Translation of micro-CT imaging into a 3D bio-printable bone model

Lucy Dascombe

A thesis submitted in partial fulfilment of the requirements of Sheffield Hallam University for the degree of Doctor of Philosophy

July 2025

Candidate declaration

I hereby declare that:

1. I have not been enrolled for another award of the university, or other academic or professional organisation, whilst undertaking my research degree.
2. None of the material contained in the thesis has been used in any other submission for an academic award.
3. I certify that this thesis is my own work. The use of all published or other sources of material consulted have been properly and fully acknowledged.
4. The work undertaken towards the thesis has been conducted in accordance with the SHU Principles of Integrity in Research and the SHU Research Ethics Policy, and ethics approval has been granted for all research studies in the thesis.
5. The thesis word count is 67,590

Name	Lucy Dascombe
Award	Doctor of Philosophy
Date of submission	24/07/2025
Research institute	Biomolecular Science Research Centre, Sheffield Hallam University
Director of studies	Dr Nicola Aberdein

Acknowledgements

I would like to start off by thanking my supervisors, Dr Nicola Aberdein, Professor Christine Le Maitre and Dr Tim Nichol. You have always shown me unconditional support, understanding and encouragement. I can safely say I am a different person to who I was at the start of this journey, I promise to not be so pessimistic of my wins! (*sometimes*). Just generally lovely and inspiring people, so I am very thankful to have your mentorship and guidance over the past few years.

Secondly, I would like to thank my family. I know you all don't understand why I want to drive myself insane with research, but you support me in my achievements regardless and celebrate my wins. For that I am thankful for you all (I promise I'm leaving 'school' now, but what did you expect after all the late nights reading when I should have been sleeping). I hope I continue to make you proud. Eloise, we built our friendship all those years ago on our shared love for science and look at us now! 14-year-old us would think we are the coolest people, and 28-year-old me agrees – we are damn cool (arguably less tattoos and piercings than younger us had imagined, I have tried to keep the bright hair going).

Now let's get into the Sheffield journey. I would not be in the position I am today without my undergraduate placement year at Dr Richards and Professor Skerry lab, where I met all the people who would stand by and support me for years to come. It was in this year that I gained a love for research, and the community that comes along with it. Ameera, who would've thought that an 11 pm message about corporation would end up like this? Kamilla, forever my kind-hearted, passionate hourglass. Meg, my hive mind, words cannot describe the love and respect I have for you – Thank you for being undoubtably my person. Special thanks to Alex, who encouraged me to apply for this 'totally not engineering and material science' PhD, for all the laughs that followed and shared enthusiasm for singing scissor sisters/Diana Ross in a cupboard. I can safely say that I cannot look at Jam shed anymore after living with you and Meg, but I wouldn't change a moment of it.

I have a lot of peers to thank who I have met along the way, especially everyone who has suffered in the final year office. Before, I mentioned the community that comes along with research, and the people I have had the pleasure of meeting along this journey are a testament to that fact. Andrea and Cristiana, thank you for all of the love and kindness. Josh, Sarah, Liv – my sardines! Thank you for all of the joy, rambles and fresh air. Charlie, my fellow book worm and nail art inspiration. Laura, thanks for all the impromptu therapy sessions and coffee dates, we are going to be okay. Ronak, thank you for sharing the world of material science with me and taking time to encourage me as a researcher. This wouldn't be an accurate acknowledgement of my research journey without mentioning the incredible Celine. Thank you for always being a friendly face, a mentor

and for always putting up with my ridiculous ideas “oh what now Lucy, you are crazy”. You truly are an inspirational woman; I am so glad to have met and learnt from you.

Sam, thank you for always leading with love, kindness, pride and undeniable support. I know this has not been easy, but silly us thought two PhD thesis submissions in 6 months would be fun. But look at what we have achieved this year. Let’s continue exploring the world together and always make the boat.

Finally, I am a bit scared of my Spotify wrapped. I predict that high school musical will be my number one artist, and I really did get my head in the game. Despite that horrible admission, I am pretty proud of myself.

This thesis is dedicated to women whose bodies work against them and continue to be misunderstood. Don’t let anything stop you.

Abstract

Biomedical research requires representative models to drive innovation and knowledge. Traditionally, monolayer cell culture studies are equipped for early-stage research prior to animal studies, however, are rarely successfully translated. In replacement, dynamic and complex three-dimensional cell culture models are under development to bridge the gap. The research presented in this study investigated the methodology involved to translate *ex-vivo* murine bones imaged by high resolution micro-computed tomography into a three-dimensional bio printable *in-vitro* bone model to reflect *ex-vivo* morphometry. Including, the associated characterisation of the model compared to native *in-vivo* murine bone and traditional monolayer culture methods. Normality of native murine bone biology is very well characterised, including the tissue composition, morphometric parameters and cellular phenotypes. These factors were summarised to inform *in-vitro* model development. Model morphology was optimised by translating *ex-vivo* bones from mice and rats, 3D models from micro-computed tomography software: CTAn, into standard tessellation language files, with different meshing algorithm, code and unit explored. Following this, the resulting models were rendered in computer assisted design software's Autodesk® Meshmixer and Fusion 360™ for the application of fused deposition modelling, stereolithography and extrusion based bioprinting. The *ex-vivo* morphology was successfully printed by both fused deposition modelling and stereolithography, inclusive of cortical and trabecular bone structures.

For the application of extrusion based bioprinting, two commercially available biomaterial inks, Bone GelXA and TissueFAB, were characterised for flow behaviour, functionality and crosslinking, as well as an in-house generated laponite® crosslinked poly (N-isopropylacrylamide, N, N'-dimethylacetamide) co-polymer, containing hydroxy-apatite nanoparticles, known as 'B-gel'. TissueFAB was removed from the study because of incompatible crosslinking, and Bone GelXA was removed due to batch-to-batch inconsistencies. In addition, to improve structural stability and the resulting fidelity of the 3D bioprinted model, a microparticle support slurry was generated and characterised. The microparticle slurry improved the bioprinted structural complexity of the bioinks. B-gel bioink was taken forward with incorporation of pre-osteoblast cell line, MC3T3-E1, with and without osteogenic differentiation media and compared against *in-*

vitro monolayer cellular behaviour. The *in-vitro* model was unable to be bioprinted in the rendered *ex-vivo* morphology despite improvements in fidelity from the microparticle support slurry. In replacement, to assess cellular phenotype and material composition a scaffold structure was bioprinted. From micro-computed tomography imaging, the *in-vitro* B-gel bioprinted constructs increased in density in both cellular conditions, suggesting osteoblast differentiation eliciting remodelling therefore enhancing the bone-like environment of the 3D *in-vitro* model. Further research is required to improve the fabrication process of bioprinting B-gel to allow the replication of bone morphology, as well as characterisation of the *in-vitro* model over a longer period to assess the full potential of remodelling to generate a replica *in-vivo* bone for the aim of reducing animal models for early-stage biomedical investigations.

Contents

List of figures

List of tables

List of abbreviations

2D – Two-dimensional

3D – Three-dimensional

AB – Acellular B-gel

ACB – Alcian blue

Alg – Alginate

ALP – Alkaline phosphatase

AM – Additive manufacturing

AR – Alizarin red

ATR – Adaptive rendering

BCLs – Bone lining cells

B-gel – Laponite® crosslinked poly (N-isopropylacrylamide, N, N'-dimethylacrylamide) co-polymer with hydroxyapatite nanoparticles

BMD – Bone mineral density

BRS – Bone research society

BV/TV – Bone volume to tissue ratio

CAD – Computer-assisted design

Cb – Cortical bone

CBV – Cortical bone volume

COL-1 – Collagen-1

CT – Computational tomography

CTM – Connect textures

DEXA – Dual-energy x-ray absorptiometry

DICOM – Digital imaging and communications

DTC – Double times cubes

EBB – Extrusion-based bioprinting

ECM – Extracellular cellular matrix

EDTA – Ethylenediaminetetraacetic acid

FDM – Fused deposition modelling

FEM – Finite element modelling

GAGs – Glycosaminoglycans

GCODE – Geometric-code

GelMA – Methacrylate gelatine

GHz – Gigahertz

H&E – Haematoxylin and eosin

HAnp – Hydroxyapatite nanoparticles

IHC – Immunohistochemistry

IHS.R – In-house slurry rehydrated

IHS.S – In-house slurry saturated

IMS – Industrial methylated spirit

iOBs – Immature-osteoblasts

LS – Life support

MB_D – MC3T3-E1 B-gel differentiated

MB_UD – MC3T3-E1 B-gel undifferentiated

MC33 – Marching cubes 33

mOBs – Mature osteoblasts

MSCs – Mesenchymal stem cells

MT – Masson's trichrome

NCPs – non-collagenous proteins

NP-gel – Laponite® crosslinked poly (N-isopropylacrylamide, N, N'-dimethylacrylamide) co-polymer

OBs – Osteoblasts

OCLs – Osteoclasts

OCN – Osteocalcin

OCs – Osteocytes

OPG – Osteoprotegerin

OPN – Osteopontin

P3G – Polygon-trochoid-profiles

PFA – Paraformaldehyde

PLA – Polylactic acid

Ply – Polygon file format

PNIPAm – Poly(*N*-isopropylacrylamide)

RANK – Receptor activator of nuclear factor kappa-B

RANKL – Receptor activator of nuclear factor kappa-B ligand

ROI – Region of interest

Runx2 – Runt-related transcription factor 2

SEM – Scanning electron microscopy

SLA – Stereolithography

SO – Safranin-o

STL – Standard tessellation language

Tb – Trabecular bone

Tb.N – Trabecular number

Tb.Sp – Trabecular separation

Tb.Th – Trabecular thickness

TBS – Tris-buffered saline (TBS)

TMD – Tissue mineral density

VB – Vertebral body

VK – Von Kossa

VOI – Volume of interest

β-GP – Beta-glycerophosphate

βTP – Beta-tricalcium phosphates

Chapter 1 – Introduction

1.1 Context of research

Early-stage biomedical research investigates organisms at various hierarchical biological levels: organelles, cells, tissues, organs, and physiological systems. Different levels of biology are essential for a comprehensive understanding of various biological mechanisms, in both physiologically healthy and diseased states (Figure 1.1) (Ayres, J. 2021; Herman, M., *et al.* 2021). To achieve this, diverse models and approaches are employed to explore or mimic biological dynamics, thereby enhancing fundamental understanding (Brosnan, S., & Postma, E. 2017; Botstein, D. 2012), and developing innovative therapeutics for disease (Stenvinkel, P., *et al.* 2021; Zhang, G. 2012).

Typically, early-stage biomedical cellular research focuses on *in-vitro* cellular approaches, such as cell culture in two-dimensional (2D) monolayers to study primary cells derived directly from living tissues, and secondary immortalised derived cells from tissues of interest (Weiskirchen, S., *et al.* 2023). However, the translation of monolayer findings is often criticised, with Sun (2022) summarising that only 3% of clinical drug development *in-vitro* studies have a probability of success, citing the problem of translation into the market due to the lack of biological relevance of initial *in-vitro* discoveries. Similar statements provided by Harrison (2016) state that 75% of novel drugs fail in clinical phases after demonstrating preclinical *in-vitro* efficacy. The conclusion is ultimately due to monolayer cultures not reflecting a dynamic biological *in-vivo* system *(*Herman, M., *et al.* 2021*)*.

In comparison, *in-vivo* studies are routinely used with a range of non-human *in-vivo* models (Figure 1.1). Scientific studies utilising animals are a longstanding practice and are vital in progressing the pipeline of drug discovery and application to humans by validating and refining results (Stein, M., *et al*. 2023; Barre-sinoussi, F., & Montagutelli, X. 2015). The general public's moral opinion of medical animal research dropped from 63% in 2002 to 52% in 2022, according to a Gallup poll in the USA (Stein, M., *et al.* 2023). However, awareness from different funding bodies, such as the national centre for the replacement, refinement and reduction (NC3Rs) of animal use in research are gaining popularity and are necessary to prompt scientists to think about their animal model

usage (Andreoli, K., *et al.* 2023; Hutchinson, I., Owen, C., & Bailey, J. 2022; Petetta, F., & Ciccocioppo, R. 2020). In 2023, 2.68 million experiments were conducted in the UK that used animal models; however, this was a 3% decrease from 2022, and the lowest reported value since 2001, according to Replacing Animal Research (Replacing animal research, 2025) and NC3Rs (NC3Rs, 2025).

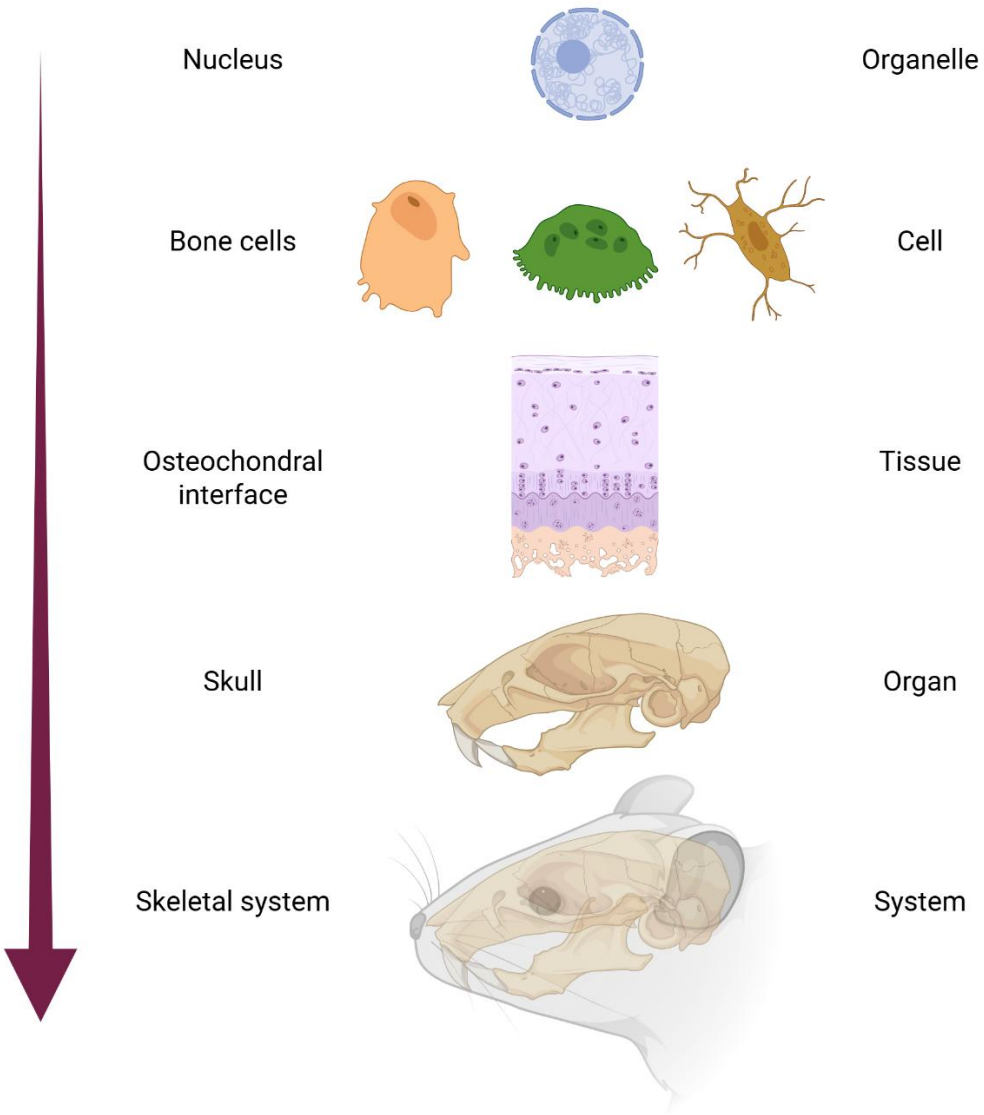

Figure 1.1. Summary of the biological structure and anatomy hierarchy, with a focus on bone.

To connect early-stage *in-vitro* research to reflect the *in-vivo* environment, reduce animal sacrifice, and improve accessibility of complex models for early-stage biomedical research, three-dimensional (3D) *in-vitro* cell culture models that closely reflect *in-vivo* tissues are gaining popularity. Different 3D models exist, including: spheroids, organoids,

and various scaffold-based systems (Moss, S., Bakirci, E., & Feinberg, A. 2025; Xie, R., *et al.* 2024; Mu, P., *et al.* 2023; Jubelin, C., *et al.* 2022; Yuste, I., *et al.* 2021), and have been shown to have varied results compared to monolayer studies, with a higher similarity to *in-vivo* dynamics (Sun, M., *et al.* 2021; Fontoura, J., *et al*. 2020; Melissaridou, S., *et al.* 2019; Soares, C., *et al*. 2012). A representative *in-vitro* bone model is required to replace early-stage *in-vivo* bone studies, to reduce the number of animals utilised for skeletal-based research without thorough testing (Stein, M., *et al.* 2023). An ideal *in-vitro* 3D bone model should reflect the environmental hierarchical composition of bone, structure, cellular and biochemical features (Wildt, B., *et al.* 2019). In addition, current 3D *in-vitro* bone models do not encompass the morphology of bone, therefore missing the relationship between structure and function of 3D *in-vitro* models (Huang, D., *et al.* 2025; Herman, M., *et al.* 2021; Schwab, A., *et al*. 2020).

1.2 The biology of bone

Bone is an organised, dynamic organ, providing a protective framework to vital organs, a site for attachment of muscles and tendons to allow locomotion, and metabolic storage (Clarke, B. 2008). For vertebrates, five types of bones make up the skeleton: flat, sesamoid, short, long and irregular, which aid in different functionalities of protection, support and locomotion (Ruberte, J., *et al*. 2023). Long bones are tubular with a hollow shaft and articulate ends, containing metabolically active bone marrow, and include the femur, tibia, fibula, and humerus. The femur primarily assists in locomotion, whereas the tibia is a weight-bearing bone working in tandem with the fibula to provide stability (Hunziker, E. 2018). Irregular bones are complex shapes which do not conform to the morphological consistency of the aforementioned bone types. These include the vertebrae of the spinal column within cervical, thoracic, lumbar, sacrum and coccyx regions (Figure 1.2). These are subdivided due to each bone's load-bearing capabilities and functionality, leading to distinct morphology (Rosello-Diez, A., & Joyner, A. 2015). The vertebral column protects the spinal cord, and is stabilised by ligaments, tendons, muscles and the intervertebral discs to allow movement of the trunk (Martin, B., Burr, B., & Sharkey, A. 1998).

Bones undergo different stages of growth, starting with bone transformation from cartilage during foetal development, referred to as endochondral ossification, and

connective tissue transformation to form bone, referred to as intramembranous ossification (Lopez, J. 2024; Watkins, J., & Mathieson, I. 2009). For human skeletal systems, long bones grow during adolescence by the epiphyseal growth plates until sexual maturity is reached, whereby the epiphyseal growth plate is sealed (Satoh, M., & Hasegawa, Y. 2022; Pines, M., & Hurwitz, S. 1991). Murine systems do not feature closure and do not stop growing (Figure 1.2); however, they shorten during sexual maturity (Jilka, R. 2013; Koh, N., *et al*. 2024). Other noticeable differences are the presence of non-fused caudal vertebrae in murine species (Figure 1.2) and the lack of osteons in cortical bone regions (Koh, N., *et al.* 2024).

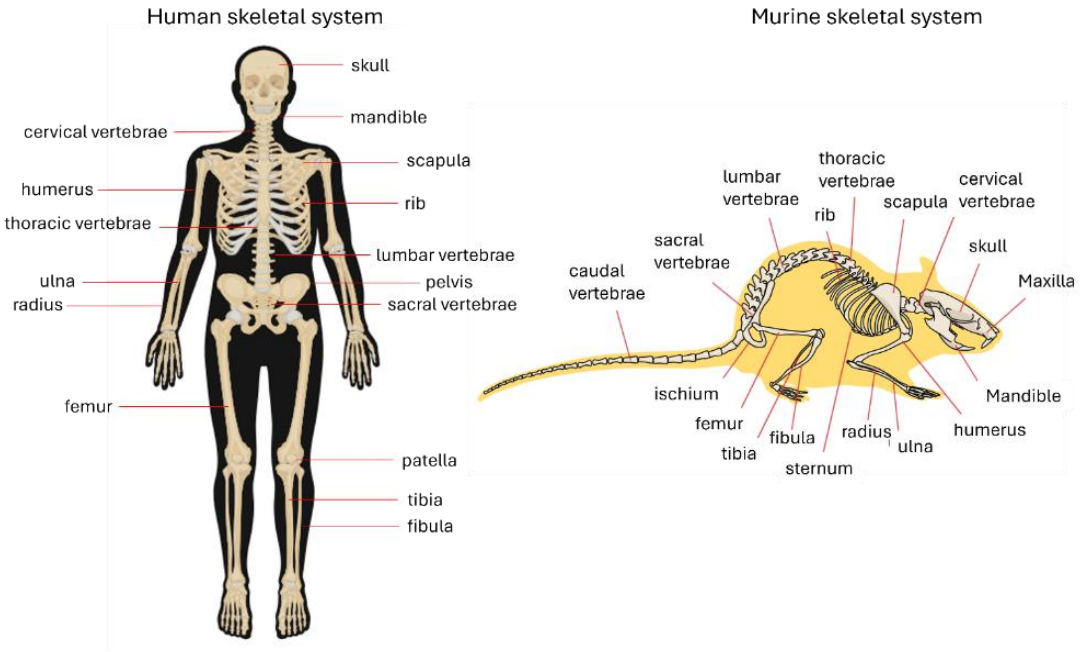

Figure 1.2 Schematic of labelled human and murine skeletal systems. *The human skeletal system shares similarities of the five main bone types to murine species; however, murine systems include caudal vertebrae and maxilla notably. Overall anatomy differs between the two mammals due to the locomotion and weight-bearing requirements of the species, whereby humans mostly walk upright using a bipedal gait, whereas murine species walk using a quadrupedal gait. Another major difference between humans and murine species is that human's long bone growth plates fuse once mature, whereas murine species persist throughout the life span.*

1.2.1 Trabecular and cortical bone

Bones are formed of four layers - periosteum, bone marrow, trabecular (Tb) and cortical (Cb) (Figure 1.3) (Clarke, B. 2008). The periosteum is the dense membranous tissue forming the outer shell of bone that contains nerves and blood vessels, connecting the skeletal system to the vascular and nervous system and separating the bone from

surrounding soft tissues (Patrick, K. 1968). The periosteum assists in structural integrity, with an inelastic membrane consisting of fibroblasts, collagen and elastin fibres that together act as a mechano-sensor to initiate osteogenic homeostasis (Li, C., & Fennessy, P. 2021). Bone marrow is a semisoft tissue fully enclosed within the cavity of bone. Marrow is split into two components: 'red' marrow that facilitates haematopoiesis with a unique microenvironment to support stem cell production and lineage commitment, and 'yellow' marrow, which is constituted of mostly adipose tissue acting as a haematopoietic reserve (Sovani, V. 2021; Taichman, R. 2005).

Tb is a network of struts (trabeculae) which are formed as either plates or rods, often referred to as a honeycomb network with the spaces filled with bone marrow (Figure 1.3) (Oftadeh, R., *et al*. 2015). Tb is highly metabolically active compared to its counterpart, Cb, due to the trabeculae increasing the surface area to volume ratio of bone due to the dynamic intricacies of the morphology (Haseltine, K., *et al*. 2021). Owing to the increased surface area, Tb aids in the hydraulic properties of bone, absorbing shock from locomotion and preventing bone fractures. Further, Tb gives structural support to the entire bone whilst minimising the mass of bone, relating to the overall function of bone – storage, protection and locomotion (Clarke, B. 2008; Oftadeh, R., *et al*. 2015).

Cb is dense, with the only spaces present being lacunae and canaliculi for bone cells and vascular channels to connect the marrow to the periosteum. Cb constitutes approximately 80% of the total bone mass, with 30% of that volume being occupied by vascular channels (Isojima, T., & Sims, N. 2021). The dense structure of Cb maintains the load-bearing functionality of bone, remaining strong, but in comparison to Tb, it has a lower surface area with decreased bone turnover rates (Augat, P., & Schorlemmer, S. 2006).

1.2.2 Structure and composition of bone – Micro/macro architecture

Fundamentally, bone architecture is hierarchical and has distinct components, which form micro and macro structures aiding in the function and health of bone (Figure 1.3). Microscopically, Cb and Tb exhibit two types of bone: woven and lamellar. Woven bone is classed as immature bone, which is produced during rapid bone formation and is

typically temporary. This type of bone is poorly organised, consisting of randomly orientated collagen fibres and mineral deposits. In contrast, lamellar bone is formed in a controlled, slow manner, resulting in a highly organised structure consisting of parallel layers of bone tissue composed of collagen fibres and minerals (Bala, Y., Farlay, D., & Boivin, G. 2012).

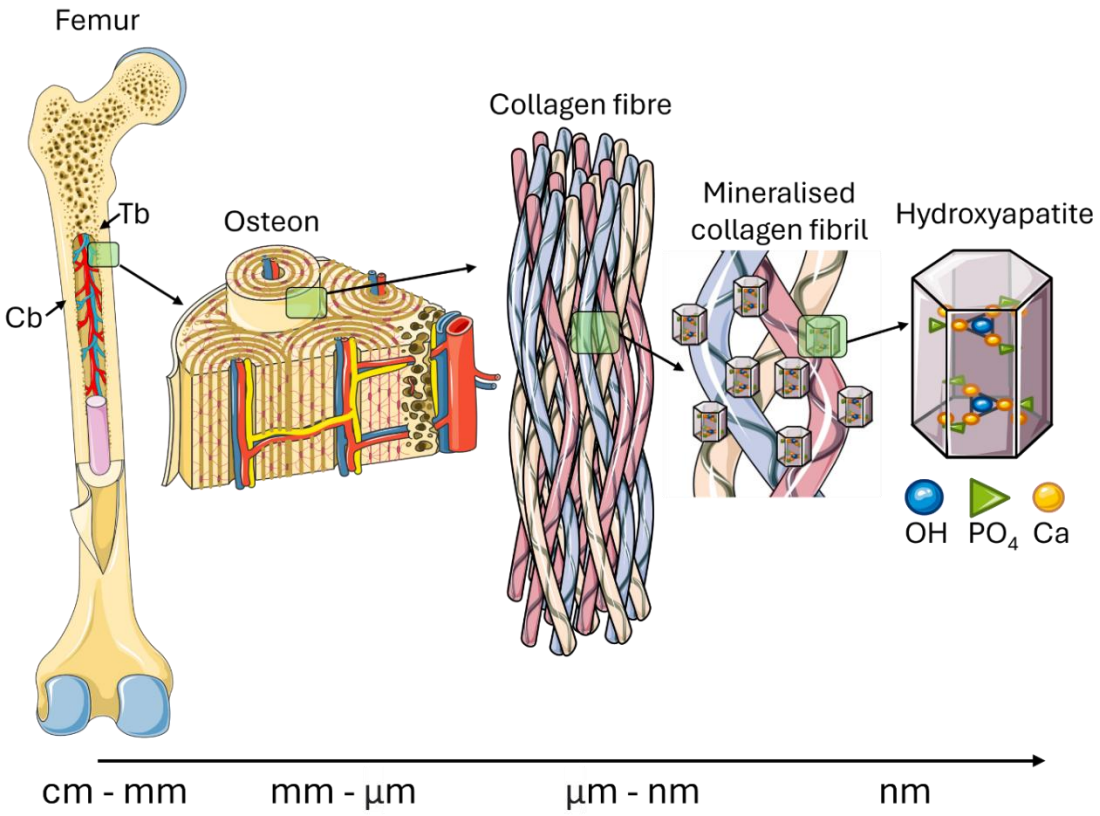

Figure 1.3 Hierarchy of bone composition. *Bone is a composite material with a microarchitecture of Cb and Tb bone, comprising osteons. The individual osteon bone tissue comprises collagen fibrils approximately 300 nm in length with a 67 nm repeating banding pattern with a 39 nm gap and 28 nm overlap zone. The inorganic composition of bone comprises nanosized plate-shaped hydroxyapatite crystallites that are approximately 20-50 nm long, 15 nm wide and 2-5 nm thick. The figure contains modified Images from Servier Medical Art (https://smart.servier.com) licenced by Creative Commons Attribution 4.0 international.*

Bone is a composite material comprising both soft (organic biological matrix), including water and collagen, as well as hard matrix (mineralised matrix), which is rich in calcium phosphates. These extracellular matrix (ECM) components provide the load-bearing properties of bone, enabling high tensile modulus and resistance to fracture from daily loading regimes, including tension, shear, torsion, bending and compression (Hart, N., *et*

al. 2017). The inorganic component of bone, known as hydroxyapatite $Ca_5(PO_4)_3(OH)$, is a crystalline composite formed from inorganic phosphate and calcium (Figure 1.3), resulting in 70% of the total bone mass. The organic phase of bone, which is composed mainly of type I collagen (COL-1) and non-collagenous proteins (NCPs) (Figure 1.3) consists of 20 – 30%, with the remaining 5 – 10% water (Brodsky, B., & Persikov, A. 2005. Feng, X. 2009). Fluctuations in composition can arise due to age, disease, treatment and hydration, resulting in changes to strength and stiffness (Surowiec, R., Allen, M., & Wallace, J. 2021).

Organic biological matrix

COL-1 is a triple-helical protein containing three polypeptide chains with a strict repeating amino acid sequence $(Gly\text{-}X\text{-}Y)_n$, commonly (Gly-proline-X) or (Gly-X-hydroxyproline), with X consisting of any other 17 amino acids (Amirrah, I., *et al*. 2022). Two chains are identical α1(I), with one α2(I) chain all cross-linked by hydrogen bonds between hydroxyproline and other charged residues. The linear chains are aligned together in parallel to form collagen fibrils, which are grouped in bundles to produce collagen fibres (Figure 1.3) (Feng, X. 2009; Brodsky, B., & Persikov, A. 2005). Aside from the abundant COL-1, types II, III, V, VI, and X collagen are present in bone tissue, contributing to osteoblast (OBs) genesis, endochondral ossification ques, and Tb regulation (Volk, S., *et al*. 2014, Acil, Y., *et al.* 2022, Komori, T., *et al.* 2022; Knuth, C., *et al*. 2019)

Aside from collagens, NCPs, including proteoglycans, glycoproteins such as osteocalcin (OCN), osteonectin and osteopontin (OPN), as well as mucins, form a small percentage of the ECM of bone, assisting in biomineralisation, structure and strength (Sroga, G., & Vashishth, D. 2012; Licini, C., *et al.* 2019). Of particular importance, during the synthesis of COL-1, proteoglycans are post-translationally added to assist in fibrillogenesis and maintenance of tissue structure. Glycosaminoglycans (GAGs), are negatively charged carbohydrate chains attached to interstitial proteoglycans with an involvement in the promotion mineralisation of collagen fibrils during osteogenesis (Rutten, L., Macias-Sanchez, E., & Sommerdijk, N. 2024; Wojtas, M., Lausch, A., & Sone, E. 2020), as well as the attraction and retention of water due to the high osmotic potential (Surowiec, R., Allen, M., & Wallace, J. 2021). Common GAGs within bone tissue include hyaluronic acid,

oligosaccharides and heparan-, chondroitin- and dermatan sulfate, all assisting with hydration and elasticity of bone (Baud'huin, M., *et al*. 2011)

Mineral chemical matrix

Hydroxyapatite nanoparticles (HAnp) constitute the major chemical component of bone, organised in a crystalline lattice (Figure 1.3). Nucleation is triggered by collagen and NCPs, with HAnp incorporation into fibrillogenesis, which begins 5 – 10 days after ECM deposition, in the woven bone tissue phase. With an increase in number, and thickness rather than length, and organisation beginning for secondary mineralisation, for the highly organised lamella bone tissue (Bala, Y., Farlay, D., & Boivin, G. 2012).

1.2.3 Bone cells

Bones constantly adapt to the surrounding environment using biological and mechanical cues by remodelling via the independent action of mesenchymal and haemopoietic stem cell lineages, OBs and osteoclasts (OCLs) to allow maintenance of mechanical and physiological integrity via Cb porosity and tissue mineral density (TMD). This, in turn, directly results in varying mechanical and morphological properties. Bone is primarily composed of the following cells: OBs, osteocytes (OCs), bone lining cells (BLCs), and OCLs (Figure 1.4) (Florencio-Silva, R., *et al*. 2015).

Osteoblasts

OBs originate from mesenchymal stromal cells (MSCs) that transition into mesenchymal osteoprogenitor cells, contained in the periosteum and bone marrow (Figure 1.3). With biochemical stimuli, notably activation of runt-related transcription factor 2 (Runx2), osterix and β-catenin the osteoprogenitor cells transition into immature-osteoblasts (iOBs) (Grigoriadis, A., Heersche, J., & Aubin, J. 1988; Rucci, N. 2008). By the induction of alkaline phosphatase (ALP) from Runx2 and osterix, ALP drives iOBs into commitment to mature osteoblasts (mOBs) (Figure 1.4). During this commitment to mOBs, OCN and OPN are upregulated (Rucci, N. 2008). Finally, mOBs can transition into BLCs, undergo apoptosis or commit to OC in a process of osteocytogenesis (Figure 1.4) (Tresguerres, F. *et al.* 2020; Dallas, D., & Bonewald, L. 2011; Franz-Odendaal, T., Hall, B., & Witten, E. 2005). As the OB transitions into an OC, ALP is reduced, and OCN, OPN and COL-1 are elevated (Bonewald, L. 2011; Tresguerres, F., *et al*. 2020).

With the primary function of synthesising the organic components of bone – collagen-rich osteoid matrix, mOBs contribute to the remineralisation process of bone remodelling. mOBs are defined as plump, cuboidal mononuclear cells that are commonly found lining the seam on the unmineralized matrix. Osteoid that has been synthesised is referred to as the endocortical surface, which is exposed to the bone marrow. The endocortical seam features a higher turnover of bone synthesis compared to other regions of Cb and Tb (Long, F., & Ornitz, D. 2013; Franz-Odendaal, T., Hall, B., & Witten, E. 2005; Matsushita, Y., *et al*. 2023).

Osteocytes

OCs are matrix-embedded cells entrapped within the bone matrix during formation in lacunae pores. OCs undergo three distinct states: osteoid OC, mineralising OC and finally, mature OC (Figure 1.4) (Dallas, D., & Bonewald, L. 2011). As mature OCs, they form extensive dendritic processes through a bone fluid-filled communication channel, named a gap junction, giving OCs a star shape with cilia and cytoplasmic processes. The most abundant bone cell, a lifespan of up to 25 years, with a primary function of being a mechanosensory cell. OCs integrate cellular cues to mechanical strain/load and report any resulting microdamage by the OCs prolongations that are throughout the calcified canaliculi within the periosteal and endosteal surfaces. The resulting mechanosensory action facilitates bone remodelling homeostasis (Wolff's law - 1892) (Bonewald, L. 2011; Buenzli, P., & Sims, N. 2015; Tresguerres, F., *et al*. 2020; Frost, M. 1994).

Bone lining cells

Originating from mOBs, BLC are the abundant flattened cells lining both the endocortical surface and Tb surfaces. Often remarked as a resting population, it still has an important role in bone remodelling and health, as a 'functional membrane' between newly formed osteoid and OCLs (Andersen, T. 2009). BLC assist in the differentiation initiation of OCLs, by production of osteoprotegerin (OPG) and the receptor activator of nuclear factor kappa-B ligand (RANK-L), thereby helping modulate the balance of bone remodelling (Wein, M. 2017).

Osteoclasts

OCLs are terminally differentiated multinucleated cells which originate from the controlled fusion of mononuclear pre-OCL cells from the hematopoietic stem cell lineage, whereby macrophages are derived (Figure 1.4) (Yahara, Y., *et al*. 2022; Sun, Y., *et al*. 2021). Known as the bone absorbing cell, OCLs are large cells (20 - 100 µm) located in Howship's lacunae on the bone surface (Soe, K., Delaisse, J., & Borggaard, X. 2021) with a notable ruffled border, and clear zones to facilitate bone resorption in acidic resorption lacunae to promote dissolution of minerals, proteins and collagenous matrix by cathepsin K enzyme (Takashi, N., Kobayashi, Y., & Udagawa, N. 2020; Aguda, A., *et al.* 2014). OCLs were thought to undergo apoptosis after resorption; however, research suggests that OCLs can acquire new nuclei from hemopoietic stem cells, contributing to rapid OCL regeneration and regulation (Jacome-Galarza, C. *et al*. 2019).

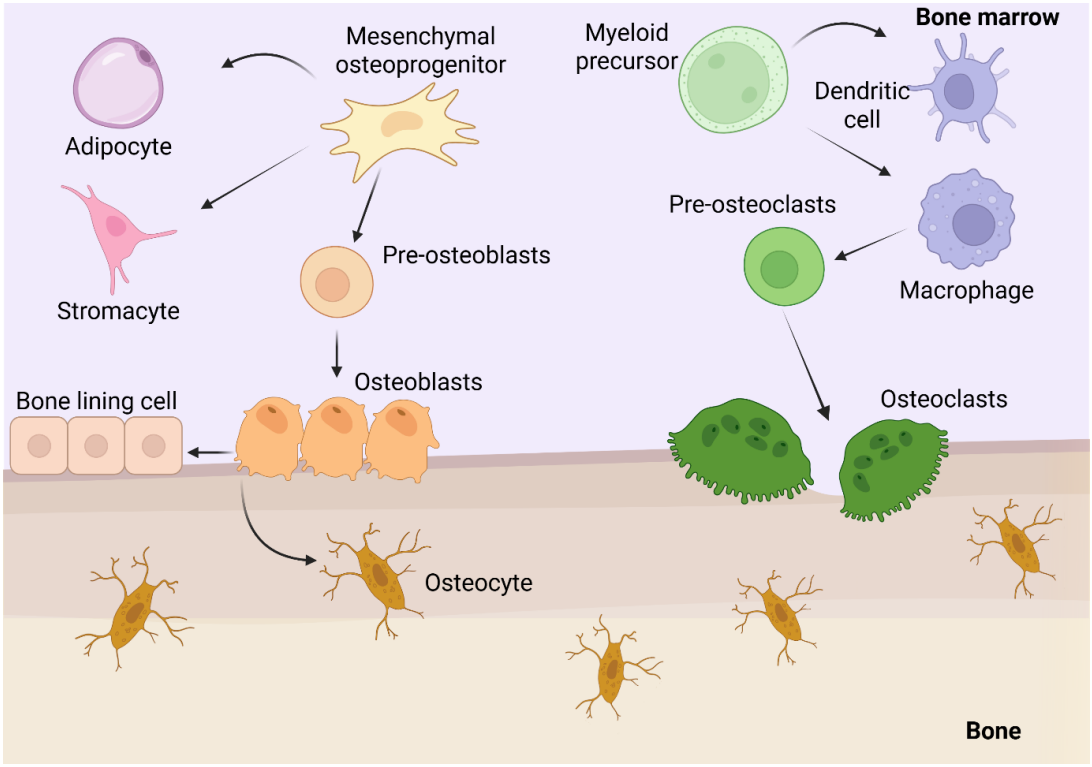

Figure 1.4. Schematic summary of bone cell lineage and differentiation.

1.2.4 Bone remodelling

Bone is a dynamic organ that is constantly responding to the surrounding environment, biomechanical and biochemical cues. The skeletal system is a reservoir of calcium, phosphorus and magnesium, regulated by bone remodelling. Calcium reserves are regulated by dietary calcium entering through the gastrointestinal tract and kidneys,

working in tandem with OBs, with loss mainly attributed to pregnancy, diet, exercise and disease (Feng, X., & McDonald, J. 2011).

Secondly, bone undergoes remodelling to replace old or damaged bone to preserve bone mass and skeletal integrity. Remodelling is a careful balance between reabsorption and deposition to remain healthy, with dysregulation often causing disease such as osteoporosis, excessive imbalance towards bone resorption resulting in bone loss with overall reduced bone strength (Tan, S., *et al.* 2014; Goldring, S. 2016). Assisting in facilitating bone remodelling, bone cells work within tandem in basic multicellular units, also known as a bone remodelling unit, to remove and replace old or damaged Cb (osteon). Consisting of resorption, reversal and formation zones (Figure 1.5), whereby OCLs resorb bone tissue, osteoprogenitors prepare the eroded surface, and finally, mOBs lay down osteoid (Loundagin, L., *et al*. 2024; Bolamperti, S., Villa, I., & Rubinacci, A. 2022).

For bone remodelling homeostasis (Figure 1.5), RANKL-RANK-OPG molecules work in tandem, released from mOBs and OCLs, controlled in tandem from OCs. In summary, OBs regulate OCL differentiation through the RANKL-RANK complex, which activates osteoclastogenesis, inhibiting apoptosis and activating mature OCLs. To allow balance, OPG, a decoy receptor, is secreted by OBs (Leon-Oliva., *et al.* 2023; Yaharam, Y., *et al*. 2022), with further control produced by OCLs from the secretion of sclerostin, which inhibits initial OBs formation (Marahleh, A., *et al*. 2023).

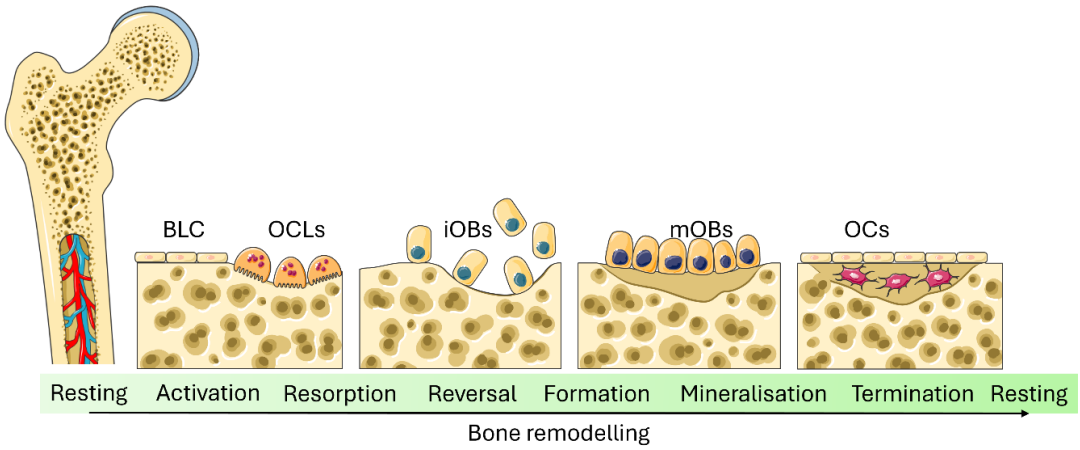

Figure 1.5 Schematic of bone remodelling. *The bone remodelling cycle consists of constant overlapping cycles: resting, activation, resorption, reversal, formation, mineralisation and termination. In a resting state, entrapped OCs sense mechanical loading and micro-damage, or factors (interleukin-6, tumour necrosis-factor-α, insulin growth factor-1 or parathyroid hormone) are released into the bone microenvironment. When initiated, the BLC and OCs are increasing expression of RANKL to initiate osteoclastogenesis by interaction with RANK. OCLs initiate bone resorption, followed by the breakdown of old bone and release factors typically stored in the bone matrix (bone morphogenetic proteins, transforming growth factor beta and fibroblast growth factors) that recruit iOBs to the reabsorbed area. OCLs then either interact with mOBs, which initiate the formation of new osteoid and lamellar bone or undergo apoptosis. mOBs become trapped in the newly formed mineralised osteoid and differentiate into OCs. The resting bone environment is maintained until a new trigger activates the cycle. The figure contains modified Images from Servier Medical Art (https://smart.servier.com) licenced by Creative Commons Attribution 4.0 international.*

1.3 The importance of *in-vivo* models

Within the bone research community, animal *in-vivo* models are used to understand development, growth, remodelling, and to mimic disease for various research applications (McGovern, J., *et al.* 2018). A wide range of animals are used, with an annual value for bone research-specific research that is challenging to report due to the variation in reporting, published status, and study types. Owen (2018) reports that in 2015, 25,381 musculoskeletal studies were conducted with *in-vivo* models (Owen, R., & Reilly, G. 2018). However, in the past 10 years (2014 – 2024), a total of 37,009 studies were published on the PubMed scientific literature database with the terms “bone” and “*in-vivo*”. In addition, 28,721 results were produced when the terms “mouse” and “bone” were searched. Similar research for bone-related studies with “rat” and “animal model” returned 13,855 and 28,418 studies, respectively. The results are in a downward trend, from a peak in 2021. In contrast, “*in-vitro* model” returned 935 results, and “3D

models" with 9,911 results, with both terms in an upward trend of publication (PubMed, National Institutes of Health).

Murine species, particularly mice and rats, are the most commonly used animals in bone research (Figure 1.2), with Zwierzyna (2017) reporting up to 78%, from the 95% total of frequently reported animals utilised for research (NC3Rs). As a species, they are favoured due to their ease of handling, lower costs, and quick experimentation times due to rapid ageing (Prankel, S. 2012). Murine species are relatively well biologically characterised, with well-defined genetics and biology, making them a good model for studying bone physiology, disease mechanisms and treatment effects (Vandamme, T. 2014; Mukherjee, P., *et al*. 2022; Gomes, P., & Fernandes, M. 2011). In addition to murine species, larger mammals are also used as research models; ovine, canine, porcine, and bovine, albeit less frequently due to associated cost, but these models more closely match human bone structure and biomechanics (Beagan, M., *et al*. 2024). Smaller models, such as zebrafish, are also employed (Dietrich, K., *et al.* 2021), however, they have simple anatomy and differences in bone formation and structure (Busse, B., *et al.* 2019). Often, research laboratories do not have direct access to *in-vivo* facilities, with only an estimated 160 research establishments with animal facilities in the UK, reports Skidmore (2020), with the exact number of laboratories without being difficult to predict, but to facilitate *in-vivo* experimentation would require costly outsourcing.

Stein (2023) reported a statement on behalf of the European calcified tissue society, emphasising the importance and major advancements in bone research that have relied on the use of *in-vivo* models; however, they suffer from reproducibility in results across different research groups. Stein (2023) refers to the advancement in both *in-silico* and *in-vitro* techniques, helping to bridge the gap between benchtop to clinical translation for preliminary research with improved characterisation and more thorough early-stage investigations before *in-vivo* model implementation; however, data still suffers from the problem of reproducibility, therefore improved standardised models are required. The statement concludes that *in-vivo* studies cannot and should not be completely replaced before clinical trials (Stein, M., *et al.* 2023).

1.4 Two-dimensional *in-vitro* models

2D *in-vitro* monolayer studies are important opening experiments in biomedical research, ultimately allowing the simplicity of investigating cell behaviour, interactions and response in a controlled environment (Figure 1.6). Monolayer culture is a core technique in biomedical research due to the ease of culture, accessibility, low-associated expense and the high reproducibility between technical replicates (Segeritz, C., & Vallier, L. 2017). However, it is widely accepted that culturing surface morphology alters biological cellular behaviour *in-vitro*, such as bone (Qin, L., *et al*. 2020) and compared to 3D *in-vitro* cell cultures (Gheytanchi, E., *et al.* 2021; Chen, C., *et al*. 2009). Monolayer cultures do not replicate the complex interactions or behaviours seen in different *in-vivo* environments (Li, Y., & Kilian, K. 2015).

For 2D *in-vitro* studies, polystyrene flasks gained popularity in the 1970s compared to glass cultureware (Moro, L., *et al*. 2024). Polystyrene flasks were typically used in a non-treated state for non-adherent cells or surface-coated to generate highly energetic oxygen ions, which oxidise the surface polystyrene chains (Curtis, A., *et al.* 1983). Today, different polystyrene flasks, such as Nunclon™ delta-treated and CellBIND®, are widely used, which are comprised of treated polystyrene with hydrophilic surface modification to facilitate improved cellular adherence (Weiskirchen, S., *et al*. 2023). This surface is not biologically, mechanically, or chemically representative of physiological tissue. It has been shown that cultureware can change the behaviour, phenotype and morphology of cells (Kapalczynska, M., *et al.* 2016), notably resulting in increased cellular tension (Juarez-Moreno, K., *et al.* 2022), which causes pronounced focal adhesions (Yamaguchi, N., & Knaut, H. 2022), actin stress fibres (Lee, S., & Kumar, S. 2016) and Tyrosine-protein kinase YES-associated deregulation influencing up-regulated cell proliferation (Jensen, C., & Teng, Y. 2020; Yang, B., et al. 2019).

An example of surface mechanobiology affecting phenotype is the widely used multi-potent MSCs, whereby the phenotype can change based on cultureware and stiffness of the environment alone (Jeske, R., *et al*. 2021; Yang, Y., *et al*. 2018). When cultured on stiff substrates, MSCs have an increased osteogenic potential, whereas softer substrates show increased adipogenic potential (Zonderland, J., & Moroni, L. 2021; Gonzalez-Cruz, R., Fonseca, V., & Darling, E. 2012). Alternatively, MSCs can be driven into a specific

phenotype, despite the cultureware, by additives in the cell culture growth medium (Fitzgerald, J., *et al*. 2023). Osteogenic potential of MSCs can be achieved by dexamethasone, ascorbic acid, and beta-glycerophosphate (β-GP) (Fakhry, M., *et al*. 2013), whereas adipogenic differentiation is driven by dexamethasone, phosphodiesterase inhibitor and insulin (Scott, M., *et al.* 2011).

The practice of 2D culturing is standardised within the scientific community as a core technique, allowing consistency, reproducibility, low cost and reduced animal use (Mattes, W. 2020; Hirsch, C., & Schildknecht, S. 2019). However, the technique is slowly becoming untrustworthy in producing translatable preliminary clinical results. Further, comparing 2D and 3D cell culture models produces varied results (Figure 1.6) (Sun, M., *et al.* 2021; Fontoura, J., *et al*. 2020; Melissaridou, S., *et al.* 2019; Soares, C., *et al*. 2012). Abbas (2023) showed that human colorectal cancer cells varied in cell viability, cell number, and expression of genes of interest when cultured in spheroids compared to monolayer culture. Zschenker (2012) reported whole genome microarray analysis on human lung cell line A549, with upregulation of genes associated with ECM and adhesion in 2D compared to 3D. A significant difference was also noted in the response to anti-cancer drugs, with 3D resulting in reduced toxicity (Abbas, Z., *et al.* 2023), with similar findings supported by Muguruma (2020) with triple negative breast cancer cells.

1.5 Three dimensional *in-vitro* models

3D cell culture allows cells to interact in a more physiologically relevant environment compared to 2D monolayer culture, referred to as the bridge between monolayer and *in-vivo* models (Xie, R., *et al.* 2024; Urzi, O., *et al.* 2023; Edmondson, R., *et al.* 2014). Various 3D models exist (Figure 1.6); scaffold-based, encouraging cell-ECM interaction or scaffold-free, encouraging cell-cell interaction (Maltman, D., & Przyborski, S. 2010), and each form of 3D model has various considerations, and applications based on the experimental aim of each independent research study (Xie, R., *et al.* 2024). Scaffold-free models are utilised in bone research; however, they are more commonly used as a tool for modelling malignancy, by allowing cancer cells to self-organise and interact into spheroids (Figure 1.6) (Araugo, T., *et al*. 2024), often mimicking a tumour featuring a hypoxic core and proliferative edges. Baek (2016) reported that osteosarcoma spheroids were generated using low-adhesion cell culture plates for preclinical drug testing

efficacy. Alternatively, Rimann (2014) reports the optimisation of hanging drop osteosarcoma spheroids. Similarly, but utilising a primary cell source, bone organoid models are emerging, albeit in a simplistic design of either scaffold-free (Hall, G., *et al.* 2019) or scaffold-embedded (Klotz, B., *et al.* 2019; Park, Y., *et al*. 2021) and only encompassing one bone-associated stem cell type, compared to the complexity and advancement of intestinal organoids (Tian, C., *et al.* 2023) (Figure 1.6). Bone-on-a-chip scaffold models utilise microfluidics to assist in the physiological microenvironment of tissues (Figure 1.6), with complex microenvironment and cell interactions achievable (Zhang, Y., *et al.* 2023; Leung, C., *et al*. 2022; Mansoorifar, A., *et al.* 2022), such as a BMU tri-culture chip whereby Woo (2025) aimed to replicate the process of bone remodelling. The model is still under development and holds great promise for a dynamic *in-vitro* bone model, but suffers from technical complexity, small scale, and high technical variability (Woo, S., *et al.* 2025).

Alternative scaffold-embedded *in-vitro* 3D bone models exist with either primary or secondary cells and are widely reported as the most common method to mimic native bone ECM (Figure 1.6) (Zauchner, D., *et al.* 2024; Yang, R., *et al.* 2023; Maji, S., & Lee, H. 2022; Sitarski, A., *et al*. 2017). Hydrated scaffolds, referred to as hydrogels mimic the integral aspect of structural anatomy, and often comprise of growth factors, polysaccharides and proteins, including collagen, fibronectin, laminin, and elastin (Section 1.2.2) (Li, L., *et al*. 2024; Nicolas, J., *et al.* 2020; Geckil, H., *et al.* 2010), and inclusion provides a structural framework that encourages tissue maturation (Lin, X., *et al.* 2020). For bone-specific *in-vitro* models, the scaffold framework encourages mineralisation if availability of suitable cells (Matsushita, Y., *et al*. 2023; Hwang, P., & Horton, J. 2019; Kartsogiannis, V., & Ng, K. 2004), bioactive components (Szwed-Georgiou, A., *et al.* 2023; Saten, V., *et al.* 2022; Zhao, Z., *et al.* 2020) and biochemical ques, such as bone morphogenic proteins (Shi, S., *et al.* 2009; Li, C., *et al.* 2006), vascular endothelial growth factor (Burger, M., *et al.* 2022; Hu, K., & Olsen, B. 2016; Cenni, E., Perut, F., & Baldini, N. 2011). Mineralisation of 3D scaffold-based *in-vitro* models reflects the native complex composite material of bone, mimicking both inorganic and organic compositions (Hart, N., *et al*. 2017). The research conducted in this report will focus on scaffold-based 3D models, with the addition of bioactive HAnp (Li, L., *et al.* 2024; Abere,

D., *et al.* 2022), and iOBs, MC3T3-E1 secondary matrix depositing cells (Sudo, H., *et al.* 1983).

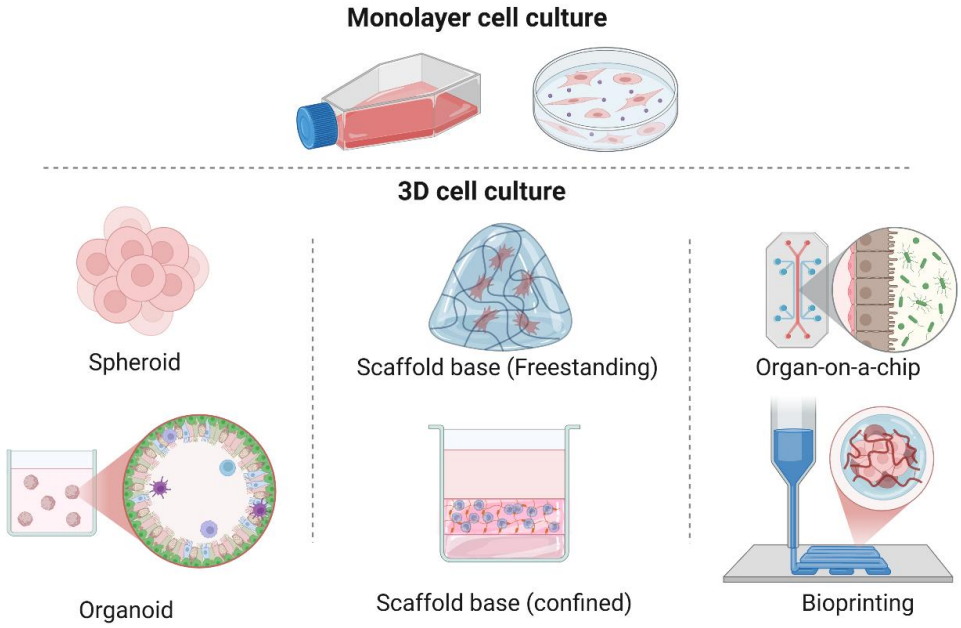

Figure 1.6. Summary schematic of monolayer and 3D cell culture in-vitro models used for biomedical investigations.

1.6 Three-dimensional extrusion bioprinting

Various approaches are utilised for generating a representative 3D *in-vitro* bone model; however, the method of bioprinting is a revolutionary technique for the fabrication of precise structures in exact XYZ orientations (Figure 1.6) (Chen, X., *et al.* 2023; Boularaoui, S., *et al*. 2020). In the extrusion-based bioprinting (EBB) process, the bioink is loaded into a cartridge and extruded by either pneumatic extrusion or mechanical extrusion, that is, piston or screw-based extrusion. Layer-by-layer deposition of bioinks, with the inclusion of cells and bioactive constituents, builds a 3D ECM-mimicking model (Holland, I. 2025; Dharmaraj, J., *et al.* 2024).

EBB requires biologically compatible ink, referred to as bioink, that is typically suited to the organ intended to mimic, termed biomimicry. Bioink is formulated of viscous biomaterials to facilitate printability, functionality and biocompatibility (Figure 1.7) (Garcia-Villen, F., *et al.* 2021; O'Connell, C., *et al.* 2020). Printability is defined by Naghieh (2021) as a material's capability to form and maintain reproducible 3D scaffolds from bioink, and directly impacts the resulting 3D EBB structure, mechanical and biological

properties (Figure 1.7). Biocompatibility is essential for promoting cell growth, proliferation and differentiation, to allow cells to function in a native phenotype (Choi, J., *et al.* 2023; Kim, J. 2023). Finally, functionality refers to the appropriate bioink being able to suitably be deposited in the exact XYZ co-ordinates, and function as a suitable ECM for 3D *in-vitro* culture (Chen, X., *et al.* 2023; Naghieh, S., & Chen, S. 2021; Gopinathan, J., & Noh, I. 2018).

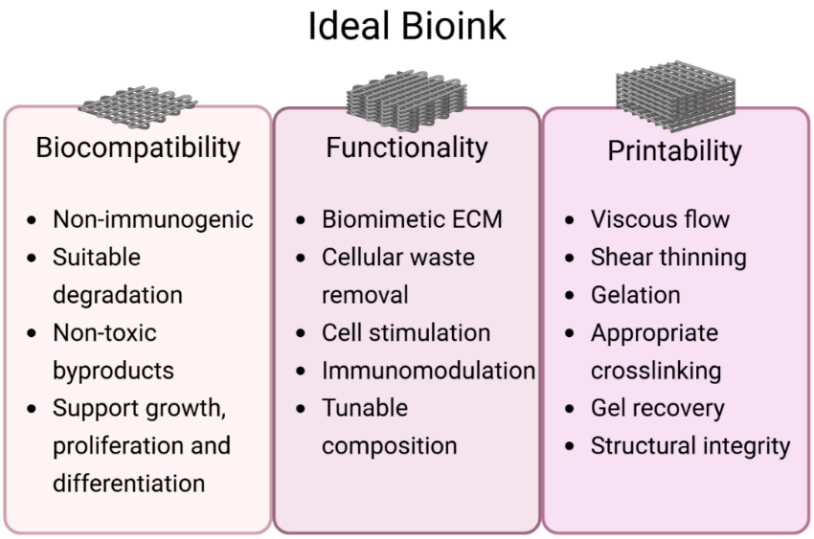

Figure 1.7. Summary of the properties required for a suitable bioink for the method of extrusion based bioprinting.

1.6.1 Bone-associated biomaterials

Inorganic

Bone consists of around 70% of inorganic calcium HA particles, and are essential in native bone tissues mechanical strength, formation and remodelling assisting functionality of the structure (Surowiec, R., Allen, M., & Wallace, J. 2021; Feng, X. 2009; Brodsky, B., & Persikov, A. 2005). Naturally, as calcium phosphate is a main bone component, combining calcium crystals into 3D *in-vitro* bone models is a common choice for inclusion in a bone bioink (Ielo, I., *et al.* 2022). Three types are often reported (Wang, W., & Yeung, K. 2017), HA and beta-tricalcium phosphates (βTP), or a combination of the two referred to as biphasic calcium phosphates, with each calcium source having different benefits in bone models. HAnp is biocompatible, bioactive, osteoconductive, and mechanically strong. It lacks immunogenicity, mimicking the structural and functional aspects of native bone closely; however, it does not degrade readily (Hua, Y., *et al. 2021*), therefore being

more suited to remodelling-based *in-vitro* models (Soleymani, S., & Naghib, S. 2023; Abere, D., *et al.* 2022; Scheinpflung, J., *et al.* 2018).

Different concentrations of HAnp are utilised, dependent on cellular state, fabrication method and material used for the generation of *in-vitro* models. For example, GelMA constructs have been reported with a concentration of 0.5 – 5% wt of HAnp without eliciting cell toxicity (Yue, K., *et al.* 2015), whereas Alg-based bioprinted constructs have been reported with the ranges of 0.5 – 10% wt of HAnp (Bendtsen, S., *et al.* 2017). β-TP are resorbable in comparison to HAnp, being suited to short-term *in-vitro* culture periods (Murphy, M., *et al.* 2013). Due to this, inclusion within *in-vitro* models is typically represented by fast bioabsorption and replacement by matrix mineralisation remodelling action, however the resorption rate can often reduce the mechanical structure of the scaffold if the dynamic is unbalanced, causing collapse of stability (Zheng, C., & Zhang, M. 2023; Bohner, M., Santoni, B., & Dobelin, N. 2020; Li, Y., *et al.* 2019; Todo, M., & Arahira, T. 2013). Various concentrations of βTP are reported (0.5% to 60% wt), often tailored with the viscosity and mechanical strength required for the 3D *in-vitro* model that is being developed, and the associated fabrication technique (Amiri, M., *et al.* 2024; Zhang, Y., *et al.* 2020).

To combat the considerations of using each source independently, some studies report using biphasic calcium phosphate for the benefit of both short-term and long-term mineral sources, enabling balance of resorption and remodelling when optimised per model (Tran, D., *et al*. 2024; Mofakhami, S., & Salahinejad, E. 2021; Tomco, M., *et al.* 2017). For example, Arinzeh (2005) reports a 20% HA and 80% βTP composition that promotes bone formation yet is degradable, whereas Shao (2021) reports 30:70% HA: βTP that has the best rate of OB-like cell differentiation with balanced degradation that mimics native animal bone growth. Mazón (2013) tested three ratios with COL *in-vivo,* with no scaffold bridging a 6 mm defect after 60 days; however, 60:20:20 (HA: βTP: COL) revealed the best progression (Mazón, P., *et al.* 2013). Alternatively, different bioactive components can be utilised in 3D *in-vitro* bone models, with Bai (2023) summarising research studies that have shown evidence of osteogenesis with calcium, cobalt, copper, fluoride, lithium, magnesium, silicon, silver, and zinc (Bai, L., *et al.* 2023). Alternatively, bone ceramics (Yuan, H., *et al.* 2010) and natural constituents like ground fish bones

(Torres, B., *et al.* 2024), eggshells (Neunzehn, J., *et al.* 2015), and shellfish are also reported (P. Vijayakumar., 2020).

Organic

Reflecting the composite material of native bone, an organic biological matrix comprising water and collagen is reflected by hydrogels (Table 1.1) (Feng, X. 2009; Brodsky, B., & Persikov, A. 2005). Hydrogel-based bioinks are ever-developing within the field of biomedical tissue engineering. Defined as crosslinked polymeric networks that possess high water contents (Tibbitt, M., & Anseth, K. 2009), hydrogels are utilised in 3D *in-vitro* models to mimic ECM by acting as a functional scaffold. Bioinks for the application of extrusion-based bioprinting are comprised of ECM mimicking biomaterials, either used independently (Table 1.1), but are more commonly used in combination to tailor the bioink characteristics to the intended application to achieve biomimicry (Hospodiuk, M., *et al.* 2017).

Hydrogels are classified into two groups: naturally or synthetically derived (Table 1.1). Nature-derived biomaterials have the benefit of being a sustainable source whilst being a suitable biological, structural and functional material for cells (Khoeini, R., *et al.* 2021; Ramiah, P., *et al.* 2020). However, compared to synthetically derived hydrogels, naturally derived hydrogels have a higher degree of variability and are mechanically weak. Synthetic polymer-based bioinks can be tailored with degradation and mechanical property requirements; however, generation often uses toxic solvents, non-biological melting points and lack the biological cues found in natural organic biomaterials (Hospodiuk, M., *et al.* 2017). Furthermore, after deposition, bioinks typically require appropriate cross-linking or sol-gel transition during the fabrication process (Table 1.1), to improve structural and mechanical stability of the polymeric network, and if appropriate, allow cellular health for culturing (GhavamiNejad, A., *et al.* 2021). Different methods of crosslinking application are utilised, for example, UV, visible or near infrared light are applied once the 3D model has finished bioprinting with a suitable duration to not elicit DNA damage (Nieto, D., *et al.* 2020; Xu, C., *et al.* 2018). Efficient and timely crosslinking of the 3D bioprinted structure is vital as the high water-content biomaterials can flow, or spread on the print-bed, resulting in increasing variability (Fu, Z., *et al.* 2021).

Table 1.1. Summary table of commonly reported biomaterials utilised as bioinks for the application of 3D in-vitro bone model fabrication.

Bioink	Source	Crosslinking/sol-gel transition	References
Silk fibroin	Natural protein from bombyx mori (silkworms).	Chemical, thermal, ionic, and physical.	Farokhi, M., *et al.* 2021; Dan, X., *et al*. 2025
Chitosan	Natural polysaccharide.	Thermal and ionic.	Bharadwaj, T., *et al.* 2024; Maturavongsadit, P., *et al.* 2021; Ressler, A. 2022
Hyaluronic acid	Natural glycosaminoglycan.	Photopolymerisation and enzymatic.	Badhe, R., *et al.* 2023; Ghorbani, F., *et al.* 2023; Hwang, H., & Lee, C. 2023
Collagen	Natural protein from animal sources.	Thermal, Ionic.	Debnath, S., *et al.* 2025; Osidak, E., *et al.* 2020
Gelatine	Denatured collagen, a natural protein, animal source.	Thermal.	Chiticaru, E., *et al.* 2024; Ozenler, A., *et al.* 2024; Waidi, Y., *et al.* 2024
Alginate	Natural, seaweed polysaccharide.	Ionic.	Wu, Y., *et al.* 2024; Farshidfar, N., *et al.* 2024; Choe, G., *et al.* 2022; Lee, J., *et al.* 2020
Gellan gum	Natural, bacterial polysaccharide.	Ionic.	Loukelis, K., *et al.* 2025; Bastos, A., *et al*. 2024
Poly (ethylene glycol)	Synthetic hydrophilic polymer.	Photo polymerisation, enzymatic and ionic.	Unagolla, J., *et al.* 2024; Tilton, M., *et al.* 2023
Polycaprolactone	Synthetic biodegradable polymer.	Thermal.	Kim, W., *et al.* 2024; Cunniffe, G., *et al.* 2017
Cellulose	Natural, polysaccharide derived from plant biomass or bacteria.	Ionic, thermal and physical.	Maturavongsadit, P., *et al.* 2021
Gelatine meth acrylamide	Semisynthetic derivate of natural gelatine	Photopolymerization and thermal.	Dobrisan, M., *et al.* 2024; Zhu, Y., *et al.* 2024; Yi, S., *et al.* 2022; Irmak, G., *et al.* 2019
Agarose	Natural polysaccharide from algae.	Ionic and thermal.	Mukundan, L., *et al.* 2025; Campos, D., *et al.* 2015

The research presented in this report used both commercially available bioinks (Bone GelXA and TissueFAB™) and in-house synthesised synthetic hydrogel: Laptonite® Poly (N-isopropylacrylamide-co-N, N-dimethylacrylamide) (L-PNIPAm-co-DMAc) polymer, which is supplemented with HAnps (Thorpe, A., et al. 2016a; Boyes, V., et al. 2021). The commercial bioinks' true formulation, concentration and composition are not officially disclosed; however, it can be hypothesised, based on crosslinking and material behaviour, that both bone GelXA and TissueFAB™ are predominately composed of alginate (Alg), and gelatine meth acryloyl (GelMA) (Badhe, R., *et al*. 2024; Anerillas, L., *et al.* 2021).

1.6.2 Alginate

Naturally occurring heteropolysaccharide with different seaweed and algae origins, Alg is frequently used as a hydrogel for 3D *in-vitro* models, including bone applications (Farshidfar, N., *et al.* 2023; Venkatesan, J., *et al.* 2020). Consisting of monomers of β-D-mannuronic acid and α-L-guluronic acid connected by a β-(1-4) glycosidic bond, Alg often has a large diversity of structures and molecular weights (Qosim, N., *et al*. 2024). Alg can undergo sol-gel transition in the presence of bivalent cations, such as calcium chloride, by ionic exchange of sodium counter ions, resulting in a chained molecular backbone (Abka-Khajouei, R., *et al.* 2022).

Stiffness and printability of Alg as a bioink can be controlled by concentration (Freeman, F., & Kelly, D. 2017), availability and duration of ion exposure, and the addition of constituents (Erickson, A., *et al.* 2018). For example, Wu (2024) reports 3D bioprinted 10 - 15% Alg lattice scaffolds supplemented with 10% wt. βTP for a bone *in-vitro* application. The addition of βTP significantly improved the material viscosity, and 10% Alg enhanced cellular proliferation (Wu, Y., *et al*. 2024). Alternatively, Iglesias-Mejuto (2021) developed Alg lattice scaffolds (testing 6, 8 and 10% wt) with HAnp (0, 8, 16 and 24% wt), with 10% Alg reported as structurally stable, and increasing concentrations of HAnp enhancing stability but also increasing brittleness (Iglesias-Mejuto, A., & García-González, C. A. 2021). Different constitutions of Alg-based bioinks are also reported, with Tharakan (2022) using Alg/COL bioink supplemented with strontium calcium polyphosphate, which resulted in a stable construct for cell viability over a 21-day culture period (Tharakan, S., *et al.* 2022). Alternative studies are reported, with Alg represented as a

common basis for a bone bioink (Korkeamaki, J., *et al.* 2025; Datta, S. 2023; Liu, S., *et al.* 2023; Im, S., *et al.* 2022; Lee, J., *et al.* 2020).

1.6.3 Gelatine meth acryloyl

GelMA is prepared through the synthesis of gelatine with chemically modified methacrylic anhydride, whereby the degree of methacryloylation is adjusted to produce a biomaterial with tunable characteristics (Yue, K., *et al.* 2015). In addition to the thermo-responsive nature of gelatine, by chemically modifying with methacrylic anhydride, radical polymerisation, e.g. UV light exposure, forms covalent crosslinks, to produce a hydrogel structure with independent stability (Fu, Z., *et al.* 2024; Bulcke, A., *et al.* 2000).

Zhu (2024) summarises that GelMA as an independent bioink has weak mechanical strength and therefore requires transformation into a composite bioink to become functional for bone *in-vitro* development, a conclusion in agreement to Zhou (2023). For example, Liu (2025) embedded electro-spun fibres, which have undergone mineralisation into GelMA bioink to produce a bioink with great mechanical properties, and diverse in nanostructure (Liu, X. *et al.* 2025). Allen (2022) optimised composite bioprinted hydrogels with GelMA and various HAnp concentrations (5, 10 and 20 mg/mL), producing structurally stable scaffolds with maintained cellular viability. Increased concentration of HAnp produced increased osteogenic activity (Allen, N., *et al.* 2022).

1.6.4 Laptonite® nano clay-based L-PNIPAm-co-DMAc polymer

Laptonite® is a synthetic smectite disc-shaped clay with a typical diameter of 30 nm and a thickness of 0.92 nm (Figure 1.8A). Magnesium 2^+ and Li^+ cations are present in the octahedral sites, with Na^+ cations within the interlayer space, and the resulting electrostatic interactions promote the formation of nanoparticle stacks in dry conditions, and colloidal dispersions in water (Figure 1.8B) (Tomas, H., *et al.* 2018). Laptonite® has a reported density of 2.53 g/cm^3 and an estimated 5.2 x10^{17} discs/g (Felbeck, T., *et al*. 2016; Grabolle, M., *et al.* 2016). Poly (*N*-isopropylacrylamide-co-*N, N*-dimethylacrylamide) is a thermo-responsive synthetic co-polymer of *N*-sioproyplacrylamide and *N,N*-dimethylacrylamide, whereby the physical properties of

the material alter when exposed to external stimuli, in this instance temperature of below 37 °C (Tang, L., *et al.* 2021; Bauri, K., *et al.* 2012).

Synthetic Laptonite® L-PNIPAm-co-DMAc polymer remains as a liquid (globule state) at temperatures above 37 °C (Figure 1.8C) and irreversibly shifts to a gel (coil state) when the temperature drops below 37 °C (Figure 1.8D) (Boyes, V., *et al.* 2021). The synthesis and polymerisation of the material have been previously described by Boyes (2021), where azobisisobutyronitrile is used at temperatures exceeding 80 °C to induce thermal dissociation of the polymer, resulting in the hydrophobic globule conformation of the Laptonite® co-polymer in a colloidal suspension (Figure 1.8C). Upon cooling, the PNIPAm chains change from globule to coil conformation, entangling the neighbouring clay platelets within polymer chains, thereby forming a non-degradable, stable hydrogel (Figure 1.8D) (Boyes, V., *et al.* 2021).

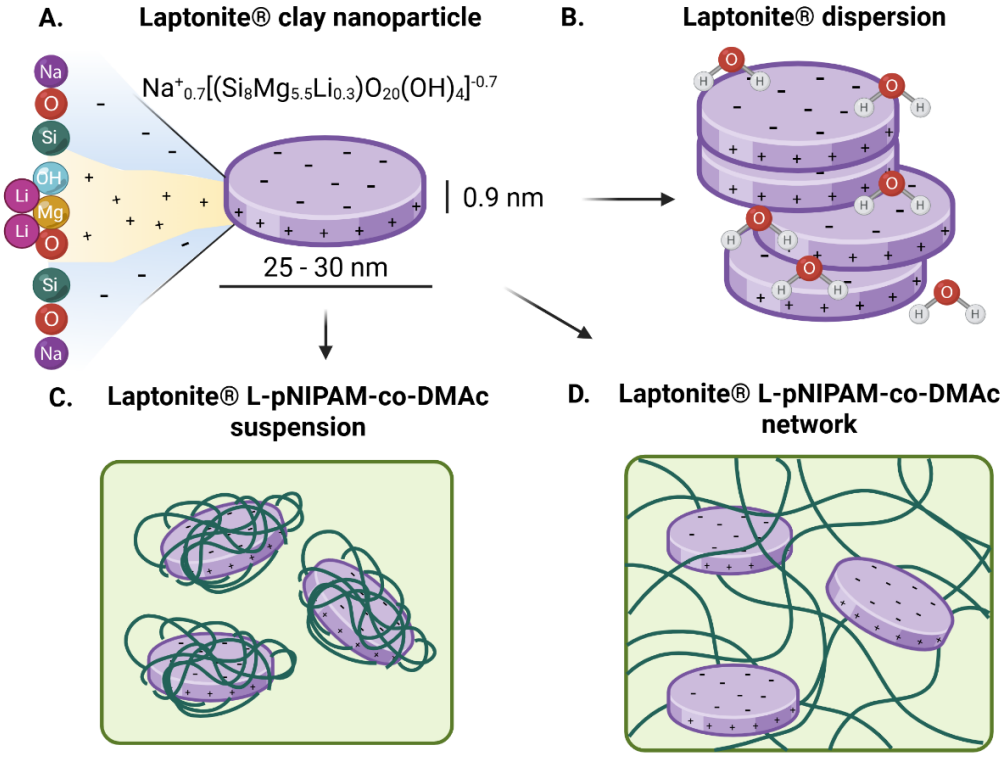

Figure 1.8. Laptonite® clay nanoparticle dimensions and chemical structure (A), in dispersion (B), suspension (C) and polymer network (D).

Previously developed as a therapeutic hydrogel for intervertebral disc degeneration (Cherif, H., *et al.* 2024; Snuggs, J., *et al.* 2023; Vickers, L., *et al*. 2019; Thorpe, A., et al. 2016a) and an injectable hydrogel scaffold to support bone augmentation (Thorpe, A.,

et al. 2018; Thorpe, A., *et al.* 2016b), the polymer was appealing to optimise for 3D bioprinting due to the tunability, mechanical stability from pre-printing sol-gel transition, biocompatibility, and the emerging interest in developing new bioinks that differ from those traditionally investigated (Sakr, M., *et al*. 2025; Garcia-Villen, F., *et al.* 2021) (Table 1.1).

Similar Laptonite®-based hydrogel materials have been developed for different biomedical applications, such as drug delivery (Li, H., *et al.* 2024; Li, Y., *et al*. 2011; Aguzzi, C., *et al.* 2007), incorporation with contrast agents for bioimaging (Rania, M., *et al.* 2016) and a bioactive nanomaterial (Reffitt, D., *et al.* 2003). Mihaila (2013) demonstrated Laptonite® suspension in growth medium to induce osteogenic differentiation in primary MSCs, in the absence of osteogenic factors, by the increased expression of differentiation markers associated with bone remodelling (Mihaila, S. *et al.* 2013).

Alternative bioprinting studies utilising Laptonite® incorporated in hydrogels are limited; however, Li (2024) investigated drug delivery of metformin to bone defects by inclusion of the drug in a 3D printed GelMA nano-clay hydrogel scaffold, with reasonable structural 3D stability. When the hydrogel was cultured in the same environment as cells, viability was maintained, and no toxicity was detected in *in-vitro* studies when the hydrogel was pasted onto bone defects in mice (Li, H., *et al*. 2024). Similar results on Laptonite® modified GelMA were reported by Mi (2024), however, osteogenesis was also shown (Mi, B., *et al*. 2024). Further, Osteogenesis was promoted by a laptonite® gelatine based bioink, both *in-vitro* with MSCs loaded onto the surface of a lattice scaffold, and *in-vivo* within a rat muscle pouch with no cytotoxicity recorded (Miao, S., *et al.* 2022). An alternative application of direct bioink, Zhou (2021) fabricated a laptonite® reinforced Pluronic F-127 sacrificial ink to create accurate channels in microfluidic devices, with the sacrificial ink acting as a structural support (Zhou, K., *et al.* 2021). Similarly, Afghah (2020) created a nano-clay hydrogel support bath to facilitate the success of bioprinting complex 3D structures.

Laptonite™ is incorporated into a Poly(*N*-isopropylacrylamide) (PNIPAm) based hydrogel, that can autonomously alter the physical and chemical properties when exposed to external stimuli (Willner, I. 2017; Jochum, F., & Theato, P. 2012), as well as alter volume by extruding or absorbing water, resulting in further alterations to the polymeric network

microstructure (Ullah, F., *et al*. 2015). Close to human body temperature, PNIPAm surfaces are hydrophobic, encouraging cell attachment, in contrast to below 20 °C where PNIPAm becomes hydrophilic, promoting detachment of cell-sheets (Sanzari, I., *et al.* 2020; Dzhoyashvili, N., *et al.* 2016). Ferrira (2018) summarises research exploiting the polymers' temperature/amphipathic behaviour to develop cell-sheet transplantation tissues from patients' autologous cells (Ferreira, N., *et al.* 2018). PNIPAm has limited bioink applications; however, Navara (2022) describes a novel PNIPAm co-polymerised GelMA bioink capable of producing structures on a micrometre scale, into a poloxamer heated support bath that encourages true filament fidelity. The bioink can be utilised in cellular +/- conditions, and the use is open-ended for different bioprinting applications (Navara, A., *et al.* 2022).

1.7 Study importance

2D monolayer *in-vitro* studies are not biologically representative of the native dynamics, composition or morphology of bones. Alternatively, *in-vivo* studies are ethically challenged, expensive and often do not allow comprehensive characterisation in early-stage biomedical studies, resulting in clinical failure. To bridge the gap between simple monolayer studies and *in-vivo* studies, 3D *in-vitro* models are a valuable resource to reflect the dynamic environment of native tissue whilst allowing for biological investigations. Various *in-vitro* bioprinted bone models utilising different compositions of inorganic and organic biomaterials have been previously published in the wider literature; however, they exist as simple structures. This study aims to develop a methodological pipeline of translating *ex-vivo* bones imaged by high-resolution micro-CT into 3D printable models (*In-vitro* and anatomical model inclusive) to develop an *in-vitro* bone model encompassing Cb and Tb structures, whereby composition and relevant bone remodelling markers will be assessed compared to *in-vivo* composition and cellular dynamics. In addition, extrusion-based bioprinting of commercial and in-house generated bioinks is investigated for suitability, with a microparticle support slurry generated and characterised to assist in achieving the overall aims of the study.

1.8 Thesis aims

The research presented in this thesis outlines the process of rendering *ex-vivo* murine bone captured by high-resolution micro-CT imaging for 3D model fabrication, of EBB, fused deposition modelling (FDM) and stereolithography (SLA). In addition, this research aims to optimise an *in-vitro* 3D EBB bone model, based on *ex-vivo* murine bone morphometry, by investigating bioink printing parameters and creation of a micro-particle support slurry. The resulting 3D *in-vitro* model is characterised against *in-vivo* bone, by investigating associated bone related markers, composition and behaviour over 21 days. It can be hypothesised that the physical structure of a biomaterial scaffold can independently induce osteogenesis in the absence of osteogenic media.

- Investigate the morphological structure and cell biology of bone architecture in *ex-vivo* mammalian murine species to inform the development of a physiologically relevant 3D *in-vitro* mouse bone model.
- Develop an informed workflow to render micro-CT images into 3D computer-assisted design model.
- Design and deliver an informative workshop on the developed method of translating *ex-vivo* micro-CT captured imagery into a 3D printable model by utilising computer-assisted design software.
- Evaluate the impact of the developed method within the wider bone scientific community.
- Optimise the bone bioink composition, fidelity and printability.
- Generate and characterise the of micro-particle support bath.
- Determine the impact on cellular viability of MC3T3-E1 pre-osteoblasts from the process of 3D bioprinting.
- Evaluate the osteogenic potential of 3D bioprinted *in-vitro* constructs in +/- osteogenic growth medium, compared to 2D monolayer culture.

Chapter 2 – Investigating murine bone biology

Summary of the structure, composition and function of bone to inform the development of an in-vitro 3D bone model

2.1 Introduction

2.1.1 Murine model selection

Murine models account for a large proportion of *in-vivo* models used in bone research (Stein, M., *et al.* 2023), with mice being the most commonly used animal in biomedical research. Various species of mice and rats exist for different specifications of research, such as studies that require genetically identical animals, or identification of biological impacts of knocking out specific genes of interest (Hickman, D., *et al*. 2016; Hefferan, T., *et al.* 2003). Mature Sprague Dawley rat models were selected for this study to represent the ossified mature stage of bone (Ruberte, J., *et al.* 2023). A common inbred strain of laboratory mouse, C57, was also utilised in this study as an alternative frequently used research model. Both the C57 and Sprague Dawley models are inbred animal strains, favoured for reliability and reproducibility within *in-vivo* studies (Song, H., & Hwang, D. 2017).

The research in this report aims to explore the similarities and differences of composition and morphology in a standard control species of both rat and mice, inclusive of bones of interest that are commonly investigated, the tibia, femur and vertebral body. The purpose of the research question is to define a 'control' bone, to be used for development into a 3D *in-vitro* bone model that aims to incorporate standard bone architecture and representative biology.

2.1.2 Bone imaging

Different non-destructive imaging techniques can be utilised to visualise bone morphology and overall bone health. In the medical investigation and diagnosis field, computational tomography (CT) is typically used to detect injury, diagnose bone diseases and cancer, as well as evaluate treatments (Hsieh, J., & Flohr, T. 2021; Rubin, G. 2014), with a typical resolution of 70 – 1000 µm (Plessis, A., *et al.* 2017). Dual-energy x-ray absorptiometry (DEXA) and magnetic resonance imaging are also frequently used to determine bone density and assess bone disease (Tadros, S., *et al*. 2023). However, for biomedical laboratory research, bench-top micro-CT imaging is more readily available for experimentation with small mammal models.

Micro-CT uses cone beam x-ray radiation as a source to capture 2D planar images of a rotating sample with a flatbed detector with a typical attainable voxel size of 2.6 - 26 µm, fluctuations are based on the model available (Plessis, A., *et al.* 2017). Briefly, as an x-ray passes through the tissue, the intensity of the beam is diminished according to the equation $I_X = I_{0e}^{-ux}$, where I0 is the intensity of the beam, X is the distance from the source, IX is the intensity of the beam at distance X from the source, and U is the linear attenuation coefficient (mm^{-1}) (Vasarhelyi, L., *et al.* 2020; Stauber, M & Muller, R. 2008). The images captured, when translated into grey pixels, represent the attenuation of the x-rays transversing the sample from which a 3D projection can be reconstructed in binary format for accurate visualisation when thresholded appropriately (Campbell, G., & Sophocleous, A. 2014).

The suitability of an object to undergo micro-CT imaging is determined by both atomic number and density, with the influence of object volume, contrast and composition of the mineral impacting the attainable attenuation and resulting contrast, which influences the quality of the images obtained (Plessis, A., *et al.* 2017). Dense, inorganic mineralised tissues, such as bone, provide the best contrast for micro-CT and is the gold star method for assessing bone micro/macro architecture, with complete external and internal visualisation (Kim, Y., *et al*. 2021; Singhal, A., Grande, J., & Zhou, Y. 2013).

2.1.3 Aims and objectives

Investigate the physiological standard in bone architecture in *ex-vivo* mammalian murine species to inform the development of a physiologically relevant 3D *in-vitro* bone model.

To image and quantify the internal and external micro/macro architecture of *ex-vivo* mammalian tibia, femur and VB, utilising the technique of micro-CT.

Characterisation of *ex-vivo* mammalian bone composition and biological phenotype by histological and immunochemistry techniques.

2.2 Materials and methods

2.2.1 Experimental design

Micro-CT and immunohistochemistry (IHC) were employed to evaluate the standard state of *ex-vivo* murine bone, focusing on morphological architecture and cellular populations (Figure 2.2.1). Different species of murine *ex-vivo* bone, including mice and rats, were chosen to undergo micro-CT evaluation due to their frequent use as biological models within the bone research community for *in-vivo* biomedical investigations (Mukherjee, P., *et al*. 2022; Abubakar, *et al.* 2017). Non-destructive micro-CT imaging facilitates 3D morphometry analysis of 3D objects, delivering information on the depth and complexity of bone microarchitecture. Further, remodelling markers specific to bone-building OBs were selected to undergo standard cellular population investigation via histology and IHC staining.

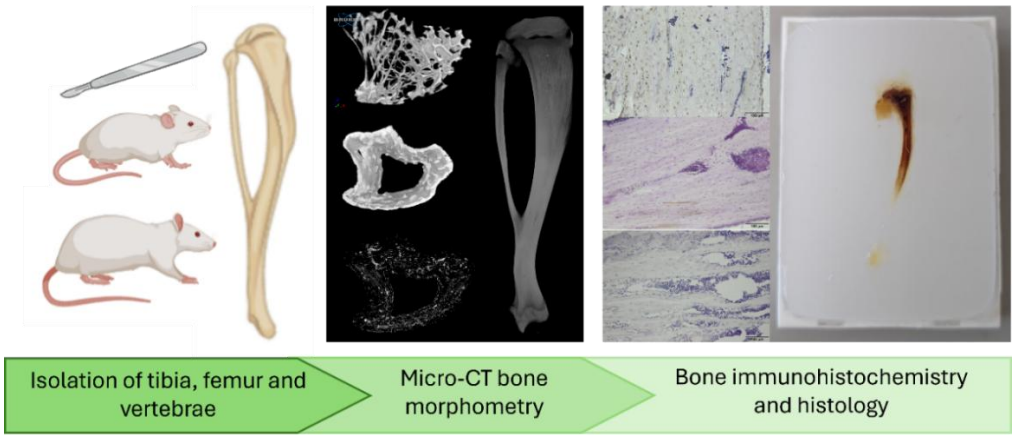

Figure 2.2.1. Summary of experimental design to investigate the internal/external architecture of bone, composition and cellular populations.

2.2.2 Tissue collection, dissection and storage

Mixed sex ex-breeder Sprague Dawley rat samples (n = 6 total, n = 3 male and n = 3 female), aged 26 +/- 1 weeks old and fed a normal diet (Table 2.2.1), as well as mixed-sex, unknown age Sprague Dawley (n = 1 male, n = 2 female) were also obtained from Biological Service Unit at University of Sheffield which were sacrificed using schedule 1 certified method before collection. Samples were collected via whole-body fresh dissection to isolate the tibia, femur, and vertebral bones (VB). Male, mouse C57 samples (n = 3), aged 24 +/- 2 weeks and fed a normal diet (Table 2.2.1), were collected and dissected via the same method, however, completed by Alexander Williamson.

***Table 2.2.1 Identification, weight and length of Sprague Dawley mixed-sex rat samples**, (n = 6), and **C57 male mice**, (n=3).*

Identification	Weight (g)	Length - nose to anus (cm)
Rat - Female 1, Mature	364	23.5
Rat - Female 2, Mature	315.6	22.9
Rat - Female 3, Mature	394.9	24.5
Rat - Male 1, Mature	466.8	23.8
Rat - Male 2, Mature	467.2	23.5
Rat - Male 3, Mature	460.9	25.5
Mouse – Male 1, Mature	41.2	Unknown
Mouse – Male 2, Mature	37.1	Unknown
Mouse – Male 3, Mature	45.6	Unknown

For murine samples, the vertebrae were dissected below the ribcage to the pelvis using a scalpel to maintain spinal integrity, harvesting the lumbar spine. The right and left tibiae were collected via dislocation of the femoral head to remove the intact hind limbs, followed by a scalpel separation of the femur and ankle. Excess soft tissue was removed. Bones were fixed in 4% w/v paraformaldehyde (PFA) (j61899.AP, VWR international, UK) supplemented with 26 mM sodium dihydrogen orthophosphate dihydrate (10723621, Thermo-fisher scientific, UK), and 34 mM disodium hydrogen orthophosphate dehydrate (10122880, Thermo-fisher scientific, UK) to reduce mineral diffusion, for 36 to 48 hours at 4°C, before being transferred to 70% v/v ethanol (459844, Sigma-Aldrich, UK) for storage until experimentation.

2.2.3 Micro-Computed tomography imaging and processing

Mouse and rat, right tibiae, right femora and lumbar three (L3) vertebrae were scanned using micro-CT (SkyScan 1272, Bruker Micro-CT, Belgium) with a resolution of 9 μm voxels by wrapping the bone in moistened tissue paper, and mounted into a plastic scanning tube which was then secured onto the stage of the micro-CT. All bones were rehydrated in $_{dd}H_20$ for 24 hours before imaging for density. Tibiae and vertebrae were scanned with a proximal orientation and femora with a distal orientation, to the standard

anatomical position to incorporate the sample's respective growth plates within the field of view. A 0.5 mm aluminium filter was used for mouse samples, and a 1 mm aluminium filter for rats. A 2016x1344 camera lens was used consistently, with a 10W power source providing different source voltage: source current of 55 kV:160 μA for mouse, and 65 kV:140 μA for rat. Flat-field detector calibration was performed before scanning to minimise ring artefacts and improve the signal-to-noise ratio by reaching a suitable signal transmission/detection percentage. Scans were performed with 360° rotation, with three x-ray projections acquired every 0.3 – 0.5 degrees.

To accurately determine the TMD and BMD of rat and mice samples, calcium hydroxyapatite rods—2 mm radius for mouse, 8 mm for rat (Bruker, Belgium)—with densities of 0.3 and 1.25 gHA/cm^3 were scanned using the previously mentioned parameters.

Software analysis of the x-ray outputs was completed using NRecon (NRecon 2.1.0.2, Bruker Micro-CT, Belgium), which generated a 3D reconstruction from the 2D x-ray projections. Images were optimised using an appropriate post-alignment compensation, +1 smoothing filter (Gaussian window kernel), 40% beam hardening correction, and appropriate ring artefact correction. A threshold of 0 – 0.12 mm^{-1} was selected to represent the transition between pore and bone tissue for all rat and mouse samples. Visualisation software, CT Vox, was used for qualitative visualisation of entire samples, density and thickness. Pseudo-colour was applied for the entire samples, whereas density and thickness visualisation for mouse and rat were calibrated (Chapter 2, sections 2.2.4.3 and 2.2.4.4). All reconstructed samples were rotated in alignment within the trans-axial plane in the software Data Viewer.

2.2.4 Region of interest segmentation

Post-reconstruction analysis was performed using CTAn (CTAn 1.15.4.0, Bruker, Belgium). Tb (metaphyseal) and Cb (metaphyseal) volume of interest (VOI) for tibiae and femora were selected using the bridge-break of the growth plate as a suitable and consistent landmark. Cancellous bone was selected as VOI for the VB (Figure 2.2.2). Region of interest (ROI) of Tb, Cb and total architecture were created by freehand drawing. Landmark selection for long bones was referenced to the chondrocyte seam, referred to

as ‘bridge break’, in the growth plate that reflects the transition from proliferative zone to hypertrophic zone in the epiphyseal growth plate. The distal femoral head growth plate features four islands that break in the centre, whereas the proximal tibiae have two. For the VB, the body was isolated from processors and pedicles using the user-defined thinnest point of Cb. VB inferior growth plate was selected, with landmark selection following the break of the chondrocyte seam and transition into mature trabecular from primary spongiosa.

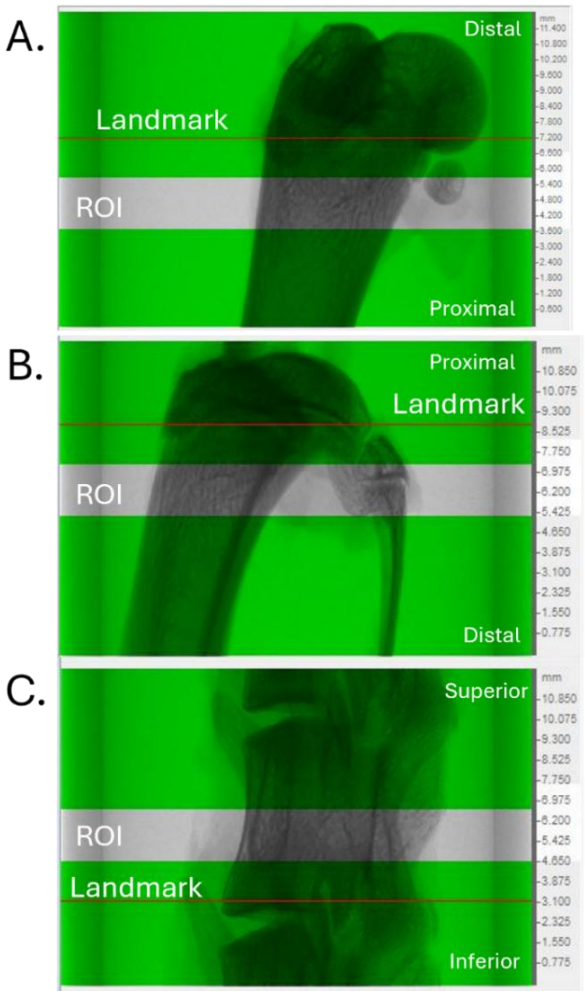

Figure 2.2.2 Region of interest selection projections in rat femur, tibia and L3 VB. *The appropriate landmark is represented by a red line in the projection, with the region of interest visualised by grey space in replacement of green space. For rats, a 2 mm height of ROI was selected for Tb & Cb analysis (shown). The tibia offset was 0.5 mm, 3mm for the femur, and 1 mm for L3 VB (shown). For mice, a 1.5 mm height of ROI was selected for Tb & Cb analysis (not shown) with a 0.5 mm offset used for all bone types.*

2.2.4.1 CTAn three-dimensional morphometry

3D bone morphometry analysis was completed for Tb and Cb independently. For rat and mouse Tb, the ROI was loaded into CTAn. Global thresholding was selected with output to image of 70 – 255, followed by despeckling. Finally, 3D analysis was selected with additional values (Table 2.2.2). For rat and mouse Cb, the greyscale threshold selected was 120 – 255, with despeckling applied, and 3D analysis performed with basic output values selected (Table 2.2.2). CSV files were produced.

2.2.4.2 CTAn porosity

Porosity was determined in the Cb by inverting the binarisation of bone to highlight the pore space, with a threshold of 120 – 255. The binarised bone underwent sweeping and despeckling to further segment. Bitwise and morphological operations were completed, with a final despeckling to retain only the VOI saved as a BMP. Finally, a 3D analysis was performed (Table 2.2.2) with porosity calculated using the following (Equation 2.2.1).

$$Porosity\ of\ total\ cortical\ volume\ (\%) = \frac{Pore\ volume\ (mm-1)}{Total\ cortical\ and\ pore\ volume\ (mm-1)} x\ 100$$

Equation 2.2.1. Equation for calculating porosity of cortical bone.

2.2.4.3 CTAn trabecular thickness

Trabecular VOIs had a threshold of 70 – 120 applied and despeckling. Following this, 3D individual object analysis was completed, with thickness and separation saved. For visualisation in CT Vox, the output ROI underwent contrast stretching, followed by saving bitmaps and BMP as output file type. The output BMP was opened in CT Vox, with the minimum and maximum thickness values of the total study, per species, applied as an appropriate colour-coded scale bar.

2.2.4.4 CTAn bone & tissue mineral density

Scanned phantoms were reconstructed and thresholded identically irrespective of bone samples, with a height of 1.5 mm selected for ROI segmentation of the inner 60% of the individual phantoms. To accurately calibrate the software, the attenuation coefficient (AC) values were obtained from the binary view data set summary. The AC output values were inputted into the BMD histogram, with the associated CaHA density to result in the

following calibration (Equation 2.2.2). After calibration, the 0.3 g/cm^3 phantom produced a TMD of 0.29 g/cm^3, and the 1.25 g/cm^3 phantom produced a TMD of 1.24 g/cm^3.

$$BMD = \frac{AC - 0.0074621052631579}{0.0335263157894737}$$

Equation 2.2.2 Bone and tissue mineral density histogram calculation based on known phantom calibration.

Independent ROIs of Tb and Cb were loaded into CTAn with the appropriate calibrations set per species, with binary histograms produced. Cb value was taken from the mean of all AC values, defined as Tissue mineral density (TMD) (g/cm^3), whereas Tb was taken from the mean (total) of all AC values, referred to as Bone mineral density (BMD) (g/cm^3) (Table 2.2.2).

Table 2.2.2. Description of analytical outputs from micro-CT imaging. *Descriptions adapted from Bouxsein, M., et al. 2010 & Kazama, J., et al. 2010. Bone morphometric parameters investigated in this study are listed below.*

Variable	Abbreviation / Standard Unit	Description of the algorithm output
Trabecular Number	Tb.N (mm^{-1})	The average number of trabeculae per unit length in an ROI, detected by spatial densitometry.
Trabecular Thickness	Tb.Th (mm)	Average thickness of trabeculae in 3D space, detected by spatial densitometry.
Trabecular separation	Tb.Sp (mm)	Average distance between trabeculae in 3D space.
Bone volume fraction	BV/TV (%)	The segmented bone volume ratio to the region's total volume of interest is based on spatial densitometry, e.g., highlighting medullary marrow space.
Cortical bone volume	CBV (mm^{-1})	The total volume of calcified bone based on spatial densitometry
Cortical bone pore volume	Porosity (%)	Total volume of pore space within the calcified bone, after inversion of density.
Tissue mineral density	TMD (g/cm^{-3})	Total volumetric density of calcium hydroxyapatite. Mean pixel tissue mineral density for total calcified bone, excluding soft tissue space.
Bone mineral density	BMD (g/cm^{-3})	Total volumetric density of calcium hydroxyapatite. Mean pixel bone mineral density for the trabecular bone area within the soft tissue space.

2.2.5 Decalcification and tissue preparation

Following micro-CT analysis, rat bones underwent destructive processing. Bones were decalcified with agitation over 3 - 4 weeks at 4 °C in excess solution volume compared to the sample in 20% ethylenediaminetetraacetic acid (EDTA) (#A10713.36, ThermoFisher, UK), adjusted to pH 7.4 with sodium hydroxide. The EDTA buffer was replaced every three days, after phosphate-buffered saline (pH 7.4) washes. Micro-CT scout views were obtained every 3 - 4 days to ensure full decalcification of samples (Figure 2.2.3). Rat bones were placed in a tissue processor (Leica TP 1020, UK) for dehydration through 70%, 80% and 95% ethanol for 45 minutes each, followed by 3 changes of 100% ethanol. The tissue was cleared by 2 changes of xylene for 1 hour each and embedded by repetitive changes of paraffin for 1 hour. Rat bone samples underwent standard embedding in paraffin (Histocore Arcadia II, UK), followed by 8 μm sections cut using a microtome (Leica RM2235, UK) fitted with a diamond blade onto positively charged slides (Leica Biosystems, UK). The floated sections were left to dry at 37 °C for 2 weeks before histological and IHC staining procedures.

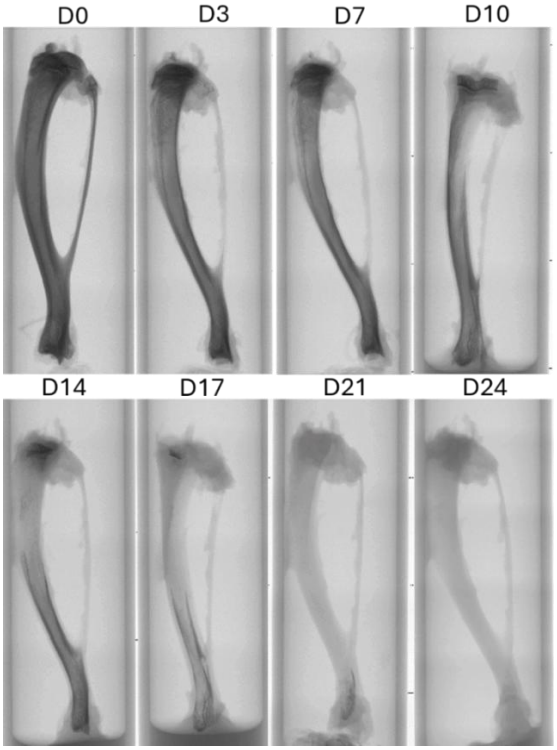

Figure 2.2.3 Micro-CT image projections of total rat tibiae decalcification. *Rat tibiae, femur and lumbar vertebrae underwent decalcification to allow tissue processing for histological and immunostaining. Representative images of tibiae shown.*

2.2.6.1 Haematoxylin and eosin staining

Samples underwent paraffin removal using sub-X (Leica microsystems, UK) for 3 x 5 minutes before rehydration through a series of industrial methylated spirit (IMS) baths. Samples were then placed in $_{dd}H_20$ before staining with filtered Mayer's Haematoxylin (Leica microsystems, UK) for 1 minute, followed by 'bluing' under running tap water for 5 minutes. Alcoholic eosin (Lecia Microsystems) was used for counterstaining for 1 minute. Sections were then dehydrated for 3 x 5 minutes in IMS and cleared for 3 x 5 minutes in Sub-X. Coverslips were mounted to samples using Eukitt quick hardening mounting medium (#03989, Merck, UK) and left to dry before sections were assessed.

2.2.6.2 Masson Trichrome staining

Samples underwent paraffin removal using sub-X (Leica Microsystems, UK) for 3 x 5 minutes before rehydration through a series of IMS baths. Masson's trichrome (MT) staining kit (Atom Scientific, UK) was used according to the manufacturer's method. Samples were stained with equal parts of Wiegert's iron haematoxylin for 20 minutes, followed by washing in water for 1 minute. Samples were differentiated in a 1% acid alcohol solution before 'bluing' under running tap water for 5 minutes. Ponceau fuchsin was applied for 5 minutes, followed by a wash in $_{dd}H_20$, before further staining with phosphomolybdic acid for 15 minutes. Samples were transferred to methyl blue solution, without rinsing, for 5 minutes. Slides were washed in water, followed by 3 x 5 minutes in IMS and cleared for 3 x 5 minutes in Sub-X. Coverslips were mounted to samples using Eukitt quick hardening mounting medium (#03989, Merck, UK) and left to dry before sections were assessed.

2.2.6.3 Alcian blue staining

Paraffin removal using sub-X (Leica microsystems, UK) for 3 x 5 minutes before rehydration through a series of IMS baths was conducted. Samples underwent staining in 1% alcian blue (ACB) solution (pH 2.5) for 30 minutes at room temperature, followed by washing in running tap water for 2 minutes and rinsing briefly in $_{dd}H_20$. To each sample, 0.1% nuclear fast red solution was applied as a counterstain for 5 minutes, with the washing in running tap water for 1 minute. Dehydration of 3 x 5 minutes in IMS and cleared for 3 x 5 minutes in Sub-X. Coverslips were mounted to samples using Eukitt quick

hardening mounting medium (#03989, Merck, UK) and left to dry before sections were assessed.

2.2.6.4 Safranin O staining

Samples underwent paraffin removal using sub-X (Leica Microsystems, UK) for 3 x 5 minutes before rehydration through a series of IMS baths. Equal parts of Wiegert's iron haematoxylin were applied for 5 minutes, with samples washed in running tap water for 10 minutes afterwards. Samples were stained with 0.4% aqueous fast green for 4 minutes, followed by rinsing in two changes of 1% acetic acid for 5 minutes each. Freshly prepared 0.125% safranin-o (SO) was applied before dehydration of 3 x 5 minutes in IMS and clearing for 3 x 5 minutes in Sub-X. Coverslips were mounted to samples using Eukitt quick hardening mounting medium (#03989, Merck, UK) and left to dry before sections were assessed.

2.2.6.5 Immunohistochemistry

IHC was conducted to assess the proteins of interest (Table 2.2.3). Samples underwent paraffin removal using sub-X (Leica microsystems, UK) for 3 x 5 minutes before rehydration through a series of IMS baths before endogenous peroxidases were blocked with 3% w/v hydrogen peroxide in IMS containing five drops of concentrated 37% hydrogen chloride for 1 hour at room temperature. Sections underwent a 5-minute wash in H_2O, a 2 x 5-minute wash in 1X tris-buffered saline (TBS), prepared by diluting a 10X stock of TBS (200 mM Tris(hydroxymethyl)aminomethane and 1500 mM sodium chloride, adjusted to pH 7.5)

Each primary antibody underwent optimisation for a suitable antigen retrieval method (Table 2.2.3): none, heat, and enzyme. For heat antigen retrieval, samples were submerged in tris antigen retrieval buffer (50 mM Tris, pH 9.5) and paired with a non-stick Teflon™ strip, clamped in place with a blank microscope slide with a bulldog clip. Sections underwent steaming (Russell Hobbs) for 10 minutes in Tris-antigen retrieval buffer and moved to $_{dd}H_20$ to allow separation of Teflon™ from the sample. For enzyme antigen-retrieval, samples were submerged in pre-heated enzyme antigen-retrieval buffer containing 300 µL of 1% w/v α-chymotrypsin and 0.1% calcium chloride for 30 minutes at 37°C.

Following antigen retrieval, slides were washed in 1X TBS for 3 x 5 minutes. A hydrophobic barrier PAP pen was used, and a blocking buffer (25% normal goat serum and 1% bovine serum albumin in 1X TBS) was applied for 2 hours at room temperature in a humidified box to limit non-specific antibody-protein interactions. Following incubation, sections were incubated overnight at 4 °C with the protein of interest antibody diluted (Table 2.2.3) in blocking buffer; anti-caspase-3, anti-Runx2, anti-ALPPL2, anti-OCN, anti-OPN, anti-COL-1, and anti-ki67 (Proteintech) or a rabbit IgG isotype (Abcam, ab183910) at an appropriate concentration as the primary antibody of interest.

Table 2.2.3 Primary antibody and antigen retrieval conditions for IHC staining of rat femur and tibiae. *All antibody concentrations and antigen retrieval methods were independently optimised, using a range of three antibody concentrations and three antigen retrieval methods – None, heat, and enzyme.*

Primary Antibody	**Antigen Retrieval**	**Concentration of primary antibody(μg/ml)**
Rabbit Anti-Caspase-3 (600μg) – Proteintech 19677-1-AP	None	1.2
Rabbit Anti-Runx2 (600μg) – Proteintech 20700-1-AP	Heat – 0.05 M Tris. pH 9.5	12
Rabbit Anti-ALPPL2 (260μg) – Proteintech 18506-1-AP	Heat – 0.05 M Tris. pH 9.5	2.6
Rabbit Anti-osteocalcin (500μg) – Proteintech 23418-1-AP	None	10
Rabbit Anti-osteopontin (700μg) – Proteintech 22952-1-AP	Enzyme – 1X TBS (pH 7.5) with CaCl and α-chymotrypsin	3.5
Rabbit Anti-Collagen Type I (500μg) – Proteintech 14695-1-AP	Enzyme – 1X TBS (pH 7.5) with $CaCl_2$ and α-chymotrypsin	1
Rabbit Anti-Ki67 (600μg) – Proteintech 28074-1AP	Enzyme – 1X TBS (pH 7.5) with $CaCl_2$ and α-chymotrypsin	1.2

Sections were washed in 1X TBS for 3 x 5 minutes, and pre-diluted secondary antibody GTX Rabbit biotin (21537, SLS) was applied for 30 minutes at room temperature. Sections were washed in 1X TBS for 3 x 5 minutes before the addition of Vectorstain elite ABC reagent (PK-7100, 2B scientific, UK) for 30 minutes at room temperature before developing with 0.08% v/v H_20_2 and 0.65 mg/ml 3,3'-diaminobenzidine tetrahydrochloride for 20 minutes at room temperature. Samples were washed in water for 5 minutes. Sections were then dehydrated for 3 x 5 minutes in IMS and cleared for 3 x 5 minutes in Sub-X. Coverslips were mounted to samples using Eukitt quick hardening mounting medium (#03989, Merck, UK) and left to dry before sections were assessed.

2.2.7 Image capture

Representative images were taken microscopically using an Olympus BX60 microscope, and images were captured using CellSens software (Olympus, UK) and a MicroCapture v5.0 RTV digital camera (Q imaging, Buckinghamshire, UK).

2.2.8 Statistical analysis

All micro-CT data were presented in the form of individual data points, with mean values displayed for normally distributed data and median values for non-parametric data. For morphometric analysis, Shapiro-Wilk normality testing was completed, with significance determined by multiple unpaired T-Tests (two-tailed) followed by the Holm-Sidak method. For TMD/BMD analysis, Shapiro-Wilk normality testing was completed, followed by One-Way ANOVA and post hoc Holm-Sidak test. $P < 0.05$ was defined as statistically significant in this study.

2.3 Results

2.3.1 Murine *ex-vivo* bone morphometry

Micro-CT imaging and analysis allow the visualisation and quantification of different murine bone types. Hand-drawn ROIs were used to define regions of Cb and Tb for 3D quantification for all mouse and rat bones of interest: Femur, tibia and L3 VB (Figure 2.3.1). Between species, qualitatively, the bones featured similar morphology; however, it was clear that rat bones contained a higher level of architectural complexity compared to mouse bones, with increased porosity and apparent Tb.N (Figure 2.3.1).

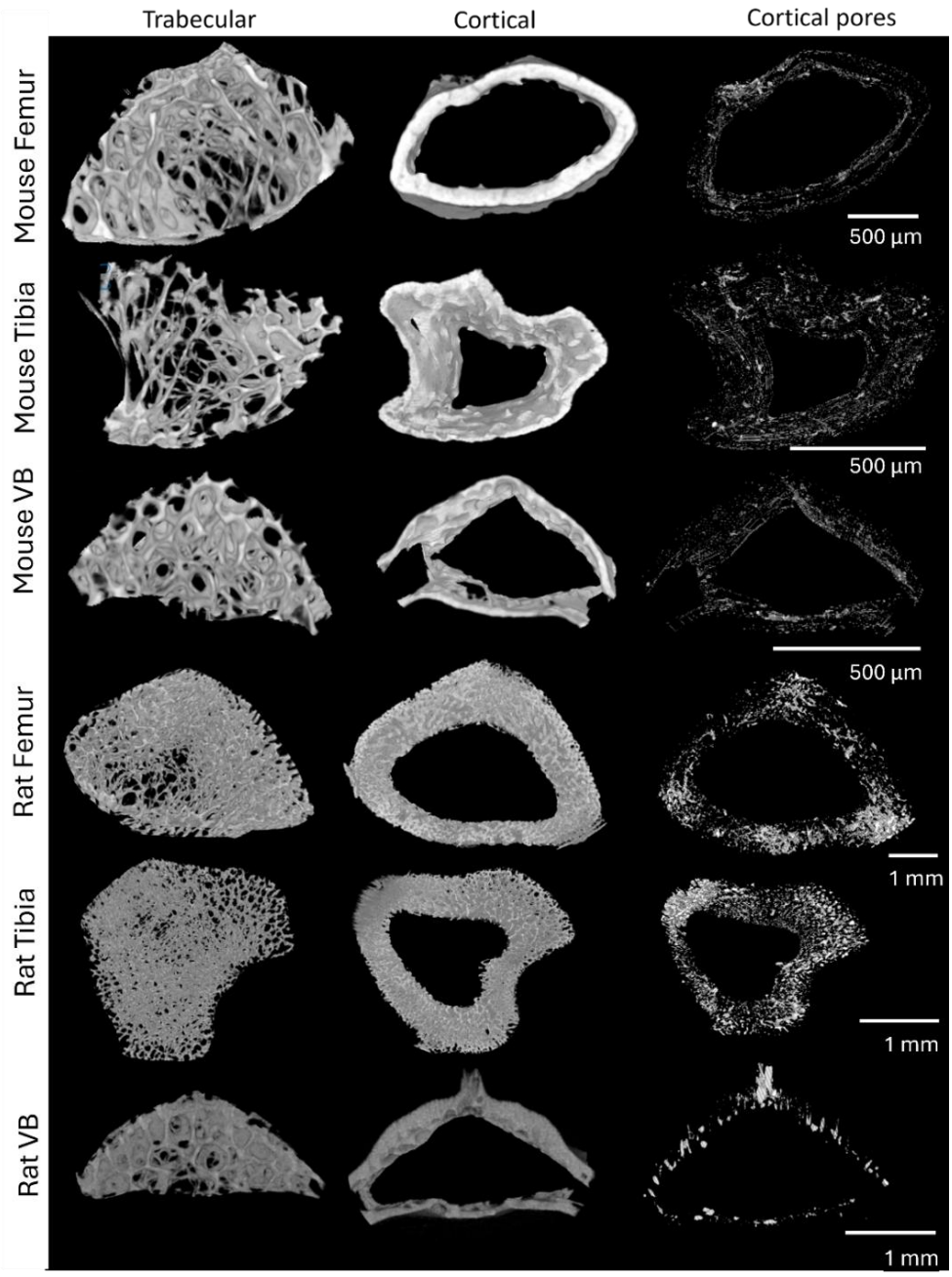

Figure 2.3.1 Representative schematic of mouse and rat bone regions of interest for morphological analysis of femur, tibia and L3 VB. *Each bone type was segmented into Tb, Cb and pore regions of interest for 3D morphological analysis. For mice, Tb and Cb analysis was completed on a 1.5 mm section taken 0.5 mm from the growth plate break landmark for the femur, tibia, and L3 VB. For rats, Tb and Cb analysis were completed on a 1.5 mm section taken 0.5 mm from the growth plate break landmark for the femur, tibia, and L3 VB. Pseudo-density colour was applied. n = 3, scale bars are 500* µm for mouse and 1 mm for rat.

From the Cb ROIs and porosity segmentation (Figure 2.3.1), 3D quantitative analysis was performed. The overall bone volume of mice was statistically significant compared to the bone volume of both male and female rats in both tibia ($P < 0.0001$) and femur ($P <$

0.0001) (Figure 2.3.2A). High intra-sample variance in the male rat tibia was discovered, compared to all other samples (Figure 2.3.2A). In comparison to porosity, a different trend could be seen. The rat male tibia and femur contain a lot of variances inter-population compared to rat female and mouse, resulting in a statistical difference between these groups (Figure 2.3.2B). The VB was shown to have consistent porosity between populations in the different groups.

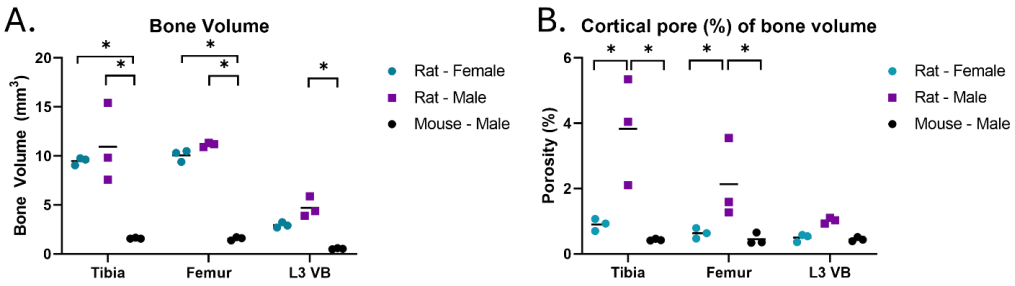

Figure 2.3.2 Cortical bone morphometry quantitative analysis outputs for mouse and rat bone regions of interest. *1.5 mm ROI of mouse Cb, and 2 mm ROI of rat Cb was selected for 3D morphometry analysis. A) Bone volume (mm^3) quantification of tibia, femur and L3 VB male and female rats and male mouse, B) porosity (%) quantification of tibia, femur and L3 VB male and female rats, and male mouse. n = 3, Mean represented, with T-Test multiple comparisons per bone type, P < 0.05.*

Tb.Th ranges between different bone types and between species. The variance of bone micro-architecture complexity was qualitatively visualised (Figure 2.3.3A/B). Statistically ($P < 0.0015$), Tb.Th was different between all species in the tibia (Figure 2.3.3C). Overall, across bone types Tb.Th was not statistically different, with male rats having the highest overall Tb.Th (Figure 2.3.3C). Trabecular number (Tb.N) for tibia and femur show no statistical difference between samples and species, whereas for the L3 VB the female and male rats were statistically different ($P = 0.0287$, 0.0264, respectively) to the mouse (Figure 2.3.3D). Trabecular separation (Tb.Sp) has great intra-sample variance, with a statistical difference ($P = 0.0174$) between male and female rat tibia (Figure 2.3.3E). The L3 VB showed a statistical significance between rat and mouse samples (Figure 2.3.3E), perhaps linked to the high Tb.N seen in mouse L3 VB compared to the rat samples (Figure 2.3.3D). Bone volume to tissue ratio (BV/TV) was varied for female rat tibia compared to male rat and male mouse, with this difference seen in the femur. L3 VB was consistent between species and conditions (Figure 2.3.3F).

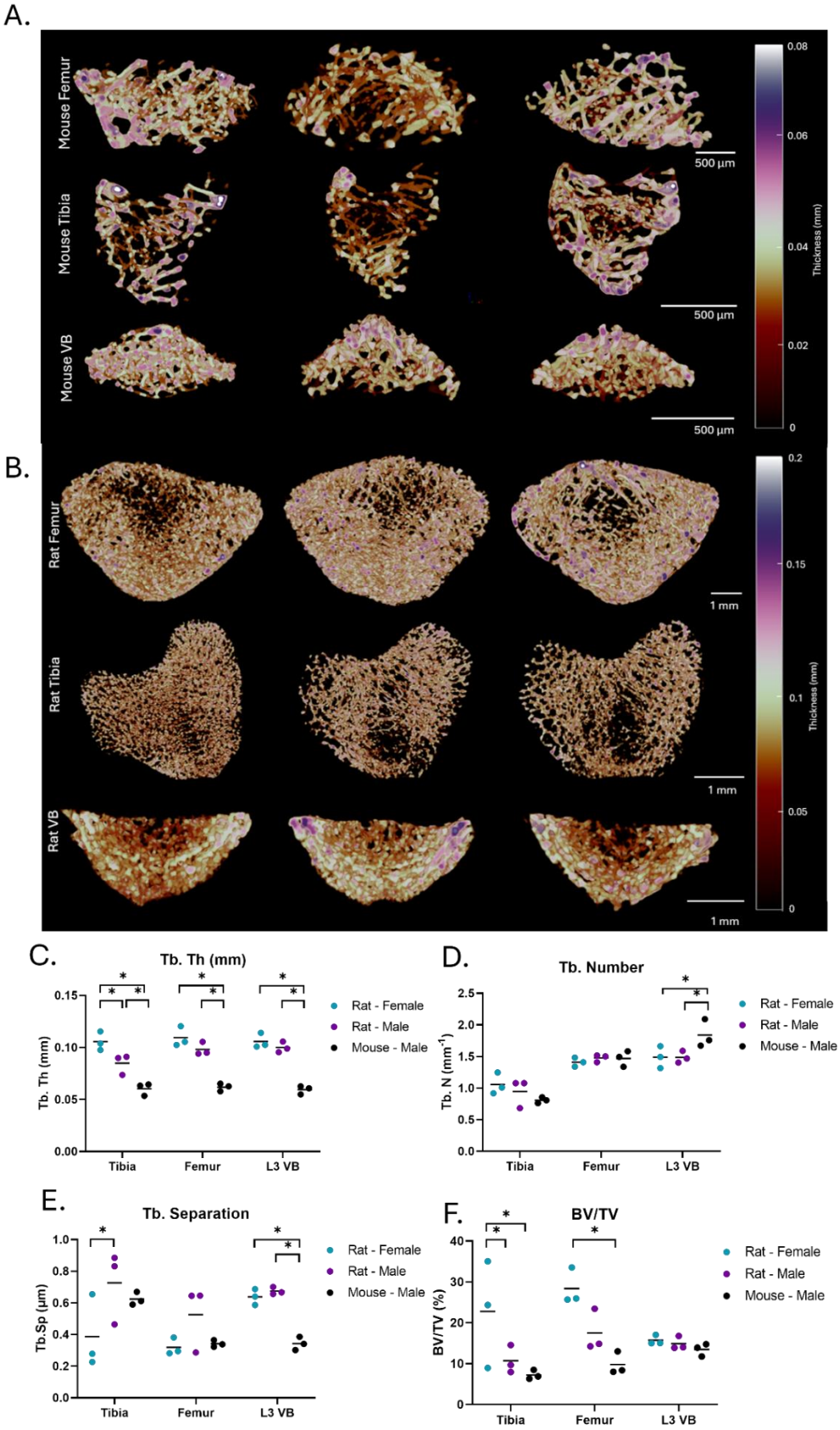
A.
Mouse Femur
Mouse Tibia
Mouse VB
500 µm
500 µm
500 µm
0.08
0.06
0.04
0.02
0
Thickness (mm)
B.
Rat Femur
Rat Tibia
Rat VB
1 mm
1 mm
1 mm
0.2
0.15
0.1
0.05
0
Thickness (mm)
C.
Tb. Th (mm)
Tb. Th (mm)
0.15
0.10
0.05
0.00
Tibia
Femur
L3 VB
Rat - Female
Rat - Male
Mouse - Male
D.
Tb. Number
Tb. N (mm-1)
2.5
2.0
1.5
1.0
0.5
0.0
Tibia
Femur
L3 VB
Rat - Female
Rat - Male
Mouse - Male
E.
Tb. Separation
Tb.Sp (µm)
1.0
0.8
0.6
0.4
0.2
0.0
Tibia
Femur
L3 VB
Rat - Female
Rat - Male
Mouse - Male
F.
BV/TV
BV/TV (%)
40
30
20
10
0
Tibia
Femur
L3 VB
Rat - Female
Rat - Male
Mouse - Male

Figure 2.3.3 Region of interest trabecular thickness colour-coded 3D models of mouse bones and morphometry 3D quantitative analysis. *All segmented Tb samples are shown, representing the diversity between samples. A) ROIs shown were used for mouse Tb analysis, with thickness colour-coded scale bar, 0 – 0.08 mm, shown from low thickness (brown) to high thickness (purple). Scale bars represent 500* μm. *B) All ROIs shown were used for male rat Tb analysis, with a thickness colour-coded scale bar, 0 – 0.2 mm, shown from low thickness (brown) to high thickness (purple). Scale bars represent 1 mm. C) Tb separation (*μm) *quantification of tibia, femur and L3 VB male and female rats, and male mouse, D) Tb number (mm^{-1}) quantification of tibia, femur and L3 VB male and female rats, and male mouse, E) Tb thickness (mm) quantification of tibia, femur and L3 VB male and female rats, and male mouse. F) Bone volume to tissue ratio (%) quantification of tibia, femur and L3 VB male and female rats and male mouse. n = 3, Mean represented, with T-Test multiple comparisons per bone type, P < 0.05.*

2.3.2 Murine bone composition

Rat bones underwent decalcification and sectioning for further investigation into cellular phenotype. Haematoxylin and eosin (H&E) staining was used to visualise the standard tissue architecture (Figure 2.3.4A) and cellular components (Figure 2.3.4B). Tb could be identified within bone marrow regions, connected to Cb. The periosteum surrounded the Cb, and blood vessels were visualised connecting the marrow to the highly vascularised surface (Figure 2.3.4A/B), where the arrows and labels indicate the structures described. Regions of BLCs, OBs and OCs were visualised within the Tb, surrounded by bone marrow containing white blood cells and adipose droplets. Within the Cb, resorption pits containing OCLs, surface lining OBs and an increased population of OCs were noted. Cells were morphologically identified by location and being either single or multi-nucleated; however, cells would require specific protein marker identification to confirm phenotype (Figure 2.3.4A/B). OCs could be visualised in ACB stain, in reabsorption pits within the Cb, with OCs in individual crypts within the Cb and Tb. No physiological differences were observed between male and female rats (Figure 2.3.4D). SO staining showed strong regions of proteoglycan staining within Tb structures, with less staining visualised in Cb (Figure 2.3.4C). ACB staining allowed visualisation of rich mucin regions within both Cb and Tb. In general, male tibia and femurs demonstrated strongly stained regions of both proteoglycans and mucins compared to female tibia and femur (Figure 2.3.4D).

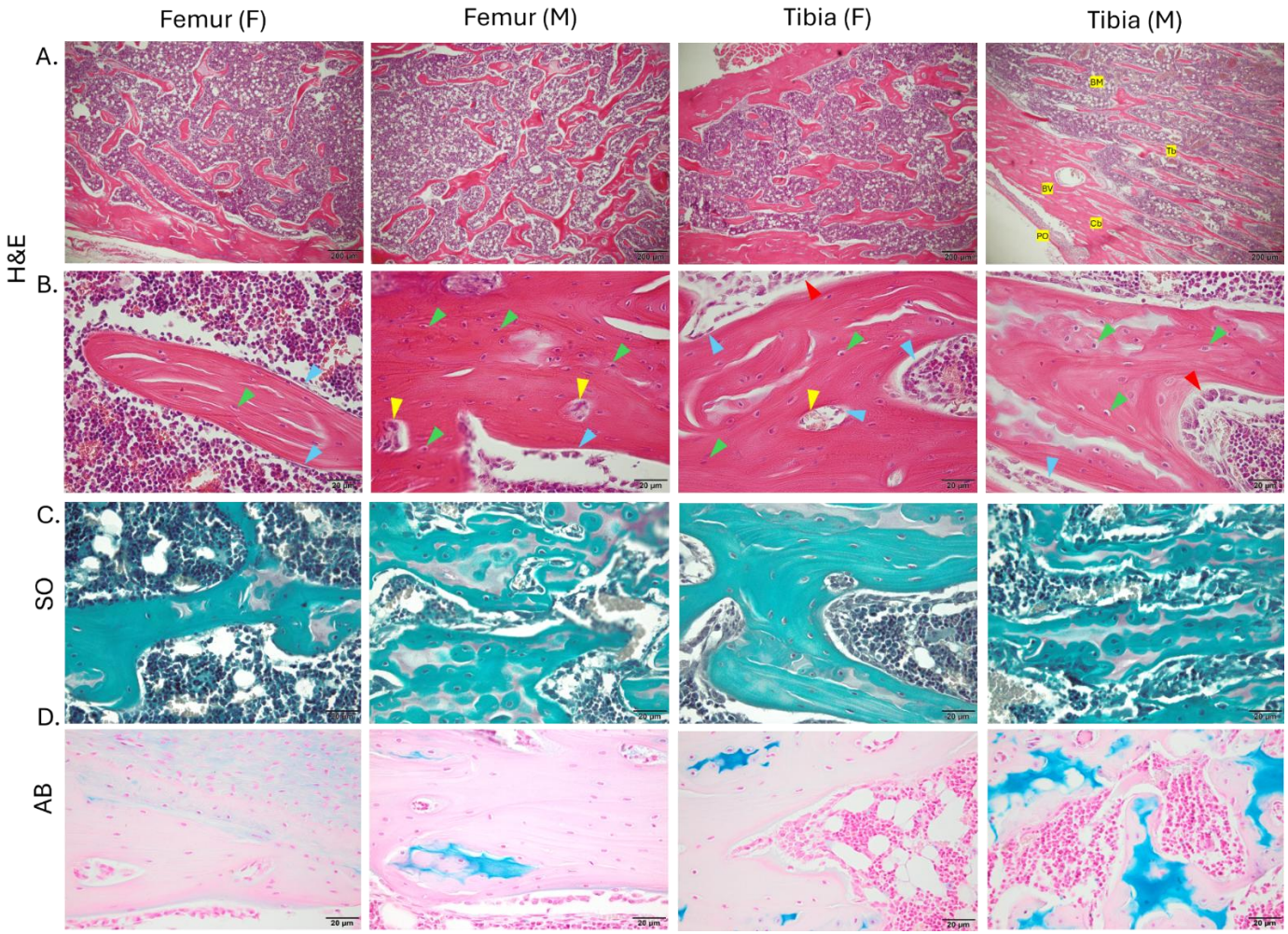

Figure 2.3.4 Histology stains on male and female rat, tibia and femur. *A) Tissue architecture is identified, trabecular bone (Tb), cortical bone (Cb), bone marrow (BM), blood vessel (BV) and periosteum (PO), scale bar represents 200 µm, B) Cellular population is identified by arrows, OCs (green), OCLs (yellow), OBs (blue), BLC (red), C) Safranin-O (SO) allows visualisation of proteoglycan-rich regions (red/pink), and bone (green). D) Alcian blue (ACB) represents regions of mucins and proteoglycans (blue), nucleus (strong pink) and connective tissue (pale pink). Scale bar for (B, C & D) represents 20 µm. n = 3, representative image shown.*

Rod-shaped standards called phantoms with a known density of calcium hydroxyapatite were scanned and reconstructed using the same parameters as the bones, allowing accurate calibration of CTAn software to determine BMD and TMD. BMD represents the Cb region, and TMD represents the trabecular region surrounded by the bone marrow cavity, with each region independently measured by Cb and Tb defined ROIs. Figure 2.3.5A represents a qualitative summary of male and female rat tibia, femur and L3 VB, as well as the male mouse tibia, femur and L3 VB.

Female rat bones had the highest density (BMD & TMD) averages in all bones, visualised both qualitatively in representative images (Figure 2.3.5A) and quantitatively (Figure 2.3.5B/C). Statistical differences in BMD were between the rats (male and female) and mice in both the femur and L3 VB (Figure 2.3.5B). Interestingly, no statistical difference was found in the tibia for BMD (Figure 2.3.5B). For TMD, the female rat tibia was statistically different from both male rat ($P = 0.0175$) and male mouse ($P = 0.0013$), with no difference between the male conditions (Figure 2.3.5C). The femur and L3 VB had statistical differences between rats (male and female) and mice (Figure 2.3.5C).

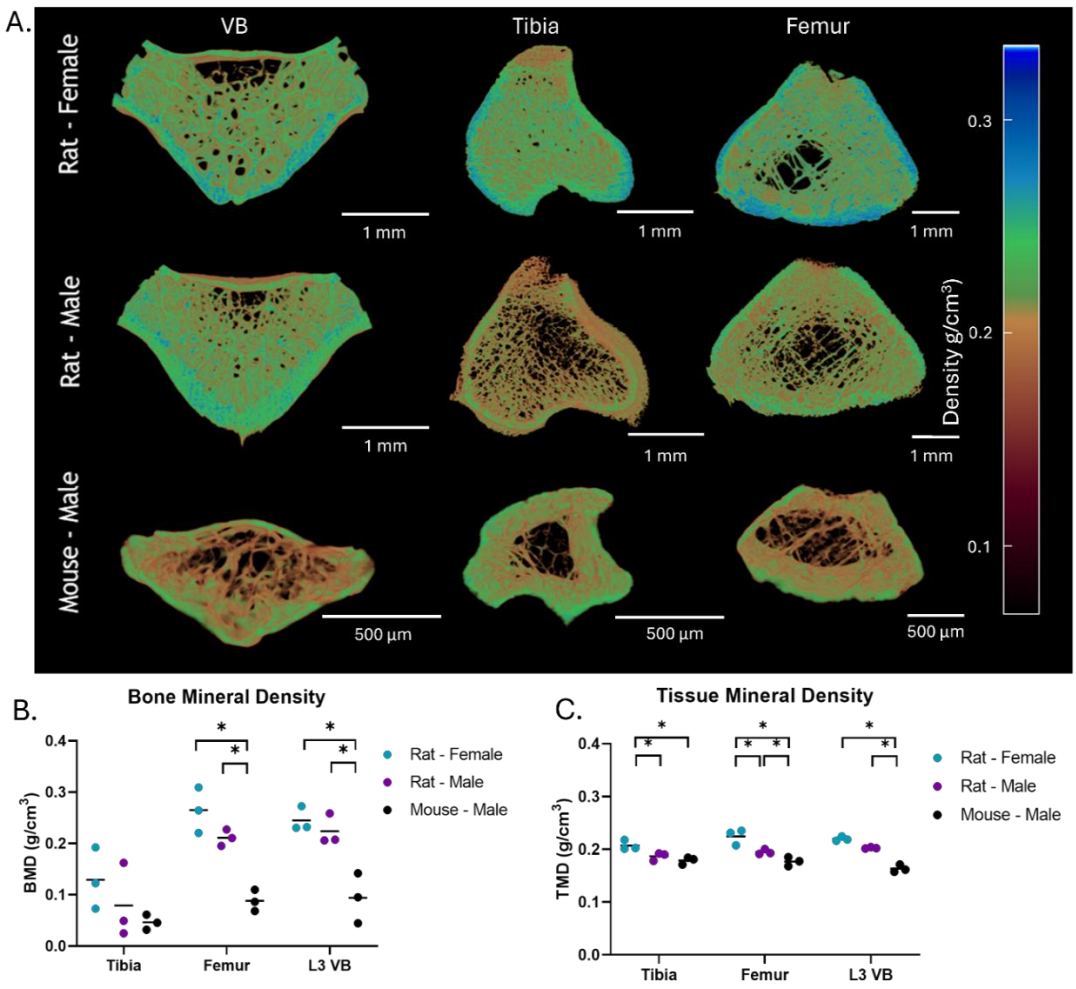

Figure 2.3.5 Region of interest density colour-coded 3D models of murine bones and density calibrated bones and tissue mineral density. *A) Mouse and rat L3 VB, tibia and femur shown. All ROIs shown were used for 3D model analysis, with a density colour-coded scale bar, 0 – 0.35 g/cm³, shown from low density (red) to high density (blue). Density was calibrated against known CaHA phantoms of 0.3 and 1.25 g/cm³. A representative 3D model is shown for each group. B) Bone mineral density (g/cm³) of all bones and murine samples, C) Tissue mineral density (g/cm³) of all bones and murine samples, n = 3. Median represented, with One-way ANOVA, multiple comparisons per bone type, P < 0.05.*

Bones were decalcified to allow efficient processing and sectioning, leaving behind the collagenous matrix. MT revealed the regions of collagen present in bones, represented by the intense blue staining for newly formed collagen and red staining for cytoplasm and muscle. Qualitatively, Tb had a lower abundance of collagen compared to Cb. Whereas Cb had stronger regions of collagen and ossified tissue (Figure 2.3.6A). COL-1 was the most abundant protein in bone, with strong positive regions around and within the OBs and BLC (Figure 2.3.6B). Interestingly, in the male tibia representative image, the transition of OBs into OCs from the reduction of immunopositivity from the endosteal surface into the Cb bone region could be visualised.

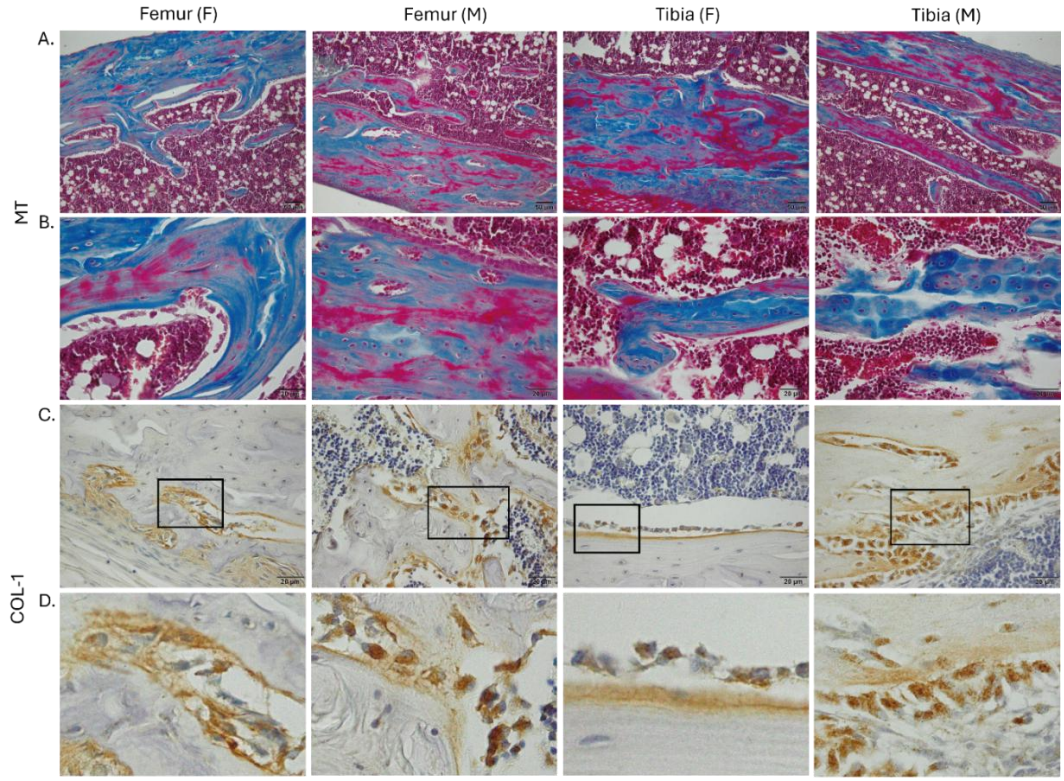

Figure 2.3.6. Masson trichrome histological stain and collagen-1 IHC on male and female rat tibia and femur. *8 µm sections. A & B) The histological stain represents collagen (blue), cytoplasm and muscle (pink) and nuclei (black). C) Immunopositivity of collagen-1 is represented by brown staining, with magnified regions highlighted by black boxes (D). n = 3, representative image shown, (A) scale bar represents 50 µm, and (B & C) scale bar represents 20 µm.*

2.3.3 Immunohistochemical evaluation of osteoblast differentiation markers in rat tibia and femur

IHC allows the detection and visualisation of proteins of interest within histologically preserved samples. Runx2 and ALP represent the early stages of OB differentiation and could be detected as immunopositivity in OBs on the endosteal seam and surface of the trabeculae in all bones (Figure 2.3.7A and 2.3.7C). ALP could also be detected in OCs, as well as in white blood cells within the bone marrow (Figure 2.3.7A/B). Despite the clear staining intensity of Runx2 in OBs, immunopositivity could be detected in OCLs and within the bone marrow niche, which may be due to non-specific binding during the endogenous peroxidase block within the IHC method, as this region was also positive within the IgG control. In Figure 2.3.7C, Runx2 could be qualitatively visualised in the

female tibia representative image of the transition of OBs into the commitment to OCs as staining intensity declines from the endochondral surface into the Cb bone region.

OPN and OCN represent the later stages of OB differentiation, commitment and maturity, with OCN positivity detected in OBs, OCs and OCLs in all bones (Figure 2.3.8A/B), as well as non-specific endogenous peroxidases within bone marrow only in the IgG control, whereby bone cells were negatively stained. Surprisingly, OPN was not detected in the samples (Figure 2.3.8C) despite its well-known role in cell adhesion and mineralisation and previous optimised conditions on rat bone samples.

Despite the abundant cellular populations commonly found in native bone, bone cells have a slow turnover. Ki-67 was a proliferation marker utilised here, and no cells were shown to have positivity in the preserved bone samples (Figure 2.3.9A). Caspase-3 (CAS-3) is a key protease involved in apoptosis, programmed cell death; however, CAS-3 is also involved with bone remodelling of osteoclastogenesis and differentiation of mOBs from iOBs. Immunopositivity could be detected in OBs (Figure 2.3.9B).

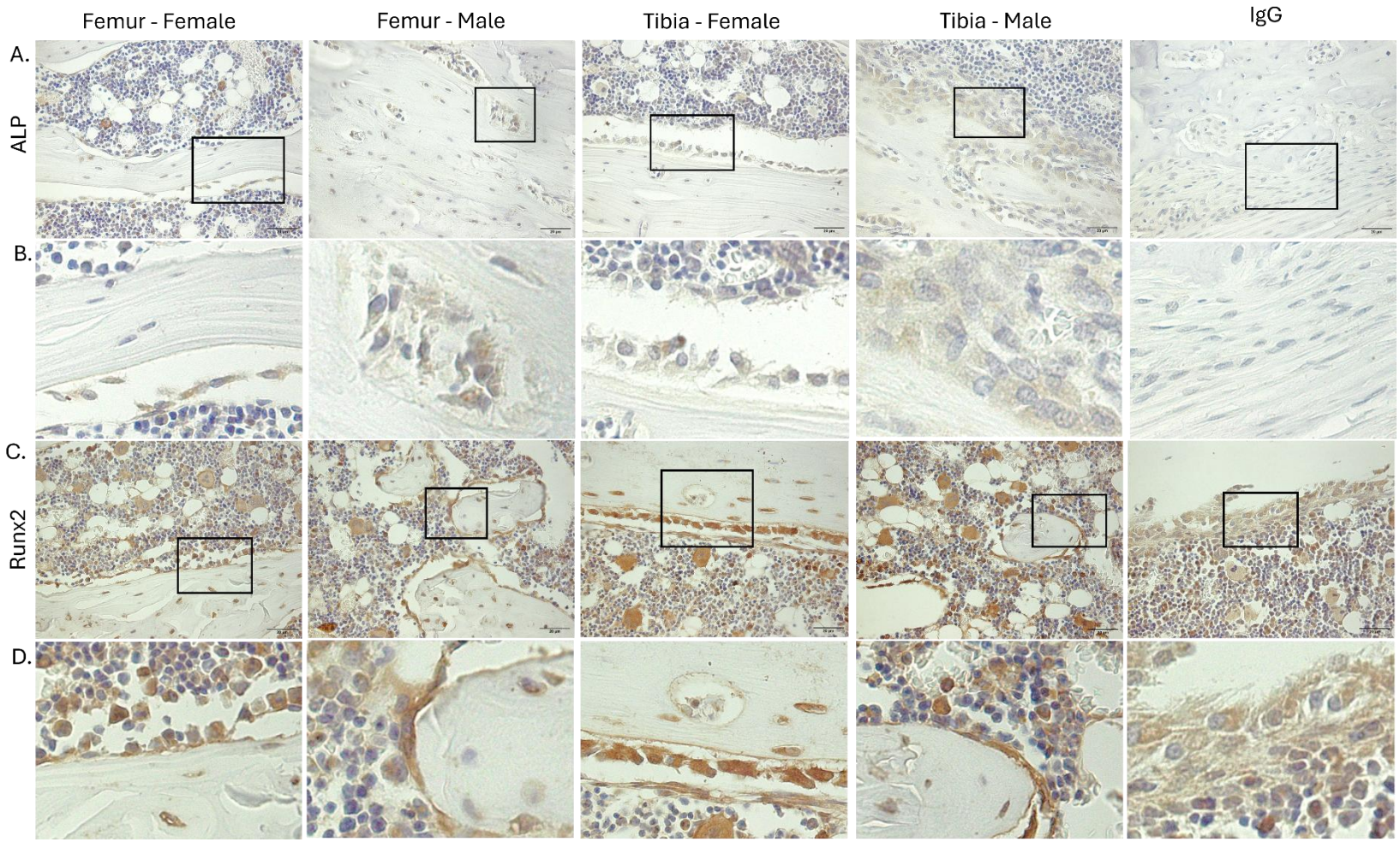

Figure 2.3.7 Alkaline phosphatase and runt-related transcription factor-2 immunohistochemistry on male and female rat, tibia and femur. *8 µm sections were used; immunopositivity is represented by brown staining. A) Alkaline phosphatase (ALP), B) magnified regions highlighted by black boxes, C) runt-related transcription factor-2 (Runx2), D) magnified regions highlighted by black boxes. IgG controls are shown. n = 3, representative image shown, scale bar represents 20 µm.*

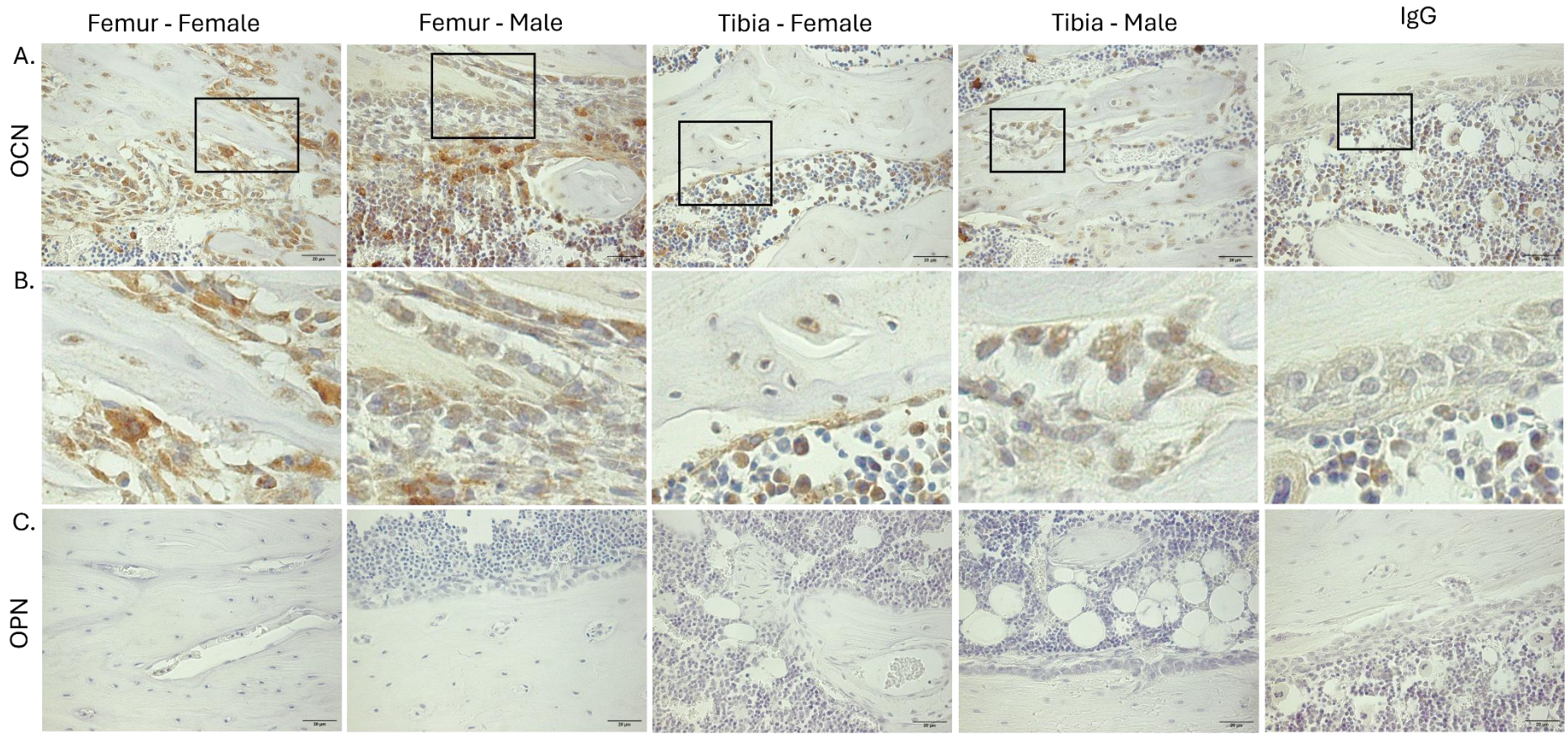

Figure 2.3.8 Osteocalcin and osteopontin immunohistochemistry on male and female rat, tibia and femur. *8 µm sections were used; immunopositivity is represented by brown staining**.** A) Osteocalcin (OCN), B) magnified regions highlighted by black boxes, C) Osteopontin (OPN). IgG controls are shown. n = 3, representative image shown, scale bar represents 20 µm.*

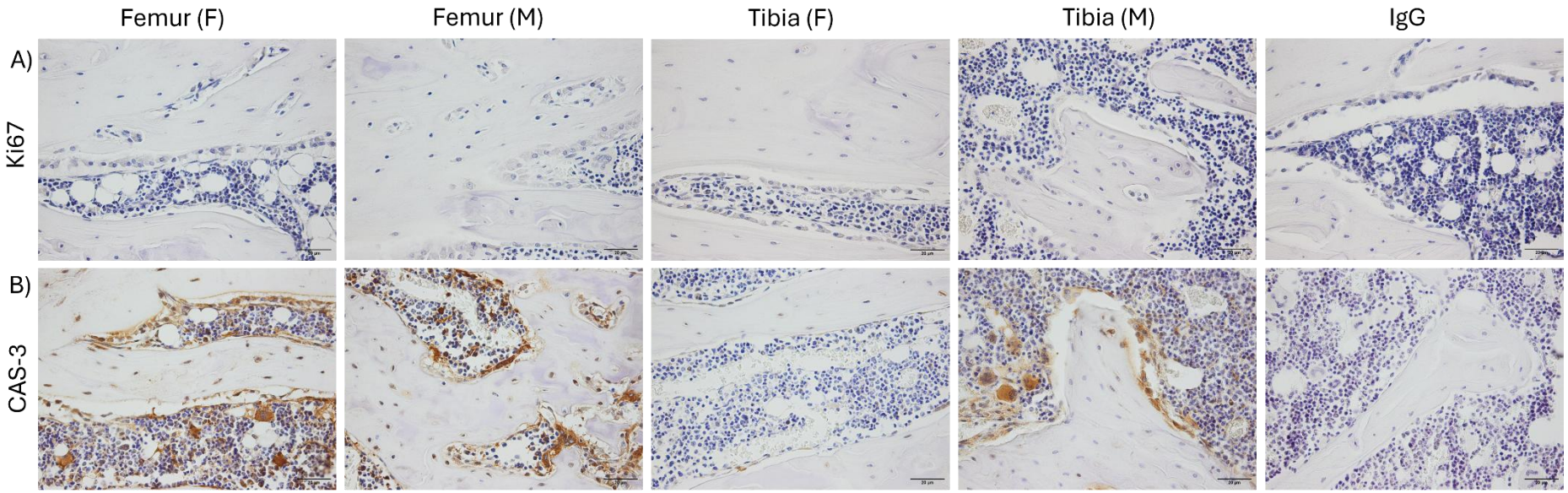

Figure 2.3.9. Ki67 and caspase-3 immunohistochemistry on male and female rat, tibia and femur. *8 µm sections were used; immunopositivity is represented by brown staining. A) Ki67 B) Caspase-3 (CAS-3). IgG controls are shown. n = 3, representative image shown, scale bar represents 20 µm.*

2.4 Discussion

This chapter aimed to determine the similarities and differences in bone architecture in murine species, with the characterisation of bone microarchitecture, composition and biological phenotype. The progressive research of developing an *in-vitro* bone model required a biological framework of native bone to act as a control, as well as translation of the 3D reconstructed bone projection into a 3D model. This was achieved via micro-CT scanning to visualise the internal and external micro/macro architecture of *ex-vivo* murine bone using high-resolution micro-CT, which was combined with histological and IHC analysis to characterise native bone composition and biological phenotype.

Various murine bones were investigated in the study to obtain values on frequently reported Cb and Tb morphometric bone parameters by the high-resolution imaging technique micro-CT. Three bones were selected for investigation: tibia, femur and lumbar VB, due to being the most frequently investigated bone types within the bone biomedical community (Prasanna, L., *et al*. 2025). Another key outcome from micro-CT was to produce a consistent ROI containing both Cb and Tb, to be used in the latter described research, for bone *in-vitro* model development. For this reason, average morphometric bone values and ROIs were defined as a characterised control, obtained from two frequently used *in-vivo* murine species, mouse and rat.

2.4.1 Murine model selection

As a research project aiming to reduce and refine animal usage in biomedical bone research, different conditions of bone development were not assessed, with ex-breeder rats chosen as the final model to continue in this study due to the mature ossified state of the skeleton, and associated cost. Alongside rats, lean C57 male mice, aged 24 +/- 2 weeks, were imaged after being used in another study conducted by Williamson (2023), to further emphasise the benefit of reducing animal usage.

Rats, of unknown age, were obtained from a teaching facility, as waste products, were originally investigated; however, due to the early developmental stage, the long bones of interest, tibia and femur, had excessive regions of cartilage and did not feature a consistent epiphyseal region (Koh, N., *et al*. 2024). This resulted in inconsistent landmark selection to achieve an equal ROI for the quantification of Cb and Tb. Martin (2003)

reported that in rats, by micro-CT imaging of the proximal tibia, epiphyseal bridges begin increasing between 3 and 10 months of age, with a peak reached at 5 months on average, whereby it remained constant up to 30 months. Immature bones can also feature increased 'porosity' compared to mature bones; however, this is often unossified regions of bone, namely cartilage undergoing intramembranous ossification, therefore not representing a true model of mature ossified bone (Jilka, R. 2013; Koh, N., *et al*. 2024).

Limited research exists comparing and characterising the morphological differences of bones in different species, which is interesting considering that an ideal *in-vivo* model to suit all bone research does not exist; the model used will depend on the study objectives (Abubakar, A. *et al*. 2016; Chevier, A., *et al*. 2014). In 1998, Aerssens reported on the interspecies differences between human, dog, pig, cow, sheep, chicken, and rat utilising Cb from the femur, and Tb from the L2 VB, based on the observation of 'baseline' values in animal models compared to humans, when utilised for research purposes, were missing in literature. The research conducted in Aerssens' (1998) study, however, was limited, with mechanically destructed bone that has undergone milling used to report on BMD. This method removes the distinction between Cb and Tb in addition to architectural complexity. Humans were reported to have a similar BMD to that of dogs and pigs, with sheep and rats having the biggest differences. Furthermore, no statistical analysis was performed, but results did emphasise the macro-differences in species (Aerssens, J., *et al.* 1998).

2.4.2 Murine bone architecture

In 2010, Bouxsein emphasised the importance of Tb.Th, Tb.N, Tb.Sp, and BV/TV quantification for assessment of Tb micro-architecture and remodelling, above other parameters. For micro-CT analysis, different considerations need to be highlighted as it is accepted that any changes in either scanning parameters, voxel size, binary assignment, or ROI selection during quantification result in output differences (Oliviero, S., *et al.* 2019; Pauwels, R., *et al*. 2015; Campbell, G., & Sophocleous, A. 2014; Verdelis, K., *et al*. 2011; Bouxsein, M. *et al*. 2010; Hara, T., *et al*. 2002). In the research presented here, commercially available CTAn was used; however, different software, such as Scanco, ImageJ/BoneJ, and dragonfly, are widely used for analysis in various bone studies

(Steiner, L., Synek, A., & Pahr, D. 2020; He, R., *et al*. 2019). Doube (2010) reported that CTAn, scanco and boneJ yielded similar results on Tb cubes scanned on the same micro-CT system; however, no statistical analysis was reported. Verdelis (2011) compared three different micro-CT systems (Scanco 35, Bruker Skyscan 1172, and GE Healthcare eXplore Locus SP), with the associated analysis software. Up to an 80% variance was noted for Tb.Th, and 150% difference for Tb.N, which was significant between the systems. This literature is important to highlight, as comparisons of morphometric output parameters to other studies should not be direct, with methods of data collection and analysis typically resulting in differences.

Traditionally, for micro-CT morphometry Cb analysis is completed at a different offset from the landmark (Figure 2.2.2) to the Tb analysis (Oliviero, S. *et al*. 2019; Campbell, G., & Sophocleous, A. 2014; Bouxsein, M. *et al*. 2010). For this study, an appropriate ROI incorporating both Cb and Tb was selected for progressive research, as explained in the subsequent chapters of this report. Due to this decision, the Cb is likely to be more vascularized and porous than the typical reported values in wider literature (Lafage-Proust, M., *et al.* 2015).

Trabecular bone, in particular the number of trabeculae (Tb.N), is a variable condition based on the *in-vivo* model investigated. The Tb.N can be altered by the ongoing bone remodelling processes, specifically the balance and regulation between OBs and OCLs. In addition, species, age, sex, mechanical stress, hormonal changes and nutrition can result in biological fluctuations (Rodriguez, V., *et al.* 2024; Sequeira, L., *et al.* 2020; Nieves, J. 2017; Jia, M., *et al*. 2013). It is understood that hormones have a great impact on both Tb and Cb structure, resulting in altered function. In males, testosterone supports periosteal bone expansion and prevents Tb loss (Tenuta, M., *et al*. 2025), whilst in females, estrogen prevents loss to both Cb and Tb volume (Cauley, J. 2015). As ex-breeder mature rats, in particular the female rats that underwent pregnancy and lactation periods, it was hypothesised that females would have reduced bone volume and increased porosity compared to males due to the natural fluctuations of estrogen, and demand on calcium reserves during pregnancy and lactation (Lujano-Negrete, A., *et al*. 2022; Kovacs, C. 2001). Due to the age of the rats used in this study, > 6 months, it

can be assumed that only one reproductive cycle was completed before sacrifice. No loss of bone volume was discovered in this study between female and male rats.

In a study conducted by Bowman (2002), Sprague Dawley rat maternal tibia, age of sacrifice was not specified, were assessed via binary histomorphometry indices after two reproductive cycles, with assessments completed after different lactation periods after weaning. The study showed a rapid increase in Tb.N after the lactation period, with an increase in Tb.Th from 0.4 mm to 0.6 mm after 4 weeks (Bowman, B. 2002). A second study, conducted by Bakker (2018) supported the findings by Bowman (2002), however, utilising the imaging technique of micro-CT, and inclusion of the assessment of tibia, femur and lumbar vertebra of rats, species not specified, aged 14 – 19 months after two to three reproductive cycles (Bakker, C. *et al.* 2018). In Bakker's (2018) study, the proximal tibia, Tb.N remained reduced for up to 12 weeks for the model following reproduction, ~2.5 mm^{-1} throughout compared to a range of 4.5 mm^{-1} decreasing to 2.7 mm^{-1} from week 0 to week 12 of the study for the virgin models. Tb.Th was increased in the reproduced model compared to the virgin model in all time points, with week 0 and week 12 having a statistical difference (Bakker, C., *et al.* 2018). In the L4 VB, Tb.N was significantly reduced in the reproductive group compared virgin, 2.7 mm^{-1} compared to 3.5 mm^{-1}, respectively. No statistical difference was identified for Tb.Th between the two groups, with a reported average of 0.08 mm. In the femur Cb, no statistical difference was reported for bone volume between the two groups (Bakker, C., *et al*. 2018).

To further explore physiological and morphological 'standard' *in-vivo* biomedical models, Shim (2022) conducted a study to determine the bone structure of ageing (6 – 22 months) C57 male and female mice. The mice were fed a standard diet, with the femur, tibia and L3 vertebrae imaged by micro-CT with a resolution of 15 µm (Shim, J., *et al.* 2022). The Tb ROI offset from the landmark reported was equal to that presented in this study, 0.5 mm, whereas the Cb measurement was 1 mm (Shim, J., *et al*. 2022) compared to 1.5 mm used in this study. In the male femur, Tb.Th did not significantly change with age, a range of 0.07 – 0.09 (mm) (Shim, J., *et al*. 2022), with 0.05 – 0.07 mm reported in this study. Tb.N reported by Shim from 12 – 22-month-old mice did not match that of this study (6 – 7 months), 1.5 +/- 0.5 mm^{-1}, as with aged 12-month Tb.Sp 0.3 +/- 0.1 µm (Shim, J., *et al*. 2022). An overall trend in all reported bones is that Tb.Th remains

constant with no statistical significance on age, Tb.N decreases with age, resulting in increased Tb.Sp. Males have increased BV/TV, Tb.Th, and Tb.N compared to females (Shim, J., *et al.* 2022).

Bones do not have exact physiological consistency. Natural biological variance is present between age, sex and disease state 'matched' species; therefore, a standard control bone model can only achieve average morphometry. However, as reported in various literature (Nieves, J. 2017; Barak, M., Lieberman, D., & Hublin, J. 2013; Wray, A., Okita, N., & Ross, C. 2011), the morphometric values reported in this study are within the range of normality for the murine models used.

2.4.3 Murine bone composition

Continued utilisation of the non-destructive technique of micro-CT provided an insight into the bone's inorganic structure. Alternatively, and more frequently clinically reported, DEXA is used to assess mineral density of large body vertebrates (Tadros, S., *et al*. 2023; Haseltine, K., *et al*. 2021). However, higher resolution is possible with micro-CT for research purposes, with calibration performed in the current study where micro-CT binarization scale was completed using 0.3 and 1.25 gHA/cm^3 calibration rods. Mice's bone density alters depending on strain, age and sex (Kranioti, E., Bonicelli, A., & Garcia-Donas, J. 2019), as reflected in this study. Beaucage (2016) reports BMD of male C57 mice total whole bodies from ages of 2 – 52 weeks, with a substantial increase from ~0.08 g/cm^3 to 0.3 g/cm^3 from week 2 to 8, respectively, whereby a small progressive increase can be seen until week 52. No individual bones were reported (Beaucage, K. *et al*. 2016). Moriishi (2022) supports the findings of a higher density found in Cb, compared to Tb, with 0.15 and 0.07 g/cm^3, respectively in C57BL/6N male mice. Further, Paragerogiou (2020) reported C57BL male mice femoral Cb TMD of ~ 0.1 g/cm^3, whereas different strains of mice, DBA and C3H, had raised TMD of 0.11 g/cm^3 (Paragerogiou, L., *et al.* 2020).

A decrease in BMD will typically result in increased bone porosity (Kranioti, E., Bonicelli, A., & Garcia-Donas, J. 2019), an interesting correlation was discovered for the male rats against female rats. It was originally hypothesised that females have a reduced BMD/TMD compared to males due to pregnancy and lactation periods (Degennaro, V.,

et al. 2021). Ho (2011) reported with DEXA, rat virgin female tibia average as 0.15 g/cm^3 compared to 0.12 g/cm^3 ovariectomized, Rodriguez (2024) male femur average as ~ 0.18 g/cm^3 as control against 0.1 g/cm^3 for streptozotocin-induced diabetic rats with DEXA, and Li (2013) reporting both femur and VB as 0.21 g/cm^3 and 0.2 g/cm^3, respectively with a significant decreases in ovariectomised female virgin rats. Further from this, even the region from which measurements are taken can alter the output value, as reported by Choi (2024), who noticed the differences in BMD within the medial and lateral regions of both tibia and femur in human patients assessed with DEXA, due to the load bearing associated with locomotion.

Rat bones underwent decalcification and tissue processing for histological and phenotypic investigations. At this stage, due to equipment malfunction, samples were destroyed. Due to this, the remaining samples were used for histological investigations within this study, instead of the original purpose of mechanical analysis by a 3-point bend test (Wang, L., *et al*. 2022; Bailey, s., & Vashishth, D. 2021; Martain, R. 2007). Impact of the loss mechanical analysis for the presented research will be discussed in Chapter 7.

As standard, H&E was completed to visualise the general tissue composition, architecture and cellular presence – all three bone cell types were visualised. No qualitative architectural difference was noted between the tibia and femur from males and females (Jia, M., *et al.* 2013). Alongside this, ACB and SO were completed to visualise the NCP component of bone histologically (Zinck, N., & Franz-Odendaal. 2020). Regions of proteoglycans were more concentrated in the metabolically active Tb, compared to being dispersed in Cb, perhaps due to higher regions of unossified collagenous tissue undergoing bone remodelling in Tb (Heath, S., *et al*. 2023; Lim, J. *et al*. 2013; Jia, M. *et al*. 2013).

Collagen is an integral part of bone biology, released by OBs which line the endocortical and trabecular surface. Collagen is highlighted by the blue stain, in MT throughout both Tb and Cb, which is classically used to histologically investigate bone remodelling and calcification. During the bone remodelling process, collagen becomes denser with a higher frequency of cross-linking and different molecular arrangement, causing newly formed bone to be stained blue, whereas ECM is stained red as represented by higher abundance within Cb regions compared to Tb (Lee, C., *et al.* 2019; Jia, L., *et al.* 2013; Lim,

J., *et al.* 2013). Wu (2020) investigated the changes in collagen abundance and structure in healthy and diseased (osteoarthritis or osteonecrosis) femoral heads from human patients, revealing the decrease of newly formed collagen in diseased states, with only mature bone remaining (Wu, Z., *et al.* 2020), thereby showing the bones presented in this study were in a healthy condition.

2.4.4 Bone cell differentiation markers

The cellular population constituting healthy bone and remodelling is well established. In mature bone, OCs are the most abundant cell type, of 90 – 95% (Mullender, M., *et al.* 1996), OBs constitute only 4 – 6% of cells in total bones (Capulli, M., Paone, R., & Rucci, N. 2014; Basso, N., *et al*. 2005), and OCLs constitute approximately 1% (Alizae, M. 2008). With a research focus on bone remodelling and driving OB differentiation to influence matrix deposition in an *in-vitro* bone model, the OB population were further investigated to assess the protein presence and location within the bone architecture. Runx2, OCN, osteonectin, OPN and ALP are OB markers which are frequently reported on to assess remodelling within bones (Franz-Odendaal, T., Hall, B., & Witten, E. 2005), as different proteins increase in abundance due to cellular phenotype stage of OBs and in turn, the physiological impact OBs have on the bone environment.

The murine models used in this study were classified as mature; therefore, osteogenic activity is reduced compared to immature models (Beaucage, K. *et al*. 2016; Safadi, A., Livne, E., & Reznick, A. 1997; Nishimoto, S., *et al*. 1985), perhaps resulting in no detectable OPN positivity due to bone maintenance (Lin, C., *et al*. 2022; Si, J. *et al.* 2020). Perrien (2002) describes post-proliferative OBs proving negative for OPN positivity, in contrast to active bone remodelling by assisting in biomineralisation (Depalle, B., *et al.* 2021). Smith (2020) reports OCN levels fluctuating naturally during ageing in males, circulating in a ‘U’ shaped trend of high in youth, declining in maintenance before rising again in mature bones. Aside from age, research conducted by Hiam (2021) reports different basal levels of OCN in males and pre-menopausal females, in agreement with Michelsen (2013).

IHC is a very widely used detection technique in biomedical investigations, with different steps of optimisation required to block non-specific binding of background tissue to

show the true positivity of the antibody used. A particularly important step for bones is to block endogenous peroxidases due to the bone marrow containing myeloid cells (Tsutsumi, Y. 2021). Within this study, optimised antibody concentrations were pre-determined before all samples were conducted at the same time for each protein of interest. Unfortunately, due to time constraints and material availability, this experiment could not be repeated to attempt to remove endogenous peroxidase background staining for the bones at this stage. IgG controls for all proteins of interest for bone samples are shown, showing background endogenous staining positivity in both Runx2 and OCN, but clear intensity of positivity can be visualised in OBs, which was not observed in IgG controls, demonstrating specificity within these cells.

2.4.5 Conclusion

Bone is a dynamic organ with a complex architecture that is constantly adapting to the surrounding environment, with a multifaceted composition assisting the functionality and physiology. Overall bone architecture, Cb and Tb, is consistent between species typically used for *in-vivo* biomedical investigations; however, various factors influence the micro/macro bone architecture, resulting in differing Tb.N, and composition, such as BMD, perhaps attributed to differences in sex. Despite efforts being made to age and sex match tissues, natural biological differences are evidenced within the same bone types (Tibia, femur and VB), and when comparing to current literature, it was clear that no consistent value for morphometric outputs exists.

From the investigation, a range of values will be taken into consideration, such as median Tb.N, Tb.Th and TMD, to develop an *in-vitro* bone model that aims to achieve biomimicry of biological architecture. As discussed further in chapter 3, bone type (tibia, femur and VB) and species have limitations of creation for the process of 3D bioprinting; however, the information gathered that has been presented here will assist in development.

Chapter 3 – *In-silico* generation of a 3D printable bone model

Method and considerations of computer assisted design manufacturing a 3D bio-printable bone model derived from ex-vivo murine bones obtained by micro-CT high-resolution imaging.

3.1 Introduction

Additive manufacturing (AM) is the computer-controlled technological process of fabricating physical 3D geometries directly from computer-assisted design (CAD) models within an XYZ spatial location, through an additive process. The resulting 3D model's function, structure, and customisation are at the forefront when deciding the specific AM technique and the required materials. There are two distinct types of AM, 3D printing and 3D bioprinting. Common 3D printing techniques include FDM, SLA, selective laser sintering, and electron beam melting (Lakkala, P., *et al.* 2023; Palmquist, A., *et al*. 2023; Naeem, O., *et al.* 2022; You, Y. *et al*. 2022; Awad, A., *et al*. 2020) whereas 3D bioprinting commonly includes EBB, inkjet, laser-assisted and SLA (Wu, C., *et al.* 2023; Kacarevic, Z., *et al*. 2018). AM advancement has assisted in innovations in aerospace, automotive, functional prototypes, anatomical models, biomedical research and healthcare such as customisable prosthetics and implants (Acierno, D., & Patti, A. 2023; Lakkala, P., *et al.* 2023; Kumar, R., Kumar, M., & Chohan, J. 2021; Prasher, A., *et al*. 2021).

3.1.1 Overview of three-dimensional printing techniques

Rapid prototyping techniques, such as FDM, form plastic-based mm – cm range models. FDM is an extrusion-based technique that utilises thermoplastics to deposit a 3D design layer-by-layer (Kristian, R., *et al*. 2021). In contrast, SLA is a photopolymerization technique which uses a thermosetting liquid resin bath to cure a 3D design layer-by-layer into a hardened plastic, with a scale in the µm – cm range (Lakkala, P., *et al.* 2023). EBB printing generates a 3D design by expelling a gel-based compound via pneumatic pressure through a nozzle layer-by-layer, often in µm – mm range. However, larger models can be printed in the cm range, using non-Newtonian biomaterials, often containing bioactive materials and live cells, defined as bioinks (Zhang, J., *et al*. 2021). An overview of the three highlighted techniques is summarised in Figure 3.1.1.

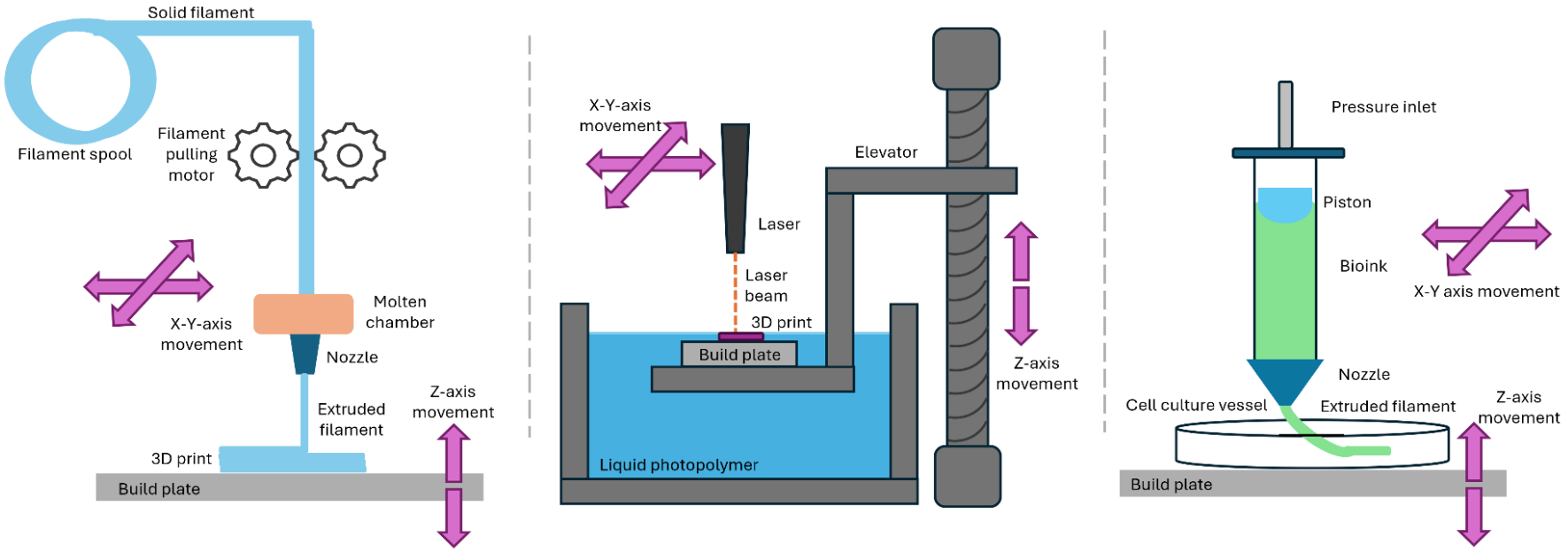

Figure 3.1.1. General mechanism of action for fused deposition modelling, stereolithography and extrusion bioprinting. *A) FDM 3D models are produced by feeding a solid filament of thermoplastic from a large spool into a molten chamber, with the capillary flow of a non-Newtonian fluid through a nozzle for layer deposition onto the print bed, followed by layer-to-layer adhesion in the geometrical formation. Sacrificial supports are required to 3D print complex geometries, B) SLA uses a photochemical laser to cross-link chemical monomers into polymers onto a build plate, layer-by-layer. SLA can achieve complex geometries with minimal supports required in the building process, C) Extrusion bioprinting uses controlled pneumatic pressure, or mechanically driven piston, to deposit individual layers, or droplets of viscous rheological bioinks in a geometrical formation. The bioink is contained within cartridges, and geometry complexity depends on the material used and if a printing support bath is used.*

3.1.2 Three-dimensional printing applications

The breakthrough benefit of 3D bioprinting biological structures is to create biological models that can mimic native tissue architecture. Overall, it is accepted that 3D *in-vitro* cultures present improved cellular dynamics and complexity by the addition of an ECM compared to standard monolayer culture (Chapter 1, section 4 – 5, Chapter 6) (Yoon, H., *et al*. 2025; Izumiya, M., *et al*. 2021). The comparison of 2D and 3D *in-vitro* studies and their use in the preliminary stages of biomedical research continues to be investigated (Sun, M., *et al.* 2021; Fontoura, J., *et al*. 2020; Melissaridou, S., *et al.* 2019; Soares, C., *et al*. 2012). Notably, the national centre for the replacement, refinement and reduction of animals in research (NC3Rs) and other humane research organisations continue to fund innovative research projects for the development of alternative animal models in the biomedical science field (Yuste, I., *et al*. 2021; Caleb, J., & Yong, T. 2020; Sitarski, A., *et al*. 2018).

EBB printing is quickly becoming readily available in tissue bioengineering laboratories due to the gentle processing conditions for live cell cultures. EBB has the potential to be used for a wide range of *in-vitro* applications due to limitless CAD design in combination with the increased availability of 3D EBB biomaterials (Badhe, R., *et al.* 2023; Szwed-feorgiou, A., *et al.* 2023; Dec, P., Modrzejewski, A., & Pawlik, A. 2022; Gao, C., *et al.* 2017). Major themes of research for 3D EBB printing include a pre-clinical pipeline for novel drug discovery (Gao, G., *et al*. 2021), tissue engineering (Germaini, M., *et al*. 2022; Gleadall, A., *et al*. 2018; Zhang, Z., & Wang, X. 2017), regenerative personalised medicine (Lam, E., *et al*. 2023; Bagaria, V., Bhansali, R., & Pawar, P. 2018) and biological based therapies (Bandyopadhyay, A., Mitra, I., & Bose, S. 2020). The resolution and reproducibility of EBB constructs are limited with current technology (Zandrini, T., *et al*. 2023), however, the field of tissue engineering is rapidly developing with innovation in resolution (Guida, L., Cavallaro, M., & Levi, M. 2024; Wu, C., Zhu, Y., & Woo, Y. 2023), material complexity (Jose, J., *et al.* 2024; Wan, H., *et al.* 2024), and AM processes (Liu, Y., & Sing, S. 2023; Memarzadeh, A., *et al.* 2023).

FDM and SLA within biomedical research have limited purposes for cellular research due to the biologically destructive nature during production and the bio-incompatibility of the materials required (Kafle, A., *et al*. 2021), however, developments have been made

in the fabrication of tissue and organ anatomical models, customisable prosthetics, and implants (You, Y., *et al*. 2022; Deshmane, S., *et al*. 2021 Kumar, R., Kumar, M., & Chohan, J. 2021; Tack, P., *et al*. 2016); as well as, µm-gauge needles and tablets for drug delivery (Lakkala, P., *et al.* 2023; Hoffmann, L., Breitkreutz, J., & Quodbach, J. 2022; Caudill, C., *et al*. 2021).

Polymer 3D models generated via printing fabrication methods, FDM and SLA, allow improved geometry, resolution and complexity compared to EBB, notably SLA with overall improved scalability, reproducibility, and long-term storage (Deshmane, S., *et al*. 2021). FDM is the most widely accessible form of 3D printing, due to the low cost of the 3D FDM printers and associated materials, whereas SLA is beneficial for speed, resolution and complexity (Lakkala, P., *et al.* 2023).

3.1.3 Three-dimensional printing materials

Consideration of printing material for all 3D printing/bioprinting techniques are varied per method, with important decisions to be made on material or ink, concerning the associated limitations of each fabrication method. The restrictions of each material define the attainable dimensions of the 3D model, the morphology, reproducibility, printability and overall structural complexity of the final 3D generated model (Bouzaglou, O., Golan, O., & Lachman, N. 2023). FDM most commonly uses thermoplastic polymers, which are cheap, easily colour-customisable, biodegradable over a prolonged period, and recyclable due to no chemical bonding taking place to form the model. Polylactic acid (PLA), $C_3H_4O_2$ is the most used filament biopolymer for FDM prototyping and is produced by condensing lactic acid, which is obtained from renewable resources through fermentation, such as corn, sugar and beets. PLA can be formulated into a composite polymer, enhancing the flexibility (Kristiawan, R., *et al.* 2021; Tumer, E., & Erbil, H. 2021). FDM systems can also facilitate specially created ‘material inks’ which can be formed from a fusion of pharmaceutical agents, excipients and binders incorporated into thermoplastic polymers for 3D printed pharmaceutical agents (Chai, X., *et al.* 2017), however more research is required in this field due to limited availability of biodegradable thermoplastic polymers for human consumption (Lakkala, P., *et al.* 2023).

The SLA method requires resin containing photopolymers and photo-initiators. The photopolymers contain monomers that are cured with ultraviolet light to form solid macromolecules, by the generation of modifying reactive species. Crosslinking degree, or stiffness, can be controlled by light exposure time, and wavelength applied to the model during curing (Curti, C., Kirby, D., & Russell, C. 2024; Kam, D., *et al*. 2024). Similar to FDA, a 'material ink' can be generated by loading the photocuring resin with drugs (Lakkala, P., *et al.* 2023), for example, Prasher (2021) generated a pharmaceutical agent loaded oesophageal-targeted 3D SLA printed ring. Whereby testing within an *in-vivo* environment showed controlled elution kinetics based on crosslink density (Prasher, S., *et al.* 2021), however, more research needs to be completed on the biocompatibility of these materials long term to achieve FDA approval.

As with any manufacturing process, considerations and rules need to be met to achieve an effective end product (Bouzaglou, O., Golan, O., & Lachman, N. 2023; Wickramasinghe, S., Do, T., & Tran, P. 2020). For FDM, the major consideration is nozzle size and print speed. The standard size of 0.4 mm often produces a good balance between print speed, precision, and resolution (Elhattab, K., Bhaduri, S., & Sikder, P. 2022). Smaller nozzles are key for detailed prints, with a minimum size of 0.1 mm possible; however, these often incur blockages and failed prints. Larger nozzles can also be used, up to 2 mm, but the quality of the print may suffer due to inconsistent flow and the requirement for even heat displacement on the material (Czyzewski, P., *et al*. 2022). Other major considerations include the generation of supports for overhangs and complex shapes. Supports are generated often in CAD, but more detailed control over placement is found in slicer software, such as Cura, or simplify3D. For SLA less is required to be considered aside from material choice and cross-linking degree, with supports also required for overhangs or thin (below the mm range) wall thickness.

EBB requires extensive research for material choice and printing considerations (Chapter 1, section 1.6.1 and chapter 5, sections 5.1.1 and 5.1.4), as biomaterials options are extremely varied in application. However, the majority of bio-inks are hydrogel-shear thinning materials which enable the deposition of ink in a specific orientation through the process of EBB (Gogoi, D., Kumar, M., & Singh, J. 2024). Hydrogel-cell suspensions are typically printed in a liquid gel solution state, often undergoing further gelling

transitions that are chemically, physically or mechanically triggered and normally crosslinked after the extrusion process of the bioink to improve stability (Chen, X. *et al.* 2023; Zhang, J., *et al.* 2021; Gungor-Ozkerim, P. *et al*. 2018). Complex structures require printing supports, such as micro-particle support baths, which support the ink during the extrusion process (Ombergen, A., *et al.* 2023; Brunel, L., Hull, S., & Heilshorn, S. 2022; Shiwarski, D., *et al.* 2021).

3.1.4 Three-dimension imaging techniques

Alongside the choice of material, different geometries can be generated within a 3D space. Different 3D medical imaging techniques, such as CT (micro- and nano-inclusive), DEXA, and magnetic resonance imaging (Mandolini, M., *et al*. 2022; Virzi, A., *et al.* 2019), make it possible to create high-resolution replicas of biological structures using CAD. As previously discussed, (Chapter 2.1.2), micro-CT uses x-ray radiation to capture 2D planar images, which can be translated into a 3D projection using binarised grey pixels of information (Stauber, M & Muller, R. 2008). Typically, dense in-organic mineralised tissues, such as bone, provide the best contrast for micro-CT visualisation, however for soft organic tissues to be visualised on micro-CT contrast agents are required such as Lugol's Iodine (Heimel, P., *et al*. 2019), Iohexol (Self, T., *et al.* 2020) and graphene oxide (Aminu, A., *et al.* 2022) can be used (He, Y., *et al.* 2022; Ashton, J., *et al*. 2014; Wathen, C., *et al*. 2013) which enable the approach described to be replicated on a variety of tissue types. Reconstructed projections can be exported as a variety of file types, such as standard tessellation language (STL) and polygon file format (Ply) or digital imaging and communications in medicine (DICOM) (Flaxman, T., *et al.* 2021; Kamio, T., *et al.* 2020), dependent on the imaging and reconstruction system (Steiner, L., Synek, A., & Pahr, D. 2020; He, R., *et al*. 2019). Thereby making the biological structures available for CAD, translatable to a 3D printable model. Alternatively, CAD software can be used to generate originally designed models.

3.1.5 Standard tessellation language – Meshing algorithm, file output, code and units

To generate a 3D model, the entire object surface requires a triangulated mesh boundary. By generating a mesh, a subdivision of a continuous geometric domain is produced to provide information on surface structure, tolerance and boundaries (Figure

3.1.2B) (He, Y., *et al.* 2022; Lee, C., *et al.* 2020). Structured, or mapped mesh, follows three tessellation rules: no overlapping or gaps; tiles must be regular consistent polygons; and each vertex must look identical. The algorithm is complex as the geometrical calculations are completed in a 2D space; however, this can sometimes cause errors when the mesh is translated into a 3D geometry. Unstructured, or direct meshing is the alternative, with vertices connected in irregular patterns for more complex shapes and surfaces, however this method tends to produce a higher frequency of meshing errors as the algorithm attempts to mesh the entire 3D geometry, without sub-dividing into 2D planes of reads (Yu, K., *et al*. 2022; Wang, M., Gao, J., & Wang, X. 2017). 3D model outputs vary depending on the selection of the triangle meshing algorithm (Figure 3.1.3A) applicable to the 2D Z-stack created by the micro-CT scanning process, available in CTAn, which is the software utilised for this workflow.

The current CTAn meshing algorithms include marching cubes 33 (MC33), double times cubes (DTC) and adaptive rendering (ATR). MC33 is an algorithm to extract 2D surface mesh from a 3D volume by iterating across the volume in the VOI, searching for regions which cross the level of interest to create a uniform mesh across the boundary of information. Simply, the entire VOI is split into empty cells and if the cells contain voxel information, it is compiled into a 2D mesh with neighbouring voxels (Figure 3.1.2A), which is then filtered into a 3D polygonal mesh model to represent the triangular surface according to standard meshing rules (Figure 3.1.2B) (Custodio, L., Pesco, S., & Silva, C. 2019; Lee, T., & Lin, C. 2001; Lorensen, B., & Cline, H. 1987). DTC is similar to MC33; however, fewer regions are read as actions, therefore producing a smaller file size and reduced surface detail (Preim, B., & Botha, C. 2014). Lastly, ATR is an algorithm designed by Bruker, and the mesh characteristics follow meshing rules, like MC33 and DTC, to the 3D model but with higher control by selected parameters found in CTAn, e.g., reduced locality, reduces noise between detected pixels, and tolerance-defined accuracy between pixel borders to assist in a successful mesh generation with minimal boundary errors.

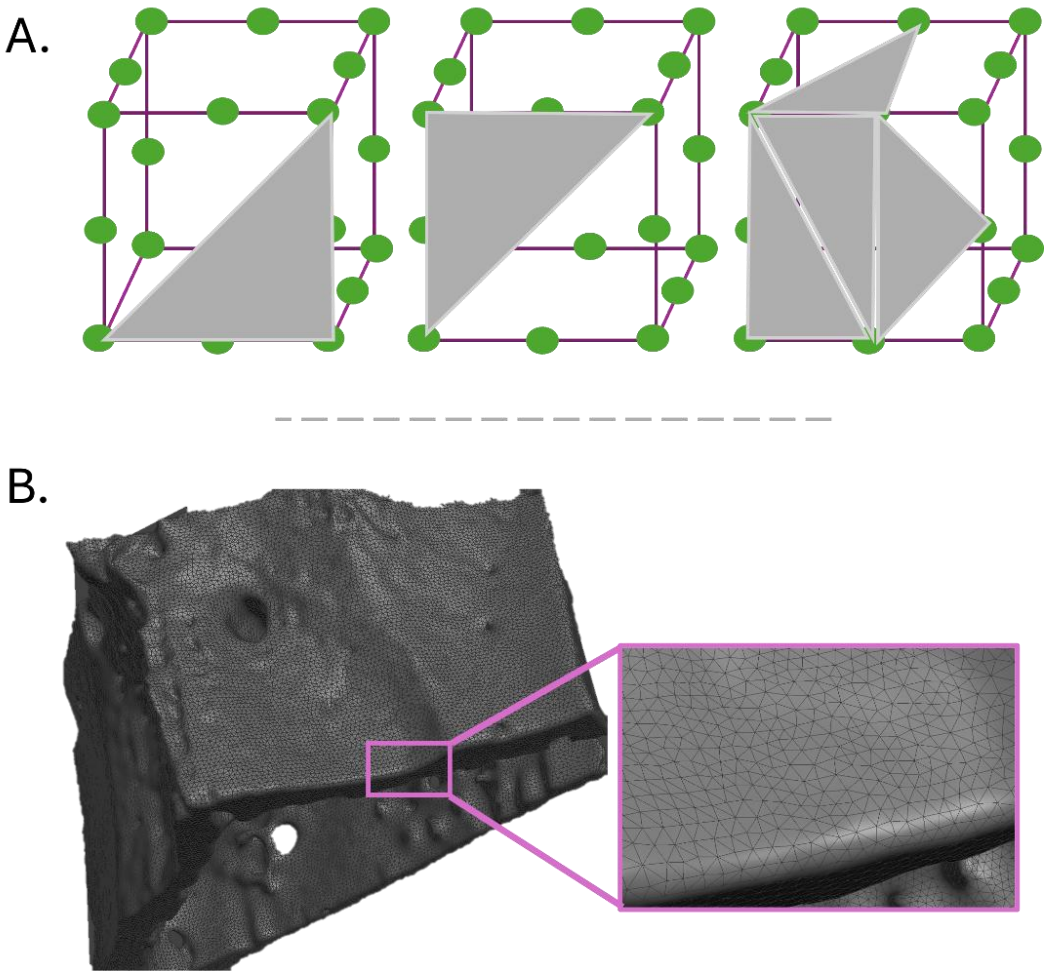

Figure 3.1.2. Examples of topologically different isoform configurations of marching cubed 33 meshing algorithms, and the resulting tessellated mesh wireframe on a mouse VB*. A) Marching cubed 33, double times cubed, and adaptive rendering all follow the same principal of mesh generation but differ with the volume of information, accuracy and quantity of empty cell reads. Mesh is defined by both vertices (green) and triangles (grey), combined to form 3D information. B) Adaptive rendering tessellated wireframe on mouse VB rendered surface, with zone of artificial magnification (purple).*

Despite the choice of algorithm, different 3D model file types can be exported. This includes STL, ply, connect textures (ctm) and polygon-trochoid-profiles (p3g). STL and ply are widely accepted mesh file types, whereas ctm and p3g are Bruker-specific file types. STL files are most widely and reliably used within CAD software interfaces; therefore, focus within this chapter will utilise this file type (Kamio, T., *et al.* 2020; Hallgren, S., *et al.* 2016). 3D models can be exported as either ASCII or binary, with ASCII encoding coordinates of the vertices of each triangle in the exact location producing a highly complex 3D model, whereas binary encodes the components of unit vectors normalised to each triangle (Isenburg, M., & Snoeyink, J. 2002). Lastly, the 3D model can be exported

in different units (µm, voxel, mm and inch) to alter the overall dimension of the model in proportion to the original scanning resolution.

3.1.6 Computer-assisted design, standard tessellation language and geometry code

Traditionally, CAD is used to computationally design, modify and simulate a 3D model for real-life applications from drawings, or basic geometry (Squares, circles and rectangles etc.) by engineers and designers in a wide variety of professions, within bio-engineering field this is often utilised for the finite element modelling (FEM) analysis (Oliviero, S., *et al*. 2019; Baghdadi, L., Steinman, D., Ladak, H. 2005). The design process can begin from scratch, alternatively, an existing 3D STL can be used, or the DICOM model can be imported into the design space interface for 3D printing/bioprinting. In the context of translating an STL model into a 3D model, CAD is used to transform the orientation, size and, if desired, shape of the model (Kamio, T., *et al*. 2020).

Different approaches and interfaces can be applied to model rendering based on the software availability, proposed end-model functionality and intended 3D printing technique. Autodesk® meshmixer (Prasher, A., *et al.* 2021), free CAD, and Rhino are open-source CAD software with user-friendly interfaces and self-directed learning materials available online with sufficient capabilities for basic rendering. Whereas Autodesk® Fusion 360®, Autodesk® Inventor, Blender® and SolidWorks (BioCAD™) require a paid licence to access but enable detailed analysis of models and CAD rendering possibilities. Various Python libraries exist and are being developed for CAD generation and rendering; however, they require more user optimisation and confidence with coding compared to the aforementioned interfaces (Smeets, S., Renaud, N., & Willenswaard, L. 2022; Hart, K, & Rimoli, J. 2020).

The final step in the 3D imaging to 3D printed model pipeline is to slice the 3D rendered CAD model. Slicer software is required to translate STL 3D models into toolpath geometry code (G-CODE) instructions, which is the language that commands the actions of the 3D printer and ultimately the printing of the 3D model (Tomiyama, T., *et al*. 2009). It is not uncommon for slicer software to be incorporated into 3D bioprinters, as typically the smaller and simplistic models contain less information and use simple toolpath GCODE directions, which dictate the movement of the extruder in the case of FDM and

EBB, or laser in SLA (Montalti, A., Ferretti, P., & Santi, G. 2024). Manufacturers for FDM and SLA may recommend a specific slicer software to be used with the 3D printers, and depending on the input file, STL or DICOM (Kamio, T., *et al*. 2020), or STLs generated from CAD, different software may be required (Yong-Sang, L., *et al.* 2022; Sljivic, M., *et al*. 2019). Free open-source software is readily available, such as Cura Ultimaker, craftware, slic3r, 3D slicer image computing platform and Lychee, with purchasable software including Simplify3D, SelfCAD and Repetier.

3.1.7 Aims and objectives

Develop an informed workflow to render micro-CT images into 3D computer-assisted design model.

Investigate the computational decisions required to translate micro-CT high resolution imaging 3D models into a 3D printable model.

Generate *in-silico* 3D models of trabecular and cortical bone rendered from micro-CT *ex-vivo* outputs of murine tibia, femur and VB that are suitable for 3D printing applications.

3.2 Materials and methods

3.2.1 Experimental design

Micro-CT imaging was used to obtain high-resolution 3D computational information on bone morphometry and physiology (Chapter 2). This information was translated into a CAD suitable for 3D printing using standard tessellation language STL (Figure 3.2.1). The resulting STL 3D model was exported in different meshing algorithms, code and units, with file size and 3D tessellation errors investigated. Finally, the 3D model was rendered in different CAD software for the application of EBB, FDM and SLA.

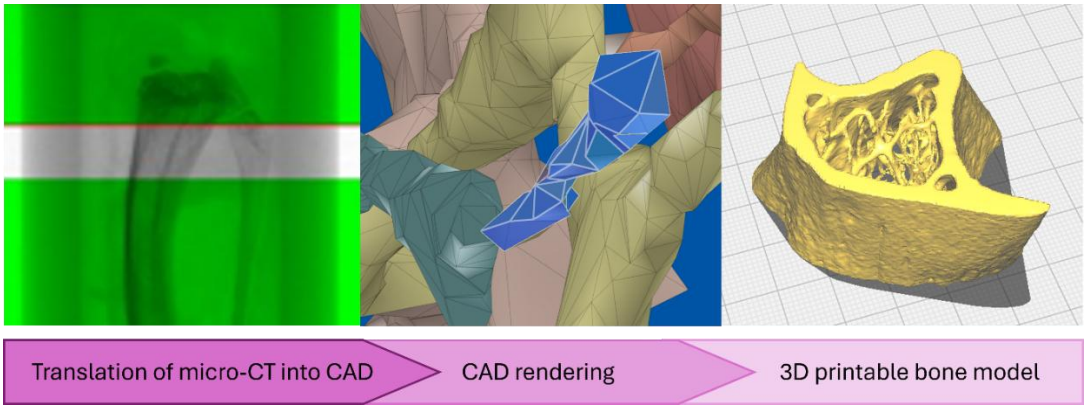

Figure 3.2.1. Summary schematic of experimental design to translate micro-CT ex-vivo bone imaging into a 3D printable bone model.

3.2.2 Standard tessellation language generation and evaluation of algorithm, unit and code

Tissue collection, micro-CT imaging and VOI segmentation of murine tibiae, femur and VB for mouse and rat were previously described (Chapter 2, section 2.2), however, a ROI was selected to enclose both Tb and Cb regions. In the custom processing of CTAn (1.21.2.0 CTAn, SkyScan), 3D model generation was selected as an available plug-in. To assess the difference between meshing algorithms, code and unit, n = 3 mouse tibia were exported in every variation of the meshing algorithm (MC33, DTC, and ATR), in ASCII or binary code, and unit (μm, voxel, mm and inch) as STL files. All STL visualisation, processing and rendering were completed on a Windows 10 Enterprise PC system, with 16 GB RAM and an Intel® Core™ i5-8500 CPU @ 3 GHz. Models were uploaded to MeshMixer (Version 11.0.544) to visualise errors, tessellation total and dimensions. ATR

with +1 smoothing, binary and mm were the selected conditions for the generation of the STL model to progress with rendering and different 3D printing techniques. As optimised output had been determined, rat and mouse tibia, femur and VB were exported as STLs for evaluation. For the final rendered STL models, the median bone of all bone morphometry values was taken forward as a representative bone model.

3.2.3 Standard tessellation language statistical analysis

All data was represented as individual data points, with mean values displayed. When appropriate, Shapiro-Wilk normality testing ($P > 0.05$) was completed. Normally distributed data underwent Tukey's multiple comparison test ($P < 0.05$) within each bone type. For different meshing algorithms file size and errors, the mean of the algorithms was compared.

3.2.4 Standard tessellation language rendering

Rendering was completed in both Autodesk® meshmixer and Autodesk® Fusion 360™. In meshmixer, basic rendering was completed to eliminate errors, re-size the model and ensure the 3D model was manifold. Manifold refers to a 3D tessellated surface that is free from breakages and becomes a solid structure. The mesh was repaired for errors by uploading the STL model into the interface, selecting analysis, followed by the inspector. Errors in the mesh were repaired using the hole fill mode with the smooth fill option. Finally, the model was made manifold using the edit feature. Make solid was selected, with the accurate type selected to minimise changes to detail. Once rendering was completed, the model was exported as an STL file.

Basic rendering was completed in Autodesk® Fusion 360™, to mimic the process completed in meshmixer before complex rendering for more detailed tessellation and information control. For basic rendering, the model was imported into the workspace, with tessellation frequency altered by 20%, utilising the mesh feature in the design workspace. The modify tab allowed proportional editing of the tessellation by reducing or re-meshing. The mesh was then repaired using the stitch and fix function. The basic STL was exported. Following this, for complex rendering, face groups were generated to analyse the different isoform components of the model. In the design workspace, the prepare mesh was selected with the generation of face groups and fast type was used.

Once face groups were generated, the model was inspected for any overhangs and structures that were not connected to the main body of the model, as this was hypothesised to increase the probability of a failed 3D print. Offending isoforms were deleted from the model by visualising different orientations and perspectives. Once appropriate, the face groups were combined. The process highlighted any further unsupported structures, which were removed from the model. The resulting STL models were exported.

3.2.5 Slicing and fabrication of fused deposition modelling and stereolithography of three-dimension tibia models

The mouse tibia and femur were selected for further processing. For EBB, the BioX™ bioprinter contained built-in slicer software. Rendered files were uploaded and visualised on the printer, determining the number of slices and geometrical information. No supports were added to the STL.

For FDM, the model was sliced for the printer to process. The rendered STL model was uploaded into Ultimaker Cura, a freely available slicing software. Following this, the model was re-sized within the edit feature (Table 3.2.1). Transform was selected, with coordinate space to local frame and uniform scaling selected to ensure translation of model volume in proportionate sizing to the method of 3D printing/bioprinting (Table 3.2.1), and rotation of model optionally applied to ensure even weight distribution and suitable centre of gravity of the model. The 3D printer stage and upper limits were input into the software, with the model fixed to the build plate.

The infill density of the printer was selected, 20% was used with a grid infill pattern and 0.8 mm minimum shell thickness. Two conditions of GCODE support were generated: connecting the model to the build plates only and connecting the model to itself and to the build plate. Supports were printed in sacrificial filament (Table 3.2.2). Selecting the slice function, the software generated the associated GCODE for the STL model, enabling translation of the 3D model into a 3D printer system. Typically, this will be completed by connecting a computer to the 3D printer with the GCODE file available, or direct printing from Cura, however, in instances of saving the model's generated GCODE, this can be completed by exporting the model.

Table 3.2.1 The original XYZ coordinates of mouse tibia, followed by translation of appropriate size for bio-printing, FDM and SLA. *Depending on the form of 3D printing/bioprinting, and the material used, different total volumes can be achieved to replicate the original morphological complexity of the scanned object. Adaptive rendering, mm and binary were used, with size translation using the scale function in Ultimaker Cura. Meshmixer models were translated by a 1913% increase from the original model, whereas Autodesk models underwent a 98% reduction to generate equal-dimension models.*

Model	X (mm)	Y (mm)	Z (mm)
Micro-CT STL output	2.55	2.48	1.51
Extrusion-based bioprinting	25.5	24.8	15.1
Filament deposition modelling	54	58	33
Stereolithography	54	58	33

Open-source SLA slicer software, Lychee was selected for ease of use. Rendered models were uploaded into the software interface and scaled appropriately (Table 3.2.1) using the scale function. Automatic supports were generated per model, followed by exporting the model for 3D printing.

Printing of FDM and SLA models was completed by Mr David Chorlton (Table 3.2.2). Completion and failure of FDM and SLA fabrication are documented with photographic evidence and qualitatively summarised. Completion is defined as a finished 3D model being produced, with no errors or excess spooling occurring during the printing process. FDM models with soluble supports underwent washing under warm water for 48 hours to remove sacrificial filament.

Table 3.2.2 Fused deposition modelling and stereolithography materials.

Printing material	Distributor and colour descriptor
PLA+ filament 1.75 mm, 1KG	*eSUN, AC – Bone White*
Siraya Tech Simple V2 water washable 3D printer resin, 1KG	*Siraya Tech Store – Grey V2*
Water soluble support material, ø 1.75 mm, 500g	*Xioneer Store – White*

3.3 Results

3.3.1 Standard tessellation language algorithm, unit and code optimisation on mouse tibia

To enable the development of the pipeline, the mouse tibia was selected as an example bone to generate a 3D STL model for determining optimal algorithm, unit and code. Binary code collectively produced a reduced, consistent file size amongst different units (Figure 3.3.1A) compared to ASCII, which varies between units (Figure 3.3.1B). All algorithms produced a different total file size, for both binary ($P < 0.0001$) (Figure 3.3.1A) and ASCII ($P < 0.0001$) (Figure 3.3.1B) in all conditions, which could be attributed to the level of complexity captured in the STL model (Figures 3.3.1E/F/G). All algorithms produced mesh errors (Figure 3.3.1C/D), whereby MC33 produced the highest frequency compared to DTC ($P < 0.0001$) for both ASCII and binary, and ATR ($P = 0.0022$ & 0.005, for ASCII and binary, respectively); however, meshing errors could be repaired in further rendering methods, but this would risk further deviation from the original imaged *ex-vivo* bone model.

Each unit produced a different dimension of the output model intra-algorithm, as expected (Table 3.3.1). Matched units between different algorithms also produced slight discrepancies in dimension, therefore highlighting the difference in complexity produced by changing algorithms. Each algorithm, despite the end product unit, produced an equal frequency of triangles and vertices, meaning that the isoform produced standardised increases in geometry whilst still abiding by standard tessellation rules.

Considering the detail that can currently be captured with different 3D printing techniques, it was questioned whether the level of detail of surface morphometry and porosity in Figure 3.3.1 could be replicated. For this reason, ATR with binary code and mm unit translation was taken forward as the algorithm of choice for 3D printing.

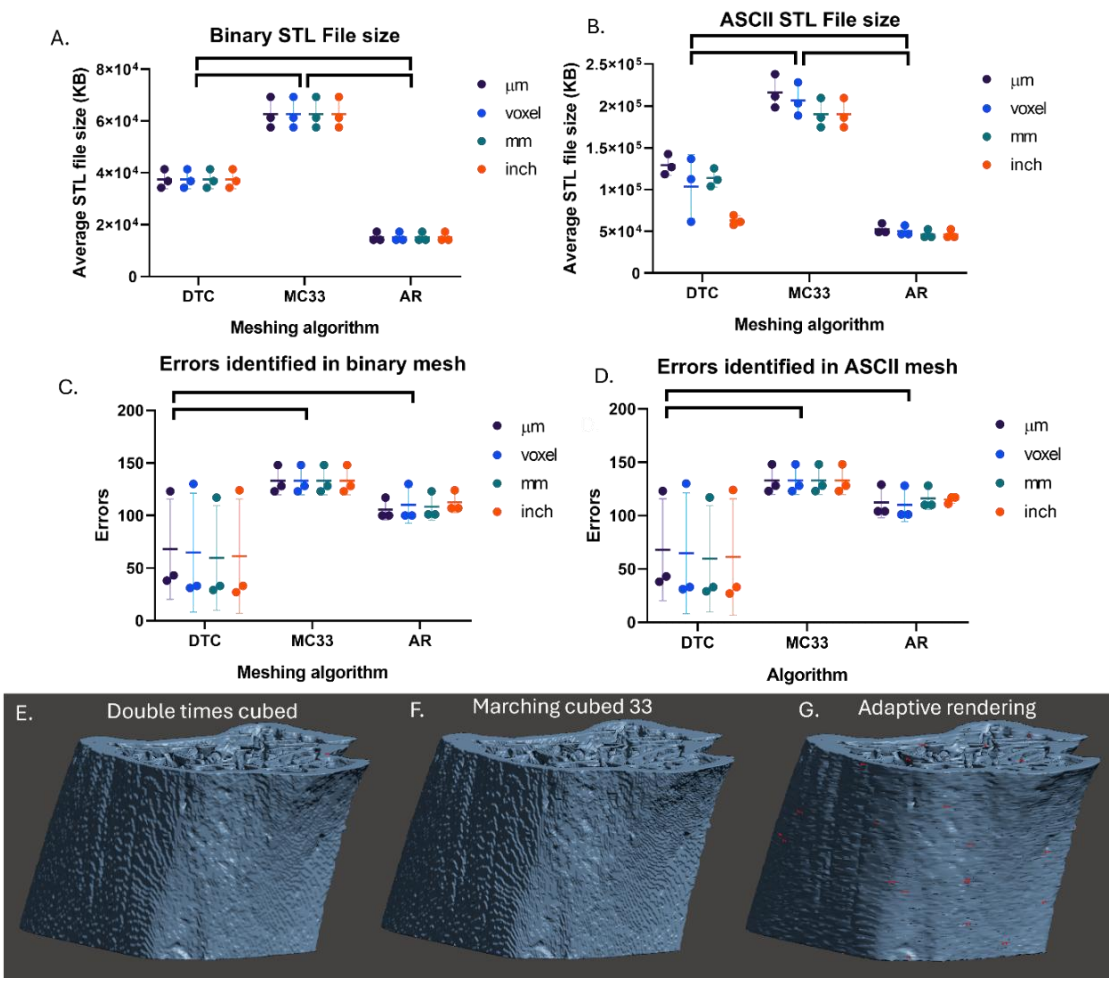

Figure 3.3.1. C57 Tibia exported into Autodesk® Meshmixer, inclusive of all potential 3D model tessellation conditions from CTAn to determine file size differences and mesh errors. *Mouse tibiae were imaged with micro-CT with 9 µm voxel pixelation and reconstructed with a binarisation of 0 – 0.12. A 1.5 mm VOI was exported as double times cubed (DTC), marching cubed 33 (MC33) and adaptive rendering (ATR) in either binary or ASCII code, and various units (um, voxel, mm, and inch). All generated STL models were exported into Autodesk meshmixer, A) Binary file size, B) ASCII file size, C) Errors identified in binary mesh, D) Errors identified in ASCII mesh, n = 3, Two-way ANOVA with Tukey's multiple comparisons test against each meshing algorithm, $P < 0.05$. All projections are binary mm, with mesh errors highlighted by red pixels, E) Double times cubed, F) Marching cubed 33, G) Adaptive rendering.*

Table 3.3.1. Average STL dimensions and tessellation values from different algorithms and units from C57 mouse tibia. *VOI of 1.5 mm (Y-axis) was subjected to different algorithms and unit options in CTAn and uploaded into Autodesk Meshmixer to visualise XYZ dimensions and total mesh tessellation of the STL files. n = 3, mean values reported, ASCII and binary produced equal values.*

Algorithm	Unit	Size (mm)			Mesh	
		X	Y	Z	Triangles	Vertices
Double times cubed	*µm*	2,442.7 ± 12.5	1,505.9 ± 8.0	2,667.7 ± 13.2	768,563 ± 15,4320	383,890 ± 75,300
	voxel	271.0 ± 5.0	167.0 ± 3.5	296.0 ± 6.0	768,563 ± 15,4320	383,890 ± 75,300
	mm	2.4 ± 0.02	1.5 ± 0.01	2.7 ± 0.02	768,563 ± 15,4320	383,890 ± 75,300
	inch	0.1 ± 0.002	0.1 ± 0.002	0.1 ± 0.002	768,563 ± 75,300	383,890 ± 75,300
Marching cubed 33	*µm*	2,447.9 ± 13.0	1,511.9 ± 8.5	2,678.9 ± 14.0	1,284,328 ± 25,350	641,610 ± 12,700
	voxel	180.4 ± 4.5	112.0 ± 2.5	201.0 ± 5.0	1,284,328 ± 25,350	641,610 ± 12,700
	mm	2.4 ± 0.02	1.5 ± 0.01	2.7 ± 0.02	1,284,328 ± 25,350	641,610 ± 12,700
	inch	0.1 ± 0.002	0.1 ± 0.002	0.1 ± 0.002	1,284,328 ± 25,350	641,610 ± 12,700
Adaptive rendering	*µm*	2,447.6 ± 11.5	1,511.9 ± 8.5	2,677.8 ± 13.0	317,613 ± 6,500	158,117 ± 3,200
	voxel	272.0 ± 5.0	168.0 ± 3.5	297.5 ± 6.0	317,621 ± 6,500	158,117 ± 3,200
	mm	2.4 ± 0.02	1.5 ± 0.01	2.7 ± 0.02	317,612 ± 6,500	158,116 ± 3,200
	inch	0.1 ± 0.002	0.1 ± 0.002	0.1 ± 0.002	317,619 ± 6,500	158,116 ± 3,200

3.3.2 Standard tessellation language *ex-vivo* bone visualisation and processing

All bone VOIs were exported from CTAn as STL files directly, with no CAD rendering. File size between bone types showed no statistical difference in the VB between species, however, the femur and tibia featured a wide range of file sizes (Figure 3.3.2A). For the tibia, no difference was noted between mouse and rat (F), compared to rat (M) ($P < 0.0001$ and 0.0002, respectively). In comparison, the femur bones represented statistical differences for the mouse against both rat sexes, $P = 0.0067$ and $P = 0.0005$ for females and males, respectively. The increase in complexity of bone structure for rats compared to mice is reflected in increased tessellation (Figure 3.3.3C) and resulting file size (Figure 3.3.2A).

Further, STL files above a file size of an estimated 36,000 KB resulted in the model rendering incorrectly in the BioX™ bioprinter interface (Figure 3.3.2B), excluding all but two mouse VB models that had a file size of below 35,500 KB (Figure 3.3.2A).

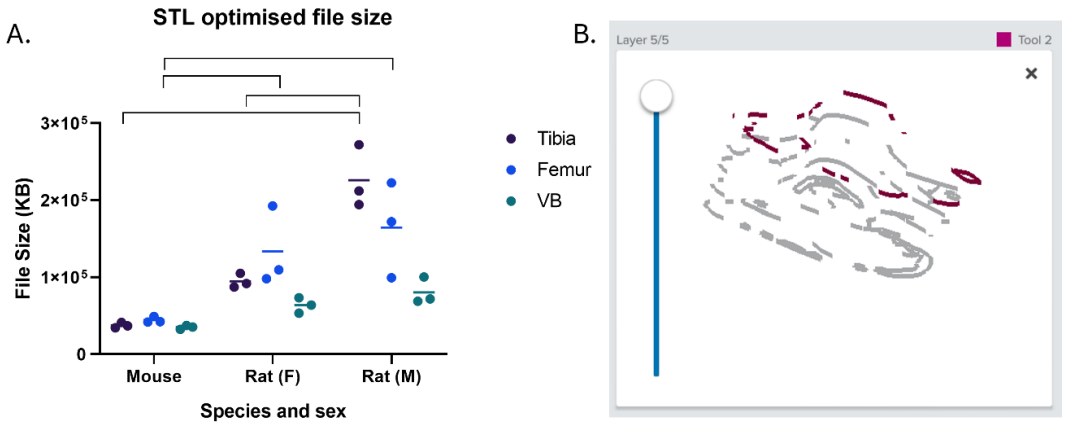

Figure 3.3.2. File size of STL output from CTAn of mouse, and rat (F + M) tibia, femur and VB. *A) 1.5 mm mouse VOI and 2 mm rat VOI were exported from CTAn with adaptive rendering, in binary and mm units. Mean values of file size are represented with statistical significance defined (< 0.05). n = 3. B) STL file of mouse VB inputted directly from CTAn to the BioX, representing failed slicing of the model due to high file size, n = 9. Representative picture shown.*

All bone VOIs were uploaded into meshmixer for visualisation and rendering. Consistent with the file size (Figure 3.3.2A), VB for all species and sexes featured the lowest quantity of vertices among all bone types. Increased vertices (Figure 3.3.3) resulted in increased file size (Figure 3.3.2A) for all model conditions. Rat (M+F) STL models were successfully

loaded, however, any actions performed on the CAD software of the models caused the failure of the computer system used for this research. The increased complexity of the rat bone structures, compared to mouse bones, can be qualitatively visualised and translated into a very complex *in-silico* 3D model (Figure 3.3.3B/C). Due to the complexity of the morphology and therefore the large STL file size, rat bones were removed from further downstream analysis and processing. Mouse bones were successfully uploaded into the Meshmixer interface, with a comparatively reduced file size due to the reduced structural complexity of the native bones. The VB was removed from the study due to the thin layer of Cb around the Tb that would require manual thickening of the walls to be rendered into the model, deviating from the original morphology. The exclusion of bone types and species was required for a more focused experimental approach, leaving the mouse tibia and femur within the study (Figure 3.3.3A).

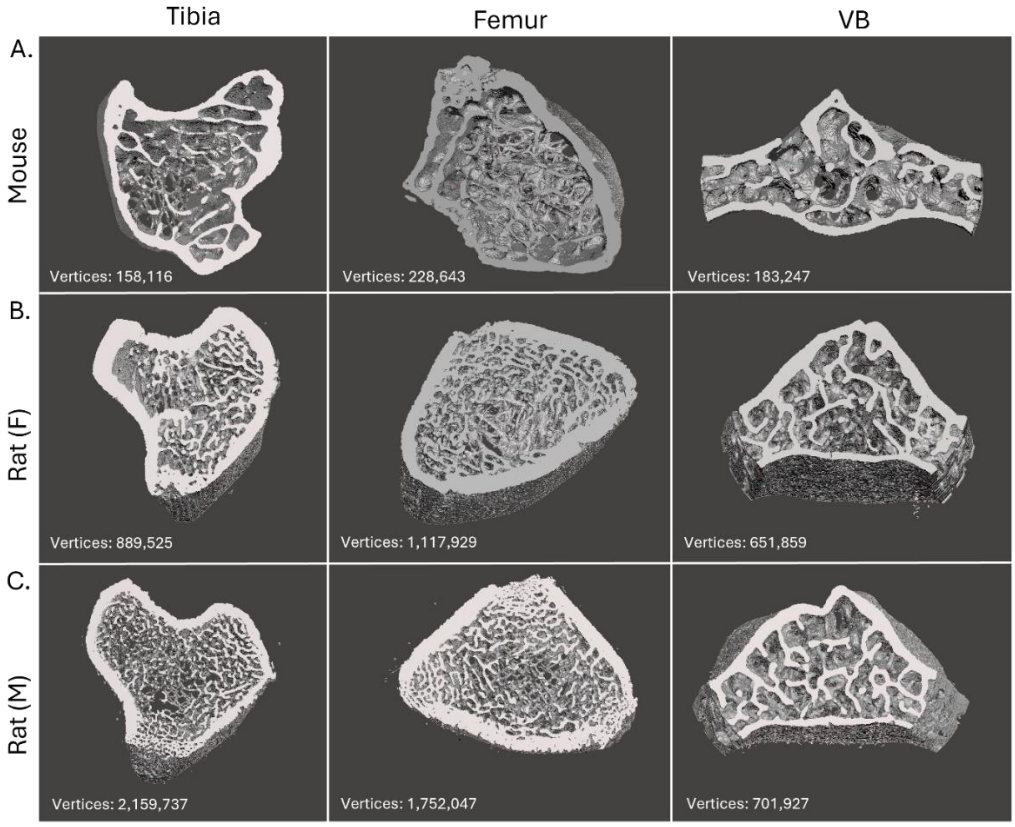

Figure 3.3.3. STL file outputs from micro-CT imaging and CTAn 3D model generation. *A) 1.5 mm VOI for mouse, and B/C) 2 mm VOI for rat. ROI of both Cb and Tb were exported as STL files with Adaptive rendering +1 smoothing, binary and mm units were used to tessellate the object surface. STL models were uploaded into CAD software Meshmixer for visualisation of models and vertex counts. n = 3, representative model shown.*

3.3.3 Standard tessellation language computer assisted design rendering

Rendering the model can allow a smoother model to be produced that is manifold (solid), as well as scaled to the required size. Reduction of tessellation can further reduce file size, but benefits in minimising complexity, producing a smoother surfaced model that a 3D printer can capture within the limits of printing and material resolution (Guida, L., Cavallaro, M., & Levi, M. 2024). Different CAD software tessellates with different algorithms, which are unknown to the average user, resulting in tessellation and structural differences from software choice alone (Figure 3.3.4A/B). Rendering options are varied between CAD software; however, reduction of tessellation, making a manifold and fixing any errors are vital processes to be completed to ensure printability of the 3D model without printing errors. However, each CAD software and action performed on the model will alter the geometry of the model from the original (Figure 3.3.4C/D).

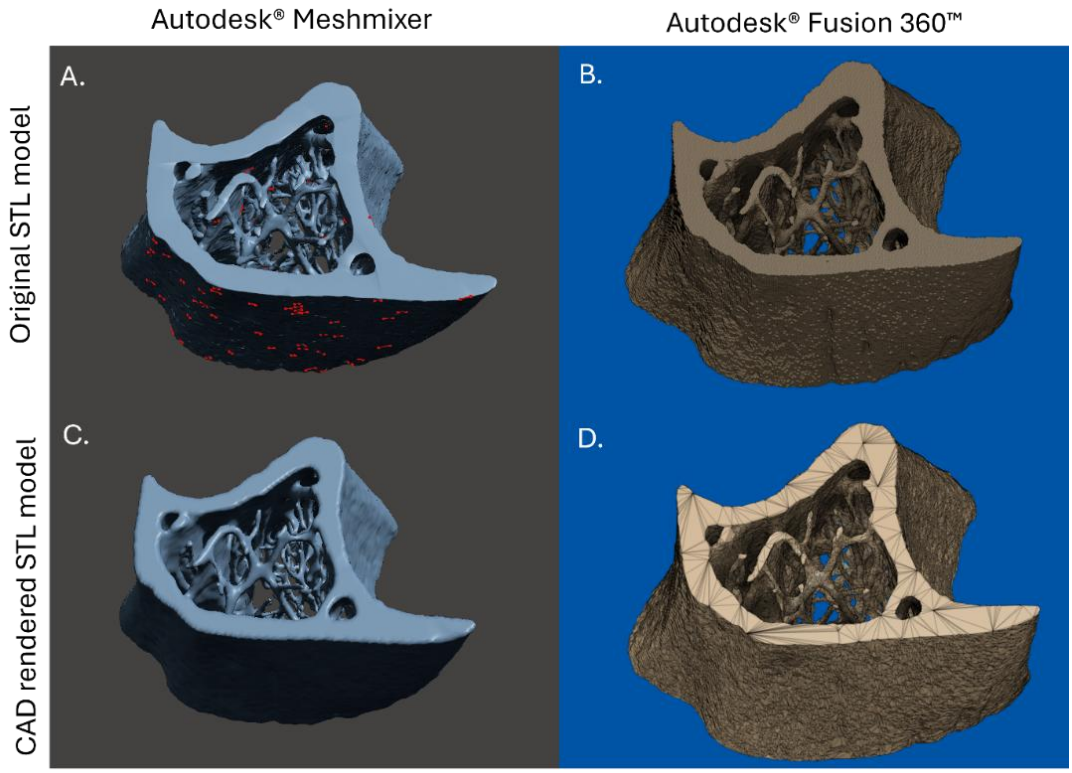

Figure 3.3.4. Tibia mesh rendering in Autodesk® Meshmixer and Autodesk® Fusion 360™. *Adaptively rendered with binary code tibia uploaded into both Autodesk® meshmixer and Autodesk® fusion 360™. The original STL model is shown in both interfaces (A & B), with the rendered output STL from meshmixer (C), and Fusion 360™ (D).*

The complex architecture that is produced in biological bone samples is supported by surrounding tissues, namely BM. To produce a 3D-printed anatomical bone model, this tissue was removed and segmented to isolate bone during micro-CT imaging, often isolating Tb structures from Cb due to manually chosen segmentation during the drawing of ROIs. To assess if unsupported Tb will interfere with printing success, the unconnected Tb can be removed in CAD software. An example can be seen in Figure 3.3.5, whereby unsupported Tb is identified and isolated (Figure 3.3.5A/B/C/D), before being removed from the 3D model (Figure 3.3.5E). This process requires time to visualise the model in different orientations and magnifications. Leaving any unconnected Tb structures will result in an increased chance of an error-bound model once tessellated face groups have been generated. Face groups represent structures that are grouped following standard tessellation rules, with connecting structures able to be linked to joining face groups and as a result, highlight unconnected Tb structures.

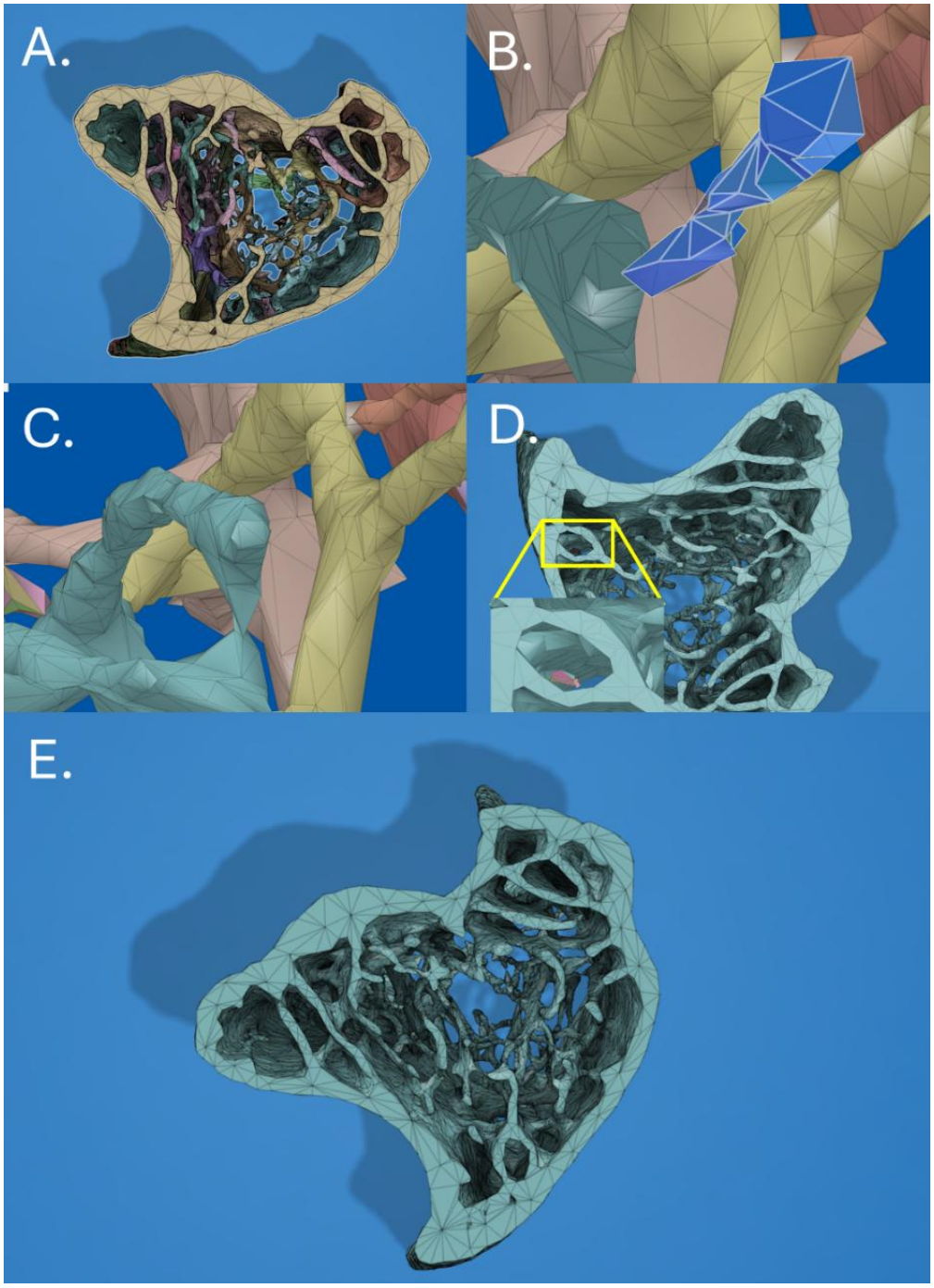

Figure 3.3.5. Identification and removal of unconnected trabecular structures in Autodesk Fusion 360™. A 1.5 mm VOI of C57 mouse tibia was exported as an STL with an adaptive rendering algorithm, binary format and mm unit. *Following the basic rendering of a 20% reduction in tessellation and repairing mesh in Fusion 360™ (Figure 3.3.4D), a detailed analysis can be completed to improve future printability by removing unconnected biological structures. A) Mouse Tibia with face-groups generated to visualise tessellation in different planes, the green box represents the area shown in the manual zoom, B) zoomed area of Tb structures, with unconnected Tb identified (blue), C) Unconnected Tb structure removed, D) Identifying and removing small objects by orbiting the model with different perspectives, E) Face-groups combined with all non-supported structures removed from the model.*

3.3.4 Slicing the rendered 3D *ex-vivo* bone models

Slicer software translates a 3D model into 2D planar XYZ information, in the form of GCODE, for 3D printing. The bioprinter used in this study, BioX™ contains a built-in slicer software. All rendered STL models from Autodesk meshmixer and Autodesk Fusion 360® were uploaded into the interface and produced equal sliced renders of the model, consisting of 76 layers (Figure 3.3.6). The process of EBB for the rendered *ex-vivo* model will be further explored in chapter 5.

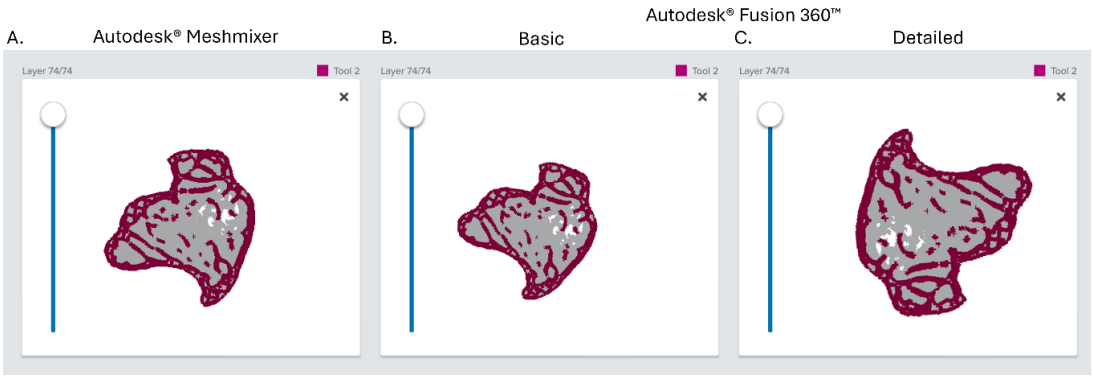

Figure 3.3.6. Mouse tibia STL rendered and uploaded to BioX bioprinter. *The ex-vivo bone model consists of 74 layers, with the current layer visualised in red. The model's dimensions are summarised in table 3.2.1.A) Meshmixer basic, B) Fusion 360™ basic, C) Fusion 360™ detailed.*

The complex biological shape may rely on sacrificial supports for the printing process, for a successful print. The type/method of 3D printing is determined by the location, frequency and requirement of the supports. For FDM, supports are added in two conditions: build plate connection only (Figure 3.3.7B) and everywhere (Figure 3.3.7C). SLA generates supports connected to the build plate and inner unsupported structures (Figure 3.3.7D). For each model, the supports generated highlight the variance in the different rendering processes by the location of supports – and the file size output. FDM slicing increases the file size of the STL models (Figure 3.3.7B/C), compared to SLA slicing, which reduces the overall file size (Figure 3.3.3D).

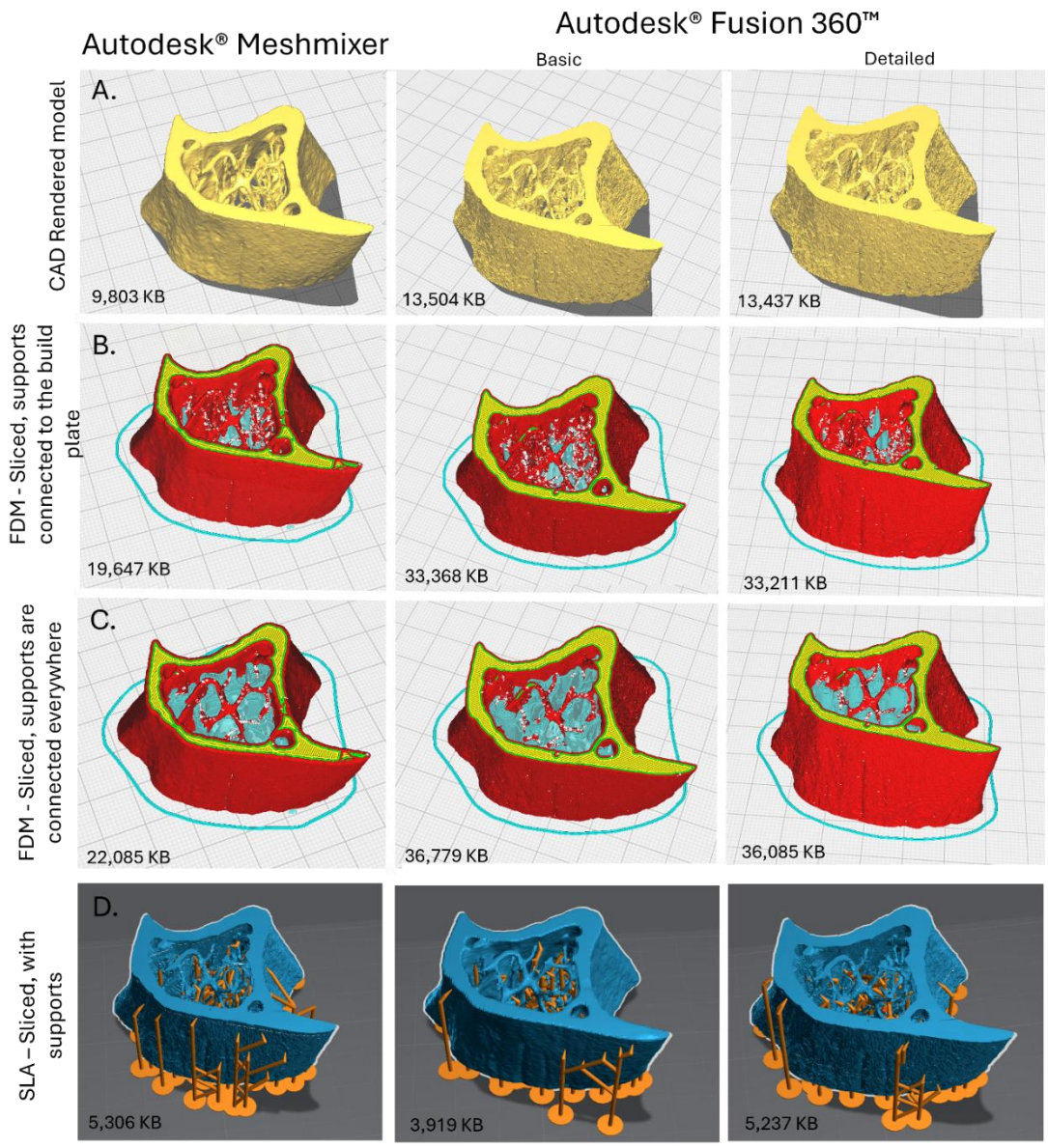

Figure 3.3.7. STL models rendered in Autodesk® Meshmixer and Fusion 360™, with FDM models sliced in Ultimaker Cura 5.9.0, and SLA sliced in Lychee. *Rendered models are uploaded into either Cura or Lychee. The Cura interface models underwent either supports built to the build plate only, or everywhere within the 3D model. All models were translated to the same coordinates; X: 54 mm, Y: 58 mm, Z: 33 mm. File size can be visualised in each tile for the respective model. Colour code for Cura: Inner wall (green), top (yellow), infill (orange), shell (red), supports (blue). Colour code for Lychee: 3D model (blue), supports (orange).*

3.3.5 Three-dimension *ex-vivo* bone model

FDM 3D tibiae models were successfully printed with no support, inclusive of Cb and Tb structures (Figure 3.3.8); however, the models suffered from filament stringing resulting in deviation from the original rendered STL models (Figure 3.3.4 & 3.3.5). This was particularly evidenced within the Tb region, perhaps due to the dead space and frequent

stop/start motion, resulting in over-extrusion of filament (Figure 3.3.8). Individual layers of the print were visible, and discrepancies in structure were identified, particularly within the Tb regions, between the three different CAD software's (Figure 3.3.8). Removal of Tb structures was essential for a successful print, as all conditions managed to be produced a printable 3D model with no errors during the FDM process.

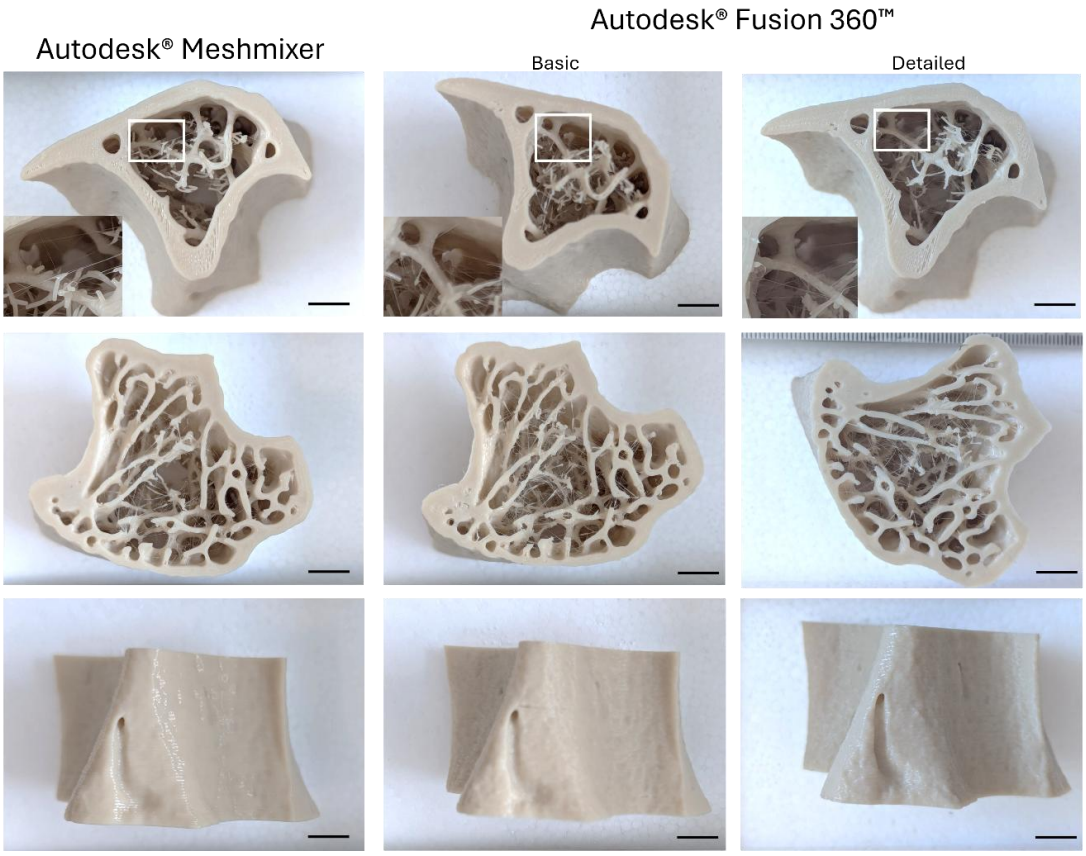

Figure 3.3.8. Fused deposition model printed ex-vivo murine tibia bone, with no structural supports. *Rendered and sliced murine tibia was printed with polylactic acid polymer. 3D printing was completed with no structural supports from all three CAD renders. Artificial magnified region represented by a white box. Representative images shown of different model orientations, n = 1 of each CAD rendered condition, scale bar represents 1 cm.*

To improve printing accuracy, particularly for the overhanging Tb structures, printing supports were used in two different positions; build plate only and everywhere (Figure 3.3.9). Supports to build plate only infilled the bottom layers, and frequency of sacrificial support reduced as the printing process progressed. Only one area of Cb shell featured supports due to the overhang of the structure (Figure 3.3.9). The sacrificial supports everywhere printed within the entirety of the central cavity of the tibia, surrounding the overhanging Tb structures. Similarly, supports were used on the Cb to enhance detail

(Figure 3.3.9). All rendered models from the different CAD software's produced different support locations (*not shown*), as represented in the slicer software (Figure 3.3.7).

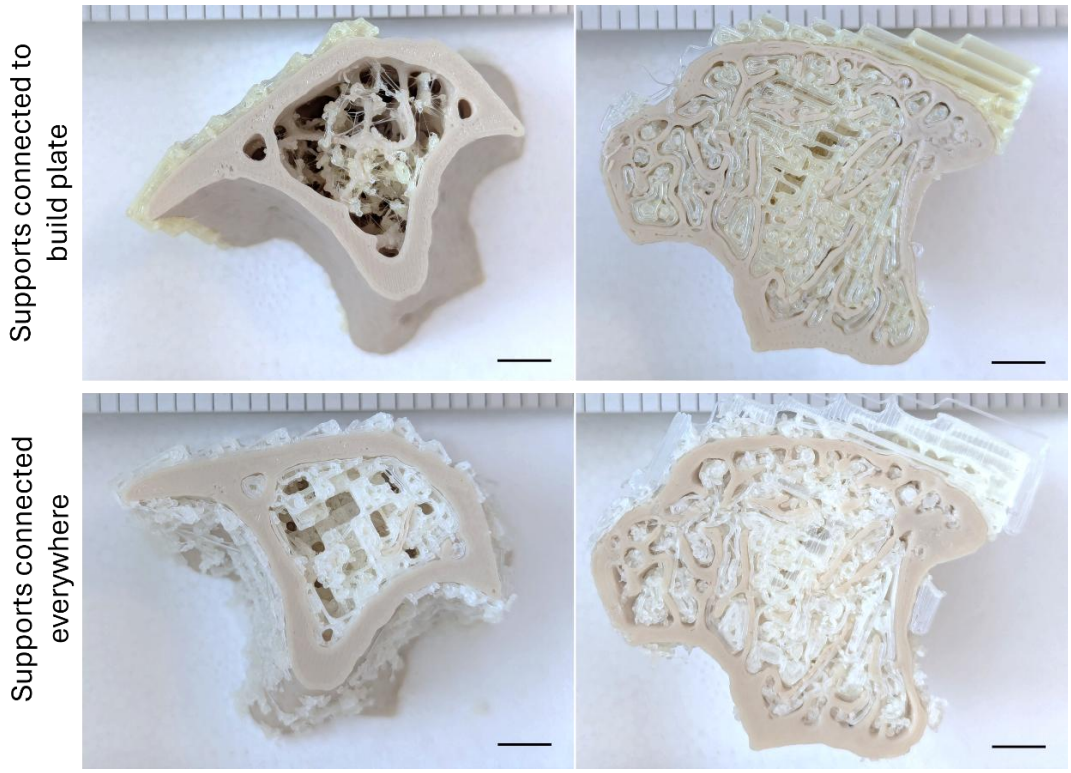

Figure 3.3.9. Example of Fused deposition model printed ex-vivo murine tibia bone, with structural supports. *Autodesk® fusion 360™ basic rendered and sliced murine tibia was printed with polylactic acid polymer. 3D printing was completed with A) structural supports connected to build plate only B) structural supports everywhere. Representative images shown of different model orientations, n = 1 of each CAD rendered condition (not shown), scale bar represents 1 cm.*

Following build plate only support (Figure 3.3.7 and 3.3.9) removal, the architecture of the 3D models was revealed. Between the three CAD fabrication methods (Figure 3.3.4 and 3.3.5) no errors were recognised for the Cb shell, however individual layers of filament were visualised. For the Tb structures, over-extrusion of filament was evident in all conditions by the filament stringing (Figure 3.3.10), resulting in deviation from the original STL *ex-vivo* mouse tibia (Figure 3.3.3). No qualitative improvement of accuracy of the architecture can be determined from the addition of build-plate only support (Figure 3.3.10), compared to no support (3.3.8).

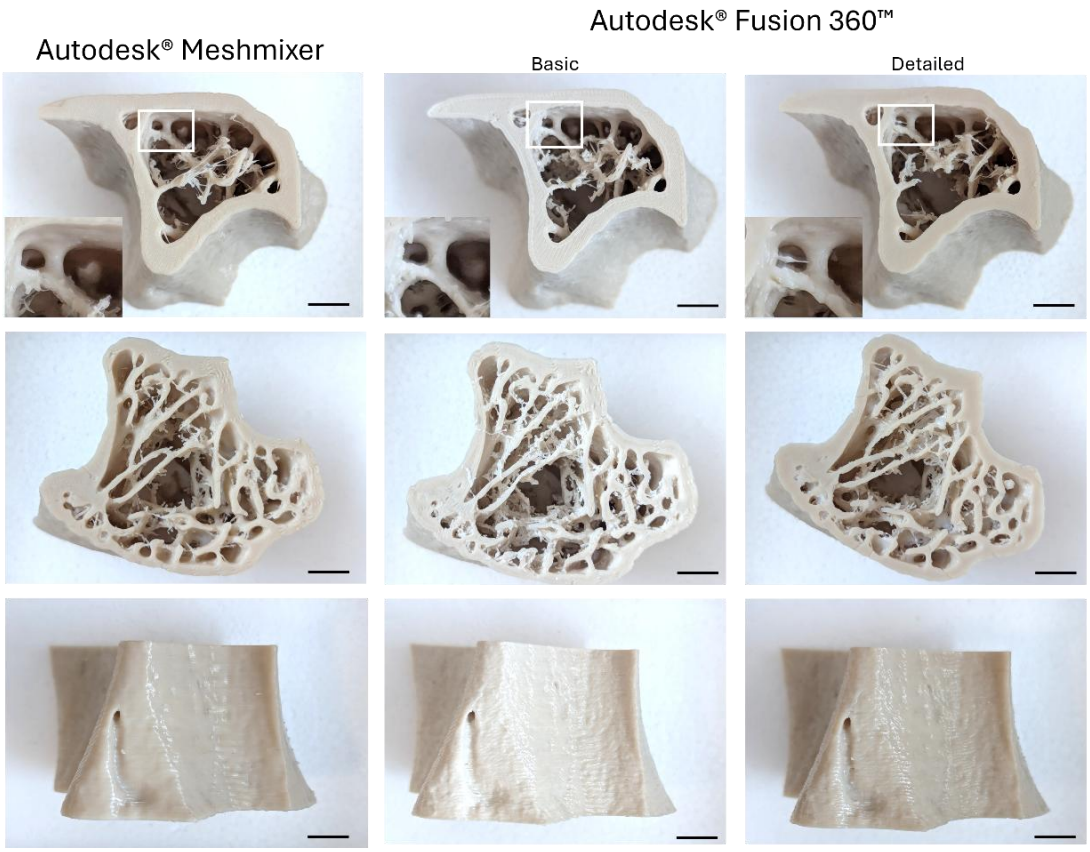

Figure 3.3.10. Fused deposition model printed ex-vivo murine tibia bone, with structural supports connected to build plate only. *Rendered and sliced murine tibia was printed with polylactic acid polymer. Structural supports were removed after 3D printing was completed. Artificial magnified region represented by a white box. Representative images shown of different model orientations, n = 1 of each CAD rendered condition.*

Sacrificial support everywhere resulted in printing errors during the process of FDM, as evidenced by Autodesk® Fusion 360™ detailed model where the Cb shell features gaps between filament layers that resulted in a broken 3D model during the support removal process. Further gaps can be visualised in both Autodesk® Fusion 360™ conditions Cb shell (Figure 3.3.11). In addition, Tb structures were reduced (Figure 3.3.11) compared to build plate only (Figure 3.3.8) and no supports (Figure 3.3.10). Meshmixer rendered 3D model suffered from over extrusion of filament, compared to Fusion 360™ (Figure 3.3.11).

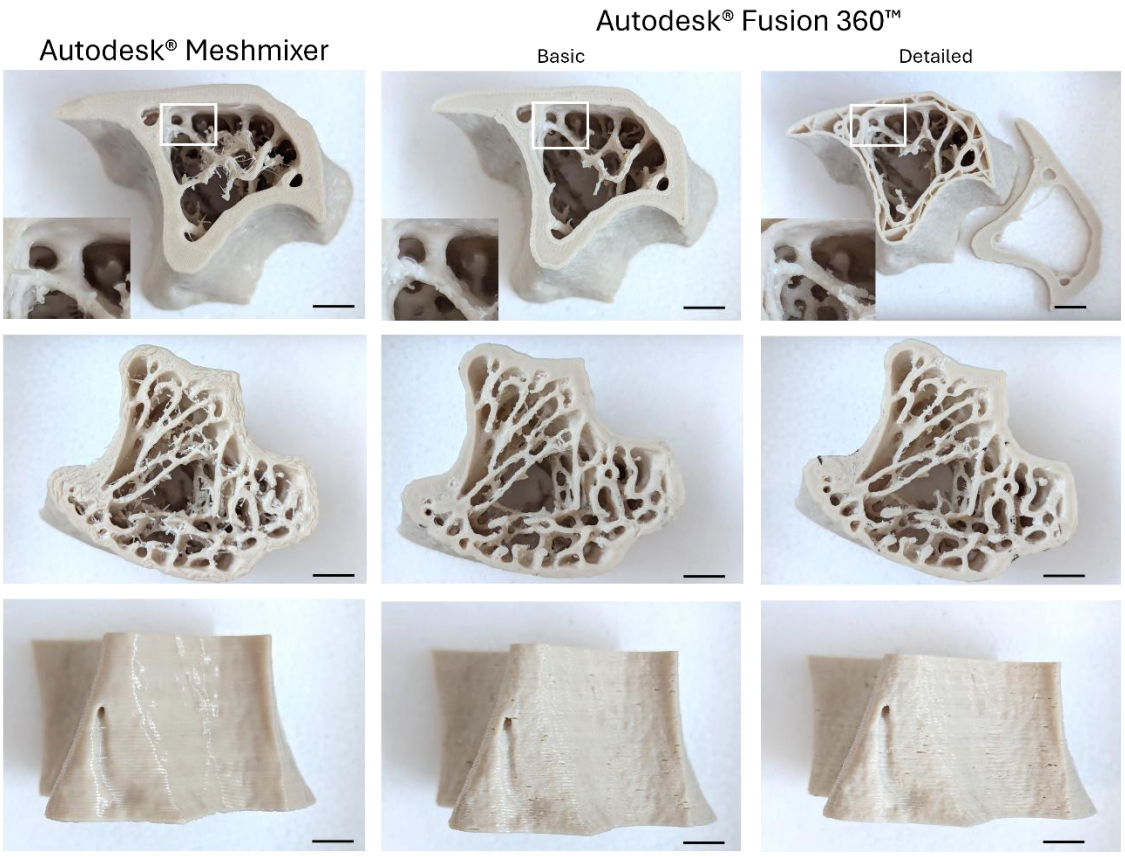

Figure 3.3.11. Fused deposition model printed ex-vivo murine tibia bone, with structural supports everywhere. *Rendered and sliced murine tibia was printed with polylactic acid polymer. Structural supports were removed after 3D printing was completed. Artificial magnified region represented by a white box. Representative images shown of different model orientations, n = 1 of each CAD rendered condition.*

Resin printed models by the process of SLA were printed with minimal structural supports. The models feature very detailed texture on the Cb shell surface compared to the original input micro-CT STL model, and defined Tb overhanging structures are also noted. Differences can be visualised between the three different CAD models within the Tb region, particularly from meshmixer compared to fusion models (Figure 3.3.12). Compared to FDM printed models (Figure 3.3.8/3.3.10/3.3.11), SLA models produced detailed and accurate biomimicry (Figure 3.3.12).

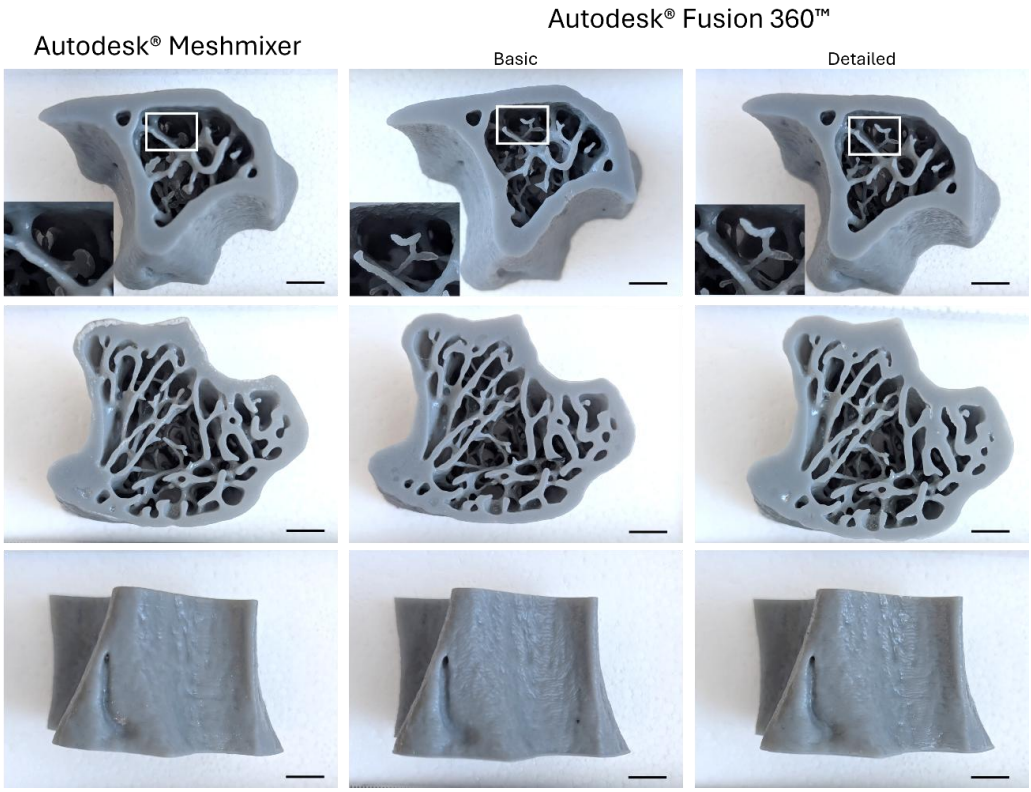

Figure 3.3.12. Stereolithography model printed ex-vivo murine tibia bone. *Rendered and sliced murine tibia was printed with resin from all three CAD renders. Artificial magnified region represented by a white box. Representative images shown of different model orientations, n = 1 of each CAD rendered condition, scale bar represents 1 cm.*

3.4 Discussion

This chapter aimed to investigate the translation of micro-CT high-resolution imaged *ex-vivo* bone VOI, incorporating both Cb and Tb into 3D printable (FDM, and SLA)/EB models. The successful generation of a biological 3D model is ambiguous and depends on the required end product. No standard singular successful rendering method exists due to the number of choices that can be made to enhance the likelihood of a successful 3D print. Furthermore, this methodological process and the considerations mentioned above are rarely explored and summarised to aid with the generation of a standard bone model to be rendered and 3D printed in different formats. The summarised method can be applied to any model obtained through the same acquisition. The rendering process of the 3D model should be tailored to the intended application, printing technique, and materials used within the fabrication process (Capellini, K., *et al.* 2024). 3D FDM and SLA murine tibia bones inclusive of Cb and Tb were successfully printed, with the different parameters explored.

Within the method described, considerations were made and tailored towards the 3D printing/bioprinting method to reduce deviation from the original *ex-vivo* imaged 3D model whilst achieving the success of printing. The intention of the standardised 3D model produced here is open-ended and could be used in several different research possibilities within the biomedical research industry, such as disease modelling and utilising the model as a healthy control, as well as an anatomical learning tool (Capellini, K., *et al.* 2024; Tripodi, N., *et al.* 2020).

3.4.1 Biological three-dimension model acquisition

Obtaining a biological CAD model dataset is becoming a more freely available process (Blackburn, D., *et al.* 2024); however, the method presented here utilised Bruker software CTAn. Alternative biological geometry can be obtained with different approaches, not strictly from obtaining original images by micro-CT or DEXA (Flaxman, T., *et al*. 2021; Preim, B., & Botha, C. 2014). Lee (2020) shares an open-source method of meshing biological structures in blender™, for the utilisation of graphics in gaming software. Other freely available software for the generation of realistic biological geometries includes Virtual Cell, and Cell Organiser, as well as different community sharing platforms available for open-source medical imaging files to be downloaded and

translated for different research purposes, or originally designed STLs such as GrabCAD (Rahmani, R., *et al*. 2024). Typically, biological researchers favour simplistic CAD models to investigate cellular interactions and the surrounding environment, due to the difficulty of mimicking physiological structures. However, design-specific research to replicate anatomical structures is progressing. For example, Moxon (2024) generated an intervertebral disc in CAD software bioCAD™, with two definite structures to mimic native anatomy. The study utilised a suspended layer AM method and achieved good accuracy of the structure from 3D bioprinting (Moxon, S., *et al.* 2024).

Alternatively, there are many mesh generation algorithm packages available for Python; notably PyMesh, Gmsh, SALOME and MeshKit (Hart, K,. & Rimoli, J. 2020). Smeets (2022) describes a nano-mesh tool within the Python library that enables the generation of a 3D mesh from a 2D image, furthering the possibility of creation and experimentation. In contrast to designing the anatomical model directly, Homan (2016) designed a gasket (empty mould) using a custom MATLAB script and the toolpath of a 3D proximal tubule construct in a custom Python script (MeCode), both scripts exporting GCODE. This method allowed 3D proximal tubule constructs to be generated with high precision (Homan, K., *et al*. 2016). Literature around the subject is limited, whilst a high frequency of information is shared on public forums by community users it is not reported by controlled experimentation.

3.4.2 Evaluation of the computer assisted design rendering process

Mesh application on biological models has been extensively studied for objects within the discipline of FEM analysis to run simulations to determine mechanical properties of the objects (Nemade, A., & Shikalgar, A. 2020; Burkhart, T., Andrews, D., & Dunning, C. 2013 Baghdadi, L., Steinman, D., & Lodak, H. 2005), preservation of specimens in a 3D space and creating interactive displays for scientific accessibility for public communities (Blackburn, D., *et al.* 2024). Referring to FEM analysis, mesh resolution dictates directly the quality of the simulation, visualisation and eventual diagnostic possibility, with it being accepted that the higher resolution produces the most reliable results, resulting in a very high frequency mesh and large data sets (Sorgente, T., *et al.* 2023). Evaluation of mesh decisions and applications is rarely considered for translating a medically imaged organ into a 3D printable model, whereby the mesh interface from the high-

resolution imagery is reduced due to the volume of information contained (Figure 3.3.2/3) (Wang, M., Gao, J., & Wang, X. 2017) to facilitate external printability with different materials (Flaxman, T., *et al*. 2021).

It was evident that the high-resolution output *ex-vivo* bone STL models, inclusive of Cb and Tb, required rendering, and a reduction in file size to be 3D printed/bioprinted. Optimisation of rendering the *ex-vivo* bone models was an extensive, high computational demand, and a timely process. The process is associated with a multitude of rendering possibilities in the chosen software, and considerations needed to be undertaken for a successful final product (Oropallo, W., & Piegl, L. 2015). It was apparent that to successfully render models, file size needed to be reduced, resulting in reduced tessellation and vertices quantity (Wang, M., Gao, J., & Wang, X. 2017). He (2022) investigated the voxel size impact on the number of resulting vertices of the resulting mesh of liver samples that were enhanced with contrast dyes and imaged by micro-CT, for FEM analysis. The study discovered that the increased resolution improved the accuracy of the resulting surface mesh for biological morphology; however, this was at the cost of processing time and demand on the computational processor, based on the high volume of information (He, Y., *et al*. 2022).

Errors in tessellation may arise from small scanning artefacts from the original image acquisition. This may insert incorrect structural information when translated to a tessellated surface by the different algorithms (Montalti, A., Ferretti, P., & Santi, G. 2024). Originally, *ex-vivo* bones were imaged at 9 µm voxel width. Ford (2016) assessed the difference in 2D slice thickness on the influence of 3D reconstruction of CT cranium scans. Higher resolution scans produced artefacts which caused a loss of detail of the biological morphology, compared to a clinical standard cranium model of 0.625 mm slice thickness (Ford, J., & Decker, S. 2016). Further research investigating the difference in original imaging resolution, with resulting tessellation error, would be useful to provide insight into this observation. Another factor is the porosity of the bone, causing space within the tessellated surface without connections for the chosen algorithm to match, perhaps causing the high file size and vertices of the rat (M) bone samples by the significant difference of Cb porosity compared to rat (F) and mouse tibia and femur.

Different algorithms, units and code produce deviations from the original STL model, *ex-vivo* bone, with the CAD software and rendering process resulting in further deviations. It is difficult to state the degree of deviation from the original *ex-vivo* input for each step, as each software runs on different algorithms. The observation of deviation by different CAD rendering processes was supported experimentally by Kamio (2020), Abad-Coronel (2023), Rungrojwittayakul (2019), and mathematically explored by Hallgren (2016). The researchers compared the resulting tessellation and 3D prints from different CAD systems, suggesting the tessellated surface ambiguity between the different systems is due to the widely used STL file format and translation of the mesh boundaries between different software algorithms (Abad-Coronel, C., *et al.* 2023; Kamio, T., *et al.* 2020; Rungrojwittayakul, O., *et al.* 2019; Hallgren, E., *et al.* 2016). The STL file format follows an unstructured tessellation, highlighted in the Cb tessellated structure in Fusion 360™, following inconsistent geometric rules which facilitate curvature in the mesh. As a result, it may perhaps assist in the error production of the biological structures' mesh due to the imperfect geometric textured surface. The meshing algorithm Autodesk® Fusion™ states in the software configuration is adaptive meshing, and it is unstated for Audodesk® Meshmixer. It could be suggested that different CAD software identify mesh errors with different boundaries.

The original 3D model was transformed for application into three different 3D printing/bio-printing techniques: FDM, SLA and EBB, to assess the ability of translating *ex-vivo* bone VOI into a 3D model. Different considerations were made for each fabrication method, notably size difference between the two-3D printing techniques; FDM and SLA, and bioprinting, due to material considerations and the build plates associated with each method, but ultimately the resolution capabilities of each system (Guida, L., Cavallaro, M., & Levi, M. 2024). Alongside this, FDM and SLA required slicing software to translate the STL model into GCODE (Figure 3.3.7), whereas the EBB technique (Chapter 5 and 6) utilised the CellInk Bioprinter.

3.4.3 *Ex-vivo* bone computer assisted design model suitability

The subject matter of translation into CAD for this research was a VOI of *ex-vivo* bone. Biologically, the surface of bone is not a perfectly smooth compact surface; instead, frequent remodelling occurs, causing pits of reabsorption, as well as being a highly

vascular surface with pores to allow connection from the BM to the periosteum (Goldring, S. 2016; Tan, S., *et al.* 2014). As well as the surface, the bone is curved with no sharp edges, resulting in the tessellated surface requiring a higher frequency of vertices compared to a flat, smooth surface. Additionally, further complexity is added by the presence of metabolically active Tb struts, which are structurally connected to the dense Cb shell and supported by surrounding BM tissue.

Wang (2017) investigated the importance of reduction of different algorithm generated tessellation of hip and femur bones for processability, suggesting a 97.5% reduction of tessellation of the entire bone whilst still maintaining overall 3D model structural morphology. In the study an Intel®Xeon®E5606 processor was used, running at 2.13 Ghz (Wang, M., *et al.* 2017), which was less than that used in this study, of 3 Ghz. There is no reported consensus on the recommended processing power for efficient CAD processing in this context. This limiting factor will be dependent on the user and technology availability, as computer systems will have different graphic processing units, random access memory, read/write speeds and central processing unit limitations (Shi, L., *et al.* 2012).

The *ex-vivo* bones were imaged in high resolution to capture morphological information and to produce a representative 3D CAD model from the bones imaged within the study. This decision has ultimately assisted in the complexity of the geometrical surface produced in the final exported STL models, extensive file size, and the resulting errors present in the mesh due to the chosen algorithm matching connecting surface morphology to geometry information. Different sample populations were removed from this study for different reasons. All rats (M+F) were removed due to large file size and resulting tessellation, causing computational failure when attempting rendering. VB models were removed because of unsuitability in downstream workflows due to the requirement of extensive rendering of false walls, resulting from VOI segmentation and 3D analysis (Chapter 2, section 2.2.4). Inclusion would have caused a considerable deviation from the original *ex-vivo* model, as well as an increased chance of printing failure and wall collapse due to a lack of structure.

As far as the researchers are aware, no research exists in translating both Tb and Cb into a 3D bio-printable model for different forms of 3D printing/bio-printing, with most

research focusing either on simple lattice structures (Xiao, L., *et al*. 2024; Tang, M., *et al.* 2022; Luttrell, L., *et al.* 2019), or macro-porous architecture of biomaterials (Jiao, J., *et al.* 2023; Martinez-Garcia, F., *et al*. 2022; Ahmed, E. *et al.* 2013). Lattice structures do not encompass the overall important micro-architecture structure of bone, inclusive of Cb and Tb. The Tb structures required detailed rendering to enable a complete manifold STL model to be produced, either by the process of removing unconnected structures or adjusting the tessellation frequency of the overall model to ensure secure joints between Cb and Tb. Ultimately, the inclusion of Tb structures resulted in exploring the requirement of printing supports to be added within slicer software, or a 3D EBB support bath to be required (Budharaju, H., *et al.* 2024; Brunel, L., Hull, S., & Heilshorn, S. 2022; Zhou, K., *et al.* 2022) (Chapter 5) by enhancing complexity. For the FDM 3D printed models, the Tb structures resulted in filament stringing, perhaps due to the size and frequency of stopping/starting. Interestingly, the FDM printed models with no sacrificial support resulted in models with less filament stringing, and printing errors. Further research is required to compare the 3D FDM and SLA models to the original *ex-vivo* bone STL model to determine accuracy and error.

Alternative anatomy models have been developed for 3D FDM and SLA printing, including patient-derived vascular anatomical models by Nguyen (2023). The DICOM obtained 3D models underwent rendering in CAD software 3matic to improve printability, in a similar process as described in this study by smoothing, removing artefacts and fixing meshing errors, whereby supports were required to 3D print the structures successfully (Nguyen, P., *et al.* 2023). Furthermore, Valls-Esteve (2023) evaluated the process of transforming patient-specific diseased models from DICOM, originally captured by CT or MRI, for the end purpose of surgical planning. The models were rendered for different 3D printing methods, including FDM and SLA, whereby printing supports, transformation of size and rendering of the model, including smoothing, and fixing mesh errors, were completed in Autodesk® Meshmixer (Valls-Esteve, A., *et al.* 2023). Both Nguyen (2023) and Valls-Esteve (2023) do not report on deviation from the original physiology but agree that different methods of printing require various considerations and rendering to allow successful printing of the 3D anatomical models.

3.4.4 Fused deposition modelling and stereolithography three dimension printed *ex-vivo* bone model

Two methods of large-scale AM were explored, to visualise the impact of different fabrication methods on the 3D models despite equal 3D STL input. It is clear that SLA produced models with elevated detail, and reduced printing errors compared to FDM models despite the inclusion of structural sacrificial supports. All FDM models suffered from over-extrusion for Tb structures. Similar conclusions were made by Anadioti (2022) who reported significant deviations in all dimensions for FDM dental implants compared to the original CAD input, whereas SLA only produced deviations in one dimension. Anadioti (2022) used a very simplified block model, with no intricate architecture (Anadioti, E., *et al*. 2022). In further detail, McMenamin (2014) reported for anatomy printing with FDM, any structures above 10 mm were accurate in size, with an average error of 1.25% across all filament deposition above this size. Below 10 mm, error increased to 14.52%, and below 4 mm filament had an error of 17.92% (McMenamin, P., *et al*. 2014).

Technique and resolution for fabrication via FDM has improved in the last 10 years, Ahn (2024) printing a filament diameter of 1.75 mm accurately, whereas Behseresht (2024) has developed a closed-loop control printing system that self-recognises printing deviations and self-corrects during the printing process. For SLA, improvements continue to be made as well (Iftekar, S., *et al*. 2023). Msallem (2024) discusses the significant advancements of the fabrication method in recent years with high accuracy achieved with new SLA technology when printing an anatomical skull and mandible (Msallem, B., *et al.* 2024), compared to a previously published study printing the same model with different technology (Msallem, B., *et al.* 2020).

Future research would focus on analysing the accuracy of the printed 3D models, to the original 3D CAD rendered models and input micro-CT STL model. Abad-Coronel (2023), Rungrojwittayakul (2019) and Mitsouras (2017), have attempted to analyse the deviation from the original model to the finalised CAD, however, in the 3D printed format. Rungrojwittayakul (2019) explored the difference between two model builds (solid and hollow infill) and printing techniques (liquid interface production and digital light processing) on the ‘trueness’ of the output model in comparison to the original input

model. They found no significant difference between the two builds when using the same printer, however difference was noted when comparing the two printing techniques with the same build. Abad-Coronel (2023) utilised four different CAD software, and 3D printed mandible models using FDM, rescanning the models and analysing deviation by 3D Geomatic control X software by superimposing the printed model onto the original CAD. No statistical difference was discovered; however, each software had a different degree of accuracy and precision compared to the original model. Finally, in a study conducted by Mitsouras (2017), a 3D SLA printed cervical vertebrae model dimensions deviated based on the original model capture method, of CT and MRI, despite equal CAD rendering and fabrication methods applied (Mitsouras, D., *et al.* 2016). All three studies represent the deviations that result from original imaging techniques, fabrication method, and CAD software selection.

3.4.5 Conclusion

Translating micro-CT high-resolution imaged of *ex-vivo* bones into 3D STL models is a process that requires extensive optimisation and knowledge of the entire AM process. Including the initial scanning resolution, sample complexity and selected algorithm to capture the information, to the continued process of rendering the 3D model for commonly used 3D printing/ bio-printing techniques. Within this study, different *ex-vivo* bone models, inclusive of Cb and Tb structures, from mouse and rat were utilised as standard bones used commonly within the biomedical bone research community. The bones were exported as STL models in optimised conditions, to make an informed workflow for the process of rendering 3D models from CTAn. The workflow can be utilised for different biomedical research involving 3D printing/bio-printing techniques; however, due to limitations of the biological complexity of the structures resulting in excessive isoforms influencing file size, and tessellation error, this research aim was unable to be achieved for all original *ex-vivo* murine bones.

Mouse tibia STLs were successfully rendered utilising different CAD software, with different techniques employed to produce 3D models for the application of FDM, SLA and EBB with reduced tessellation but minimal deviation from the original STL file. All models were sliced appropriately for the different printing techniques, FDM, SLA and EBB. The *ex-vivo* mouse tibia was successfully printed with both fabrication methods of

FDM and SLA, however FDM produced a model with clear deviations from the original STL model from the micro-CT input, compared to SLA. Further, the different CAD rendering processes produced 3D models with deviations per model, in both fabrication methods of FDM and SLA.

Chapter 4 – Dissemination of micro-CT to 3D CAD model workflow

Training the bone research community of the developed pipeline of translation of micro-CT imaging into 3D printable models.

4.1 Introduction

4.1.1 'From CT to 3D printed models' workshop context

The body of research aimed to determine the efficacy of an educational workshop developed to instruct participants about translating micro-CT data into 3D-printable STL files, and further model rendering to ensure translation and printability (Figure 4.1.3). The research pipeline used in the workshop was developed during the presented doctoral research (Chapter 3), and the wider application possibilities in a relevant field of research were evaluated.

The workshop featured an overview of the main topics: AM, micro-CT, and CAD, followed by first hand practice using CAD software to generate a rendered *in-silico* 3D model. For micro-CT, Bruker software CTAn was introduced; for CAD, Autodesk® software meshmixer v.11.0 and Fusion 360™ v.2.0 were used. The information delivered on CT was broad, with more detailed information on AM and CAD, including definitions and summaries, to allow exploration of different 3D printing methods and different output applications (Bucking, T., *et al.* 2017; Rengier, F. *et al*. 2010). Participants were provided with a detailed handout aid, which included definitions, considerations, and simple instructions on the process from micro-CT to 3D model rendering (Supplementary Figure S6). A practical workshop titled 'From CT to 3D printed models' was delivered at the Bone Research Society (BRS) national meeting (10/07/2024) to twelve participants.

4.1.2 Learning theory

Activity-based workshops allow participants to develop their knowledge and practical skills via an interactive learning experience. Activity-based learning forces participants to reflect and engage with the ideas and concepts presented (Michael, J. 2006), therefore helping to understand and improve knowledge, creativity, and comprehension within their research interests. Activity-based learning is rooted in the cognitive and constructivist learning theories from Brunner (1960;1966) and Vygotsky (1978) whereby knowledge is not passive but actively built up through learning, which involves the construction of knowledge from experience.

The information-based approach, also known as a passive form of learning, is an efficient way to ensure all participants have equal information and understanding of the subject

area before the requirement of active participation, which will reinforce the information taught (Armstrong, J. 2011). By delivering multi-faceted information, the opportunity for each participant, despite prior knowledge and expertise, to learn a new skill or gain a new perspective was vital. By combining activity-based learning with an information-rich approach, the intention was to provide an interactive environment (Noreen, R., & Rana, A. 2019; Doherty, P. 2007) for participants with the tools to comprehend and follow the research pipeline that has been optimised and outlined.

Dissemination of information at an accessible level was vital to allow the exchange of skills and knowledge within the community, with novel scientific methods particularly useful to researchers in a relevant field. Dissemination of research allows an increase in visibility, impact, and influence and helps drive the field forward by incorporating a multi-disciplinary approach (Ravinetto, R., & Singh, J. 2023; National Institute for health care and Research, 2019; Besley, J., *et al*. 2018; Marin-Gonzalez, E., *et al*. 2016; Jucan, C., & Jucan, M. 2014). By designing a workshop based on practical skills, participating researchers may use the newly developed skills and knowledge within their research allowing progression and innovation.

4.1.3 Aims of the workshop

1. To gain an understanding of the importance of 3D model design and algorithm selection in influencing the resulting standard tessellation language 3D model. In addition, how 3D design should be changed based on 3D model application and how different applications (extrusion, fused deposition modelling and stereolithography impact the downstream workflow.
2. To practice rendering 3D STL models utilising two different CAD software's, for the application of 3D extrusion bioprinting.

4.2 Materials and methods

4.2.1 Experimental design

Participants were offered the opportunity to complete a pre-workshop questionnaire to inform the researcher and teacher of familiarity with techniques covered in the workshop. Post-questionnaires were generated to evaluate the effectiveness of handouts, presentation delivery, and participants' knowledge development. In addition, questionnaires were utilised to determine success in teaching new skills to a range of scientific backgrounds and interests. Questionnaires and workshop handouts are attached as supplementary data (Supplementary Figure S4, S5 and S6). All participants received an information guide explaining the study (Supplementary Figure S3).

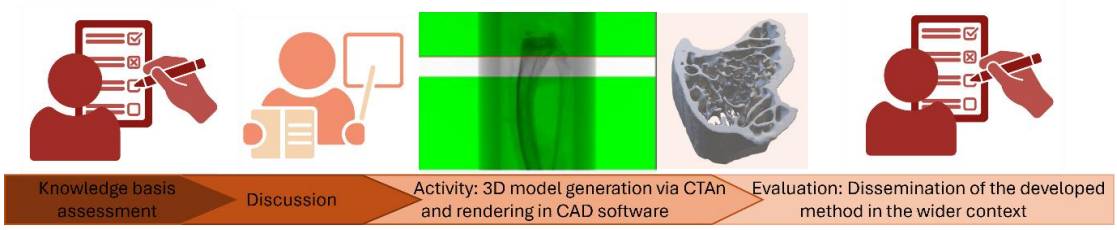

Figure 4.2.1 Experimental design of workshop context and evaluation. *Participants were taken through the different experimental considerations required for the generation of 3D models intended for 3D printing / bio-printing based on micro-CT outputs. Finally, participants completed pre- and post-questionnaires to assess knowledge.*

4.2.2 Bone Research Society dissemination event

The workshop was proposed to the BRS committee, with ethical approval from the researcher's institution (Ethics ID – ER66185031) and material preparation of content completed by the first-named researcher. The workshop and meeting were advertised to BRS members, as well as the wider scientific community. The session, from '*CT to 3D printing'*, offered 22 places for a 2-hour activity-based workshop. From this, 14 participants attended the workshop however, only 12 were active participants. The BRS national meeting workshop was hosted at the Diamond, University of Sheffield in a computer suite to provide participants with IT equipment and software.

All active participants had attended a previous workshop that discussed the themes and functionality of micro-CT, therefore a basic level of understanding of the theory behind micro-CT was assumed. The information delivered was a broad scope of the field of AM,

CT, and CAD processing with a high focus on activity-based learning. All participants were provided with computers pre-loaded with a 1.5 mm VOI mouse C57 Tibia STL obtained by a 9 µm scan with an Al 0.5 mm (55 kV:160µA) filter. The STL was generated with AM in binary with mm unit, and all information on generation was delivered to participants including meshing algorithm and 3D model file type. As CTAn is a licensed software, this was not available for casual usage. CAD software meshmixer and Autodesk® Fusion 360™ are publicly available, and as a result, were made available on participants' computers.

4.2.3 Data collection

To evaluate the session, questionnaires were created (Supplementary Figure S4/S5). Questionnaires contained both dichotomous questions and open-ended questions. Nine completed pre-questionnaires and 10 completed post-questionnaires were returned from the session, anonymously, with coding applied to enable pre and post questionaries to be associated.

4.2.4 Data analysis

Data collection was collated, matched by identification codes, and scanned as PDF files on an internal drive. No identifiable participant information was collected. Multiple choice questions were altered into the binary score, ‘yes’, ‘maybe’, and ‘no’ equating to 1 if a positive selection, 0.5 for maybe or 0 if a negative selection. Data was processed in Prism v8.1.1 (GraphPad software) by parts of whole doughnut charts to represent the proportion of choice selection. Comment-based answers were divided into keywords and themes of answers, with frequency of theme summarised in bold contained in a table or summarised in a bar chart. Statistical analysis was unable to be performed due to the small population size.

4.3 Results

4.3.1 Pre-workshop questionnaire

The pre-workshop questionnaire was developed to measure the level of knowledge and understanding of the core topics, micro-CT, AM, and CAD software from the attending participants. Micro-CT had a higher percentage of familiarity amongst participants (Figure 4.3.1A), 67% compared to CAD software, 34% (Figure 4.3.1D). For micro-CT, of the participants who identified familiarity with the technique only 67% had experience analysing data (Figure 4.3.1B). Imagej (Bonej), CTAn, and Amira were identified as the most frequently used software (Figure 4.3.1C).

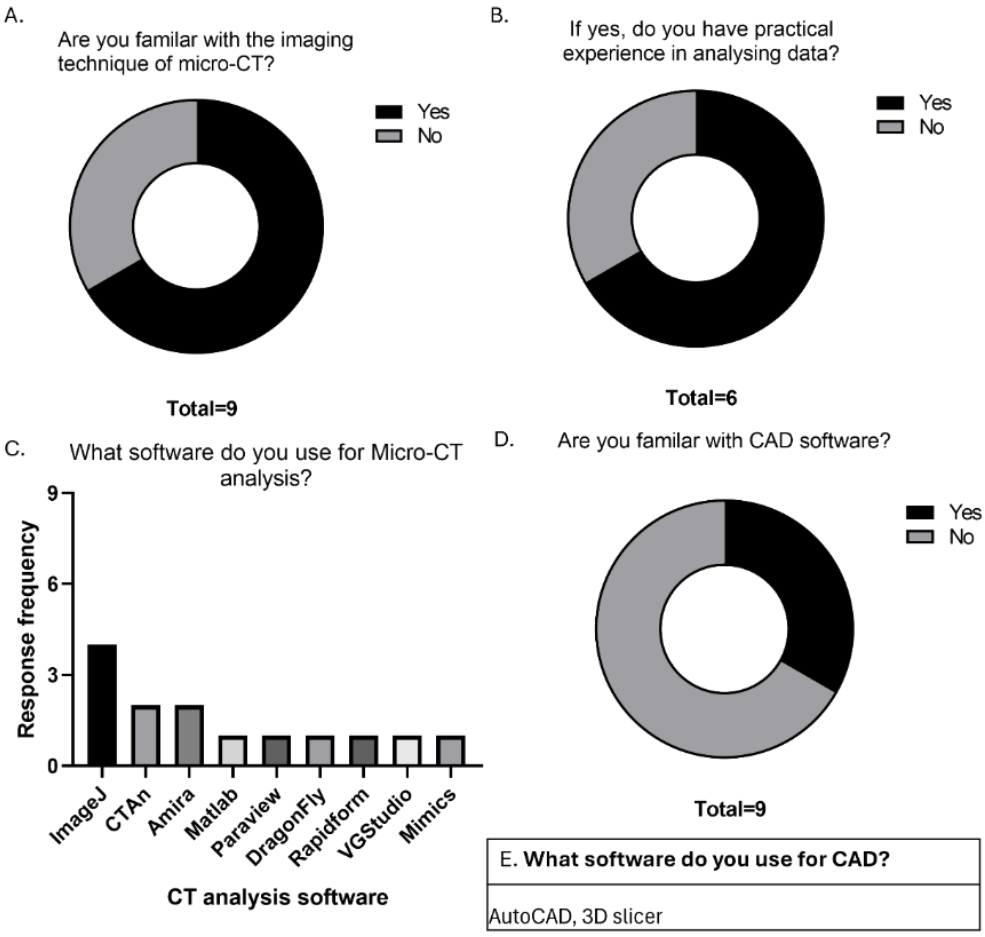

Figure. 4.3.1. Investigation into familiarity with techniques, and scope of relevancy. *Nine responses were collected, for the intention of understanding the range of knowledge between attending participants. A) Participant micro-CT familiarity B) Micro-CT analysis experience, C) Scope of software used for micro-CT, D) CAD familiarity, E) Scope of software used for CAD. n = 9.*

AM has two main branches: 3D printing and 3D bio-printing, with further subdivisions of the different techniques. Each technique requires different considerations and preparation of 3D models due to the printing processes and materials associated with each technique. For this group of participants, 56% did not know what type of 3D printer (Figure 4.3.2A) or materials (Figure 4.3.2B) they had access to, compared to 44% who had an awareness of the printer and material. Bio-printing and FDM were identified as the most common techniques, with 22% of total participants having access to either technique, compared to 11% who had access to stereolithography and ceramic 3D printers. Attendees stated research interests in a broad range of areas including Bone, medical anatomy, and dental models.

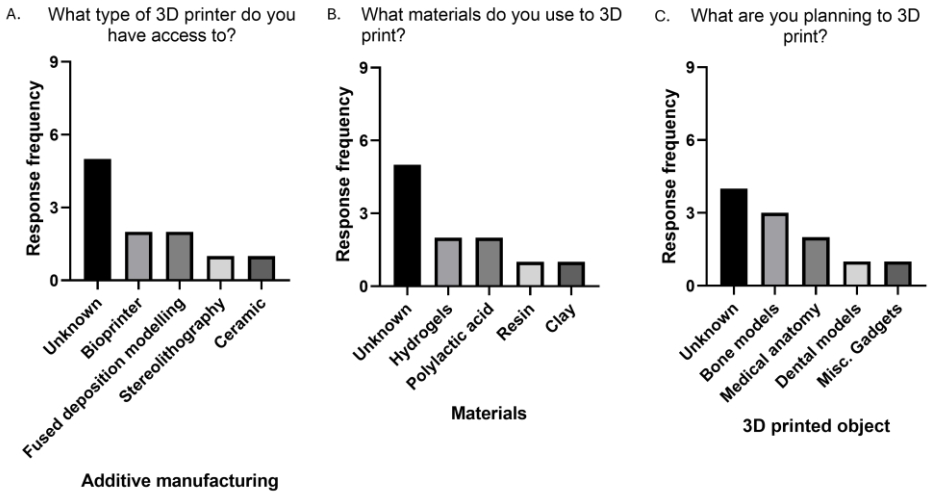

Figure 4.3.2. Investigation into availability, materials, and application of 3D printing. *Nine responses were collected, for the intention of understanding the knowledge and 3D printing equipment available for attending participants. A) 3D printer access, B) Material access, C) intended 3D model output. n = 9.*

To understand why participants decided to attend the workshop, it was important to decipher how the workshop would fit into their research. All participants believed that transferring micro-CT data to 3D models was useful for their research (Figure 4.3.3A), demonstrating the workshop's content impact on the wider scientific community by encouraging skills and knowledge. Interestingly, a wide variety of responses were provided for their reasoning including validating methods, educational tools, and pre-surgical planning being the most frequent answers (Figure 4.3.3B). Participants' expectations (Figure 4.3.3C) were similar, with an increase in knowledge for all listed processes.

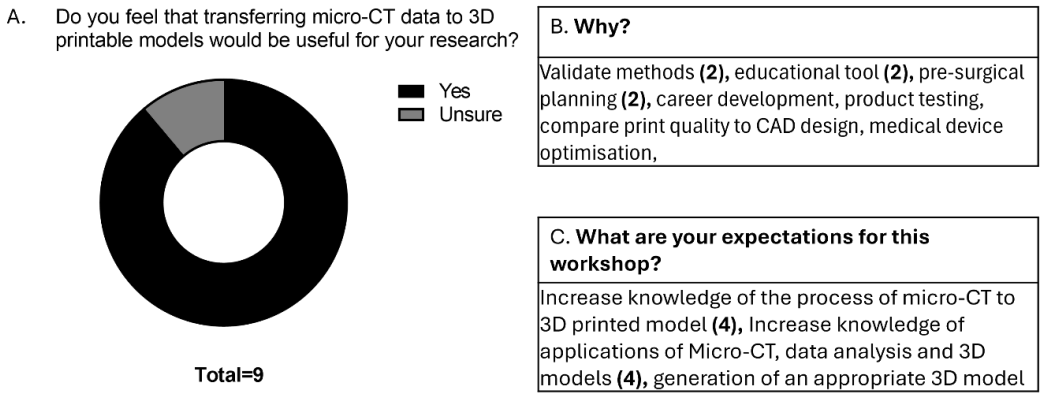

Figure 4.3.3. Investigation into participants' purposes and expectations for attending the workshop. *Nine responses were collected, to comprehend the anticipated outcome and relevance to current research. A) Use in research, B) Expansion of information, C) expectations for workshop content. n = 9.*

4.3.2 Post-workshop questionnaire

The post-workshop questionnaire was designed to investigate the effectiveness of the dissemination of knowledge. The participants reported a 100% success of the workshop in meeting the participants' initial expectations (Figure 4.3.4A). Following this, the content of the workshop was 100% relevant to the participants' research, indicating the relevance and importance of the information to the wider scientific community. The expansion of knowledge was the most common response when asked why the workshop would be useful to their research (Figure 4.3.4B/C). The workshop materials provided to the participants were deemed clear and helpful in assisting independent learning (Figure 4.3.4D), and furthering understanding (Figure 4.3.4E).

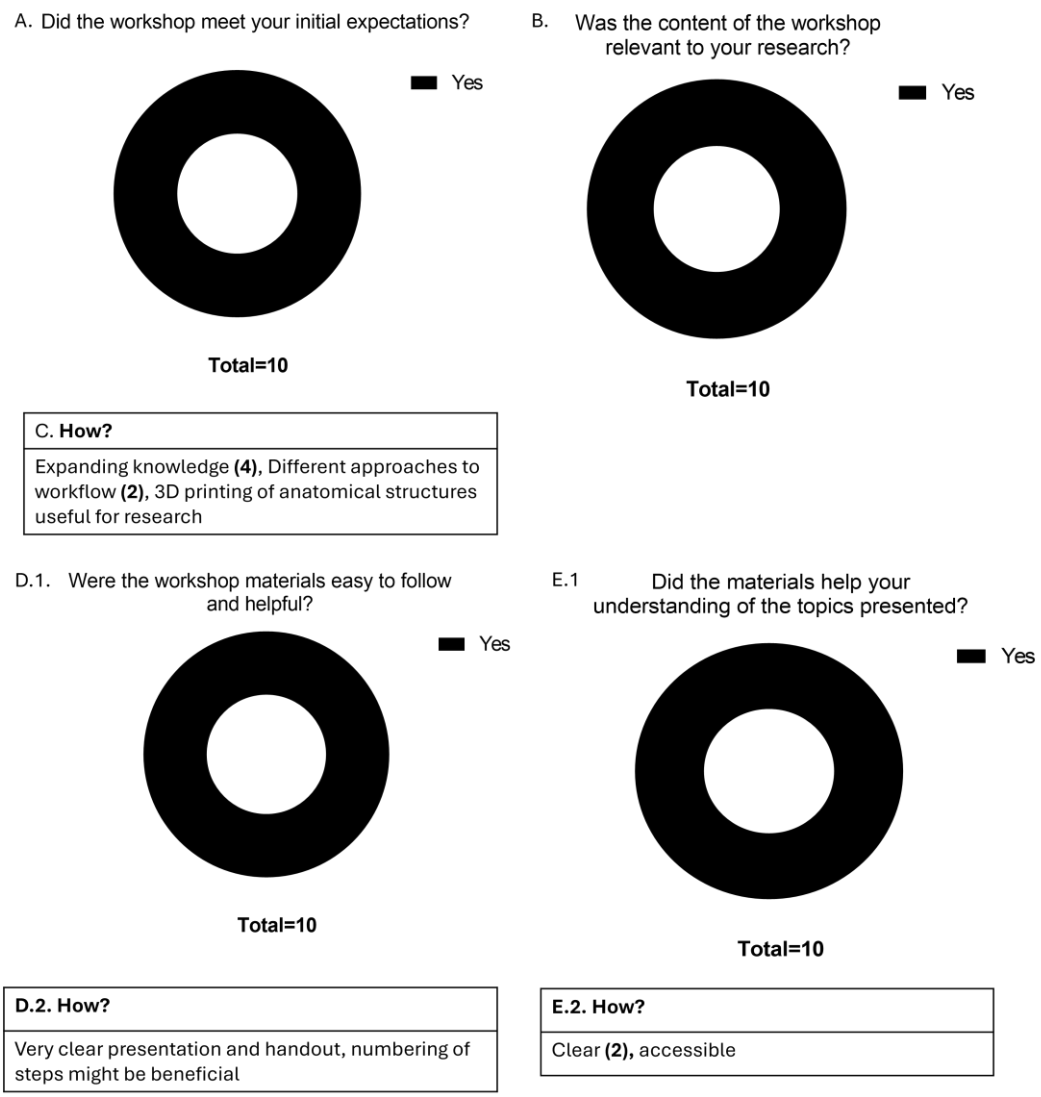

Figure 4.3.4. Understanding the relevance of the information to the participant's scientific research. *Ten responses were collected, to comprehend the success in delivery of content and the impact on individual research. A) Content meeting expectations, B) Relevance in research, C) Expansion of information, D/E) Evaluation of materials. n = 10*

As an early career researcher, it was important to receive feedback on the materials generated, the presentation, and the information provided to ensure effective knowledge transfer. All participants had positive feedback and stated that the materials provided, and the format of the workshop ensured that they left the workshop with a new skill or had a new awareness of the considerations for all micro-CT, AM, and CAD software (Figure 4.3.5).

A. **What was the most valuable part of the workshop for your research?**	B. **What techniques did you learn?**
Learning CAD software **(5)**, technical considerations for 3D printing capabilities **(2)**, evaluation of bones from a different workflow, practical activity to directly learn	CAD software (Fusion 360 + meshmixer) **(6),** working with 3D data, improved CAD rendering skills

C. Do you feel confident in transferring micro-CT data to 3D printable models?

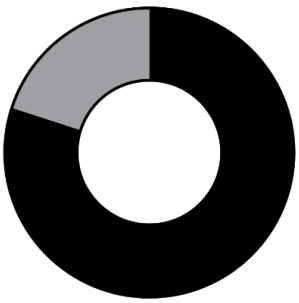

Total=10

D. **Why?**
Not used a 3D printer before, but materials and information provided will inform and help

E. **Are there any improvements you would suggest for future workshops?**
None **(7)**, over-view of the presenter's research, simple files to practice on at home, visualisation of a 3D printed model based on the taught process

Figure 4.3.5. Determining the output value of attending the workshop for the participants*. Ten responses were collected, to investigate the new skills and knowledge obtained. A) Value in attendance, B) Techniques learned, C) Confidence in the method, D) Expansion of information, E) Feedback for workshop improvement. n = 10.*

Overall, 67% and 34% of participants had previous micro-CT and CAD knowledge, respectively. Of the participants who had knowledge gaps in both micro-CT and CAD, 67% stated that they had improved in the technique of processing micro-CT data to a rendered CAD model, with only 33% unsure (Table 4.3.1). Of the 33% of participants who had no prior micro-CT knowledge, 67% reported improved confidence, with 33% unsure. Finally, of the 66% of participants with no prior CAD knowledge, 67% reported improved confidence, with 33% unsure. Of all reporting participants, 100% reported an improved knowledge of the overall process taught.

Table 4.3.1. Evaluation of prior micro-CT and CAD knowledge, compared to confidence in methodological process post-workshop. *Responses from the participants who completed both the pre- and post-questionnaire were, to evaluate the progression in the knowledge of key concepts. n = 9.*

Participant ID	Prior micro-CT knowledge	Prior CAD knowledge	Confidence in micro-CT to rendered CAD model method post workshop
P1	Yes	No	Unsure
P2	Yes	Yes	Yes
P3	No	No	Unsure
P4	No	No	Yes
P5	No	No	Yes
P6	Yes	No	Yes
P7	Yes	No	Yes
P8	Yes	Yes	Yes
P9	Yes	Yes	Yes

4.4 Discussion

4.4.1 Evaluation of questionnaire design

The opportunity to present and teach an optimised methodological workflow workshop, which was developed as part of my PhD fellowship, was a rewarding experience as an early career researcher. To evaluate the success of knowledge delivery throughout the workshop process, a pre- and post-workshop questionnaire was generated enabling feedback from participants on their level of understanding before and after the workshop. Areas that were assessed included the materials they were provided with, the knowledge gained, and if they felt confident with their new skills which were constructed through the experience.

Within the questionnaires, two types of questions were employed: dichotomous and open-ended (Boynton, P., & Greenhalgh, T. 2004; Fink, K. 1996). Dichotomous questions allowed for clear and definitive answers to be obtained, in this case, options of yes, maybe, and no. Dichotomous questions were used to inform the researcher of the depth of knowledge of the participants attending the workshop on all main themes: micro-CT, AM, and CAD rendering, as well as to determine the success of information dissemination. Dichotomous questions can be openly criticised by forcing participants to make a choice they do not completely agree with, causing bias (Choi, B., & Pak, A. 2004). To combat this, open-ended questions were also included to offer participants the option to include their own opinions (Schaeffer, N., & Dykema, J. 2011). As a result, participants provided more detailed responses, including thought processes and specific information of their own working knowledge.

Open-ended questions are often criticised, as general open-ended questions do not typically produce qualitative or quantitative data and therefore lack clarity on how to analyse and report findings (O'Cathain, A., & Thomas, K. 2004). By summarising open-ended questions, frequency tables were able to be generated to allow an unbiased consensus between participants, such as micro-CT analysis software usage.

4.4.2 Workshop skills taught to participants

The workshop utilised Bruker CTAn as the micro-CT analysis software and the method of generating the un-rendered 3D STL model. Information presented in the workshop

included details on the interface and the capabilities of the software to ensure participants were equally informed. Due to CTAn being a licensed software, this was not available for open use during the workshop; however, materials were provided to explain the interface to users, as well as demonstrating bone analysis and 3D model generation. Bruker CTAn software and equipment are widely used within the bone scientific research community (Walker, E., *et al*. 2021; Salmon, P., *et al.* 2015; Campbell, G., & Sophocleous, A. 2014; Bouxsein, M., *et al*. 2010), however different software options exist including open-use; ImageJ plug-in (BoneJ), (El-Gizawy, A., *et al*. 2023; Domander, R., Felder, A. A., & Doube, M. 2021; Salmon, P., *et al.* 2015 Double, M., *et al*. 2010), DragonFly (Xi, R., *et al*. 2024; Viero, A., *et al.* 2022) and MatLab (Sefa, S., *et al*. 2023; Wankier, Z., *et al.* 2021), as well as further licensed software Amira (Beitlitum, I., *et al*. 2021; Veneziano, A., *et al*. 2021; Pratt, I., & Cooper, D. 2017), all of which were software's recorded as being used by participants. BoneJ, dragonfly, Amira, and MATLAB, in theory, support the exportation of 3D tessellated models due to the meshing ability from the reconstruction of standard TIF files (Koyama, H., *et al*. 2023; Wang, N., *et al*. 2021), however, these processes would require ample optimisation and the use of multiple software packages, as explored by Bucking (2017). Despite this methodology being presented with the use of CTAn, this method of translating CT to 3D printable models is achievable by different open-source software package programs depending on experimental pipelines and software availability/familiarity (Flaxman, T., *et al.* 2021).

AM approaches were explored with the participants. Due to the varied responses provided, it was apparent that many participants were unsure of the different 3D printing/bio-printing techniques available to them. It is undisclosed if this is due to knowledge gaps of techniques, or unfamiliarity with equipment availability in different research institutes, highlighting an improvement in the questionnaire to investigate this information in future. Unfamiliarity with micro-CT as a technique was unexpected, due to the premise of the workshop location, i.e. within the BRS Meeting and following an initial workshop on micro-CT and FEM. It was anticipated that participants would have a higher degree of knowledge of micro-CT processes due to the prominence of the imaging technique within the bone research field, compared to both CAD and AM techniques.

From this, more detailed information on different applications, including various CAD software options (Kizilkaya, A., & Kara, A. 2024; Bucking, T. *et al*. 2017), was included in the handout. The main emphasis of the information was a simple step-by-step guide on how to use two different CAD software programmes: Meshmixer and Fusion 360™. The two Autodesk® CAD options were employed to ensure participants reached a successful end goal of 3D model rendering due to the experience of the lead researcher, but also due to the ample supportive material online and within the software interfaces for the participants. The approach to focus on CAD from the three original aims was favourable for the active participants, as all participants stated improved knowledge in this area.

4.4.3 Determining the success of the workshop

The post-workshop questionnaire was designed to evaluate the dissemination of knowledge to the participants, but mostly to aid evaluation of the materials provided and to scope how this research method fits within the wider scientific community. All active reporting participants agreed that the workshop met their initial expectations of content. Additionally, all participants commented that the presented information was relevant to their research, further demonstrating the methodology's relevance within the wider scientific community. This was due to expanding the individual's knowledge and showcasing different approaches to workflows by showing alternative information.

It should be noted that participants were required to self-register for the workshop presented; therefore, it was assumed that participants had an interest in the topic or were already active within some of the themes of the workshop. This demonstrated that improved knowledge by all participants drives satisfaction, relevance of information and expectations of attending. All learners had an increase in confidence and knowledge in the subject areas: micro-CT, CAD and AM, summarising the success in the overall aim of dissemination of knowledge and methodology to the scientific community.

For the small population size of specialised individuals who participated in this study, it can be concluded that undertaking the workshop based on the developed method was a positive experience that taught new skills and improved knowledge. To further expand on conclusions and improve the study, a larger sample size of participants would better

represent the population and improve the relevance of findings by allowing statistical analysis to be conducted (Serdar, C., *et al*. 2021; Martinez-Mesa. J. *et al*. 2014).

Further to the post-workshop questionnaire, to determine impact on participants skills long-term it would have been beneficial to pursue a follow-up questionnaire. This would include questions on

4.4.4 Conclusion

Dissemination of this AM pipeline was successfully delivered at the BRS meeting, with taught materials and workflow allowing participants to learn new skills and enhance their knowledge surrounding the subject area of micro-CT imaging and using CAD software for 3D modelling of biological structures. All participants rendered a 3D CAD model from the original *ex-vivo* bone STL 3D model provided to them, by using the methods evaluated by the research project.

Chapter 5 – Optimisation of bioprinted bone

Optimisation, evaluation and considerations required for the development of a bioprinted in-vitro bone model.

5.1 Introduction

The long-term objective of 3D bioprinting is to develop 3D biocompatible models, that closely mimic living tissues with improved physiological relevance for either humans (*In-vivo*) or biomedical research models (*In-vitro*). Biomaterial solutions, referred to as bio-inks in this application (Dell, A., *et al.* 2022), are varied in composition based on the 3D printing method, incorporation of living cells and/or biomolecules and the intended 3D model. Material characteristics, notably viscosity and flow behaviour known as rheology, dictate the possible fidelity and complexity of the resulting 3D bioprinted model (Gungor-Ozkerim, P., *et al.* 2019).

5.1.1 Bioink

Ideally, a bioink composition is aligned towards the intended experimental organ, with printability and appropriate rheological behaviour considered for the bioprinting method used. Hydrogels are preferable bioinks for EBB due to excellent biocompatibility and controllable permeability, allowing a hydrated yet mechanically supportive 3D environment (Dell, A., *et al.* 2022). For instance, skin is a commonly fabricated bioprinted model that incorporates high concentrations of water, and natural polymers such as collagen, cellulose, chitosan and hyaluronic acid, often using different layers of similar hydrogel bioinks to replicate the hydrated dynamic ECM layers of skin basement membranes (Arabpour, Z., *et al.* 2024; Kang, M., *et al.* 2022). Similarly, liver bioprinted models predominantly use natural hydrogel polymers; however, the biomaterials typically have increased stiffness, such as gelatine and Alg and use one bioink type for the entire model (Ali, A., *et al.* 2024).

Bone, as previously discussed (Chapter 1, section 1.2.2), comprises organic and inorganic components; therefore, an appropriate bioink to mimic this tissue requires both these attributes. Typically, collagen is supplemented with HAnp or other suitable bioactive components to achieve a biomimetic ink (Bakhiary, N., Liu, C., & Ghorbani, F. 2021). Many different approaches of biomaterials to mimic bones have been explored, including HAnp within polymer hydrogels (Badhe, R., *et al*. 2023; Li, N., Guo, R., & Zhang, Z. 2021). Chapter 1, section 1.6.1 summarises different biomaterial constituents that have been frequently used previously to mimic bone in a bioprinting approach.

The research presented here investigated commercially available bioink (Bone GelXA and TissueFAB™) and an in-house synthesised hydrogel (Boyes, V., *et al*. 2021; Thorpe, A., *et al.* 2016a) to develop a suitable *in-vitro* bioprinted bone model to capture accurate fidelity to a previously generated CAD bone mouse tibia (Chapter 3, section 3.3.3). The commercial inks' true formulation, concentration and composition are not disclosed; however, it can be hypothesised, based on crosslinking and material behaviour, to be composed of Alg and GelMA (Figure 5.1.1) (Badhe, R., *et al*. 2024; Anerillas, L., *et al.* 2021). Whereas the in-house generated hydrogel is known to be Laponite® (N-isopropylacrylamide, N, N'-dimethylacrylamide) co-polymer with 0.5 mg/ml HAnp (B-gel) (Boyes, V., *et al*. 2021; Thorpe, A., *et al.* 2016a; Thorpe, A., *et al.* 2016b) which is a thermally responsive hydrogel, that transitions from a colloidal nanocomposite suspension above 37 °C into a sterically entangled hydrogel network when the temperature drops below 37 °C (Figure 5.1.1).

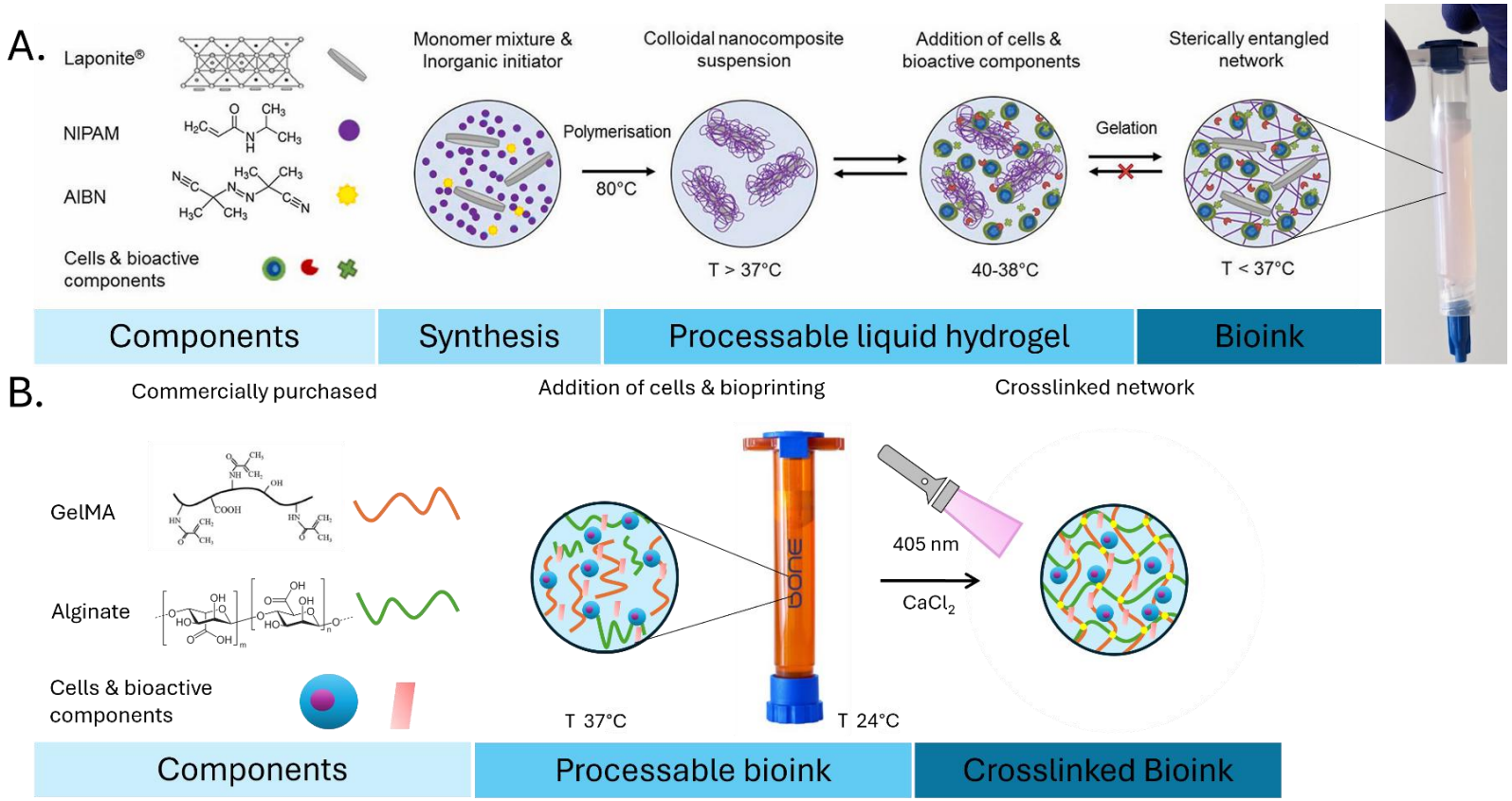

Figure 5.1.1. Commercially available bone GelXA bioink and in-house generated B-gel (adapted from Boyes, V. 2021). *A) Overview of the components, synthesis and processing of in-house generated Laponite® crosslinked poly (N-isopropylacrylamide, N, N'-dimethylacetamide) co-polymer with 0.5 mg/ml hydroxyapatite nanoparticles and cellular components from hydrogel to structural bioink, B) overview of the components and processing of bone GelXA bioink to crosslinked bioink.*

Important attributes of bioink include printability, which is defined by the rheological properties, owing to the flowability and deformability of the material during the EBB process, which determine the shape and structural stability of the final printed structure (Bakhtiary, N., Liu, C., & Ghorbani, F. 2021; Riberio, A., *et al*. 2017; Paxton, N., *et al.* 2017). Bioinks are typically pseudoplastic shear-thinning materials, with the benefit of bioinks becoming thinner with an easier flow when subjected to shear stress, causing the material to be deposited from a suitable nozzle in the intended XZY orientation (Ribeiro, A., *et al.* 2017). In general, a trade-off between printability and biocompatibility exists, in which stiffer, more viscous materials exhibit accurate shape fidelity, whereas softer, less viscous materials provide a suitable environment for biocompatibility with higher deviation of shape fidelity compared to the original STL, with minimal shape complexity (Jungst, T., *et al.* 2016). It is important to consider a bioink's functionality and composition without compromising printability, stability, and biocompatibility, which remains challenging when creating complex architecture.

5.1.2 Microparticle support bath for extrusion-based bioprinting

To improve structural complexity and overall filament fidelity, a class of assistive materials for 3D extrusion-based bioprinting has gained popularity (Budharaju, H., *et al.* 2024; Brunel, L., Hull, S., & Heilshorn, S. 2022; Zhou, K., *et al*. 2022). These materials include support baths, where bio-inks are printed, or sacrificial inks, which are printed alongside the desired shape and then later removed (Yang, S., *et al*. 2025; Liu, S., *et al.* 2022). Support baths are typically yield-stress materials, e.g. a material that can undertake stress without irreversible deformation, that provide physical confinement during the printing process to improve print resolution and overall, EBB shape fidelity, and they can 'self-heal' after filament deposition (Daly, A., *et al.* 2021; Lee, A., *et al.* 2019; Highley, C., *et al*. 2015). Typically, once the bioprinting process has been completed and the bioink has transitioned into a solid state, the model is either removed manually (Moxon, S., *et al.* 2024) or the support bath is melted away (Shiwarski, D., *et al*. 2021). Printing into a support bath, as opposed to an open-air stage, whereby materials suffer from the unavoidable effects of gravity at the air-water interface (Sarabi, M., Yetisen, A., & Tasoglu, S. 2013; Ombergen, A., *et al*. 2023; Shiwarski, D., *et al*. 2021), keeps the printed bio-ink hydrated, suspended in place with lower interfacial tension. Therefore,

improving the possibility of transitioning soft biomaterials into a bio-ink by preventing structural collapse and improving print fidelity (McCormack, A., *et al.* 2020), and the opportunity of printing structural overhangs. Sacrificial inks are typically equipped to create hollow internal architectures, such as vascular-like networks within microfluidic devices (Wang, X., *et al.* 2023; Pan, B., *et al.* 2022; Kolesky, D., *et al*. 2014), or combined with bioinks to modify the printability of the biomaterial of interest with a removal mechanism once printing has completed (Liu, S., *et al.* 2022; Ying, G., *et al*. 2018).

Wu (2011) developed a support bath which is comprised of photocurable Pluronic F-127 diacrylate, which physically supports omnidirectional bioprinting and inspired a new branch of research to improve the complexity of 3D EBB printed structures. Soon after, a gelatine microparticle slurry, defined as a semi-liquid mixture containing micro-particles suspended in solution (McClendon, M., *et al.* 2024), arose from an ethanol-induced coacervation process developed by the research group led by Adam Feinberg was published (Hinton, T., *et al.* 2015). Named freeform reversible embedding of suspended hydrogels, the microparticle slurry facilitated the EBB of complex architecture with a filament resolution of ~ 100 µm by allowing shear-thinning materials to be deposited and supported by a self-healing medium (Shiwarski, D., *et al.* 2021; Lee, A., *et al*. 2019; Hinton, T., *et al.* 2015). Closely following Feinberg, Thomas Angelini developed a similar granular gel support bath whereby the gel system solidified, entrapping the deposited filament in suspension and negating the effects of surface tension and gravity in a process of jamming/unjamming tension (Bhattacharjee, T., *et al.* 2015). The gel system was formed of Carbopol ETD 2020 polymer, which is a polyacrylic acid, designed for thickening surfactant systems (Oelschlaeger, C., *et al.* 2022), and supports low interfacial tension of materials for defined structures. The achievable resolution of this system was limited to granule size; however, it can support a filament thickness of ~ 100 µm, and the 3D bioprinted structure required crosslinking before removal from the suspension (Duraivel, S., *et al*. 2022; Bhattacharjee, T., *et al.* 2016). Alternative methods involving support baths for EBB include utilising blended agarose as a support medium (Mirdamadi, E., *et al.* 2019), bioprinting directly into a mould (Zhou, L., *et al.* 2023), and alternative microparticle polymer suspensions (Highley, C., Rodell, C., & Burdick, J. 2015).

An in-house slurry (IHS), ethanol-induced coacervation of gelatine, was adapted from the method developed by Adam Feinberg for the application of 3D bioprinting (Lee, A., *et al*. 2019; Hinton, T., *et al.* 2015) as a result of no commercially available product during the early stages of the research presented in this thesis. The protocol required optimisation and adaptation to create a reproducible product fit for purpose. Feinberg have recently licensed their microparticle slurry under the name of LifeSupport™ (LS) (FluidForm™), which was used as a comparative control to the IHS optimised here.

5.1.3 Micro-particle support bath composition

Typically, microparticle support baths constitute a gel phase that will be formed from either synthetic or natural polymers, suspended in solution, which contributes to self-healing properties, and with a low (below 37 °C) melting point, which allows the release of the 3D printed structure (Brunel, L., Hull, S, & Heilshorn, S. 2022; McCormack, A., *et al*. 2020; Highley, C., Rodell, C., & Burdick, J. 2015). The benefit of a self-healing support bath is the ability to reform around the deposited bioink without impediment, allowing the morphology to include overhangs. The shape of the microparticles in the slurry solution assists in the function of the material, with spherical structures passing without resistance compared to irregular structures that are more likely to interfere with material flow (Zeng, G*., et al*. 2023). This has been shown to increase print resolution and print fidelity, so the resulting printed object more closely resembles the target STL 3D model (Hinton, T., *et al.* 2015; Bhattacharjee, T., *et al.* 2015; Highley, C., Rodell, C., & Burdick, J. 2015) as the full-sized cardiac model printed with collagen by Lee (2019), mm-sized cardiac model printed with decellualrised human omental hydrogel Noor (2019) and the kidney model Zhang (2024).

Gelatine

Gelatine is a natural biopolymer consisting of an amphoteric polymer that is derived from collagen by thermal denaturing or partial hydrolysis of collagenous materials, such as mammalian skins, carp skin or demineralised bones (Jannat, B., *et al.* 2020; Ninan, G., *et al.* 2012). The properties of gelatine are altered by several biological factors, such as source material age and the intrinsic parameters, including chemical composition; molecular weight distribution, and amino acid composition (Mad-Ali, S., *et al.* 2017). For

mammalian gelatine, derived from skin, bones and connective tissues, type A is cationic, resulting from the partial acid hydrolysis, whereas type B gelatine is anionic, derived from an alkali-based treatment. Type A gelatine is derived from porcine, whereas type B is bovine (Mikhailov, O., *et al*. 2023; Jannat, B., *et al*. 2020). During alkaline hydrolysis treatment, the gelatine undergoes partial removal of asparagine and glutamine amide groups, increasing aspartic and glutamic acid content. This increase in carboxyl groups results in type B gelatine having negatively charged properties, with a lower isoelectric point of around 4.7 – 5.5, compared to type A, which has an isoelectric point of 6 – 9 (Goudie, J., *et al*. 2023). The melting point and gelling point of mammalian gelatines are similar, with Ninan (2012) reporting 32 °C and 34 °C for melting and 31.6 °C and 31.8 °C for gelling of bovine and porcine, respectively.

Upon gelling, gelatine can undergo conformational changes to the gelled structure based on the surrounding environment and concentration. For the generation of microspheres, different approaches can be undertaken, such as water-in-water emulsification (Chen, J., *et al.* 2021; Beldengrun, Y., *et al*. 2018), double emulsion oil-in-water-in-oil, which results in microspheres with more control on shape, size, porosity and stability (Zhang, L., & Yu, Y. 2023; Zhang, T., *et al*. 2020), electro spraying (Atay, E., *et al.* 2018), microfluidics (Moreira, A., Campos, J., & Miranda, J. 2022) and various coacervation processes including ethanol-induced (Figure 5.1.2) (Pei, Y., *et al*. 2021; Timilsena, Y., *et al*. 2019), and Alg encapsulation (Chavarri, M., *et al.* 2010).

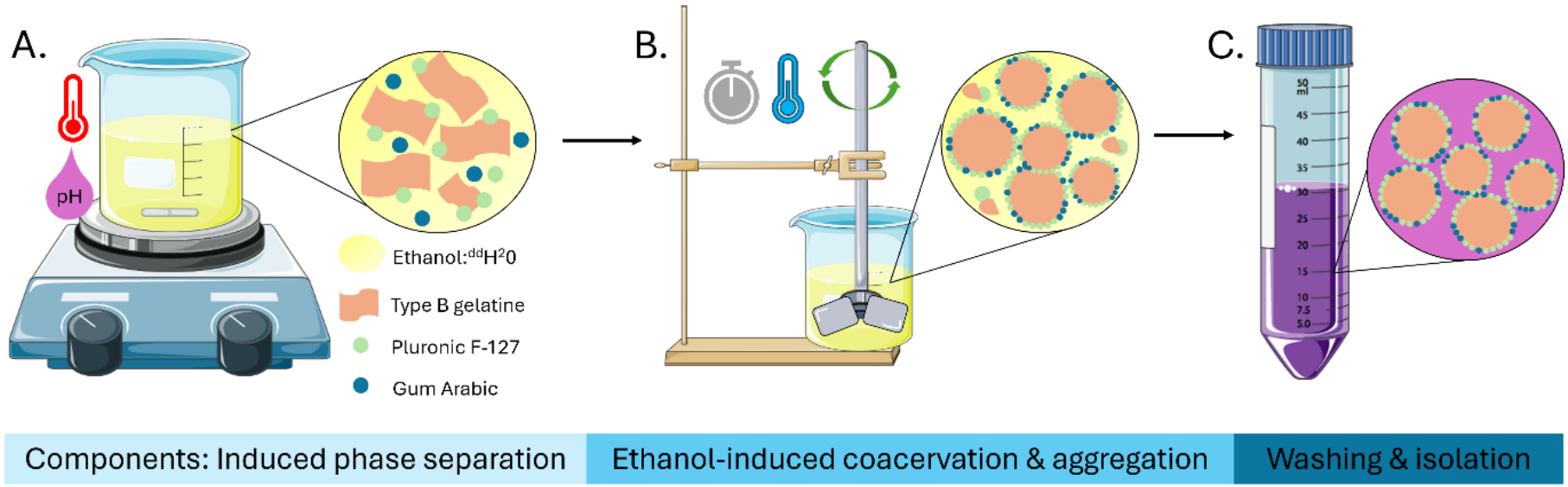

Figure 5.1.2. Schematic of the generation of gelatine microparticles through the process of ethanol-induced coacervation. *Coacervation is a process driven by electrostatic interactions between two aqueous phases, ethanol and water. A) The ethanol phase induces a phase separation in a homogenous gelatine solution, resulting in a polymer-rich phase driven by ethanol acting as a poor solvent for gelatine. The solution is heated and pH adjusted. B) Microspheres are encouraged by aggregation with an impeller whilst gelatine undergoes gelling, resulting in spheroid morphology supported by Pluronic F-127 and gum Arabic. C) Resulting microspheres are collected, compacted and washed for the removal of excess non-gelled material and concentration of microparticles. The washing buffer can consist of cross-linking buffers, such as calcium chloride or growth medium. The figure contains modified Images from Servier Medical Art (https://smart.servier.com) licenced by Creative Commons Attribution 4.0 international.*

Pluronic-F127

Pluronic-F127 (EO_{99}-PO_{69}-EO_{99}) is an amphiphilic block copolymer that self-assembles in different structures, particularly nanosized direct and reverse micelles (Naharros-Molinero, A., *et al.* 2022). The Pluronic family exists as a triblock structure, with a central hydrophobic poly (propylene oxide) segment linked to two lateral hydrophilic poly (ethylene oxide) chains. The behaviour of this material is controlled by the Pluronic type, dictated by chain length, concentration in solvent, temperature, pH and the presence of external additives (Di Spirito, N., Grizzuti, N., & Pasquino, R. 2024). Pluronic assists in the self-assembling morphology of micelle aggregates, further referred to as spheres, within this reaction due to temperature control and poor water solubility, whereby self-assembly transformation is spontaneous. Typically, micelles assemble in the size range of 10 – 100 nm and are primarily used as a nanotherapeutic containing bioactive component or therapeutic for drug delivery (Bhalodi, K., Kothari, C., & Butani, S. 2024), however when combined with a polymer the controlled self-assembling can form different morphologies, and sizes (Yao, Y., *et al*. 2021).

Gum Arabic

Gum Arabic is a polysaccharide formed from arabinogalactan, a combination of D-galactose and L-arabinose, produced from the dried sap of *Acacia Senegal* and *Acacia seyal* trees. It has been used predominantly as an emulsion stabiliser in a wide range of applications within many different industries (Yao, Y., *et al.* 2021; Atgie, M., *et al.* 2019). Within this study, gum Arabic is used as a microsphere stabiliser to assist in retaining the spherical shape morphology, which occurs during the alcohol coacervation process, as well as the spontaneous self-assembly of the micelles. Riberio (2016) investigated the improved stability of gold nanoparticles when using gum Arabic in various physiological pH conditions, such as intestinal (pH 6.8) and gastric (pH 1.2), thereby improving the above described microparticle slurry by facilitating stability in multiple conditions, such as different pH's which can assist biomaterial crosslinking conditions for some materials.

5.1.4 Assessment of flow behaviour of biomaterials

The support bath micro-particle slurry and different bio-inks are physical materials whereby their characteristics define the method of printing success and the production

of a high-fidelity 3D bio-printed model; therefore, investigating and characterising the rheological flow behaviour of the differing materials is vital when reporting on functionality (Budharaju, H., *et al.* 2024; Brunel, L., Hull, S., & Heilshorn, S. 2022; Habib, M., & Khoda, B. 2022; Zhou, K., *et al.* 2022). Rheology is undertaken to investigate a material's deformation and flow behaviour in response to motion, defined as shear stress (Figure 5.1.3) (Herrada-Manchon, H., *et al.* 2023; Habib, M., & Khoda, B. 2022). The microparticle slurry and bioink all undergo different transitions of stress and flow during the process of 3D bioprinting, which impacts viscosity, enabling the structured fluid materials to behave in a characteristic way to extrude, for bioinks (Bercea, M. 2023; Habib, M., & Khoda, B. 2022), plus the balance of flow and recovery, for microparticle support slurries (Gillispie, G., *et al.* 2023; Amorim, P., *et al.* 2021; Townsend, J., *et al.* 2019).

Fluids are defined by viscosity, which characterises different fluid behavioural flow patterns in response to stress (Wilson, D. 2017). Newtonian fluids, most associated with water, do not change in response to stress such as shear forces, whereas non-Newtonian fluids behave in diverse ways in response to stress, this includes Bingham plastic; pseudoplastic; and dilatant (Malkin, A., Derkach, S., & Kulichikhin, V. 2023) (Figure 5.1.3). A structured fluid dispersion is defined as a material which includes particles or droplets suspended in a carrier liquid, such as a microparticle slurry (Figure 5.1.2). The viscosity of the liquid phase in dispersions plays a significant role, whereby the microparticle support slurry has a liquid phase of growth medium which classifies it as a Newtonian fluid without additives of serum (Cantarero-Rivera, F., *et al.* 2024; Poon, C. 2022), and with B-gel (Figure 5.1.1) which has a carrier liquid of water, another Newtonian fluid (Berstad, D., *et al.* 1988). However, due to the total composition of the materials by the addition of micro/nanoparticles, the flow behaviour is likely to change when the materials are in motion since particles will be forced to slide along each other in motion, and under stress resulting in flow resistance with increased particle size, and concentration often resulting in altered viscosity (Figure 5.1.3) (Gao, T., *et al*. 2018; Tian, X., *et al*. 2009).

Further from the characteristic flow resistance, materials can have different responses to stress based on their viscous flow behaviour, as viscosity is shear-dependent. This

includes being either shear-thinning or shear-thickening (Figure 5.1.3) (Amorim, P., *et al.* 2021). Shear-thinning is defined as a decrease in viscosity in response to increased shear rates, whereas shear-thickening causes viscosity to increase with increased shear rates. Materials can also be viscoelastic, displaying a mixture of viscous and elastic behaviours, depending on the storage (G') and loss (G") modulus ratio (Gillispie, G., *et al*. 2020). Elasticity is the ability to resist a distorting force and return to the original state when the force has been removed, represented by a higher G' compared to a material with a higher ability to dissipate flow, typically visualised by a higher G" (Gao, T., *et al.* 2018). Thereby, a viscoelastic material enables fluid flow with resistance to deformation with shape retention to behave both like a liquid and a solid (Eckert, C., *et al*. 2025; Hull, S., *et al*. 2023).

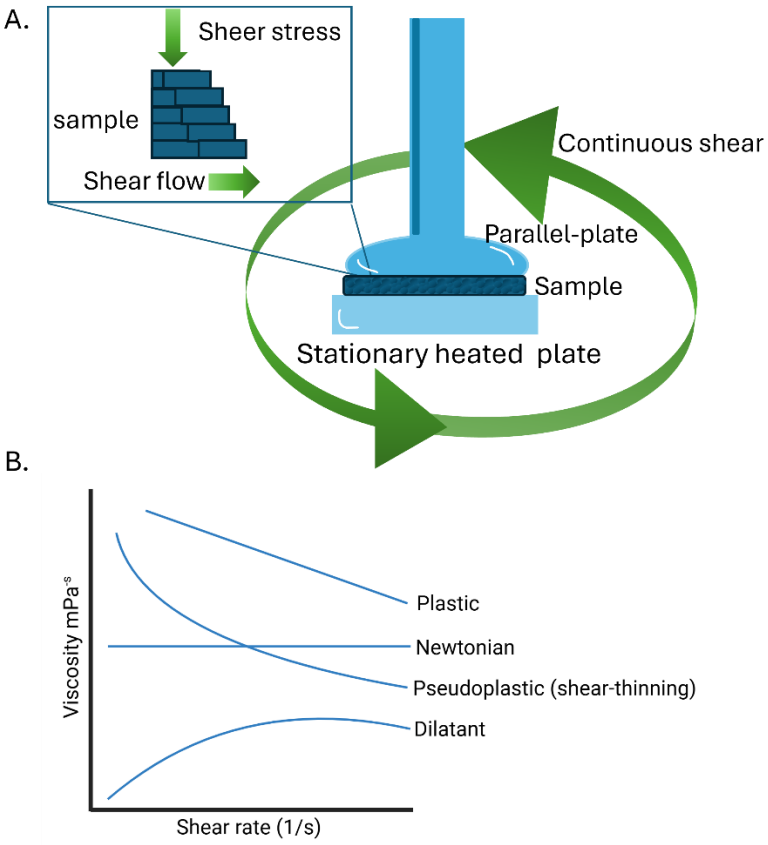

Figure 5.1.3. Schematic of continuous shear rheology and viscosity characteristic flow behaviour. *A) Viscosity can be determined by a rheometer under shear stress using continuous shear of a parallel plate to determine the shear flow of varied materials. B) Viscosity is recorded throughout shear rate, and the resulting flow resistance is characteristic of different material behaviours, including Newtonian, pseudoplastic with either shear thinning or thickening behaviour, plastic, and dilatant.*

5.1.5 Aims and objectives

Optimisation of bioink composition, fidelity and printability.

To investigate the composition and properties of bioink for accurate bioprinting of pre-designed 3D control models derived from CAD data. Ensuring fidelity in shape, structure, and material composition by high-resolution micro-CT, rheology and qualitative assessment.

Generation and characterisation of micro-particle support bath.

Investigate and characterise the rheological properties of a micro-particle support bath, assessing its effectiveness in enhancing structural accuracy during the 3D bioprinting process.

5.2 Materials and methods

5.2.1 Experimental design

This study evaluated both commercially available and in-house formulated biomaterials for their suitability in 3D extrusion-based bioprinting and the generation of an *in-vitro* bone model (Figure 5.2.1). The flow behaviour of each bioink was characterised with rheometry, whilst printing fidelity was assessed under varying printing parameters to determine optimal conditions for structural accuracy. Inorganic material composition was investigated for consistency by high-resolution micro-CT imaging, and 3D bioprinted constructs were optimised for micro-CT imaging. Further, in-house generated and commercially available micro-particle support slurry morphology and diameter were characterised with light microscopy, and flow behaviour was investigated with rheological investigations. The optimised slurry was used to improve filament accuracy of the original STL input 3D model (Figure 4.2.1).

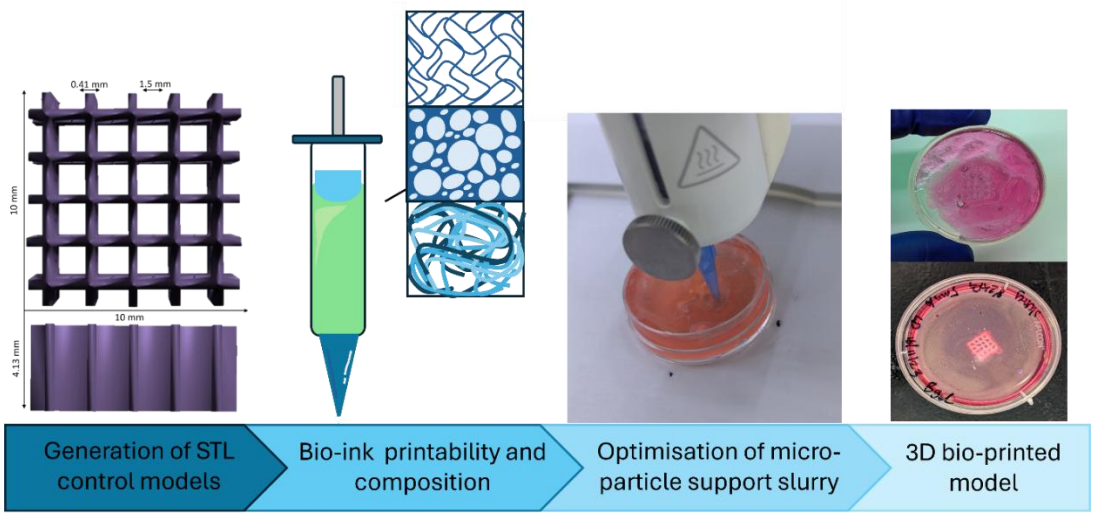

Figure 5.2.1. Experimental design to investigate suitable bioink composition, printability and fidelity, plus characterisation of micro-particle support slurry.

5.2.2 Control standard tessellation models

Two CAD models were generated to evaluate different 3D EBB parameters and associated bioinks. Model generation was completed using open-source software Autodesk® TinkerCAD (www.tinkercad.com). First, a singular filament of 10 mm length and 0.413 mm width/height was created to assess individual filament dimensions during the printing process (Figure 5.2.2). Secondly, a 3D lattice model with known dimensions was generated to assess layering and, most importantly, height capabilities of EBB and different bioinks. A third model of a lattice with the same dimensions, however, only a height of 0.41 mm was generated (Figure 5.2.2). The 3D models were exported in STL binary format.

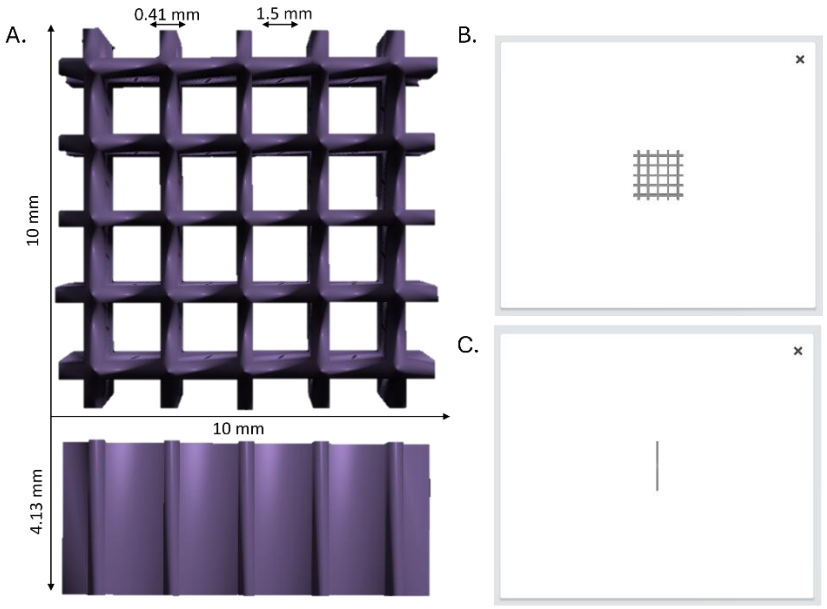

Figure 5.2.2 Known dimension control lattice and line. *A) Computer-assisted design generated a lattice that was composed of solid box shapes, manipulated into rectangles, and snapped to the building plate. The 3D model was exported in the standard tessellation language binary format. B) Lattice uploaded to BioX™ bioprinter interface, C) 10 mm length, and 0.41 mm width line uploaded to BioX™ bioprinter interface.*

5.2.2.1 Three-dimension extrusion based bioprinting

All EBB experimentation was completed with the BioX bioprinter (Cellink, Switzerland), with a conical 22G nozzle fitted to a 3 ml bioink cartridge, either pre-loaded by the manufacturer or prepared in-house (Table 5.2.1). Bioprinting was predominantly completed in 35 mm Petri dishes (Table 5.2.1), however, 6 well Nunc™ plates (Thermo-fisher, UK) were utilised for Bone GelXA experiments. Finally, the BioX bioprinter (CellInk,

Switzerland) was calibrated manually for the printing vessel (either a 6-well Falcon Corning plate or 35 mm Falcon plastic petri dish), by dictating the centre of the vessel with the nozzle tip just above the plasticware. As a standard, EBB experiments were completed in a laminar flow biological safety cabinet, which had undergone thorough cleaning with 70% IMS and UV cycles with the printer *in situ*. The BioX HEPA filter was changed yearly.

Table 5.2.1. Materials used for 3D bioprinting.

Bioprinting accessory	**Distributor and catalogue number**
Empty 3 ml cartridge	SLS, 917753-1EA
22G conical nozzle	SLS, COR6167
End caps for 3 ml cartridge	SLS, 917001-1EA
Pistons	SLS, 916749-1EA
Tip caps for 3 ml cartridge	SLS, 916773-1EA
Female Luer Lock Connector	Merck, C4681-10EA
3 ml Luer Lock syringe	SLS, SYR6160
35 mm petri dish	Fisher Scientific, 10390961

5.2.2.2 B-gel

Laponite®-pNIPAM-co-$DMAc_{13}$ hydrogel was synthesised by Essa Abdusalam or Ronak Janani (Materials and Engineering Research Institute) as per the previously published method (Thorpe, A., *et al.* 2016a). The polymerised biomaterial was stored in a glass vial in colloidal state at 60 °C in an oven, with any transferring of the polymer completed in a sterile temperature-controlled glovebox (Coy, USA) at 40 °C to increase processing time. The hydrogel with no HAnp (NP-gel) was generated by placing an appropriate volume into an empty cartridge and allowing the hydrogel to transition into a gel at < 37°C. A second hydrogel with 0.5 mg/ml HAnp added, generating (B-gel) was prepared by removing an appropriate volume of hydrogel into an empty 3 ml luer lock syringe containing the HAnp. The hydrogel was transferred back and forth between the cartridge and syringe quickly using the female luer lock connector. This was completed carefully to avoid the introduction of air bubbles, whereby the polymer finished in the bioprinting

cartridge, mixing via constant inverting was performed to ensure homogenous incorporation of HAnp. The hydrogel was allowed to transition into a gel at < 37°C. As standard, the transitioned bioink (B-gel) was placed into a temperature-controlled printhead *(Cellink, Switzerland)* and allowed to acclimatise to 34 °C for 10 minutes before the cartridge was fitted with a 22G conical nozzle (Table 5.2.2). B-gel is ultimately a hydrogel throughout; however, for clarification of state and application, polymer hydrogel refers to the liquid state, gel refers to the transformed form, whereas bioink refers to the temperature transitioned state.

5.2.2.3 Cellink GelXA

Bone GelXA bioink *(Cellink, Switzerland)* was heated in a temperature-controlled printhead *(Cellink, Switzerland)* at 37 °C for 10 minutes. For acellular printing, 50 µL of media was added to the pre-loaded cartridge by removal of the bioink utilising a female luer lock connector and a 3 ml luer lock syringe. The bioink was mixed thoroughly between the cartridge and syringe before finally being replaced inside the printing cartridge. For bioinks loaded with cells (Chapter 6), the same method was utilised; however, the cell pellet was resuspended in 50 µL of media and then mixed as described for the mixing of acellular media. Once the cartridges were prepared, the temperature-controlled printhead was reduced to 24 °C for 5 minutes prior to printing. Once bioprinting was completed (Table 5.2.2), constructs were photo-crosslinked under the 405 nm LED module for 60 seconds, followed by ionic crosslinking with 200 mM $CaCl_2$ for 2 minutes.

5.2.2.4 TissueFAB®

An appropriate volume of acellular TissueFAB® bioink Alg(Gel)ma-UV/365 nm (Sigma, 926159-10ml) was transferred into an empty 3 ml cartridge after 30 minutes of gentle warming in a 37 °C incubator. The printed constructs were photo-crosslinked under the 365 nm UV module for a minimum of 120 seconds, followed by a wash with 200 mM $CaCl_2$ for 2 minutes.

5.2.2.5 Bioprinting conditions

Table 5.2.2. Summary of extrusion bioprinting experimental conditions for optimisation of the B-gel and GelXA. *Printing pressures were visually assessed by extruding a range of low pressures until a consistent filament deposition was achieved. The printing pressure often had variability during the 3D bioprinting process, however, speed remained constant.*

Experimental summary	Bioink used	Printing conditions	Crosslinking
Single filament fidelity assessment	Bone GelXA (Acellular)	45, 50, 55 kPa @ 10 mm/s, 7, 10, 13 mm/s @ 50 kPa.	None
	Bgel (Acellular)	75, 80, 85 kPa @ 10 mm/s, 7, 10, 13 mm/s @ 85 kPa.	None – heat transitioned
	Bgel (Cellular)	65, 70, 75 kPa n@ 10 mm/s, 7, 10, 13 mm/s @ 75 kPa.	None – heat transitioned
	TissueFAB® (Acellular)	5 – 15 kPa @ 5 mm/s	None
1-layer lattice optimised from single filament fidelity	Bone GelXA (Acellular)	55 kPa, 10 mm/s.	60s 405 LED exposure, 200mM $CaCl_2$ for 2 mins.
	Bgel (Acellular)	185 kPa, 10 mm/s.	None – heat transitioned
	Bgel (Cellular)	75 kPa, 7 mm/s.	None – heat transitioned
	TissueFAB® (Acellular)	18 kPa @ 10 mm/s	5-minute wash in 200 mM $CaCl_2$ & 60s under 365 nm light module
10-layer lattice – micro-CT optimisation & microparticle support slurry optimisation.	TissueFAB® (Acellular)	19 kPa @ 5 mm/s	10-minute wash in 200 mM $CaCl_2$ & 300s under 365 nm light module
	B-gel (Acellular)	High variability: 40 – 65 kPa @ 10 mm/s.	None – heat transitioned
	B-gel (Cellular)	High variability. Average 40 – 60 kPa @ 10 mm/s.	None – heat transitioned
	Bone GelXA (Acellular)	High variability. Average 20 – 105 kPa @ 10 mm/s.	60s 405 LED exposure, 200mM $CaCl_2$ for 2 mins.

5.2.3 Rheological measurement of bioinks

To investigate the flow viscosity of the bioinks, ~500 µL of bioink was loaded onto a rheometer (Physica MCR 301, Anton Paar) equipped with a 20 mm diameter parallel plate configuration and a maintained gap of 1 mm. For GelXA, three different batches underwent investigation of sheer stress at 24°C. B-gel and NP-gel were investigated at 30, 34, and 37°C, with three independent batches of B-gel analysed at 34 °C to represent the printing temperature. A continuous shear rate strain-controlled amplitude sweeps from 0.01 1Hz to 100 1 Hz (with 1% strain) were used to determine the linear viscoelastic region and apparent yield stress. Data was recorded in Microsoft Excel, and viscosity was presented with GraphPad Prism 8.0 on a logarithmic scale.

5.2.4 Microparticle slurry optimisation

The microparticle slurry was originally published by Lee (2019), however, this published method required further optimisation to be able to be replicated in-house. The different conditions that underwent optimisation are summarised in Table 5.2.3.

Table 5.2.3. Summary of optimised parameters for in-house generated micro-particle slurry.

Condition	***Conditions tested***	***Method***
Origin of gelatine	Porcine (type A) and bovine (type B).	2.0% (w/v) gelatine used was either from a type A (porcine) or type B (bovine) source.
Beaker size	5L, 1L.	The heated solution was placed under an overhead stirrer in either a 5L or 1L beaker.
Time of stirring	0, 30, 60, 90, 120, 150, 180, 210, 240, 270, 300, 330, 360, 390, 420, 450 (minutes).	During the coacervation process, a 1 ml sample was taken at 30-minute intervals ranging from 0 – 450 mins. Room temperature fluctuations were between 16 – 23 °C during the experimental timeframe. The resulting morphology was visualised under light microscopy. Temperature was also measured at the time intervals.
pH	Control of pH after the addition of each chemical.	All dissolved reagents were added into the 50% (v/v) water: absolute ethanol solution independently, with the pH adjusted to 6.25 after each addition.
Insulation	Room temperature cooling and insulated box cooling.	The coacervation process was completed either at room temperature in a fume hood or inside a Styrofoam box.
Impeller specifications		A crossed stirrer blade shaft (10 cm total blade length and 5 cm diameter) or a dual centrifugal stirrer shaft (35 cm length and 5 cm diameter) was used.
Wash buffer	200 mM calcium chloride, α-MEM.	Once the coacervation process was completed, and the liquid phase removed, the resulting slurry was washed in either 200 mM calcium chloride or α-MEM with no additives.

5.2.5 Microparticle slurry generation – optimised method

Microparticle gelatine slurry was prepared using a coacervation technique to produce micro-particles. Two percent (w/v) gelatine type B (Thermo-Fisher, UK), 0.25% (w/v) Pluronic-127 (Thermo-Fisher, UK) and 0.1% (w/v) gum Arabic (Thermo-Fisher, UK) were simultaneously dissolved in a 50% (v/v) water: absolute ethanol solution at 45 °C with a 20 mm magnetic stirrer in a 1L beaker. The dissolved solution was adjusted to pH 6.25 with 30% hydrochloric acid. To continue the controlled coacervation process, the beaker was sealed with parafilm and placed inside an insulated box to minimise evaporation and

strive for controlled cooling. The beaker inside the insulated box was placed under an overhead stirrer with a rotational speed of 600 rpm and a crossed stirrer shaft (10 cm length and 5 cm diameter) for 4 hours. The resulting slurry was divided equally into 50 mL Falcon tubes and allowed to cool to ~24 °C with gentle agitation to avoid compaction (Figure 5.2.2A). The solution phase was removed and replaced with 10 mL media (Alpha MEM - Gibco, UK) w/o serum, and centrifuged at 500 g for 5 minutes to collect the gelatine microparticles, with the excess supernatant removed. The microparticles were washed twice with α-MEM to disrupt the pellet and create a suspension to avoid complete aggregation (Figure 5.2.2B). The resulting slurry was either used instantly after 1 hour UV exposure and named IHS saturated (IHS.S), or frozen overnight before lyophilisation at -50 °C 0 mBar for 48 - 86 hours. The lyophilised microparticle slurry was divided into 1G samples and kept at RT in airtight conditions until use (Figure 5.2.2C).

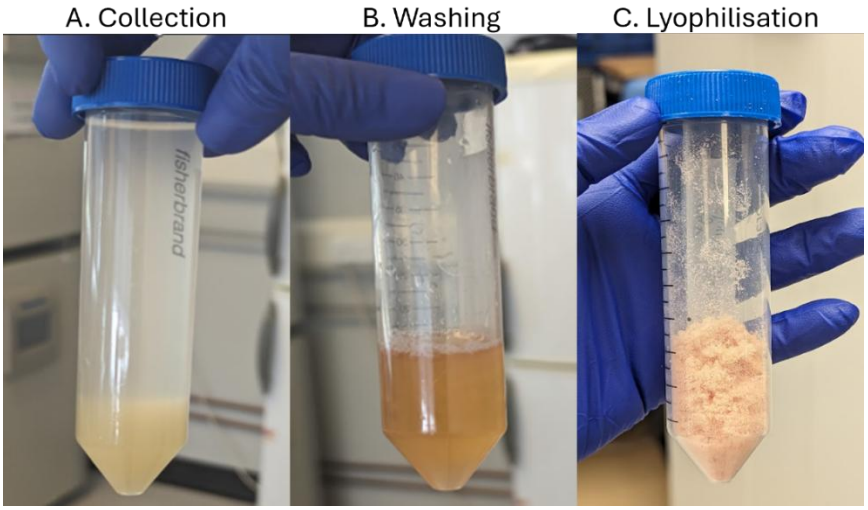

Figure 5.2.2. Overview of in-house slurry process. *A) Collection of the total resulting slurry. Polymer-rich phase is visualised at the bottom of the Falcon tube. B) Removal of the liquid phase, with washing and compacting of the gel microparticle phase. C) Lyophilised microparticles.*

Lyophilised samples were rehydrated, named IHS rehydrated (IHS.R) in various volumes of media (concentrations of 41 mg/ml, 50 mg/ml and 62.5 mg/ml) and immediately vortexed for 1 minute, followed by incubation at RT for 15 minutes. The IHS.R underwent centrifugation at 2000 g for 5 minutes, followed by supernatant removal. The pelleted IHS.R was then dislodged, followed by further centrifugation at 2000 g for 5 minutes. The slurry was then ready for immediate use at room temperature. For sterile microparticles,

all hardware was autoclaved or cleaned with 70% IMS before ultraviolet (UV) sterilisation in a biosafety cabinet. All original materials were measured in a sterile environment.

5.2.6 FRESH Life Support™ rehydration

Three different batches of FRESH life support™ (LS) microparticles (FluidForm™) were used as a control against IHS.R, which became commercially available during the PhD. LS was rehydrated in various volumes of media (concentrations of 41 mg/ml, 50 mg/ml and 62.5 mg/ml) and immediately vortexed for 1 minute, followed by incubation at RT for 15 minutes. The LS underwent centrifugation at 2000 g for 5 minutes, followed by supernatant removal. The pelleted LS was then dislodged, followed by further centrifugation of 2000 g for 5 minutes. The resulting LS slurry could then be used immediately at room temperature.

5.2.7 Microparticle slurry size characterisation

To assess microparticle (IHS.S, IHS.R and LS) size and uniformity, the microparticle slurry was diluted in 1X PBS solution and imaged with brightfield using an inverted microscope (Olympus IX81, Cytation 5 bioTek, and EVOS x1 core) with a digital camera (Olympus DP75) in various magnifications of 40X, 200X and 400X. The particles were evaluated (n = 3) in ImageJ (National Institutes of Health) to analyse the average particle Feret diameter. Four random fields of view were collected, and 50 individual particles were measured to assess shape distribution, classified as either sphere, fused or rod morphology, and sphere size distribution, by measuring width and length diameter (Figure 5.2.3). The criteria used for assessing the 3D morphology in a 2D image were that the entire perimeter was in focus, and the shape must fall under the three defined categories (sphere, fused and rod) (Figure 5.2.3).

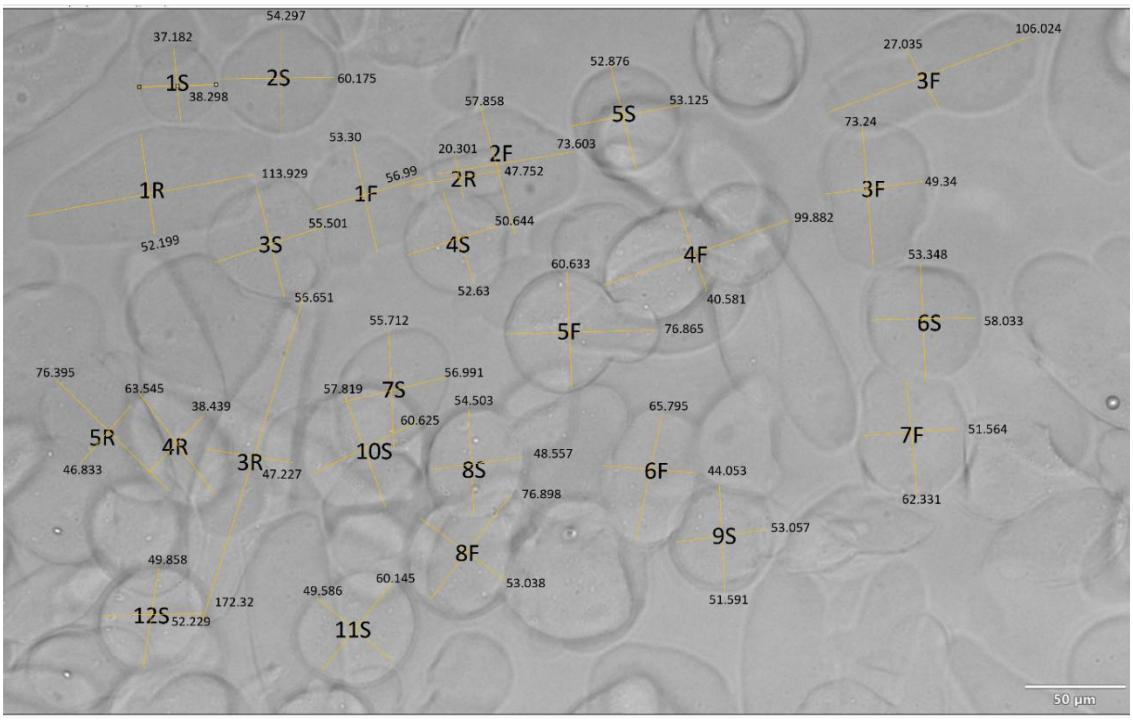

Figure 5.2.3. Light microscopy analysis of microparticle slurry. *The criteria used for assessing the 3D morphology in a 2D image was that the entire perimeter was in focus, the shape must fall under the three defined categories (sphere, fused and rod), and the diameter measurements must cross the centre of the sphere represented by yellow lines. Above represents count of each shape, e.g. 1S is the 1st sphere counted, R is rod, and F is fused shape.*

5.2.8 Microparticle rheological behaviour characterisation

To evaluate the rheological fluid properties of the gelatine microparticle support bath, neat wet compacted slurry and various rehydrated lyophilised samples were loaded onto a rheometer (Physica MCR 301, Anton Paar) equipped with a 20 mm diameter parallel plate at 23°C, with a maintained gap of 1 mm. A shear rate strain-controlled amplitude sweep from 0.01% to 100% strain at a frequency of ramp logarithmic was used to determine the linear viscoelastic region and apparent yield stress.

An amplitude-frequency sweep was performed on 50 mg/ml IHS.R and LS. The microparticle sample was added to 20 mm diameter parallel plates at 20 °C. The bottom plate was fitted with sandpaper to avoid artificial movements of the sample. A moisture trap was used to avoid drying effects on the sample. A strain controlled amplitude sweep of 0.1 – 50% was applied under a constant 0.5 N force, with 1 Hz of data collection for 5 minutes to determine the apparent yield stress and linear viscoelastic region. Storage (G') and Loss (G") modulus were collected (n = 1). Following the identification of the

linear viscoelastic region, thixotropy was performed. Three stages of assessment were completed: rest, strain and recovery. The rest stage was defined as 0.1% strain at 1 Hz for 200s, then 50% strain was then applied for 200s at 1 Hz, followed by a recovery stage of 0.1% strain at 1 Hz for 300s. Storage (G') and Loss (G") moduli were collected.

5.2.9 In-house slurry rehydration for bioprinting

For bioprinting with GelXA and B-gel, 50 mg/ml IHS.R was utilised. The IHS.R was rehydrated as previously stated, and ~ 4 ml was used per construct, roughly half full of a 35 mm petri dish or 6-well plate. After the deposition of bio ink and completion of printing, the petri dish/6 well plate was placed in standard incubator conditions for 30 minutes. Following the release of the construct due to the melting of IHS.R, the construct was washed 2X in media before manual removal and placement in an appropriate well plate for the continuation of culturing.

5.2.10.1 Optimisation of visualisation of 3D printed structures and total cartridge

Five different batches of GelXA and 3 different batches of B-gel were imaged. All samples were imaged within their respective cartridges. All appropriate GelXA and B-gel bioprinted constructs were imaged at 9 μm voxels, 0.25 mm aluminium filter, 2016x1344 camera with a 10W power source, resulting in 55 kV:160 μA source voltage. Scans were performed with 180° rotation, with two x-ray projections acquired every 0.8°. NRecon (NRecon 2.1.0.2, Bruker Micro-CT, Belgium) generated a 3D reconstruction from X-ray projections. Images were independently optimised using an appropriate post-alignment compensation, +1 smoothing filter (Gaussian window kernel), 40% beam hardening correction, and appropriate ring artefact correction. A threshold of 0 – 0.12 mm^{-1} was selected to represent the transition from air space to biomaterial.

Various approaches to the sample staging for micro-CT imaging of 3D printed structures were considered. For bone GelXA, first, the construct was wrapped in moist tissue paper and placed inside a sealed bijou and secured onto the stage of the micro-CT. Second, the construct was submerged in $_{dd}H_20$ and placed on top of damp tissue paper, inside a sealed bijou. Finally, a UV-sterilised Styrofoam block was placed inside the tube and covered with a layer of parafilm. The bioprinted construct was carefully placed atop the

parafilm seal with a small, sterilised spatula, and growth media was slowly added until surface tension reached the top of the construct.

For B-gel bioprinted constructs, the same approach of mounting under a growth medium was trialled. Following this, constructs were embedded within warm 0.15% agar and allowed to solidify in a 37 °C incubator before being imaged. Alongside this, iron oxide particles obtained from HotHands™ were measured by an infrared temperature gun in different weights to determine the surrounding temperature inside a bijou tube. Finally, constructs were placed inside an empty bijou edge after undergoing snap-freezing in liquid nitrogen, fixing in 4% PFA or no treatment.

5.2.10.2 Quantification of total cartridge biomaterial using micro-CT imaging

To calibrate for TMD, 2 mm radius calcium hydroxyapatite rods with densities of 0.3 and 1.25 gHA/cm^3 were scanned using the previously mentioned parameters inside the bijou tube. AC was obtained and updated on the software as previously stated (Chapter 2, section 2.2.4.4). Individual cartridges were then loaded into CTAn, and TMD (g/cm^3) (Table 5.2.4) was recorded.

For individual particle analysis, cartridges were loaded into CTAn. For B-gel and GelXA batches 1 – 3, a threshold of 65 – 255 was applied to represent the transition between air and HAnp/particles, whereas GelXA batches 4 – 5 required a threshold of 100 – 255. Despeckling of < 30 white voxels was completed, with the individual object analysis task list selected to calculate diameter and thickness (Table 5.2.4) into a separate file. Following this, 3D analysis with basic and additional outputs was selected (Table 5.2.4), with the thickness image output into a new folder. To visualise the thickness matched HAnp/particles, the thickness output images were opened, with a new task list of filtering with contrast stretching in 3D space applied, bitmaps saved inside the ROI, followed by shadow and data set selected. The final output thickness images were uploaded to CT Vox, with each independent thickness range applied to the same colour gradient to individually represent the thickness range per cartridge.

Table 5.2.4. Descriptions of analytical outputs from micro-CT imaging*. The total cartridges of biomaterial parameters investigated in this study.*

Variable	Abbreviation / standard unit	Description of the algorithm output
Number of particles	Particle. N	Number of individual particles, irrespective of size
Particle thickness	Particle. Th (mm)	Smallest dimension of an irregularly shaped particle
Particle diameter	Particle Diam (mm)	Largest diameter of an irregularly shaped particle
Tissue mineral density	TMD (g/cm^3)	Total volumetric density of calcium hydroxyapatite, or dense particles. Mean pixel tissue mineral density for total space, excluding air space.

5.2.11 Data and statistical analysis

All rheological, micro-CT, micro-particle slurry particle and filament analysis data were recorded in Microsoft Excel and presented with GraphPad Prism 8.0. All micro-CT data, rheological data and microparticle diameter analysis were presented in the form of individual data points, with mean or median value displayed by processing in GraphPad Prism 8.0. For microparticle diameter and individual filament analysis, Shapiro-Wilk normality testing was completed with significance determined by multiple unpaired T-Tests (two-tailed) followed by the Holm-Sidak method. If discovered to follow a normal distribution, Tukey's multiple comparison one-way ANOVA was completed. Non-parametric data, Kruskal-Wallis multiple comparison, was conducted. $P < 0.05$ was defined as statistically significant in this study.

5.3 Results

5.3.1 Investigation of bioink fidelity

The influence of printing pressure, speed and nozzle size on printing fidelity was investigated for three independent bioinks. Two bioinks (Bone GelXA and B-gel) underwent individual filament extrusion optimisation, testing the impact of a range of suitable pressures for the ink on filament length and width. The most consistent pressure after visual qualitative inspection was taken forward to assess different printing speeds. True analysis of length and width based on altering parameters was completed post-experimentation. TissueFAB™ was not investigated for individual filament deposition in the same methodological manner.

Firstly, extrusion pressure for bone GelXA and B-gel ink was assessed by testing the initial filament length deposition on the BioX interface. Initial pressure tests were performed to ensure ink was free flowing from the end of the nozzle – this was classed as the baseline. The pressure value was then altered within a +/- 20 kPa range of the baseline to visualise the differences in pressure on printing consistency, as well as accuracy. For the bone GelXA conical nozzle, filament began extruding inconsistently at 35 kPa; therefore, the range of 45 – 55 kPa was selected, with 45 kPa having overall precision to the true length; however, 55 kPa was the most consistent filament length generation (Figure 5.3.1A/E). Between triplicate samples, 50 kPa was selected to assess printing speed due to the overall filament consistency with lack of 'blowouts' of ink (Figure 5.3.1A/B/G), as well as no gaps in the entire filament (Figure 5.3.1G). Speeds of 7, 10, and 13 mm/s were chosen as standard between all bioink conditions, with 7 mm/s producing the highest precision to true length compared to 10 and 13 mm/s (Figure 5.3.1F); however, they featured large blowouts compared to 10 mm/s. Overall, despite different selections of parameters, the material did not print consistently for an individual filament.

From the same 10 mm length filament experiment, filament width was measured for all conditions of pressure and speed at 25%, 50% and 75% of the total length of each filament. No pressure parameter selected produced a filament diameter of exactly 0.41 mm, with a wide distribution visualised between all distances of the filament and

'blowouts' were more frequent in the 75% region of the filament (Figure 5.3.1C). Interestingly, changing speed impacted filament width variably (Figure 5.3.1D). Although no statistical difference was observed ($P > 0.05$), 10 mm/s produced the most consistent filament width compared to 7 and 13 mm/s. Overall, 55 kPa and 10 mm/s were selected as the most consistent parameters to print bone GelXA with, as previously selected qualitatively, which resulted in the 1-layer lattice visualised. Qualitatively, the lattice individual filaments have high variability, representing inconsistency of bioink deposition (Figure 5.3.1G). The resulting lattice was successfully crosslinked by a 60-second wash in 200 mM $CaCl_2$ after 60 s under the 405 nm light module to initiate both photo and ionic-crosslinking.

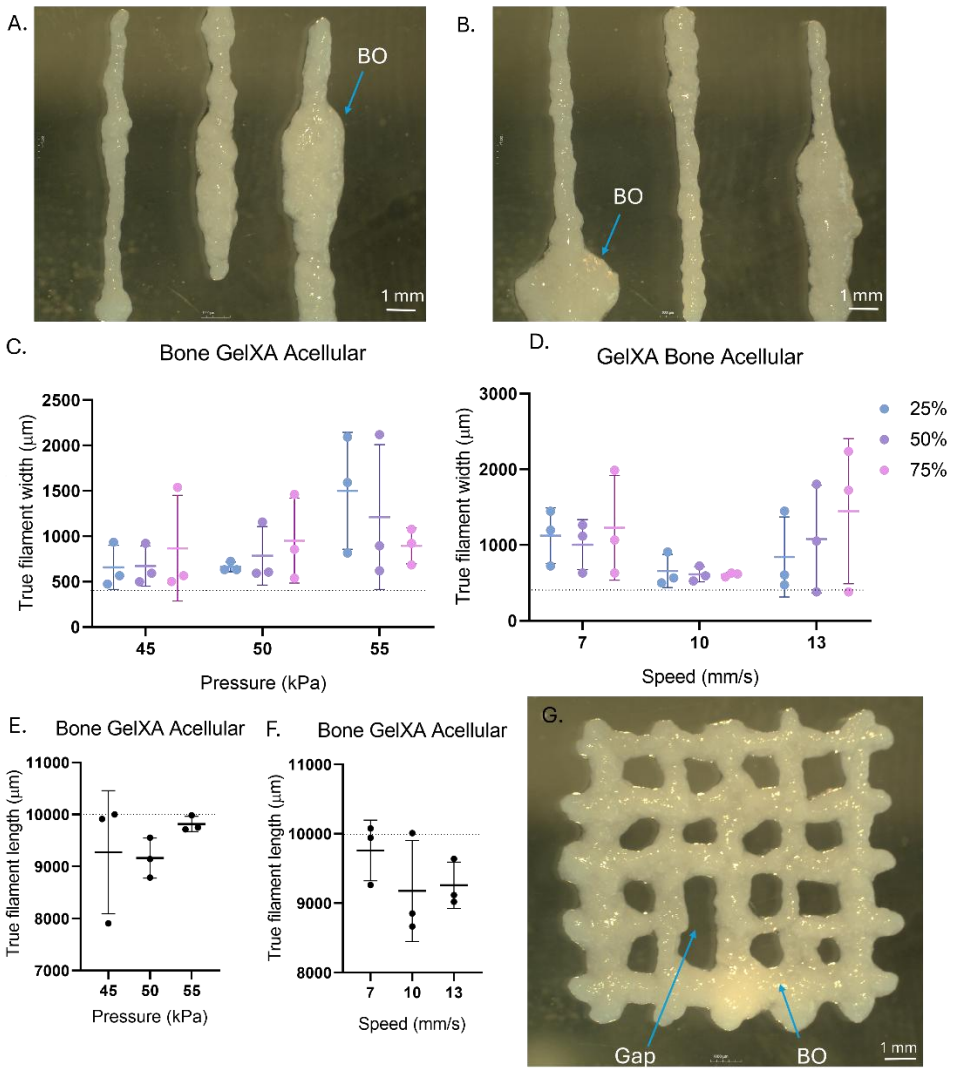

Figure 5.3.1. Filament length analysis on GelXA based on changes in printing pressure and speed. *STL designed dimension is highlighted by a dashed line, at 10 mm in length, and 0.41 mm in diameter. All inks are printed with a 22G conical nozzle. A) Visualisation of 10mm in length printed filament from different pressures 45, 50 and 55 (left to right) with 10 mm/s, B) Visualisation of 10 mm in length printed at different speeds (7, 10, 13 mm/s) at 50 kPa, C) Quantification of filament width at different printing pressures, at 25, 50 and 75% of total individual length, D) Quantification of filament width at different printing speeds, at 25, 50 and 75% of total individual length, E) Quantification of filament length with different printing pressures, F) Quantification of filament length with different printing speeds, G) resulting 1-layer latticed printed with qualitatively decided parameters of 55 kPa and 10 mm/s. Blowouts (BO) and gaps in deposition examples are highlighted with blue arrows. The scale bar represents 1 mm, ns, n = 3.*

B-gel fidelity was assessed in both acellular and cellular conditions. Overall, no parameter was able to attain high fidelity to the pre-defined dimensions of the 10 mm in length and 0.41 mm in diameter STL model. Printing pressure for AB began at 70 kPa, with the range of 75, 80 and 85 kPa selected which all produced consistent filament

deposition (Figure 5.3.2A), however from qualification the closest pressure to 10 mm length was 85 kPa, with a significant difference observed compared to 75 kPa (P = 0.0411) (Figure 5.3.2E). Based on visual inspection of consistency, 85 kPa was selected to assess different printing speeds, with 7 mm/s producing the closest to 10 mm length (Figure 5.3.2F). All parameters produced varied results between replicates, representing low consistency of the bioink. Filament width was more consistent between replicates and distances for pressure, especially at 25% distance for 75 kPa. The consistency at 25% distance does not maintain, with statistical difference against 80 kPa (P = 0.0189) and 85 kPa (P = 0.0321) (Figure 5.3.2C). Speed changes caused varied filament width (Figure 5.3.2D). Finally, a 1-layer lattice was printed with 85 kPa at a speed of 10 mm/s, with an undefined structure, as it was observed that the material had a high affinity for itself, causing deformations from the intended lattice structure (Figure 5.3.2G). However, compared to bone GelXA, individual filaments were deposited without 'blow-outs' and gaps, representing a more suitable option for bioprinting the shape in its entirety. No cross-linking was required, as the material was thermally responsive rather than chemically or ionically cross-linked.

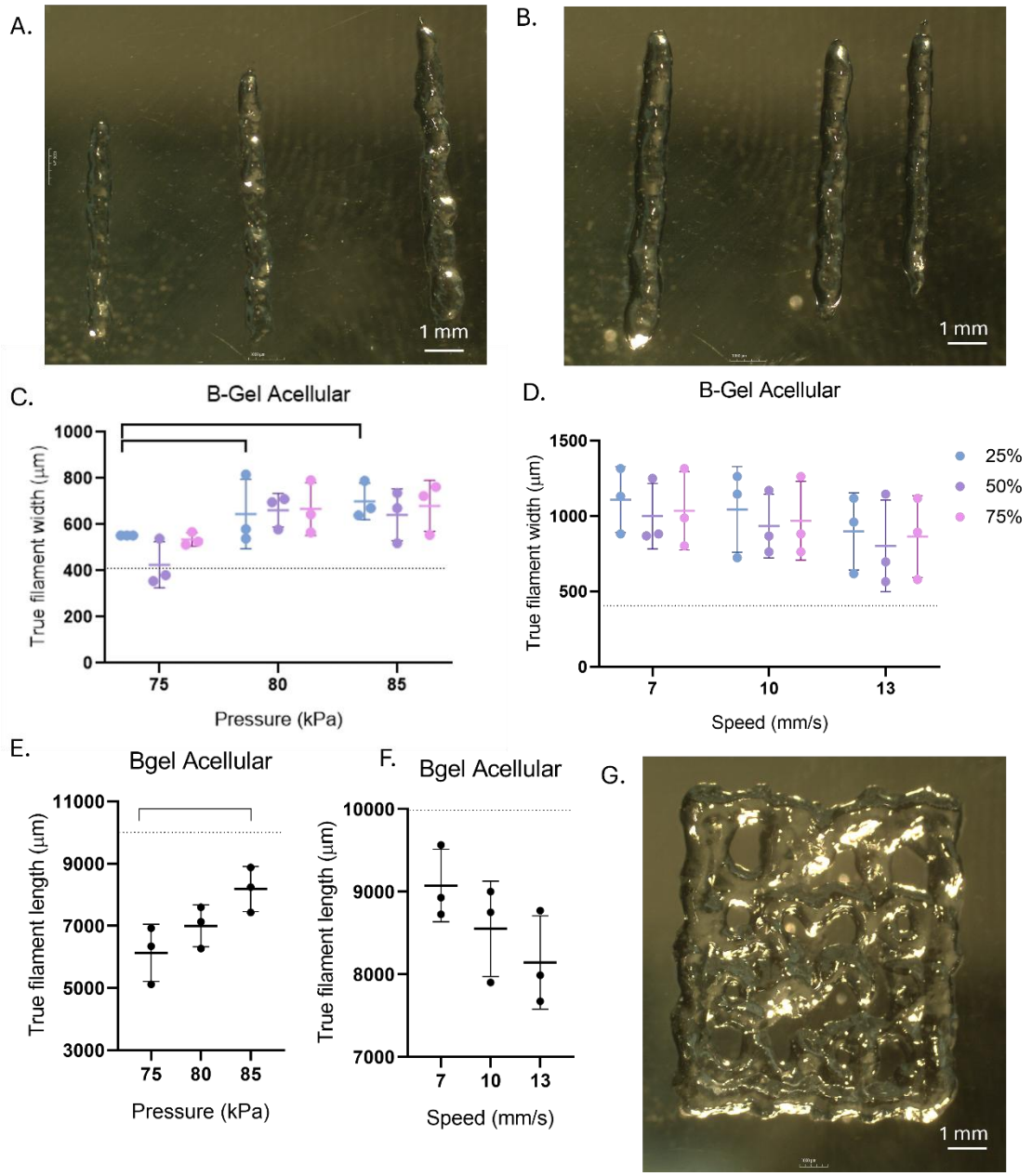

Figure 5.3.2. Filament analysis on acellular B-gel based on changes in pressure and speed. *STL designed dimension is highlighted by a dashed line, at 10 mm in length, and 0.41 mm in diameter. Printed with a 22G conical nozzle. A) Visualisation of filament from different pressures 75, 80, 85 (left to right) with 10 mm/s, B) Visualisation of filament printed at different speeds (7, 10, 13 mm/s) at 85 kPa, C) Quantification of filament diameter with printing pressures, D) Quantification of filament diameter with printing speeds, E) Quantification of printing pressures on filament length, D) Quantification of printing speeds on filament length, F) Quantification of filament diameter with printing pressures G) resulting 1-layer latticed printed with qualitatively decided parameters of 85 kPa and 10 mm/s, . Scale bar represents 1 mm, representative image shown, One-way ANOVA, Tukey's multiple comparison with significance defined as $P < 0.05$, $n = 3$.*

Printing pressure for cellular conditions was selected as 65, 70, and 75 kPa. The difference in filament deposition between the pressures was very apparent (Figure 5.3.3A), especially with each pressure producing highly variable lengths (Figure 5.3.3E). Seventy-five kPa was selected for further studies as the most consistent filament deposition. Seven mm/s produced the closest to 10 mm length when printed at 75 kPa, with a significant difference (P = 0.0418 and 0.0040) against 10 and 13 mm/s, respectively (Figure 5.3.3F). Accurate filament width was obtained by one replicate of 13 mm/s printed at 75 kPa in the 75% increment (Figure 5.3.3D), with overall closeness to 0.14 mm width seen with less variability between replicates in B-gel cellular bioprinting. Cellular conditions (Figure 5.3.3A/B) produced reduced length compared to acellular conditions (Figure 5.3.2A/B) in all pressure conditions, with cellular ink requiring overall reduced pressure (65 – 75 kPa) to extrude filament compared to acellular (75 – 85 kPa).

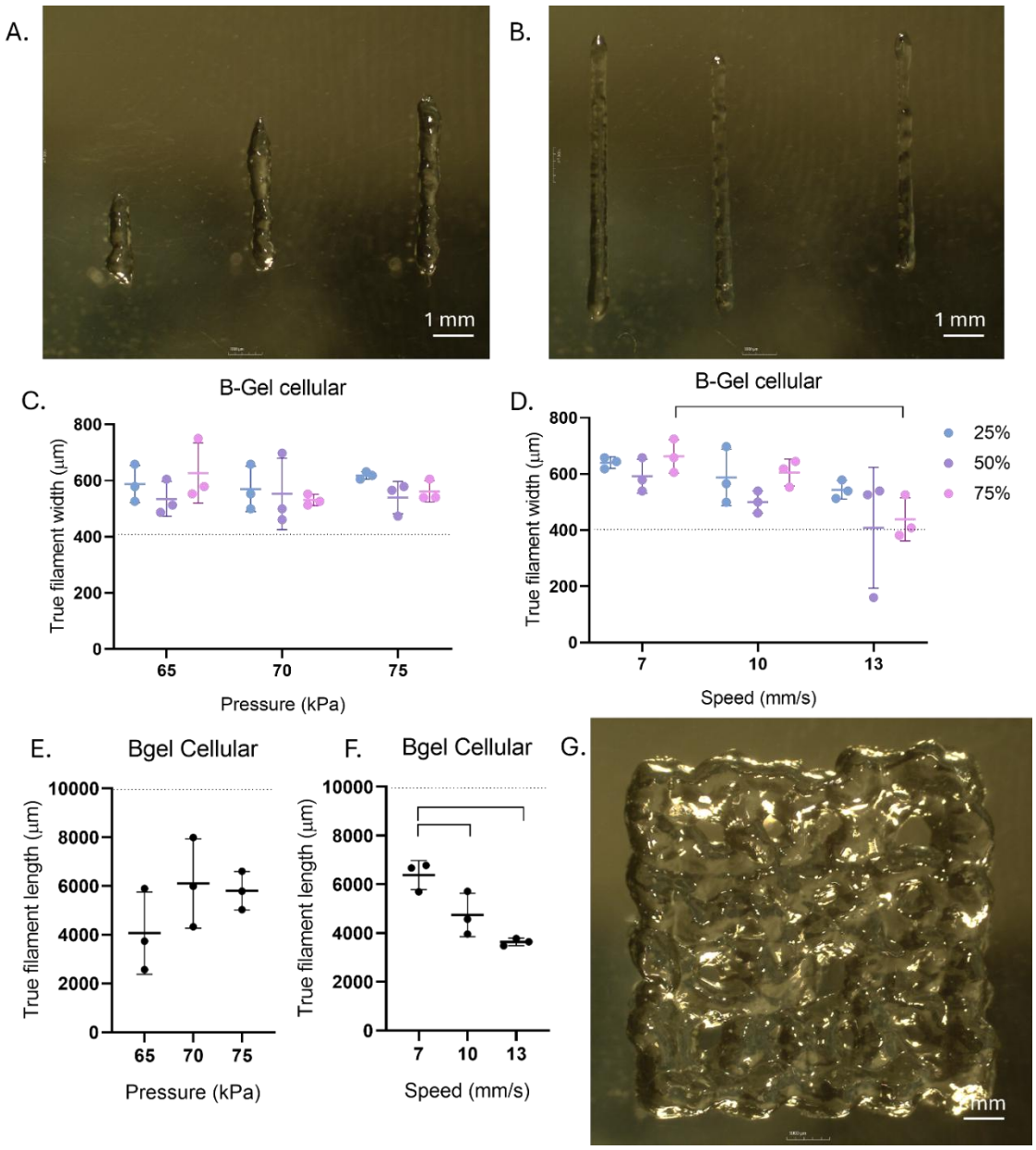

Figure 5.3.3. Filament length analysis on cellular B-gel based on changes in printing pressure and speed. *STL designed dimension is highlighted by a dashed line, at 10 mm in length, and 0.41 mm in diameter. All inks are printed with a 22G conical nozzle. A) Visualisation of 10mm in length printed filament from different pressures 65, 70, 75 (left to right) with 10 mm/s, B) Visualisation of 10 mm in length printed at different speeds (7, 10, 13 mm/s) at 75 kPa, C) Quantification of filament diameter with different printing pressures, D) Quantification of filament diameter with different printing speeds, E) Quantification of printing pressures impact on filament length, F) Quantification of printing speeds impact on filament length, G) resulting 1-layer latticed printed with qualitatively decided parameters of 75 kPa and 7 mm/s. Scale bar represents 1 mm, representative image shown, One-way ANOVA Tukey's multiple comparison with significance defined as $P < 0.05$, $n = 3$.*

Experimentation was completed on both B-gel conditions with a needle nozzle instead of a conical nozzle. For acellular, initial printing pressures were raised to 175, 180 and 185 kPa, and for cellular raised to 160, 165 and 170 kPa. Conical nozzles were selected for progressive experimentation due to the reduced pressure required for extrusion, with cellular viability integral for an *in-vitro* model, a consideration discussed in Chapter 6. The bone GelXA was not printed with the needle nozzle due to inconsistency and a lack of extrusion between conditions.

TissueFAB® is an alternative commercially available bioink, consisting of Alg and GelMA – precise composition and concentrations unknown, tailored to cross-link at 365 nm. Initial line filament printing required low pressures for extrusion; however, no clear trend was visualised from increasing print pressure and the impact on the filament (Figure 5.3.4A). For example, 9 & 10 kPa initially showed consistent deposition of ink; however, after trailing another range, pressures of 10 – 13 kPa did not print consistently. A 6 well plate of 1-layer lattices was printed at 15 kPa (Figure 5.3.4B.1), and produced inconsistent structures (not shown), however, this experimental aim was to assess crosslinking of the structures. As per the manufacturer's recommendations, the lattices underwent 60 s crosslinking at 365 nm, with a 5-minute incubation submerged in 200 mM $CaCl_2$, and upon incubation in PBS, the lattice structures had dissolved (Figure 5.3.4B.2). The 10-layer lattice structures were then printed at 19 kPa. The resulting structures printed more consistently compared to previous attempts, however air bubbles within the individual filament were visualised (Figure 5.3.4C.1). The structures underwent more intense cross-linking methods, with a 10-minute incubation in 200 mM $CaCl_2$ and 300s under the 365 nm light module (Figure 5.3.4C.2). The structures were washed in media and incubated for 30 minutes, which resulted in stable acellular structures (Figure 5.3.4C.3). Further optimisation and incorporation of this material was discontinued within the research project due to excessive lead time of the product which did not fit within the research duration, and unsuitability for *in-vitro* cultures (Chapter 6) with such extensive cross-linking required to produce a stable structure.

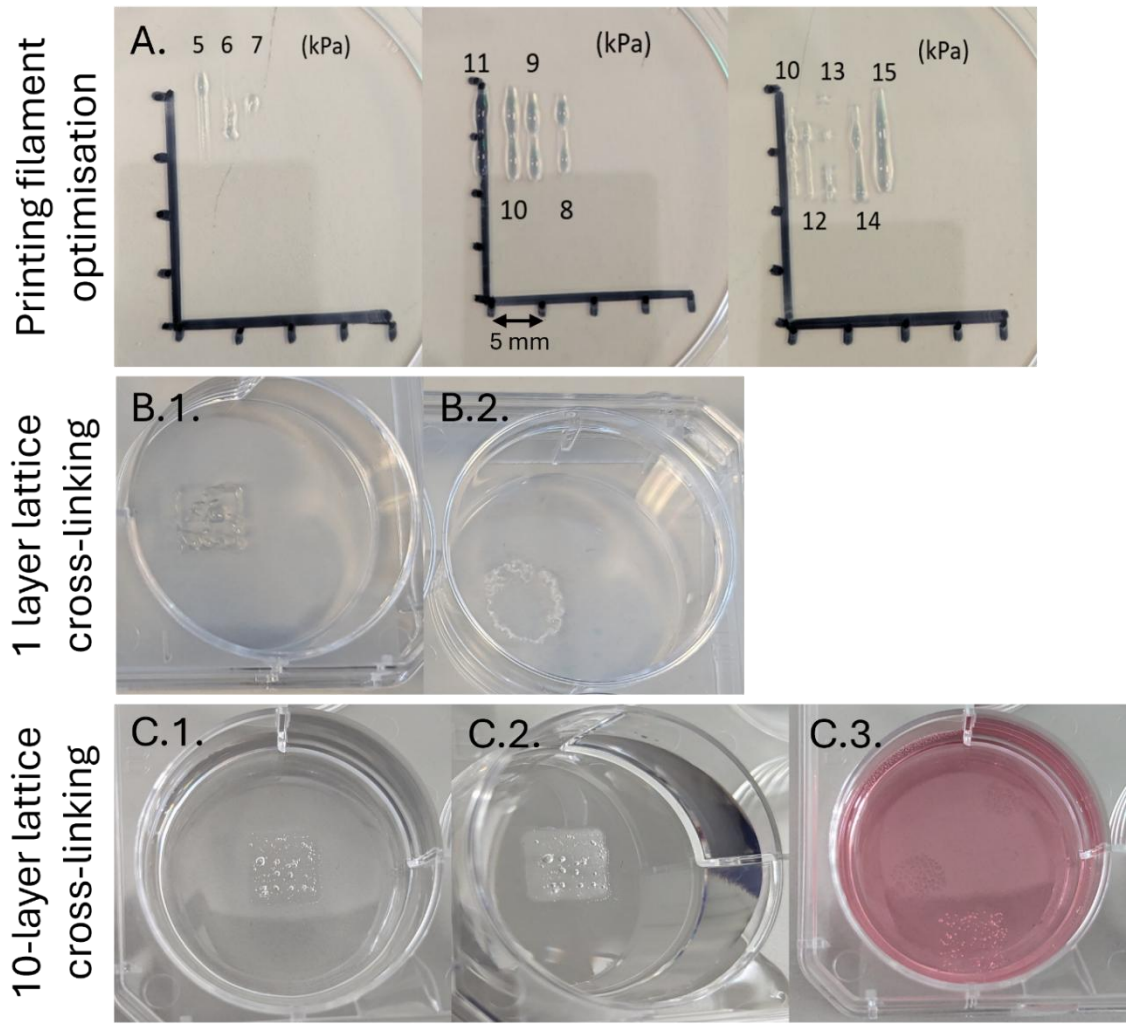

Figure 5.3.4. TissueFAB® 3D bioprinting optimisation. *TissueFAB® Alg(Gel)MA – Vis 365 nm (Acellular) bioink optimisation, A) individual 10 mm filaments printed at a range of pressure from 5 – 15 kPa @ 5 mm/s, B.1) represents a 1 layer lattice printed at 15 kPa @ 5 mm/s, B.2) lattice after crosslinking in 200 mM $CaCl_2$ and 60s under 365 light module, after 30 minutes incubation at 37* °C*, C.1) 10 layer printed lattice printed at 19 kPa @ 5 mm/s, C.2) 10 layer printed lattice after crosslinking in 200 mM $CaCl_2$ and 300s under 365 light module, C.3) lattice after 30 minute incubation at 37* °C, washed in α-MEM. n = 1, representative images taken with a camera.

The assessment of extrusion consistency was visually completed at the time of each independent experiment. It became apparent during 3D bioprinting experimentation, each experiment required differences in printing pressure (Table 5.2.2) between different cartridges of material and, most importantly, during the printing process itself. It was often required to slowly increase printing pressure as ink inside the cartridge was reduced after consecutive 3D prints. From initial investigations of attempting to bioprint 10-layer lattices, a support medium was required to improve 3D EBB fidelity, especially

since height and structural complexity were required to bioprint a 3D model based on *ex-vivo* bone morphology, inclusive of Tb and Cb architecture (Chapter 3, Figure 3.3.6).

5.3.2 Bioink rheological analysis

The flow behaviour of the acellular bioinks was explored to assess viscosity at different shear rates, at appropriate temperatures for bioprinting the materials. Both biomaterials, GelXA and B-gel, presented shear stress dependence resulting in thinning viscous behaviour characteristic of shear-thinning pseudoplastics. For GelXA, the three different batches showed similar trends; however, at higher shear rates of > 10 (1/s) difference in viscosities was observed between the batches (Figure 5.3.5A). As an in-house generated material with no standard protocol and adapted for bioprinting, the Laptonite™ co-polymer viscosity was observed at different temperatures, further characterised by assessing the viscosity of the gel with HAnp and without HAnp – named B-gel and NP-gel, respectively. The viscosity trend of B-gel and NP-gel was equal at each temperature, representing a shear-thinning fluid, and representing no difference in viscosity due to the presence of HAnp within the biomaterial. Determining printing temperature at first was completed by depositing filament at a range of temperatures, 30 – 37 °C, whereby temperatures above 36 °C would cause a 'blow out' of filament (*not shown*). The temperature change, impacting the viscosity of B-gel, is clear by the difference in viscosity of B-gel/NP-gel at 37 °C, compared to 30 °C and 34 °C, at higher rates of shear stress, whereby higher temperatures decreased viscosity (Figure 5.3.5B). Finally, different batches of B-gel showed no difference in viscosity behaviour between batches (Figure 5.3.5A), when measured at 34 °C, suggesting material consistency. Statistical difference ($P = 0.0056$) was reported between GelXA and B-gel (Figure 5.3.5A).

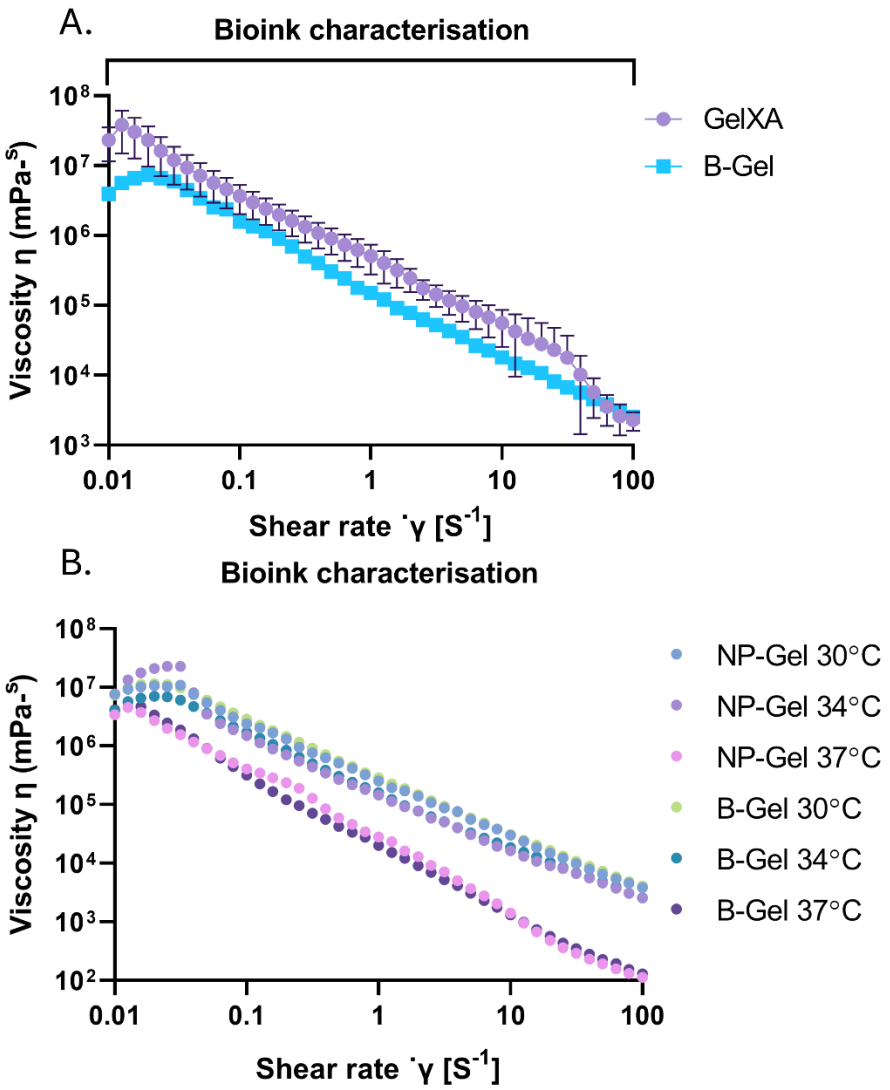

Figure 5.3.5. Viscosity versus shear rate curve of acellular bone GelXA, B-gel and NP-gel. *Oscillatory shear strain frequency sweep with a 20 mm parallel plate, A) Bone GelXA at 24 °C and B-gel at 34 °C n = 3, paired two-tailed t-test was used to statistically analyse viscosity at each corresponding shear rate, (P < 0.05), B) B-gel and NP-gel viscosity at 30, 34 and 37 °C, n = 1.*

5.3.3 Microparticle slurry optimisation and morphology characterisation

The initial production attempts of in-house-generated slurry produced irregular, non-consistent morphology. At first, no spherical morphology was observed; instead, long, thin rods were produced after 24 hours (Figure 5.3.6A). Once an insulated environment was introduced to ensure controlled cooling, spherical morphology was identified; however, the structure was highly variable (Figure 5.3.6B). It was shown that utilising a 1L beaker in place of a 5L beaker was key to improving suspension collision, resulting in improved spherical morphology (Figure 5.3.6C), however, the resulting particles were

still highly variable. A different stirring rod was trialled (Figure 5.3.6D) with improvement to the intended morphology. Type B gelatine was used in place of type A due to the different ionic characteristics, which yielded greatly improved morphology compared to previous trials with type A (Figure 5.3.6E), with final pH adjustments being completed after the addition of each reagent (Figure 5.3.6F) producing spherical morphology; however, it remained highly inconsistent. At this stage, temperature and time were not controlled for the duration of the stirring process.

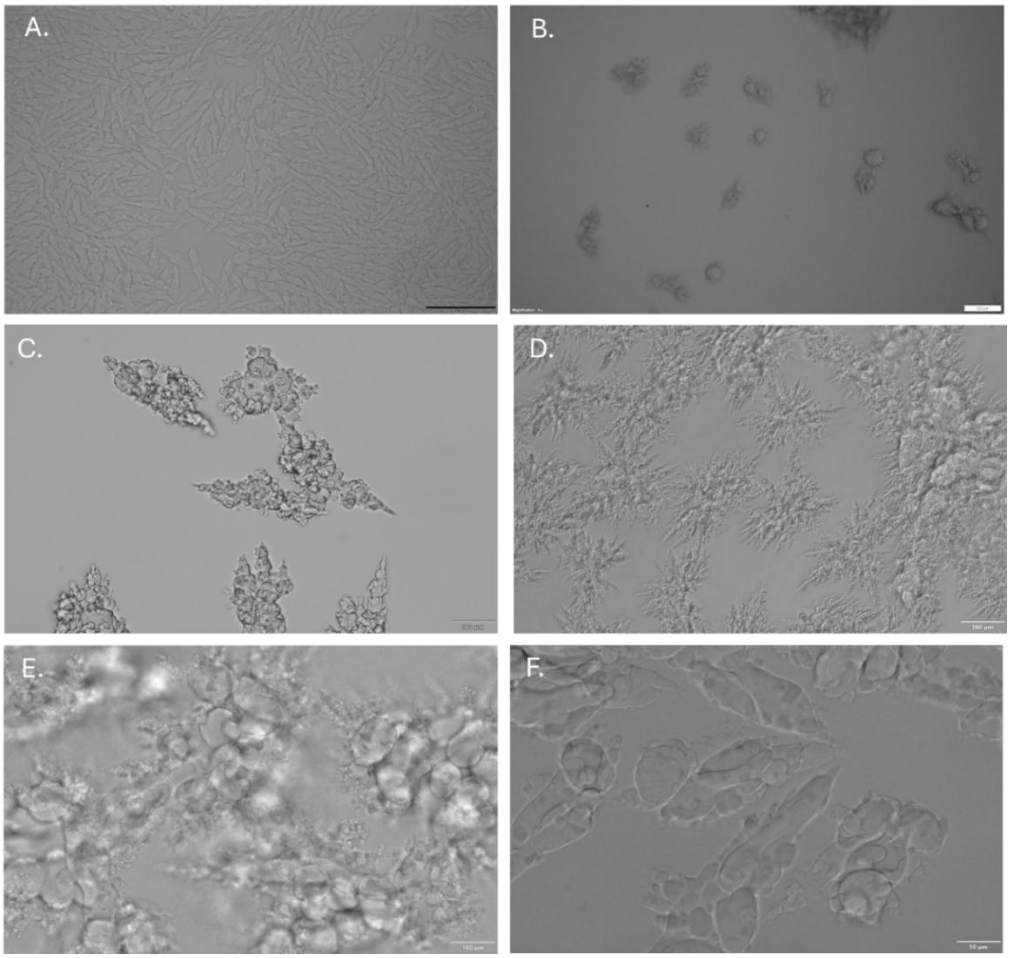

Figure 5.3.6. Morphology of early-stage optimisation of generating a micro-particle support slurry. *Based on a method published by Lee et al. (2019). All conditions presented were stirred overnight at 600 rpm. All changes to reagents and method are stated here, with reagent concentration, volume, starting temperature and pH remaining constant. A) Type A gelatine, 5 L beaker, dual stirrer at RT, scale bar represents 100 µm B) Type A gelatine, 5 L beaker, dual stirrer, insulated box, C) Type A gelatine, 1 L beaker, dual stirrer, insulated box, D) Type A gelatine, 1 L beaker, cross stirrer, insulated box, E) Type B gelatine, 1 L beaker, cross-stirrer, insulated box, F) Type B gelatine, adjustment of pH of solute before addition of reagents 1 L beaker, cross-stirrer, insulated box—representative images shown, scale bar represents 200 µm for A, B, 100 µm for C, D & E, and 50 µm for F. n = 1.*

Once a spherical morphology was identified, the final optimisation considerations were time and temperature during the coacervation process, as all previous experiments (Figure 5.3.6) had been completed with a 24-hour, overnight stirring process. To assess the optimal time for stirring, the slurry's morphology was evaluated during the coacervation process at 30-minute intervals. It was initially hypothesised that time was the critical condition for forming spherical uniform microparticles. After the first technical repeat (RT ~23 °C), 240 minutes was selected as the optimal time for morphology (Figure 5.3.7G), with 0 – 120 minutes not showing consistent spherical formation (Figure 5.3.7A/D), whereas 360 minutes onwards showed signs of thinning and disruption of spheroid morphology (Figure 5.3.7J/M). Progressive experiments requiring new batches were made based on this result of time as the critical factor; however, inconsistencies with microparticle size were being observed after post-processing and analysis. Technical repeats, RT ~21 °C and ~16 °C, revealed different microparticle morphology and size at different times compared to RT 23 °C (Figure 5.3.7).

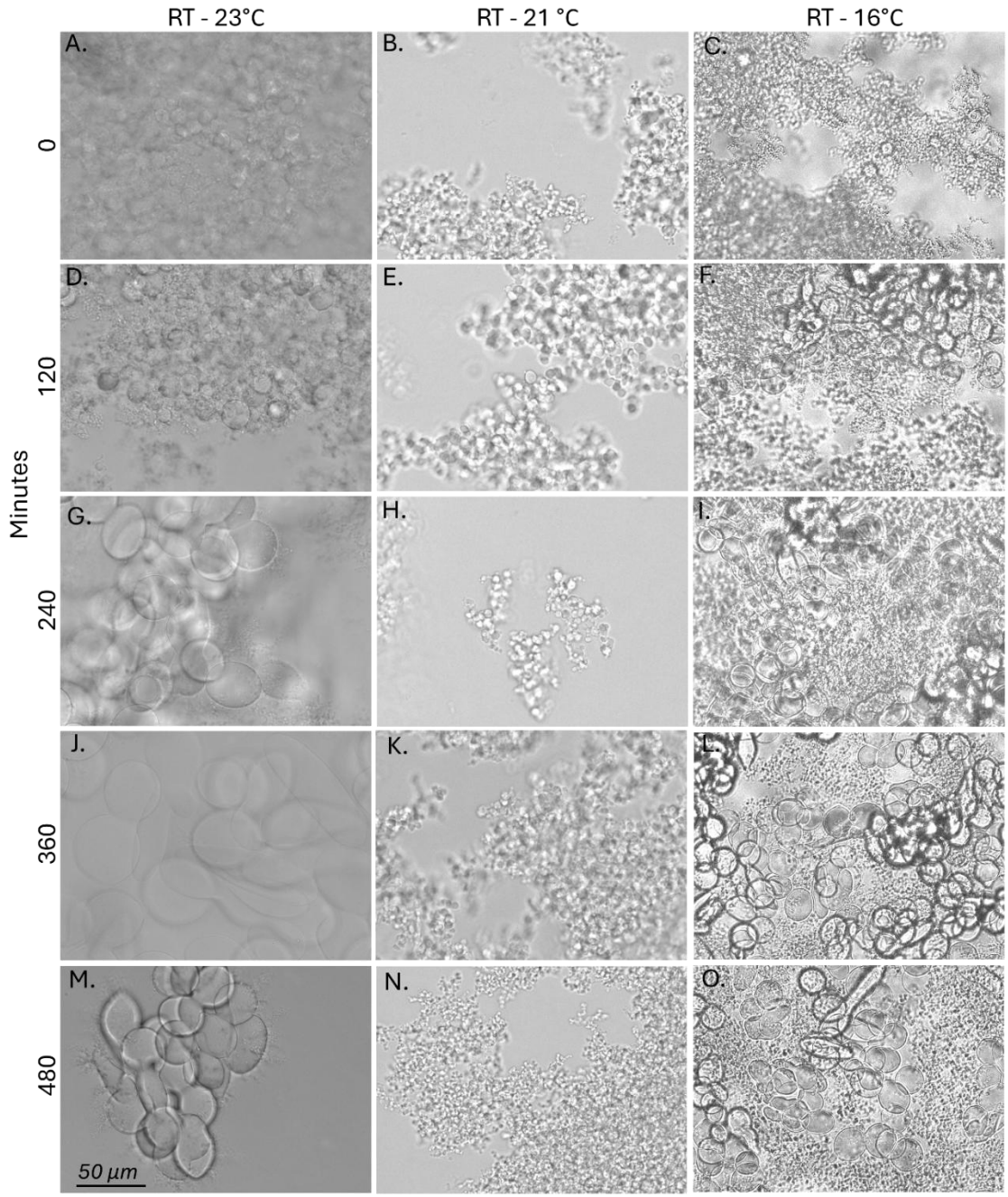

Figure 5.3.7. Morphology of in-house generated slurry during the coacervation process over time. *IHS was generated with type B gelatine in a 1L beaker inside an insulated box with a cross-stirrer blade shaft. A sample was taken every 30 minutes, with every 120 minutes represented above. 0 min A) 23 °C, B) 21 °C, C) 16 °C, 120 min D) 23 °C, E) 21 °C, F) 16 °C, 240 mins G) 23 °C, H) 21 °C, I) 16 °C, 360 mins J) 23 °C, K) 21 °C, L) 16 °C, 480 minutes, M) 23 °C, N) 21 °C, O) 16 °C. The representative images shown, scale bar represents 50 µm, n = 3.*

Investigation of temperature, compared to time, revealed altered cooling times of the microparticle slurry were dependent on room temperature during the coacervation process (Figure 5.3.8). For example, at 23 °C RT following 120 minutes, the microparticle slurries' temperature was 34 °C, compared to 16 °C RT and the slurry being 26 °C. Following Newton's law of cooling (Ilyin, S. 2024), the change in room temperature had a direct impact on the cooling rate of the microparticle slurry, and therefore the temperature of gelation of the bovine gelatine that begins gel transition at temperatures below 35 °C, with full solidification around 25 °C (Ninan, G., *et al*. 2014). To further expand, RT 23 °C the slurry reached below 35 °C at 150 minutes, both RT 21 °C and RT 18 °C reached a slurry below 35 °C at 120 minutes, and RT 16 °C reached below 35 °C at 30 minutes, representing the variation in cooling times based on surrounding ambident temperature despite using an insulating box within the method (Figure 5.3.8).

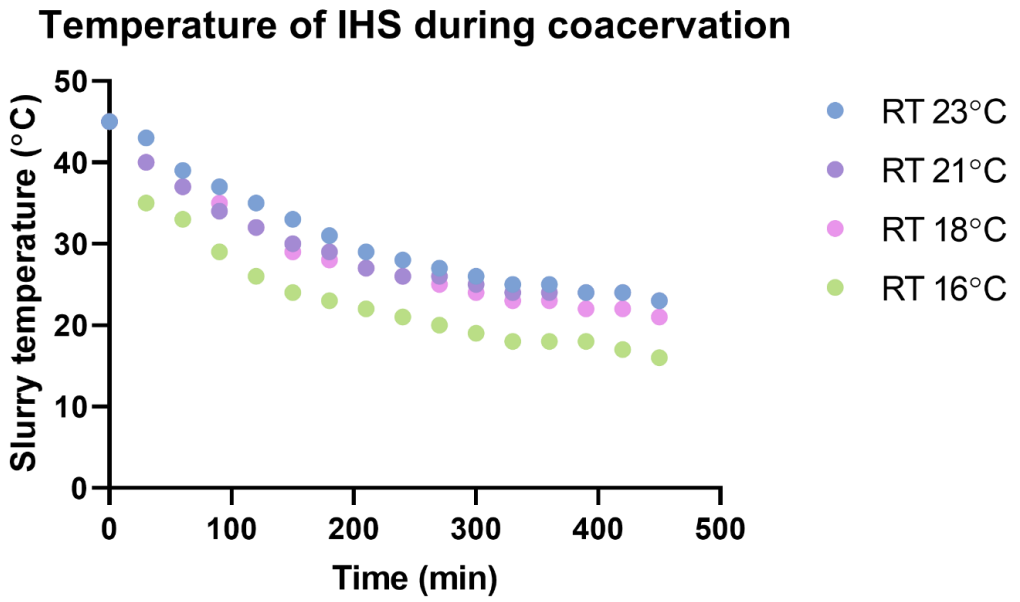

Figure 5.3.8. Cooling curve of in-house generated microparticle slurry over time. *Temperature was taken at 30-minute intervals from 0 – 480 minutes, from four independent experiments conducted at a range of lab room temperatures (23 °C, 21 °C, 18 °C and 16 °C at time 0), n = 1 for each temperature.*

IHS.S required washing with a buffer to remove any excess waste product and to concentrate the resulting microparticles. The post-processing method was not found to interfere with microparticle morphology (Figures 5.3.9A/B), and the microparticle slurry was usable 24 hours after creation at room temperature (Figure 5.3.9C). To establish a

concentration of microparticle slurry for accuracy and consistency of flow behaviour, lyophilisation was completed, and this was shown not to affect the resulting morphology once rehydrated (Figure 5.3.9D). LS, a commercially available gelatine microparticle, was used as a control against the in house-slurry (Figure 5.3.9E).

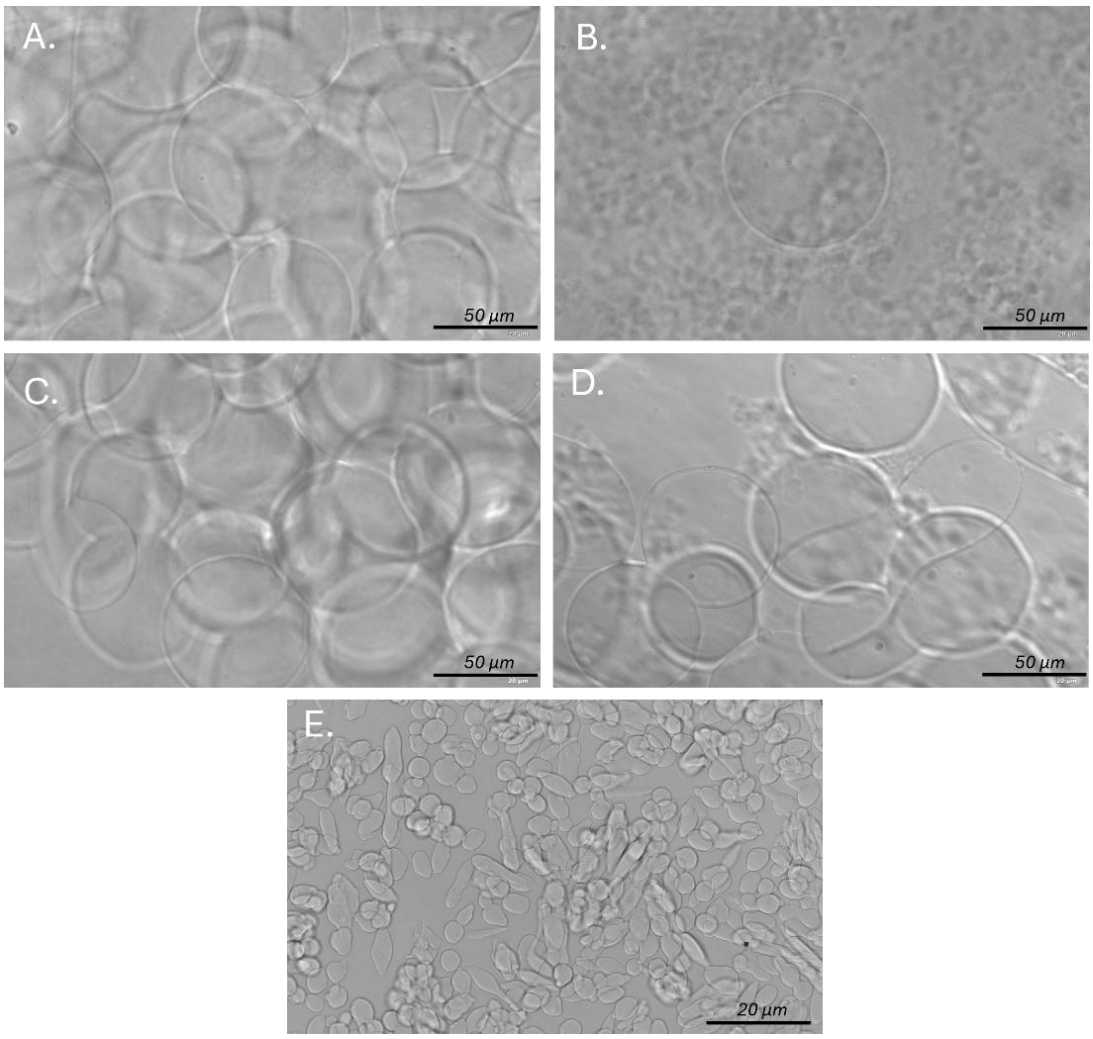

Figure 5.3.9. Morphology of optimised in-house generated slurry during post-processing, 400X. *After the coacervation process (240 minutes), microparticle slurry requires post-processing of compaction, washing, usage or lyophilisation. A) compaction of microparticles, B) microparticles after 2X washing, C) microparticles after 24 hours for use in freshly generated bioprinting experiments and D) microparticles after overnight -20 °C, lyophilisation and rehydration, E) Life support after rehydration. The representative image shown, the scale bar represents 50 µm (A, B, C, D) and 20 µm (E). Optimised IHS n = 11 and LS n =3.*

Microparticle shape was classified into three prominent morphologies (Sphere, fused and rod) that represent the transition between morphologies (Figure 5.2.3). All conditions (LS, IHS.R & IHS.S) underwent object classification (%) in ImageJ, whereby it

was discovered that overall, the IHS generated microparticle slurries had a higher percentage of spheres compared to the commercially available LS (Figure 5.3.10). Overall, sphere morphology classification in each condition was statistically different compared to rod and fused (P = 0.0001), with the different conditions of microparticle slurry representing statistical difference between LS and IHS for sphere morphology (P = 0.0002 for IHS.S, and P = 0.014 for IHS.R). Rod morphology was significantly lower in both IHS conditions compared to LS (P = 0.0062 and P = 0.0144 for IHS.S and IHS.R, respectively).

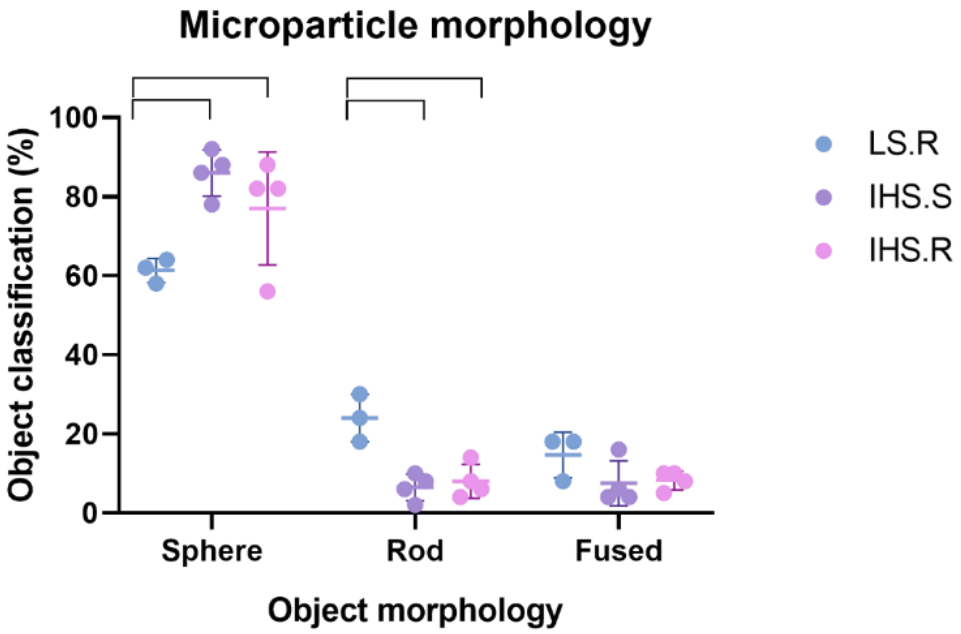

Figure 5.3.10. Microparticle shape analysis of rehydrated life support commercial slurry, saturated and rehydrated in-house generated slurry*. Light microscopy imaging was used to capture a representative field of view, with particle shape determined as rod, sphere or fused morphology with ImageJ on 50 particles, with each replicate average defined as a data point. Tukey's multiple comparison of morphology (%) was statistically evaluated between the different microparticle slurry conditions ($P < 0.05$). LS n = 3, IHS n = 4.*

From the objects classified as spheres, size analysis was completed by measuring the average diameter (Figure 5.2.3) within the different batches and conditions. For the IHS, the difference in diameter was investigated for the process of using saturated neat slurry, compared to the process of lyophilisation and rehydration (Figure 5.3.11A). Between replicates, only IHS.1 represented a statistical difference ($P < 0.05$) between IHS.S and IHS.R from the 50 spheres measured, with progressive batches of IHS generating more

consistent sphere sizes. Rehydrated batches were then compared to LS, a lyophilised product that requires rehydration, whereby inconsistency between batches of IHS was discovered by significant differences against LS.R for all IHS.R ($P < 0.05$) (Figure 5.3.11B). LS.1 was significantly different from LS.2 ($P = 0.0035$), with a statistical difference between all IHS.R replicates ($P < 0.0001$). IHS.R batches were shown to have a statistical difference in size ($P < 0.05$) apart from IHS.1.R against IHS.2.R, and IHS.3.R against IHS.4.R. This discovery represents the inconsistency in the production of microparticle size in both commercially produced and in-house produced slurries.

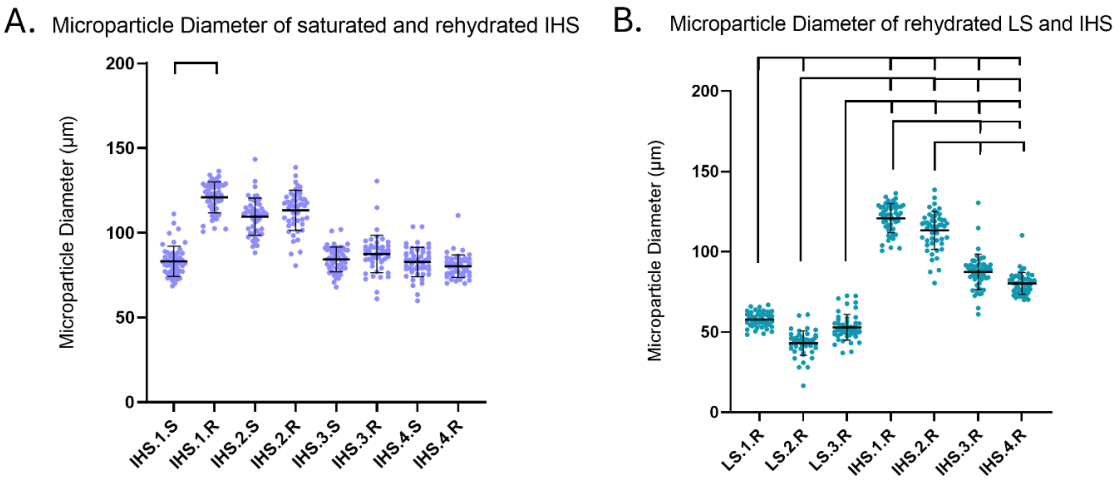

Figure 5.3.11. Microparticle diameter analysis of in-house slurry, saturated and rehydrated, and life support. *Light microscopy imaging was used to capture a representative field of view, with particle diameter analysis performed with ImageJ on 50 particles. A) Diameter analysis of Saturated and rehydrated in-house slurry (IHS), B) Diameter analysis of commercial life support and rehydrated in-house slurry (IHS). Normality testing was completed using Shapiro-Wilk, showing non-parametric distribution. Kruskal-Wallis was performed using multiple comparisons (P < 0.05), with (A) investigating the difference from IHS.S to IHS.R per batch and (B) comparing diameter across all conditions and batches. LS n = 3 and HIS n = 4.*

5.3.4 Flow behaviour analysis of microparticle support slurry

The flow behaviour of the microparticle slurry was characterised by oscillatory rheological testing. First, the viscosity of IHS.R.3 in various concentrations, in comparison to IHS.S.3 was assessed to represent the difference in flow behaviour (Figure 5.3.12A). The neat slurry did not have an exact concentration compared to the rehydrated samples, resulting in variation of viscosity (Figure 5.3.12A). The overall profile of the material, however, has not altered from a viscoelastic material with a non-Newtonian flow profile of a pseudoplastic. As predicted, the increased concentration of material

caused an increased viscosity under shear, resulting in decreased flow behaviour compared to a low concentration of slurry (Figure 5.3.12A).

Viscosity between the rehydrated batches of IHS and LS revealed differences in flow behaviour between all conditions at lower shear rates (Figure 5.3.12B), whereby under ‘γ 10 S/1 the different batches and conditions begin to cluster with similar viscosities. All profiles represent a viscoelastic material with a non-Newtonian flow profile of a pseudoplastic; however, the different batches of IHS.R show variations in viscosity profiles, e.g. IHS.3 has the lowest viscosity, whereas IHS.4 has the highest viscosity overall. This is an interesting result, considering the sphere diameter for IHS.3 and IHS.4 are the only batches which are not significantly different (Figure 5.3.11B). LS has a consistent viscosity and flow behaviour between batches, compared to IHS (Figure 5.3.12B). Overall, all materials become more viscous at a higher rate, following the same fluid behaviour of a non-Newtonian fluid (Figure 5.3.12).

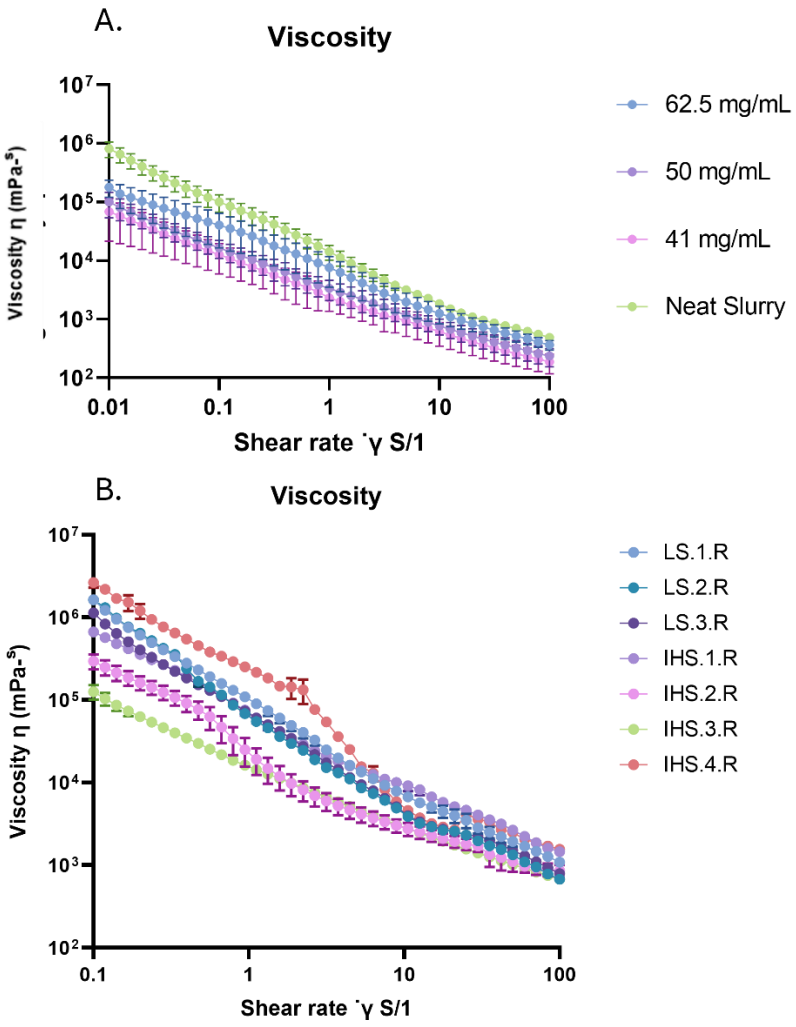

Figure 5.3.12. Viscosity curve of different concentrations of in-house lyophilised and rehydrated slurry in comparison to freshly made neat slurry*. A) In-house slurry (IHS) underwent lyophilisation and rehydration with alpha-MEM in the following concentrations: 62.5, 50 and 41 mg/ml before oscillation rheological investigations. The neat slurry was freshly made and immediately assessed. B) 50 mg/ml of IHS and LS were rehydrated for oscillation rheological investigations. Different concentrations of IHS n = 1, different batches of IHS n = 4, and LS n = 3.*

Identification of the linear viscoelastic (LVE) region allows appropriate stress to be applied to the material without imposing irreversible damage on the material (Figure 5.3.13A). For LS, the LVE was 0.1 – 3 % shear strain, and for IHS, the LVE was 0.1 – 2 %. The LVE was selected instead of the linear viscoliquid region (LVL) as this was representative of the bio-printing experiment, and to be inclusive of both samples 0.1 – 2% was defined as an appropriate LVE region. Both IHS and LS proved to have different destruction regions, with different stress applied. For IHS, the destruction region began at 23% stress, whereas LS was 39%.

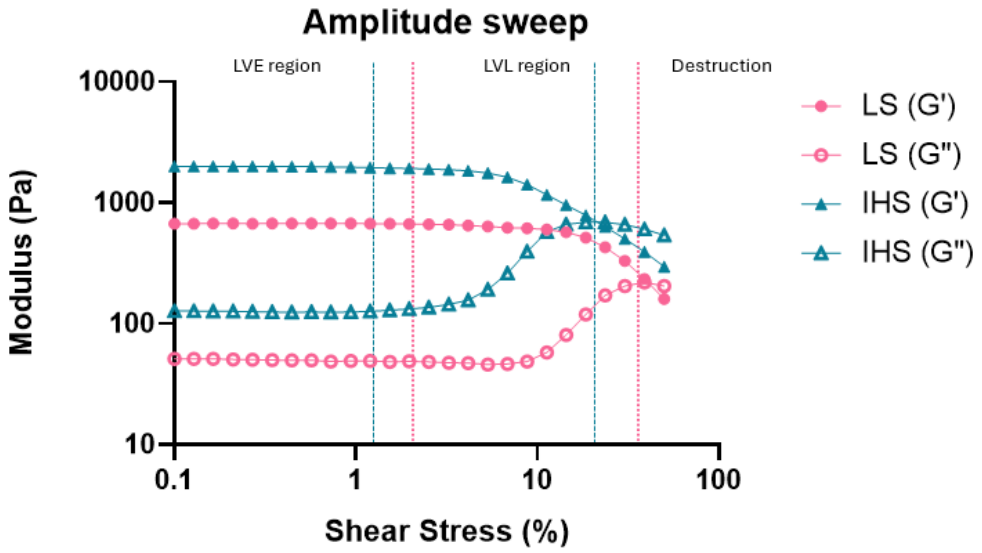

Figure 5.3.13. Amplitude strain curve for the identification of the linear viscoelastic region of life support and in-house generated slurry. *Storage (G') and loss (G") modulus were assessed for 50 mg/ml Life support (LS), and 50 mg/ml in-house slurry (IHS), n = 1.*

To further explore the flow characteristics of both materials for bioprinting applications, the destructive region was explored to assess if an excessive region of shear stress, 50%, applied to the microparticle slurry could cause destruction to the material, and if recovery of the material's mechanical properties was possible over-time after strain, even at extremes. Recovery was defined as the return of the material's viscosity to its original state after a period of stress is removed (Gao, T., *et al.* 2018). Both materials responded immediately to strain removal (Figure 5.3.14A/B), representing the materials' immediate recovery from a bio-printing nozzle passing through and biomaterial deposition, and further classifying the material as a pseudoplastic flow behaviour with a shear thinning profile. The G' G" crossover point is also visualised during this experimentation, signifying the transition between elastic and viscous behaviour, known as the gel point. Once strain was applied, the material crossed from an elastic gel material (G'), to a viscous liquid material (G"), with this behaviour seen in both materials (Figure 5.3.14A/B). Interestingly, despite the materials having the same pseudoplastic viscosity profile (Figure 5.3.12B), LS G' is higher than G" in rest and recovery periods (Figure 5.3.14A), suggesting that the material behaved more like a solid with elastic properties, compared to a liquid with viscous properties as IHS.

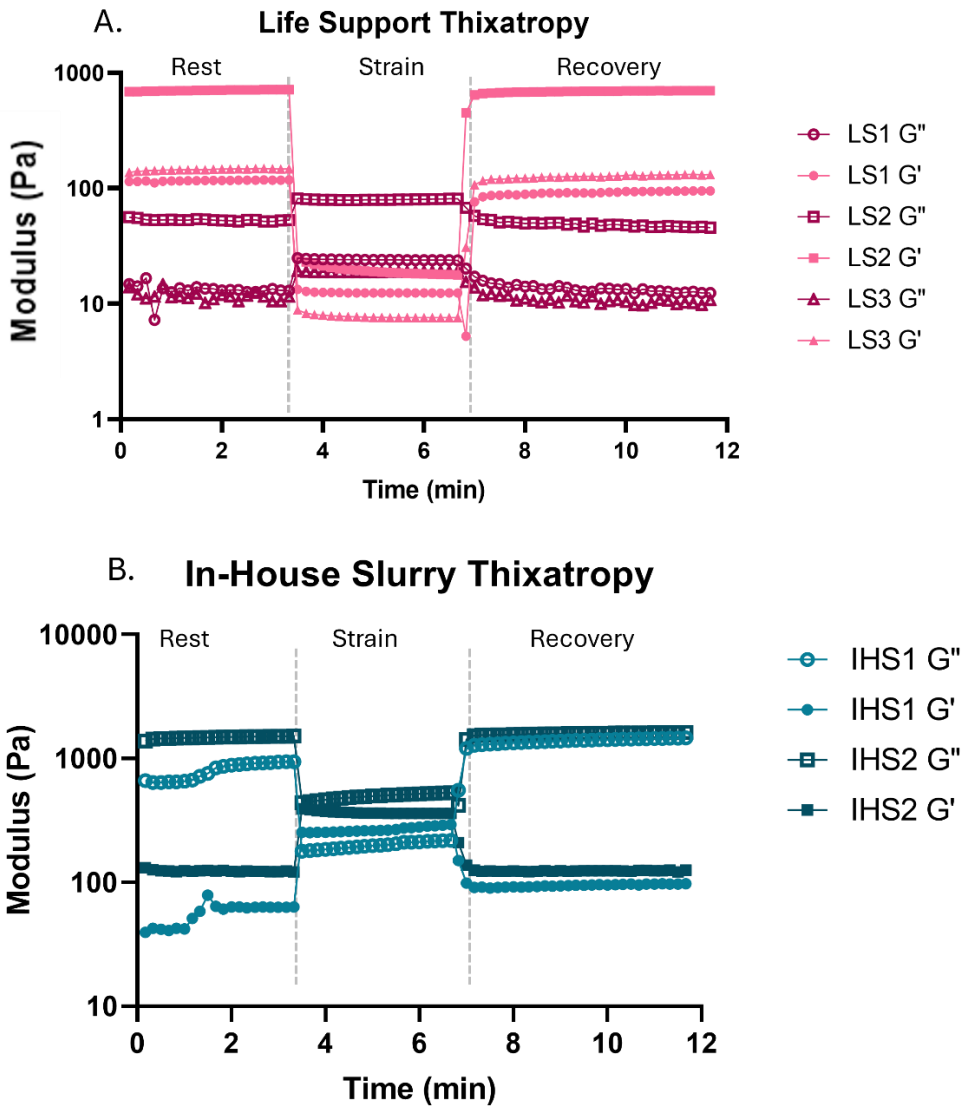

Figure 5.3.13. Thixotropy destructive material response analysis on life support and in-house slurry. *Following the Identification of the linear viscoelastic region of life support and in-house slurry, the response of the material to destructive strain was assessed by oscillation with 50% strain applied. A) Storage (G') and loss (G") modulus were assessed for 50 mg/ml LS N=3, B) Storage (G') and loss (G") modulus were assessed for 50 mg/ml IHS n = 2.*

5.3.5 Optimisation of 3D bioprinting control structures in microparticle support slurry

Initial optimisation of bioprinting control structures was completed with bone GelXA. To assist in crosslinking to produce a stable structure with reduced sheer thinning of the bioink, $CaCl_2$ in various concentrations of 20 – 200 mM wash was used as the IHS wash buffer. Bioprinting in the absence of a microparticle slurry produced an inconsistent construct (Figure 5.3.14A), compared to the construct printed in media-washed slurry

(Figure 5.3.14B). Interestingly, when bioprinting in $CaCl_2$ washed slurry, the filaments deposited did not adhere to each layer, therefore producing a construct that unravelled due to the cross-linked filament surface not allowing further material attachment (Figure 5.3.14C/D/E). As a result, media-washed only IHS was used in future experimentation. LS was not assessed with GelXA.

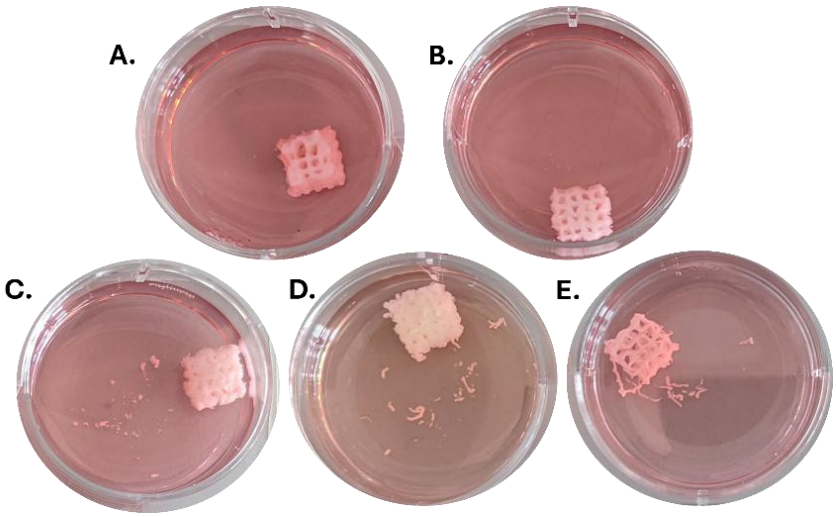

Figure 5.3.14. Bone GelXA bioprinting in microparticle conditions*. A) Bone GelXA bioprinted w/o a microparticle support bath, B) Bone GelXA bioprinted within in house slurry saturated (IHS.S), only media washed, C) Bone GelXA bioprinted within IHS.S, washed with 20 mM $CaCl_2$, D) Bone GelXA bioprinted within IHS.S, washed with 100 mM $CaCl_2$, E) Bone GelXA bioprinted within IHS.S, washed with 200 mM $CaCl_2$. n = 1 technical replicate, representative picture shown.*

B-gel did not require ionic or photoinitiated crosslinking, only temperature transition, which was performed before bioprinting. Similar to GelXA, in the absence of support slurry, B-gel produced an inconsistent construct that tended to constrict on the sides when the construct was printed to full height (Figure 5.3.15A), with undefined individual filaments. Alternatively, when B-gel was printed in IHS.R, a construct with qualitative similarity to the intended control model was produced, with defined individual filaments, pores and a shell, visualised both embedded within the IHS.R (Figure 5.3.15B), and after release of the construct > 37 *°C* (Figure 5.3.15C). Surprisingly, bioprinting B-gel in LS resulted in B-gel not self-adhering, similar to that seen for Bone GelXA in various $CaCl_2$ conditions (Figure 5.3.15C/D/E), and produced a non-stable construct, whereby no defined filaments were obtained, pores were not observed, and the shell disintegrated (Figure 5.3.15D).

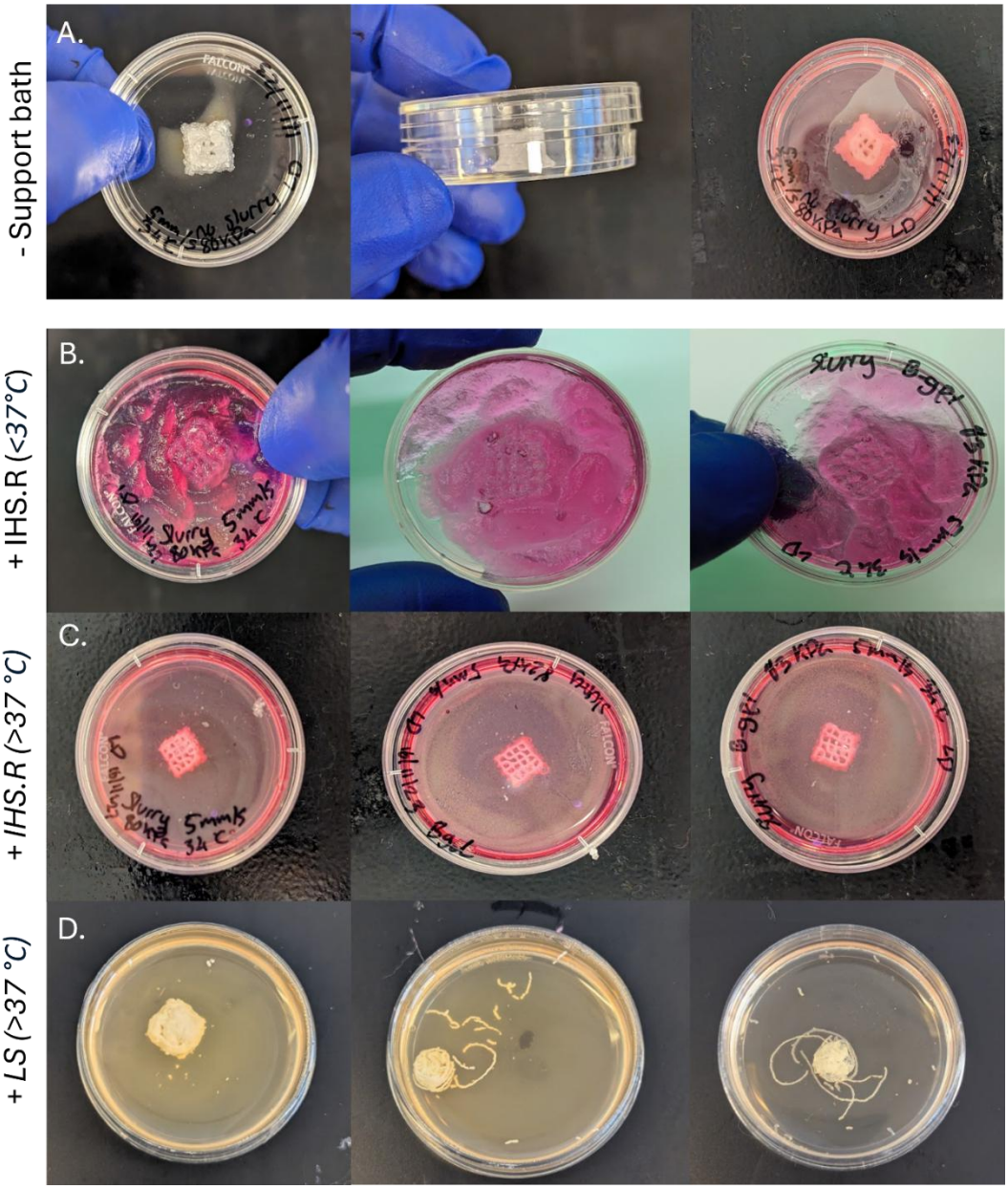

Figure 5.3.15. B-Gel bioprinting in microparticle conditions. *A) B-gel bioprinted w/o a microparticle support bath, B) B-gel bioprinted in in-house slurry rehydrated support bath below 37°C, C) B-gel bioprinted within in-house slurry rehydrated support bath above 37°C, D) B-gel bioprinted in life support above 37°C. A representative picture is shown of the result.*

It should be noted that despite initial optimised bioprinting parameters and micro-particle slurry conditions, bioprinting both GelXA and B-gel was challenging, with a high volume of replicates required due to inconsistent bioprinting during technical repeats (Figure 5.3.16). Printing parameters were consistently monitored to adjust bioink filament deposition; however, when bioprinting within microparticle slurry, visualisation of filament was obscured, B-gel features an opaque appearance in temperatures < 37 *°C*

(Figure 5.3.15B). Often, it was required to alternate between bioprinting +/- microparticle slurry, to monitor bioprinting filament deposition, and adjust printing parameters throughout the cartridge, as well as change nozzles if recurrent blockages occurred (Figure 5.3.16).

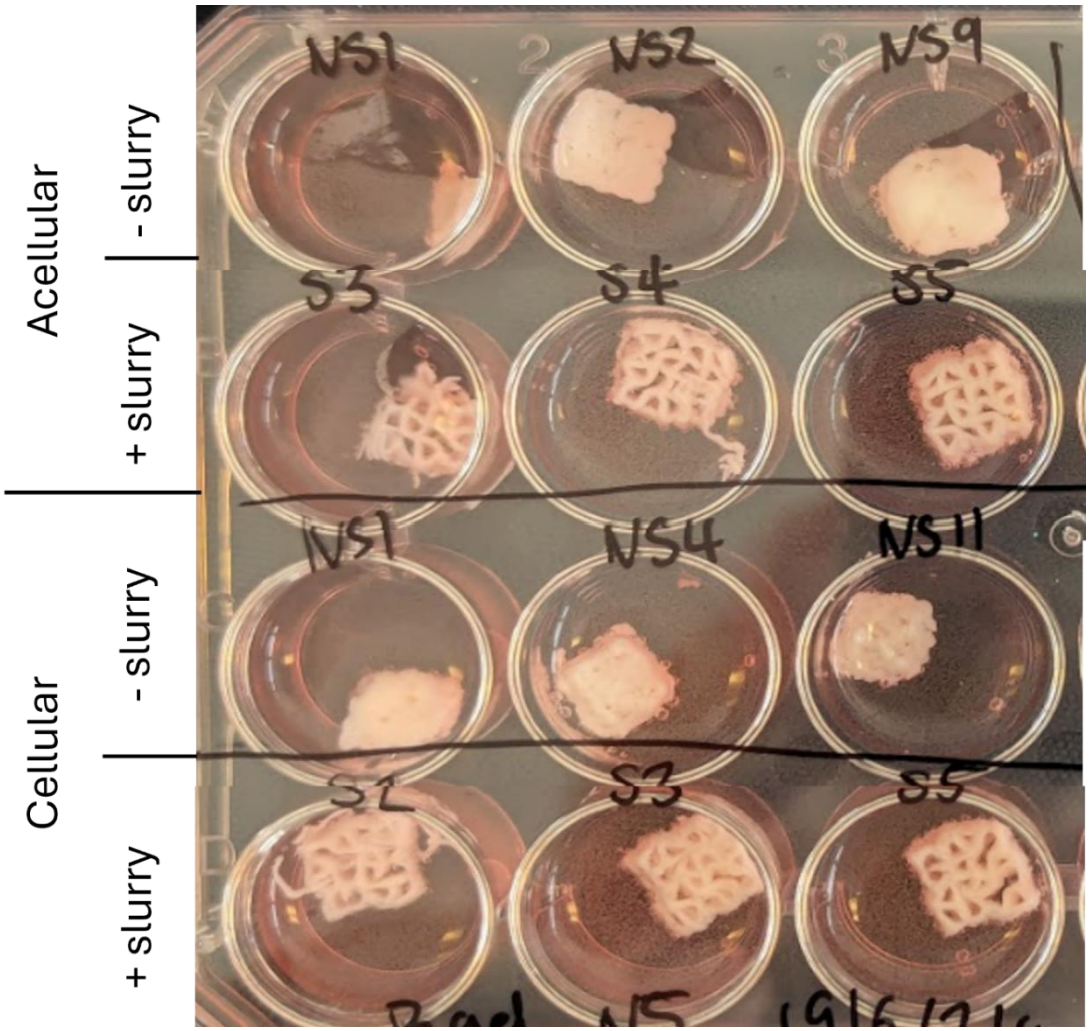

Figure 5.3.16. Example of bioprinting inconsistency within the same technical replicate. *B-gel +/- cellular conditions, bioprinted +/- in house rehydrated slurry above 37°C. A representative picture was taken showing the variation of bioprinting within the same experiment.*

5.3.6 Optimisation of high-resolution micro-CT imaging of bioink and bioprinted control constructs

The quantification of fidelity of 3D bioprinted constructs is typically completed on a 2D basis, using photographs (Figure 5.3.1/2/3). Initial optimisation for the quantification of 3D bioprinted constructs using micro-CT required the 3D bioprinted constructs to be placed within the chamber whilst maintaining structural integrity and hydration and

reduce scanning artefacts. Scanning time and radiation from the x-ray source was another key consideration, as cellular constructs would be scanned in future experimentation. Initially, bone GelXA constructs were optimised with a bijou tube to contain constructs in a sterile environment throughout. Similar to the method of scanning bone, by wrapping the construct in damp tissue paper, however, this did not support complex structures, causing collapse, this method also had the disadvantage of failing to maintain sterility (Figure 5.3.17A). To reduce shrinkage and morphology collapse, sterile $^{dd}H_20$ was used, however, this caused strong movement artefacts in the resulting scan (Figure 5.3.17B). Finally, the bioprinted construct was placed on top of a UV-sterilised Styrofoam block, covered with a small layer of parafilm, and surrounded by appropriate warm growth medium, whereby the meniscus surface tension assisted in reducing the bioprinted construct from moving during scanning rotation (Figure 5.3.17C). This method of micro-CT scanning produced a better understanding of the impact of utilising a micro particle slurry for bioprinting, whereby the benefit in the resulting printed structure can be visualised in the lateral visualisation plane by reduced constriction of the bioprinted shell (Figure 5.3.17C).

In addition, a micro-CT analysis was performed as a method to compare bioprinted dimensions to the original STL lattice structure (Figure 5.2.2). By segmenting the boundaries of the lattice structure, measurements such as overall volume, height, width, and pore width could be taken to determine deviation from the original STL model (Figure 5.3.17D/E/F).

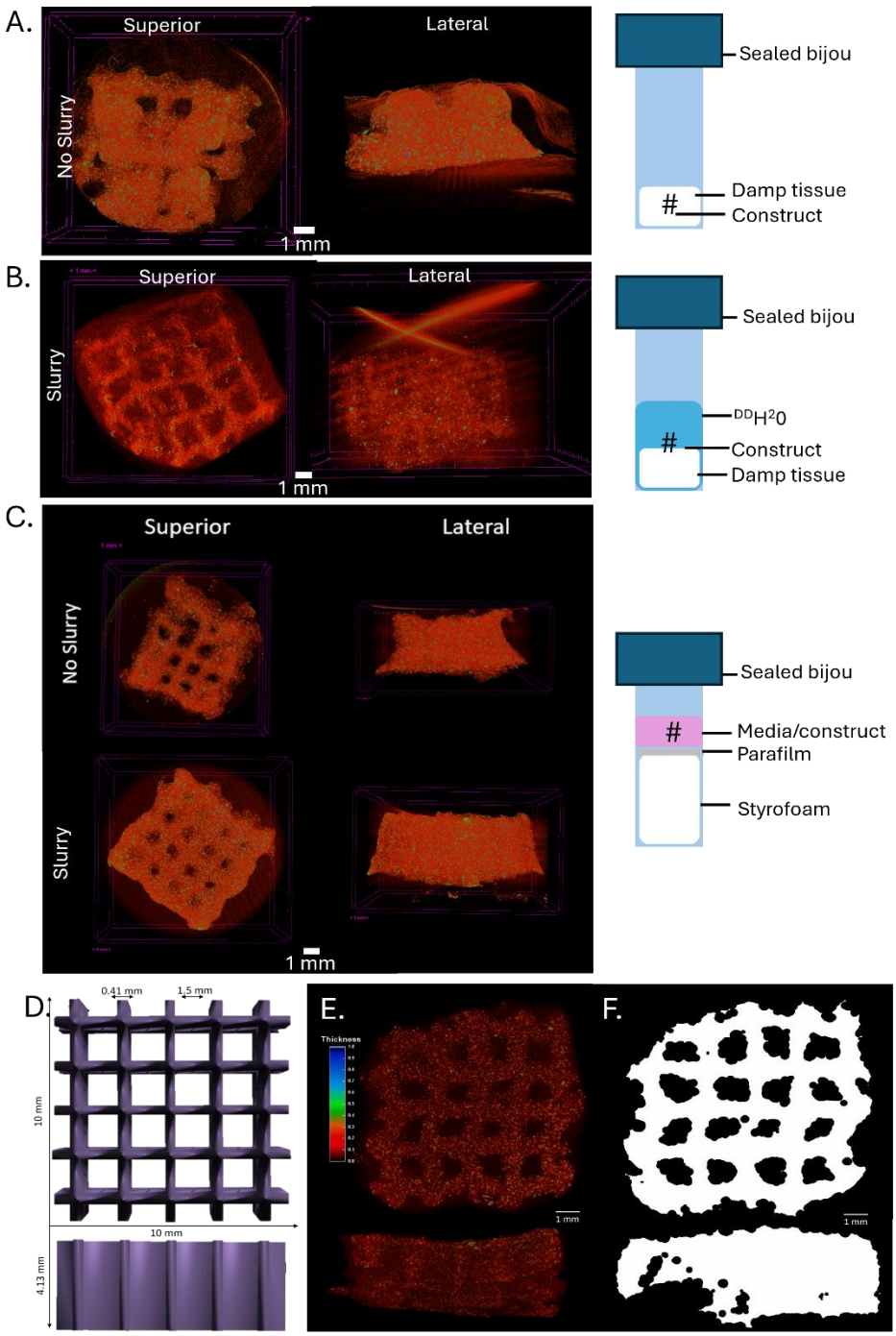

Figure 5.3.17. Optimisation of micro-CT imaging bone GelXA bioprinted lattice structures. *All constructs were imaged at 9 µm and reconstructed with a binary threshold of 0 – 0.12. A) Bone GelXA construct printed w/o slurry, placed in a bijou tube covered in damp tissue, B) Bone GelXA construct printed with slurry, placed on amount of damp tissue within a bijou tube submerged in $^{dd}H_20$, C) Bone GelXA constructs printed +/- slurry placed on top of a Styrofoam block, submerged in growth medium underneath the meniscus. D) dimension defined 3D lattice, E) projection of GelXA bioprinted construct in slurry, F) thresholded lattice for intention of 3D dimensional analysis compared to original 3D lattice model. n = 1, pseudo-colour applied to represent arbitrary density, scale bar represents 1 mm.*

B-gel is a thermo-responsive material; therefore, capturing the true fidelity in temperatures below 37 °C proved challenging as the material reduced in size upon cooling (Figure 5.3.18A), compared to in culture at 37 °C (Figure 5.3.18B). First, a similar approach to imaging GelXA was trialled (Figure 5.3.18C); however, due to the material difference whereby B-gel is mainly constituted of water, visualisation against warmed media was challenging due to the lack of difference in the density between the two materials. To support the structure and visualise fidelity, the construct was embedded within agar; however, this also impeded visualisation of the construct, as well as being defined as destructive (Figure 5.2.18D). Snap freezing and fixing the construct were investigated; however, no improvement on retaining > 37 °C morphology was achieved, with both techniques also being destructive (Figure 5.2.18E/F), with the snap frozen construct defrosting by the end of the imaging protocol, causing artefacts from sample movement (Figure 5.2.18E). Constructs were placed on the edge of a sterile bijou tube, which allowed visualisation of volume and density (Figure 5.2.18G). Iron oxide was investigated as an exothermic source; however, it did not generate high enough temperatures in the surrounding environment to maintain above 37 °C for the duration of the imaging process (Figure 5.2.18H), which was already reduced to a minimum time. Further optimisation was not continued due to time constraints; therefore, future constructs were imaged by placing the construct on the edge of a sterile bijou (Figure 5.2.18G), eliminating the opportunity for 3D fidelity analysis.

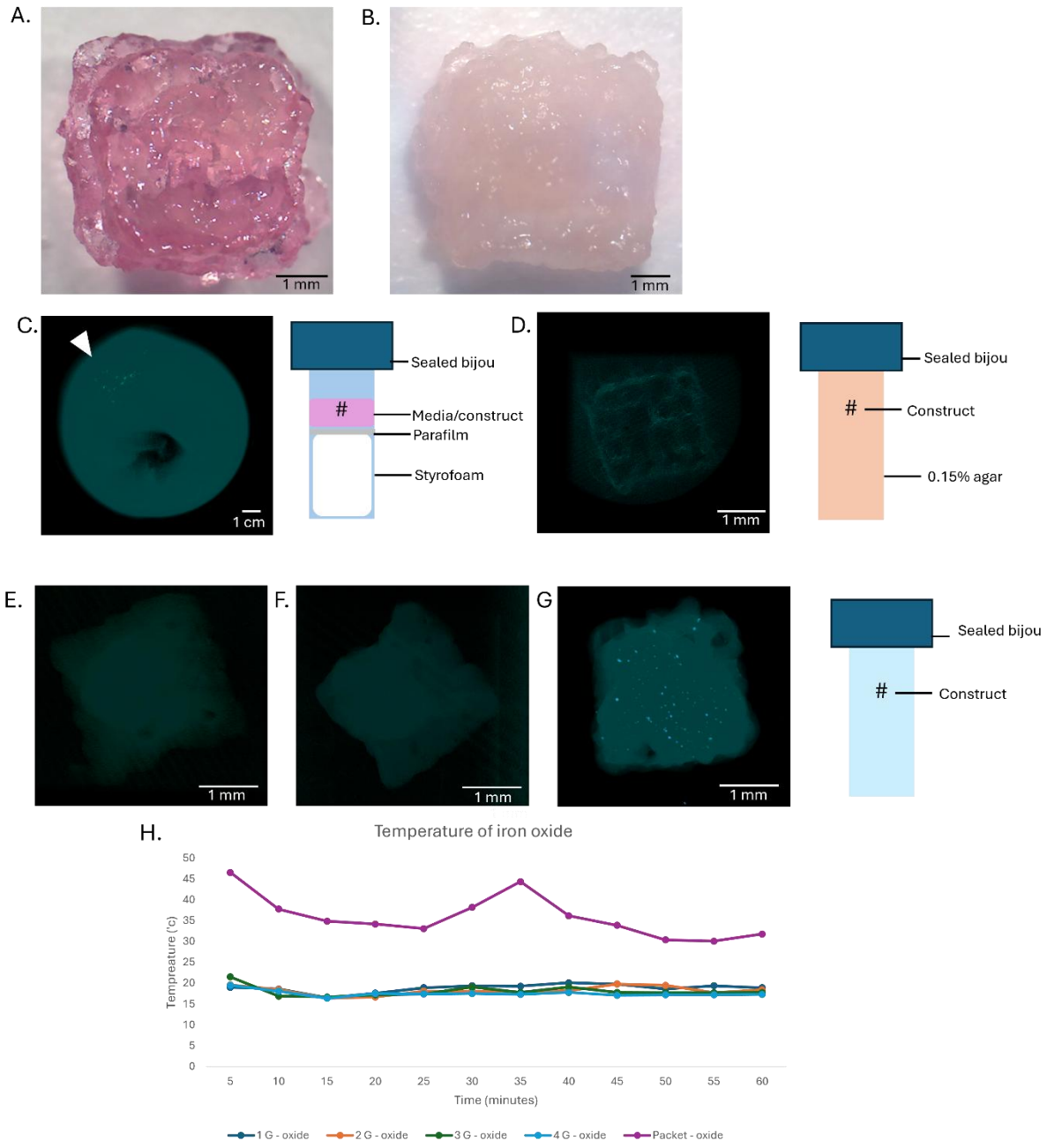

Figure 4.2.18. Optimisation of micro-CT imaging B-gel bioprinted lattice structures. *All constructs were imaged at 9 µm and reconstructed with a binary threshold of 0 – 0.12. All lattices were printed – IHS.R during optimisation. A) B-gel printed lattice at <37°C, B) B-gel printed lattice at >37°C, C) B-gel printed lattice placed on top of a Styrofoam block, submerged in growth medium underneath the meniscus. White arrow indicates location of bioprinted construct. D) B-gel printed lattice submerged in 37 °C 0.15% agar and allowed to cool, E) snap frozen B-gel printed lattice and immediately imaged, F) 4% PFA fixed B-gel printed lattice, G) B-gel printed lattice placed on surface of bijou, H) Various weights of Iron oxide (1, 2, 3 and 4g) temperature over 60 minutes, contained within a sealed bijou and measured with a infrared thermometer, compared to original packet heat. n = 1, scale bar represents 1 mm for A, B, D, E, F, G and 1 cm for C. Pseudo-density applied to micro-CT projections in CT Vox.*

Micro-CT total cartridge particle analysis

Throughout the optimisation of bio-printing GelXA, highly variable inconsistencies with printing parameters were noted, especially printing pressure (Table 5.2.2). As previously explored, the bioinks did not always have consistent filament deposition and would often 'blow out' or 'jump' filament, resulting in highly inconsistent filament printing (Figure 5.3.1) despite the exact protocol followed, with appropriate adjustments made. Micro-CT imaging was used to visualise entire, unopened, cartridges of GelXA bioink (Figure 5.3.19A/B/C), revealing highly inconsistent TMD (g/cm^3) concentrations (Figure 5.3.19G). In contrast, B-gel, showed HAnp distribution was homogenous throughout the biomaterial (Figure 5.3.19D/E/F), whereby minimal blockages occurred during bio-printing over the various experimentations, despite pressure fluctuations (Table 5.2.2).

Binarised analysis on the different batches of GelXA requires further consideration, as B1 & B2 allowed consistent 3D analysis binarisation for identification of particles, thus allowing TMD to match that of B-gel (Figure 5.3.19G). GelXA B3 – B5 could not be thresholded within equal boundaries of 65 – 255, as a high volume of particles were not included with the threshold, and therefore did not produce a representative output of density. Alternatively, the B-gel and GelXA B1&B2 could not have raised thresholds, as this caused exaggerated enhancement of particle number; therefore, different binarised thresholds were applied (Figure 5.3.19G) within the same workflow, reducing the accuracy of results for TMD overall.

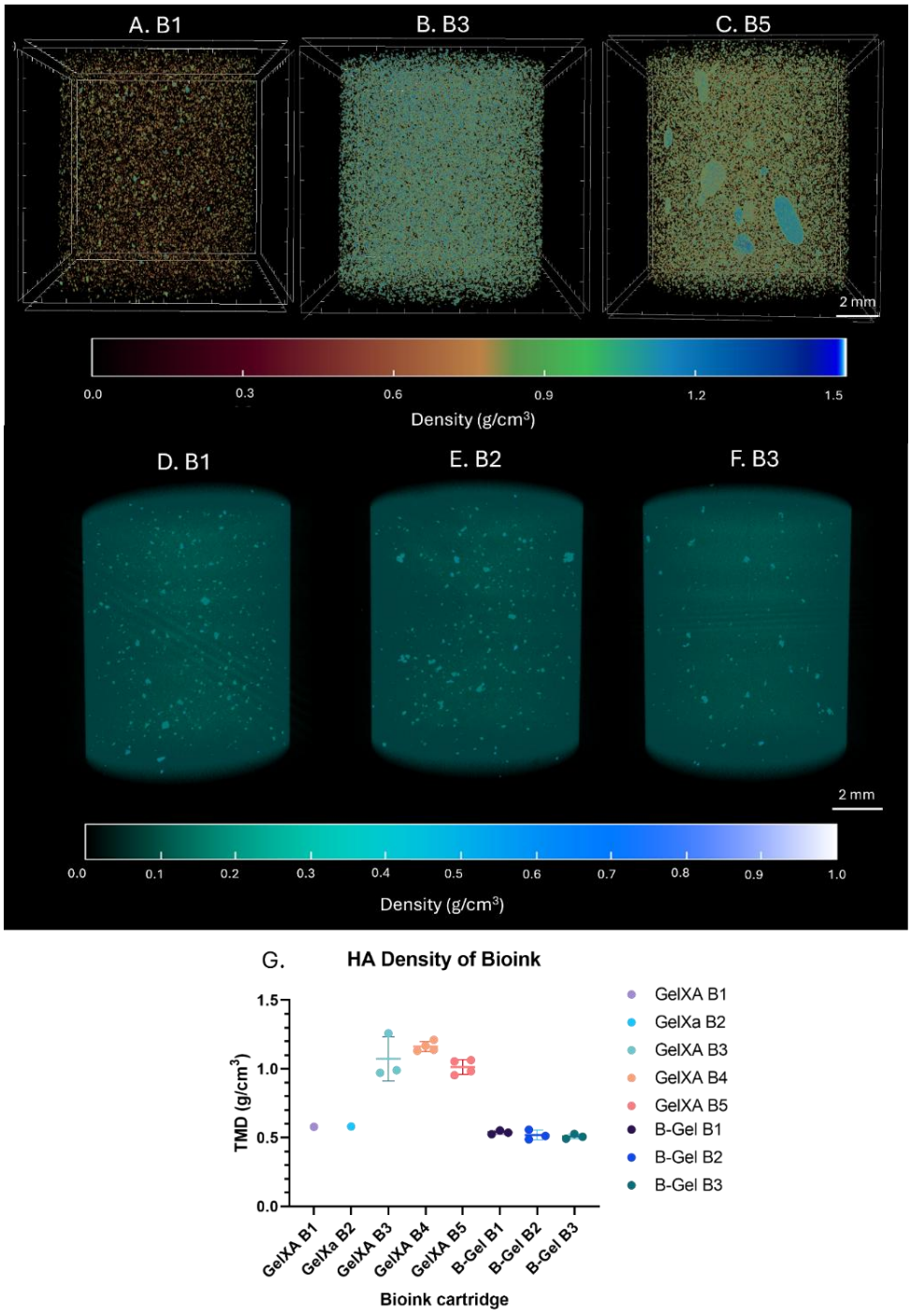

Figure 5.3.19. Bone GelXA and B-gel total cartridge micro-CT imaging. *Cartridges were imaged at 9 µm and reconstructed with a binary threshold of 0 – 0.12. CT Vox was used for visualisation of the total field of view, with TMD VOI of 2 mm. A) Batch 1 of bone GelXA, B) Batch 3 of bone GelXA, C) Batch 5 of bone GelXA, D) Batch 1 of B-gel, E) Batch 2 of B-gel, F) Batch 3 of B-gel, G) TMD quantification of 2 mm VOI. GelXA B1 & B2 and all B-gel required a threshold of 65 – 255, whereas GelXA B3 – B5 required a threshold of 100 – 255 for particle identified and TMD analysis. H) 22G nozzle blocked from bioprinting with batch 5 of GelXA. GelXA batch 1/2 n =1, batch 3/4/5 n = 3, B-gel batch 1/2/3 n = 3. Statistical analysis cannot be completed due to the low n of batch 1/2.*

HAnp individual particle thickness/diameter was explored to further characterise the bioinks used within this study (Figure 5.3.20A/21A). Thickness represents the smallest dimension of an irregularly shaped particle, whereas the diameter is the largest dimension of an irregularly shaped particle (Table 2.2.4). Reporting on both values gives a perspective of the overall morphology of the irregular HAnp/particles present in the investigated bioinks.

It was discovered that the particle diameters in batches 4 and 5 were consistently blocking the 22G nozzle used (Figure 5.3.20E), therefore not allowing deposition of any ink, with constant waste of materials. A 22G nozzle has an inner width of 0.41 mm, whereas HAnp visualised in latter batches, had particle sizes of up to 2 mm in width. Aside from the large particle sizes visualised, batch density variation may produce inconsistent cell environments in future work (Chapter 6), invalidating technical replicates.

No statistical differences were visualised for the average HAnp thickness in all batches of B-gel ($P > 0.05$), despite cellular or acellular conditions (Chapter 6), with an average particle diameter of 0.91029 mm in total (Figure 5.3.21B). The maximum particle diameter average for all inks imaged was 0.55708 mm, larger than the 0.413 mm inner diameter of the conical nozzle used for 3D EBB, however, no frequent nozzle blockages were noted during active experimentation (Figure 5.3.21C). Lastly, despite no statistical difference ($P > 0.05$), the number of HAnp present in the VOI of B-gel was inconsistent between batches, perhaps suggesting further improvement of consistency in homogenising the bio-ink, cells and HAnp during creation (Figure 5.3.21F).

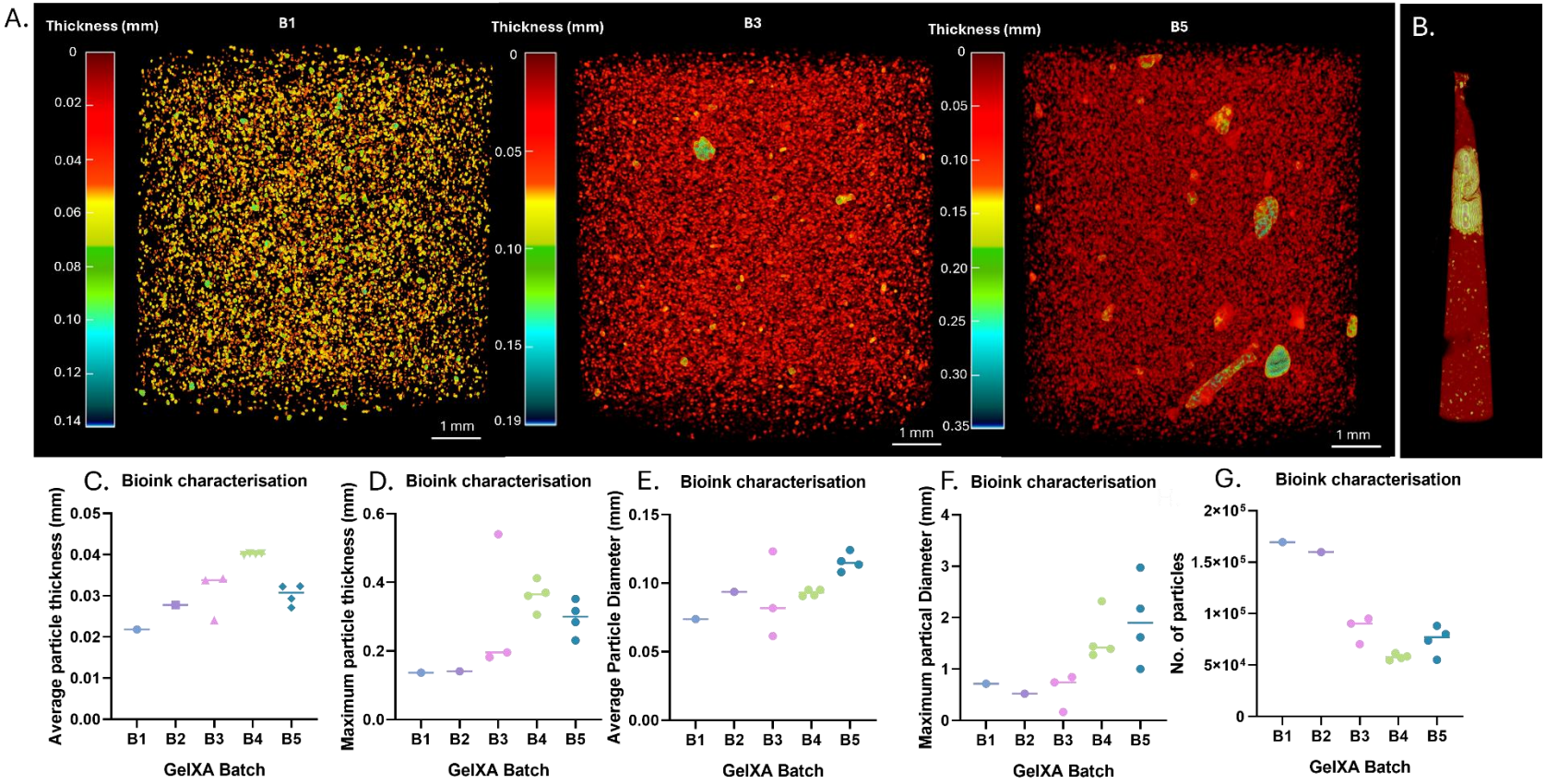

Figure 5.3.20. Bone GelXA particle visualisation and quantification by micro-CT imaging. *Five different batches of GelXA had cartridges imaged at 9 µm and reconstructed with a binary threshold of 0 – 0.12. A) Individual particle analysis was performed, with B1- 2 thresholded at 65 – 255, and B3 – 5 thresholded at 100 – 255 for appropriate particle visualisation. Individual batches were colour-coded as appropriate to output particle thickness and visualised in CT Vox. The scale bar represents 1 mm. B) 22G nozzle imaged at 9 µm and reconstructed with a binary threshold of 0 – 0.12. The nozzle was collected during a 3D bioprinting experiment. C) Average particle thickness (mm) of GelXA batches, D) Maximum particle thickness (mm) of GelXA batches, E) Average particle diameter (mm) of GelXA batches, F) Maximum particle diameter (mm) of GelXA batches, G) Number of particles. n = 5, no statistical analysis can be completed due to no replicates for B1-2.*

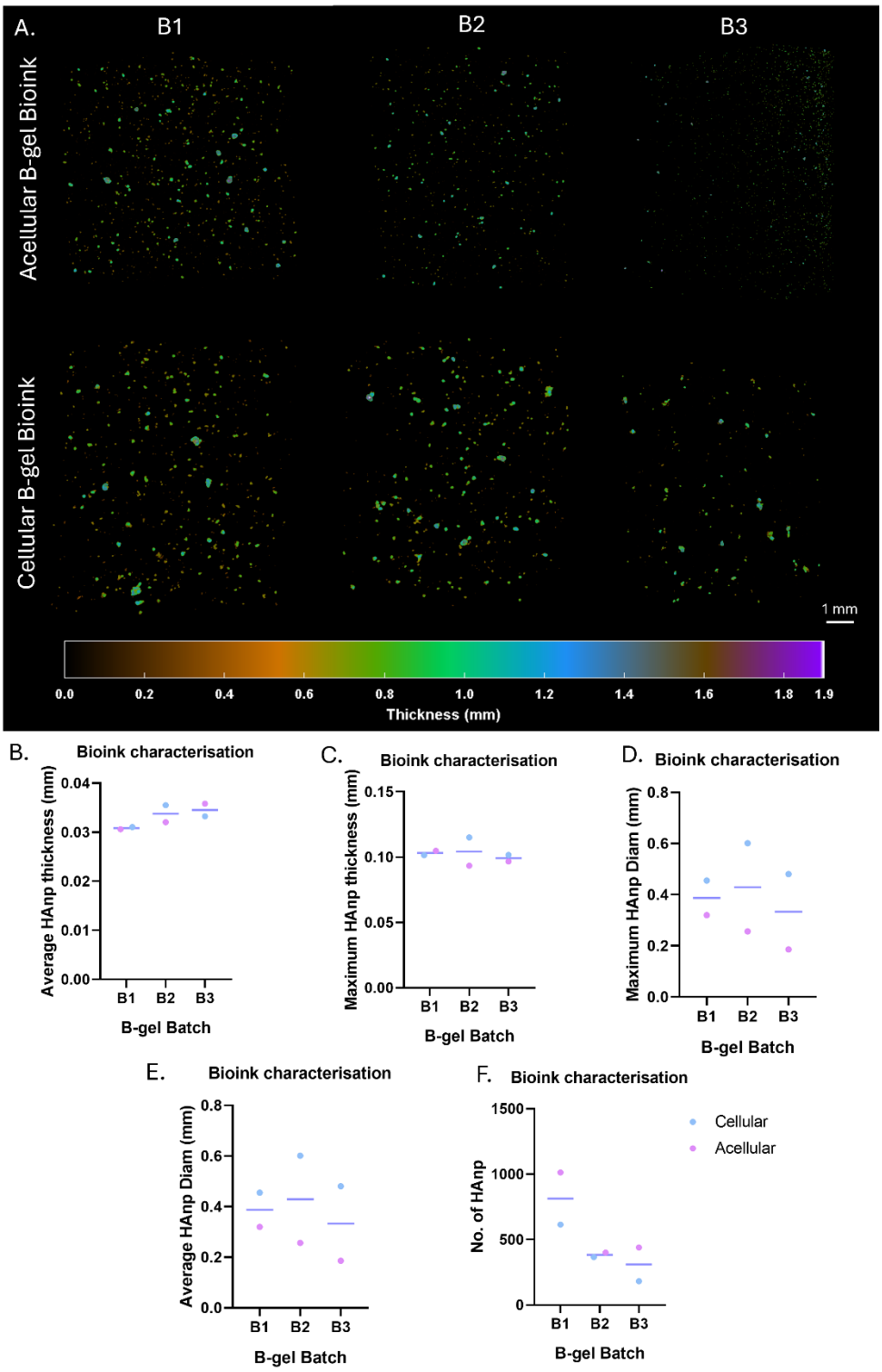

Figure 5.3.21. Hydroxyapatite nanoparticle characterisation of different batches of B-gel bioink*. B-gel cartridges were imaged at 9 µm, with an aluminium 0.25mm filter followed by reconstruction of 0 – 0.12. Individual particle analysis was completed in CTAn, and thickness coding was applied. A) Cartridges were imaged in CT Vox, with thickness colour coding applied., B) Average particle diameter, C) Maximum hydroxyapatite diameter, C) Number of hydroxyapatite nanoparticles. n = 3, Tukey's two-way ANOVA between different batches revealed no statistical difference.*

5.3.7 Three-dimensional bioprinted *ex-vivo* tibia structures

For both conditions, the full 37-layer CAD model was unable to be printed with the current bioprinting method as this would result in collapse of the model, or the requirement for more than 3 ml of B-gel material (*not shown*). Instead, the printing process was halted at 17 layers for all models (Figure 5.3.22). All three CAD modelling methods resulted in bio printable models, with no noticeable differences could be detected between the different rendering processes (Figure 5.3.22A/C). Similar to previous results (Figure 5.3.15/5.3.16/5.3.17), the impact of including a microparticle support slurry is clear by reducing shrinkage after heating and improving structural stability during the bioprinting process (Figure 5.3.21B/D). Despite the unsuccessful completion of bioprinting the *ex-vivo* bone model, Cb structure had good definition in all rendered models, and by the inclusion of IHS, Tb structures were identified (Figure 5.3.22D), compared to without IHS (Figure 5.3.22C).

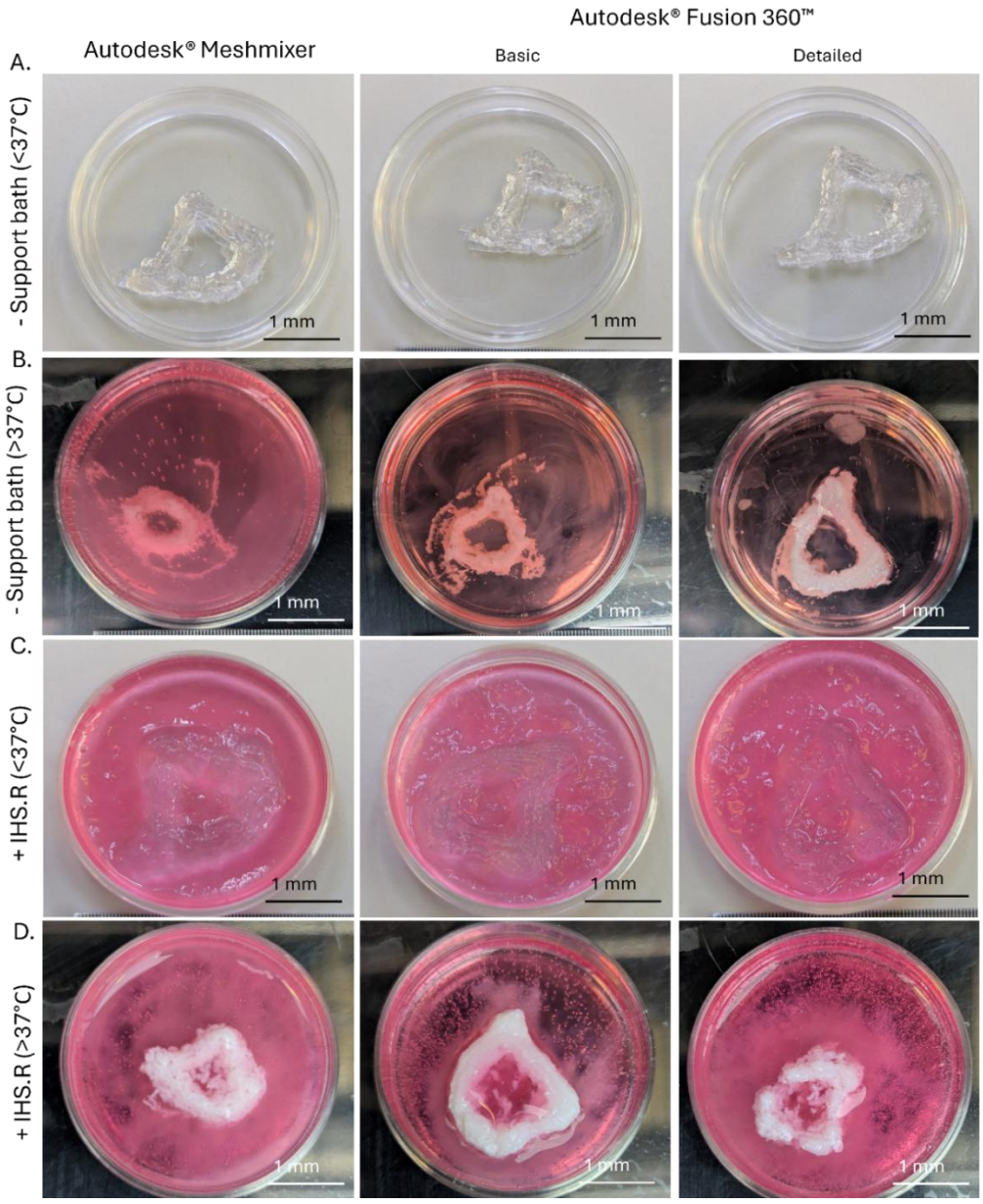

Figure 5.3.22. Bioprinted in-silico designed ex-vivo tibia bone. *Acellular B-gel bioprinted with previously rendered murine tibia bone, A) B-gel bioprinted without IHS at room temperature, B) B-gel bioprinted without IHS at 37 °C, C) B-gel bioprinted with IHS at room temperature, D) B-gel bioprinted with HIS at 37 °C. Representative picture taken, scale bar represents 1 mm.*

5.4 Discussion

Bioprinting is an exciting and progressive technique, with a substantial benefit being the ability to generate complex structures with high resolution; however, many challenges exist that require extensive optimisation, consideration and characterisation. The research presented aimed to optimise and determine the composition, suitability, printability and fidelity of bioinks, GelXA, TissueFAB™ and B-gel, to achieve bioprinting of a complex architecture of bone inclusive of Cb and Tb. To assist in structural complexity and stability, a micro-particle support slurry was produced, optimised and characterised.

5.4.1 Bioink composition and consistency

Within the research presented, different hydrogel bioinks were explored. Commercially available inks were initially selected, as this allowed a higher degree of reproducibility, reliability, convenience and accessibility between different researchers in various research facilities. Ultimately, the purpose would be to allow a more consistent 3D *in-vitro* bone model to be used for biomedical investigations (Chiticaru, E., & Ionita, M. 2024). Alternatively, an in-house generated but previously characterised hydrogel, Laptonite™ co-polymer +/- HAnp (Snuggs, J*., et al.* 2023; Boyes, V., *et al*. 2021; Thorpe, A., *et al*. 2016a; Thorpe, A., *et al*. 2016b) was investigated for the possibility of translating an injectable hydrogel into a functional bioink. Ali (2024) reported in a systematic study for liver bioprinted models that only 8% of studies utilised commercially available bioinks, with 83% utilising custom, in-house generated bioinks, emphasising the preference for in-house bioink use. The trend of utilising in-house generated bioinks limits progressive research between different institutes. This, therefore, limits the opportunity for a widely characterised material to be used for different applications in the overall goal of generating a suitable *in-vitro* 3D model, unless systems can be shared easily between laboratories. However, despite the benefit of increased accessibility to commercial bioinks, a range of considerations and negatives are clear. This includes lack of composition knowledge and control, long lead time for materials, increased cost, and batch inconsistencies that can be found, as revealed within this study, whereby the material is not fit for purpose resulting in a higher frequency of error, with a large cost on time, funding and research progress.

Aside from batch inconsistencies, complete material composition is not exclusively revealed, and therefore, limited adjustments to the composition and concentrations can be made to the bioink to improve fidelity and printability, limiting application. Chiticaru (2024) suggests the bone GelXA formulation is GelMA, xanthan gum, lithium phenyl-2,4,6-trimethylbenzoylphosphinate, Alg, calcium phosphate tribasic, HAnp, D-mannitol, and HEPES buffer solution. All components are commonly used within bioinks, either to improve the structural stability of the ink or as the biocompatible base (Chaurasiya, A., *et al*. 2024; Tolmacheva, N., *et al.* 2024; Mukherjee, K., *et al*. 2024; Chen, S., *et al.* 2023; Zhu, M., *et al.* 2019). TissueFAB™ is listed as an alg and GelMA bioink that crosslinked under 365 nm UV, and 200 mM $CaCl_{2;}$ however, no further specification of concentration or other materials is provided.

Previously investigated by Boyes (2021), the composition of B-gel can be altered by the addition of N, N' – dimethylacrylamide comonomer, HAnp and gelatine in various concentrations, resulting in a change in mechanical and rheological properties. For the research conducted, the same composition of NP-gel was used consistently as utilised by Snuggs (2023). Perhaps a more focused research approach to improving printability and resulting fidelity by tailoring the B-gel composition for the strict application of bioprinting could be investigated; however, in the materials' current state, the in-house generated bioink featured a higher success rate of physical printing compared to commercially sourced bioinks. In addition, COL could be investigated as a further additive to the hydrogel in a similar approach to Alaman-Diez (2023) by generating COL laptonite™ hydrogels for spheroid generation, as well as Ding (2022) with COL-polyacrylamide hydrogels, to further tailor the bioink to a bone-like composition.

5.4.2 Bioink printability

Printability is typically determined by two different methods: rheological viscosity or physical trial-and-error printing to assess resulting fidelity (Bercea, M. 2023; Habib, M., & Khoda, B. 2022; Gao, T., *et al.* 2018). For example, the Herschel-Bulkley model is employed to characterise the viscosity to produce flow curves (Gillispie, G., *et al*. 2023), as represented by the data obtained in this study. Both GelXA and B-gel represented pseudoplastic flow behaviour with shear-thinning properties, whereby viscosity decreased based on shear stress, which was applied to the material. Classically, a

pseudoplastic viscoelastic material is ideal for bioinks to enable complex flow behaviour to act as a fluid during flow yet present the characteristics of a soft solid to exhibit fidelity and return to the original state after deposition (Amorim, P., *et al*. 2021).

Tian (2009) used the Herschel-Bulkley model to determine the alterations of viscosity of Alg & HAnp bioinks based on different concentrations of the components, as well as the impact of temperature. Within the research, 1% Alg with 20% HAnp produced a bioink which was almost Newtonian in behaviour, with increased concentrations of Alg, up to 5% adjusting the flow behaviour to pseudoplastic. Altering the HAnp concentration from 10 to 50% increased viscosity dramatically, representing increased stiffness; however, this gave rise to difficulty in material manipulation. Similarly, with temperature, a higher temperature represented a decrease in viscosity, generating an almost Newtonian behaviour material that allowed easy handling of the biomaterial, e.g. producing filled cartridges. When the material was cooled, stiffness increased, indicating the material will have higher shape retention (Tian, X., *et al.* 2009).

A similar approach of characterising B-gel viscosity by altering temperature, and +/- HAnp was used within this study, however, commercial bioinks were strictly used as provided with the standard protocol followed with investigative rheology revealing inconsistency of material under increased shear-rate. This is attributed to the inconsistent particle density, thickness and diameter discovered within the batches by micro-CT imaging. Compared to B-gel, whereby density, thickness and diameter have no statistical differences, resulting in a consistent pseudoplastic material with sheer-thinning behaviour. Unlike widely used bioinks that are cross-linked post-printing, B-gel/NP-gel is thermally transitioned after the handling stage to allow suitable transferring into equipment due to the Newtonian liquid-like behaviour (Snuggs, J., *et al.* 2023; Boyes, V, *et al.* 2021). Investigating the viscosity of B-gel at different temperatures revealed that the transitioned bioink's viscosity was temperature-dependent, with decreasing temperature increasing viscosity, therefore reducing flow at low shear rates. Temperature increases decrease viscosity, resulting in increased flow at low shear rates. For this, 34 °C was discovered to be appropriate flow behaviour to produce filament that allows shape retention, suitable extrusion pressure and biocompatibility, as further explored in chapter 6.

To further characterise the rheological behaviour of the bioink, in particular B-gel, the materials recovery response to stress, it would have been beneficial to define the storage modulus (G') and loss modulus (G") ratio to determine if the material is solid-like or liquid-like, with elastic properties. As discussed by Gao (2018), typically only viscosity is reported on for bioinks concerning bioprinting, and although this is a vital characteristic for the application of bioprinting, the G'/G" ratio indicates the ability of the material to resist deformation, by the material behaving elastically and, eventually, structural stability long term (Gao, T., *et al.* 2018). Bioprinting as a technique transfers stress to the bioink at different stages, and therefore, it is beneficial for the material to resist deformation during this mechanical process (Amorim, P., *et al.* 2021). Previously investigated by Boyes (2021) it was reported that at 25 °C within a range of 0.1 – 6 Hz through a frequency sweep, the NP-gel behaved like a viscoelastic solid by a greater G' compared to G".

5.4.3 Bioink fidelity

Characterising bioinks' viscosity on a rheometer assists in predicting the viscosity and printability of the material; however, EBB is a challenging, timely manual process involving different equipment, and considerations are required to minimise discrepancies in temperature, composition and processing time to allow consistent printability. Plus, assessing the material in practice is important due to the artefacts of natural deformation in free space due to gravity and surface tension (Ombergen, A., *et al.* 2023; Sarabi, M., *et al.* 2023), compared to the artificial environment of confinement during rheology. Gravity and surface tension cause compression of structures printed with height and cause morphology to have reduced surface area (Riberio, A., *et al*. 2017), as well as collapse of individual filaments when layered (Naghieh, S., & Chen, X. 2021), altering fidelity.

It was initially clear that the reproducibility of parameters resulting in filament deposition was going to be an ongoing challenge to achieve consistent fidelity to mimic that of the pre-designed STL control model. This is due to altering printing parameters, which resulted in different filament fidelity. However, printing parameters would often need to be altered in different technical repeats to ensure the printability of individual filaments. In addition to the same technical repeat due to the ever-changing volume of

bioink within the cartridge, contact of ink to the heated printhead and environmental fluctuations (Straußm, S., Schroth, B., & Hubbuch, J. 2022). A review published by Naghieh (2021) highlighted in detail the many different challenges and considerations required for 3D bioprinting, with the precision, accuracy and reproducibility mentioned as a clear major challenge for the progressive field of 3D bioprinting to achieve success in translation from *in-vitro* to *in-vivo* applications.

Each technical repeat was conducted in the same systematic method to ensure appropriate printability and resulting fidelity of the individual bioinks. Pressure was always optimised first per bioink to ensure the extrusion of the filament. After printing speed was tailored towards improving fidelity and printing success, however, in progressive experiments, this was kept at 10 mm/s for method consistency between technical repeats due to high fluctuations discovered between pressure. For an initial investigation into achievable fidelity, a singular filament was bioprinted with a range of pressures and speeds. In progressive technical experiments, bioprinted filament fidelity is determined *post hoc* with a visual qualitative evaluation of the extruded filaments made in real time. This method allowed initial success of experimental progression whereby time-sensitive bioinks with cellular components can be printed (Chapter 6). However, it is highly subjective and causes high variability between different bioinks and experimental repeats, resulting in a lack of reproducibility.

Paxton (2017) describes the requirements for utilising a variety of nozzle sizes, pressures and speeds throughout a study. By investigating the impact of rheological variation of different bioinks post printing, with a conclusion that the printing parameters should be reported within a window range, as each technical repeat of bioprinting was not mathematically able to be matched. Further, Riberio (2017) investigated the fidelity, collapse and fusion on individually printed lattice structures and the resulting impact of different printing parameters, whereby technical repeats showed high variability. Straußm (2022) suggests improving the active qualitative decision-making causing variability by replacing printing pressure with constant flow rate. However, this method was developed for an independent bioprinter, whereby most tissue engineering research laboratories do not have access. Instead, commercial bioprinters focus on pneumatic printing pressure.

The research presented here investigated three different bioink compositions for optimisation for translation into a 3D *in-vitro* bone model. Kim (2023) reported on the difference in line width and height based on the differences in speed when printing with three different bioinks for the development of a 3D *in-vitro* liver model, including gelatine-based, digested decellularised liver and combination. All bioinks require different printing parameters to achieve optimal line width and length fidelity. The study presents a good example that increasing speed from 10 mm/min up to 160 mm/min decreased line width down to 300 µm at a maximum speed of 160 mm/min, equivalent to 2.5 mm/s, from 1200 µm average width at 10 mm/min printing speed (0.15 mm/s). Compared to the printing speeds utilised within this study, Kim (2023) utilised bioinks with increased viscosity therefore reduced sheer thinning artefacts in free space. Kim (2023) utilised strictly acellular conditions for optimisation, a 27G nozzle (200 µm inner diameter), and dispensing rate of 0.5735 µL/s able to achieve an increased resolution of filament fidelity, and increased complexity in end-product model. Once the bio-inks became cell-laden, thereby altering composition, 120 kPa pressure was used alongside 50 mm/min speed, roughly 0.8 mm/s, and a 25G nozzle (250 µm inner diameter) to achieve a maximum line width fidelity of ~840 µm, representing a deviation in initial maximum fidelity captured during pre-liminary line width analysis (Kim, M., *et al*. 2023).

Further, in the research presented here, from initial extrusion, it was frequently a requirement to alter printing parameters throughout the experimental period. For example, after ~4 constructs were bioprinted, the printing pressure would need to be increased to allow continuous filament deposition; however, after ~ 8 constructs, the pressure would need to be further reduced to below the starting pressure. Zhao (2015) investigated the impact of working time on the quality and resulting fidelity of a bioink composed of gelatine and Alg, whereby bioprinting at different time points of holding time with the same bioink cartridge produced high variation in resulting fidelity with 5 minutes producing a lattice with no structural definition, 15 minutes a detailed structure, and after 30 minutes the structural definition was negatively impacted with ‘blow-outs’ and gaps. In a review by Ramesh (2021), this phenomenon on initial increase in pressure was explored. The reported findings were explained to be because the extrusion pressure is lower for more material due to gravitational stress and surface tension,

whereas less material in the cartridge requires further pressure to push the piston down onto the material within the dead space of the cartridge. In addition, the reduced pressure towards the end of the cartridge could be due to the reduced volume of bioink and therefore will be exposed to a greater temperature, compared to the start of the experiment, despite the temperature remaining 'constant' within the printhead. No research reports, as far as the researchers are aware, on the impact of pressure changes in the dead space during the printing process and why altering parameters are required throughout, despite being reported in various literature, reporting on the challenges, as summarised above.

5.4.4 Microparticle support slurry

A microparticle slurry can be utilised to increase the complexity and resolution of a 3D bioprinted structure when using a bioink that has a low-viscosity or shear-thinning behaviour (Budharaju, H., *et al*. 2024; Zhou, K., *et al.* 2022; Brunel, L., *et al*. 2022). By using a low melting point temperature polymer, the 3D bioprinted construct can be released before further experimentation with low impact on the resulting 3D construct. The aim is to produce a material that allows the deposition of bio-ink without infringing on the resulting structure, whilst providing structural support. The idealistic material will have pseudoplastic fluid flow, have consistent microparticle size and morphology, and be able to withstand shear stress and recover appropriately. Characterisation of the fluid-flow behaviour of the microparticle slurry was important, as the purpose of the slurry is to assist in the bioprinting process by allowing the printing nozzle to move freely, without impediment, and deposit bioink in an accurate XZY location whilst providing support to the filament by reducing sheer-thinning effects by gravity. The material should act as a liquid mould to support the material and not interfere with the deposited filament.

5.4.5 Life support

During the preliminary stages of the research, no suitable commercial support bath product was available. Therefore, published methods by Lee (2019) and Hinton (2015) were adapted for this study. In late 2023, LS was released and patented to the market by FluidFormBio™ and distributed by CellInk in 2024. This product was expensive for the optimisation of bioink printability and fidelity, featuring extensive lead times to obtain three different batches of the product. Therefore, it was used as a control material for

functional characterisation against the developed IHS. LS was found to have inconsistent microparticle shape, but a consistent size of ~ 50 µm, however, it was reported by Lee (2019), to have a uniform microparticle shape and an average diameter of 25 µm. Additionally, it was reported by the specification sheet of the product to have a diameter of 30 +/- 10 µm. As of May 2025, there have been no further reported studies utilising LS as a support bath.

The flow behaviour was reported by Hinton (2015) to have a viscosity of that of Bingham plastic, compared to pseudoplastic, viscoelastic, with shear thinning properties discovered in the research presented here. Bingham plastic requires a minimum shear stress to initiate flow, whereby it begins to behave like a Newtonian fluid with a constant viscosity, compared to pseudoplastic with shear-thinning properties, whereby the viscosity decreases with increased shear rate (Herrada-Manchon, H., Fernandez, M., & Aguilar, E. 2023). The benefit of Bingham plastic is that the support medium is completely self-healing and better suited for materials with very low viscosities, low Pa range, such as strictly COL (Moss, S., *et al*. 2024; Debnath, S., *et al*. 2024), whereas pseudoplastic materials allow flow, deposition of filament, self-healing and provide more structural support for materials that have higher densities, following the gel-in-gel microparticles slurry created by Highley (2015).

Another suggested benefit of LS was that the lyophilised powder can be reconstituted with the crosslinking agent Lee (2019), in this instance, different concentrations of $CaCl_2$ were experimentally tested with IHS. However, because of the deposited ink, GelXA in this case, being submerged in a crosslinking agent, the deposited filament layers did not adhere to subsequent layers, resulting in unravelling of the printed construct, losing all shape integrity. A similar observation of bioprinting into crosslinking agent causing reduced shape integrity was reported by Ghavaminejad (2021). This suggested method was not taken forward in progressive experimentation. B-gel was bioprinted within LS reconstituted in standard growth medium, surprisingly causing the gel to not self-adhere, again resulting in the unravelling of the printed construct. Perhaps a result from apparent pH alteration compared to IHS is causing the laptonite™ clay nanoparticles to dissociate from the edges of the deposited filament. Visualised by the LS material being bright yellow despite identical growth medium used as a reconstitution buffer for HIS.R,

suggesting an acidic environment below pH 6.8, compared to typical range of pH 7.2 – 7.4 (Weiskirchen, S., *et al.* 2023). Jatav (2024) investigated the chemical stability of laponite™ in aqueous growth media, whereby the pH of 6 – 7.5 did not disrupt the OH^- ions surrounding the edge of laptonite™ within suspension, therefore not disrupting the bioink compared to pH of < 5.5 begin to disrupt OH^- ions, or pH > 7.5 begins leeching of Mg^{2+} ions. The full recipe of the commercially available LS is believed to be identical to that of published by Lee (2019) and Hinton (2015), however within the published protocols the type of gelatine, and associated pH is not disclosed as far as the researchers are aware, thus leading to a potential variation in pH of the product. Discussed by Goudie (2023) the pH of either bioink or the surrounding medium impacts the properties and morphology of hydrogels. In the instance investigated by Goudie (2023), a gelatine-based hydrogel whereby pH 5 – 10 produces a firm closed material that retains shape, whereas alternative pH environments cause dissociation of material and breakdown of hydrogel morphology (Goudie, J*., et al*. 2023).

5.4.6 In-house slurry

The in-house microparticle slurry required extensive optimisation to produce spherical particles; however, once this was achieved and used within the application of 3D bioprinting, filament deposition and complexity were greatly improved. Shape retention was visualised in both materials after relevant crosslinking and washing steps, with reduced impact of gravitational and surficial tension artefacts. Overall, producing a higher spatial resolution construct with high definition and separation of filaments.

Pitfalls during production included the type of gelatine, time of agitation and lack of control over the cooling of the solution; therefore, each batch reached gelation temperature at different time points, whereby agitation was stopped at 4 hours. The change in the experiment's final temperature can be attributed to the diversity of ambient room temperature during generation, processing time, setting up the equipment and time before post-processing begins, although every effort was made to reduce this impact and process consistently. The resulting impact of alterations of room temperature is shown by the resulting microparticles having a discrepancy range of resulting microparticle size. Further, different morphologies were often visualised within both IHS and LS with sphere, fused, and rod chosen as the classification morphology as

this represents the transition either into spherical microparticle form or the destruction of the morphology from shearing damage from the impeller. Therefore, an improvement to the method would be to determine the exact gelation temperature and stop the stirring process based on temperature, not on time.

Another consideration should be the cooling process speed, with this parameter remaining constant at 600 rpm throughout all experiments. Increasing the rotational speed during fabrication can result in smaller particle sizes, likely due to increased particle collisions and the disruption of larger aggregates. Utilising the polymer polyethyleneglycol-PLA-co-glycolic acid, Sagoe (2023) reported improvements in the uniformity of particle size and morphology of the resulting microparticles, batch-to-batch, after vigorous optimisation of polymer concentration and stirring speed, achieving tunable sizes from 50 µm to 5 µm by increasing the impeller speed (Sagoe, P., *et al.* 2023).

Despite ethanol-induced coacervation being a widely applied research technique, limited research exists that characterises the resulting morphology of gelatine coacervates in different conditions bar the notable research conducted by Pei (2021). The resulting gelatine particles' size, often in the nano-range of 340 +/-15 nm, compared to the micro-range discovered within the research presented here, utilising type B gelatine from the ethanol coacervation process with no surfactants or stabilisers (Pei, Y., *et al*. 2021). The difference in size could be attributed to the difference in gelatine concentration of 1.2% (wt.) compared to 2 % (w/v) utilised in this study, as it was reported by Pei (2021) that size could be adjusted by changing the volume ratio of aqueous gelatine and ethanol, as well as altering the gelatine concentration and ethanol temperature. In summary, the exact theory underpinning the generation of IHS microparticles presented in this study requires more in-depth research for control over resulting characteristics, in particular, size consistency.

5.4.7 Three-dimension bioprinted *in-vitro* bone model derived from *ex-vivo* bone morphometry

The overall aim of the research presented in this thesis was to develop and optimise an *in-vitro* 3D bioprinted bone model based on *ex-vivo* morphometry to achieve biomimicry for the application of early-stage biomedical investigations. Functionally, to mimic *in-vivo*

bone remodelling dynamics is explored in chapter 6, whereas bioprinting fidelity, composition and achievable accuracy were investigated in the research presented here. Despite B-gel being successfully translated into a bioink and achieving suitable resolution for dimensionally designed 3D lattice structure with the addition of IHS.R, the bioink was not suitable to bioprint the CAD-designed *ex-vivo* bone model with such a complex structure. Further research is required to improve the fabrication process of EBB, for example, an increased depth of printing vessel to allow full support of the *ex-vivo* rendered bones dimensions. Alternatively, the model could be further rendered, and a reduced VOI could be processed. As far as the researchers are aware, no study has been published for the development of a bioprinted bone in-vitro model inclusive of Cb and Tb, as architecturally this method remains a challenge.

5.4.8 Conclusion

3D extrusion bioprinting is a challenging technique that requires in-depth characterisation of the bioink's viscosity, response to stress, and achievable fidelity. Three bioinks were investigated for the use of generating an *in-vitro* bone model. In-house generated B-gel having a consistent composition with a pseudoplastic shear thinning behaviour that assisted in the consistency of extrusion, whereas commercial-sourced bone GelXA was discovered to feature high batch inconsistencies, altering the flow behaviour of the pseudoplastic material and resulting in an unsuitable product for application. TissueFAB™ did not crosslink appropriately. Further optimisation is required to improve the achievable fidelity of B-gel to match that as pre-designed in CAD, as well as improvements for consistency and reproducibility are required. The in-house generated microparticle support slurry, although inconsistent in micro-particle diameter compared to the commercially sourced counterpart LS, greatly improves the structural fidelity of complex 3D bioprinted lattice constructs as visualised in 3D by micro-CT imaging. Improvements to temperature regulation are required to produce consistent, uniform batches of the material; however, no discrepancies in output from the process of bioprinting have been recognised.

Chapter 6 – 3D bone *in-vitro* model characterisation

Investigating the cellular interaction of MC3T3-E1 pre-osteoblasts with the 3D bioprinted in-vitro bone model, to drive a bone mimic environment.

6.1 Introduction

6.1.1 Bone biology *in-vitro* studies

Bone is a dynamic tissue that is constantly undergoing remodelling by the action of three main cell types: OB, OC, and OCLs. OBs have a primary function of synthesising the collagen-rich osteoid matrix and contributing to remineralisation (Matsushita, Y., *et al*. 2023; Long, F., & Ornitz, D. 2013; Franz-Odendaal, T., Hall, B., & Witten, E. 2005). OCs are mechanosensory cells (Qin, L., *et al*. 2020), referred to as the regulators of bone remodelling homeostasis (Buenzli, P., & Sims, N. 2015; Bonewald, L. 2011). Finally, OCLs are bone-absorbing cells (Soe, K., Delaisse, J., & Borggaard, X. 2021) to enable maintenance and rebuilding of healthy bone to maintain integrity (Florencio-Silva, R., *et al*. 2015).

Different secondary and primary cell lines exist to model bone cell biology for preliminary investigations (Table 6.1.1), such as cellular interactions (Kim, J., *et al.* 2021; Remmers, S., *et al.* 2021), response to drugs (Lehmann, T., *et al*. 2023; Ramiro-Gutierrez, L., *et al.* 2016), signalling pathways (Williamson, A., *et al*. 2024), investigating genes associated with differentiation and regulation (Izumiya, M., *et al.* 2021; Hong, D., *et al.* 2010), and phenotypic characteristics of typical cell types (Kartsogiannis, V., & Ng, K. 2004). Malignant cell lines are commonly utilised *in-vitro*; however, can suffer from genetic instability, often mutating during monolayer culturing, causing variation between labs and findings when passaged for extended periods of time (Li, J., *et al*. 2019; Hynds, R., *et al.* 2018). Malignant cell lines, such as MG-63 and RAW 264.7, are commonly used in bone studies (Chatree, K., *et al.* 2023; Staehlke, S., *et al.* 2018), which are not specifically malignant-associated research (Balestri, W., *et al.* 2023; Choi, H., *et al.* 2016), as the cells exhibit OB and OCLs-like characteristics when interacting with different biomaterials (Liu, L., *et al.* 2021; Nekounam, H., *et al.* 2021).

Table 6.1.1 Immortalised cell lines commonly used in bone biology studies. Note: *Malignant-derived cell lines are not included in the summary, such as osteosarcoma-derived MG-63 osteoblasts and RAW 264.7 osteoclasts.*

Cell type	Cell line	Modelling description	Species	Considerations	Reference
Osteoblast	MC3T3-E1	Pre-osteoblasts transition into mature osteoblasts. Potential to deposit ECM and mineralise the matrix.	Murine, spontaneously immortalised.	MC3T3-E1 cells are selected for high expression of ALP. Technically difficult to experiment with cells embedded in osteogenic matrix. Primary culture is limited in passage number, and yield is variable between donors.	Chen, F., *et al*. 2023; Marozin, S., *et al*. 2021; Kartsogiannis, V., & Ng, K. 2004; Subramaniam, M., *et al*. 2002
	Primary OBs	Mature or late-stage osteoblasts. Potential to deposit ECM and mineralise the matrix.	Human, primary derived.		
	hFOB 1.19	Reflective of MSCS, able to undergo multilineage differentiation.	Human, transformed by SV40 T-antigen.		
	ST-2	Stromal cells, transformed into osteoblasts when cultured in ascorbic acid.	Murine, spontaneously immortalised.		
Osteoclast	MC3T3-G2/PA6	Preadipocyte, a potential bone marrow-derived stromal cell.	Murine, transformed by SV40 T-antigen.	Utilised mostly in co-cultures alongside osteoblasts to model the balance of bone remodelling.	Owen, R. & Reilly, G. 2018; Anaraki, P., *et al*. 2015 Udagawa, N., et al. 1989
	Peripheral blood mononuclear cell	Osteoclast precursors, selected for osteoclasts.	Human, primary derived.		
	Bone marrow-derived	Haematopoietic cells were extracted, isolated and differentiated into osteoclasts.	Human, primary derived.		
Osteocyte	MLO-Y4	Post-osteoblast transition into pre-osteocyte cells. Potential to deposit ECM and mineralise the matrix.	Murine, spontaneously immortalised.	Lack of sclerostin expression in both MLO-Y4	Chen, K., et al. 2023; Aziz, A., *et al.* 2020;

	MLO-A5	Pre-osteocyte transition into a mature osteocyte. Typically used for studying the response of osteocytes to mechanical stimuli. Potential to deposit ECM and mineralise the matrix.	Murine, spontaneously immortalised.	and MLO-A5, but present in IDG-SW3. A collagen-coated culture is required for all cell lines.	Shah, K., *et al*. 2016; Woo, S., *et al*. 2011; Barragan-Adjemian, C., *et al.* 2006
	IDG-SW3	Post-osteoblast transition into pre-osteocyte cells. Potential to deposit ECM and mineralise the matrix.	Murine, spontaneously immortalised.		

Cells are typically cultured in an isolated, monoculture environment; however, physiologically, all three cell types work in tandem. Co-culture methods have been developed to improve the complexity within 2D environments (Borciani, G., *et al.* 2020; Owen, R., & Reilly, G. 2018), as discussed by Remmers (2021), co-culture methods can be conducted in a 2D monolayer, utilising both OBs and OCs. Alternatively, co-culturing is more typical for simple gel system 3D studies, to mimic the physiological distance of bone cells (Jones, G., *et al.* 2009), focusing on OBs and OC for remodelling research (Borciani, G., *et al.* 2020). Vazquez (2014) cultured MLO-Y4 cells in 3D collagen gels, with MC3T3-E1 or MG63, an OBs and osteosarcoma cell line, respectively, cultured on top, in a similar approach to Skottke (2019) who utilised primary-derived OCs, cultured long term in collagen gels with OBs seeded onto a porous transwell insert. Further, tri-cultures inclusive of OBs, OCs and OCLs have been reported (Bernhardt, A., *et al*. 2021; Clarke, M., *et al*. 2013), however, this comes with high complexity and considerations to function *in-vitro,* such as different substrates for culturing, and different growth medium requirements (Borciani, G., *et al.* 2020; Vis, M., *et al.* 2020; Janardhanan, S. *et al.* 2012).

6.1.2 *In-vitro* MC3T3-E1 cellular osteogenic matrix-driven differentiation

iOB immortalised cell line, MC3T3-E1 cells, are a widely used OB model in both 2D and 3D *in-vitro* studies (Kartsogiannis, V., & Ng, K. 2004) that are derived from mouse calvaria (Sudo, H., *et al.* 1983). The MC3T3-E1 cells were originally cloned to maintain a high level of ALP in resting states, whereby this decreases during proliferation; however, this is now known as inducing differentiation of the iOBs into mOBs (Figure 6.1.1) (Yoon, H., *et al*. 2025). MC3T3-E1 cells are often cultured in two different conditions, with and without ascorbic acid (Franceschi, R., Lyer, B., & Cui, Y. 1994), dependent on experimental aims. Various sub-clones of MC3T3-E1 cells exist divided into mineralising (subclones 4, 8, 11, and 26) and non-mineralising (subclones 17, 20, 24, 30 and 35) (Wang, D., *et al*. 1999). Global Biological Resource Centre, ATCC offer sub-clone 4, 14, 24 and 30, with Hwang (2019) reporting that sub-clone 14 is the most commonly reported and researched; however, ATCC reports sub-clone 4 with the most cited publication associations (Metzger, W., *et al.* 2025; Yoon, H., *et al*. 2025). Notably, studies commonly do not report the subtype used (Kim, J., *et al.* 2024; Jeon, S., *et al.* 2021; Izumiya, M., *et al.* 2021; Saleh,

L., Carles-Carner, M., & Bryant, S. 2020; Cao, S., *et al.* 2015). The research presented in this study utilised MC3T3-E1 sub-clone 4.

To initiate osteogenesis, different methods are reported (Yoon, H., *et al.* 2025; Semicheva, A., *et al.* 2024; Jeon, S., *et al*. 2021; Izumiya, M., *et al.* 2021; Li, W., *et al*. 2019; Fukunishi, Y., *et al.* 2018), however, as summarised by Metzger (2025), the most widely used method utilises ascorbic acid (Hwang, P., & Horton, J. 2019). Vitamin C is the L-enantiomer of ascorbic acid, and it has been shown that vitamin C is essential in collagen formation (Brzezinska, O., *et al.* 2020; Boyera, N., Galey, I., & Bernard, B. 1998). Ascorbic acid serves as a cofactor for prolyl hydroxylase, which catalyses the hydroxylation of proline residues that are integral for the stability of the collagen triple helix (Amirrah, I., *et al*. 2022; Murad, S., *et al.* 1981). In addition, ascorbic acid is known to upregulate ALP and OCN expression, promoting mineralisation (Figure 6.1.1) (Izumiya, M., *et al.* 2021; Franceschi, R., Lyer, B., & Cui, Y. 1994; Rickard, D., *et al*. 1994). Dexamethasone and B-glycerophosphate (β-GP) are usually added in combination with ascorbic acid, with both additives promoting mineralisation (Hwang, P., & Horton, J. 2019; Tevlek, A., *et al.* 2018). Specifically, β-GP is an inorganic phosphate source, crucial in HA deposition within the excreted ECM matrix to be classified as osteogenic, serving as a substrate for ALP by hydrolysing phosphate esters (Semicheva, A., *et al.* 2024; Fratzl-Zelman, N., *et al.* 1998; Bellows, C., Aubin, J., & Heersche, J. 1991).

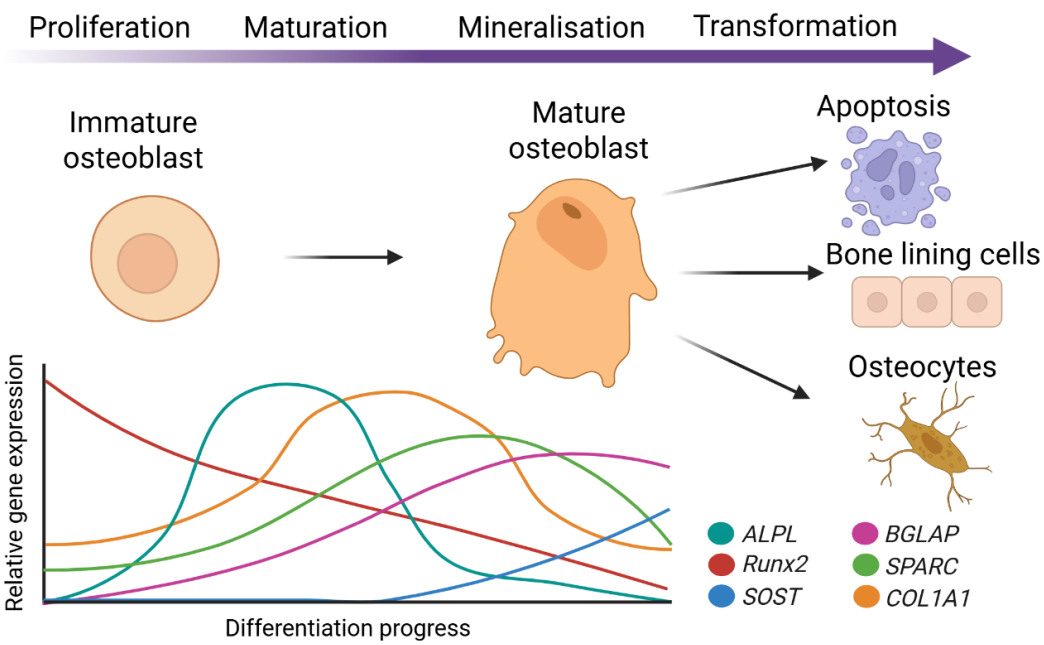

Figure 6.1.1 Summary of osteoblast differentiation with hallmark genes of interest relative expression summarised. *Originating from mesenchymal osteoprogenitor cells, immature osteoblasts (iOBs) differentiate into mature osteoblasts (mOBs) facilitated by activation of runt-related transcription factor 2 (Runx2) that drives the up-regulation of alkaline phosphatase (ALPL) expression and defines the commitment to maturation, matrix deposition by collagens, notably type-1 collagen (COL1A1) and promotes mineralisation. Osteocalcin (BGLAP), and osteopontin (SPARC) are up-regulated as Runx2 and ALPL are down-regulated, as a marker of a mOB. Finally, transition into osteocytes is defined by increased sclerostin (SOST) levels, however, mOBs can also transition into bone lining cells (BLC) or undergo apoptosis.*

6.1.3 MC3T3-E1 three-dimensional *in-vitro* studies

Utilising secondary MC3T3-E1 iOBs for 3D *in-vitro* bone model development is an attractive option, due to the ability to drive differentiation from iOBs to mOBs (Figure 6.1.1). The differentiation process allows mineral deposition, as well as matrix secretion, to further drive a bone-mimicking environment within a 3D *in-vitro* model (Yoon, H., *et al*. 2025; Izumiya, M., *et al*. 2021). In addition, 3D EBB requires extensive optimisation; therefore, it was beneficial to utilise a secondary immortalised cell line for the development of the proposed *in-vitro* bone model compared to a primary cell source, which would require phenotypic characterisation per donor, limited lifespan and yield, as well as variability between populations (Piwocka, O., *et al*. 2024; Belk, L., *et al*. 2020). B-gel has previously been reported to maintain viability of both secondary and primary cells (Cherif, H., *et al*. 2024; Snuggs, J., *et al*. 2023; Thorpe, A., *et al*. 2018; Thorpe, A., *et*

al. 2016), however has not been previously utilised as a bioink. Primary cells are utilised in 3D models with a clinical translation (Munir, A., *et al.* 2023; Maia-pinto, M., *et al.* 2020; Nasello, G., *et al*. 2020; Mcbeth, C., *et al.* 2017) however, this research focuses on the development of a biomedical preliminary *in-vitro* bone model that is physiologically relevant by utilising 3D EBB and therefore, utilising MC3T3-E1 cells was appropriate, as the OBs are commonly utilised and relatively well understood.

A variety of 3D *in-vitro* bone models exist which have used MC3T3-E1 to develop and validate different biomaterials (Fois, M., *et al.* 2024; Saleh, L., Carles-Carner, M., & Bryant, S. 2018; Li, D., *et al*. 2017), different methods of fabrication (Zhao, X., *et al.* 2022; Liu, H., *et al.* 2021; Zhu, J., *et al.* 2020) and assess osteogenic potential (Kim, J., *et al*. 2024; Sayed, S., *et al*. 2019; Zamani, Y., *et al.* 2018; Zhang, H., *et al.* 2015). For example, Latour (2024) reported the development of decellularised apple hypanthium tissue as a plant-derived cellulose material, and utilised MC3T3-E1 cells to assess the osteogenic potential, cell distribution and pore size of the material (Latour, M., *et al.* 2024). For the application and optimisation of 3D EBB application, MC3T3-E1 are reported encapsulated in different hydrogel bioinks (Lv., X., *et al.* 2024; Ozenler, A., *et al.* 2024; Khatun, M., *et al.* 2023; Maturavongsadit, P., *et al.* 2021), or alternatively seeded post-printing on ceramics and metals (Wei, J., *et al.* 2022; Tortelli, F., *et al.* 2009).

6.1.4 The influence of three-dimensional model fabrication on cell health

As previously discussed in chapters 1 and 5, different biomaterials are suitable for the application of 3D EBB. However, when bio-printing with cells encapsulated within the bioink, different considerations are required for the manufacturing process to ensure cellular viability is not negatively impacted (Figure 6.1.2). The main considerations when bioprinting with cells are rheological flow behaviour, biocompatibility, nozzle size and cell concentration. Altering these parameters can modify the shear stress that is applied to the cell during the bioprinting process, with high shear stress resulting in increased apoptosis (Cidonio, G., *et al*. 2019). Cellular damage resulting from shear stress can trigger cell death, involving the intrinsic and/or extrinsic pathways. The intrinsic pathway refers to caspase activation of the BH3 protein, leading to activation of CAS-3, whereas triggering the extrinsic pathway activates caspase-8, subsequently activating CAS-3 (Xu, H., *et al.* 2022; Shive, M., *et al*. 2002) Shear stress is unavoidable during the 3D EBB

process due to the pressure applied to extrude bioink (Paxton, N., *et al*. 2017), therefore, limiting the detrimental impact and reduction in cell viability is vital (Berg, J., *et al*. 2018). In a detailed review, Boularaoui (2020) summarises the impact of velocity on cells during bioprinting, whereby the highest impact on cells is under the piston, next to the cartridge walls, the connection from cartridge to nozzle, and the tapered nozzle (Figure 6.1.2).

Cell concentration has a direct impact on the flow behaviour of the bioink (Figure 6.1.2). For example, bioprinting with a high cell density can reduce the stiffness of the material compared to a low cell density, as well as increase the opportunity of cell collision with the cartridge walls and/or bioactive components, and mechanical pressure passing from the nozzle (Majumder, N., *et al.* 2022; Persaud, A., *et al*. 2022). Alternatively, a low cell density maintains a similar acellular material flow behaviour, but cell viability can be reduced during long-term culturing as cells require cell-cell interactions (Karvinen, J., & Kellomaki, M. 2023; Daly, A., *et al*. 2021). Various cell densities are reported (Ozenler, A., *et al*. 2024; Maturavongsadit, P., *et al*. 2021; Gillispie, G., *et al.* 2020; Zhang, J., *et al.* 2020); however, 10 million cells/ml is a standard value for 3D EBB when a nozzle size of 25 gauge (inner diameter of 0.26 mm) or larger, for bone related constructs (Leeuw, A., *et al*. 2024; You, S., *et al.* 2023; Im, S., *et al.* 2022; Gonzalez-Fernandez, T., *et al.* 2021; Mandrycky, C., *et al*. 2016).

Finally, nozzle width has a direct impact on resulting filament resolution as previously discussed (Chapter 5, section 5.4.3), however, the translation of cellular bioprinting comes with further limitations on possible resolution. Nozzle size should be appropriate to allow flow of cells and bioactive components, with limiting shear stress applied to cells (Cidonio, G., *et al*. 2019). For example, Immohr (2022) bioprinted cell-laden Alg and gelatine scaffolds with 22G and 25G nozzles, with the evaluated cell viability reduced in 25G scaffolds due to increased shear stress (Immohr, M., *et al*. 2022). In addition, filament width should be minimised to allow appropriate nutrient diffusion. For instance, Zhu (2022) presented a 3D bioprinted nanocomposite bioglass lattice model and reported cell death in the middle of the filaments and cross-over points when increasing filament width above 1.5 mm.

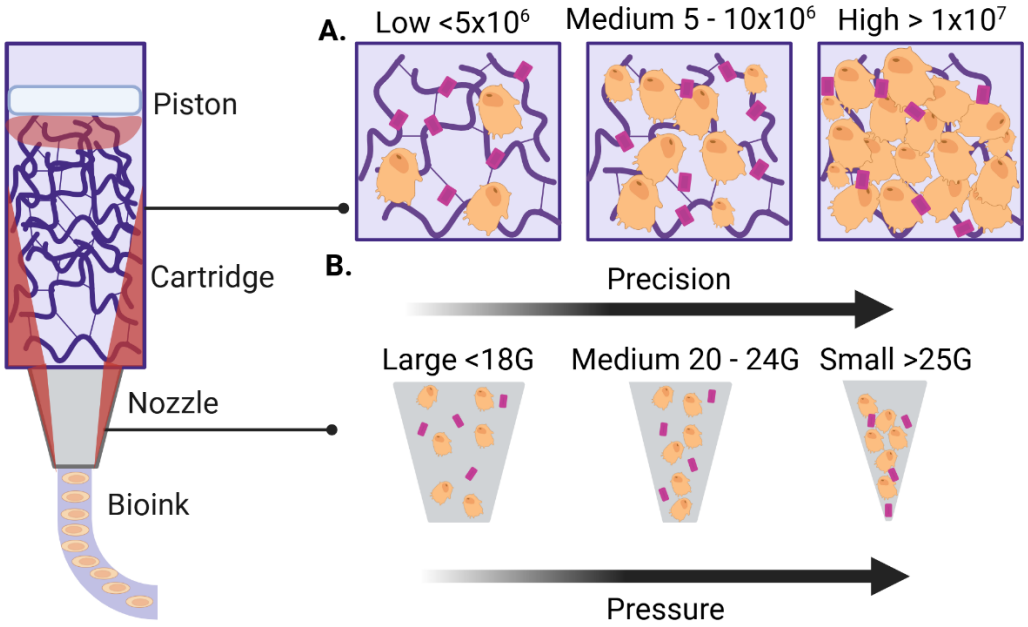

Figure 6.1.2 Schematic of 3D bioprinting considerations for maintained cell viability. *Bioprinting with cells encapsulated within bioink requires optimisation to maintain cell health during preparation, printing and recovery. Red highlights on the bioink cartridge and nozzle represent areas of stress under pressure A) Cell population can be altered based on output 3D construct, however high populations increase contact during mechanical pressure of the 3D bioprinting process, often resulting in higher rates of apoptosis. Low cellular population reduces cellular contact; medium allows cellular contact and high increases cellular contact. B) Nozzle size impacts resulting resolution of the 3D bioprinted construct, however, small nozzle sizes increase pressure on cells, resulting in higher rates of apoptosis.*

6.1.5 Characterisation of the polymer network and composition of three-dimensional bioprinted constructs

In hydrogels, the microarchitecture depends on the organisation of the polymer network during the sol-gel transition, the polymer: water concentration, and the crosslinking conditions (Martinez-Garcia, F., *et al*. 2022; Ahmed, E. *et al.* 2013). The resulting polymer network, known as the mesh size or molecular porosity, influences oxygen and nutrient diffusion and therefore maintenance of cell health and functionality (Caliari, S., & Burdick, J. 2016). Berg (2018) reported the decrease in human alveolar cell viability when Alg, gelatine and Matrigel hydrogels were tuned for reduced porosity, therefore emphasising the importance of characterising the polymer network of biomaterials utilised for *in-vitro* models.

Techniques to characterise cell-laden 3D hydrogels include confocal microscopy, Micro-CT, transmission electron microscopy, scanning electron microscopy (SEM) and atomic force microscopy (Jayawardena, I., *et al.* 2023; Kaberova, Z., *et al*. 2020). Micro-CT evaluation of hydrogel scaffolds has grown in popularity due to the non-destructive processing and the possibilities of data output from a single scan. Micro-CT imaging and analysis can produce a range of data, depending on the density of individual components of a hydrogel scaffold. This includes individual particle analysis, water-laden and freeze-dried volume, mean pore size volume to surface ratio, scaffold geometry including filament thickness (Lin, A., *et al*. 2003), and density of constructs (Luttrell, L., *et al.* 2019). Micro-CT evaluation of water-laden scaffolds is not always possible due to the nature of the scanning process, whereby the material is required to have a density higher than the air and water interface to be able to capture contrast information. Alternatively, SEM is typically utilised to visualise and quantify porosity in high magnification and high-resolution images. Capturing the porosity of a water-laden hydrogel is very insightful to the true cellular environment (Martinez-Garcia, F., *et al.* 2022). In addition, elemental dispersive x-ray can be completed alongside SEM to detect elements within the cell-laden hydrogels (Scimeca, M., *et al*. 2018).

6.1.6 Aims and objectives

Determine the impact on cellular viability of MC3T3-E1 pre-osteoblasts after the process of 3D bioprinting.

Optimise cellular visualisation techniques in 3D constructs.

Evaluate the osteogenic potential of 3D bioprinted *in-vitro* constructs in +/- osteogenic growth medium, compared to 2D monolayer culture.

Investigate OBs remodelling markers to characterise the osteogenic potential of MC3T3-E1 cells undergoing growth media-driven differentiation in both 3D *in-vitro* bone constructs and 2D monolayer cell culture, by IHC and histology techniques.

Characterise the composition and structure of bioprinted 3D *in-vitro* bone constructs undergoing differentiation by high-resolution micro-CT, SEM, histology and IHC methods.

6.2 Materials and methods

6.2.1 Experimental design

MC3T3-E1 immortalised iOBs cells were selected as a suitable cellular model to investigate the osteogenic potential of 3D bioprinted B-gel constructs. Cells were characterised in 2D monolayer cell culture (Figure 6.2.1) for differentiation of osteogenic markers expression, to allow comparison to 3D culture. MC3T3-E1 supplemented B-gel bioink was utilised to generate 3D bioprinted *in-vitro* constructs, and cellular constructs were treated with or without ascorbic acid over 21 days to evaluate matrix deposition and composition changes. The 3D bioprinted structure was investigated by micro-CT high-resolution imaging (Figure 6.2.1). Osteogenic markers and matrix composition of 3D *in-vitro* constructs were investigated by histological and IHC techniques (Figure 6.2.1) and SEM.

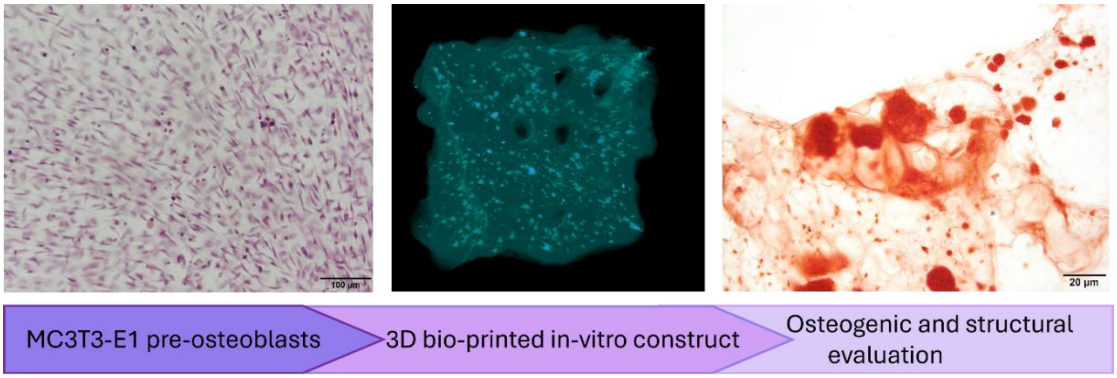

Figure 6.2.1. Experimental design to investigate MC3T3-E1 matrix deposition in response to differentiation treatment after bioprinting in B-gel to fabricate an in-vitro bone model.

6.2.2.1 Two-dimensional cell culture

Mouse immortalised iOBs cells MC3T3-E1 (ATCC, UK) were cultured and maintained at 37 °C with 5% CO_2 at undifferentiated state in ascorbic acid free, 2mM L-glutamine and 1mM sodium pyruvate α-MEM (Fisher Scientific, UK) supplemented with 10% (v/v) heat-inactivated foetal bovine serum (FBS) and 1% (v/v) penicillin. Cells were routinely passaged by washing twice with an appropriate volume of pH 7.4 PBS, followed by incubation in an appropriate volume of trypLE (Thermo-fisher scientific, UK) at 37 °C with 5% CO_2 for detachment. Cells were transferred to sterile falcon tubes, followed by centrifugation at 300 x g for 5 minutes. Supernatant was discarded, and cells

resuspended in 10% (v/v) ascorbic acid-free α-MEM and maintained at previously stated conditions in T75 flasks.

To initiate differentiation of MC3T3-E1 cells, 10 mM dexamethasone (Merck Life Sciences, UK), 10 mM β-GP (Merck Life Sciences, UK) and 50 μg/mL ascorbic acid (Merck Life Sciences, UK) were supplemented into 10% (v/v) ascorbic acid free α-MEM and sterilised with a nanopore filter. The media was changed every 72 hours for 21 days to allow differentiation.

Due to the recurrence of fungal infections in 3D *in-vitro* cultures, 1.5 μg/ml amphotericin B (Fisher Scientific, UK) was supplemented into all media conditions. Viability assay Alamar blue was used over 7 days. Alamar blue working solution (1x) was made from 100X stock of 1 mg/ml resazurin salt (Merck, 199303). Cells were incubated in the working solution for 4 hours at 37 °C with 5% CO_2. After incubation, 500 μL alamar blue solution was placed in a microplate reader with fluorescence intensity measured at an excitation wavelength of 560 nm and emission wavelength of 590 nm.

6.2.2.3 MC3T3-E1 chamber slides

MC3T3-E1 cells were seeded at a concentration of $1x10^4$/well into an 8-well glass chamber slide (Nunc Lab-Tek II). After 24 hours, the appropriate growth medium was replaced with differentiation medium. Chambers underwent fixing with 4% PFA with a 10-minute incubation on days 0, 7, 14 and 21, before washing with pH 7.4 1X PBS and storage in a damp environment at -4 °C until experimentation. Chamber moulds were removed before staining procedures.

6.2.3 Cell fluorescence

MC3T3-E1 cells underwent lipid tagging with a commercially available PKH26 fluorescent cell linker kit (Sigma Aldrich, PKH26GL) according to the manufacturer's instructions 24 hours before 3D bioprinting experimentation. Briefly, $1x10^7$ cells/mL were stained with a concentration of 2×10^{-6} M of PKH26 by pelleting cells and washing with normal growth medium without FBS. After a 5-minute incubation in the ethanolic PKH26 dye, the reaction was stopped by the addition of FBS, followed by subsequent washes in growth medium supplemented with FBS. All imaging of PKH26-stained cells was completed on an inverted microscope at an appropriate magnification. Brightfield and red fluorescence

(551 nm excitation and 567 nm emission range) were collected (Figure 6.2.2). Single-layer images were taken, as well as Z-stacks of a region of 0.5 mm and a step size of 25.47 µm. Image processing and overlaying were completed in Fuji ImageJ (Figure 6.2.2).

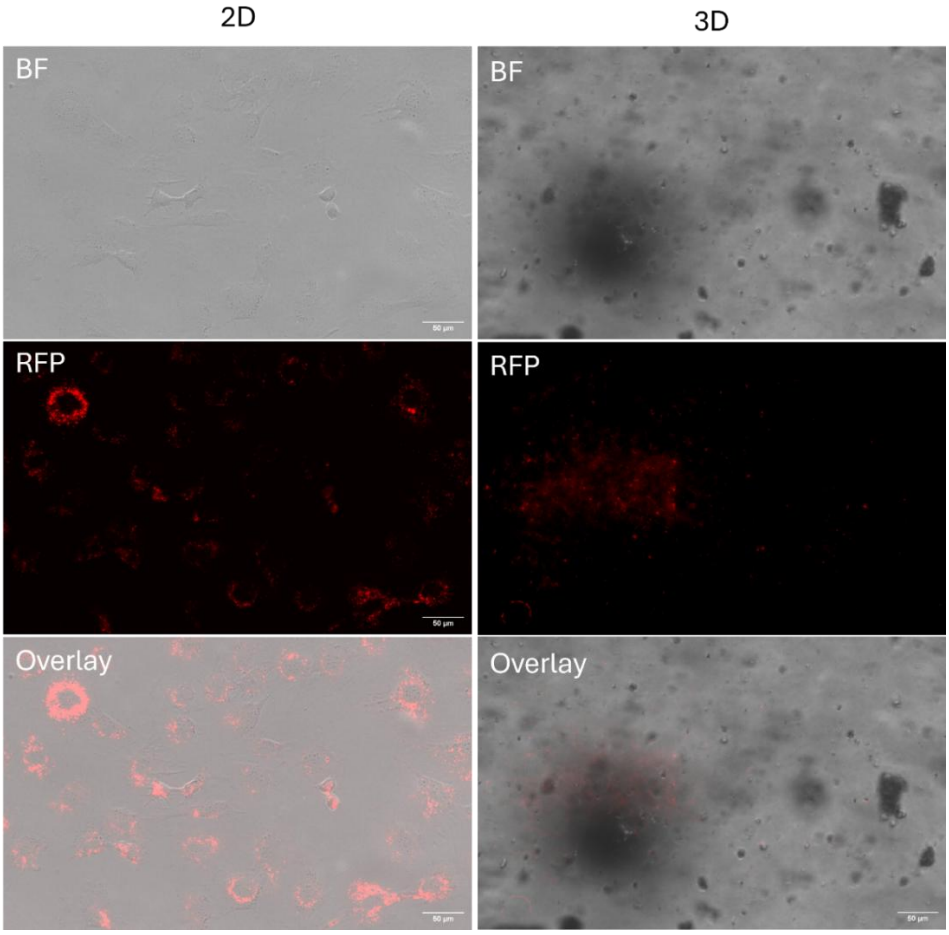

Figure 6.2.2. Example of fluorescent image capture of PKH26-stained MC3T3-E1 cells, and within 3D bioprinted construct, processed in Fuji ImageJ. *Image capture depth for 3D bioprinted constructs was limited, and the complex geometry of the 3D bioprinted structure proved difficult for cellular localisation determination. Cells were membrane-stained in lipophilic regions (cell membrane) and visualised in red fluorescent probe (RFP) regions and merged with brightfield (BF) image capture.*

6.2.4 Three-dimensional extrusion *in-vitro* bioprinting

All EBB experimentation was completed with the Bio X bioprinter (Cellink, Switzerland) with a conical 22G nozzle as previously described (Chapter 5, section 5.2.2.1), using the control lattice (Figure 5.2.1). B-gel was prepared as previously stated (Chapter 5, section 5.2.2.3), however, $5x10^6$ MC3T3-E1 PKH26 cells were supplemented. Cells were pelleted, with as much supernatant removed as possible, before being added into cooled Laponite®-pNIPAM-co-$DMAc_{13}$ hydrogel with 0.5 mg/ml HAnp, with thorough mixing

between the empty syringe and cartridge. Cellular B-gel is referred to as MB, whereas acellular B-gel is referred to as AB. AB constructs were printed with a pressure range of 40 – 65 kPa at a speed of 10 mm/s, and MB constructs with a pressure of 40 – 60 kPa at the same speed.

6.2.5 Three-dimensional cell culture

Bioprinted constructs were transferred to an appropriate vessel. Constructs bioprinted with MC3T3-E1 were equally split and cultured +/- ascorbic acid growth medium as previously described. Constructs + ascorbic acid are referred to as differentiated (MB_D), and - ascorbic acid are referred to as undifferentiated (MB_UD). Acellular bioprinted constructs (AB) were cultured in ascorbic acid conditions. All media changes were completed in a sterile hypoxia cabinet (Coy, USA) at 37 °C to decrease temperature fluctuations exposed to the 3D bioprinted constructs, with all media pre-warmed before addition.

6.2.6 Alkaline phosphatase

ALP activity was assessed using a commercially available assay kit (Merck, MAK447) according to the manufacturer's instructions. Simply, supernatant cell culture media from the 3D bioprinted *in-vitro* constructs +/- ascorbic acid (n = 3) and 2D monolayer chamber slides (n = 3) were collected on days 0, 7, 14, and 21 and stored at -20°C. For experimentation, media samples and reagents were defrosted on ice with 50 µL of each sample added in duplicate to wells of a 96-well clear-bottom plate, followed by 150 µL of supplied working reagents with suitable mixing. Optical density (OD) values were measured immediately against a tartrazine calibrant and fresh media blank at 405 nm using a Clariostar reader (BMG Labtech). OD values were taken again at 4 and 16 minutes of reaction time. ALP enzyme activity was calculated using the following equation:

$$ALP\,\frac{IU}{L} = \frac{(ODt16 - ODt0)\ x\ RunVol\ x\ 35.3}{(ODcal - ODblank)\ x\ SampleVol\ x\ time}$$

$$ALP\,\frac{IU}{L} = \frac{(ODt16 - ODt0)\ x\ 200\ x\ 35.3}{(ODcal - ODblank)\ x\ 50\ x\ 16}$$

6.2.7 Micro-computed tomography

Imaging of B-gel bioprinted constructs was completed with a resolution of 9 μm, by placing the construct on the side of a bijoux in a sterile environment. All scanning and reconstruction parameters were followed as previously described (Chapter 5, section 5.2.10.1). The TMD of all constructs was determined by 2 mm radius calcium hydroxyapatite rods with densities of 0.3 and 1.25 gHA/$cm^{3,}$ which were scanned using the previously mentioned parameters inside the bijoux tube. AC was obtained as previously stated (Chapter 2, section 2.2.4.4). Individual particle analysis was also conducted, following the threshold of 65 – 255 and the method as previously described (Chapter 5, section 5.2.10.2). The projection threshold for TMD (Figure 6.2.3A) and individual particle analysis (Figure 6.2.3B) is represented.

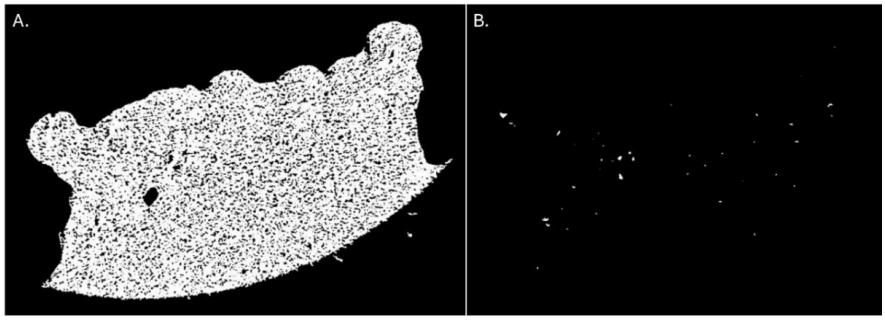

Figure 6.2.3. Representative micro-CT threshold shadow projections for volume and density analysis.

6.2.8 Construct fixing, processing and image capture

B-gel +/- MC3T3-E1 and AB bioprinted constructs were placed in 4% PFA overnight at 37 °C before washing in PBS. Samples were placed in a tissue processor, paraffin-embedding and sectioning of 8 μm thickness as previously described (Chapter 2, section 2.2.5). Histology, IHC and immunocytochemistry were completed as previously described (Chapter 2, sections 2.2.6.1 – 5), however, bioprinted constructs underwent a prolonged dehydration and clearing of 3 x 10 minutes in IMS and Sub-X due to the hydrophilic nature of the B-gel.

In addition to the previously described histology (Chapter 2, sections 2.2.6.1 – 4), Von Kossa (VK) and alizarin red (AR) histological stains were performed. VK was performed as per kit instructions (#1.00362.0001, Avantor Scientific, UK), and counterstained with 1% acidified neutral red. For AR, samples underwent paraffin removal using sub-X (Leica

Microsystems, UK) for 3 x 5 minutes before rehydration through a series of IMS baths. Slides were flooded with 40 mM AR solution at pH 4.1 for 3 minutes, with excess stain tipped off and blotted before 3 x 10 minutes in IMS and cleared for 3 x 10 minutes in Sub-X. Coverslips were mounted to samples using Eukitt quick hardening mounting medium (#03989, Merck, UK).

Representative images were taken microscopically using an Olympus BX60 microscope, and images were captured using CellSens software (Olympus, UK) and a MicroCapture v5.0 RTV digital camera (Q imaging, Buckinghamshire, UK).

6.2.9 Construct lyophilisation, scanning electron microscopy, elemental dispersion x-ray analysis and micro-computed tomography

B-gel *in-vitro* constructs were frozen at -20 °C overnight before lyophilisation at -50 °C 0 mBar for 48 hours. All lyophilised constructs were imaged using micro-CT as previously described (Chapter 6, section 6.2.7), with 3D analysis completed to determine the overall volume of the construct after water removal. For SEM, a single AB construct, which had been cultured for 21 days, was fractured to expose the interior surface morphology, attached onto an aluminium stub and 15 nm carbon coated for imaging. The fractured surface was examined using the FEI Quanta 650 (ThermoFisher, UK). Secondary electron images were obtained using a voltage of 2000 kV, with magnifications of 400X and 1000X. In addition, elemental dispersive X-ray spectroscopy was completed on the entire field of view of the 400X obtained image to generate an elemental spectrum on the chemical composition of the sample.

6.2.10 Statistical analysis

All micro-CT and ALP activity data are presented in the form of individual data points, with mean values displayed for normally distributed data and median values for non-parametric data. For micro-CT data, normality was determined by the Shapiro-Wilk method and statistical analysis was completed against day 0 for each condition by two-way ANOVA, multiple comparisons with Geisser-Greenhouse correction. For ALP activity analysis, Shapiro-Wilk normality testing was completed, followed by One-Way ANOVA and post hoc Holm-Sidak test. $P < 0.05$ was defined as statistically significant in this study, with colours representing the condition of significance for micro-CT data.

6.3 Results

6.3.1 MC3T3-E1 two-dimension characterisation

The MC3T3-E1 immortalised cell line represents iOB; however, the subclone was selected to undergo differentiation for mOBs after treatment with ascorbic acid growth medium over 21 days to initiate mineralisation to mimic ECM production. H&E revealed cellular structure and arrangement *in-vitro,* whereby over the 21-day culture period, MC3T3-E1 remained morphologically viable with clear nuclear staining despite the increase in population (Figure 6.3.1B). Amphotericin B was selected as an additive to the growth medium due to recurrent fungal infections when culturing 3D *in-vitro* constructs, whereby a concentration of 1.5 µg did not negatively impact cell viability for MC3T3-E1 grown in monolayer (Figure 6.3.1C). Finally, growth medium supernatant was collected at defined time-points to assess ALP activity, with D0 showing high ALP activity, whereby activity decreased ($P < 0.0003$) over the experimental duration (Figure 6.3.1D).

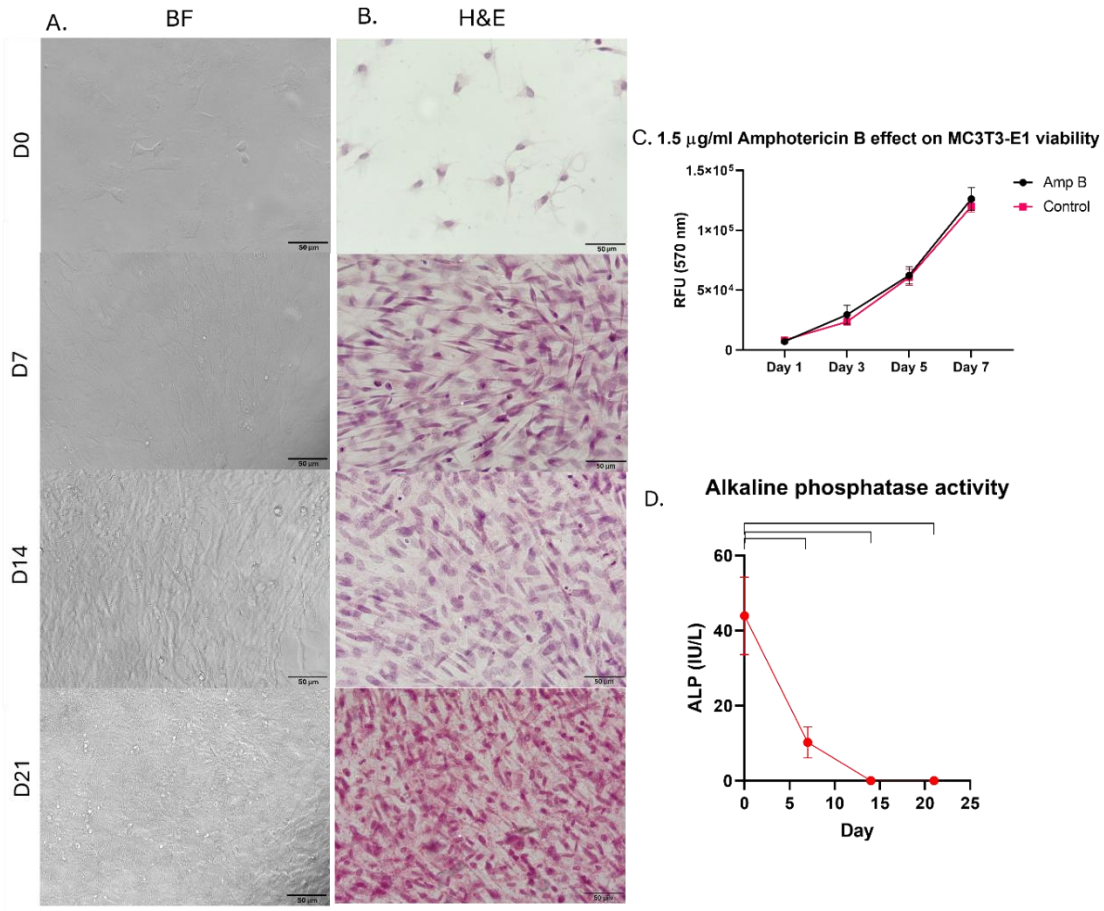

Figure 6.3.1 MC3T3-E1 monolayer over 21 days + ascorbic acid. *1x10^4 MC3T3-E1 were seeded on glass chamber slides and visualised, A) brightfield (BF) microscopy, B) haematoxylin and eosin (H&E). Scale bar represents 50 µm, n = 1, representative image shown. C) MC3T3-E1 cell viability +/- 1.5 µg/ml amphotericin B over 7 days, n = 1, D) Alkaline phosphatase activity in cell culture media from 1x10^4 MC3T3-E1 over 21 days, n = 3, Tukey's multiple comparison, P < 0.05.*

Histological staining using MT on MC3T3-E1 cells undergoing differentiation revealed increased collagenous matrix deposition over the 21-day culture period, represented qualitatively by increased blue staining (Figure 6.3.2B). MC3T3-E1 cells demonstrated immunopositivity for COL-1 within the cytoplasm and secretion on D0, D7 and D14, with no positivity detected on D21 (Figure 6.3.2A). Finally, AR represents calcium deposition which appeared to increase over the 21-day culture period, qualitatively visualised by orange/red depositions (Figure 6.3.2C).

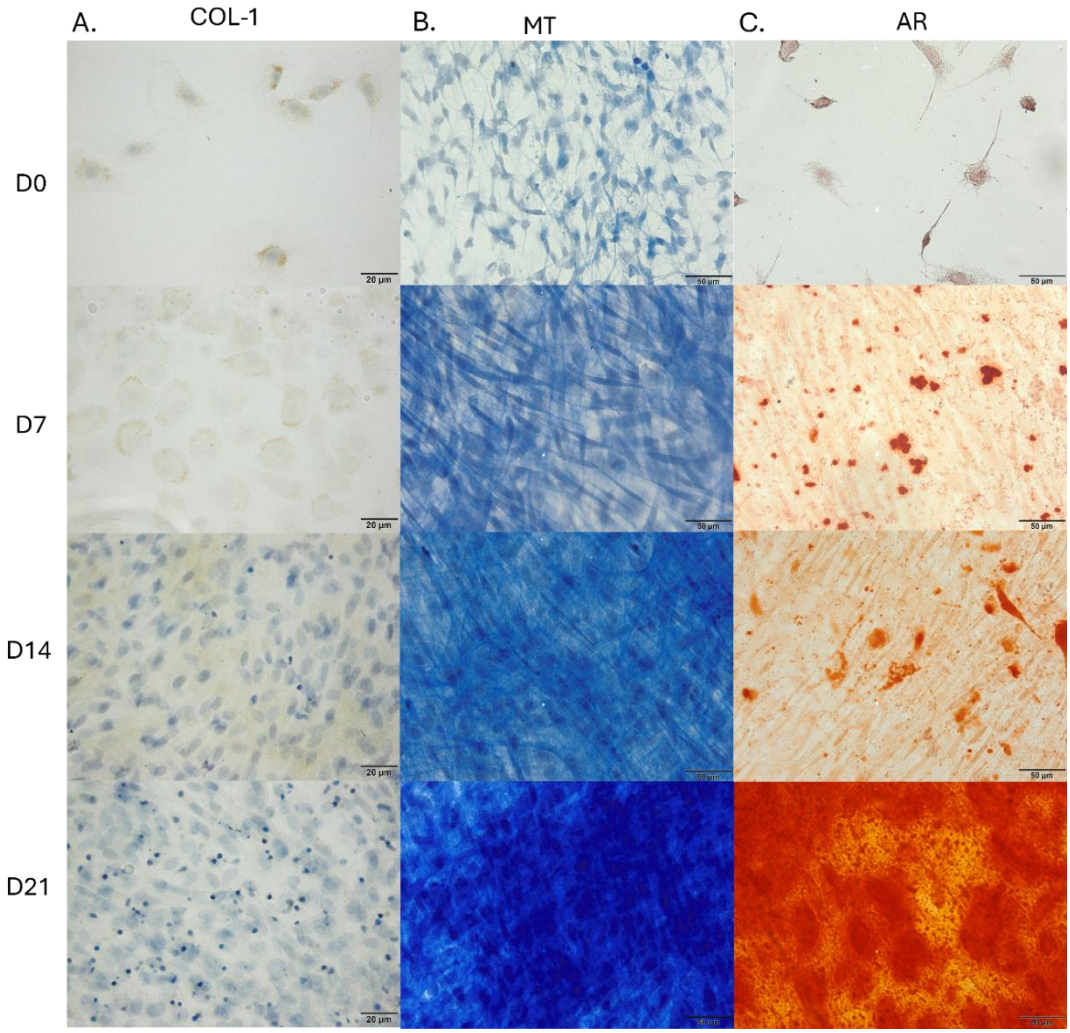

Figure 6.3.2. MC3T3-E1 monolayer histological characterisation over 21 days + ascorbic acid. *Chamber slides with 1x10^4 MC3T3-E1 over 21 days, A) Type-1 collagen (COL-1) immunohistochemistry, immunopositivity is represented by brown staining, B) Masson's trichrome (MT) in-vitro histology, C) Alizarin red (AR) in-vitro histology. The scale bar represents 20 µm for A (n = 3), and 50 µm for B/C (n = 1).*

Early OB differentiation is represented by ALP and Runx2 (Rucci, N. 2008), whereby immunopositivity was visualised in D0 (Figure 6.3.3A/B). Runx2 protein positivity was typically localised to the nucleus, whereas ALP was detected both in the cytoplasm and within the secreted matrix. ALP positivity was visualised throughout the 21-day culturing period (Figure 6.3.3B), whereas Runx2 qualitatively has strong nuclear staining on D0, and reduced nuclear positivity for the remainder of the experimentation (Figure 6.3.3A).

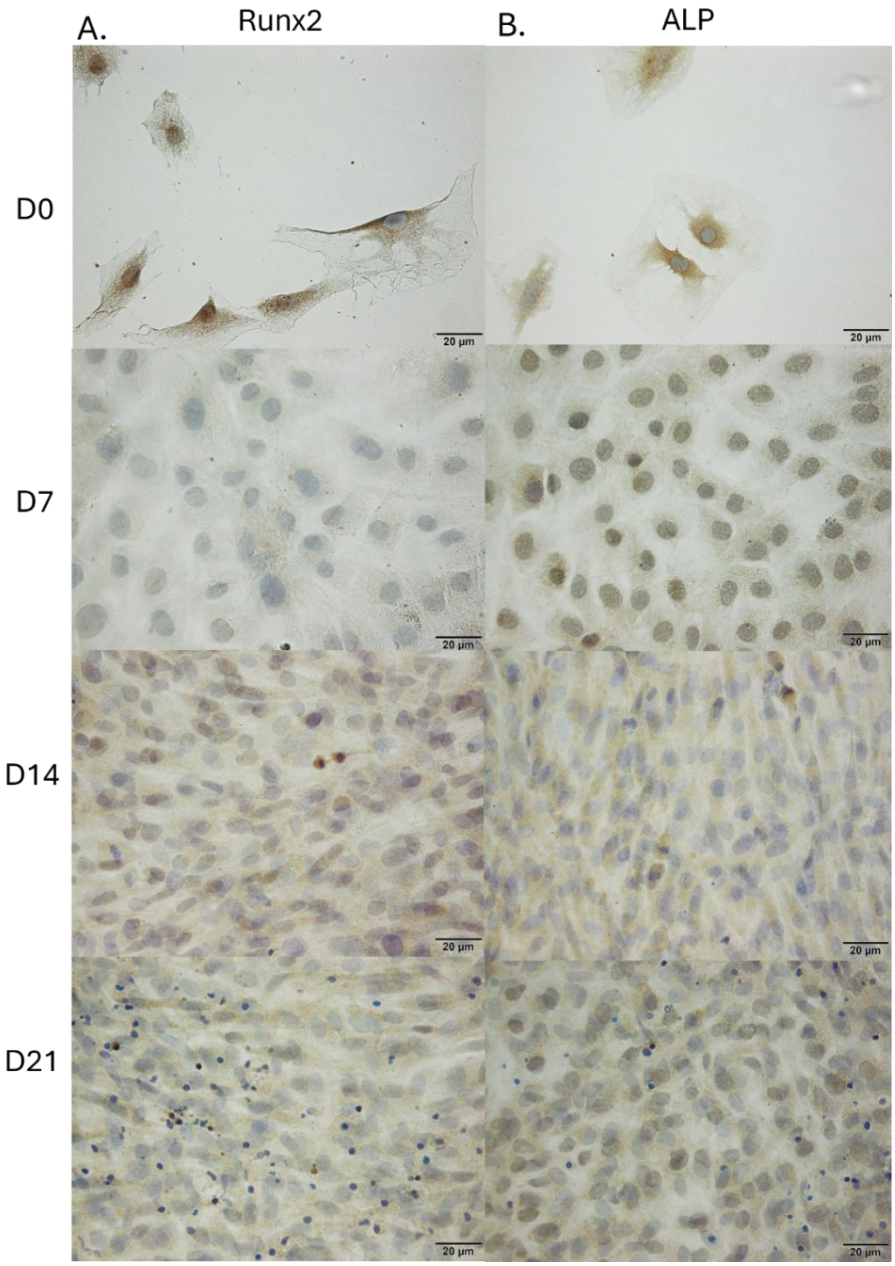

Figure 6.3.3. MC3T3-E1 monolayer immunocytochemistry characterisation over 21 days + ascorbic acid. *Chamber slides with 1x10^4 MC3T3-E1 over 21 days; Immunopositivity is represented by brown staining, A) Runx2, B) alkaline phosphatase (ALP). Scale bar represents 20 µm, n = 3.*

Late OB differentiation is typically represented by OPN and OCN (Rucci, N. 2008); however, immunopositivity is visualised at D0 (Figure 6.3.4A/B), whereby OB should be immature. OPN and OCN could both be visualised in the surrounding secreted matrix and within the cytoplasm of MC3T3-E1 cells. OPN qualitatively decreased in positivity over the 21-day culture period (Figure 6.3.4A), whereas OCN is positive on D0, D7 and D21, whereas minimal staining could be detected on D14 (Figure 6.3.4B).

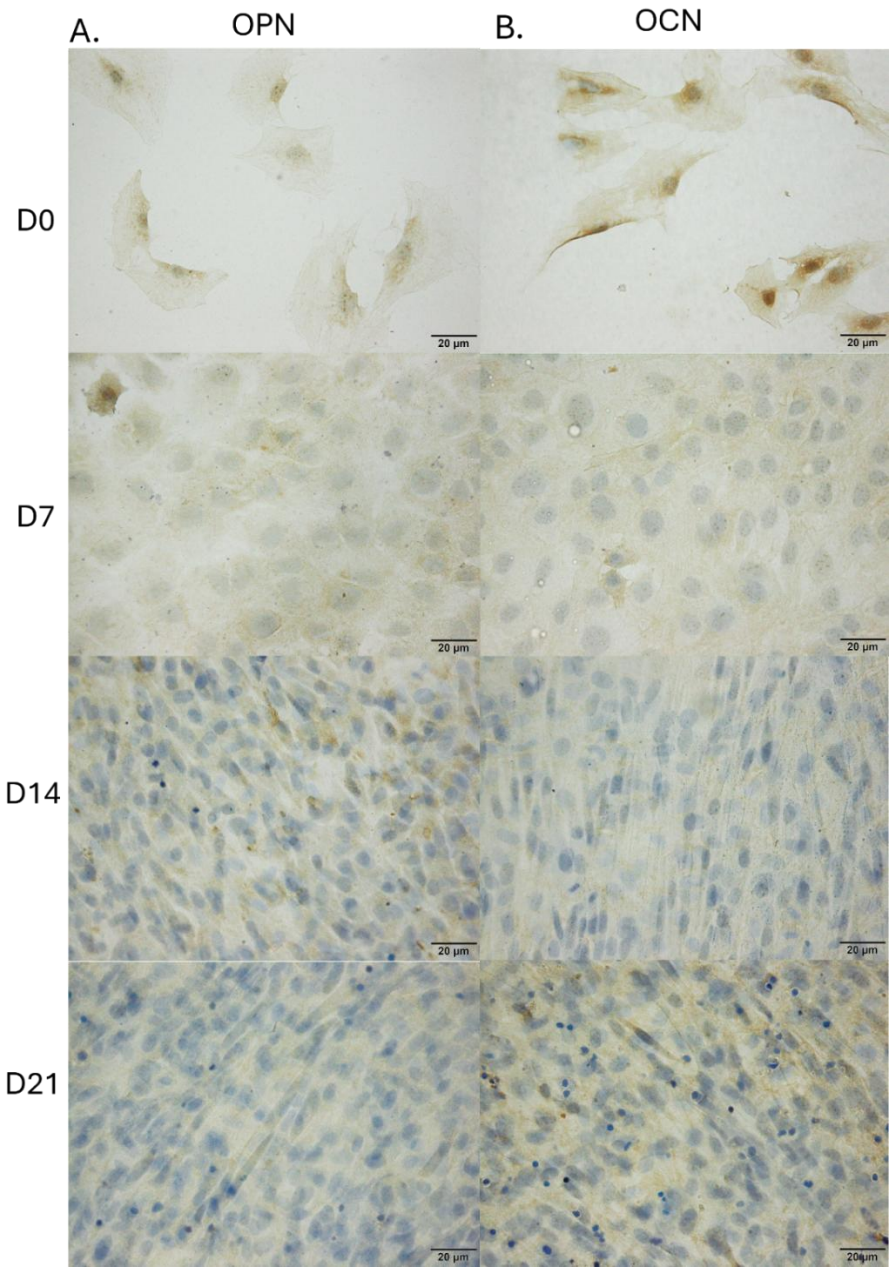

Figure 6.3.4. MC3T3-E1 monolayer immunocytochemistry characterisation over 21 day + ascorbic acid. *Chamber slides with 1x10^4 MC3T3-E1 over 21 days; Immunopositivity is represented by brown staining, A) Osteopontin (OPN), B) Osteocalcin (OCN). Scale bar represents 20 µm, n = 3.*

Cell health markers, Ki-67 associated with proliferation, and caspase 3 (CAS-3), an executioner caspase upregulated during apoptosis, were assessed during the 21-day culture period. No positivity for CAS-3 was detected (Figure 6.3.5A). All timepoints represented positivity for Ki-67, however, this is qualitatively reduced throughout the experimental duration with increased confluence (Figure 6.3.5B).

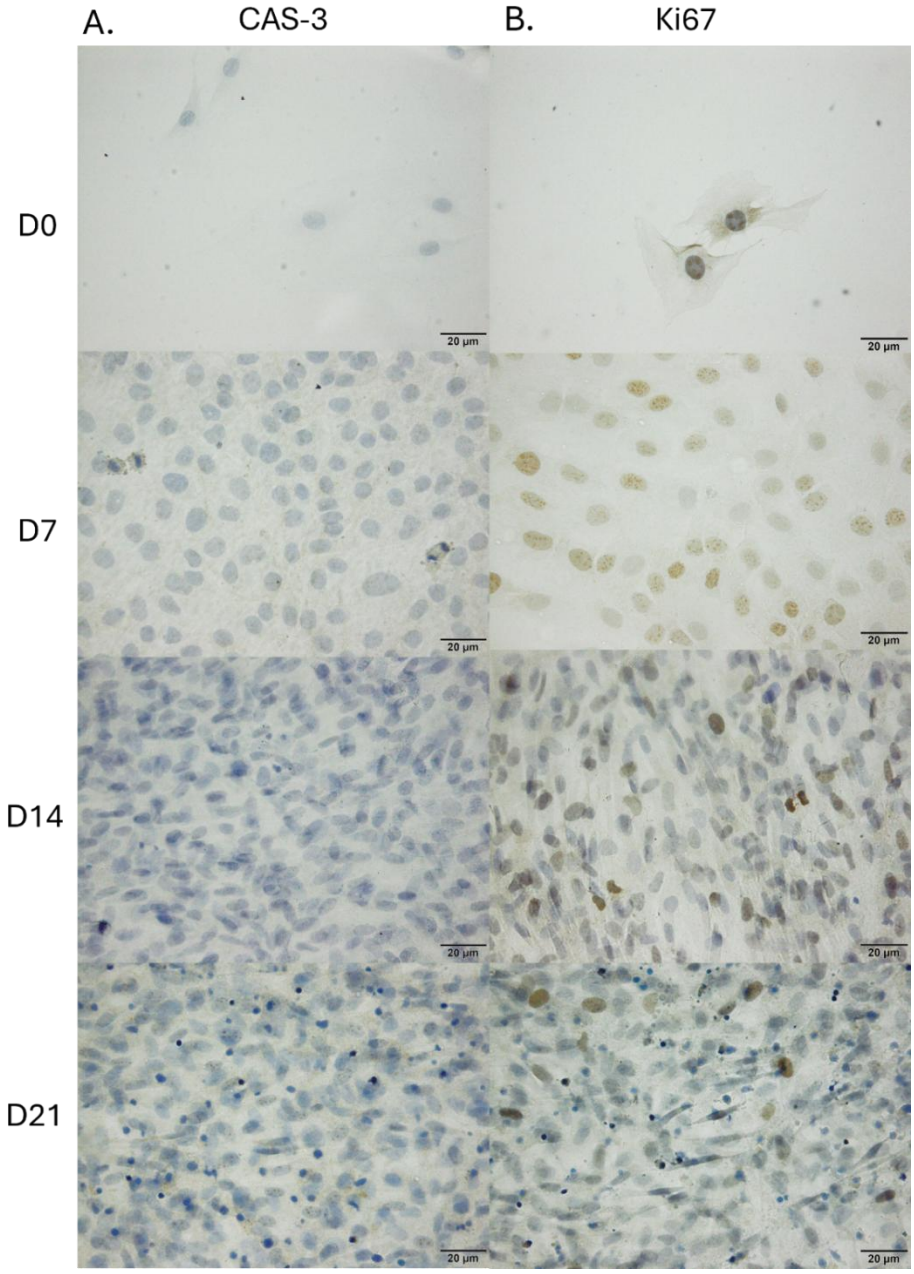

Figure 6.3.5. MC3T3-E1 monolayer immunocytochemistry characterisation over 21 days + ascorbic acid. *Chamber slides with 1x10^4 MC3T3-E1 over 21 days; Immunopositivity is represented by brown staining, A) Caspase-3 (CAS-3), B) Ki67. Scale bar represents 20 µm, n = 3.*

Cell tracker PKH26 allowed fluorescent visualisation of MC3T3-E1 cells over 21 days of treatment with ascorbic acid. D0 represents complete internalisation of dye for the MC3T3-E1 population. Full retention of the dye was not seen in the entire cellular population during the experimental duration (Figure 6.3.6); however, most of the population was still visible under fluorescence. This method was then utilised in 3D *in-vitro* cultures to visualise the presence of cells within the 3D matrix (Chapter 6, Section 6.3.2).

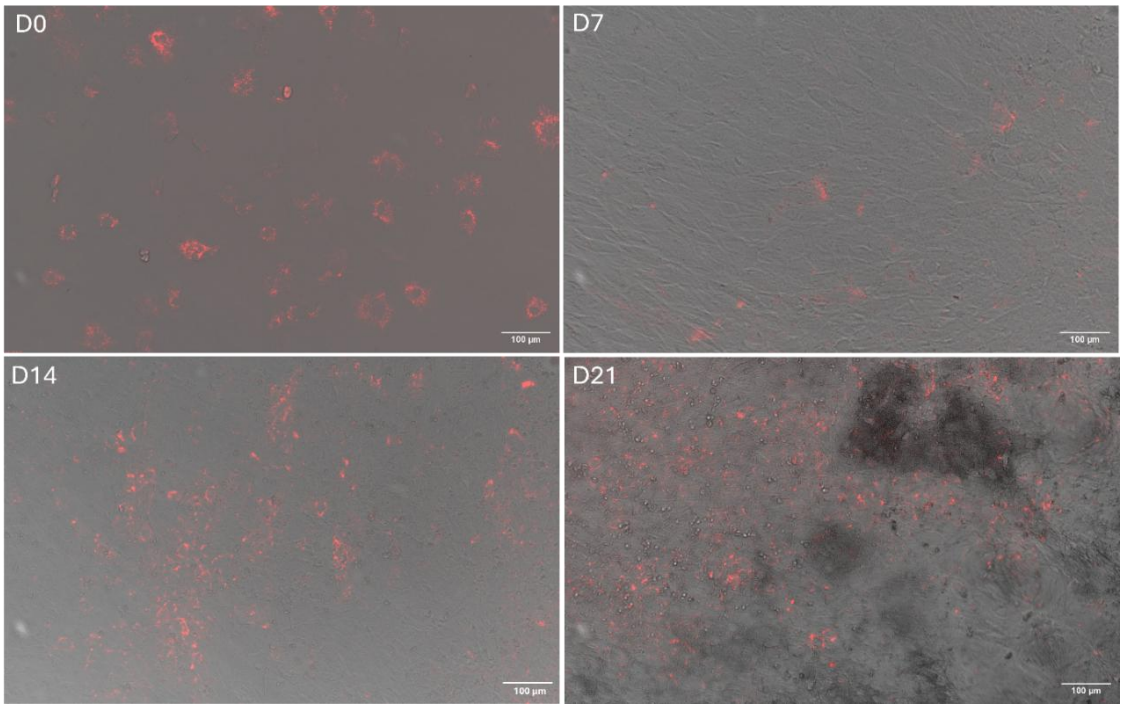

Figure 6.3.6. MC3T3-E1 monolayer fluorescent stained with cell tracker PKH26. *The scale bar represents 100 µm.*

6.3.2 Three-dimensional bioprinted *in-vitro* bone model MC3T3-E1 cell population

Monolayer images were captured to visualise fluorescently tagged cells within the B-gel, as well as the HAnp distribution within the bioprinted matrix (Figure 6.3.7). In both cellular conditions, MC3T3-E1 cells remained present during the 21 days of culturing after the process of 3D bioprinting. The 3D bioprinted constructs did not have a smooth, even surface; therefore, capturing representative images of the entire surface was challenging. It was discovered that HAnp and the B-gel were auto-fluorescent; however, despite this, MC3T3-E1 cells could be clearly distinguished from the surrounding material environment by fluorescence intensity (Figure 6.3.7). Live cell staining with

calcein AM, propidium iodide and 4',6-diamidino-2-phenoylindole was originally optimised; however, the background fluorescence was too intense, whereby no cellular detail or location could be visualised.

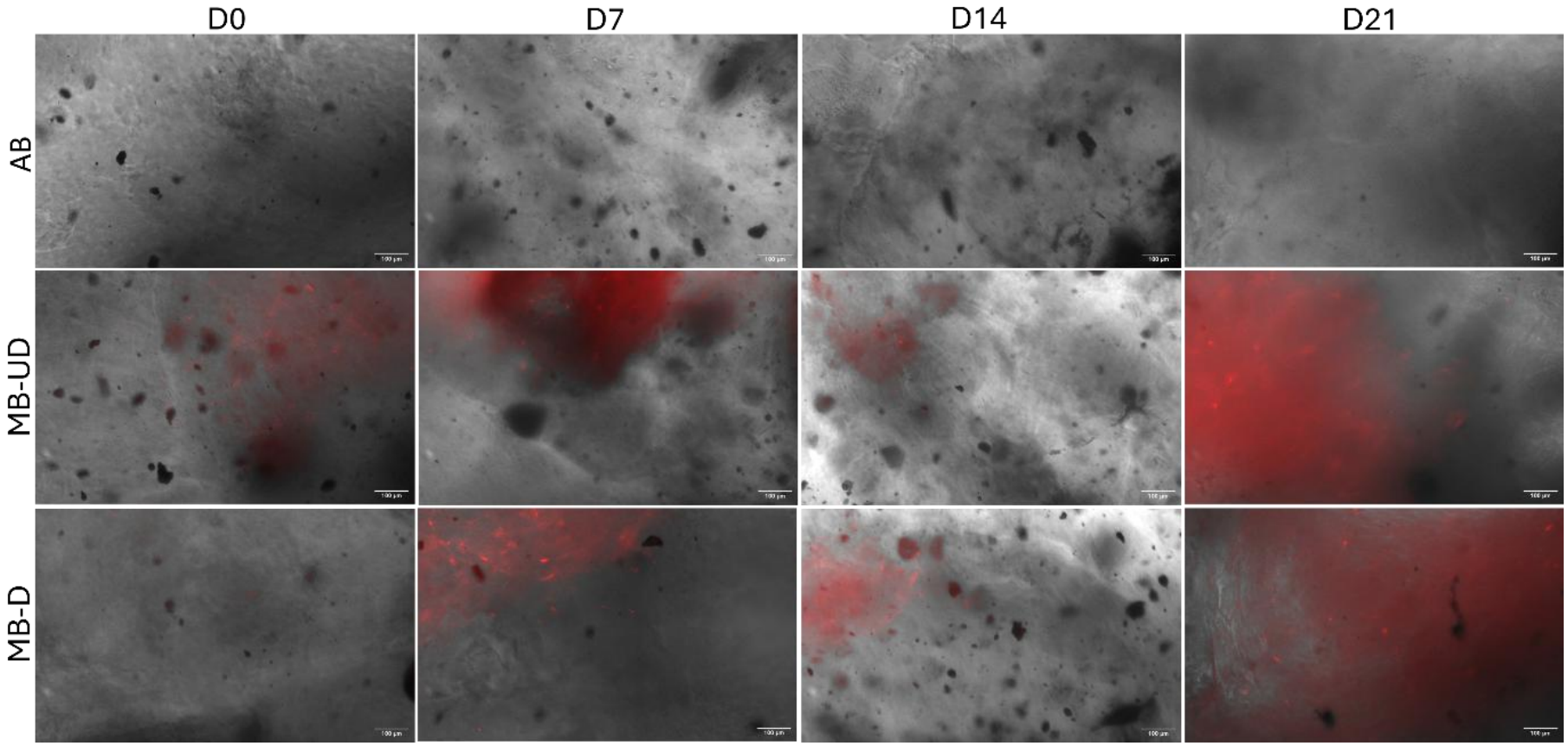

Figure 6.3.7. PKH26 lyophilic tracked MC3T3-E1 in 3D bioprinted in-vitro constructs over 21 days, +/- ascorbic acid. *Bright field and fluorescent image overlay of acellular b-gel (AB), MC3T3-E1 B-gel constructs - ascorbic acid (MB-UD), and MC3T3-E1 B-gel constructs + ascorbic acid (MB-D). The scale bar represents 100 µm, n = 3.*

MC3T3-E1 cells were visualised during the 21-day differentiation process +/- ascorbic acid (Figure 6.3.8). Qualitatively, no difference could be visualised between the population density of D0 and D21 for both conditions. The same construct was visualised per experimental repeat.

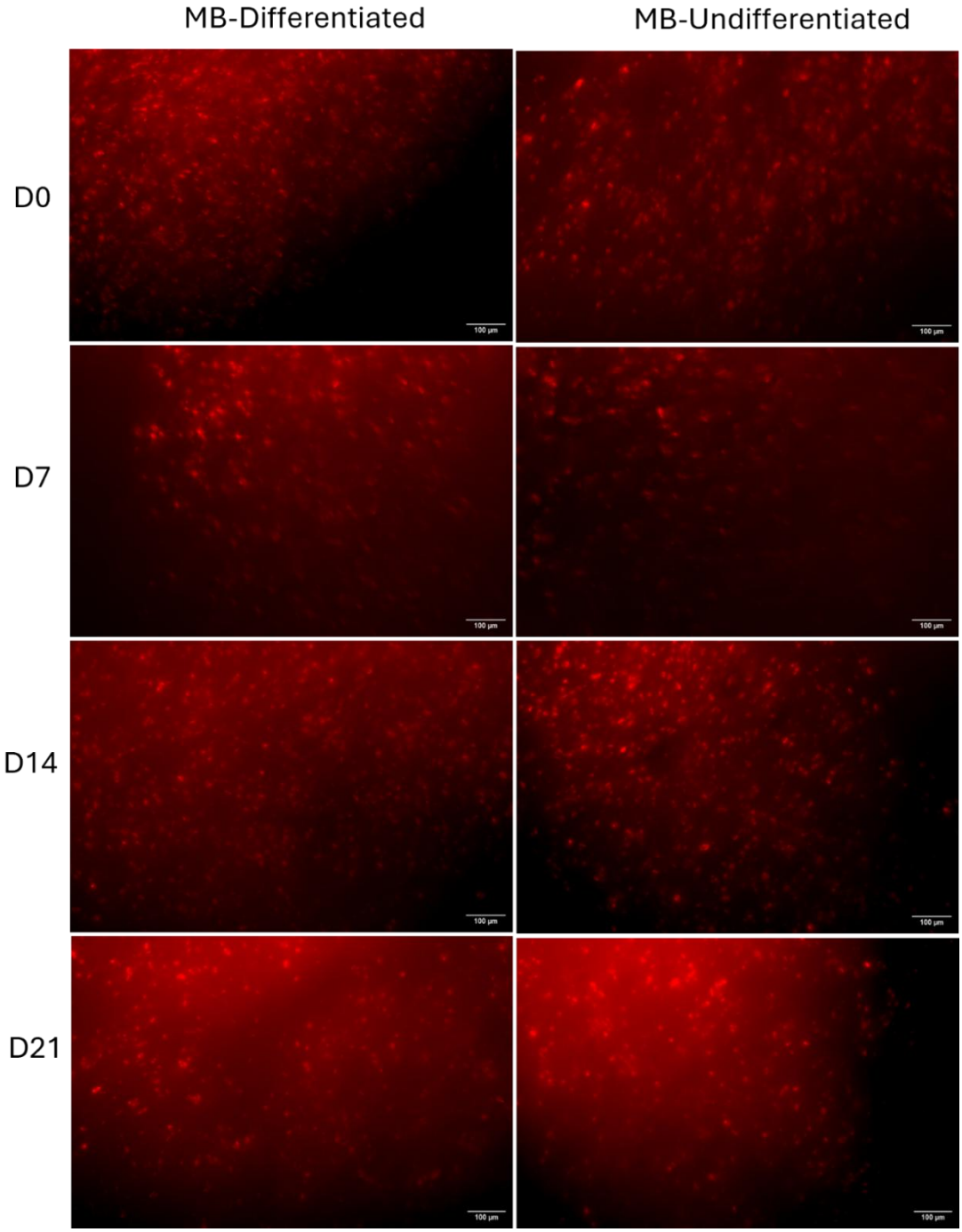

Figure 6.3.8. PKH26 lyophilic tracked MC3T3-E1 in 3D bioprinted in-vitro constructs over 21 days, +/- ascorbic acid, Z-stack. *Bright field and fluorescent z-stack image overlay of MC3T3-E1 B-gel constructs +/- ascorbic acid (differentiated and undifferentiated, respectively) over 21 days. The scale bar represents 100 µm, n = 3.*

ALP activity is an indicator of initiating OBs differentiation and driving mineralisation (Izumiya, M., *et al.* 2021; Franceschi, R., Lyer, B., & Cui, Y. 1994; Rickard, D., *et al*. 1994). Cell culture media from the same *in-vitro* bioprinted construct (n = 3) was assessed for ALP activity, with no difference between the two groups on day 0 (Figure 6.3.9). Day 7 had the most significant difference of ALP activity between MB_D and MB_UD (*P* = 0.011247), with the difference continuing on day 14 (*P* = 0.12224). Both MB_D and MB_UD followed different trends over the 21 days, with MB_D peaking in activity on D7, whereas MB_UD had the highest ALP activity on D0. No activity was detected in acellular constructs (Figure 6.3.9).

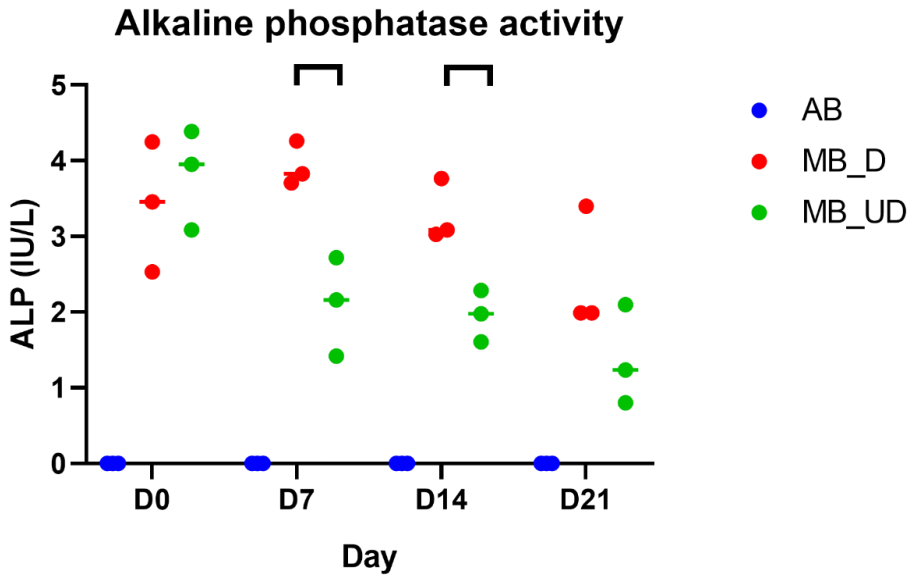

Figure 6.3.9. Alkaline phosphatase activity in 3D bioprinted in-vitro constructs cell culture media. *5 x 10^6 / mL MC3T3-E1 were bioprinted into control lattice structures, treated with +/- ascorbic acid (n = 3) MB_D and MB_UD, respectively, against acellular control (AB). Statistical difference between MB_D and MB_UD at appropriate time points, determined using the Holm-Sidak method, P < 0.05.*

6.3.3 Micro-computed tomography evaluation of the *in-vitro* bone model

Acellular, and +/- ascorbic acid MC3T3-E1 *in-vitro* constructs were imaged with micro-CT over 21 days (Figure 6.3.10A) to investigate the total volume of the individual constructs, and changes in density based on the culturing conditions. Qualitatively, construct components are visualised with a clear density-assigned colour gradient, whereby the Laptonite® nanoparticle co-polymer could be visualised in green with a low density, compared to HAnp deposits represented by blue (Figure 6.3.10A). Compared to acellular,

both cellular conditions increased overall in TMD over 21 days (Figure 6.3.10B). Acellular was statistically increased for TMD on D7 compared to D0 ($P < 0.007$); however, density then proceeded to decrease. MB_UD were not statistically different at any time point, compared to MB_D on D14 ($P < 0.035$), and D21 ($P < 0.0211$) (Figure 6.3.10B). Despite no statistical difference, all constructs decreased in overall volume over the 21 days in a similar trend (Figure 6.3.10C).

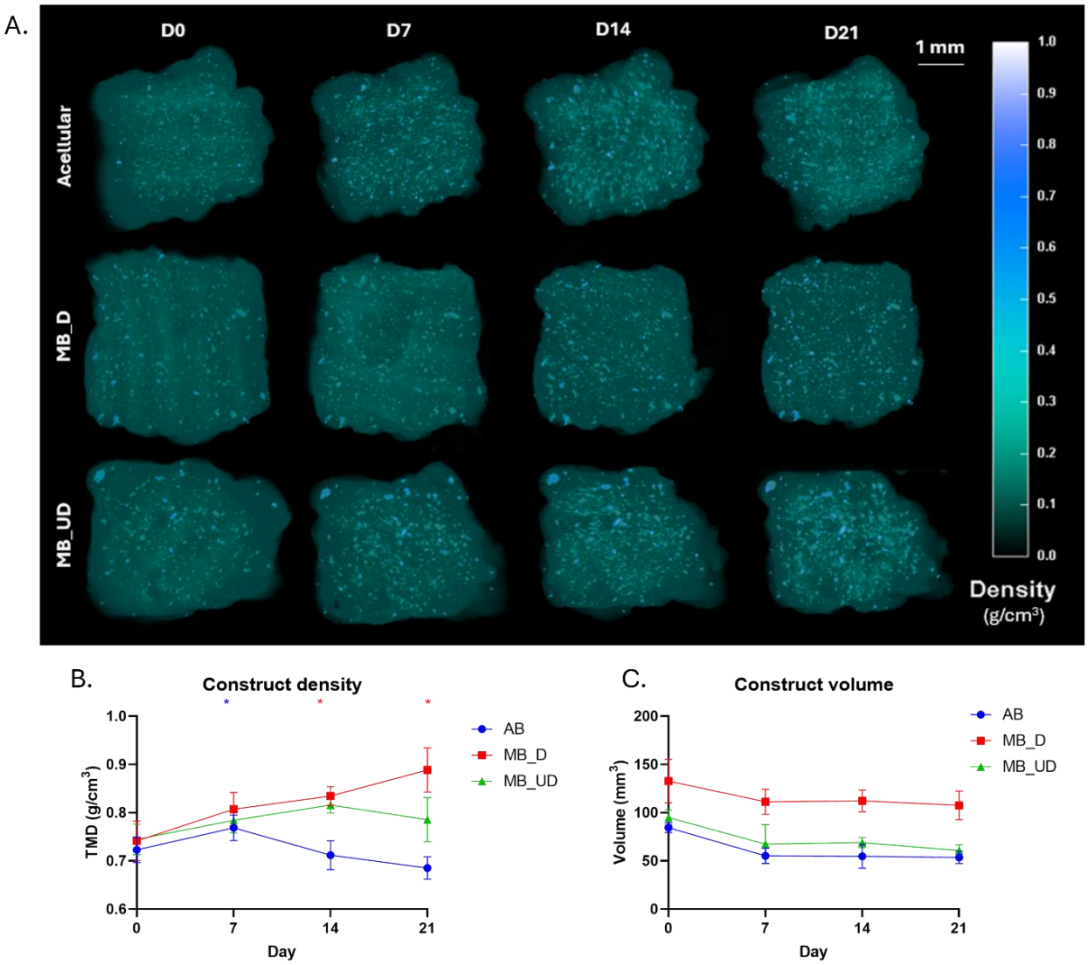

Figure 6.3.10. Micro-CT volume and density analysis of B-gel in-vitro 3D bioprinted constructs. *Constructs printed at D-1. Acellular b-gel (AB), MC3T3-E1 b-gel differentiated (MB_D), MC3T3-E1 b-gel undifferentiated (MB_UD). Each construct was imaged at 9 µm on days 0, 7, 14 and 21. A) Micro-CT projection visualisation on CT Vox, density colour coded, B) Tissue mineral density (g/cm^3) (TMD), C) total construct volume (mm^3). n = 3, two-way ANOVA multiple comparisons with Geisser-Greenhouse correction were performed against D0 for each respective condition, P < 0.05, statistical difference is represented per time point, per condition by the respective coloured Asterix.*

Further image processing allowed the segmentation of the individual HAnp for independent analysis, visualised by a colour-assigned threshold to represent particle thickness from a range of 0 – 1.9 mm (Figure 6.3.11A). The total HAnp number increased in all conditions, with statistical significance for AB ($P < 0.0363$), MB_UD ($P < 0.0224$) and MB_D ($P < 0.0242$) on D21 compared to D0 (Figure 6.3.11B). The particle diameter for AB remained similar from D0 to D21 ($P = 0.4107$), whereas MB_UD and MB_D increased the average diameter, with D21 being statistically different for MB_D ($P < 0.0446$) compared to MB_UD ($P = 0.0521$) (Figure 6.3.11C). In a similar trend, the maximum HAnp diameter increased in all conditions, with a greater difference visualised in the MB_D condition; however, this was not statistically different to D0 ($P = 0.0612$) (Figure 6.3.11D).

Noticeably, HAnp particle number (Figure 6.3.11B) and TMD (Figure 6.3.11B) were within a consistent range for all conditions on D0; however, the diameter was increased for MB_UD and MB_D on D0 (Figure 6.3.11C), perhaps suggesting that MC3T3-E1 cells interact with existing HAnp and further mineralise. In addition, the initial volume between all the constructs in the experimentation was inconsistent with an average of 104.02 mm^2 +/- 23.72 (Figure 6.3.11C), further evidencing the methodological inconsistency of 3D bioprinting for individual consistency between constructs and reproducibility.

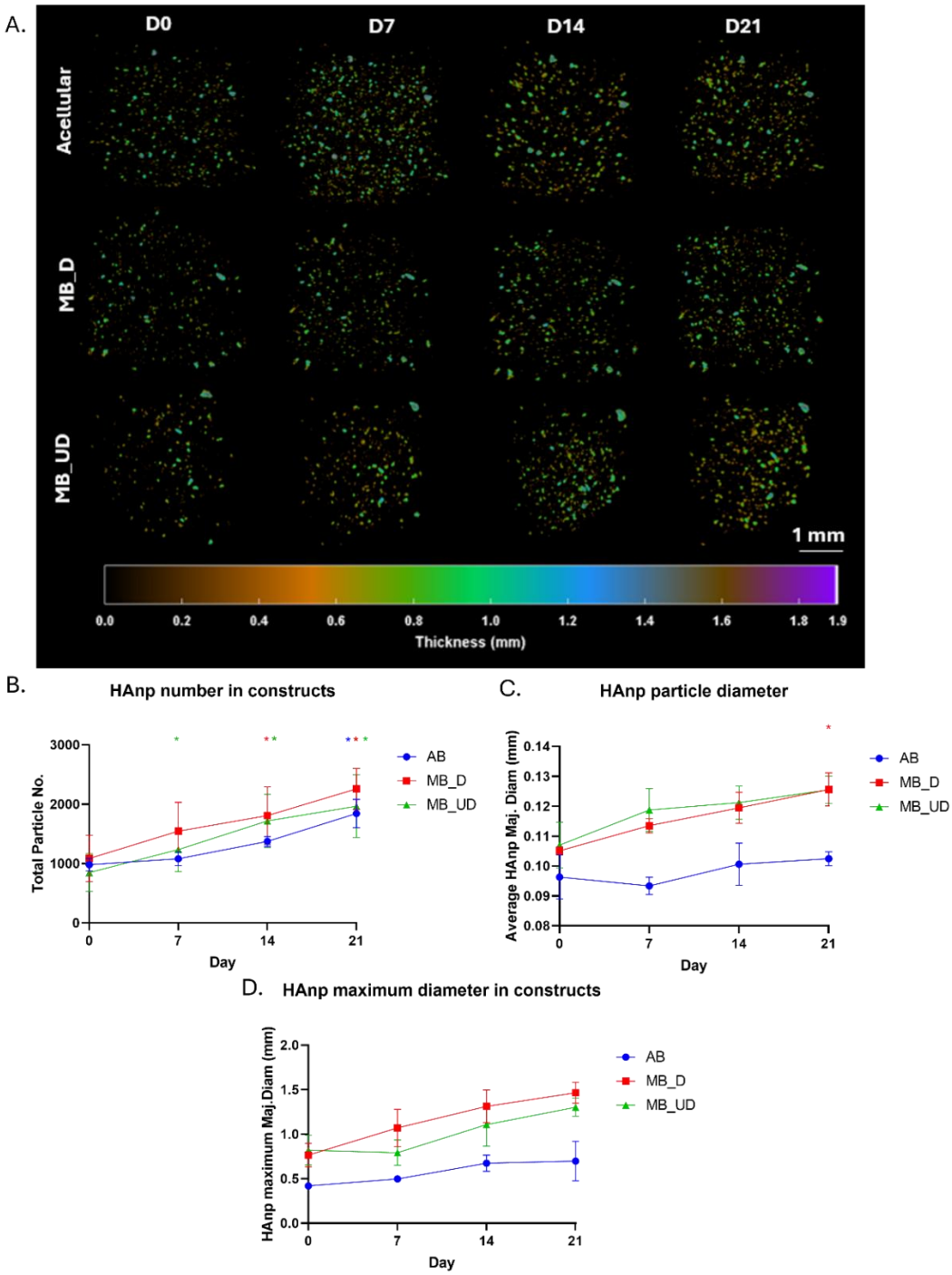

Figure 6.3.11. Micro-CT particle analysis of B-gel in-vitro 3D bioprinted constructs. *Constructs printed at D-1. Acellular b-gel (AB), MC3T3-E1 b-gel differentiated (MB_D), MC3T3-E1 b-gel undifferentiated (MB_UD). Each construct was imaged at 9 µm on days 0, 7, 14 and 21. A) Micro-CT projection visualisation on CT Vox, particle thickness colour coded, B) Total HAnp particle number, C) average hydroxyapatite nanoparticle (HAnp) major diameter (Maj. Diam) (mm), D) hydroxyapatite nanoparticle maximum Diam (mm). n = 3, two-way ANOVA multiple comparisons with Geisser-Greenhouse correction were performed against D0 for each respective condition, P < 0.05; statistical difference is represented per time point, per condition by the respective coloured asterisk.*

B-gel is a co-polymer hydrogel that contains a high concentration of water. To determine dry weight, the volume of the lyophilised constructs was quantified by micro-CT (Figure 6.3.12A). Despite not being a matched comparison of individual constructs due to the destructive nature of the experimentation, a trend of increasing volume could be visualised from D0 to D21 (Figure 6.3.12). Overall, compared to hydrated samples (Figure 6.3.10C), a loss of up to 9143% of volume (mm^3) on D0, and 5473% on D21 for dehydrated cellular conditions (Figure 6.2.12B) was observed, representing the high-water content of the *in-vitro* models in a hydrated state.

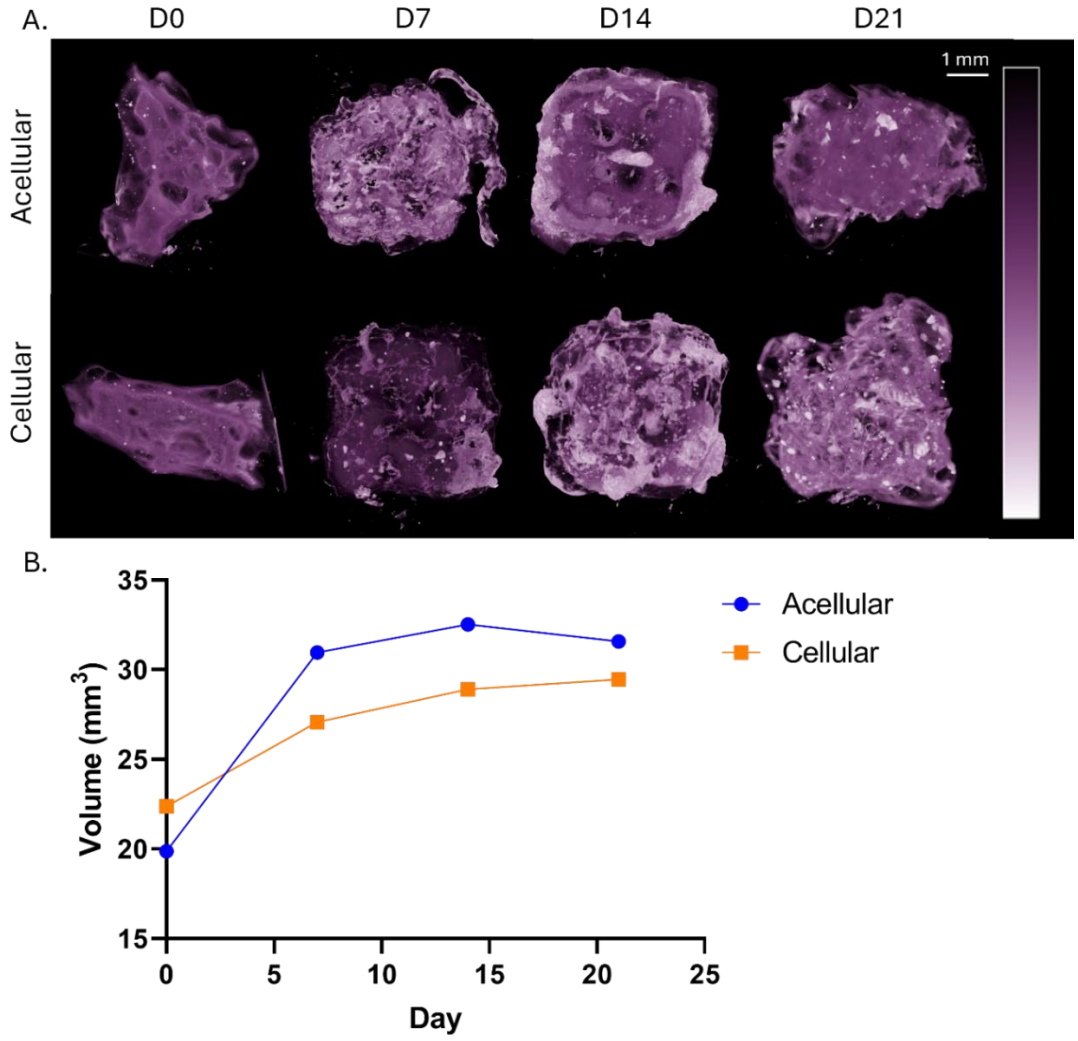

Figure 6.3.12. Micro-CT volume analysis of lyophilised 3D in-vitro bioprinted constructs. *Constructs were bioprinted at D-1. One acellular and cellular construct was fixed on days 0, 7, 14 and 21, following lyophilisation, before being imaged at 9 µm. A) Micro-CT projection of lyophilised bioprinted constructs, pseudo density applied. B) Total volume (mm^3) of acellular and cellular constructs. n = 1, scale bar represents 1 mm.*

6.3.4 Composition investigation of three-dimensional bioprinted *in-vitro* bone model

Mineralisation and cellular behaviour were investigated within the *In-vitro* bioprinted 3D constructs. Histological staining with H&E indicated cellular populations within the construct body and lining the surface in both MB_UD and MB_D (Figure 6.3.13). The porosity of B-gel could be visualised, with MC3T3-E1 cells often lining the pores, as well as the construct surface (Figure 6.3.13).

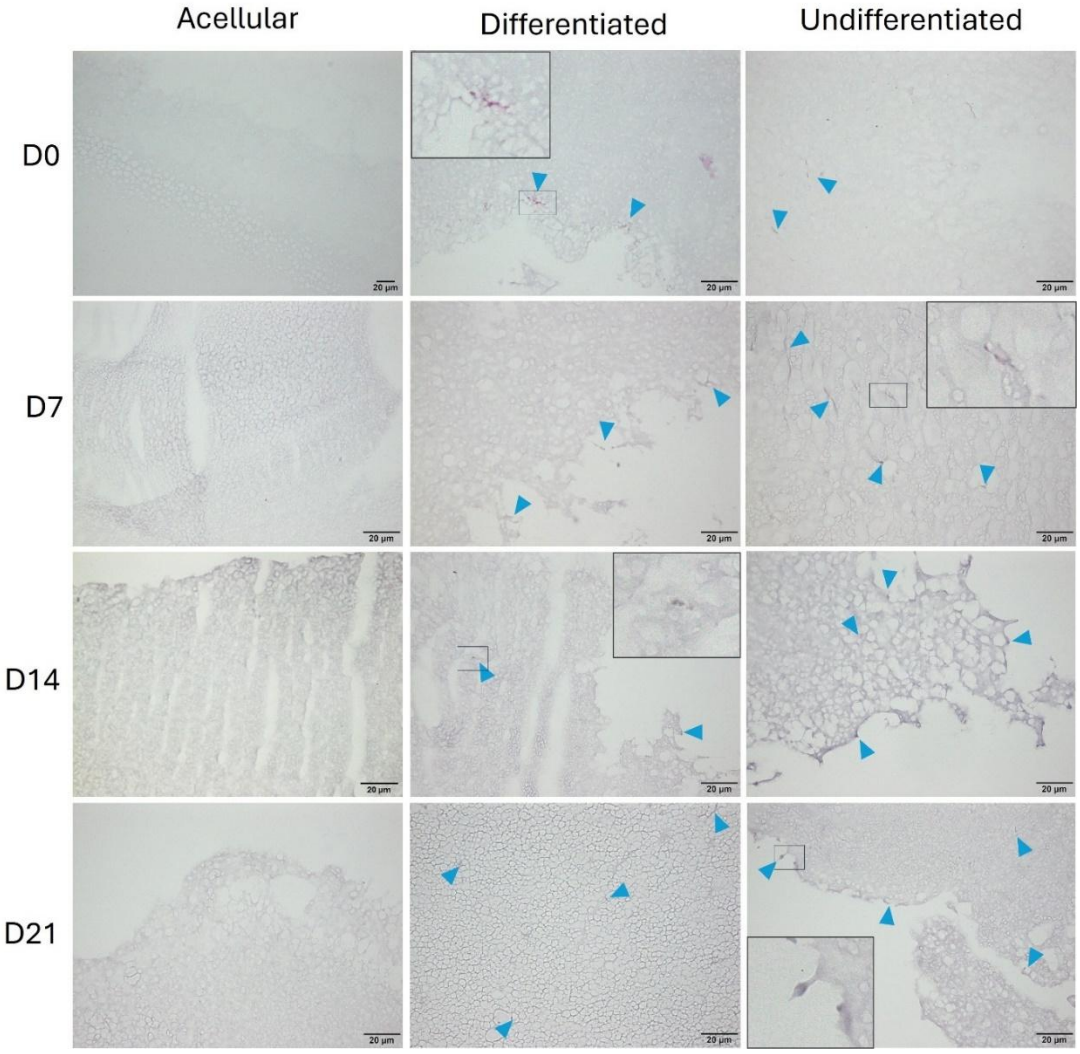

Figure 6.3.13. Haematoxylin and eosin histology on in-vitro 3D bioprinted constructs over 21 days. *8 µm sections, H&E histological stain, MC3T3E1 cells highlighted (blue arrow) in +/- ascorbic acid conditions. n = 3, representative image shown with magnified regions highlighted by black boxes, scale bar represents 20 µm.*

Calcium deposition in MB_D bioprinted 3D constructs could be visualised from D7, with increased nodules on D14 and D21 (Figure 6.3.14). MB_UD constructs increased calcium deposition by D14, with increased nodules visualised on D21, matching the intensity visualised on D14 for MB_D conditions (Figure 6.3.14). Finally, calcium deposits could be visualised on D14 and D21 for AB (Figure 6.3.14), in a similar trend of increase in TMD determined from micro-CT (Figure 6.3.10B).

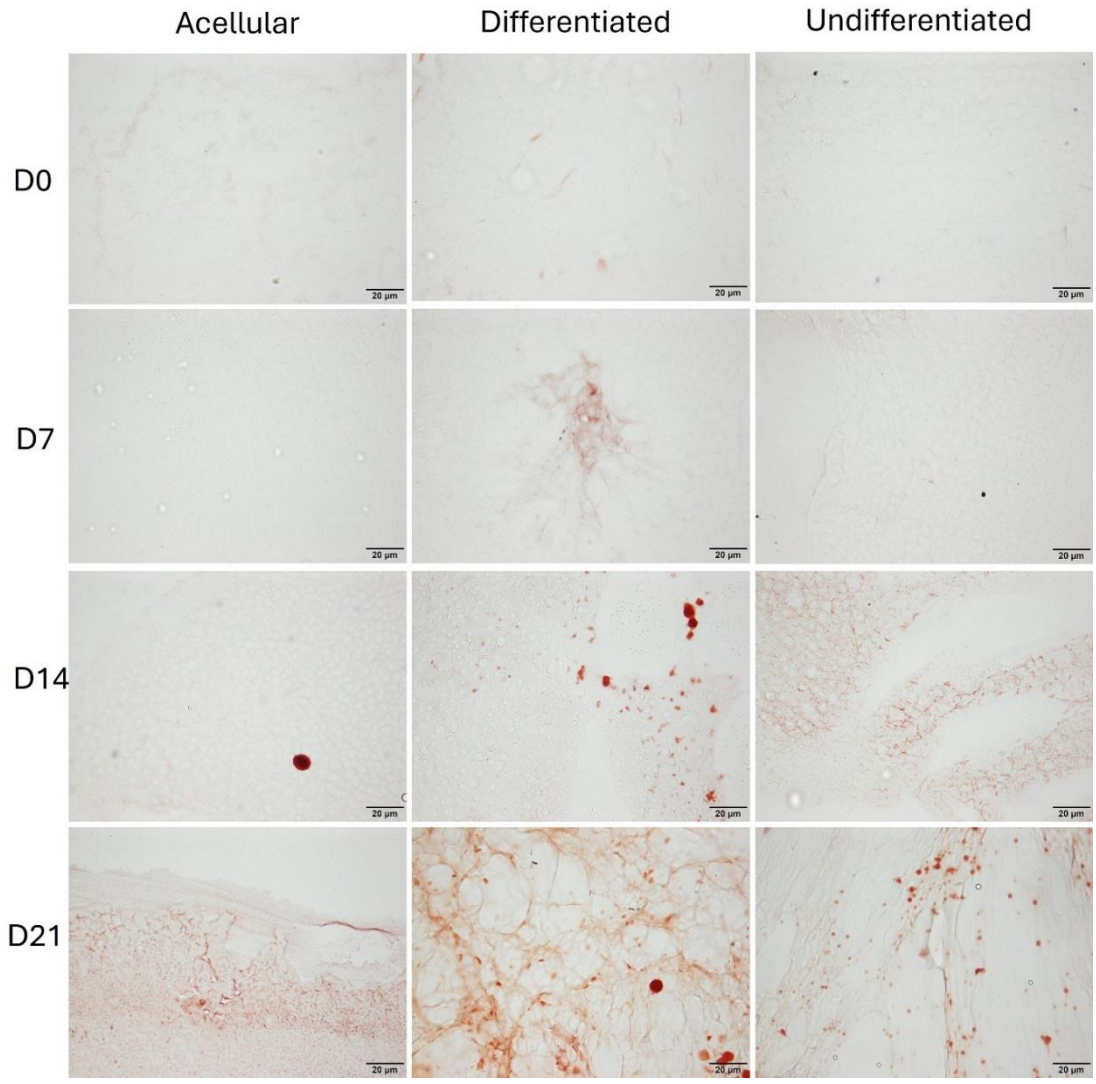

Figure 6.3.14. Alizarin red histology on in-vitro 3D bioprinted constructs over 21 days. *8 µm sections, alizarin red histological stain represents calcium deposits (red). n = 3, representative image shown, scale bar represents 20 µm.*

Similar to AR, Von Kossa histology enables the visualisation of mineralised matrix, compared to non-mineralised matrix (Figure 6.3.15), as well as improved cell visualisation compared to AR (Figure 6.3.14) and H&E (Figure 6.3.13). In a similar trend to AR, MB_D cells begin to show increased calcium deposition in the presence of HAnp from D7, with mineralised matrix represented by brown staining on D21 (Figure 6.3.15). The surrounding matrix over the 21 days in the cellular condition is stained with an increased intensity, suggesting an increase in matrix complexity of the entire *in-vitro* model.

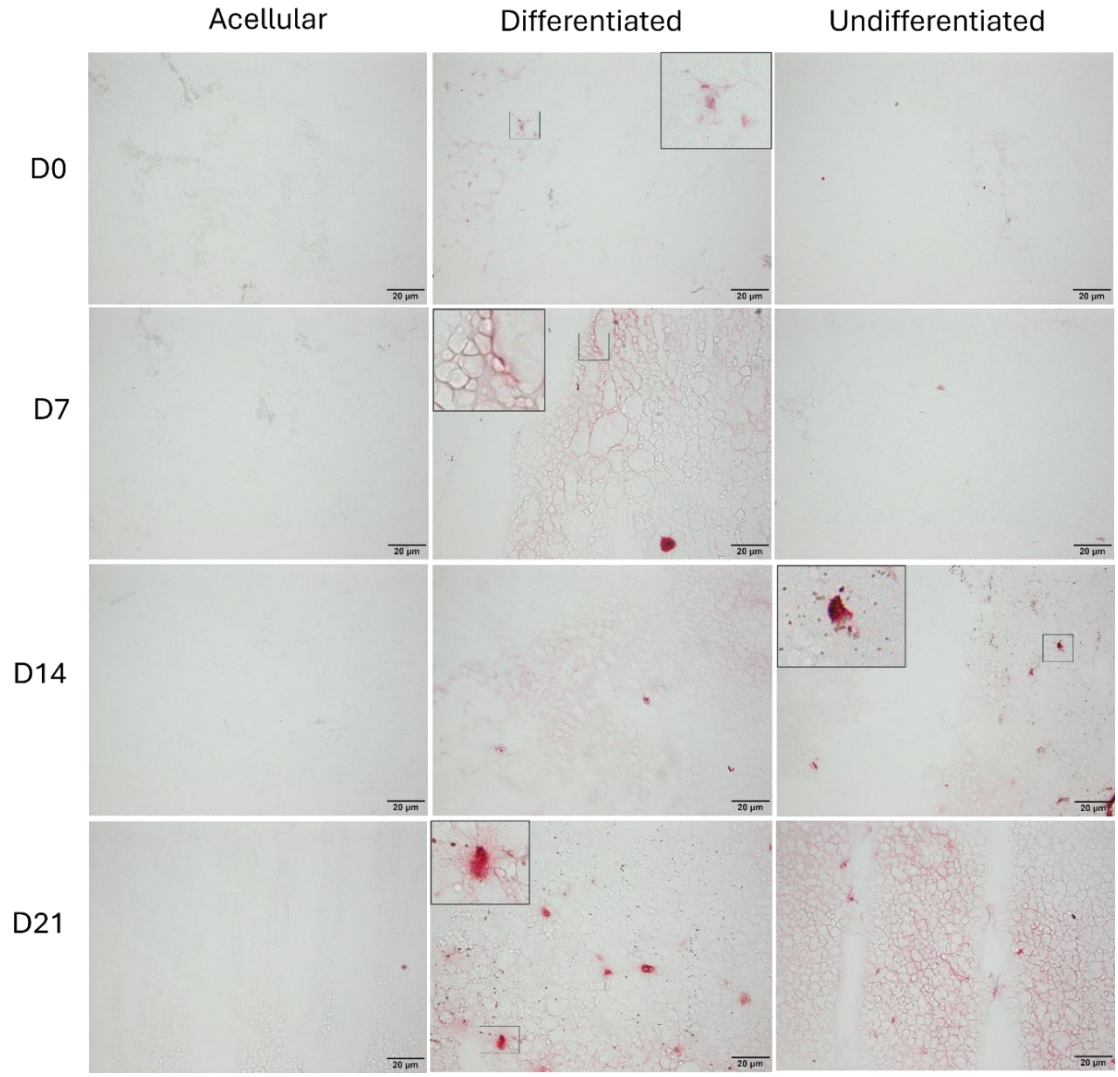

Figure 6.3.15. Von Kossa histology on in-vitro 3D bioprinted constructs over 21 days. *8 µm sections, calcium deposits (black/brown), nuclei (red) and ECM (pink). n = 3, representative image shown with magnified regions highlighted by black boxes, scale bar represents 20 µm.*

The cellular matrix was investigated by MT, with the matrix producing MC3T3-E1 identified with increased staining intensity compared to the B-gel matrix around cellular structures (Figure 6.3.16). Regions of increased staining intensity of the background matrix due to cellular differentiation are difficult to distinguish between, as the material was also stained an intense blue, despite no collagen components in the B-gel composition (Figure 6.3.16).

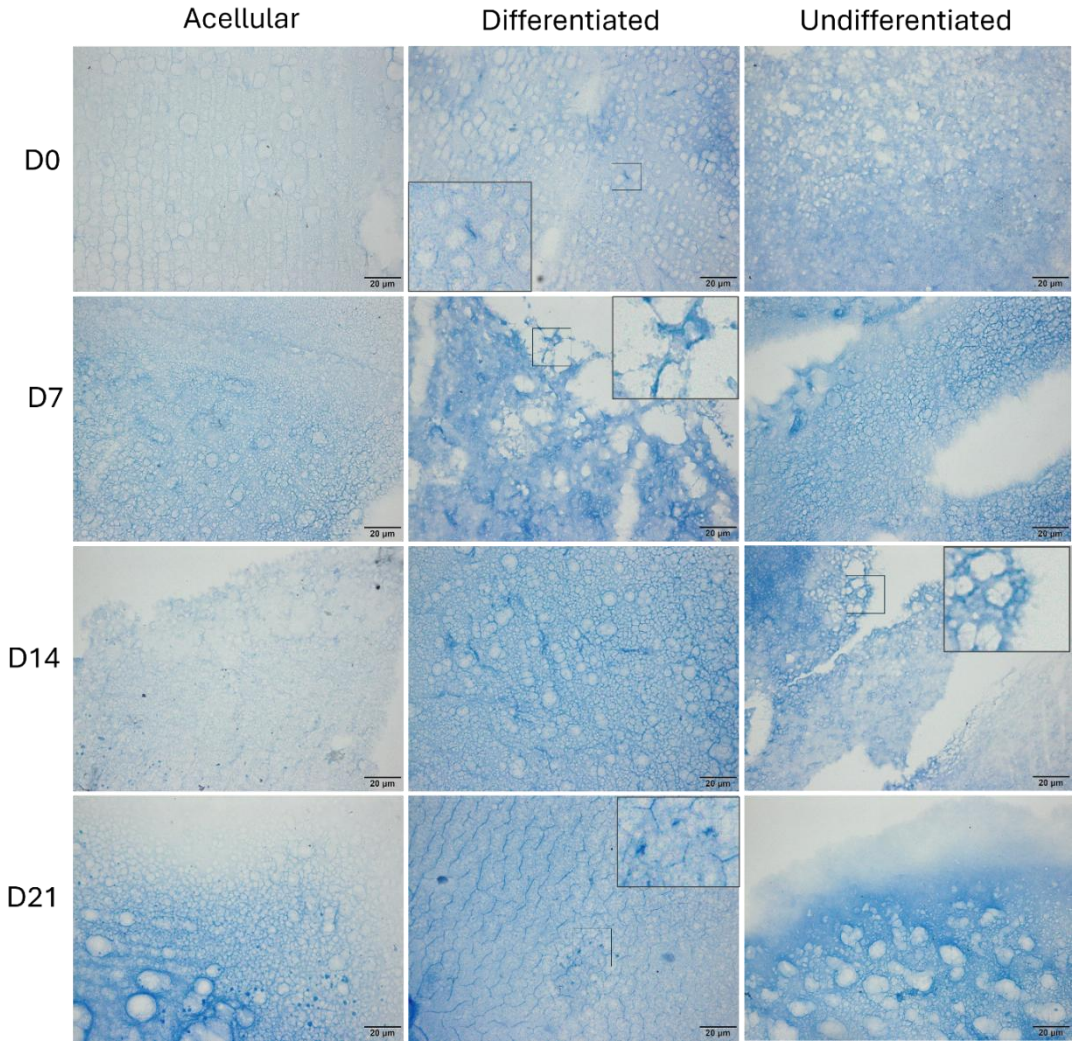

Figure 6.3.16. Massons trichrome histology on in-vitro 3D bioprinted constructs over 21 days. *8 µm sections, Massons trichrome represents collagen (blue) and nuclei (black). n = 3, representative image shown with magnified regions highlighted by black boxes, scale bar represents 20 µm.*

Further investigation on the surrounding matrix was performed by ACB and SO. Regions of mucins are identified by blue staining, and HAnp calcium deposits can be identified by purple regions (Figure 6.3.17). Pink cellular nuclei contrast to the blue/purple B-gel material, allowing clear visualisation of the cellular structures and the interaction (Figure 6.3.17). Mineralised matrix formation in the presence of HAnp could be visualised as purple nodules, and MC3T3-E1 cells were visualised interacting with these regions (Figure 6.3.17).

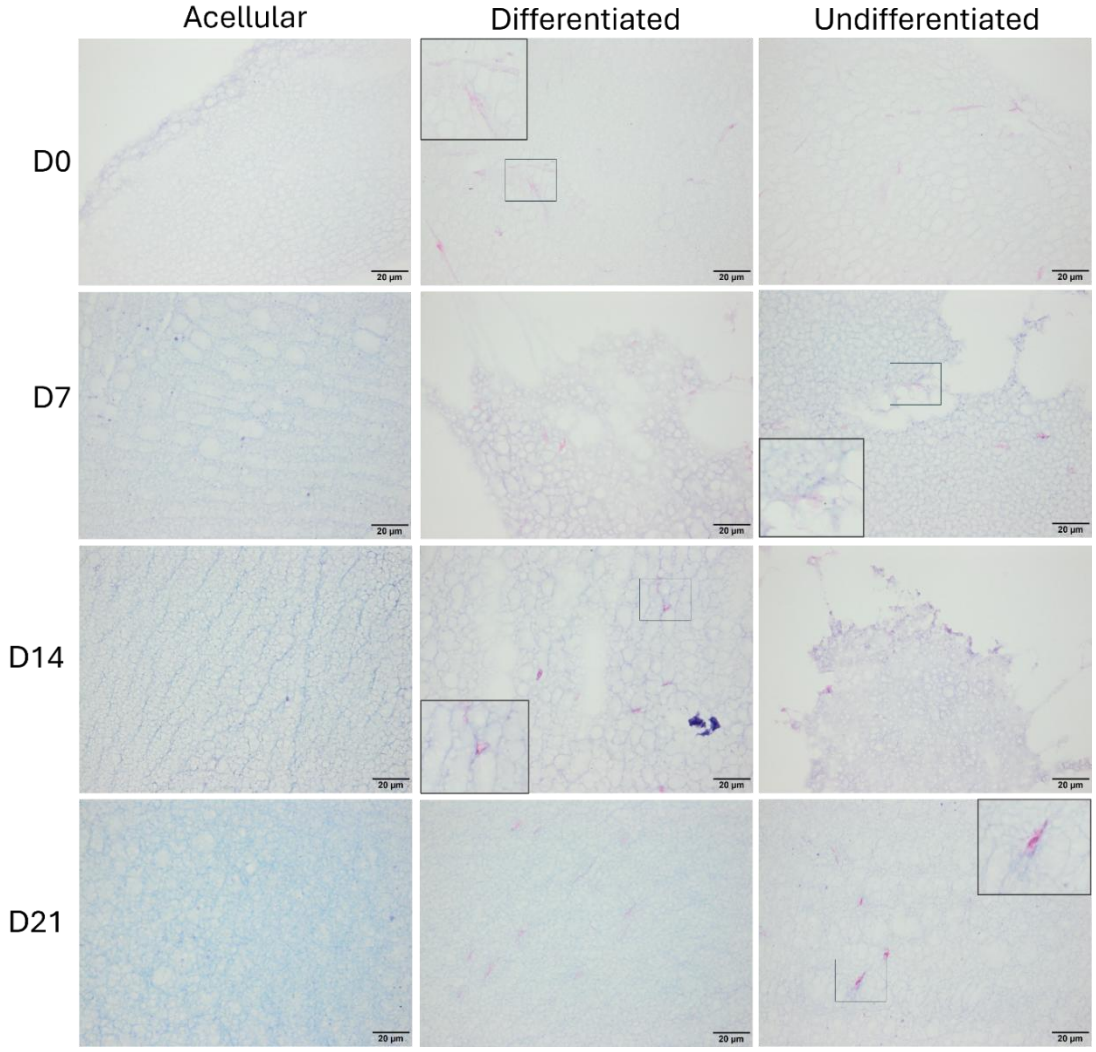

Figure 6.3.17. Alician blue & fast red histology on in-vitro 3D bioprinted constructs over 21 days. *8 µm sections, histological stains represent acidic mucins (blue), nuclei (pink) and calcium deposits (purple). n = 3, representative image shown with magnified regions highlighted by black boxes, scale bar represents 20 µm.*

For SO, green calcium deposits could be visualised within all structures from the bioink composition, with increased population surrounding the cellular structures (Figure 6.3.18). Interestingly, all conditions gradually increase in the staining intensity of pink from D0 to D21, associated with proteoglycan content within cartilage regions, therefore this stain is unreliable for reporting cellular-based changes (Figure 6.3.18).

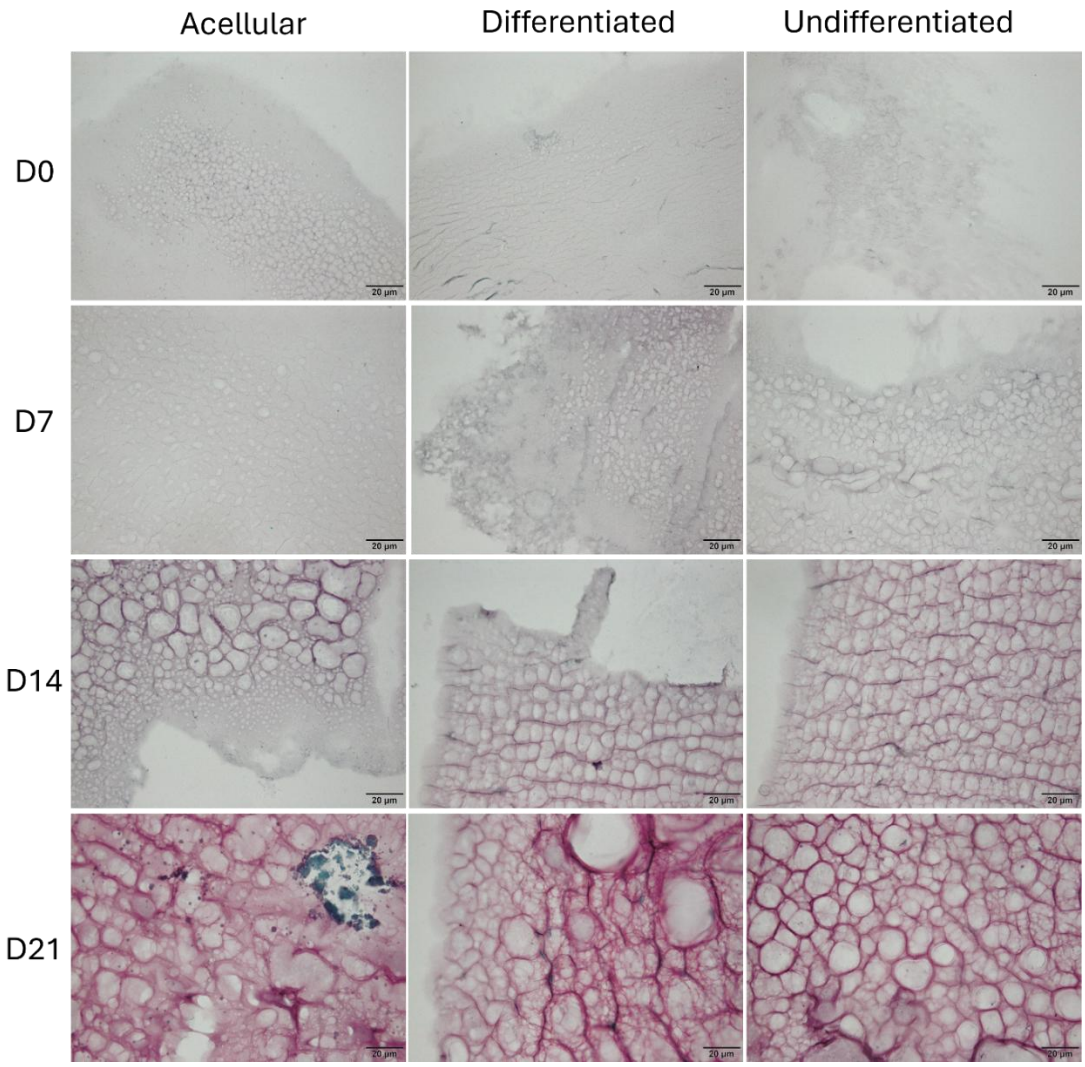

Figure 6.3.18. Safranin-O histology on in-vitro 3D bioprinted constructs over 21 days. *8 µm sections, proteoglycan-rich regions (red/pink) and calcium (green). n = 3, representative image shown, scale bar represents 20 µm.*

6.3.5 Immunohistochemical evaluation of osteoblast differentiation marker of three-dimensional bioprinted *in-vitro* bone model

To further explore the phenotype of MC3T3-E1 cells within the B-gel matrix, after the process of bioprinting, immunological staining was performed against previously identified proteins of interest associated with osteogenesis and cell function. Associated with matrix deposition, MC3T3-E1 cells were immunopositive for COL-1 in MB_UD and MB_D over the 21-day differentiation period (Figure 6.3.19).

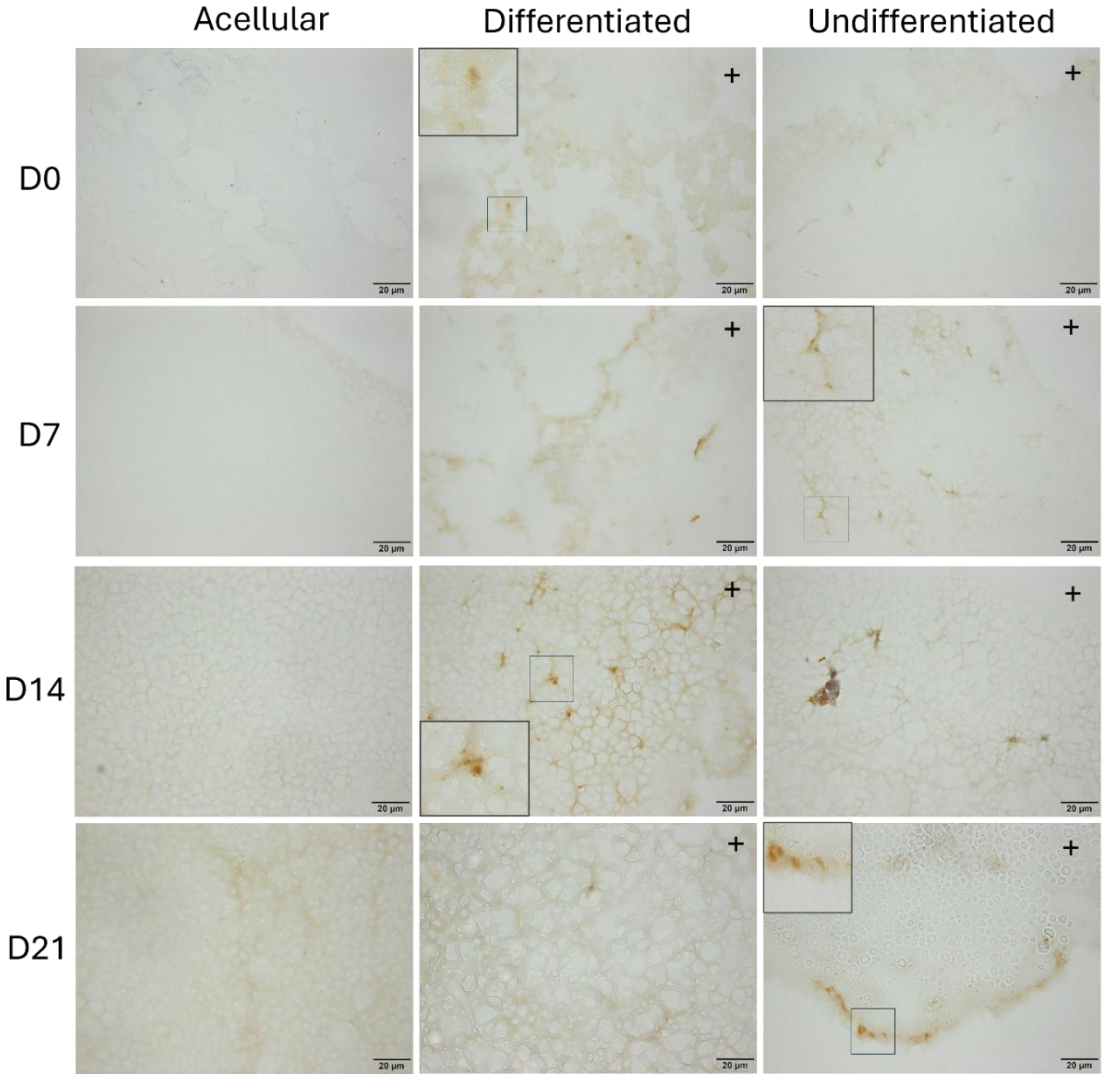

Figure 6.3.19. Type-1 collagen immunohistochemistry on in-vitro 3D bioprinted constructs over 21 days. *8 µm sections were used; immunopositivity represented by brown staining and indicated (+). n = 3, representative image shown with magnified regions highlighted by black boxes, scale bar represents 20 µm.*

Strong staining intensity for ALP was visualised in D0 for the cellular conditions, with no positivity detected in the MB_UD studied population for the remainder of experimentation (Figure 6.3.20). MB_D revealed positivity for ALP for the 21-day experiment (Figure 6.3.20), with this trend following the increased ALP activity discovered (Figure 6.3.9).

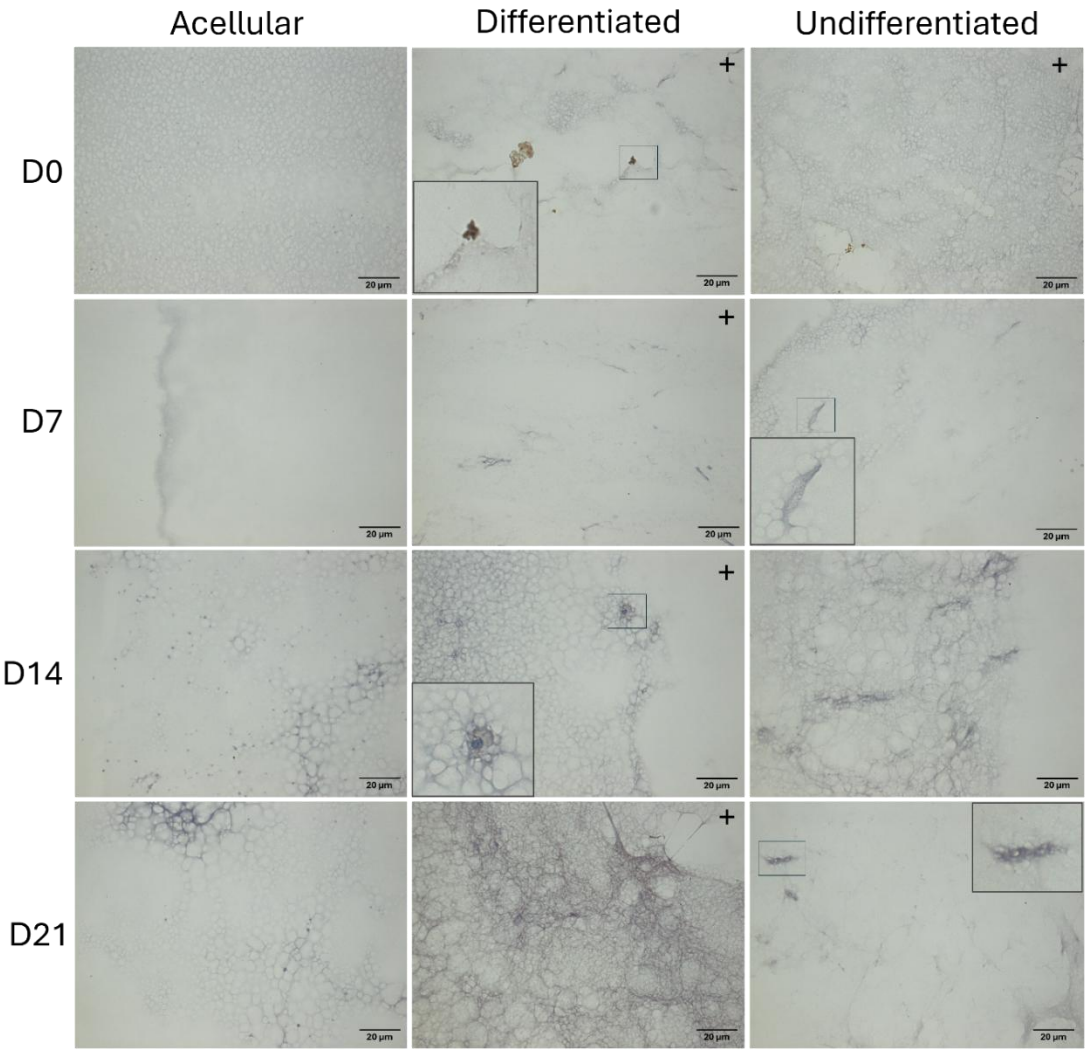

Figure 6.3.20. Alkaline phosphatase immunohistochemistry on in-vitro 3D bioprinted constructs over 21 days. *8 µm sections were used; immunopositivity represented by brown staining and indicated (+). n = 3, representative image shown with magnified regions highlighted by black boxes, scale bar represents 20 µm.*

Interestingly, MC3T3-E1 did not stain positively for Runx2 on D0 in 3D (Figure 6.3.21), compared to strong positivity in 2D (Figure 6.2.3A). D7 for MB_D, and D14 MB_UD represented the presence of Runx2, with strong intensity visualised for D7, perhaps indicating the phenotypic commitment for differentiation of iOBs into mOBs.

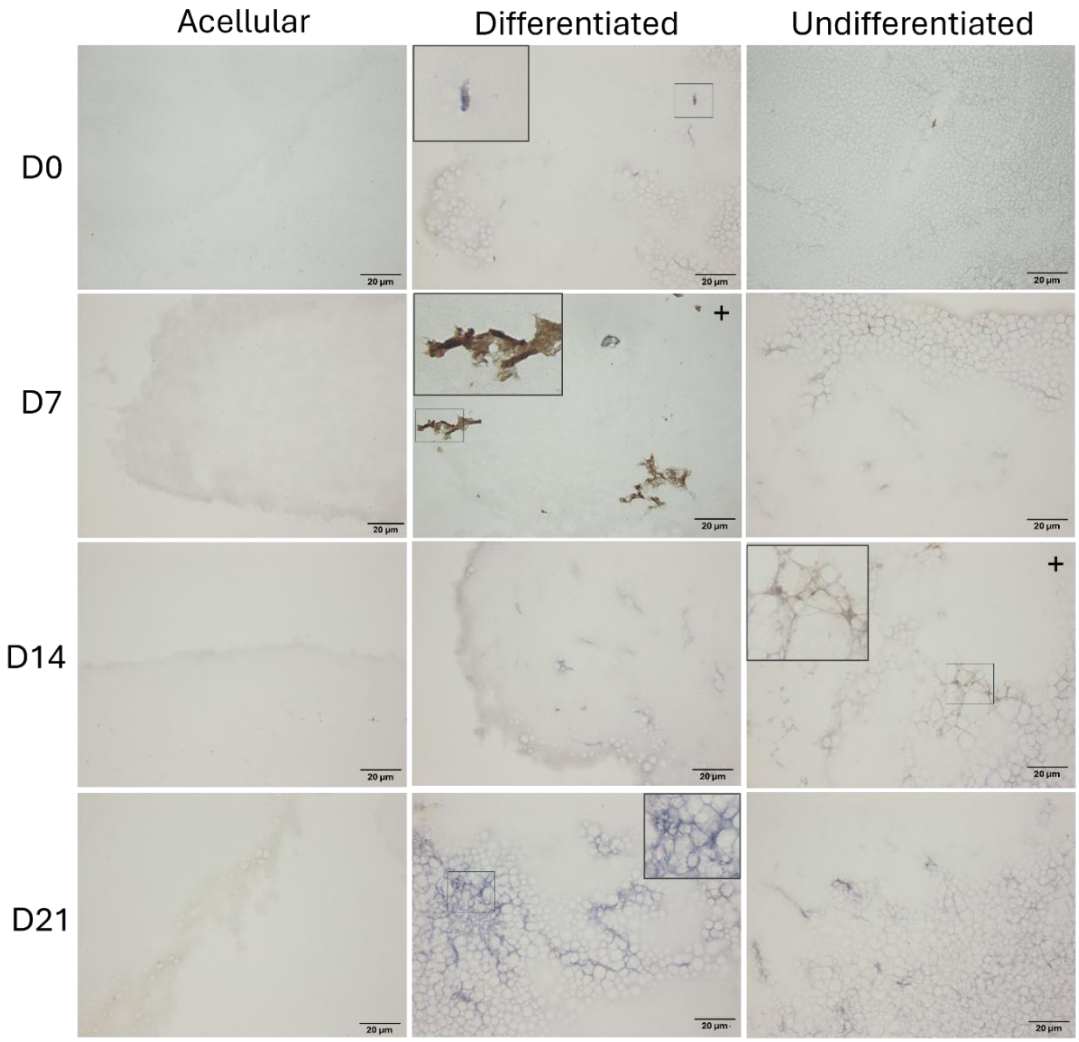

Figure 6.3.21. Runt-related transcription factor-2 immunohistochemistry on in-vitro 3D bioprinted constructs over 21 days. *8 µm sections were used; immunopositivity represented by brown staining and indicated (+). n = 3, representative image shown with magnified regions highlighted by black boxes, scale bar represents 20 µm.*

OCN IHC produced complete non-specific binding of both antigen specific, and IgG control, to the B-gel material (Supplementary, Figure S8) due to the high concentration of antibody discovered during optimisation of previous experimentation (Chapter 2, Figure 2.3.8 and supplementary, Figure S7). Apart from the controls for OCN, all other IgG controls were clear of non-specific immunopositivity staining (Supplementary, Figure S8).

Finally, OB-related OPN showed no immunopositivity for both cellular conditions in D0 and D7, with positivity visualised in D14 for MB_D and finally both cellular conditions on D21 (Figure 6.3.22). As a marker for the later stages of osteogenesis for iOBs to mOBs, OPN positivity represents cellular differentiation to show phenotype transition.

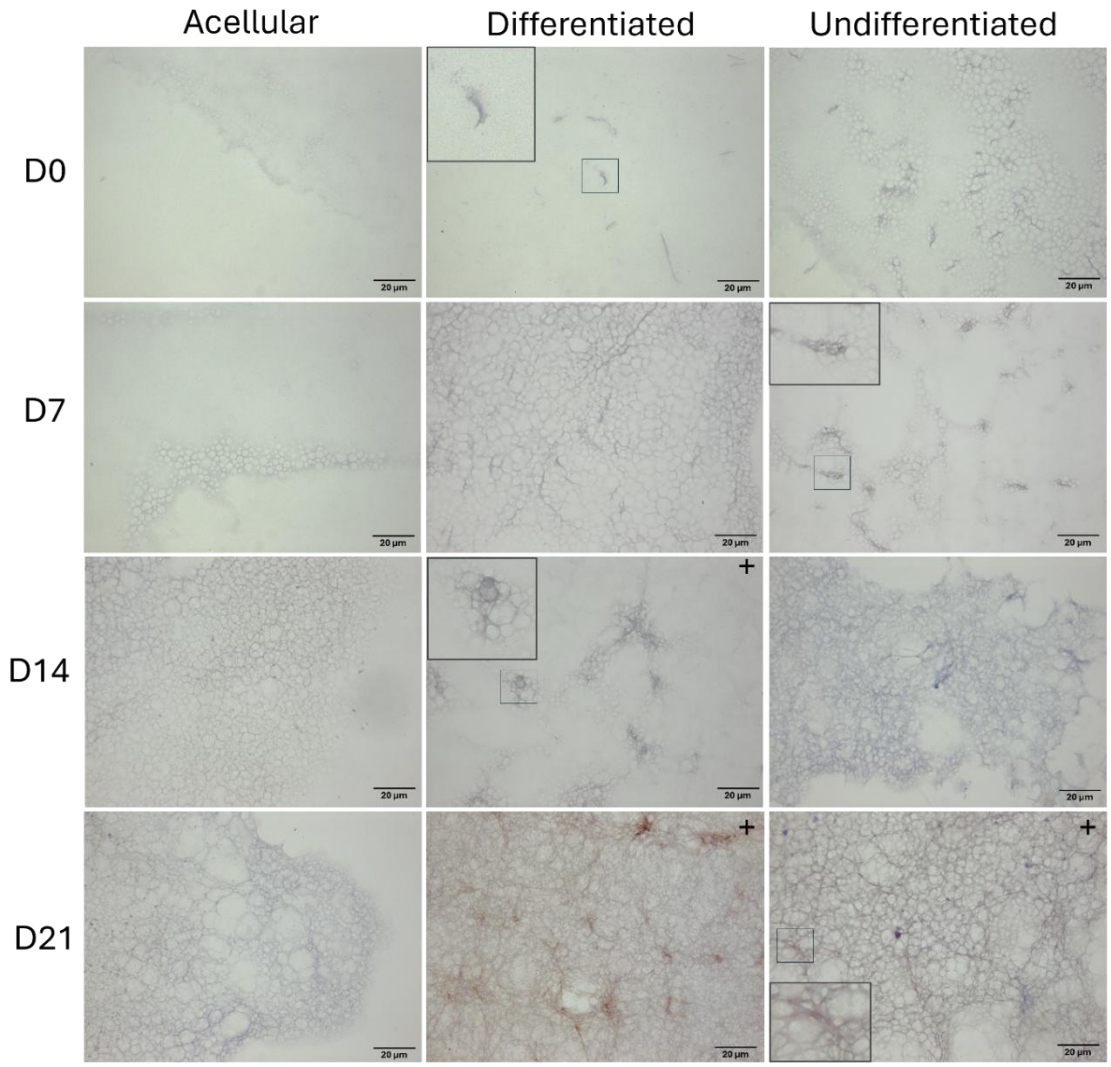

Figure 6.3.22. Osteopontin immunohistochemistry on in-vitro 3D bioprinted constructs over 21 days. *8 µm sections were used; immunopositivity represented by brown staining and indicated (+). n = 3, representative image shown with magnified regions highlighted by black boxes, scale bar represents 20 µm.*

As a marker for proliferation, Ki-67 positivity is detected in both cellular conditions on D0 and D7. On D14, no positivity was detected for MB_D compared to positivity determined for MB_UD. No positivity was detected in either cellular condition on D21, suggesting that MC3T3-E1 have undergone growth arrest (Figure 6.3.23), alluding to the cells entering a resting state by ALP positivity (Figure 6.3.20) (Yoon, H., *et al.* 2025). No positivity could be detected for CAS-3 in all cellular conditions (Figure 6.3.24), showing cells not undergoing apoptosis due to the environment during the 21 days, and further, the bioprinting process does not implicitly put excessive stress on the cells during the mechanical process.

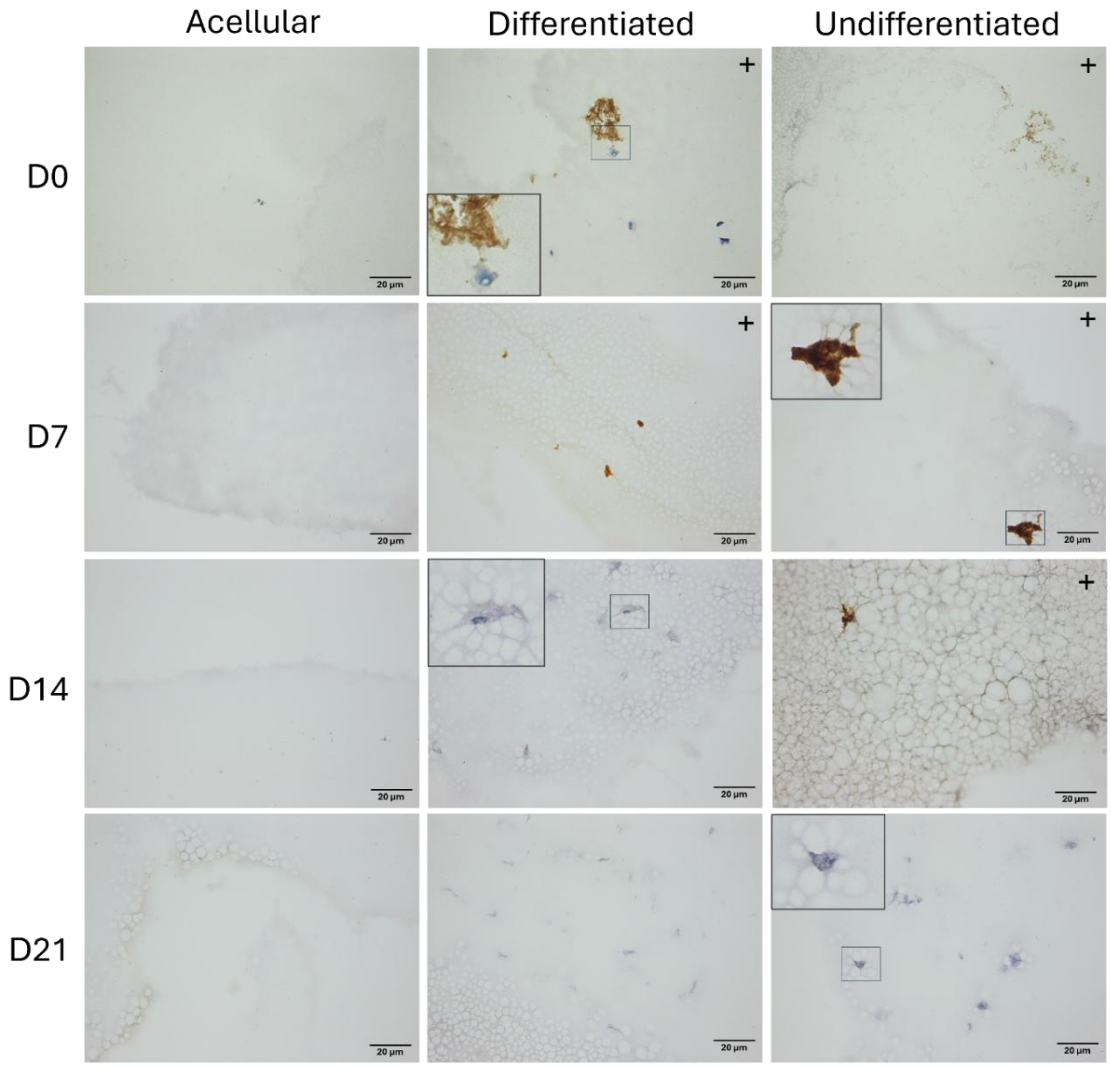

Figure 6.3.23. Ki-67 immunohistochemistry on in-vitro 3D bioprinted constructs over 21 days. *8 µm sections were used; immunopositivity represented by brown staining and indicated (+). n = 3, representative image shown with magnified regions highlighted by black boxes, scale bar represents 20 µm.*

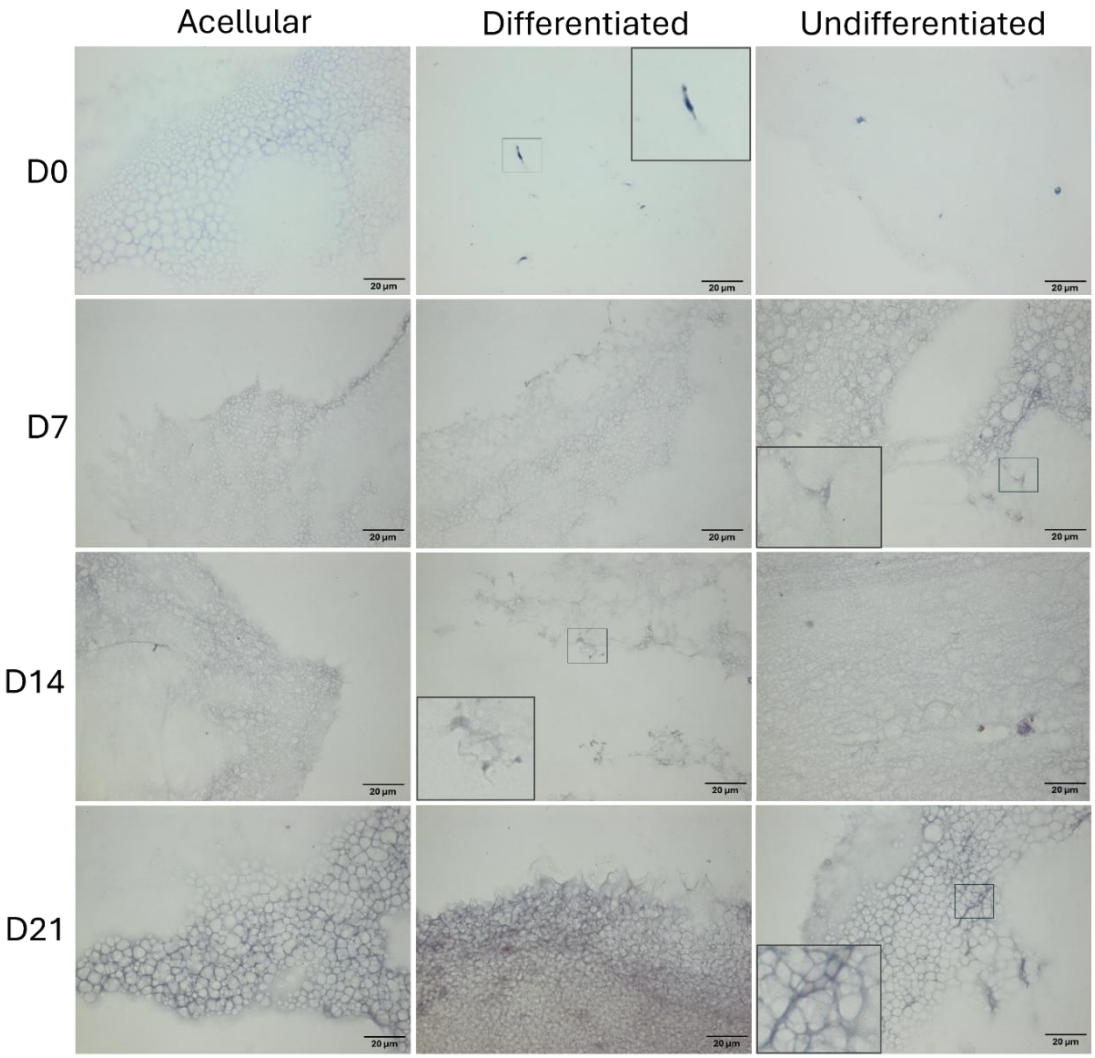

Figure 6.3.24. Caspase-3 immunohistochemistry on in-vitro 3D bioprinted constructs over 21 days. *8 µm sections were used; immunopositivity represented by brown staining and indicated (+). n = 3, representative image shown with magnified regions highlighted by black boxes, scale bar represents 20 µm.*

Quantification of immunopositivity was trialled; however, sections analysed contained low numbers of cells, and such, it was not appropriate to report percentage immunopositivity and thus +/- immunopositivity was reported. Further, the total population of negative cells across all conditions and time-points were difficult to distinguish from the surrounding background matrix.

6.3.6 Porosity of three-dimensional bioprinted *in-vitro* model

The interior morphology of B-gel features an open pore structure (Figure 6.3.25A/B), supporting the observation of an interconnected structure as visualised in all 3D *in-vitro* constructs within histology and IHC (Chapter 6, sections 6.3.4 and 6.3.5). The construct was carbon-coated to facilitate charging, resulting in a high carbon signal (Figure 6.3.25C). Silicon, sodium, magnesium, oxygen and chlorine were detected in various abundance (Figure 6.3.25C).

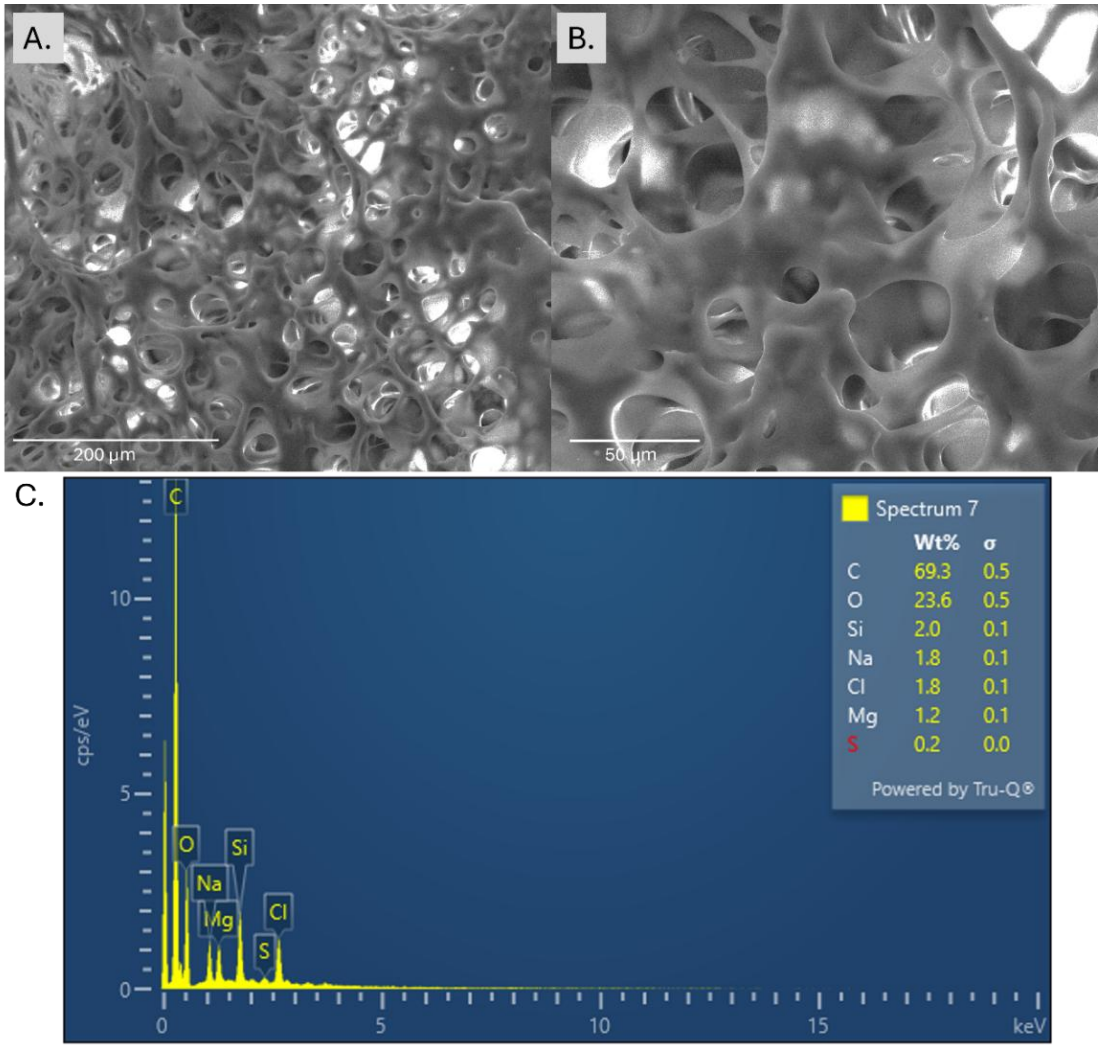

Figure 6.3.25. Scanning electron microscopy and elemental dispersive x-ray spectroscopy analysis of acellular day 21 3D bioprinted b-gel construct. *A) Representative SEM micrograph of B-gel bioprinted construct, B) Region of EDX, C) EDX mapping of carbon, oxygen, silicon, sodium, chlorine, magnesium and sulphur. n = 1, scale bar represents 200 µm (A) and 50 µm (B).*

6.4 Discussion

Biomedical research requires relevant biological models to mimic physiological and morphological dynamics to produce impactful results to drive biological knowledge and innovation. Traditionally, monolayer cell culture is utilised for preliminary *in-vitro* research; however, this method lacks biological complexity. Alternatively, *in-vivo* experimentation using animal models are expensive, biologically variable and morally questionable. In replacement, 3D models are gaining popularity as accepted and innovative preliminary research models. Different forms of 3D models exist, with spheroids, organoids, organ-on-chip and scaffold-based models being most reported (Abuwatfa, W., Pitt, W., & Husseini, G. 2024; Cacciamli, A., Villa, R., & Dotti, S. 2022). The research presented here utilised 3D EBB bioprinting with a bioink of Laptonite® crosslinked co-polymer supplemented with 0.5 mg/ml HAnp and MC3T3-E1 pre-OB secondary cells, with the impact of bioprinting on cellular health explored. MC3T3-E1 cells were treated with +/- ascorbic acid growth media to investigate the osteogenic potential and remodelling of the *in-vitro* bioprinted model.

6.4.1 MC3T3-E1 pre-osteoblast cells as a relevant cellular model

MC3T3-E1 secondary cells are very well characterised and utilised as a iOBs cell model within the bone research community, predominantly for research on differentiation and bone remodelling (Owen, R., & Reilly, G. 2018). Differentiation of iOBs into mOBs is typically divided into three stages: proliferation, matrix maturation, and mineralisation, after the treatment with organic phosphates over a 21-day period (Kartsogiannis, V., & Ng, K. 2004). The phenotype of MC3T3-E1 cells, therefore, in theory could be controlled by culturing in osteogenic conditions to drive differentiation (Izumiya, M., *et al*. 2021). It is under-reported how the environment of culturing MC3T3-E1 cells, e.g. scaffold-bound, can impact the cellular phenotype.

Bone remodelling related marker expression

As a representative Ob model, MC3T3-E1 cells are known to express bone remodelling related markers. In the research presented in this study, immunocytochemistry was utilised to determine protein positivity during the differentiation process, inclusive of cells embedded within the developing mineralised matrix. The bone-related markers

investigated were Runx2, ALP, OPN and OCN, representing different stages of native OB differentiation (Tresguerres, F., *et al*. 2020; Bonewald, L. 2011; Rucci, N. 2008), whereby all produced positivity on all timepoints. Immunocytochemistry is useful to detect the presence of proteins; however, it cannot determine quantitative expression. Yoon (2025) reports an in-depth RNA-sequencing analysis on MC3T3-E1 cells undergoing differentiation, and in summary, genes associated with proliferation are enriched until day 4, and enter matrix formation until day 10, whereby genes associated with mineralisation and matrix maturation are enriched. Compared to the in-depth overview produced by Yoon (2025), Luttrell (2019) previously conducted RNA sequencing and reported an increased expression of Runx2, ALP and osterix proteins in MC3T3-E1 over 28-days of organic phosphate and ascorbic acid driven differentiation. Izumiya (2021) reported from a 7-day study, the supporting results of Runx2, ALP and osterix expression, as well as increased expression of OCN.

In addition, Yoon (2025) highlighted the continued proliferation of MC3T3-E1 cells, suggesting that MC3T3-E1 differentiation is not as linear as previously reported and accepted (Rutkovskiy, A., *et al.* 2016; Quarles, D., *et al*. 1992). In contrast, Galindo (2005) reported that Runx2 expression is cell cycle regulation-related, with forced expression resulting in suppressing proliferation, compared to fluctuating levels (Galindo, M., *et al.* 2005). The finding of Yoon (2025) of continued proliferation after day 4 was seen in the current study, with the positivity of Ki67 throughout in the 3D *in-vitro* models, and notably the increased cellular concentration, visualised in monolayer, throughout despite continuous Runx2 expression.

Matrix deposition

After day 7 in osteogenic conditions for monolayer culture, MC3T3-E1 cells deposit matrix and become embedded (Hwang, P., & Horton, J. 2019), making the cells difficult to detach for downstream analysis without breaking down the secreted matrix. From searching literature utilising MC3T3-E1 cells for downstream applications, many studies are limited to a 7-day duration or simply use MC3T3-E1 cells with non-osteogenic media (Lehmann, T., *et al.* 2023; Wang, Q., *et al.* 2022; Izumiya, M., *et al.* 2021; Hwang, P., & Horton, J. 2019). The matrix deposited from MC3T3-E1 cells consists of an extracellular fibrillar, densely packed collagen network, displaying characteristic native banding of

COL-1 as mimicked in mouse calvaria, as characterised by Addison (2014) by transmission electron microscopy. It could be hypothesised that as cells become matrix-embedded, they begin to align along the collagen fibrils secreted (Keijzer, K., *et al.* 2025; Schaart, J., *et al*. 2024; Hu, S., *et al.* 2022), as an observation from the research presented here recognised a change in cellular alignment over the differentiation period that initiated on day 7.

The matrix composition includes expression of COL-1 and OCN as described by Addison (2014), in agreement with visualisation of positivity over the 21 days in osteogenic differentiation in this study, where COL-1 begins with intracellular positivity; however, after D14, positivity is visually secreted within the matrix. As far as the researchers are aware, no in-depth compositional protein ECM analysis has been completed on the isolated secreted matrix. In a study on isolated MC3T3-E1 cells, Luttrell (2019) reports an array of genes associated with bone matrix marker proteins over a 28-day culture period. In summary, COL-1 and COL-10 expression remains high, COL-2 and periostin decrease during maturity, and dentin matrix acidic phosphoprotein-1 and OPN increase exponentially from iOB to mOB (Luttrell, L., *et al.* 2019).

The difficulty of downstream application is represented by Luttrell (2019), whereby intact sheets of MC3T3-E1 cells embedded in the matrix were lifted off culture plates to either undergo collagenase digestion or cell lysis to investigate the secreted matrix or cellular transcriptomes at different time points, respectively. The matrix deposited by MC3T3-E1 remained important to keep intact for the progressive research presented here, to closely mimic the physiological complex biological environment, and the ossification response of OBs *in-vivo (*Yoon, H., *et al*. 2025; Xiao, G., *et al.* 2009; Franceschi, R., Lyer, B., & Cui, Y. 1994). To achieve this, MC3T3-E1 cells were cultured in glass chamber slides over 21 days to investigate proliferation, matrix secretion and maturation, mineralisation and expression of relevant proteins expressed by cytology and immunocytochemistry techniques. A consideration of immunostaining both cells and matrix results in the limitation of not separating positivity between the cells and matrix (Luttrell, L., *et al.* 2019).

Mineralisation

In addition to matrix secretion, MC3T3-E1 cells are used as a mineralisation model *in-vitro.* Mineralisation does not occur spontaneously; instead, it is dependent on a phosphate source within the culture environment. For experimental cultures utilising the accepted method of the addition of β-GP (Fratzl-Zelman, N., *et al.* 1998), mineralisation begins < day 7 and increases in concentration over the 21 days of differentiation and maturation, resulting in ossification of the secreted matrix (Yoon, H., *et al*. 2025; Semicheva, A., *et al.* 2024; Luttrell, L., *et al.* 2019). Mineralisation in monolayer culture was visualised by AR calcium deposit staining, whereby calcium deposits increase over the experimental duration, as commonly represented (Bernar, A., *et al.* 2022; Hwang, P., & Horton, J. 2019; Zhang, Y., *et al.* 2020; Shah, K., *et al*. 2016).

As discussed by Hwang (2019) mineralisation is variable between replicates and different sub-types, with sub-clone 4 proving to be the most reliable in this study. Often reported qualitative, to quantify the stain requires to be quenched and read via spectroscopy (Bao, S., *et al*. 2023; Hwang, P., & Horton, J. 2019; Zhang, Y., *et al.* 2020), or counted manually, perhaps leading to inaccuracy (Shah, K., *et al*. 2016). AR is often criticised for accuracy (Bernar, A., *et al.* 2022; Addison, W., *et al*. 2014) due to the process of staining calcium regardless of its source, e.g. salts from growth medium, precipitates, protein-bound calcium and ECM mineral (Bonewald, L. 2003; Puchtler, H., Meloan, S., & Terry, M. 1969). Addison (2014) presented an in-depth analysis of the mineral deposition of MC3T3-E1 cells using X-ray diffraction analysis in comparison to the source of mouse calvaria, with similarities in mineral crystallinity reported. Despite the increased knowledge gained from X-ray diffraction analysis, the technique is not as readily available as a histology stain and requires more in-depth analysis. Alternative methods of analysing mineralisation include calcium binding fluorescent dye (Moester, M., *et al.* 2014), ion chromatography (Souter, P., *et al*. 2011), SEM (Grue, B., & Veres, S. 2022), and Fourier-transform infrared spectrometry (Nitschke, B., *et al*. 2024; Addison, W., *et al.* 2014), however, many of these techniques are destructive.

6.4.2 Cell viability and visualisation in three-dimensional bioprinted models

3D bioprinting is challenging, with different factors within the fabrication process impacting cell health and viability. Generally, during the 3D EBB printing process, viability can be affected by temperature, pH, printing pressure, material viscosity and duration of the process. Cell biocompatibility and viability of MSCs (Thorpe, A., *et al*. 2018; Thorpe, A., *et al*. 2016a; Thorpe, A*., et al.* 2016b) and human bone marrow progenitor cells (Cherif, H., *et al*. 2024; Snuggs, J., *et al*. 2023) have been previously shown, when cultured for ~ 6 weeks in laptonite® crosslinked copolymer hydrogel +/- HAnp. As for the HAnp concentration, 0.5 mg/ml was selected based on previous research completed by Thorpe (2016b), who showed sustained viability of primary MSCs in 0.5 mg/ml HAnp, compared to declined viability in 1 mg/ml HAnp over 6 weeks. In addition, *in-vivo* biocompatibility of B-gel was investigated by subcutaneous implantation for 6 weeks in rat femurs with no adverse effects observed (Thorpe, A., *et al.* 2018). As a result of previous literature, no experimentation was undertaken on the viability of MC3T3-E1 cells in B-gel, without the process of 3D bioprinting, and MC3T3-E1 cells were positively identified during the 21-day experimental period.

The porosity of B-gel was previously investigated by Thorpe (2016a) with +/- MSCs. In standard culture conditions, AB displayed a uniform interconnecting porous network with an average pore size of 14 +/- 5 µm, with the cellular condition showing a significant size reduction, > 10 µm. The network of pores remained during the 6-week experimental period; however, shrinkage was observed. It was noted that cells were occupying the porous structure, in addition to the surface of the hydrogel (Thorpe, A., *et al.* 2016a), as visualised in the research presented here by histology techniques. In silk fibroin/COL/HAnp 3D printed porous scaffolds, Liu (2021) reports that MC3T3-E1 cells were visualised inside pores of 450 µm and on the surface. A porous network is vital for cell viability to allow a supply of nutrients, oxygen, proliferation and migration (Hao, X., *et al*. 2023; Annabi, N*., et al*. 2010), with a small pore size beneficial to maintain mechanical and structural integrity, as well as sufficient contact for sufficient oxygen and nutrient transport (Fidkowski, C., *et al*. 2005; Karageorgiou, V., & Kaplan, D. 2005). Small

pore size (<50 µm) can result in reduced cellular proliferation and migration; however, it promotes cell attachment and viability (Murphy, C., *et al.* 2010).

Reviewing the literature provides no consensus on the ideal pore size for scaffold morphology for osteogenic applications. As evaluated by Mukasheva (2024b), a broad range of 10 – 1,500 µm pore sizes is reported in different hydrogel systems with an osteogenic application, due to differences in methodologies and experimental questions, with 100 µm being the average size investigated (Huang, D., *et al.* 2025; Mukasheva, F., *et al.* 2024b; Trifonov, A., *et al*. 2024; Karageorgiou, V., & Kaplan, D. 2005). Further, Mukasheva (2024a) reported a bioprinted *in-vitro* hydrogel scaffold that consisted of a pore gradient of 10 – 300 µm, by utilising three different concentrations of gelatine and Alg bioinks. MSCs were used and showed an improvement in cellular proliferation and mineralisation with a pore gradient compared to a homogenous pore size of 150 µm (Mukasheva, F., *et al*. 2024a). Future work could include an investigation into the impact of increased pore size on B-gel, and the resulting osteogenic potential, cellular population and 3D fidelity. It is hypothesised that increased pore size will further reduce fidelity and structural integrity of the resulting 3D printed *in-vitro* construct; however, the cellular action will be improved (Cavallo, A., *et al.* 2025).

EDX analysis was also undertaken by Thorpe (2016a) and Thorpe (2016b), whereby calcium and phosphate peaks were observed in cellular conditions. In acellular constructs, similar peaks of silicon and magnesium were identified (Thorpe, A., *et al.* 2016a), as represented in this study. Silicon and magnesium are identified due to the presence of laptonite® nanoparticles, whereby the synthetic composition is hydrous-nano magnesium silicate particles (Stealey, S., *et al*. 2023). Alternative studies by Samchenko (2024) and Zhang (2019) have shown similar elemental peaks from hydrogels containing laptonite®. The limited SEM/EDX experimentation in the research presented here does not allow conclusions to be drawn on the potential effect of extrusion pressure on the porosity of hydrogels; however, the impact is theorised to be minimal due to bioprinting in a transitioned gel state (Trifonov, A., *et al*. 2024; Annabi, N., *et al.* 2010).

Printing pressure can result in varied imposed stress on the cell-containing bioink, and if the loading capacity of the cell is exceeded, the cell undergoes irreversible damage, resulting in cell death (Xu, H., *et al.* 2022). The viscosity of the material directly impacts

the extrusion pressure required; however, shear-thinning bioinks are typically utilised to minimise extrusion pressure (Riberio, B., *et al.* 2016). No definite pressure range can be defined for bioinks, or whether it will result in cell death. Valon (2019) summarised that different cells undergo apoptosis under different mechanical loads, with neuronal cell death induced by 0.2 mPa, whereas lymphoblasts undertook 85 mPa before apoptosis. For a 3D EBB application, Rahman (2025) reports that an increase in printing pressure from 50 to 100 kPa resulted in a higher degree of cell death of human bronchial epithelial cells bioprinted in a sodium Alg-carboxymethylcellulose bioink. Similarly, Fakhruddin (2018) reports an increase in cell death of primary fibroblasts in pluronic-127 from a range of 3 to 45 kPa. For bone-specific application, Loi (2023) reports a range of 80 – 125 kPa for continuous filament printing with a methyl-furan functionalised gelatine and chitosan bioink supplemented with MG-63 cells, with no detriment to viability compared to 55 – 80 kPa. Finally, Dutta (2021) printed various concentrations of Alg and gelatine bioinks with a pressure range of 100 – 300 kPa with no detriment to human MSCs. The printing pressure utilised in this study ranged from 40 – 60 kPa, with no detrimental impact on viability visualised, and a suitable filament fidelity (Chapter 5).

Cell visualisation and general imaging in 3D is challenging. Traditional microscopy techniques are fundamentally suited for thin, optically transparent cultures compared to thick, light-scattering 3D cultures that are more likely to move and distort images (Schneckenburger, H., & Richter, V. 2021; Graf, B., & Boppart, S. 2010). Confocal microscopy is commonly utilised to obtain images of 3D structures (Masaeli, E., & Marquette, C. 2020), however, for the research presented here, the height of the 3D bioprinted *in-vitro* constructs exceeded the maximum focal plane. In replacement, a cell tracker was utilised to good efficiency to assess the presence of viable cells over the duration of the experimentation; however, this method did not provide information on cell death, or total number.

Calcein AM and PI fluorescent staining are the most reported methods of quantifying populations of viable and dead cells in 3D bioprinted models that are not osteogenic (Lu, J., *et al.* 2022; Muthusamy, S., *et al*. 2021; Gu, Y., *et al.* 2018). Limited osteogenic 3D bioprinted models have been assessed by live/dead stain, including Wang (2016) whereby only day 1 and day 7 are reported from the 21-day study, and features intense

background staining of the bioink. Chen (2023) published similar results of primary OBs within a bi-phasic scaffold and only represented cell viability for day 1 and day 7, from the 21-day study. Finally, in a recent study, Leeuw (2024) reported the mineralisation of human bone-derived bioprinted lattices with primary OBs and represented viability of only day 1 and day 15, in the 71-day total study. It was discovered that calcein AM is not a suitable stain to use on mineralised *in-vitro* models, as it binds to calcium ions and emits fluorescence (Serguienko, A., *et al*. 2018; Hale, L., Ma, Y., & Santerre, R. 2000), thus providing insight into why the method did not work for the research conducted to assess viability. Alternatively, calcein AM can be utilised to assess mineralisation. For example, as shown by White (2021), the study utilised calcein AM and AZ to assess mineralisation in hydrogel microspheres undergoing differentiation and concluded that calcein AM produced more consistent results. It is not reported how the researchers segmented cellular response to mineralisation (White, K., *et al.* 2021).

6.4.3 Extracellular matrix environment of the bioprinted *in-vitro* three-dimensional bone construct

Native bone requires weeks to months, often years, under physiological loading and nutrient availability to mature and develop its mechanical properties, complex matrix composition and unique architecture (Satoh, M., & Hasegawa, Y. 2022; Pines, M., & Hurwitz, S. 1991). As widely accepted, and shown in this study, in comparison to 2D monolayer culture, the 3D *in-vitro* matrix environment is complex. However, mineralisation and matrix secretion of MC3T3-E1 cells undergoing differentiation occur more slowly compared to 2D due to the spatial separation of the cells within the 3D porous environment. An increase in cell concentration could improve cellular action compared to that used in this study. The observations were similar to Lv (2024), with MC3T3-E1 cells and a bioink of Alg, gelatine and HAnp, where increased mineralisation was visualised in 2D compared to 3D, however, cell viability decreased drastically after 21 days in culture for the 2D culture (Lv, X., *et al.* 2024). In benefit, this enriches the scaffold-based environment and allows remodelling of the biomaterial itself long-term, compared to only matrix deposition as visualised in 2D. COL-1 was positive in the 3D *in-vitro* constructs for +/- ascorbic acid conditions for the experimentation period, enriching the 3D environment with matrix deposition, and further represented by MT. In addition,

ECM composition is shown to increase in complexity with the detection of proteoglycans and mucins (Abbey, T., *et al.* 2016b). An enriched ECM is crucial for mimicking bone, supporting the scaffold, assisting in cell attachment and stability (Fan, L., *et al.* 2023).

Interestingly, culturing MC3T3-31 in the B-gel bioprinted scaffold without ascorbic acid conditions appeared to initiate differentiation of the iOBs into mOBs. The ascorbic acid-free condition began to reflect the matrix deposition and calcification of the differentiation-driven scaffolds, with an estimated 7-day delay. This is particularly emphasised in AR histology as well as runx2, OPN and Ki67 IHC. In two material-based studies, Mcbeth (2017) and Persson (2018) demonstrated the ability to drive differentiation of primary OBs and MSCs on titanium surfaces coated with GelMA and PLA supplemented with HA, respectively. In particular, Persson (2018) compared the mineralised matrix produced compared to 2D monolayer culture and reported enhanced production of mineralised matrix on the 3D scaffold compared to 2D monolayer culture after 35 days. It is known that environmental stiffness can begin to drive changes in cellular phenotype, such as MSCs into adipocyte or OBs phenotype based on environmental stiffness (Zonderland, J., & Moroni, L. 2021; Gonzalez-Cruz, R., Fonseca, V., & Darling, E. 2012). In native bone, the stiffness of the ECM influences the phenotype of OBs, with stiff ECM promoting differentiation compared to a soft environment (Zhu, S., *et al.* 2024; Zhang, T., *et al.* 2017).

To fully understand the trigger of differentiation based on environment, further experimentation on the material over the culturing period would be required to be completed, such as dynamic mechanical analysis over time to measure material elasticity (Lopez-Seerano, C., *et al*. 2024). Mechanical strength and the ability to withstand load are vital factors of native bone, with micro- and macro-structure providing strength and driving bone maturation; therefore, should be a consideration when developing an *in-vitro* bone model (Leeuw, A., *et al.* 2024; Revete, A., *et al.* 2022). The elastic modulus for bone is within the range of 17 – 20 GPa for Cb, and 10 GPa for Tb for humans (Rho, J., *et al*. 1993), and Cb of 1.58 GPa and Tb of 0.55 GPa for mice (Asgari, M., *et al.* 2019; Thiagarajan, G., *et al.* 2018). Thorpe (2016b) completed dynamic mechanical analysis on B-gel discs over 6 weeks, with the elastic modulus of 0.5 mg/mL HAnp and primary MSCs at day 0 being higher than the acellular control at 0.99 MPa, with a significant difference

observed in the MSC gels after 6 weeks 2.03 MPa, compared to acellular conditions, which remained stable (Thorpe, B., *et al*. 2016b). Hydrogel materials, specifically for the application of 3D EBB, are required to have a minimised modulus to allow extrusion (Schwab, A., *et al.* 2020), therefore, the material increasing in strength during culturing and differentiation is beneficial to mimic a bone over time, and this results from increasing the 3D *in-vitro* matrix complexity.

6.4.4 Quantification of *in-vitro* three-dimensional bone construct mineralisation

To determine remodelling and ossification of the model a combination of histology and micro-CT imaging was employed. Histological stain VK is an unreliable histological stain to complete alone, producing inconsistent mineral staining of MC3T3-E1 cells due to not staining apatite mineral, and only being specific for phosphate, as discussed by Bonewald (2003). B-gel features synthetic HAnp incorporated at a standard concentration, with further mineral deposition from MC3T3-E1 undergoing differentiation due to phosphate availability. In addition, as mentioned previously (Section 6.4.1) AR is also criticised (Addison, W., *et al*. 2014), however, these techniques are still the gold standard to report mineralisation (Bao, S., *et al*. 2023; Zhang, Y., *et al.* 2020; Hwang, P., & Horton, J. 2019), as visualised in the B-gel scaffold. Micro-CT imaging facilitated an in-depth analysis of the density, volume and individual particle analysis of the *in-vitro* bone constructs. The analysis of 3D bioprinted active *in-vitro* constructs comprised of hydrogels are not commonly reported without the addition of contrast-enhancing materials (Aminu, A., *et al.* 2022; Self, T., *et al.* 2020; Heimel, P., *et al*. 2019), or fixed before imaging (Nitschke, B., *et al.* 2024; Olaret, E., *et al.* 2021; Cengiz, I., Oliveria, J., & Reis, R. 2018), therefore by utilising this imaging technique a more novel approach of non-destructive structural and composition analysis can be completed to compliment SEM, and X-ray differentiation analysis (Grue, B., & Veres, S. 2022; Addison, W., *et al.* 2014).

Micro-CT imaging allowed the visualisation of particle distribution of the total 3D bioprinted construct during the entire experimental period. Unsurprisingly, the differentiation group increased in TMD overall, with an increase in particle number detected by micro-CT. The undifferentiated group also increased in TMD overall; however, it reduced compared to the differentiated group. Acellular constructs

decreased in TMD overall, perhaps suggesting leaching of the supplemented HAnp into the surrounding growth medium over the 21 days. It can be hypothesised for future directions, culturing the *in-vitro* constructs for longer durations, such as the 10-week study completed by Leeuw (2024) and > 1-year NC3R-funded project by Finlay (2024) would further represent increased mineralisation of the B-gel *in-vitro* constructs. Leeuw (2024) imaged 3D bioprinted lattices by micro-CT; however, a resolution of 34.5 µm was used, limiting the information gained on individual mineralisation. Reporting a mineral density of the entire gelatine/Alg/graphene lattice structures with primary iOBs showed an exponential increase from day 7 to day 70, whereby the entire lattice structure was mineralised by the endpoint. The largest increase in mineralisation occurred on day 7 to day 14 (Leeuw, A., *et al.* 2024), as reflected in the differentiation of 3D bioprinted lattices in this study.

Despite the wealth of information produced, the limitations of micro-CT *in-vitro* analysis should be highlighted. Micro-CT is a powerful imaging technique; however, resolution is limited to the selection of the user when imaging mm-sized objects. In this case of this study, the *in-vitro* construct was required to remain sterile to ensure that each time-point was matched, resulting in limited depth of resolution to facilitate appropriate storage of the construct during imaging (Plessis, A., *et al.* 2017). Consequently, all mineralised particles in the secreted matrix may not have been captured within the spatial resolution of 9 µm (Ghani, M., *et al.* 2016). As qualitatively visualised in both 2D and 3D AR results from this study, the mineral nodules produced are varied in size and continue growing throughout the 21-day period, however, often appear less than 9 µm in size prior to day 14 (Zhang, X., *et al*. 2020) and therefore this method does not capture the complete early-stage calcification. Additionally, the processing, imaging and exposure to X-rays were required to be minimised, to not negatively impact cellular viability. Long exposure to X-rays can damage DNA and cellular structures (Dukak, J., *et al.* 2016), therefore, dose management was minimised (Meganck, J., & Liu, B. 2016). No detrimental effects of X-rays were noted in this study; however, a more in-depth analysis would be required to conclude.

In addition, at 37 °C PNIPAm surfaces within the B-gel composition are hydrophobic and promote cellular growth; however, when the temperature is reduced to 20 °C, PNIPAm

becomes hydrophilic, promoting the detachment of cell sheets (Sanzari, I., *et al.* 2020). For this purpose, the temperature of the rooms and analysis was kept above 20 °C to attempt thermal stability of the construct, in addition to pre-warmed media and processing in a heated glove box. However, a clear reduction of volume can be visualised by micro-CT volume analysis, perhaps suggesting the construct is losing water content due to the drop in temperature. This phenomenon did not allow micro-CT fidelity analysis to be completed at the constructs, simply due to the construct dropping in temperature, resulting in a conformational change due to the amphipathic nature of the material (Ferreira, N., *et al.* 2018). Future work would be to include a heated stage to control micro-CT chamber temperature, to improve thermal stability (Boerckel, J., *et al*. 2014)

6.4.4 Conclusion

Bone is a dynamic organ, with a complex matrix composition and macro/micro-architecture that needs to be taken into consideration when developing a suitable *in-vitro* bone model replacement for early-stage biomedical research. The secondary iOB cell line MC3T3-E1 is frequently used as a representative OB model and is researched frequently in a 2D monolayer state. *In-vitro* 2D monolayer studies are criticised for the lack of physiological relevance, with 3D *in-vitro* studies becoming preferable in comparison.

In this study, a laptonite® co-polymer with 0.5 mg/ml HAnp bioink (B-gel) was optimised for 3D bioprinting with a lattice structure, in combination with the cell line MC3T3-E1. The extrusion bioprinting process had no significant negative impact on the cell viability of MC3T3-E1 cells during the 21-day experimental period, representing biocompatibility. By culturing in osteogenic media, compared to the laptonite® co-polymer bioprinted scaffold alone, mineral deposition was increased over the 21-day experimental period as detected by the total density and individual particle analysis of the 3D bioprinted constructs via non-destructive high-resolution micro-CT. However, the 3D environment alone was visualised to trigger differentiation. The matrix of the 3D *in-vitro* constructs undergoes increased complexity within the porous morphology, as visualised by histological and IHC techniques, whereby the phenotype of the MC3T3-E1 can be visualised and represents the transition from immature to mOBs.

Compared to traditional 2D monolayer culture, the proposed 3D *in-vitro* model more closely mimics the complexity of native bone by representing physiological remodelling by matrix deposition and gradual mineralisation. However, there is still a realistic difference between the *in-vitro* 3D model proposed within this study compared to native bone, in particular, the ability of the biomaterial used in this study to achieve accurate bioprinted morphometry and density, however, it is hypothesised that an extended culture period would further improve ossification of the 3D bioprinted polymer structure. In addition, the model requires further optimisation by the inclusion of different primary cellular populations to closely mimic the closely controlled remodelling balance visualised in native bone.

Chapter 7 – General discussion and future directions

7.1 Summary of results and impact

The work presented in this thesis investigated the methodology required to translate *ex-vivo* murine bones imaged by high-resolution micro-CT into 3D printed bone models. This included the development of an *in-vitro* bioprinted model and the evaluation of the *in-vitro* model fabrication process for a final comparison with native *in-vivo* murine bone. The outcome of this research contributes to the broader understanding of 3D *in-vitro* model fabrication for animal replacement for early-stage biomedical studies. Particularly for the context of defining the process of capturing high-resolution 3D objects and transformation into 3D printable models through CAD software, and the considerations required for a 3D extrusion-based bioprinted high-fidelity *in-vitro* model.

Chapter 2 outlined native *ex-vivo* murine bone architecture and composition, and the natural biological variance between sexes and species for bones of interest: tibia, femur and VB. In addition, morphological values of Tb and Cb were assessed, whereby the median values were used for the development of a biomimic 3D bone model in chapter 3. The binarised *ex-vivo* bone models underwent parameter and algorithm selection by exporting 3D models from CTAn software, to produce a reduced file size STL. The 3D models still encompassed the detail captured by micro-CT imaging and underwent *in-silico* rendering in CAD software to produce 3D models suitable for the application of FDM, SLA and EBB. Both FDM and SLA 3D models were printed, with SLA concluded as the most suitable fabrication method for the generation of complex structures. In summary, the research in chapters 2 and 3 produced an informed workflow for the process of translating micro-CT imaging into 3D models, for the application of *in-vitro* 3D bones. The workflow was evaluated within the wider bone research community in chapter 4, by the delivery of a workshop at a national conference, which allowed participants to successfully learn the skills developed by this research project.

With a focus on the process of EBB, chapter 5 evaluated the composition, fidelity and printability of two commercially sourced bioinks, TissueFAB™ and Bone GelXA, as well as an in-house generated hydrogel that was optimised for the process of bioprinting, Laponite® crosslinked poly (N-isopropylacrylamide, N, N'-dimethylacetamide) co-polymer containing HA nanoparticles, known as B-gel. TissueFAB™ was removed from the study due to inappropriate crosslinking requirements, and Bone GelXA was

discovered to suffer from high batch-to-batch particle inconsistency that altered flow behaviour and resulted in an unsuitable product for the process of EBB. B-gel was shown to have a consistent composition with a pseudoplastic shear thinning behaviour; however, extrusion resolution compared to the original STL models was not accurate and required further optimisation. To improve structural fidelity, a microparticle support slurry was successfully generated and characterised as a viscoelastic material with a non-Newtonian flow profile of a pseudoplastic and was shown to improve the structural complexity of the 3D bioprinted models. Despite the improvements of structure from the micro-particle slurry, B-gel was concluded as unsuitable to achieve the complex structure of the rendered *ex-vivo* tibia.

Finally, chapter 6 incorporated the iOBs cell line, MC3T3-E1, into B-gel and printed into a scaffold structure. The *in-vitro* model was cultured for 21 days, alongside acellular controls, and +/- differentiation media conditions. Models were evaluated for native bone remodelling associated processes in comparison to traditional 2D *in-vitro* monolayer models. Cellular viability was maintained, with the pneumatic process of bioprinting showing no negative impacts. Micro-CT was utilised to evaluate mineral deposition of the *in-vitro* model for the experimental duration, whereby an increase in density was visualised in differentiated media conditions. Interestingly, the *in-vitro* B-gel scaffolds without differentiation media initiated the remodelling process by the scaffold alone. In addition, the composition of the model was evaluated and shown to increase in matrix complexity. B-gel as a bioink was determined to be a suitable biomaterial to mimic bone; however, fidelity and resolution of the material and bioprinting capability require improvement to mimic the original complex STL model.

7.2 The ongoing challenge of the fabrication of biomimic complex in-vitro bone three-dimensional models

Ultimately, the limitations of the flow behaviour, and structural stability of biomaterials for the application of 3D EBB (Bakhtiary, N., Liu, C., & Ghorbani, F. 2021; Riberio, A., *et al*. 2017; Paxton, N., *et al.* 2017) are reflected in the research presented in this study, despite the improvements of using a microparticle support slurry to achieve complex architecture. Alternative bone *in-vitro* models focus on the fabrication of a scaffold structures (Xiao, L., *et al*. 2024; Tang, M., *et al.* 2022; Luttrell, L., *et al.* 2019) to evaluate

the biocompatibility and printability of various biomaterials, whereby minimal studies attempt to bioprint the complex architecture of bone, inclusive of Cb and Tb. It is true, many studies have intentions of clinical human application and therefore, overall architecture is not a focus, compared to micro/nano-structure (Jiao, J., *et al.* 2023; Martinez-Garcia, F., *et al*. 2022; Ahmed, E. *et al.* 2013), however, for studies with the application of *in-vitro* bone model development, the simple scaffold structure does not replicate *in-vivo* bone morphometry.

It remains a challenge, and various approaches of fabrication with different materials are required to determine if the complex architecture, inclusive of Cb and Tb, is able to be bioprinted with the current available 3D extrusion-based technology and the resolution limitations. Studies, as previously mentioned (Kim, M., et al. 2023) have been able to achieve filament resolution of < 300 µm for simple structures, whereas > 400 µm range is more commonly reported, dependent on nozzle width (Riberio, A., *et al.* 2017; Paxton, N., *et al.* 2014). As far as the researchers are aware, no study has been able to achieve supported over-hang structures with biomaterials, from the method of 3D EBB. This is likely the consequence of hydrogel based bioinks, whereby the compositions of the materials are predominantly water, and lack structural stability (Tibbitt, M., & Anseth, K. 2009). Alternative materials, such as bioink cements, could have suitable mechanical strength, and structural stability over time, and resist the natural deformation of gravity (Ombergen, A., *et al.* 2023; Sarabi, M., *et al.* 2023). In addition, and a more likely approach would be culturing the 3D extrusion bioprinted bone structure within the support matrix for a long period of time (Afghah, F., *et al.* 2020), and encourage matrix deposition and calcification, to fix the physiological structure, in a similar approach to Leeuw (2024), in the 71-day total study whereby the entire bioprinted construct was mineralised, capturing the initial CAD structure.

7.3 Future directions

The research presented in this thesis outlines the methods and considerations required for the development of a 3D *in-vitro* model based on *ex-vivo* bone; however, further optimisation and development are required to produce a reproducible and accurate *in-vitro* bone bioprinted model. In addition, further applications could be conducted to build on the methodology outlined in this thesis.

7.3.1 The three-dimensional standard tessellation model and computer assisted design rendering process

Various methods could be applied to further develop the *in-vitro* bone model generated. It can be concluded that the process of transformation of micro-CT imaging to a rendered STL model is appropriate and successful for use within this study, as accurate bone 3D models, inclusive of Cb and Tb, were able to be printed by the processes of FDM and SLA with direct similarity to the input *ex-vivo* bone. Future work and further development could include increasing the availability of 3D bone STL models, inclusive of the complex structures of Cb and Tb, as models only replicating Cb structures of total bones are widely available (Nguyen, P., *et al.* 2023; Valls-Esteve, A., *et al.* 2023; Leordean, D., *et al.* 2021; Grassi, L., *et al*. 2011), for disease mimicking bones such as osteoporosis (Frank, M., *et al*. 2021; Goldring, S. 2016; Tan, S., *et al.* 2014), or expanding the selection of species to include larger mammals which a stronger relevance to human architecture, such as monkeys, dogs or pigs (Hillier, M., *et al.* 2007; Aerssens, J., *et al.* 1998). Ultimately, human architecture with primary cells to generate a fully humanised model would be the ideal end point fabrication; however, this would require further model rendering to address broken tessellation, and reduction of file size to make it appropriate for processing, as well as optimisation of scanning parameters of the bones for capturing information by micro-CT.

Determination of accuracy of the fidelity of the printed 3D models (FDM, SLA and EBB) by micro-CT imaging compared to 2D was attempted, however due to various reasons, such as thermo-responsive nature of the B-gel material, as well as time constraints (FDM and SLA), experimentation was not fully completed. The accuracy in fabrication is important because deviations will have a direct impact on functionality of 3D models, for example, resulting in misalignments. In theory, the micro-CT imaged models could be

evaluated in a 3D space for accuracy in comparison to the original CAD model by either superimposing a slice of the imaged model onto the CAD 3D model in image processing systems such as ImageJ as theorised by Okamoto (2024) or 3D Geomagic control X software as utilised by Abad-Coronel (2023). Alternatively, utilising CTAn measurement tools, or once again superimposing the models to the original *ex-vivo* bone models, for complete analysis of *ex-vivo*, to CAD, to 3D model accuracy.

In addition, with the ever-increasing application of artificial intelligence (Ai), 3D STL bone models could be generated with defined prompts based on bone morphometry such as Tb.N and Tb.Sp, in Ai tools. For example text to 3D; open AI's point-E, NVIDIA's GET3D, and DeepMind's Alpha3D interfaces, alternatively image to 3D tools such as Bambu lab or Sloyd's tools (Scan2CAD, 2024). Ai is beginning to be integrated into CAD software to assist in the rendering process, such as SolidWorks (Solidworks, 2025), which may assist in the detection of tessellation errors or unconnected structures, making the rendering process more efficient for users (PTC, 2025; Autodesk, 2025). It would be interesting to validate Ai output STL models, compared to the user-defined 3D STL bone models generated, for example, in this study, to assist in pushing innovation and accessibility of relevant 3D biomimetic models, and driving the future of tissue engineering possibilities.

7.3.2 Bone relevant biomaterials and translation into functional bioinks

The major theme of research within the field of tissue engineering and the development of relevant *in-vitro* models remains the investigation of relevant biomaterials, including the composition, printing conditions, and fabrication processes. In the research presented here, two commercially available bioinks were selected for incorporation within the method development to focus on achieving complex architecture of bone, inclusive of Cb and Tb structures, and ease of accessibility for different research groups. Ultimately, batch-to-batch inconsistencies and unknown compositions did not allow for a reliable application. Perhaps, initial focus and time on the in-house biomaterial could have allowed for the properties to be tuned, to alter the hydrogel to have different flow behaviour and mechanical properties (Davern, J., *et al.* 2024; Boyes, V., *et al.* 2021) and change resulting filament fidelity to be more accurate, to allow development of the *ex-vivo* bone architecture.

As a material for the basis of mimicking bone, it was shown in this study, as well as previous research (Thorpe, A., *et al.* 2016b), that B-gel is a suitable biomaterial to promote osteogenesis with OB-related cell phenotypes. To improve the complexity of the bioink for this study, MC3T3-E1 cells underwent differentiation to produce a COL-based ECM matrix. The matrix was not fully characterised in terms of composition as this had already been described previously (Luttrell, L., *et al.* 2019; Addison, W., *et al.* 2014). Alternative methods of increasing ECM complexity could include utilising decellularised bone-derived ECM incorporated into bioink (Lee, J., *et al*. 2020), or inclusion of COL-1 directly (Alaman-Diez, P., *et al.* 2023), however, these materials naturally are thermally crosslinked (Kajave, N., *et al.* 2019), therefore inclusion would alter the printing parameters, material behaviour and require further printing optimisation.

A limitation of B-gel for the application of a bioink is the thermo-responsive nature of the material; alterations of temperature result in morphological changes (Ullah, F., *et al*. 2015). Ultimately resulting in deviation from the original STL model, perhaps also accounting for volume changes over time as visualised in this thesis and not allowing accurate fidelity assessment of the 3D model. To resolve this, a heated environment (37°C) would be required for the entirety of the fabrication process, and any experimentation applied to the *in-vitro* bone constructs to reduce temperature fluctuations.

The biomimic bone model, based on the 3D rendered *in-vitro* model did not functionally print as intended. Perhaps due to the bioink itself, or the bioprinting vessel was not appropriate for the dimensions of the CAD model. Future work would include different vessels, such as petri-dishes with increased depth and increased length nozzles to facilitate.

As previously discussed in Chapter 5, further optimisation of the microparticle slurry is required to produce uniform, consistent spherical particles. It is hypothesised that output morphology is determined by experimental stopping temperature, compared to time of stirring, which was used for most of the slurry generation. To test this, a controlled heated environment should be used for the duration of stirring, with particle morphology analysis completed for different technical repeats to determine a suitable temperature range. Further, the size of spheres could be investigated to be tunable, by

altering the mixing speed. For example, an increase in rotation speed of the impeller would result in reduced particle size due to an increase in particle collision (Herman, A., *et al*. 2021).

7.3.3 *In-vitro* cell selection, and loading regime to mimic the bone microenvironment

The resulting *in-vitro* 3D bioprinted bone model represented a dynamic environment compared to traditional monolayer models and provided evidence of the differentiation process being driven by environment alone compared to traditional osteogenic media (Hwang, P., & Horton, J. 2019; Franceschi, R., Lyer, B., & Cui, Y. 1994). To further build characterisation of the *in-vitro* 3D bone model, a fourth condition of mechanical loading would be introduced. Load-bearing is an essential characteristic of bone (Hunziker, E. 2018), with bone density changing in response to mechanical load, referred to as Wolff's Law (Bonewald, L. 2011). OBs are not known as the primary mechanosensing cells, however various studies have reported that OB inclusive 3D *in-vitro* models undergoing load have resulted in increased density, and linked to further differentiation into OCs, which are considered as the primary mechanosensing cell in bone (Pragnere, S., *et al.* 2024; Leeuw, A., *et al*. 2024). Regardless, dynamic mechanical analysis should be completed on the 3D bioprinted constructs to further investigate the viscoelastic properties (Uysal, B., *et al.* 2025), both at fabrication and during the experimental period. Experientially, mechanical analysis would be completed by 3D *in-vitro* models placed appropriately under load, by utilising similar approaches to Segovia-Gutiérrez (2025), Choi (2025) and Rotbaum (2019), with comparison of model density and cellular phenotype back to the static cell culture methods used in this thesis.

MC3T3-E1 cells, as previously mentioned, were an attractive cell source for the research conducted in this thesis due to the ability to scale up cell number due to immortalisation (Sudo, H., *et al.* 1983), availability (Hwang, P., & Horton, J. 2019), well previously characterised (Yoon, H., *et al*. 2025) and the ability to drive differentiation for osteogenesis (Metzger, W., *et al.* 2025). However, to achieve a more physiologically reflective *in-vivo* environment, primary-derived OBs implementation should be considered (Piwocka, O., *et al*. 2024; Belk, L., *et al*. 2020) once the model reaches a higher level of accuracy and reproducibility. In addition, co- and tri- culture methods

should be considered (Bernhardt, A*., et al.* 2021; Borciani, G., *et al.* 2020; Owen, R., & Reilly, G. 2018 Clarke, M., *et al*. 2013), however once again, this comes with high complexity if to function *in-vitro*, and therefore should only be implemented once the 3D structure aspect of the *in-vitro* model is more reliable and characterised. Different approaches could be utilised, such as incorporating bone cell populations in different bioink compositions for printing with multiple printheads. For example, OCs could be strictly used to print the Cb, whereas OBs would be printed as the Tb structure, and OCLs seeded onto the surface of the 3D *in-vitro* structure. Similar approaches have been undertaken by Moxon (2024) and Kibble (2025) for bioprinting of the intervertebral disc regions, Moakes (2021) with tri-layered bioprinted skin, and Berg (2021) by generating a multi-cell scaffold to mimic the lungs.

At the core, the fabrication of early stage biomedical *in-vitro* 3D bone models that mimic the dynamic environment of bone facilitates further understanding of *in-vivo* biological dynamics, in normal physiology and disease, without the requirement for unnecessary *in-vivo* experimentation. The fabrication approach undertaken in this research period solely focused on normality, by representing healthy mature bone; however, this could be altered to reflect a diseased state and is open-ended for other researchers based on their research interests. Potential applications include assessing drugs, such as bisphosphonates, to drive mineralisation *in-vitro* to mimic osteoporosis treatment (Breathwaite, E., *et al*. 2020; Sieberath, A., *et al.* 2020), or including malignant-associated cell lines to mimic osteosarcoma and metastasis (Menshikh, K., *et al.* 2025; Fischetti, T., *et al*. 2021; Datta, P., *et al.* 2020).

7.4 Concluding remarks

The contribution to knowledge demonstrated in this thesis included the evaluation of the process of translating micro-CT imaging into 3D printable models that will allow the generation of biomimic 3D models to be generated for the wider tissue engineering and bone community. In addition, the suitability of three bioinks was evaluated in terms of composition and printability for the aim of bioprinting complex structures, with an emphasis on micro-CT to facilitate compositional and structural analysis. To assist in bioprinting complex structures, an in-house microparticle slurry was generated and characterised, improving the accessibility of the material for the wider community. Finally, compared to monolayer *in-vitro* models, the 3D bioprinted *in-vitro* model more closely mimicked the native complexity of bone by matrix deposition and gradual mineralisation with both scaffold alone and differentiation growth medium; however, the material requires further optimisation to achieve *in-vivo* biomimicry, reflective of the CAD-generated *in-silico* model.

References

Abad-coronel, C., Pazan, D., Hidalgo, L., & Loyola, J. (2023) Comparative analysis between 3D-printed models designed with generic and dental-specific software. *Dentistry journal,* 11(9), 216. Doi: 10.3390/dj11090216

Abbas, Z., Al-Saffar, A., Jasim, S., & Sulaiman, G. (2023) Comparative analysis between 2D and 3D colorectal cancer culture models for insights into cellular morhological and transcriptomic variations. *Scientific reports*, 13, 18380. Doi: 10.1038/s41598-023-45144-w

Abere, D. V., Ojo, S. A., Oyatogun, G. M., Paredes-Epinosa, M. B., Niluxsshun, M. C. D., & Hakami, A. (2022). Mechanical and morphological characterization of nano-hydroxyapatite (nHA) for bone regeneration: A mini review. *Biomedical Engineering Advances*, *4*, 100056. Doi: 10.1016/j.bea.2022.100056

Abrhaley, A., Giday, M., & Hailu, A. (2024) Challenges and opportunities of translating animal research into human trials in Ethiopia. *BMC Medical Research Methodology*, 24, 211. Doi: 10.1186/s12874-024-02338-8

Abubakar, A., Noordin, M., Azmi, T., Kaka, U., & Loqman, M. (2016) The use of rats and mice as animal models in ex vivo bone growth and development studies. *Bone joint research*, 5(12), 610 – 618. Doi: 10.1302/2046-3758.512

Abuwatfa, W., Pitt, W., & Husseini, G. (2024) Scaffold-based 3D cell culture models in cancer research. *Journal of biomedical science*, 31, 7. Doi: 10.1186/s12929-024-00994-y

Acierno, D., & Patti, A. (2023) Fused deposition modelling (FDM) of thermoplastic-based filaments: process and rheological properties – An overview. *Materials (Basel),* 16(24), 7664. Doi: 10.3390/ma16247664

Acil, Y., Weitkamp, J., Wieker, H., Florke, C., Wiltfang, J., & Gulses, A. (2022) Organic bone matrix component type I and V collagen are not destructed in bisphosphonate-associated osteonecrosis of the jaw. *Medicina*, 58(11), 1690. Doi: 10.3390/medicina58111690

Addison, W., Nelea, V., Chicatun, F., Chien, Y., Tran-Khanh, N., Buschmann, M., Nazhat, S., Kaartinen, M., Vali, H., Tecklenburg, M., Franceschi, R., & McKee, M. (2014) Extracellular matrix mineralization in murine MC3T3-E1 osteoblast cultures: an ultrastructural, compositional and comparative analysis with mouse bone. *Bone*, 71, 244 – 256. Doi: 10.1016/j.bone.2014.11.003

Aerssens, J., Boonen, S., Lowet, G., & Dequeker, J. (1998) Interspecies differences in bone composition, density, and quality: potential implications for *in vivo* bone research. *Endocrinology*, 139(2), 663 – 670. Doi: 10.1210/endo.139.2.5751

Afghah, F., Altunbek, M., Dikyol, C., & Koc, B. (2020). Preparation and characterization of nanoclay-hydrogel composite support-bath for bioprinting of complex structures. *Scientific Reports*, *10*(1), 1-13. Doi: 10.1038/s41598-020-61606-x

Aguda, A., Panwar, P., Du, X., Nguyen, N., Brayer, G., & Bromme, D. (2014) Structural basis of collagen fibre degradation by cathepsin K. *The proceedings of the national academy of sciences*, 111(49), 17474-17479. Doi: 10.1073/pnas.1414126111

Aguzzi, C., Cerezo, P., Viseras, C., & Caramella, C. (2007). Use of clays as drug delivery systems: Possibilities and limitations. *Applied Clay Science*, *36*(1-3), 22-36. Doi: 10.1016/j.clay.2006.06.015

Ahmed, E. (2013) Hydrogel: preparation, characterisation, and applications: a review. *Journal of advanced research*, 6(2), 105 – 121. Doi: 10.1016.j.jare.2013.07.006

Ahn, S., Lee, H., & Cho, K. (2024) 3D printing with a 3D printed digital material filament for programming functional gradients. *Nature communications*, 15, 3605. Doi: 10.1038/s41467-024-47480-5

Alaman-Diez, P., Borau, C., Guerrero, P., Amaveda, H., Mora, M., Fraile, J., Garcia-Gaeta, E., Garcia-Aznar, J., & Perez, M. (2023) Collagen-laponite nanoclay hydrogels for tumour spheroid growth. *Biomacromolecules*, 24(6), 2879 – 2891. Doi: 10.1021/acs.biomac.3c00257

Ali, A., Wu, D., Bannach-Brown, A., Dhamrait, D., Berg, J., Tolksdorf, B., Lichtenstein, D., Dressler, C., Braeuning, A., Kurreck, J., & Hulsemann, M. (2024) 3D bioprinting of liver models: A systematic scoping review of methods, bioinks, and reporting quality. *Materials today bio*, 26, 100991. Doi: 10.1016/j.mtbio.2024.100991

Alizae, M. (2008) An overview of bone cells and their regulating factors of differentiation. *The Malaysian journal of medical sciences*, 15(1), 4 – 12.

Allen, N. B., Abar, B., Johnson, L., Burbano, J., Danilkowicz, R. M., & Adams, S. B. (2022). 3D-bioprinted GelMA-gelatin-hydroxyapatite osteoblast-laden composite hydrogels for bone tissue engineering. *Bioprinting*, *26*, e00196. Doi: 10.1016/j.bprint.2022.e00196

Amelian, A., Wasilewska, K., Megias, D., & Winnicka, K. (2017) Application of standard cell cultures and 3D in-vitro stiddue models as an effective tool in drug design and development. *Pharmacological reports,* 69(5), 861 – 870. Doi: 10.1016/j.pharep.2017.03.014

Aminu, A., Chen, W., Yin, Z., Kuniewicz, M., Walocha, J., Perde, F., Molenaar, P., Iaizzo, P., Dobrzynski, H., & Atkinson, A. (2022) Novel micro-computed tomography contrast agents to visualise the human cardiac conduction system and surrounding structures in hearts from normal, aged and obese individuals. *Translational research in anatomy*, 27, 299175. Doi: 10.1016/j.tria.2022.100175

Amiri, M. A., Amiri, D., & Hamedani, S. (2024). Thermosensitive Hydrogels for Periodontal Regeneration: A Systematic Review of the Evidence. *Clinical and Experimental Dental Research*, *10*(6), e70029. Doi: 10.1002/cre2.70029

Amirrah, I., Lokanathan, Y., Zulkiflee, I., Wee, M., Motta, A., & Fauzi, M. (2022) A comprehensive review on collagen type I development of biomaterials for tissue engineering: from biosynthesis to bioscaffold. *Biomedicines*, 10(9), 2307. Doi: 10.3390/biomedicines10092307

Amorim, P., D'Avila, M., Anand, R., Moldenaers, P., Puyvelde, P., & Bloemen, V. (2021) Insights on shear rheology of inks for extrusion-based 3D bioprinting. *Bioprinting*, 22, e00129. Doi: 10.1016/j.bprint.2021.e00129

Anadioti, E., Kane, B., Zhang, Y., Bergler, M., Mante, F., & Blatz, M. B. (2022). Accuracy of Dental and Industrial 3D Printers. *Journal of Prosthodontics : Official Journal of the American College of Prosthodontists*, *31*(Suppl 1), 30. Doi: 10.1111/jopr.13470

Anaraki, P., Patecki, M., Tkachuk, S., Kiyan, Y., Haller, H., & Dumler, I. (2015) Urokinase receptor mediates osteoclastogenesis via M-CSF release from osteoblasts and the c-Fms/PI3K/Akt/NK-kB pathway in osteoclasts. *Journal of bone mineral research*, 30(2), 379 – 388. Doi: 10.1002/jbmr.2350

Andersen, T., Sondergaard, T., Skorzynska, K., Dagnaes-Hansen, F., Plesner, T., Hauge, E., Plesner, T., & Delaisse, J. (2009) A physical mechanism for coupling bone resorption and formation in adult human bone. *The American journal of pathology,* 174(1), 239-247. Doi: 10.2353/ajpath.2009.080627

Anerillas, L., Kingham, P/. Lammi, M., Wiberg, M., & Kelk, P. (2021) Three-dimensional osteogenic differentiation of bone marrow mesenchymal stem cells promotes matrix metallopeptidase 13 (MMP13) expression in type-1 collagen hydrogels. *International journal of molecular sciences*, 22(24), 13594/ doi: 10.3390/ijms222413594

Annabi, N., Nichol, J., Zhong, X., Ji, C., Koshy, S., Khademhosseini, A., & Dehghani, F. (2010) Controlling the porosity and microarchitecture of hydrogels for tissue engineering. *Tissue engineering Part B: Reviews*, 16(4), 371 – 383. Doi: 10.1089/ten.teb.2009.0639

Arabpour, Z., Abedi, F., Salehi, M., Baharnoori, S,, Soleimani, M., & Djalilian, A. (2024) Hydrogel-based skin regeneration. *International Journal of molecular science*, 25(4), 1982. Doi: 10.339/ijms25041982

Arinzeh, T. L., Tran, T., Mcalary, J., & Daculsi, G. (2005). A comparative study of biphasic calcium phosphate ceramics for human mesenchymal stem-cell-induced bone formation. *Biomaterials*, *26*(17), 3631-3638. Doi: 10.1016/j.biomaterials.2004.09.035

Armstrong, J. (2011) Natural learning in higher education. *University of Pennsylvania Scholarly Commons.* Doi: 10.2139/ssrn.1928831

Asgari, M., Abi-Rafeh, J., Hendy, G., & Pasini, D. (2019) Material anisotropy and elasticity of cortical and trabecular bone in the adult mouse femur via AFM indentation. *Journal of the mechanical behaviour of biomedical materials*, 93, 81 – 92. Doi: 10.1016/j.jmbbm.2019.01.024

Ashton, J., Befera, N., Clark, D., Qi, Y., Mao, L., Rockman, H., Johnson, G., and Badea, C. (2014) Anatomical and functional imaging of myocardial infarction in mice using micro-CT and eXIA 160 contrast agent. *Contrast media and molecular imaging*, 9(2), 161-168. Doi: 10.1002/cmmi.1557

Atay, E., Fabra, M., Martinez-sanz, M., Gomez-Mascaraque, L., Altan, A., & Lopez-rubio, A. (2018) Development and characterisation of chitosan/gelatin electrosprayed

microparticles as food grade delivery vehicles for anthocyanin extracts. *Food hydrocolloids*, 77, 699 – 710. Doi: 10.1016/j.foodhyd.2017.11.011

Atgie, M., Chenneviere, A., Masbernat, O., & Roger, K. (2019) Emulsions stabilized by gum Arabic: how diversity and interfacial networking lead to metastability. *Langmuir*, 35(45), 14553 – 14565. Doi: 10.1021/acs.langmuir.9b02541

Augat, P., & Schorlemmer, S. (2006) The role of cortical bone and its microstructure in bone strength. *Age and aging*, 35, 27 – 31. Doi: 10.1093/ageing/afl081

Autodesk (2025) Autodesk fusion for AI in CAD. https://www.autodesk.com/solutions/computer-aided-design-with-ai (Accessed 17/06/2025)

Awad, A., Fina, F., Goyanes, A., Gaisford, S., & Basit, A. (2020) 3D printing: principles and pharmaceutical applications of selective laser sintering. *International journal of pharmaceutics,* 586, 119594. Doi: 10.1016/j.1016/j.ijpharm.2020.119594

Aziz, A., Wilmoth, R., Ferguson, V., & Bryant, S. (2020) IDG-SW3 osteocyte differentiation and bone extracellular matrix deposition are enhanced in a 3D matrix metalloproteinase-sensitive hydrogel. *ACS applied biomaterials*, 3(3), 1666 – 1680. Doi: 10.1021/ascabm.9b01227

Badhe, R. V., Chatterjee, A., Bijukumar, D., & Mathew, M. T. (2023). Current advancements in bio-ink technology for cartilage and bone tissue engineering. *Bone*, *171*, 116746. Doi: 10.1016/j.bone.2023.116746

Baek, N., Seo, O., Kim, M., Hulme, J., & An, S. (2016) Monitoring the effects of doxorubicin on 3D-spheroid tumour cells in real-time. *Dovepress*, 9, 7207 – 7218. Doi: 10.2147/OTT.S112566

Bagaria, V., Bhansali, R., & Pawar, P. (2018) 3D printing - creating a blueprint for the future of orthopaedics: current concept review and the road ahead! *Journal of clinical orthopaedics and trauma*, 9(3), 207 - 212. Doi: 10.1016/j.jcot.2018.07.007

Baghdadi, L., Steinman, D., & Ladak, H. (2005) Template-based finite-element mesh generation from medical images. *Computer methods and programs in biomedicine,* 77(1), 11 – 21. Doi: 10.1016/j.cmpb.2004.06.002

Bai, L., Song, P., & Su, J. (2023). Bioactive elements manipulate bone regeneration. *Biomaterials Translational*, *4*(4), 248. Doi: 10.12336/biomatertransl.2023.04.005

Bai, R., Li, Y., & Zhang, F. (2022) Osteopontin, a bridge links osteoarthritis and osteoporosis. *Frontiers in endocrinology*, 13, 1012508. Doi: 10.3389/fendo.2022.1012508

Bailey, S., & Vashishth, D. (2018). Mechanical Characterisation of Bone: State of the Art in Experimental Approaches—What Types of Experiments Do People Do and How Does One Interpret the Results? *Current Osteoporosis Reports*, *16*(4), 423. Doi: 10.1007/s11914-018-0454-8

Bakhtiary, N., Liu, C., & Ghorbani, F. (2021) Bioactive inks development for osteochondral tissue engineering: a mini review. *Gels*, 7(4), 274. Doi: 10.3390/gels7040274

Bakker, C., Li, Y., Zhao, H., Leavitt, L., Tseng, W., Lin, T., Tong, W., Qin, L., & Liu, X. (2018) Structural adaptations in the rat tibia bone induced by pregnancy and lactation confer protective effects against future estrogen deficiency. *Journal of bone mineral research,* 33(12), 2165 – 2176. Doi: 10.1002/jbmr.3559

Bala, Y., Farlay, D., & Boivin, G. (2012) Bone mineralization: from tissue to crystal in normal and pathological contexts. *Osteoporosis international*, 24. 2153 – 2166. Doi: 10.1007/s00198-012-2228-y

Balestri, W., Hickman, G., Morris, R., Hunt, J., & Reinwald, Y. (2023) Triphasic 3D in-vitro model for bone-tendon-muscle interfaces to study their regeneration. *Cells*, 12(2), 313. Doi: 10.3390/cells12020313

Bandyopadhyay, A., Mitra, I., & Bose, S. (2020) 3D printing for bone regeneration. *Current osteoporosis reports*, 18, 505 - 514. Doi: 10.1007/s11914-020-00606-2

Bao, S., Yu, D., Tang, Z., Wu, H., Zhang, H., Wang, N., Liu, Y., Huang, G., Liu, C., Li, X., & Guo, Z. (2023) Conformationally regulated "nanozyme-like" cerium oxide with mutliple free radical scavenging activities for osteo immunology modulation and vascularized osseointegration. *Bioactive materials*, 34(6), 64 – 79. Doi: 10.1016/j.bioactmat.2023.12.006

Barak, M., & Lieberman, D., & Hublin, J. (2013) Of mice, rats and men: trabecular bone architecture in mammals' scales to body mass with negative allometry. *Journal of structural biology,* 183(2), 123- 131. Doi: 10.1016/j.jsb.2013.04.009

Barragan-Adjemian, C., Nicolella, D., Dusevich, V., Dallas, M., Eick, J., & Bonewald, L. (2006) Mechanism by which MLO-A5 late osteoblasts/early osteocytes mineralize in culture: similarities with mineralization of lamellar bone. *Calcified tissue international*, 79(5), 340 – 353. Doi: 10.1007/s00223-006-0107

Barre-sinoussi, F., & Montagutelli, X. (2015) Animal models are essential to biological research: issues and perspectives. *Future science OA,* 1(4), FS063. Doi: 10.4155/fso.15.63

Basso, N., Jia, Y., Bellows, C., & Heersche, J. (2005) The effect of reloading on bone volume, osteoblast number, and osteoprogenitor characteristics: studies in hind limb unloaded rats. *Bone*, 37(3), 370 – 378. Doi: 10.1016/j.bone.2005.04.033

Bastidas Coral, A. P., A Hogervorst, J. M., Klein-Nulend, J., & Bakker, A. D. (2022). Biologically Relevant In Vitro 3D-Model to Study Bone Regeneration Potential of Human Adipose Stem Cells. *Biomolecules*, *12*(2), 169. Doi: 10.3390/biom12020169

Bastos, A. R., Da Silva, L. P., Maia, F. R., Franco, A., Noro, J., Silva, C., Oliveira, J. M., Reis, R. L., & Correlo, V. M. (2024). Hydroxyapatite/alginate/gellan gum inks with osteoconduction and osteogenic potential for bioprinting bone tissue analogues. *International Journal of Biological Macromolecules*, *271*, 132611. Doi: 10.1016/j.ijbiomac.2024.132611

Bateson, M., & Feenders, G. (2010) The use of passerine bird species in laboratory research: implications of basic biology for husbandry and welfare. *ILAR*, 51(4), 394 – 408. Doi: 10.1093/ilar.51.4.394

Baud'huin, M., Ruiz-velasco, C., Jego, G., Charrier, C., Gasiunas, N., Gallagher, J., Maillasson, M., Naggi, A., Padrines, M., Redini, F., Duplomb, L., & Heymann, D. (2011) lycosaminolycans inhibit the adherence and the spreading of osteoclasts and their precursors: role in osteoclastoenesis and bone resorption. *European journal of cell biology,* 90(1), 49 – 57. Doi: 10.1016/j.ejcb.2010.08.001

Bauri, K., Roy, S., Arora, S., Dey, R., Goswami, A., Madras, G., & De, P. (2012) Thermal degradation kinetics of thermoresponsive poly(N-isopropylacrylamide-co-*N,N*-dimethylacrylamide) copolymers prepared via RAFT polymerization. *Journal of thermal analysis and calorimetry*, 11, 753 – 761. Doi: 10.1007/s10973-012-2344-0

Beagan, M., Dreyer, C., Jensen, L., Jensen, H., Andersen, T., Overgaad, S., & Ding, M. (2024) The potential of sheep in preclinical models for bone infection research – A systematic review. *Journal of orthopaedic translation*, 45, 120 – 131. Doi: 10.1016/j.jot.2024.02.002

Beaucage, K., Pollmann, S., Sims, S., Dixon, J., & Holdsworth, D. (2016) Quantitative in-vivo micro-computed tomography for assessment of age-dependent changes in murine whole-body composition. *Bone reports*, 5, 70 – 80. Doi: 10.1016/j.bonr.2016.04.002

Behseresht, S., Love, A., Valdez Pastrana, O. A., & Park, Y. H. (2024). Enhancing Fused Deposition Modeling Precision with Serial Communication-Driven Closed-Loop Control and Image Analysis for Fault Diagnosis-Correction. *Materials*, *17*(7), 1459. Doi: 10.3390/ma17071459

Beitlitum, I., Rayyan, F., Pokhojaev, A., Tal, H., & Sarig, R. (2024) A novel micro-CT analysis for evaluating the regenerative potential of bone augmentation xenografts in rabbit calvarias. *Scientific reports*, 14, 4321. Doi: 10.1038/s41598-024-54313-4

Beldengrun, Y., Aragon, J., Prazeres, S., Montalvo, G., Miras, J., & Esquena, J. (2018) Gelatin/mlatodextrin water-in-water (w/w) emulsions for the preparation of cross-linked enzyme-loaded microgels. *Langmuir*, 34(33), 9731 – 9743. Doi: 10.1021/acs.langmuir.8b1599

Belk, L., Tellisi, N., Macdonald, H., Erdem, A., Ashammakhi, N., & Pountos, I. (2020) Safety considerations in 3D bioprinting using mesenchymal stromal cells. *Frontiers in bioengineering and biotechnology*, 8. Doi: 10.3389/fbior.2020.00924

Bendtsen, S. T., Quinnell, S. P., & Wei, M. (2017). Development of a novel alginate-polyvinyl alcohol-hydroxyapatite hydrogel for 3D bioprinting bone tissue engineered scaffolds. *Journal of Biomedical Materials Research Part A*, *105*(5), 1457-1468. Doi: 10.1002/jbm.a.36036

Bercea, M. (2023) Rheology as a tool for fine-tuning the properties of printable bioinspired gels. *Molecules*, 28(6), 2766. Doi: 10.3390/molecules28062766

Berg, J., Hiller, T., Kissner, M., Qazi, T., Duda, G., Hocke, A., Hippenstiel, S., Elomaa, L., Weinhart, M., Fahrenson, C., & Kurreck, J. (2018) Optimisation of cell-laden bioinks for 3D bioprinting and efficient infection with influenza A virus. *Scientific reports*, 8, 13877. Doi: 10.1038/s41598-018-31880-x

Berg, J., Weber, Z., Fechler-Bitteti, M., Hocke, A. C., Hippenstiel, S., Elomaa, L., Weinhart, M., & Kurreck, J. (2021). Bioprinted Multi-Cell Type Lung Model for the Study of Viral Inhibitors. *Viruses*, *13*(8), 1590. Doi: 10.3390/v13081590

Bernar, A., Gebetsberger, J., Bauer, M., Streif, W., & Schirmer, M. (2022) Optimisation of the alizarin red S assay by enhancing mineralisation of osteoblasts. *International journal of molecular sciences*, 24(1), 723. Doi: 10.3390/ijms24010723

Bernhardt, A., Skottke, J., Witzleben, M., & Gelinsky, M. (2021) Triple culture of primary human osteoblasts, osteoclasts and osteocytes as an *in-vitro* bone model. *International journal of molecular sciences*, 22(14), 7316. Doi: 10.3390/ijms22147316

Berstad, D., Knapstad, B., Lamvik, M., Skjolsvik, P., Torklep, K., & Oye, H. (1988) Accurate measures of the viscosity of water in the temperature range 19.5 – 25.5 degrees. *Physica A: statistical mechanics and its applications*, 151(2), 246 – 280. Doi: 10.1016/0378-4371(88)900015-5

Besley, J., Dudo, A., Yuan, S., & Lawrence, F. (2018) Understanding scientists' willingness to engage. *Sage; science communication*, 40(5). Doi: 10.1177/1075547018786561

Bhalodi, K., Kothari, C., & Butani, S. (2024) Next-generation cancer nanotherapuetics: pluronic® F127 based mixed micelles for enhanced drug delivery. *Naunyn-Schmiedeberg's archives of pharmacology*. Doi: 10.1007/s00210-024-03582-x

Bharadwaj, T., Chrungoo, S., & Verma, D. (2024). Self-assembled chitosan/gelatin nanofibrous aggregates incorporated thermosensitive nanocomposite bioink for bone tissue engineering. *Carbohydrate Polymers*, *324*, 121544. Doi: 10.1016/j.carbpol.2023.121544

Bhattacharjee, T., Gil, C., Marshall, S., Uruena, J., O'Bryan, C., Carstens, M., Keselowski, B., Palmer, G., Ghivizzani, S., Gibbs, C., Sawyer, G., & Angelini, T. (2016). Liquid-like solids support cells in 3D. *ACS biomaterials science engineering*, 2(10), 1787 – 1795. Doi: 10.1021/acsbiomaterials.6b00218

Bhattacharjee, T., Zehnder, S., Rowe, K., Jain, S., Nixon, R., Sawyer, G., & Angelini, T. (2015) Writing in the granular gel medium. *Science advances*, 1(8), e1500655. Doi: 10.11126/sciadv.1500655

Blackburn, D., Boyer, D., Gray, J., Winchester, J., Bates, J., Baumgart, S., Braker, E., Coldren, D., Conway, K., Rabosky, A., Sancha, N., Dillman, C., Dunnum, J., Early, C., Frable, B., Gage, M., Hanken, J., Maisano, J., Marks, B., Maslenikov, K., McCormack, J., Nagesan, R., Pandelix, G., Prestidge, H., Rabosky, D., Randall, Z., Robbins, M., Scheinberg, L., Spencer, C., Summers, A., Tapanila, L., Thompson, C., Tornabene, L., Watkins-colwell, G., Welton, L., & Stanley, E. (2024) Increasing the impact of vertebrate scientific collections through 3D imaging: The open Vertebrate (oVert) thematic collections network. *BioScience*, 74(3), 169 – 186. Doi: 10.1093/biosci/biad120

Boerckel, J. D., Mason, D. E., McDermott, A. M., & Alsberg, E. (2014). Microcomputed tomography: Approaches and applications in bioengineering. *Stem Cell Research & Therapy*, *5*(6), 144. Doi: 10.1186/scrt534

Bohner, M., Santoni, B. L. G., & Döbelin, N. (2020). β-tricalcium phosphate for bone substitution: Synthesis and properties. *Acta Biomaterialia*, *113*, 23-41. Doi: 10.1016/j.actbio.2020.06.022

Bolamperti, S., Villa, I., & Rubinacci, A. (2022) Bone remodelling: an operational process ensuring survival and bone mechanical competence. *Bone research*, 10(48). Doi: 10.1038/s41413-022-00219-8

Bonewald, L. (2011) The amazing osteocyte. *The journal of bone and mineral research*, 26(2), 229-238. Doi: 10.1002/jbmr.320

Bonewald, L., Harris, S., Rosser, J., Dallas, M., Dallas, S., Camacho, N., Boyan, B., & Boskey, A. (2003) Von Kossa staining alone is not sufficient to confirm that mineralization in-vitro represents bone formation. *Calcified tissue international*, 72(5), 537 – 547. Doi: 10.1007/s00223-002-1057

Borciani, G., Montalbano, G., Baldini, N., Cerqueni, G., Vitale-Brovarone, C., & Ciapetti, G. (2020) Co-culture systems of osteoblasts and osteoclasts: simulating in-vitro bone remodelling in regenerative approaches. *Acta biomaterialia*, 108, 22 – 45. Doi: 10.1016/j.actabio.2020.03.043

Botstein, D. (2012). Why we need more basic biology research, not less. *Molecular Biology of the Cell*, *23*(21), 4160. Doi: 10.1091/mbc.E12-05-0406

Boularaoui, S., Hussein, G., Khan, K., Christoforou, N., & Stefanini, C. (2020) An overview of extrusion-based bioprinting with a focus on induced shear stress and its effect on cell viability. *Bioprinting*, 20, e00093. Doi: 10.1016/j.bprint.2020.e00093

Bouxsein, M., Boyd, S., Christiansen, B., Guldberg, R., Jepsen, K., & Muller, R. (2010) Guidelines for assessment of bone microstructure in rodents using micro-computed tomography. *Journal of bone mineral research*, 25(7), 1468-1486. Doi: 10.1002/jbmr.141

Bouzaglou, O., Golan, O., & Lachman, N. (2023) Process design and parameters interaction in material extrusion 3D printing: a review. *Polymers*, 15(10), 2280. Doi: 10.3390/polym15102280

Bowman, B., Siska, C., & Miller, S. (2002) Greatly increased cancellous bone formation with rapid improvements in bone structure in the rat maternal skeleton after lactation. *Journal of bone and mineral research,* 17(11), 1954-1960. Doi: 10.1359/jbmr.2002.17.11.1954

Boyera, N., Galey, I., & Bernard, B. (1998) Effect of vitamin C and its derivatives on collagen synthesis and cross-linking by normal human fibroblasts. *International journal of cosmetic science*, 20(3), 151 – 158. Doi: 10.1046/j.1467-2494.1998.171747

Boyes, V., Janani, R., Partridge, S., Fielding, L., Breen, C., Foulkes, J., Le Maitre, C., & Sammon, C. (2017) One-pot precipitation polymerisation strategy for tuneable injectable Laponite®-pNIPAM hydrogels: polymerisation, processability and beyond. *Polymer*, 233, 124201. Doi: 10.1016/j.polymer.2021.124201

Boynton, P., & Greenhalgh, T. (2004) Hands-on guide to questionnaire research: selecting, designing, and developing your questionnaire. *British Medical Journal,*

328(7451), 1312-1315. Retrieved: http://www.jstor.org/stable/41707852 Accessed on: 04/08/2024

Breathwaite, E., Weaver, J., Odanga, J., & Lee, J. B. (2020). 3D Bioprinted Osteogenic Tissue Models for In Vitro Drug Screening. *Molecules*, *25*(15), 3442. Doi: 10.3390/molecules25153442

Brodsky, B., & Persikov, A. (2005) Molecular structure of the collagen triple helix. *Advances in protein chemistry*, 70. 301 – 339. Doi: 10.1016/S0065-3233(05)70009-7

Brosnan, S. F., & Postma, E. (2017). Humans as a model for understanding biological fundamentals. *Proceedings of the Royal Society B: Biological Sciences*, *284*(1869), 20172146. Doi: 10.1098/rspb.2017.2146

Brunel, L., Hull, S., & Heilshorn, S. (2022) Engineered assistive materials for 3D bioprinting: support baths and sacrificial inks. *Bio fabrication*, 14(3). Doi: 10.1088/1758-5090/ac6bbe

Brzezinska, O., Lukasik, Z., Makowska, J., & Walczak, K. (2020) Role of vitamin C in osteoporosis development and treatment – A literature review. *Nutrients*, 12(8), 2394. Doi: 10.3390/nu12082394

Bucking, T., Hill, E., Robertson, J., Maneas, F., Plumb, A., & Nikitichev, D. (2017) From medical imaging data to 3D printed anatomical models. *PLoS one*, 12(5), e0178540. Doi: 10.1371/journal.pone.0178540

Budharaju, H., Sundaramurthi, D., & Sethuraman, S. (2024) Embedded 3D bioprinting – an emerging strategy to fabricate biomimetic & large vascularised tissue constructs. *Bioactive materials*, 32, 356 – 384. Doi: 10.1016/j.bioactmat.2023.10.012

Buenzli, P., & Sims, N. (2015) Quantifying the osteocyte network in the human skeleton. *Bone*, 75, 144-150. Doi: 10.1016/j.bone.2015.02.016

Bulcke, A., Vogdanov, B., Rooze, N., Schancht, E., Cornelissen, M., & Berghmans, H. (2000) Structural and rheological properties of methacrylamide modified gelatine hydrogels. *Biomacromolecules*, 1(1), 31 – 38. Doi: 10.1021/bm990017d

Burger, M. G., Grosso, A., Briquez, P. S., Born, G. M., Lunger, A., Schrenk, F., Todorov, A., Sacchi, V., Hubbell, J. A., Schaefer, D. J., Banfi, A., & Di Maggio, N. (2022). Robust coupling of angiogenesis and osteogenesis by VEGF-decorated matrices for bone regeneration. *Acta Biomaterialia*, *149*, 111-125. Doi: 10.1016/j.actbio.2022.07.014

Burgmann, S., Godehardt, M., Schladitz, K., & Breit, W. (2021) *Construction and building materials*, 289. 123148. Doi: 10.1016/j.conbuildmat.2021.123148

Burkhart, T., Andrews, D., & Dunning, C. (2013) Finite element modelling mesh quality, energy balance and validation methods: A review with recommendations associated with the modelling of bone tissue. *Journal of biomechanics*, 46(9), 1477 – 1488. Doi: 10.1016/j.biomech.2013.03.022

Busse, B., Galloway, J. L., Gray, R. S., Harris, M. P., & Kwon, R. Y. (2019). Zebrafish: An Emerging Model for Orthopaedic Research. *Journal of Orthopaedic Research: Official Publication of the Orthopaedic Research Society*, *38*(5), 925. Doi: 10.1002/jor.24539

Caleb, J., & Yong, T. (2020) Is it time to start transitioning from 2D to 3D cell culture? *Frontiers molecular bioscience*, 7. Doi: 10.3389/fmolb.2020.00033

Caliari, S., & Burdick, J. (2016) A practical guide to hydrogels for cell culture. *Nature methods*, 13(5), 405 – 414. Doi: 10.1038/nmeth.3839

Campbell, G., & Sophocleous, A. (2014) Quantitative analysis of bone and soft tissue by micro-computed tomography: applications to ex-vivo and in-vivo studies. *Bonkey reports*, 3, 564. Doi: 10.1038/bonekey.2014.59

Campos, D., Blaeser, A., Korsten, A., Neuss, S., Jakel, J., Vogt, M., & Fischer, H. (2015) The stiffness and structure of three-dimensional printed hydrogels direct the differentiation of mesenchymal stromal cells toward adipogenic and osteogenic lineages. *Tissue Engineering: Part A*, 21(4), 740 – 756. Doi: 10.89/ten.TEA.2014.0231

Cantarero-Rivera, F., D'Souza, D., Dhar, M., & Chen, J. (2024) Characterisation of the dynamic viscosity of cell cultures and its effect on mixing performance in a spinner flask bioreactor. *Biochemical engineering journal.* 212, 109523. Doi: 10.1016/j.bej.2024.109523

Capellini, K., Ait-Ali, L., Pak, V., Cantinotti, M., Murzi, M., Vignali, E., Fanni, B., Clemente, A., Celi, S., & Gasparotti, E. (2024) Three-dimensional printed models as an effective tool for the management of complex congenital heart disease. *Frontiers in bioengineering and biotechnology*, 12, 1369514. Doi: 10.3389/fbior.2024.1369514

Capulli, M., Paone, R., & Rucci, N. (2014) Osteoblast and osteocyte: games without frontiers. *Archives biochemistry and biophysics*, 561, 3 – 12. Doi: 10.1016/j.abb.2014.05.003

Caudill, C., Perry, J., Iliadis, K., & Desimone, J. (2021) Transdermal vaccination via 3D-printed microneedles induces potent humoral and cellular immunity. *PNAS: biological sciences*, 118(39), e2102595118. Doi: 10.1073/pnas.2102595118

Cauley, J. (2015) Estrogen and bone health in men and women. *Steroids*, 99, 11 – 15. Doi: 10.1016/j.steroids.2014.12.010

Cavallo, A., Radaelli, G., Kayal, T., Mero, A., Mezzetta, A., Guazzelli, L., Soldani, G., & Losi, P. (2025) *Molecules*, 30(3), 649. Doi: 10.3390/molecules30030649

Cengiz, I., Oliveria, J., & Reis, R. (2018) Micro-CT a digital 3D microstructural voyage into scaffolds: a systematic review of the reported methods and results. *Biomaterials research*, 22(26). Doi: 10.1186/s40824-018-0136-8

Cenni, E., Perut, F., & Baldini, N. (2011). In vitro models for the evaluation of angiogenic potential in bone engineering. *Acta Pharmacologica Sinica*, *32*(1), 21-30. Doi: 10.1038/aps.2010.143

Chai, X., Chai, H., Wang, X., Yang, J., Li, J., Zhao, Y., Cai, W., Tao, T., & Xiang, X. (2017) Fused deposition modelling (FDM) 3D printed tablets for intragastric floating delivery of domperidone. *Scientific reports*, 7, 2829. Doi: 10.1038/s41598-017-03097-x

Chatree, K., Sriboonaied, P., Phetkong, C., Wattananit, W., Chanchao, C., & Charoenpanich, A. (2023) Distinctions in bone matrix nanostructure, composition, and

formation between osteoblast-like cells, MG-63, and human mesenchymal stem cells, UE7T-13. *Heliyon*, 9(5), e15556.

Chaurasiya, A., Pande, P., Shankar, R., Kushwaha, N., Kumar, P., Dey, K., & Chaurasiya, A. (2024) Synthesis and characterisation of novel D-mannitol based hydrogel: swelling and adsorption behaviour of heavy metal ion studies. *Journal of applied polymer science*, 141(25), e55534. Doi: 10.1002/app.55534

Chavarri, M., Maranon, I., Ares, R., Ibanez, F., Marzo, F., & Villaran, M. (2010) Microencapsulation of a probiotic and prebiotic in alginate-chitosan capsules improves survival in simulated gastro-intestinal conditions. *International journal of food microbiology,* 142(2), 185 – 189. Doi: 10.1016/j.ijfoodmicro.2010.06.022

Chen, C., Hsieh, P., Wang, G., Chen, W., & Yeh, M. (2009) The influence of surface morphology and rigidity of the substrata on cell motility. *Materials letters*, 63(21), 1872 – 1875. Doi: 10.1016/j.matlet.2009.05.073

Chen, F., Zhang, Y., Peng, P., Huang, X., Qui, Z., Liu, B., Yang, T., Yang, B., & Guo, Y. (2023) Isolation and culture of human primary osteoblasts: comparing the effects of differences in method details on osteoblast characteristics. *Genes and diseases*, 11(2), 546 – 549. Doi: 10.1016/j.gendis.2023.03.024

Chen, H., Gonnella, G., Huang, J., Di-Silvio, L. (2023) Fabrication of 3D bioprinted bi-phasic scaffold for bone-cartilage interface regeneration. *Biomimetics*, 8(1), 87. Doi: 10.3390/biomimetics8010087

Chen, J., Guo, J., Yang, X., & Nicolai, T. (2021) Water-in-water-in-water emulsions formed by cooling mixtures of guar, amylopectin and gelatine. *Food hydrocolloids*, 118, 106763. Doi: 10.1016/j.foodhyd.2021.106763

Chen, K., Chen, H., Deng, L., Yang, K., & Qi, J. (2023) IDG-SW3 cell culture in a three-dimensional extracellular matrix. *Journal of visualised experiments*, 201. Doi: 10.3791/64507

Chen, S., Wang, Y., Lai, J., Tan, S., & Wang, M. (2023) Structure and properties of gelatin methacryloyl (GelMA) synthesized in different reaction systems. *Biomacromolecules*, 24(6), 2928 – 2941. Doi: 10.1021/acs.biomac.3c00302

Chen, X., Anvari-Yazdi, F., Duan, X., Zimmerling, A., Gharraei, R., Sharma, N., Sweilem, S., & Ning, L. (2023) Biomaterials / bioinks and extrusion bioprinting. *Bioactive materials*, 28, 511 – 536. Doi: 10.1016/j.bioactmat.2023.06.006

Cherif, H., Li, L., Snuggs, J., Li, X., Sammon, C., Li, J., Beckman, L., Haglund, L., & Le Maitre, C. (2024) Injectable hydrogel induces regneration of naturally degenerate human intervertebral discs in a loaded organ culture model. *Acta Biomaterialia*, 176, 201 – 220. Doi: 10.1016/j.actbio.2023.12.041

Chiticaru, E., & Ionita, M. (2024). Commercially available bioinks and state-of-the-art lab-made formulations of bone tissue engineering: A comprehensive review. *Materials Today bio*, 29, 101341. Doi: 10.1016/j.mtbio.2024.101341

Choe, G., Lee, M., Oh, S., Seok, J. M., Kim, J., Im, S., Park, S. A., & Lee, J. Y. (2022). Three-dimensional bioprinting of mesenchymal stem cells using an osteoinductive bioink

containing alginate and BMP-2-loaded PLGA nanoparticles for bone tissue engineering. *Biomaterials Advances*, *136*, 212789. Doi: 10.1016/j.bioadv.2022.212789

Choi, B., & Pak, A. (2004) A catalogue of biases in questionnaires. *Preventing chronic disease,* 2(1), A13.

Choi, H., Lee, J., Lee, J., Sung, H., Shin, J., Shin, J., Wu, Y., & Kim, J. (2016) MG-63 cells proliferation following various types of mechanical stimulation on cells by auxetic hybrid scaffolds. *Biomaterials research*, 20, 32. Doi: 10.1186/s40824-016-0079-x

Choi, J., Lee, E. J., Jang, W. B., & Kwon, M. (2023). Development of Biocompatible 3D-Printed Artificial Blood Vessels through Multidimensional Approaches. *Journal of Functional Biomaterials*, *14*(10), 497. Doi: 10.3390/jfb14100497

Choi, S., Hunt, E., Shangin, E. A., Bahranifard, Z., Nguyen, E., Collins, C. J., & Whittington, A. R. Dynamic Micromechanical Characterization of 3D Printed Bone In Vitro Models Manufactured via Vat Photopolymerization. *Advanced Functional Materials*, 2418547. Doi: 10.1002/adfm.202418547

Choi, Y., Yoon, J., Shin, Y., & Lee, S. (2024) The difference in bone mineral density between femur and tibia is related to tibia deformation in end stage knee osteoarthritis. *The knee*, 51, 173 – 180. Doi: 10.1016/j.knee.2024.09.008

Cidonio, G., Glinka, M., Dawson, J., & Oreffo, R. (2019) The cell in the ink: improving bio fabrication by printing stem cells for skeletal regenerative medicine. *Biomaterials*, 209, 10 – 24. Doi: 10.1016/j.biomaterials.2019.04.009

Clarke, B. (2008) Normal bone anatomy and physiology. *Clinical journal American Society of Nephrology*. 3, 131 – 139. Doi: 10.2215/CJN.04151206

Clarke, M., Sundaresan, A., Vanderburg, C., Banigan, M., & Pellis, N. (2013) A three-dimensional tissue culture model of bone formation utilising rotational co-culture of human adult osteoblasts and osteoclasts. *Acta biomaterials*, 9(8), 7908 – 7916. Doi: 10.1016/j.actbio.2013.04.051

Cuanalo-Contreras, K., & Benkmann, D. (2022) Towards more human and humane testing: the role of the device supplier industry. *Alternative lab animals*, 50(1), 62 – 70. Doi: 10.1177/026119211073132

Cunniffe, G., Gonzalez-Fernandez, T., Daly, A., Sathy, B., Jeon, E., & Kelly, D. (2017) Three-dimensional bioprinting of polycaprolactone reinforced gene activated bioinks for bone tissue engineering. *Tissue Engineering: part A*, 23(18), 891 – 900. Doi: 10.1089/ten.tea.2016.0498

Curti, C., Kirby, D., & Russell, C. (2024) Systematic screening of photopolymer resins for stereolithography (SLA) 3D printing of solid oral dosage forms: investigation of formulation factors on printability outcomes. *International journal of pharmaceutics*, 653, 123862. Doi: 10.1016/j.ijpharm.2024.123862

Curtis, A., Forrester, J., McInnes, C., & Lawrie, F. (1983) Adhesion of cells to polystyrene surfaces. *Journal of Cell Biology*, 97(5), 1500 – 1506. Doi: 10.1083/jcb.97.5.1500

Custodio, L., Pesco, S., & Silva, C. (2019) An extended triangulation to the marching cubes 33 algorithm. *Journal of the Brazilian computer society*, 25(6). Doi: 10.1186/s13173-019-0086-6

Dallas, S., & Bonewald, L. (2011) Dynamics of the transition from osteoblast to osteocyte. *The annals of the New-York academy of sciences*, 1192(1), 437-443. Doi: 10.1111/j.1749-6632.2009.05246

Daly, A., Davidson, M., & Burdick, J. (2021) 3D bioprinting of high cell-density heterogeneous tissue models through spheroid fusion within self-healing hydrogels. *Nature communications*, 12, 753. Doi: 10.1038/s41467-021-21029-2

Dan, X., Chen, H., Li, S., Xue, P., Liu, B., Zhang, Z., Lei, L., Li, Y., & Fan, X. (2025). Silk Fibroin as a 3D Printing Bioink for Tissue Engineering Applications. *Applied Materials Today*, *44*, 102775. Doi: 10.1016/j.apmt.2025.102775

Datta, P., Dey, M., Ataie, Z., Unutmaz, D., & Ozbolat, I. T. (2020). 3D bioprinting for reconstituting the cancer microenvironment. *Npj Precision Oncology*, *4*(1), 1-13. Doi: 10.1038/s41698-020-0121-2

Datta, S. (2023) Advantage of alginate bioinks in bio fabrication for various tissue engineering applications. *International journal of polymer science*, 2023(1), 6661452. Doi: 10.1155/2023/6661452

Davern, J. W., Hipwood, L., Bray, L. J., Meinert, C., & Klein, T. J. (2024). Addition of Laponite to gelatin methacryloyl bioinks improves the rheological properties and printability to create mechanically tailorable cell culture matrices. *APL Bioengineering*, *8*(1), 016101. Doi: 10.1063/5.0166206

De Araújo, T. B. S., Nogueira, R. L. R., Siquara da Rocha, L. D. O., Bastos, I. N., Dias, R. B., Souza, B. S. D. F., Lambert, D. W., Coletta, R. D., Silva, V. A. O., & Gurgel Rocha, C. A. (2024). Enhancing scaffold-free spheroid models: 3D cell bioprinting method for metastatic HSC3–Oral squamous carcinoma cell line. *SLAS Discovery*, *29*(4), 100158. Doi: 10.1016/j.slasd.2024.100158

Debnath, S., Agrawal, A., Jain, N., Chatterjee, K., & Player, D. (2025) Collagen as a bio-ink for 3D printing: a critical review. *Journal of materials chemistry B*, 13, 1890 – 1919. Doi: 10.1039/D4TB01060D

Dec, P., Modrzejewski, A., & Pawlik, A. (2022) Existing and novel biomaterials for bone tissue engineering. *International journal of molecular sciences*, 24(1), 529. Doi: 10.3390/ijms24010529

Degennaro, V., Brandi, M., Cagninelli, G., Casciaro, S., Ciardo, D., Conversano, F., Pasquo, E., Gonnelli, S., Lombardi, F., Pisani, P., & Ghi, T. (2021) First assessment of bone mineral density in healthy pregnant women by means of radiofrequency echo graphic Mult spectrometry technology. *Gynaecology and reproductive biology*, 263, 44 – 49. Doi: 10.1016/j.ejogrb.2021.06.014

Dell, A., Wagner, G., Own, J., & Geibel, J. (2022) 3D bioprinting using hydrogels: cell inks and tissue engineering applications. *Pharmaceutics*, 14(12), 2596. Doi: 10.3390/pharmaceutics14122596

Depalle, B., McGilvery, C., Nohakhti, S., Aldegaither, N., Shefelbine, S., & Porter, A. (2021) Osteopontin regulates type I collagen fibril formation in bone tissue. *Acta biomaterialia*, 120, 194 – 202. Doi: 10.1016/j.actbio.2020.04.040

Deshmane, S., Kendre, P., Mahajan, H., & Jain, S. (2021) Stereolithography 3D printing technology in pharmaceuticals: a review. *Drug development and industrial pharmacy,* 9, 1362 – 1372. Doi: 10.1080/03639045.2021.1994990

Dharmaraj, J. J., Navasingh, R. J., Krolczyk, G., & Pitchumani, S. V. (2024). Extrusion-Based Bioprinting in a Cost-Effective Bioprinter. *Machines*, *12*(8), 518. Doi: 10.3390/machines12080518

Di Spirito, N., Grizzuti, N., & Pasquino, R. (2024) Self-assembly of pluronics: A critical review and relevant applications. *Physics of fluids*, 36(11). Doi: 10.1063/5.0238690

Dietrich, K., Fiedler, I., Kurzyukova, A., Lopez-Delgado, A., McGowan, L., Geurtzen, K., Hammond, C., Busse, B., & Knopf, F. (2021) Skeletal biology and disease modelling in zebrafish. *Journal of bone and mineral research*, 36(3), 436 – 458. Doi: 10.1002/jbmr.4256

Dietrich, K., Fiedler, I., Kurzyukova, A., Lopez-Delgado, A., McGowan, L., Geurtzen, K., Hammond, C., Busse, B., & Knopf, F. (2021) Skeletal biology and disease modelling in zebrafish. *Journal of bone and mineral research*, 36(3), 436 – 458. Doi: 10.1002/jbmr.4256

Ding, Y., Tang, R., Feng, Y., Yuan, M., Li, H., & Yuan, M. (2022) synthesis and characterisation of high resilience collagen-polyacrylamide semi-interpenetrating network hydrogel. *Materials today communications*, 32, 103955. Doi: 10.1016/j.mtcomm.2022.103955

Dobrisan, M., Lungu, A., & Ionita, M. (2024) A review of the current state of the art in gelatin methacryloyl-based printing inks in bone tissue engineering. *Virtual and physical prototyping*, 19, e2378003. Doi: 10.1080/17452759.2024.2378003

Doherty, P. (2007) From passivity to interactivity: How the traditional lecture has evolved as a method of instruction. *ITB*, 8(1), 4. Doi: 10.21427/D7VB3J

Domander, R., Felder, A. A., & Doube, M. (2021) BoneJ2 – refactoring established research software. *Wellcome open research*, 6, 37. Doi: 10.12688/wellcomeopenres.16619.2

Double, M., Klosowski, M., Arganda-Carreras, I., Cordelieres, F., Dougherty, R., Jackson, J., Schmid, B., Hutchinson, J., & Shefelbine, S. (2010) Bonej; free and extensible bone image analysis in ImageJ. *Bone*, 47(6), 1076-1079. Doi: 10.1016/j.bone.2010.08.023

Dudak, J., Zemlicka, J., Karch, J., Patzelt, M., Mrzilkova, J., Zach, P., Hermanova, Z., Kvacek, J., & Frejci, F. (2016) High-contrast X-ray micro-radigraphy and micro-CT of ex-vivo soft tissue murine organs utilizing ethanol fixation and large area photon-counting detector. *Scientific reports*, 6, 30385. Doi: 10.1038/srep30385

Duraivel, S., Subramaniam, V., Shisolm, S., Scheutz, G., Sumerlin, B., Bhattacharjee, T., & Angelini, T. (2022) Leveraging ultra-low interfacial tension and liquid-liquid phase

separation in embedded 3D bioprinting. *Biophysics reviews*, 3(3), 031307. Doi: 10.1063/5.0087387

Dutta, S., Hexiu, J., Patel, D., Ganguly, K., & Lim, K. (2021) 3D-printed bioactive and biodegradable hydrogel scaffolds of alginate/gelatine/cellulose nanocrystals for tissue engineering. *International journal of biological macromolecules,* 167, 644 – 658. Doi: 10.1016/j.ijbiomac.2020.12.011

Dzhoyashvili, N., Thompson, K., Gorelov, A., & Rochev, Y. (2016) Film thickness determines cell growth and cell sheet detachment from spin-coated poly(N-Isopropylacrylamide) substrates. *ACS applied materials & interfaces*, 8(41), 27564 – 27572. Doi: 10.1021/acsami.6b09711

Eckert, C., Schmidt, S., Faber, J., Detsch, R., Vielreicher, M., Lamberger, Z., Stahlhut, P., Sandor, S., Karimi, T., Schmid, R., Arkudas, A., Friedrich, O., Budday, S., Lang, G., Kengelbach-Weigand, A., & Bosserhoff, A. (2025) An alginate-cellulose based bioink mimics the viscoelastic features of the melanoma microenvironment and its influence on cell cycle and invasion. *Bioprinting*, 46, e00384. Doi: 10.1016/j.bprint.2024.e00384

Edmondson, R., Broglie, J. J., Adcock, A. F., & Yang, L. (2014). Three-Dimensional Cell Culture Systems and Their Applications in Drug Discovery and Cell-Based Biosensors. *Assay and Drug Development Technologies*, *12*(4), 207. Doi: 10.1089/adt.2014.573

El-Gizawy, A., Ma, X., Pfeiffer, F., Schiffbauer, J., & Selly, T. (2023) Characterisation of microarchitectures, stiffness, and strength of human trabecular bone using micro-computed tomography (micro-CT) scans. *Biomed*, 3(1), 89-100. Doi: 10.3390/biomed3010007

Elhattab, K., Bhaduri, S., & Sidker, P. (2022) Influence of fused deposition modelling nozzle temperature on the rheology and mechanical properties of 3D printed β-tricalcium phosphate (TCP)/Polylactic acid (PLA) composite. *Polymers*, 14(6), 1222. Doi: 10.3390/plym14061222

Erickson, A. G., Laughlin, T. D., Romereim, S. M., Sargus-Patino, C. N., Pannier, A. K., & Dudley, A. T. (2018). A Tunable, Three-Dimensional In Vitro Culture Model of Growth Plate Cartilage Using Alginate Hydrogel Scaffolds. *Tissue Engineering. Part A*, *24*(1-2), 94. Doi: 10.1089/ten.tea.2017.0091

Fakhruddin, K., Hamzah, M., & Razak, S. (2018) Effects of extrusion pressure and printing speed of 3D bioprinted construct on the fibroblast cells viability. *OP conference series: materials science and* engineering, 440, 012042. Doi: 10.1088/1757-899X/440/1/012042

Fakhry, M., Hamade, E., Badran, B., Buchet, R., & Magne, D. (2013) Molecular mechanisms of mesenchymal stem cell differentiation towards osteoblasts. *World journal of stem cells*, 5(4), 136 – 148. Doi: 10.4252/wjsc.v5.i4.136

Fan, L., Ren, Y., Emmert, S., Vuckovic, I., Stojanovic, S., Najman, S., Schnettle, R., Barbeck, M., Scheneke-Layland, K., & Xiong, X. (2023) The use of collagen-based materials in bone tissue engineering. *International journal of molecular sciences*, 24(4), 3744. Doi: 10.3390/ijms24043744

Farias, B., Rizzi, F., Riberio, E., Diaz, P., Cadaval Jr, T., Dotto, G., Khan, M., Manoharadas, S., Pinto, L., & Reis, G. (2023) Influence of gelatin type on physiochemical properties of electrospun nanofibers. *Scientific reports*, 13, 151995. Doi: 10.1038/s41598-023-42472-9

Farokhi, M., Aleemardani, M., Solouk, A., Mirzadeh, H., Teuschl, A., & Redl, H. (2021) Crosslinking strategies for silk fibroin hydrogels: promising biomedical materials. *Biomedical materials,* 16, 022004. Doi: 10.1088/1748-605X/abb615

Farshidfar, N., Iravani, S., & Varma, R. S. (2023). Alginate-Based Biomaterials in Tissue Engineering and Regenerative Medicine. *Marine Drugs*, *21*(3), 189. Doi: 10.3390/md21030189

Felbeck, T., Lezhnina, M., Resch-Genger, U., & Kynast, U. (2016). Red emissive nanoclay hybrids in transparent aqueous dispersion—Towards optical applications in biophotonics. *Journal of Luminescence*, *169*, 728-732. Doi: 10.1016/j.jlumin.2014.11.039

Feng, X. (2009) Chemical and biochemical basis of cell-bone matrix interaction in health and disease. *Current chemical biology*, 3(2), 189 – 196. Doi: 10.2174/187231309788166398

Feng, X., & McDonald, J. (2011) Disorders of bone remodelling. *Annual review of pathology: mechanisms of disease,* 6, 121 – 145. Doi: 10.1146/annurev-pathol-011110-130203

Ferreira, N., Ferreira, L., Cardoso, V., Boni, F., Souza, A., & Gremiao, M. (2018) Recent advances in smart hydrogels for biomedical applications: from self-assembly to functional approaches. *European polymer journal*, 99, 117 – 133. Doi: 10.1016/j.eurpolymj.2017.12.004

Fidkowski, C., Kaazempur-mofrad, M., Borenstein, J., Vacanti, J., Langer, R., & Wang, Y. (2005) Endothelialised microvasculature based on a biodegradable elastomer. *Tissue engineering,* 11(2), 302 – 309. Doi: 10.1089/ten.2005.11.302

Fink, K. (1996) How to conduct surveys: A step-by-step guide. *London: sage publications*. Accessed 04/08/2024

Finlay, M., Hill, L., Neag, G., Patel, B., Chipara, M., Lamont, H., Frost, K., Patrick, K., Lewis, J., Nicholson, T., Edwards, J., Jones, S., Grover, L., & Naylor, A. (2024) A detailed methodology for a three-dimensional, self-structuring bone model that supports the differentiation of ostblasts towards osteocytes and the production of a complex collagen-rich mineralised matrix. *F1000 research*, 12, 357. Doi: 10.12688/f1000research.130779.3

Fischetti, T., Pompo, G. D., Baldini, N., Avnet, S., & Graziani, G. (2021). 3D Printing and Bioprinting to Model Bone Cancer: The Role of Materials and Nanoscale Cues in Directing Cell Behavior. *Cancers*, *13*(16), 4065. Doi: 10.3390/cancers13164065

Fitzgerlad, J., Shaw, G., Murphy, M., & Barry, F. (2023) Media matters: culture medium-dependent hypervariable phenotype of mesenchymal stromal cells. *Stem cell research & therapy*, 14(363). Doi: 10.1186/s13287-023-03589-w

Flaxman, T., Cooke, C., Miguel, O., Sheikh, A., & Singh, S. (2021) A review and guide to creating patient specific 3D printed anatomical models from MRI for benign gynecologic surgery. *3D printing in medicine*, 7(17). doi: 10.1186/s41205-021-00107-7

Florencio-Silva, R., Sasso, G., Sasso-cerri, E., Simoes, M., & Cerri, P. (2015) Biology of bone tissue: structure, function, and factors that influence bone cells. *Biochemistry research international*, 2015(1). Doi: 10.1155/2015/421746

Fois, M., Griensven, M., Giselbrecht, S., Habibovic, P., Truckenmuller, R., & Birgani, Z. (2024) Mini-bones: miniaturized bone *in-vitro* models. *Trends in biotechnology*, 42(7), 910-928. Doi: 10.1016/j.tibtech.2024.01.004

Fontoura, J., Viezzer, C., Santos, F., Ligabue, R., Weinlich, R., Puga, R., Antonow, D., Severino, P., & Bonorino, C. (2020) Comparison of 2D and 3D cell culture models for cell growth, gene expression and drug resistance. *Materials science and engineering: C*, 107, 110264. Doi: 10.1016/j.msec.2019.110264

Ford, J., & Decker, S. (2016) Computed tomography slice thickness and its effects on three-dimensional reconstruction of anatomical structures. *Journal of forensic radiology and imaging*, 4, 43 – 46. Doi: 10.1016/j.jofri.2015.10.004

Franceschi, R., Lyer, B., & Cui, Y. (1994) Effects of ascorbic acid on collagen matrix formation and osteoblast differentiation in murine MC3T3-E1 cells. *Journal of bone mineral research*, 9(6), 843 – 854. Doi: 10.1002/jbmr.5650090610

Frank, M., Reisinger, A. G., Pahr, D. H., & Thurner, P. J. (2021). Effects of Osteoporosis on Bone Morphometry and Material Properties of Individual Human Trabeculae in the Femoral Head. *JBMR Plus*, *5*(6), e10503. Doi: 10.1002/jbm4.10503

Franz-Odendaal, T., Hall, B., & Witten, P. (2005) Buried alive: How osteoblasts become osteocytes. *American association for anatomy*, 235(1), 176 – 190. Doi: 10.1002/dvdy.20603

Fratzl-Zelman, N., Fratzl, P., Horander, H., Grabner, B., Varga, F., Ellinger, A., & Klaushofer, K. (1998) Matrix mineralisation in MC3T3-E1 cell cultures initiated by beta-glycerophosphate pulse. *Bone*, 23(6), 511 – 520. Doi: 10.1016/s8756-3282(98)00139-2

Freeman, F., & Kelly, J. (2017) Tuning alginate bioink stiffness and composition for controlled growth factor delivery and to spatially direct MSC fate within bioprinted tissues. *Scientific reports*, 7(1), 17042. Doi: 10.1038/s41598-017-17286-1

Frost, M. (1994) Wolff's law and bone's structural adaptations to mechanical usage: an overview for clinicians. *The Angle orthodontist*, 64(3), 175-188. Doi: 10.1043/0003-3219(1994)064

Fu, Z., Naghieh, S., Xu, C., Wang, C., Sun, W., & Chen, X. (2021) Printability in extrusion bioprinting. *Biofabrication*, 13(3), 033001. Doi: 10.1088/1758-5090/abe7ab

Fukunishi, Y., & Tabata, Y. (2018) Osteogenic differentiation enhances the MC3T3-E1 secretion of glycosaminoglycans with an affinity for basic fibroblast growth factor and bone morphogenetic protein-2. *Regenerative therapy*, 8, 58 – 62. Doi: 10.1016/j.reth.2018.02.001

Galindo, M., Pratap, J., Young, D., Hovhannisyan, H., Im, H., Choi, J., Lian, J., Stein, J., Stein, G., & Wijnen, A. (2005) The bone=specific expression of runx2 oscillates during the cell cycle to support a G_1-related antiproliferative function in osteoblasts. *Journal of biological chemistry*, 280(21), 20274 – 20285. Doi: 10.1074/jbc.M413665200

Gao, C., Peng, S., Feng, P., & Shuai, C. (2017) Bone biomaterials and interactions with stem cells. *Bone research*, 5, 17059. Doi: 10.1038/boneres.2017.59

Gao, Ge., Ahn, M., Cho, W., Kim, B., & Cho, D. (2021) 3D printing of pharmaceutical application: drug screening and drug delivery. *Pharmaceutics*, 13(9), 1373. Doi: 10.3390/pharmaceutics13091373

Gao, T., Gillispie, G., Copus, J., Jumar, A., Seol, Y., Atala, A., Yoo, J., & Lee, S. (2018) Optimisation of gelatine-alginate composite bioink printability using rheological parameters: a systematic approach. *Biofabrication*, 10(3), 034106. Doi: 10.1088/1758-5090/aacdc7

García-Villén, F., Ruiz-Alonso, S., Lafuente-Merchan, M., Gallego, I., Sainz-Ramos, M., & Pedraz, J. L. (2021). Clay Minerals as Bioink Ingredients for 3D Printing and 3D Bioprinting: Application in Tissue Engineering and Regenerative Medicine. *Pharmaceutics*, *13*(11), 1806. Doi: 10.3390/pharmaceutics13111806

Geckil, H., Xu, F., Zhang, X., Moon, S., & Demirci, U. (2010). Engineering hydrogels as extracellular matrix mimics. *Nanomedicine (London, England)*, *5*(3), 469. Doi: 10.2217/nnm.10.12

Ghani, M., Zhou, Z., Ren, L., Li, Y., Zheng, B., Yang, K., & Liu, H. (2017) Investigation of spatial resolution characteristics of an in-vivo micro computed tomography system. *Nuclear instruments and methods in physics research section A: accelerators, spectrometers, detectors and associated equipment*. 807, 129 – 136. Doi: 10.1016/j.nima.2015.11.007

GhavamiNejad, A., Ashammakhi, N., Wu, X. Y., & Khademhosseini, A. (2020). Crosslinking Strategies for Three-Dimensional Bioprinting of Polymeric Hydrogels. *Small, 16*(35), e2002931. Doi: 10.1002/smll.202002931

Gheytanchi, E., Naseri, M., Karimi-Busheri, F., Atyabi, F., Mirsharif, E., Bozorgmehr, M., Ghods, R., & Madjd, Z. (2021) Morphological and molecular characteristics of spheroid formation in HT-29 and Caco-2 colorectal cancer cell lines. *Cancer Cell International*, 21, 204. Doi: 10.1186/s12935-021-01898-9

Ghorbani, F., Ghalandari, B., Khajehmohammadi, M., Bakhtiary, N., Tolabi, H., Sahranavard, M., Fathi-Karkan, S., Nazar, V., Niar, S., Armoon, A., Ettelaei, M., Banizi, M., & Collins, M. (2023) Photo-cross-linkable hyaluronic acid bioinks for bone and cartilage tissue engineering applications. *International materials reviews,* 68(7), 901 – 942. Doi: 10.1080/09506608.2023.2167559

Gillispie, G., Copus, J., Uzun-per, M., Yoo, J., Atala, A., Niazi, M., & Lee, S. (2023) The correlation between rheological properties and extrusion-based printability in bioink artifact quantification. *Materials & design*, 233, 112237. Doi: 10.1016/j.matdes.2023.112237

Gillispie, G., Han, A., Uzun-Per, M., Fisher, J., Mikos, A., Niazi, M., Yoo, J., Lee, S., & Atala, A. (2020) The influence of printing parameters and cell density on bioink printing outcomes. *Tissue engineering Part A: Research advances*, 26(24), 1349 – 1358. Doi: 10.1089/ten.2020.0210

Gleadall, A., Visscher, D., Yang, J., Thomas, D., & Segal, J. (2018) Review of additively manufactured tissue engineering scaffolds: the relationship between geometry and performance. *Burns Trauma*, 6, 19. Doi: 10.1186/s41038-018-0121-4

Gogoi, D., Kumar, M., & Singh, J. (2024) A comprehensive review on hydrogel-based bio-ink development for tissue engineering scaffolds using 3D printing. *Annals of 3D printed medicine*, 15, 100159. Doi: 10.1016/j.stlm.2024.100159

Goldring, S. (2016) Differential mechanisms of de-regulated bone formation in rheumatoid arthritis and spondylarthritis. *Rheumatology*, 55(2), 56 – 60. Doi: 10.1093/rheumatology/kew345

Gomes, P., & Fernandes, M. (2011) Rodent models in bone-related research: the relevance of calvaria defects in the assessment of bone regeneration strategies. *Laboratory animals*, 45(1). Doi: 10.1258/la.2010.010085

Gonzalez-Cruz, R., Fonseca, V., & Darling, E. (2012) Cellular mechanical properties reflect the differentiation potential of adipose-derived mesenchymal stem cells. *PNAS: biological sciences*, 109(24), 1523 – 1529. Doi: 10.1073/pnas.1120349109

Gonzalez-Fernandez, T., Tenorio, A., Campbell, K., Silva, E., & Leach, J. (2021) Alginate-based bioinks for 3D bioprinting and fabrication of anatomically accurate bone grafts. *Tissue Engineering Part A: Research Advances,* 27(17), 1168 – 1181. Doi: 10.1089/ten.tea.2020.0305

Goudie, K., McCreath, S., Parkinson, J., Davidson, C., & Liggat, J. (2023). Investigation of the influence of pH on the properties and morphology of gelatin hydrogels. *Journal of polymer science*, 61(19), 2316 – 2332. Doi: 10.1002/pol.20230141

Grabolle, M., Starke, M., & Resch-Genger, U. (2016) Highly fluorescent dye-nanoclay hybrid materials made from different dye classes. *Langmuir*, 32(14), 3506 – 3513. Doi: 10.1021/acs.langmuir.5b04297

Graf, B., & Boppart, S. (2010) Imaging and analysis of three-dimensional cell culture models. *Methods of molecular biology*, 591, 211 – 227. Doi: 10.1007/978-1-60761-404-3_13

Grassi, L., Nraiech, N., Schileo, E., Ansaloni, M., Rochette, M., & Viceconti, M. (2011) Evaluation of the generality and accuracy of a new mesh morphing procedure for the human femur. *Medical engineering and physics*, 33(1), 112 – 120. Doi: 10.1016/j.medengphy.2010.09.014

Grigoriadis, A., Heersche, J., & Aubin, J. (1988) Differentiation of muscle, fat, cartilage, and bone from progenitor cells present in a bone derived clonal cell population: effect of dexamethasone. *Journal of cellular biology*, 106, 2139 – 2151. Doi: 10.1083/jcb.106.6.2139

Grue, B., & Veres, S. (2022) Effect of increasing mineralization on pre-osteoblast response to native collagen fibril scaffolds for bone tissue repair and regeneration. *Journal of applied biomaterials and functional materials*, 20(3), 228080002211040. Doi: 10.1177/22808000221104000

Gu, Y., Lei, Z., Du, X., Fan, Z., Wang, L., Sun, W., Cheng, Y., Zhu, Y., & Chen, C. (2018) Reversible physical crosslinking strategy with optimal temperature for 3D bioprinting of human chondrocyte-laden gelatine meth acryloyl bioink. *Journal of biomaterial applications*, 33(5), 088532821880586. Doi: 10.117/0885328218805864

Guida, L., Cavallaro, M., & Levi, M. (2024) Advancements in high-resolution 3D bioprinting: exploring technological trends, bioinks and achieved resolutions. *Bioprinting*, 44, e00376. Doi: 10.1016/j.bprint.2024.e00376

Gungor-Ozkerim, O., Inci, I., Zhang, Y., Shademhosseini, A., & Dokmeci, M. (2018) Bioinks for 3D bioprinting: an overview. *Biomaterial science*, 6(5), 915-946. Doi: 10.1039/c7bm00765e

Gungor-Ozkerim, P. S., Inci, I., Zhang, Y. S., Khademhosseini, A., & Dokmeci, M. R. (2018). Bioinks for 3D bioprinting: An overview. *Biomaterials Science*, *6*(5), 915. Doi: 10.1039/c7bm00765e

Habib, M., & Khoda, B. (2022) Rheological analysis of bio-ink for 3D bio-printing processes. *Journal of manufacturing processes*, 76, 708 – 718. Doi: 10.1016/j.jmapro.2022.02.048

Hale, L., Ma, Y., & Santerre, R. (2000) Semi-quantitative fluorescence analysis of calcein binding as a measurement of in-vitro mineralization. *Calcified tissue international*, 67(1), 80 – 84. Doi: 10.1007/s00223001101

Hall, G. N., Mendes, L. F., Gklava, C., Geris, L., Luyten, F. P., & Papantoniou, I. (2020). Developmentally Engineered Callus Organoid Bioassemblies Exhibit Predictive In Vivo Long Bone Healing. *Advanced Science*, *7*(2), 1902295. Doi: 10.1002/advs.201902295

Hallgren, S., Perjryd, L., & Ekengren, J. (2016) 3D data export for additive manufacturing – improving geometric accuracy. *Science direct: Procedia CIRP*, 50, 518 – 523. Doi: 10.1016/j.procir.2016.05.046

Hao, X., Miao, S., Li, Z., Wang, T., Xue, B., Chen, J., Xian, C., & Bi, L. (2023) 3D printed structured porous hydrogel promotes osteogenic differentiation of BMSCs. *Materials & Design,* 227, 111729. Doi: 10.1016/j.matdes.2023.111729

Hara, T., Tanck, E., Homminga, J., & Huiskes, R. (2002) The influence of microcomputed tomography threshold variations on the assessment of structural and mechanical trabecular bone properties. *Bone*, 31(1), 107 – 109. Doi: 10.1016/s8756-3282(02)00782-2

Harrison, R. K. (2016). Phase II and phase III failures: 2013–2015. *Nature reviews drug discovery*, 15, 817 – 818. Doi: 10.1038/nrd.2016.184

Hart, K., & Rimoli, J. (2020) MicroStructPy: A statistical microstructure mesh generator in python. *Software X*, 12, 100595. Doi: 10.1016/j.softx.2020.100595

Hart, N., Nimphius, S., Rantalainen, T., Ireland, A., Sifarikas, A., & Newton, R. (2017) Mechanical basis of bone strength: Influence of bone material, bone structure and muscle action. *Journal of musculoskeletal and neuronal interactions*, 17(3), 114 – 139.

Haseltine, K., Chukir, T., Smith, P., Jacob, J., Bilezikian, J., & Farooki, A. (2021) Bone mineral density: clinical relevance and quantitative assessment. *The journal of nuclear medicine*, 62(4), 446 – 454. Doi: 10.2967/jnumed.120.256180

He, R., Tu, M., Huang, L., Tsai, M., Wu, J., & Hsu, J. (2019) Improving the prediction of the trabecular bone microarchitectural parameters using dental cone-beam computed tomography. *BMR Medical Imaging*, 19, 10. Doi: 10.1186/s12880-019-0313-9

He, Y., Anderson, B., Cazoulat, G., Rigaud, B., Almodovar-Abreu, L., Pollard-Larkin, J., Balter, P., Liao, Z., Mohan, R., Odisio, B., Svensson, S., & Brock, K. (2022) Optimisation of mesh generation for geometric accuracy, robustness, and efficiency of biomechanical-model-based deformable image registration. *American association of physicists in medicine*, 50(1), 323-329. Doi: 10.1002/mp.15939

Heath, S., Han, Y., Hua, R., Roy, A., Jiang, J., Nyman, J., & Wang, X. (2023) Assessment of glycosaminoglycan content in bone using Raman spectroscopy. *Bone*, 171. Doi: 10.1016/j.bone.2023.116751

Hefferan, T. E., Evans, G. L., Lotinun, S., Zhang, M., Morey-Holton, E., & Turner, R. T. (2003). Effect of gender on bone turnover in adult rats during simulated weightlessness. *Journal of Applied Physiology*. Doi: 0951775

Heimel, P., Swiadek, N., Slezak, P., Kerbl, M., Schneider, C., Numberger, S., Redl, H., Teuschl, A., & Hercher, D. (2019) Iodine - enhanced micro-CT imaging of soft tissue on the example of peripheral nerve regeneration. *Contrast media & molecular imaging*, 7483745. Doi: 10.1155/2019/7483745

Herman, A., Gan, J., & Yu, A. (2021) The effects of rotation speed and mixer size on granular flow and mixing in bladed mixers. *Powders and grains*, 249, 03036. Doi: 10.1051/epjconf/2021249-3-36

Herman, M., Aiello, B., DeLong, J., Garcia-Ruiz, H., Gonzalez, A., Hwang, W., McBeth, C., Stojkovic, E., Trakselis, M., & Yakoby, N. (2021) A unifying framework for understanding biological structures and functions across levels of biological organisation. *Integrative and comparative biology*, 61(6), 2038 – 2047. Doi: 10.1093/icb/icab167

Herrada-Manchon, H., Fernandez, M., & Aguilar, E. (2023) Essential guide to hydrogel rheology in extrusion 3D printing: how to measure it and why it matters? *Gels*, 9(7), 517. Doi: 10.3390/gels9070517

Hickman, D., Johnson, J., Vemulapalli, T., Crisler, J., & Shepherd, R. (2016) Commonly used animal models. *Principals of animal research for graduate and undergraduate students*, 117 – 175. Doi: 10.1016/B978-0-12-802151-4.00007-4

Highley, C., Rodell, C., & Burdick, J. (2015) Direct 3D printing of shear-thinning hydrogels into self-healing hydrogels. *Advanced materials*, 27(34), 5075-5079. Doi: 10.1002/adma.201501234

Hillier, M. L., & Bell, L. S. (2007). Differentiating Human Bone from Animal Bone: A Review of Histological Methods. *Journal of Forensic Sciences*, *52*(2), 249-263. Doi: 10.1111/j.1556-4029.2006.00368.x

Hinton, T., Jallerat, Q., Palchesko, R., Park, J., Grodzicki, M., Shue, H., Ramadan, M., Hudson, A., & Feinberg, A. (2015) Three-dimensional printing of complex biological structures by freeform reversible embedding of suspended hydrogels. *Science Advances*, 1(9). Doi: 10.1126/sciadv.1500758

Hirsch, C., & Schildknecht, S. (2019) In-vitro research reproducibility: keeping up high standards. *Frontiers in pharmacology*, 10, 1484. Doi: 10.3389/fphar.2019.01484

Ho, H., Wu, J., & Lin, W. (2011) Flemingia macrophylla extract ameliorates experimental osteoporosis in ovariectomized rats. *Evidence-based complementary and alternative medicine*, 2011(18), 752302. Doi: 10.1098/ecam/nep179

Hoffmann, L., Breitkreutz, J., & Quodbach, J. (2022) Fused deposition modelling (FDM) 3D printing of the thermo-sensitive peptidomimetic drug enalapril maleate. *Pharmaceutics*, 14(11), 2411. Doi: 10.3390/pharmaceutics14112411

Holland, I. (2025). Extrusion bioprinting: Meeting the promise of human tissue biofabrication? *Progress in Biomedical Engineering (Bristol, England)*, *7*(2), 023001. Doi: 10.1088/2516-1091/adb254

Homan, K., Kolesky, D., Skylar-scott, M., Herrmann, J., Obuobi, H., Moisan, A., & Lewis, J. (2016) Bioprinting of 3D convoluted renal proximal tubules on perfusable chips. *Science Reports*, 6, 34845. Doi: 10.1038/srep34845

Hong, D., Chen, H., yu, H., Liang, Y., Wang, C., Lian, Q., Deng, H., & Ge, R. (2010) Morphological and proteomic analysis of early stage of osteoblast differentiation in osteoblastic progenitor cells. *Experimental cell research*, 316(14), 2291 – 2300. Doi: 10.1016/j.yexcr.2010.05.011

Hospodiuk, M., Dey, M., Sosnoski, D., & Ozbolat, I. T. (2017). The bioink: A comprehensive review on bioprintable materials. *Biotechnology Advances*, *35*(2), 217-239. Doi: 10.1016/j.biotechadv.2016.12.006

Hsieh, J., & Flohr, T. (2021) Computed tomography recent history and future perspectives. *Journal of medical imaging*, 8(5), 052109. Doi: 10.1117/1.JMI.8.5.052109

Hu, K., & Olsen, B. R. (2016). The roles of vascular endothelial growth factor in bone repair and regeneration. *Bone*, *91*, 30. Doi: 10.1016/j.bone.2016.06.013

Hu, S., Meng, Z., Zhou, J., Li, Y., Su, Y., Lei, Q., Mao, M., Qu, X., He, J., & Wang, E. (2022) Enhanced attachment and collagen type I deposition of MC3T3-E1 cells via electrohydrodynamic printed sub-microscale fibrous architectures. *International journal of bioprinting*, 8(2), 514. Doi: 10.18063/ijb.v8i2.514

Hua, Y., Wu, J., Wu, H., Su, C., Li, X., Ao, Q., Zeng, Q., Zhu, X., & Zhang, X. (2021). Exposure to hydroxyapatite nanoparticles enhances Toll-like receptor 4 signal transduction and overcomes endotoxin tolerance in vitro and in vivo. *Acta Biomaterialia*, *135*, 650-662. Doi: 10.1016/j.actbio.2021.09.006

Huang, D., Li, Z., Li, G., Zhou, F., Wang, G., Ren, X., & Su, J. (2025) Biomimetic structural design in 3D-printed scaffolds for bone tissue engineering. *Materials today biology*, 32, 101664. Doi: 10.1016/j.mtbio.2025.101664

Hull, S., Lou, J., Lindsay, C., Navarro, R., Cai, B., Brunel, L., Westerfield, A., Xia, Y., & Heilshorn, S. (2023) 3D bioprinting of dynamic hydrogel bioinks enabled by small molecule modulators. *Science advances*, 9(13). Doi: 10.1126/sciadv.ade7880

Hulley, P., Papadimitriou-Oliveri, I., & Knowles, H. (2020) Osteoblast-osteoclast coculture amplifies inhibitory effects of FG-4592 on human osteoclastogenesis and reduces bone resorption. *JBMR Plus*, 4(7), e10370. Doi: 10.1002/jbm4.10370

Hunziker, E. (2018) Elongation of the long bones in humans by the growth plates. *Nestle Nutrition Institute Workshop Series*, 89, 13 – 23. Doi: 10.1159/000486489

Hutchinson, I., Owen, C., & Bailey, J. (2022). Modernising Medical Research to Benefit People and Animals. *Animals: An Open Access Journal From MDPI*, *12*(9), 1173. Doi: 10.3390/ani12091173

Hwang, H. S., & Lee, S. (2023). Recent Progress in Hyaluronic-Acid-Based Hydrogels for Bone Tissue Engineering. *Gels*, *9*(7), 588. Doi: 10.3390/gels9070588

Hwang, P., & Horton, J. (2019) Variable osteogenic performance of MC3T3-E1 subclones impacts their utility as models of osteoblast biology. *Scientific Reports*, 9, 8299. Doi: 10.1038/s41598-019-44575-8

Hynds, R. E., Vladimirou, E., & Janes, S. M. (2018). The secret lives of cancer cell lines. *Disease Models & Mechanisms*, *11*(11), dmm037366. Doi: 10.1242/dmm.037366

Ielo, I., Calabrese, G., Luca, G. D., & Conoci, S. (2022). Recent Advances in Hydroxyapatite-Based Bio composites for Bone Tissue Regeneration in Orthopaedics. *International Journal of Molecular Sciences*, *23*(17), 9721. Doi: 10.3390/ijms23179721

Iftekar, S. F., Aabid, A., Amir, A., & Baig, M. (2023). Advancements and Limitations in 3D Printing Materials and Technologies: A Critical Review. *Polymers*, *15*(11), 2519. Doi: 10.3390/polym15112519

Iglesias-Mejuto, A., & García-González, C. A. (2021). 3D-printed alginate-hydroxyapatite aerogel scaffolds for bone tissue engineering. *Materials Science and Engineering: C*, *131*, 112525. Doi: 10.1016/j.msec.2021.112525

Ilyin, S. (2024) structural rheology in the development and study of complex polymer materials. *Polymers*, 16(17), 2458. Doi: 10.3390/polym16172458

Im, G. (2014) Coculture in musculoskeletal tissue regeneration. *Tissue engineering part B, reviews*, 20(5). Doi: 10.1089/ten.teb.2013.0731

Im, S., Choe, G., Seok, J., Yeo, S., Lee, J., Kim, W., Lee, J., & Park, S. (2022) An osteogenic bioink composed of alginate, cellulose nanofibrils, and polydopamine nanoparticles for 3D bioprinting and bone tissue engineering. *International journal of biological macromolecules*, 205, 520 – 529. Doi: 10.1016/j.ijbiomax.2022.02.012

Immohr, M., Adrego, F., Teichert, H., Schmidt, V., Sugimura, Y., Bauer, S., Barth, M., Lichtenberg, A., & Akhyari, P. (2022) 3D-bioprinting of aortic valve interstitial cells: impact of hydrogel and printing parameters on cell viability. *Biomedical materials*, 18, 15004. Doi: 10.1088/1748-605X/ac9f91

Irmak, G., Demirtas, T., & Gumusdereligoglu, M. (2019) Highly methacrylated gelatine bioink for bone tissue engineering. *ACS biomaterials science & Engineering*, 5(2), 831 – 845. Doi: 10.1021/acsbiomaterials.8b00778

Isenburg, M., & Snoeyink, J. (2002) Coding with ASCII: compact, yet text-based 3D content. *IEEE Xplore*. Doi: 10.1109/TDPVT.2002.1024125

Isojima, T., & Sims, N. (2021) Cortical bone development, maintenance and porosity: genetic alterations in humans and mice influencing chondrocytes, osteoclasts, osteoblasts and osteocytes. *Cellular and molecular life sciences*, 78(15), 5755 - 5773. Doi: 10.1007/s00018-021-03884-w

Izumiya, M., Ueda, K., Ishia, H., Ma, C., Ideta, H., Sobijma, A., Ueshiba, K., Uemura, T., Saito, N., & Haniu, H. (2021) Evaluation of MC3T3-E1 cell osteogenesis in different cell culture media. *International journal of molecular sciences*, 22(14), 7752. Doi: 10.3390/ijms22147752

Jacome-Galarza, C., Percin, G., Muller, J., Mass, E., Lazarov, T., Eitler, J., Rauner, M., Yadav, V., Crozet, L., Bohm, M., Loyher, P., Karsenty, G., Waskow, C., & Geissmann, F. (2019) Developmental origin, functional maintenance and genetic rescue of osteoclasts. *Nature*, 568(7753), 541 – 545. Doi: 10.1038/s41586-019-1105-7

Janardhanan, S., Wang, M. O., & Fisher, J. P. (2012). Coculture Strategies in Bone Tissue Engineering: The Impact of Culture Conditions on Pluripotent Stem Cell Populations. *Tissue Engineering. Part B, Reviews*, *18*(4), 312. Doi: 10.1089/ten.teb.2011.0681

Janarthanan, G., & Noh, I. (2018) Recent trends in bioinks for 3D printing. *Biomaterials research*, 22, 11. Doi: 10.1186/s40824-018-0122-1

Jannat, B., Ghorbani, K., Kouchaki, S., Sadeghi, N., Eslamifarsani, E., Rabbani, F., & Beyramysoltan, S. (2020) Distinguishing tissue original of bovine gelatin in processed products using LC/MS technique in combination with chemometrics tools. *Food chemistry*, 319, 126302. Doi: 10.1016/j.foodchem.2020.126302

Jatav, S., & Joshi, Y. (2014) Chemical stability of laponite in aqueous media. *Applied clay science*, 97, 72 – 77. Doi: 10.1016/j.clay.2014.06.004

Jeon, S., Lee, J., Jang, H., Lee, Y., Kim, B., Kang, M., Shin, Y., Shin, S., Hong, S., & Han, D. (2021) Spontaneously promoted osteogenic differentiation of MC3T3-E1 pre-osteoblasts on ultrathin layers of black phosphorus. *Material Science Engineering C: material biology applied*. Doi: 10.1016/j.msec.2021.112309

Jeske, R., Yuan, X., Fu, Q., Bunnell, B., Logan, T., & Li, Y. (2021) In-vitro culture expasion shifts are the immune phenotype of human adipose-derived mesenchymal stem cells. *Frontiers in immunology*, 12, 621744. Doi: 10.3389/fimmu.2021.621744

Jia, M., Chen, S., Zhang, B., Liang, H., Feng, J., & Zong, Z. (2013) Effects of constitutive β-catenin activation on vertebral bone growth and remodelling at different post-natal stages in mice. *PLOS ONE,* 8(9), e7409. Doi: 1-.1371/journal.pone.0074093

Jiao, J., Hong, Q., Zhang, D., Wang, M., Tang, H., Yang, J., Qu, X., & Yue, B. (2023) Influence of porosity on osteogenesis, bone growth and osteointegration in trabecular tantalum scaffolds fabricated by additive manufacturing. *Frontiers: biomaterials*, 11. Doi: 10.3389/fbioe.2023.1117954

Jilka, R. (2013) The relevance of mouse models for investigating age-related bone loss in humans. *Journal of gerontology series A: Biological sciences and medical sciences*, 68(10), 1209 – 1217. Doi: 10.1093/gerona/glt046

Jochum, F., & Theato, P. (2013) Temperature- and light-responsive smart polymer materials. *Chemistry society reviews*, 42, 7468 – 7483. Doi: 10.1039/C2CS35191A

Jones, G., Motta, A., Marshall, M., Haj, A., & Cartmell, S. (2009) Osteoblast: osteoclast co-cultures on silk fibroin, chitosan and PLLA films. *Biomaterials*, 30(29), 5376 – 5384. Doi: 10.1016/j.biomaterials.2009.07.028

Jose, J., Peter, A., Thajudeen, K., Pereira, M., Athira, P., Bhat, S., & Michel, H. (2024) Recent advances in the design and development of bioink formulations for various biomedical applications. *Results in engineering*, 22, 102060. Doi: 10.1016/j.rineng.2024.102060

Juarez-Moreno, K., Chavez-Garcia, D., Hirata, G., & Vazquez-Duhalt, R. (2022) Monolayer (2D) or spheroids (3D) cell cultures for nanotoxicological studies? Comparison of cytotoxicity and cell internalization of nanoparticles. *Toxicology in-vitro*, 85, 105461. Doi: 10.1016/j.tiv.2022.105461

Jubelin, C., Munoz-Garcia, J., Griscom, L., Cochonneau, D., Ollivier, E., Heymann, M., Vallette, F., Oliver, L., & Heymann, D. (2022) *Cell & Bioscience*, 12, 155. Doi: 10.1186/s13578-022-00887-3

Jucan, M., & Jucan, C. (2014) The power of science communication. *Procedia – Social and behavioural sciences*, 149, 461 – 466. Doi: 10.1016/j.sbspro.2014.08.288

Jungst, T., Smolan, W., Schacht, K., Scheibel, T., & Groll, J. (2016) Strategies and molecular design criteria for 3D printable hydrogels. *Chemical reviews*, 116(3), 1496-1539. Doi: 10.1021/acs.chemrev5b00303

Kacarevic, Z., Rider, P., Alkildani, S., Retnasingh, S., Smeets, R., Jung, O, Ivanisevic, Z., & Barbeck, M. (2018) An introduction to 3D bioprinting: possibilities, challenges and future aspects. *Materials*, 11(11), 2199. Doi: 10.3390ma11112199

Kafle, A., Luis, E., Silwal, R., Pan, H., Shrestha, P., & Bastola, A. (2021) 3D/4D printing of polymers: fused deposition modelling (FDM), selective laser sintering (SLS), and stereolithography (SLA). *Polymers*, 13(18), 3101. Doi: 10.3390/polym13183101

Kajave, N., Schmitt, T., Nguyen, T., & Kishore, V. (2019) Dual crosslinking strategy to generate mechanically viable cell-laden printable constructs using methacrylate collagen bioinks. *Material science engineering C: Materials and biology applied*. 107, 110290. Doi: 10.1016/j.msec.2019.110290

Kam, D., Rulf, O., Reisinger, A., Lieberman, R., & Magdassi, S. (2024) 3D printing by stereolithography using thermal initiators. *Nature communications*, 15, 2285. Doi: 10.1038/s414167-024-46532-0

Kamio, T., Suzuki, M., Asaumi, R., & Kawai, T. (2020) DICOM segmentation and STL creation for 3D printing: a process and software package comparison for osseous anatomy. *3D printing in medicine,* 6(1), 17. Doi: 10.1186/s41205-020-00069-2.

Kang, M., Jang, J., Jo, H., Kim, W., Kim, B., Chun, H., Lim, D., & Han, D. (2022) Advances and innovations of 3D bioprinting skin. *Biomolecules*, 13(1), 55. Doi: 10.3390/biom13010055

Kapalczynska, M., Kolenda, T., Przybyla, W., Zajaczkowska, M., Teresiak, A., Filas, V., Ibbs, M., Blizniak, R., Luczewski, L., & Lamperska, K. (2016) 2D and 3D cell cultures – a comparison of different types of cancer cell cultures. *Archives of medical science*, 14(4), 910-919. Doi: 10.5114/aoms.2016.63742

Karageorgiou, V., & Kaplan, D. (2005) Porosity of 3D biomaterial scaffolds and osteogenesis. *Biomaterials*, 26(27), 5474 – 5491. Doi: 10.1016/j.biomaterials.2005.02.002

Kartsogiannis, V., & Ng, K. (2004) Cell lines and primary cell cultures in the study of bone cell biology. *Molecular and cellular endocrinology*, 228(1), 79 – 102. Doi: 10.1016/j.mce.2003.06.002

Karvinen, J., & Kellomaki, M. (2023) Design aspects and characterisation of hydrogel-based bioinks for extrusion-based bioprinting. *Bioprinting*, 32, e00274. Doi: 10.1016/j.bprint.2023.e00274

Kazama, J., Koda, R., Yamamoto, S., Narita, I., Gejyo, F., & Tokumoto, A. (2010) Cancellous bone volume is an indicator for trabecular bone connectivity in dialysis patients. *Clinical Journal of the American society of nephrology*, 5(2), 292-298. Doi: 10.2215/CJN.04150609

Keijzer, K., Tsingos, E., & Merks, R. (2025) How cells align to structured collagen fibrils: a hybrid cellular Potts and molecular dynamics model with dynamic mechanosensitive focal adhesions. *Frontiers in Cell developmental biology*, 12. Doi: 10.3389/fcell.2024.1462277

Khatun, M., Bhattacharyya, A., Gunbayar, M., Jung, M., & Noh, I. (2023) study on bio responsive gelatin-hyaluronic acid-genipin hydrogel for high cell-density 3D bioprinting. *Gels*, 9(8), 601. Doi: 10.3390/gels9080601

Khoeini, R., Nosrati, H., Akbarzadeh, A., Eftekhari, A., Kavetskyy, T., Khalilov, R., Ahmadian, E., Nasibova, A., Datta, P., Roshangar, L., Deluca, D. C., Davaran, S., Cucchiarini, M., & Ozbolat, I. T. (2021). Natural and Synthetic Bioinks for 3D Bioprinting. *Advanced NanoBiomed Research*, *1*(8), 2000097. Doi: 10.1002/anbr.202000097

Kibble, M. J., Ferreira, M. J., Usta, Y. H., Van den Akker, G. G., Moxon, S. R., Baird, P., Hoyland, J. A., Domingos, M. A., & Richardson, S. M. (2025). Suspension bioprinted whole intervertebral disc analogues enable regional stiffness- and hypoxia-regulated

matrix secretion by primary human nucleus pulposus and annulus fibrosus cells. *Acta Biomaterialia*, *200*, 378-389. Doi: 10.1016/j.actbio.2025.05.015

Kim, J. (2023). Characterization of Biocompatibility of Functional Bioinks for 3D Bioprinting. *Bioengineering*, *10*(4), 457. Doi: 10.3390/bioengineering10040457

Kim, J., Kumar, S., Park, C., & Kim, C. (2024) Development of cell-laden photopolymerized constructs with bioactive amorphous calcium magnesium phosphate for bone tissue regeneration via 3D bioprinting. *International journal of biological macromolecules*, 267, 131412. Doi: 10.1016/j.ijbiomac.2024.131412

Kim, J., Lyu, H., Jung, C., Lee, K., Han, S., Lee, J., & Cha, M. (2021) Osteogenic response of MC3T3-E1 and Raw 264.7 in the 3d-encapsulated co-culture environment. *Tissue engineering and regenerative medicine*, 18, 387 – 397. Doi: 10.1007/s13770-020-00321-0

Kim, M., Jeong, W., & Kang, H. (2023) Liver dECM-gelatin composite bioink for precise 3D printing of highly functional liver tissues. *Journal of functional biomaterials*, 14(8), 417. Doi : 10.3390/jfb14080417

Kim, Y., Brodt, M., Tang, S., & Silva, M. (2021) Micro-CT for scanning and analysis of mouse bones. *Methods molecular biology*, 2230, 169 – 198. Doi: 10.1007/978-1-0716-1028-2

Kizilkaya, A., & Kara, A. (2024) Impact of different CAD software programs on the marginal and internal fit of provisional crows: An *in vitro* study. *Heliyon*, 10(2), e24205. Doi: 10.1016/j.heliyon.2024.e24205

Klotz, B. J., Oosterhoff, L. A., Utomo, D. L., S Lim, D. K., Vallmajo-Martin, D. Q., Clevers, P. H., F Woodfield, T. B., P Rosenberg, J. W., Malda, P. J., Ehrbar, D. M., Spee, D. B., & Gawlitta, D. D. (2019). A Versatile Biosynthetic Hydrogel Platform for Engineering of Tissue Analogues. *Advanced Healthcare Materials*, *8*(19), e1900979. Doi: 10.1002/adhm.201900979

Knuth, C., Sastre, A., Fahy, N., Witte-bouma, J., Ridwan, Y., Strabbing, E., Koudstaal, M., Peppel, J., Wolvius, E., Narcisi, R., & Farrell, E. (2019) Collagen type X is essential for successful mesenchymal stem cell-medicated cartilage formation and subsequent endocondral ossification. *European cells and materials*, 38, 106 – 122. Doi: 10.22203/eCM.v03a09

Koh, N., Miszkiewicz, J., Fac, M., Wee, N., & Sims, N. (2024) Preclinical rodent models for human bone disease, including a focus on cortical bone. *Endocrine reviews*, 45(4), 493 – 520. Doi: 10.1210/endrev/bnae004

Kolesky, D., Truby, R., Gladman, S., Busbee, T., Homan, K., & Lewis, J. (2014) 3D bioprinting of vascularised, heterogeneous cell-laden tissue constructs. *Advanced materials*, 26(19), 3124-3130. Doi: 10.1002/adma.201305506

Komori, T., Ji, Y., Pham, H., Jani, P., Kilts, T., Kram, V., Li, L., & Young, M. (2022) Type VI collagen regulates endochondral ossification in the temporomandibular joint. *JBMR plus*, 6(1), e10617. Doi: 10.1002/jbm4.10617

Korkeamaki, J., Rashad, A., Ojansivu, M., Karvinen, J., Koivisto, J., Syverud, K., Kellomaki, M., Miettinen, S., & Mustafa, K. (2025) Systematic development and bioprinting of novel nanostructured multi-material bioinks for bone tissue engineering. *Biofabrication*, 17(2). Doi: 10.1088/1758—50900/ada63b

Kovacs, C. (2001) Calcium and bone metabolism in pregnancy and lactation. *The journal of clinical endocrinology and metabolism*, 86(6), 2344 – 2348. Doi: 10.1210/jcem.86.6.7575

Koyama, H., Kishi, K., Mikoshiba, S., & Fujimori, T. (2023) An imageJ-based tool for three-dimensional registration between different types of microscopic images. *Development, growth & differentiation,* 65(1), 65-74. Doi: 10.1111/dgd.12835

Kranti, E., Bonicelli, A., & Garcia-Donas, J. (2019) Bone-mineral density: clinical significance, methods of quantification and forensic applications. *Dove press*, 2019(8), 9 – 21. Doi: 10.2147/RRFMS.S164933

Kristian, R., Imaduddin, F., Ariawan, D., Ubaidillah., & Arifin, Z. (2021) A review on the fused deposition modelling (FDM) 3D printing: filament processing, materials, and printing parameters. *Open engineering*, 11(1). Doi: 10.1515/eng-2021-0063

Kumar, R., Kumar, M., & Chohan, J. (2021) The role of additive manufacturing for biomedical applications: a critical review. *Journal of manufacturing processes*, 64, 828-850. Doi: 10.1016j.jnapor.2021.02.022

Lafage-Proust, H., Roche, B., Langer, M., Cleret, D., Bossche, A. V., Olivier, T., & Vico, L. (2015). Assessment of bone vascularization and its role in bone remodeling. *BoneKEy Reports*, *4*, 662. Doi: 10.1038/bonekey.2015.29

Lai, Y., Li, Y., Cao, H., Long, J., Wang, X., Li, L., Li, C., Jia, Q., Teng, B., Tang, T., Peng, J., Eglin, D., Alini, M., Grijpma, D. W., Richards, G., & Qin, L. (2019). Osteogenic magnesium incorporated into PLGA/TCP porous scaffold by 3D printing for repairing challenging bone defect. *Biomaterials*, *197*, 207-219. Doi: 10.1016/j.biomaterials.2019.01.013

Lakkala, P., Munnangi, S., Bandari, S., & Repka, M. (2023) Additive manufacturing technologies with emphasis on stereolithography 3D printing in pharmaceutical and medical applications: a review. *International Journal of Pharmaceutics*, 5, 100159. Doi: 10.1016/j.ijpx.100159

Lam, E., Yu, F., Zhu, S., & Wang, Z. (2023) 3D bioprinting for next-generation personalised medicine. *International journal of molecular sciences*, 24(7), 6357. Doi: 10.3390/ijms24076357

Latour, M., Tarar, M., Hickey, R., Cuerrier, C., Catelas, I., & Pelling, A. (2024) Decellularized apple-derived scaffolds for bone tissue engineering in-vitro and in-vivo. *Journal of visualised experiments,* 204. Doi: 10.3791/65226

Lee, A., Hudson, A., Shiwarski, D., Tashman, J., Hinton, T., Yerneni, S., Bliley, J., Campbell, P., & Feinberg, A. (2019) 3D bioprinting of collagen to rebuild components of the human heart. *Science*, 365(6452), 482 – 487. Doi: 10.1126/science.aav9051

Lee, C., Laughlin, J., Moody, J., Amaro, R., McCammon, A., Holst, M., & Rangamani, P. (2020) An open-source mesh generation platform for biophysical modeling using realistic

cellular geometries. *Biophysical journal,* 118 (5), 1003 – 1008. Doi: 10.1016/j.bpj.2019.11.3400

Lee, C., Lee, J., Han. S., Kim, Y., Choi, Y., Jeon, K., & Jung, H. (2019) Site-specific and time-course changes of post-menopausal osteoporosis in rat mandible: comparative study with femur. *Scientific reports*, 9(1), 1 – 9. Doi: 10.1038/s41598-019-50554-w

Lee, J., Hong, J., Kim, W., & Kim, G. H. (2020). Bone-derived dECM/alginate bioink for fabricating a 3D cell-laden mesh structure for bone tissue engineering. *Carbohydrate Polymers*, *250*, 116914. Doi: 10.1016/j.carbpol.2020.116914

Lee, S., & Kumar, S. (2016) Actomyosin stress fibre mechanosensing in 2D and 3D. *F1000 Research*, 5. Doi: 10.12688/F1000research.8800.1

Lee, T., & Lin, C. (2001) Growing-cube isosurface extraction algorithm for medical volume data. *Computerised medical imaging and graphics,* 25(5), 405-415. Doi: 10.1016/s095-6111(00)00084-7

Leenaars, C., Kouwenaar, C., Stafleu, F., Bleich, A., Ritskes-Hoitinga, M., Vries, R., & Meijboom, F. (2019) Animal to human translation: a systematic scoping review of reported concordance rates. *Journal of Translation Medicine*, 17, 223. Doi: 10.1186/s12967-019-1976-2

Leeuw, A., Graf, R., Lim, P., Zhang, J., Schadli, G., Peterhans, S., Rohrbach, M., Giunta, C., Ruger, M., Rubert, M., & Muller, R. (2024) Physiological cell bioprinting density in human bone-derived cell-laden scaffolds enhances matrix mineralization rate and stiffness under dynamic loading. *Frontiers in bioengineering and biotechnology*, 12. Doi: 10.3389/fbior.2023.1310289

Lehmann, T., Iwanczyk-skalska, E., Harasymczuk, J., Jagodzinski, P., & Glowacki, M. (2023) Gene expression in MC3T3-E1 cells treated with diclofenac and methylprednisolone. *Genes*, 14(1), 184. Doi: 10.3390/genes14010184

Leon-Oliva, D., Barrena-Blazquezx, S., Jimenez-Alvarez, L., Fraile-Martinez, F., Garcia-Montero, C., Lopez-Gonzalez, L., Torres-Carranza, D., Garcia-Puente, L., Carranza, S., Alvarez-mon, M., Alvarez-Mon, M., Diaz, R., & Ortega, M. (2023) The RANK-RANKL-OPG system: a multifaceted regulator of homeostasis, immunity, and cancer. *Medicina*, 59(10), 1752. Doi: 10.3390/medicina59101752

Leordean, D., Vilău, C., & Dudescu, M. C. (2021). Generation of Computational 3D Models of Human Bones Based on STL Data and CAD Software Packages. *Applied Sciences*, *11*(17), 7964. Doi: 10.3390/app11177964

Leung, C. M., De Haan, P., Kim, G., Ko, J., Rho, H. S., Chen, Z., Habibovic, P., Jeon, N. L., Takayama, S., Shuler, M. L., Frey, O., Verpoorte, E., & Toh, Y. (2022). A guide to the organ-on-a-chip. *Nature Reviews Methods Primers*, *2*(1), 1-29. Doi: 10.1038/s43586-022-00118-6

Li, C., & Fennessy, P. (2021) The periosteum: a simple tissue with many faces, with special reference to the antler-lineage periostea. *Biology direct*, 16(17). Doi: 10.1186/s13062-021-00310-w

Li, C., Vepari, C., Jin, H., Kim, H. J., & Kaplan, D. L. (2006). Electrospun silk-BMP-2 scaffolds for bone tissue engineering. *Biomaterials*, *27*(16), 3115-3124. Doi: 10.1016/j.biomaterials.2006.01.022

Li, D., He, F., He, J., Deng, X., Liu, Y., Liu, Y., Ye, Y., & Yin, D. (2017) From 2D to 3D: the morphology, proliferation and differentiation of MC3T3-E1 on silk fibroin/chitosan matrices. *Carbohydrate polymers*, 178, 69 – 77. Doi: 10.1016/j.carbpol.2017.09.035

Li, H., Mao, B., Zhong,. J., Li, X., & Sang, H. (2024) Localised delivery of metformin via 3D printed GelMA-nanoclay hydrogel scaffold for enhanced treatment of diabetic bone defects. *Journal of orthopaedic translation*, 47, 249 – 260. Doi: 10.1016/j.jot.2024.06.013

Li, J., Settivari, R., & LeBaron, M. (2019) Genetic instability of in-vitro cell lines: implications for genetic toxicity testing. *Environmental and molecular mutagenesis*, 60(6), 559 – 562. Doi: 10.1002/em.22280

Li, L., Li, H., Wang, Q., Xue, Y., Dai, Y., Dong, Y., Shao, M., & Lyu, F. (2024) Hydroxyapatite nanoparticles promote the development of bone microtissues for accelerated bone regeneration by activating the FAK/Akt pathway. *ACS biomaterial science engineering*, 10(7), 4463 – 4479. Doi: 10.1021/acsbiomaterials.4c00574

Li, L., Wang, S., Chen, Y., Dong, S., Zhang, C., Liao, L., & Zhang, W. (2024). Hydrogels mimicking the viscoelasticity of extracellular matrix for regenerative medicine: Design, application, and molecular mechanism. *Chemical Engineering Journal*, *498*, 155206. Doi: 10.1016/j.cej.2024.155206

Li, N., Guo, R., & Zhang, Z. (2021) Bioink formulations for bone tissue regeneration. *Frontiers in bioengineering and biotechnology,* 9. Doi: 10.3389/fbioe.2021.630488

Li, W., Zhang, S., Liu, J., Liu, Y., & Liang, Q. (2019) Vitamin K2 stimulates MC3T3-E1 osteoblast differentiation and mineralisation through autophagy induction. *Molecular medicine reports*, 19(5), 3675 – 3684. Doi: 10.3892/mmr.2019.10040

Li, Y., & Kilian, K. A. (2015). Bridging the gap: From 2D cell culture to 3D micro-engineered extracellular matrices. *Advanced Healthcare Materials*, *4*(18), 2780. Doi: 10.1002/adhm.201500427

Li, Y., Maciel, D., Tomas, H., Rodrigues, J., Ma, H., & Shi, X. (2011) pH sensitive laponite/alginate hybrid hydrogels: swelling behaviour and release mechanism. *Soft matter*, 7, 6231 – 6238. Doi: 10.1039/C1SM05345K

Licini, C., Vitale-Brovarone, C., & Mattioli-Belmonte, M. (2019) Collagen and non-collagenous proteins molecular crosstalk in the pathophysiology of osteoporosis. *Cytokine and growth factor reviews*, 49, 59 – 69. Doi: 10.1016/j.cytogfr.2019.09.001

Lim, J., Lee, J., Yun, H., Shin, H., & Park, E. (2013) Comparison of bone regeneration rate in flat and long bone defects: Calvarial and tibial bone. *Tissue engineering and regenerative medicine*, 10(6). Doi: 10.1007/s13770-013-1094-9

Lin, A., Barrows, T., Cartmell, S., & Guldberg, R. (2003) Microarchitecture and mechanical characterisation of oriented porous polymer scaffolds. *Biomaterials*, 24(3), 481 – 489. Doi: 10.1016/s0142-9612(02)00361-7

Lin, C., Chen, Z., Guo, D., Zhou, L., Lin, S., Li, C., Li, S., Wang, X., Lin, B., & Ding, Y. (2022) Increased expression of osteopontin in subchondral bone promotes bone turnover and remodelling and accelerates the progression of OA in a mouse model. *Aging*, 14(1), 253 – 271. Doi: 10.18632/aging.203707

Lin, X., Patil, S., Gao, G., & Qian, A. (2020). The Bone Extracellular Matrix in Bone Formation and Regeneration. *Frontiers in Pharmacology*, *11*, 757. Doi: 10.3389/fphar.2020.00757

Liu, H., Qin, L., Liu, H., Li, F., Fan, Y., Meng, L., Sun, X., Zhan, C., Luo, R, Luo., Wang, C., Zhang, J., & Li, R. (2021) Effects of fiber cross-angle structures on the mechanical property of 3D printed scaffolds and performance of seeded MC3T3-E1 cells. *ACS omega*, 6(49), 33665 – 33675. Doi: 10.1021/acsomega.1c04672

Liu, L., Mu, H., & Pang, Y. (2021) Caffeic acid treatment augments the cell proliferation, differentiation, and calcium mineralisation in the human osteoblast-like MG-63 cells. *Pharmacognosy,* 17, 73, 38 – 44. Doi: 10.4103/pm.pm_186_20

Liu, S., Kilian, D., Ahlfeld, T., Hu, Q., & Gelinsky, M. (2023) Egg white improves the biological properties of an alginate-methylcellulose bioink for 3D bioprinting of volumetric bone constructs. *Biofabrication,* 15(2). Doi: 10.1088/1758-5090/acb8dc

Liu, S., Wang, T., Li, S., & Wang, X. (2022) Application status of sacrifical biomaterials in 3D bioprinting. Polymers, 14(11), 2182. Doi: 10.3390/polym14112182

Liu, X., Wang, B., Ma, J., & Hu, H. (2025). Biomineral/VEGF-functionalized fibre - enhanced 3D printed GelMA hydrogel to facilitate bone regeneration through osteogenesis and angiogenesis modulation. *International Journal of Biological Macromolecules*, *312*, 143991. Doi: 10.1016/j.ijbiomac.2025.143991

Liu, Y., & Sing, S. (2023) A review of advances in additive manufacturing and the integration of high-performance polymers, alloys, and their composites. *Material sciences in additive manufacturing*, 2(3), 1587. Doi: 10.36922/msam.1587

Loi, G., Stucchi, G., Scocozza, F., Cansolino, L., Cadamuro, F., Delgrosso, E., riva, F., Ferrari, C., Russo, L., & Conti, M. (2023) Characterisation of a bioink combining extracellular matrix-like hydrogel with osteosarcoma cells: preliminary results. *Gels*, 9(2), 129. Doi: 10.3390/gels9020129

Long, F., & Ornitz, D. (2013) Development of the endochondral skeleton. *Cold spring harbour perspectives in biology,* 5(1). Doi: 10.1101/cshperspect.a008334

Lopez, J. (2024) Bone development and growth. *International journal of molecular sciences*, 25(12), 6767. Doi: 10.3390/ijms25126767

Lopez-Serrano, C., Cote-Paradis, Y., Habenstein, B., Loquet, A., Coz, C., Ruel, J., Laroche, G., & Durrieu, M. (2024) Integrating mechanics and bioactivity: a detailed assessment of elasticity and viscoelasticity at different scales in 2D biofunctionalized PEGDA hydrogels for targeted bone regeneration. *ACS applied material interfaces*, 16(30), 39165 – 39165. Doi: 10.1021/acsami.4c10755

Loukelis, K., Kontogianni, I., Vlassopoulos, D., & Chatzinikolaidou, M. Extrusion-Based 3D Bioprinted Gellan Gum/Poly(vinyl alcohol)/Nano-Hydroxyapatite Composite Bioinks

Promote Bone Regeneration. *Advanced Healthcare Materials*, 2500365. Doi: 10.1002/adhm.202500365

Loundagin, L., Harrison, K., Wei, X., & Cooper, D. (2024) Understanding basic multicellular unit activity in cortical bone through 3D morphological analysis: new methods to define zones of the remodelling space. *Bone*, 179, 116960. Doi: 10.1016/j.bone.2023.116960

Lu, J., Huang, J., jin, J., Xie, C., Xue, B., Lai, J., Cheng, B., Li, L., & Jiang, Q. (2022) The design and characterisation of a strong bio-ink for meniscus regeneration. *International journal of bioprinting*, 8(4), 600. Doi: 10.18063/ijb.v8i4.600

Lujano-Negrete, A., Rodriguez-Ruiz, M., Skinner-Taylor, C., Perez-Barbosa, L., Garza, J., Garcia-Hernandez, P., Espinosa-Banuelos, L., Gutierrez-Leal., Jezzini-Martinez, S., & Galarza-Delgado, D. (2022) Bone metabolism and osteoporosis during pregnancy and lactation. *Archives of osteoporosis*, 17(1), 36. Doi: 10.1007/s11657-022-01077-x

Luttrell, L., Dar, M., Gesty-Palmer, D., El-Shewy, H., Robinson, K., Haycraft, C., & Barth, J. (2019) Transcriptomic characterisation of signalling pathways associated with osteoblastic differentiation of MC3T3-E1 cells. *PLOS: one*, 14(1), e0204197. Doi: 10.1371/journal.pone.0204197

Lv, X., Zhang, C., Liu, X., Li, P., & Yang, Y. (2024) 3D bioprinting technology to construct bone reconstruction research model and its feasibility evaluation. *Frontiers in bioengineering biotechnology*, 12, 1329078. Doi: 10.3389/fbior.2024.13228078

Mad-Ali, S., Benjakul, S., Prodpran, T., & Maqsood, S. (2017) Characteristics and gelling properties of gelatine from goat skin as affected by drying methods. *Journal of food science and technology*, 54(6), 1646-1654. Doi: 10.1007/s13197-017-2597-5

Maia-pinto, M., Brochado, A., Teixeria, B., Sartoretto, S., Uzeda, M., Alves A., Alves, G., Calasans-Maia, M., & Thire, R. (2020) Biomimetic mineralisation on 3D printed PLA scaffolds: on the response of human primary osteoblasts spheroids and *in-vivo* implantation. *Polymers*, 13(1), 74. Doi: 10.3390/polym13010074

Maji, S., & Lee, H. (2022). Engineering Hydrogels for the Development of Three-Dimensional In Vitro Models. *International Journal of Molecular Sciences*, *23*(5), 2662. Doi: 10.3390/ijms23052662

Majumder, N., Mishra, A., & Ghosh, S. (2022) Effect of varying cell densities on the rheological properties of the bioink. *Bioprinting*, 28, e00241. Doi: 10.1016/j.bprint.2022.e00241

Malda, J., Visser, J., Melchels, F., Jungst, T., Hennink, W., Dhert, W., Groll, J., & Hutmacher, D. (2013) 25th anniversay article: Engineering hydrogels for biofabrication. *Advanced materials*, 25(36), 5011-5028. Doi: 10.1002/adma.201302042

Malkin, A., Derkach, S., & Kulichikhin, V. (2023) Rheology of gels and yielding liquids. *Gels*, 9(9), 715. Doi: 10.3390/gels9090715

Maltman, D., & Przyborski, S. (2010) Developments in three-dimensional cell culture technology aimed at improving the accuracy of in-vitro analyses. *Biochemical Society Transactions*, 38(4), 1074 – 1075. Doi: 10.1042/BST0381072

Mandolini, M., Brunzini, A., Facco, G., Mazzoli, A., Forcellese, A., & Gigante, A. (2022) Comparison of three 3D segmentation software tools for hip surgical planning. *Sensors*, 22(140, 5242. Doi: 10.3390/s22145242

Mandrycky, C., Wang, Z., Kim, K., & Kim, D. (2016) 3D bioprinting for engineering complex tissues. *Biotechnology advances*, 34(4), 422 – 434. Doi: 10.1016/j.biotechadv.2015.12.011

Mansoorifar, A., Gordon, R., Bergan, R., & Bertassoni, L. E. (2020). Bone-on-a-chip: Microfluidic technologies and microphysiologic models of bone tissue. *Advanced Functional Materials*, *31*(6), 2006796. Doi: 10.1002/adfm.202006796

Marahleh, A., Kitaura, H., Ohori, F., Noguchi, T., & Mizoguchi, I. (2023) The osteocyte and its osteoclastogenic potential. *Frontiers in endocrinology*, 14. Doi: 10.3389/fendo.2023.1121727

Marin-Gonzalez, E., Malmusi, D., Camprubi, L., & Borrell, C. (2016) The role of dissemination as a fundamental part of a research project: Lessons learned from SOPHIE. *International journal of social determinants of health and health services,* 47(2). Doi: 10.1177/0020731416676227

Marozin, S., Simon-Nobbe, B., Irausek, S., Chung, L., & Lepperdinger, G. (2021) Kinship of conditionally immortalized cells derived from fetal bone to human bone-derived mesenchymal stroma cells. *Scientific Reports*, 11, 10933. Doi: 10.1038/s41598-021-90161-2

Martin, B., Burr, B., & Sharkey, A. (1998) Skeletal biology. *Skeletal tissue mechanics*. Spinger, New York, NY. Doi: 10.1007/978-1-4757-2968-9_2

Martin, E., Ritman, E., & Turner, R. (2003) Time course of epiphyseal growth plate fusion in rat tibiae. *Bone*, 32(3), 261-267. Doi: 10.1016/S8756-3282(02)00983-3

Martin, R. (2007) The importance of mechanical loading in bone biology and medicine. *Journal of musculoskeletal neuronal interactions*, 7(1), 48 – 53. PMID: 17396005

Martinez-Garcia, F., Fischer, T., Hayn, A., Mierke, C., Burgess, J., & Harmsen, M. (2022) A beginner's guide to the characterisation of hydrogel microarchitecture for cellular applications. *Gels*, 8(9), 535. Doi: 10.3390/gels8090535

Matsushita, Y., Liu, J., Chu, A., Ono, W., Welch, J., & Ono, N. (2023) Endosteal stem cells at the bone-blood interface: A double-edged sword for rapid bone formation. *Bioassays*, 46(3), 2300173. Doi: 10.1002/bies.202300173

Mattes, W. (2020) *In-vitro* to *in-vivo* translation. *Current opinion in toxicology*, 24, 114 – 188. Doi: 10.1016/j.cotox.2020.09.001

Maturavongsadit, P., Narayanan, L., Chansoria, P., Shirwaiker, R., & Benhabbour, R. (2021) Cell-laden nanocellulose/chitosan-based bioinks for 3D bioprinting and enhanced osteogenic cell differentiation. *ACS applied biomaterials*, 4(3), 2342 – 2353. Doi: 10.1021/acsabm.0c01108

Mazón, P., Calvo-Guirado, J. L., Delgado Ruiz, R. A., Ramírez Fernández, M. P., Negri, B., Abboud, M., & De Aza, P. N. (2014). Comparison of three hydroxyapatite/β-tricalcium phosphate/collagen ceramic scaffolds: An in vivo study. *Journal of Biomedical Materials Research Part A*, *102*(4), 1037-1046. Doi: 10.1002/jbm.a.34785

McBeth, C., Lauer, J., Ottersbach, M., Campbell, J., Sharon, A., & Sauer-Budge, A. (2017) 3D bioprinting of GelMA scaffolds triggers mineral deposition by primary human osteoblasts. *Biofabrication*, 9(1), 015009. Doi: 10.1088/1758-50-90/aa53bd

McClendon, M., Ji, W., Greene, A., Sai, H., Sangji, M., Sather, N., Chen, C., Lee, S., Katchko, K., Jeong, S., Kannan, A., Weiner, J., Cook, R., Driscoll, A., Lubbe, R., Chang, K., Haleem, M., Chen, F., Qiu, R., Chun, D., Stock, S., Hsu, W., Hsu, E., & Stupp, S. (2024) A supramolecular polymer-collagen microparticle slurry for bone regeneration with minimal growth factor. *Biomaterials,* 302, 122357. Doi: 10.1016/j.biomaterials.2023.122357

McCormack, A., Highley, C., Leslie, N., & Melchels, F. (2020) 3D printing in suspension baths: keeping the promises of bioprinting afloat. *Trends in biotechnology,* 38(6), 584 – 593. Doi: 10.1016/j.tibtech.2019.12.020

McGovern, J. A., Griffin, M., & Hutmacher, D. W. (2018). Animal models for bone tissue engineering and modelling disease. *Disease Models & Mechanisms*, *11*(4), dmm033084. Doi: 10.1242/dmm.033084

McMenamin, P. G., Quayle, M. R., McHenry, C. R., & Adams, J. W. (2014). The production of anatomical teaching resources using three-dimensional (3D) printing technology. *Anatomical Sciences Education*, *7*(6), 479-486. Doi: 10.1002/ase.1475

Meganck, J., & Liu, B. (2016) Dosimetry in micro-computed tomography: a review of the measurement method impacts, and characterisation of the quantum GX imaging system. *Molecular imaging and biology*, 19(4). 499 – 511. Doi: 10.1007/s11307-016-1026-x

Melissaridou, S., Wiechec, E., Magan, M., Jain, M., Chung, M., Farnebo, L., & Roberg, K. (2019) The effect of 2D and 3D cell cultures on treatment response, EMT profile and stem cell features in head and neck cancer. *Cancer Cell International*, 19, 16. Doi: 10.1186/s12935-019-0733-1

Memarzadeh, A., Safaei, B., Tabak, A., Sahmani, S., & Kizilors, C. (2023) Advancements in additive manufacturing of polymer matrix composites: a systematic review of techniques and properties. *Materials Today Communications,* 36, 106449. Doi: 10.1016/j.mtcomm.2023.106449

Menshikh, K., Gobbo, V. A., Nascimben, M., Hannula, M., Cochis, A., Serra, T., Massera, J., Pandit, A., & Rimondini, L. (2025). 3D-printed β-TCP scaffold as a bone-mimicking environment for an engineered model of osteosarcoma: In vitro properties and transcriptomic insights. *Materials Today Bio*, *32*, 101766. Doi: 10.1016/j.mtbio.2025.101766

Metzger, W., Ammo, T., Sossong, D., Bubel, M., Mattes, C., Stumpf, H., Spater, T., Laschke, M., & Pohlemann, T. (2025) Establishing a simple protocol to induce the osteogenic differentiation of MC3T3-E1 cells in 2D and its transfer to 3D spheroid cultures. *Biotechnology and histochemistry*, 1 – 14. Doi: 10.1080/10520295.2025.2489501

Mi, B., Zhang, J., Meng, H., Xu, Y., Xie, J., Hao, D., & Shan, L. (2024). Laponite modified methacryloyl gelatin hydrogel with controlled release of vascular endothelial growth factor a for bone regeneration. *Biochemical and Biophysical Research Communications*, *733*, 150714. Doi: 10.1016/j.bbrc.2024.150714

Miao, S., Zhou, J., Liu, B., Lei, X., Wang, T., Hao, X., Cheng, P., Wu, H., Song, Y., Pei, G., & Bi, L. (2022). A 3D bioprinted nano-laponite hydrogel construct promotes osteogenesis by activating PI3K/AKT signaling pathway. *Materials Today Bio*, *16*, 100342. Doi: 10.1016/j.mtbio.2022.100342

Michael, J. (2006) Where's the evidence that active learning works? *Advanced physiological education,* 30(4), 159-167. Doi: 10.1152/advan.00053.2006

Michelsen, J., Wallaschofski, H., Friedrich, N., Spielhagen, C., Rettig, R., Ittermann, T., Nauck, M., & Hannemann, A. (2013) Reference intervals for serum concentrations of three bone turnover markers for men and women. *Bone,* 57(2), 399 – 404. Doi: 10.1016/j.bone.2013.09.010

Mihaila, S., Gaharwar, A., Swami, A., Patel, A., Sant, S., Reis, R., Marques, A., Gomes, M., & Khademhosseini, A. (2013) Bioactive silicate nanoplatelets for osteogenic differentiation of human mesenchymal stem cells. *Advanced materials,* 25(24), 3257 – 3385. Doi: 10.1002/adma.201300584

Mikhailov, O. (2023) Gelatin as it is: histroy and modernity. *International journal of molecular sciences*, 24(4), 3583. Doi: 10.3390/ijms24043583

Mirdamadi, E., Muselimyan, N., Koti, P., Asfour, H., & Sarvazyan, N. (2019) Agarose slurry as a support medium for bioprinting and culturing freestanding cell-laden hydrogel constructs. *3D printing additive manufacturing*, 6(3), 158 – 164. Doi: 10.1089/3dp.2018.0175

Mitsouras, D., Lee, T. C., Liacouras, P., Ionita, C. N., Pietilla, T., Maier, S. E., & Mulkern, R. V. (2016). 3D Printing of MRI-Visible Phantoms and MR Image-Guided Therapy Simulation. *Magnetic Resonance in Medicine*, *77*(2), 613. Doi: 10.1002/mrm.26136

Moester, M., Schoeman, M., Oudshoorn, I., Beusekom, M., Mol, I., Kaijzel, E., Lowik, C., & Rooij, K. (2014) Validation of a simple and fast method to quantify in-vitro mineralisation with fluorescent probes used in molecular imaging of bone. *Biochemical and biophysical research communications*, 443(1), 80 – 85. Doi: 10.1016/j.bbrc.2013.11.055

Mofakhami, S., & Salahinejad, E. (2021). Biphasic calcium phosphate microspheres in biomedical applications. *Journal of Controlled Release*, *338*, 527-536. Doi: 10.1016/j.jconrel.2021.09.004

Montalti, A., Ferretti, P., & Santi, G. (2024) From CAD to G-code: strategies to minimizing errors in 3D printing process. *Journal of manufacturing science and technology*, 55, 62-70. Doi: 10.1016/j.jcirpj.2024.09.005

Moreira, A., Campos, J., & Miranda, J. (2022) Characterisation of gelatine microparticle production in a flow-focusing microfluidic system. *Colloids and surfaces A:*

Physicochemical and engineering aspects. 647, 129079. Doi: 10.1016/j.colsurfa.2022.129079

Moriishi, T., Ito, T., Fukyama, R., Qin, X., Komori, H., Kaneko, H., Matsuo, Y., Yoshida, N., & Komori, T. (2022) Sp7 transgenic mice with a markedly impaired lacunocanalicular network induced Sost and reduced bone mass by unloading. *International Journal of Molecular Science*, 23(6), 3173. Doi: 10.3390/ijms23063173

Moro, L., Guarnier, L., Azevedo, M., Fracasso, J., Lucio, M., Castro, M., Dias, M., Livero, F., & Riberio-Paes, J. (2024) A brief history of cell culture: from Harrison to organs-on-a-chip. *Cells*, 13(24), 2068. Doi: 10.3390/cells13242068

Moss, S., Bakirci, E., & Feinberg, A. (2025) Engineering the 3D structure of organoids. *Stem cell reports*, 20(1), 102379. Doi: 10.1016/j.stemcr.2024.11.009

Moss, S., Shiwarski, D., & Feinberg, A. (2024) FRESH 3D bioprinting of collagen types I, II, and III. *ACS biomaterials science & engineering*, 11(1), 556 – 563. Doi: 10.1021/acsbiomaterialss.4c01826

Moxon, S., McMurran, Z., Kibble, M., Domingos, M., Gough, J., & Richardson, S. (2024) 3D bioprinting of an intervertebral disc tissue analogue with a highly aligned annulus fibrosus via suspended layer additive manufacture. *Bio-fabrication*, 17(1), 015005. Doi: 10.1088/1758-5090/ad8379

Msallem, B., Sharma, N., Cao, S., Halbeisen, F., Zeilhofer, H., & Thieringer, F. (2020) Evaluation of the dimensional accuracy of 3D-printed anatomical mandibular models using FFF, SLA, SLS, MJ and BJ printing technology. *Journal of clinical medicine*, 9(3), 817. Doi: 10.3390/jcm9030817

Msallem, B., Vavrina, J. J., Beyer, M., Halbeisen, F. S., Lauer, G., Dragu, A., & Thieringer, F. M. (2024). Dimensional Accuracy in 3D Printed Medical Models: A Follow-Up Study on SLA and SLS Technology. *Journal of Clinical Medicine*, *13*(19), 5848. Doi: 10.3390/jcm13195848

Mu, P., Zhou, S., Lv, T., Xia, F., Shen, L., Wan, J., Wang, Y., Zhang, H., Cai, S., Peng, J., Hua, G., & Zhang, Z. (2023) Newly developed 3D in-vitro models to study tumour-immune interaction. *Journal of experimental & clinical cancer research,* 42, 81. Doi: 10.11186/s13046-023-02653-w

Muguruma, M., Teraoka, S., Miyahara, K., Ueda, A., Asaoka, M., Okazaki, M., Kawate, T., Kuroda, M., Miyagi, Y., & Ishikawa, T. (2020) Differences in drug sensitivity between two-dimensional and three-dimensional culture systems in triple-negative breast cancer cell lines. *Biochemical and biophysical research communications*, 533(3), 268 – 274. Doi: 10.1016/j.bbrc.2020.08.075

Mukacheva, F., Moazzam, M., Yernaimanova, B., Shehzad, A., Zhanbassynova, A., Berillo, D., & Akilbekova, D. (2024a) Design and characterisation of 3D printed pore gradient hydrogel scaffold for bone tissue engineering. *Bioprinting*, 39, e00341. Doi: 10.1016/j.bprint.2024.e00341

Mukasheva, F., Adilova, L., Dyussenbinov, A., Yernaimanova, B., Abilev, M., & Akilbekova, D. (2024b) Optimising scaffold pore size for tissue engineering: insights across various

tissue types. *Frontiers in bioengineering and biotechnology,* 12. Doi: 10.3389/fbioe.2024.1444986

Mukherjee, K., Dutta, P., Badwaik, H., & Giri, T. (2024) Xanthan gum and its composed-based hydrogels. *Polysaccharide hydrogels for drug delivery and regenerative medicine,* 2024, 89 – 108. Doi: 10.1016/B978-0-323-95351-1.00017-X

Mukherjee, P., Roy, S., Ghosh, D., & Nandi, S. (2022) Role of animal models in biomedical research: a review. *Laboratory animal research*, 38, 18. Doi: 10.1186/s42826-022-00128-1

Mukundan, L. M., Rajasekaran, R., Das, S., Seesala, V., Ganguly, D., Kumar, N., Dhara, S., & Chattopadhyay, S. (2025). Tailoring of agarose hydrogel to modulate its 3D bioprintability and mechanical properties for stem cell mediated bone tissue engineering. *International Journal of Biological Macromolecules*, *309*, 142795. Doi: 10.1016/j.ijbiomac.2025.142795

Mullender, M., Huiskes, R., Versleyen, H., & Buma, P. (1996) Osteocyte density and histomorphometry parameters in cancellous bone of the proximal femur in five mammalian species. *Journal of orthopaedic research*, 14(6), 972 – 979. Doi: 10.1002/jor.1100140618

Munir, A., Reseland, J., Tiainen, H., Haugen, H., Sikoriski, P., Christiansen, E., Reinholt, F., Syversen, U., & Solberg, L. (2023) Osteocyte-like cells differentiated from primary osteoblasts in an artificial human bone tissue model. *JBMR plus*, 7(9), e10792. Doi: 10.1002/jbm4.10792

Murad, S., Grove, D., Lindberg, K., Reynolds, G., Sivarajah, A., & Pinnell, S. (1981) Regulation of collagen synthesis by ascorbic acid. *PNAS*, 78(5), 2879 – 2882. Doi: 10.1073/pnas.78.5.2879

Murphy, C., Haugh, M., & O'Brien, F. (2010) The effect of mean pore size on cell attachment, proliferation and migration in collage-glycosaminoglycan scaffolds for bone tissue engineering. *Biomaterials*, 31(3), 461 – 466. Doi: 10.1016/j.biomaterials.2009.09.063

Murphy, M. B., Suzuki, R. K., Sand, T. T., Chaput, C. D., & Gregory, C. A. (2013). Short Term Culture of Human Mesenchymal Stem Cells with Commercial Osteoconductive Carriers Provides Unique Insights into Biocompatibility. *Journal of Clinical Medicine*, *2*(3), 49. Doi: 10.3390/jcm2030049

Muthusamy, S., Kannan, S., Lee, M., Sanjairaj, V., Lu, W., Fuh, J., Sriram, G., & Cao, T. (2021) 3D bioprinting and microscale organisation of vascularised tissue constructs using collagen-based bioink. *Biotechnology and bioengineering*, 118(8), 3150 – 3163. Doi: 10.1002/bit.27838

Naeem, O., Bencharit, S., Yang, I., Stilianoudakis, S., Carrico, C., & Tufekci, E. (2022) Comparison of 3-dimensional printing technologies on the precision, trueness, and accuracy of printed retainers. *American journal of orthodontics and dentofacial orthopaedics,* 161(4), 582-591. Doi: 10.1016/j.ajodo2021.03.016

Naghieh, S., & Chen, X. (2021) Printability – a key issue in extrusion-based bioprinting. *Journal of pharmaceutical analysis*, 11(5), 564 – 597. Doi: 10.1016/j.jpha.2021.02.001

Naharros-Molinero, A., Caballo-Gonzalez, M., Javier de la Mata, F., & Garcia-Gallego, S. (2022) Direct and reverse Pluronic micelles: Design and characterisation of promising drug delivery nano systems. *Pharmaceutics*, 14(12), 2628. Doi: 10.3390/pharmaceutics14122628

Nasello, G., Alaman-Diez, P., Schiavi, J., Perez, M., McNamara, L., & Garcia-Aznar, J. (2020) Primary human osteoblasts cultured in 3D microenvironment create a unique representative model of their differentiation into osteocytes. *Frontiers in bioengineering and biotechnology*, 8, 336. Doi: 10.3389/fbior.2020.00336

National institute for health care and research. (2019) How to disseminate your research. Retrieved from: https://www.nihr.ac.uk/documents/how-to-disseminate-your-research/19951 Accessed on: 02/08/2024

Navara, A. M., Kim, Y. S., Xu, Y., Crafton, C. L., Diba, M., Guo, J. L., & Mikos, A. G. (2022). A dual-gelling poly(N-isopropylacrylamide)-based ink and thermoreversible poloxamer support bath for high-resolution bioprinting. *Bioactive Materials*, *14*, 302-312. Doi: 10.1016/j.bioactmat.2021.11.016

Nekounam, H., Kandi, M. R., Shaterabadi, D., Samadian, H., Mahmoodi, N., Hasanzadeh, E., & Faridi-Majidi, R. (2021). Silica nanoparticles-incorporated carbon nanofibers as bioactive biomaterial for bone tissue engineering. *Diamond and Related Materials*, *115*, 108320. Doi: 10.1016/j.diamond.2021.108320

Nemade, A., & Shikalgar, A. (2020) The mesh quality significance in finite element analysis. *Journal of mechanical and civil engineering*, 17(2), 44 – 48. Doi: 10.9790/1684-1702054448

Neunzehn, J., Szuwart, T., & Wiesmann, H. (2015) Eggshells as natural calcium carbonate source in combination with hyaluronan as beneficial additives for bone graft materials, an in-vitro study. *Head & Face medicine*, 11, 12. Doi: 10.1186/s13005-015-0070-0

Nguyen, P., Stanislaus, I., McGahon, C., Pattabathula, K., Bryant, S., Pinto, N., Jenkins, J., & Meinert, C. (2023) Quality assurance in 3D-printing: a dimensional accuracy study of patient-specific 3D-printed vascular anatomical models. *Frontiers in medical technology*, 5, 1097850. Doi: 10.3389/fmedt.2023.1097850

Nicholas, J., Magli, S., Rabbachin, L., Sampaolesi, S., Nicotra, F., & Russo, L. (2020) 3D extracellular matrix mimics: Fundamental concepts and role of materials chemistry to influence stem cell fate. *Biomacromolecules*, 21(6), 1968 – 1994. Doi: 10.1021/acs.biomac.0c00045

Nieto, D., Marchal Corrales, J. A., & Moroni, L. (2020). Fundamentals of light-cell–polymer interactions in photo-cross-linking based bioprinting. *APL Bioengineering*, *4*(4), 041502. Doi: 10.1063/5.0022693

Nieves, J. (2017) Sex-differences in skeletal growth and aging. *Biomechanics*, 15, 70 – 75. Doi: 10.1007/s11914-017-0349-0

Ninan, G., Joseph, J., & Aliyamveettil. Z. (2012) A comparative study on the physical, chemical and functional properties of carp skin and mammalian gelatines. *Journal of food science and technology*, 51(9), 2085 – 2091. Doi: 10.1007/s13197-012-0681-4

Nishimoto, S., Chang, C., Gendler, E., Stryker, W., & Nimni, M. (1985) The effect of aging on bone formation in rats: biochemical and histological evidence for decreased bone formation capacity. *Calcified tissue international,* 37(6), 617 – 624. Doi: 10.1007/BF02554919

Nitschke, B., Beltran, F., Hahn, M., & Grunlan, M. (2024) Trends in bioactivity: inducing and detecting mineralisation of regenerative polymeric scaffolds. *Journal of material chemistry*, 12, 2720 – 2736. Doi: 10.1039/D3TB02674D

Noor, N., Shapira, A., Edri, E., Gal, I., Wertheim, L., & Dvir, T. (2019) 3D printing of personalised thick ad perfusable cardiac patches and hearts. *Advanced science*, 6(11), 1900344. Doi: 10.1002/advs.201900344

Noreen, R., & Rana, A. (2019) Activity-based teaching versus the traditional method of teaching in mathematics at the elementary level. *Bulletin of education and research*, 41(2), 145-159. Retrieved from: https://files.eric.ed.gov/fulltext/EJI229426.pdf, Accessed on: 02/08/2024

O'Cathain, A., & Thomas, K. (2004) "Any other comments?" Open questions on questionnaires – a bane or a bonus to research? *BMC Medical Research Methodology*, 4, 25. Doi: 10.1186/1471-2288-4-25

O'Connell, C., Ren, J., Pope, L., Zhang, Y., Mohandas, A., Blanchard, R., Duchi, S., & Onofrillo, C. (2020) Characterisation bioinks for extrusion bioprinting: printability and rheology. 3D bioprinting. *Methods in molecular biology*, vol 2140. Humana, NY. Doi: 10.1007/978-1-0716-0520-2_7

Oelschlaeger, C., Marten, J., Peridont, F., & Willenbacher, N. (2022). Imaging of the microstructure of Carbopol dispersions and correlation with their macro elasticity: a micro- and macro ecological study. *Journal of rheology*, 66, 749 – 760. Doi: 10.11122/8.0000452

Oftadeh, R., Perez-Viloria, M., Villa-Camacho, J., Vaziri, A., & Nazarian, A. (2015) *Biomechanics and mechanobiology of trabecular bone: a review. Journal of biomechanic engineering*, 137(1), 0108021 – 01080215. Doi: 10.1115/1.4029176

Okamoto, T., & Ura, S. (2024) Verifying the accuracy of 3D-printed objects using an image processing system. *Journal of manufacturing and materials processing*, 8(3), 94. Doi: 10.3390/jmmp8030094

Olaret, E., Stancu, I., Iovu, H., & Serafilm, A. (2021) Computed tomography as a characterisation tool for engineered scaffolds with biomedical applications. *Materials*, 14(22), 6763. Doi: 10.3390/ma14226763

Oliviero, S., Giorgi, M., Laud, P., & Dall'Ara, E. (2019) Effect of repeated in vivo micro-CT imaging on the properties of the mouse tibia. *PLOS ONE*, 14(11). E0225127. Doi: 10.1371/journal.pone.0225127

Ombergen, A., Chalupa-Gantner, F., Chansoria, P., Colosimo, B., Costantini, M., Comingos, M., Dufour, A., Maria, C., Groll, J., Jungst, T., Levato, R., Malda, J., Margarita, A., Maruqette, C., Ovsianikov, A., Petiot, E., Read, S., Surdo, L., Swieszkowski, W., Vozzi, G., Windisch, J., Zenobi-wong, M., & Gelinsky, M. (2023) 3D bioprinting in microgravity: opportunities, challenges, and possible applications in space. *Advanced healthcare materials*, 12(23), e2300443. Doi: 10.1002/adhm.202300443

Oropallo, W., & Piegl, L. (2015) Ten challenges in 3D printing. *Engineering with computers*, 32, 135 – 148. Doi: 10.1007/s00366-015-0407-0

Osidak, E., Kozhukhov, V., Osidak, M., & Domogatsky, S. (2020) Collagen as bioink for bioprinting: a comprehensive review. *International Journal of bioprinting*, 6(3), 270. Doi: 10.18063/ijb.v6i3.270

Owen, R., & Reilly, G. (2018) In-vitro models of bone remodelling and associated disorders. *Frontiers in bioengineering and biotechnology*, 6, 134. Doi: 10.3389/fbioe.2018.00134

Ozenler, A., Distler, T., Akkineni, A., Tihminlioglu, F., Gelinsky, M., & Boccaccini, A. (2024) 3D bioprinting of mouse pre-osteoblasts and human MSCs using bioinks consisting of gelatine and decellularised bone particles. *Biofabrication*, 16(2), 025027. Doi: 10.1088/1758-5090/ad2c98

Ozenler, A., Distler, T., Akkineni, A., Tihminlioglu, F., Gelinsky, M., & Boccaccini, A. (2024) 3D bioprinting of mouse pre-osteoblasts and human MSCs using bioinks consisting of gelatin and decellularized bone particles. *Biofabrication*, 16(2). Doi: 10.1088/1758-5090/ad2c98

Palmquist, A., Jolic, M., Hryha, E., & Shah, F. (2023) Complex geometry and integrated macro-porosity: clinical applications of electron beam melting to fabricate bespoke bone-anchored implants. *Acta biomaterials*, 156, 125 – 145. Doi: 10.1016/j.actbio2022.06.002

Pan, B., Shao, L., Jiang, J., Zou, S., Kong, H., Hou, R., Yao, Y., Du, J., & Jin, Y. (2022) 3D printing sacrifical templates for manufacturing hydrogel constructs with channel networks. *Materials & Design*, 222. 111012. Doi: 10.1016/j.matdes.2022.111012

Papageorgiou, M., Foger-Samwald, U., Wahl, K., Kerschan-Schindl, K., & Pietschmann, P. (2020) Age- and strain- related differences in bone microstructure and body composition during development in inbred male mouse stains. *Calcified tissue international*, 106, 431 – 443. Doi: 10.1007/s00223-019-00652-8

Park, Y., Cheong, E., Kwak, G., Carpenter, R., Shim, H., & Lee, J. (2021). Trabecular bone organoid model for studying the regulation of localized bone remodelling. *Science Advances*. Doi: 10.1126/sciadv.abd6495

Patrick, K. (1968) Anatomy, physiology and pathology of the blood supply of bones. *The journal of bone and joint surgery*, 50(4), 766-783.

Pauwels, R., Faruangsaeng, T., Charoenkarn, T., Ngonphloy, N., & Panmekiate, S. (2015) Effect of exposure parameters and voxel size on bone structure analysis in CBCT. *Dentomaxillofacial radiology,* 44(8). Doi: 10.1259/dmfr.20150078

Paxton, N., Smolan, W., Bock, T., Melchels, F., Groll, J., & Jungst, T. (2014) Proposal to assess printability of bioinks for extrusion-based bioprinting and evaluation of rheological properties governing bio printability. *Biofabrication*, 9(4), 044107. Doi: 10.1088/1758-5090/aa8dd8

Paxton, N., Smolan, W., Bock, T., Melchels, F., Groll, J., & Jungst, T. (2017) Proposal to assess printability of bioinks for extrusion-based bioprinting and evaluation of rheological properties governing bio printability. *Biofabrication*, 9(4), 044107. Doi: 10.1088/1758-5090/aa8dd8

Pei, Y., Zheng, Y., Li, Z., Liu, J., Zheng, X., Tang, K., & Kaplan, D. (2021) Ethanol-induced coacervation in aqueous gelatin solution for constructing nanospheres and networks: morphology, dynamics and thermal sensitivity. *Journal of colloid and interface science*, 582, 610 – 618. Doi: 10.1016/j.jcis.2020.08.068

Perrien, D., Brown, E., Aronson, J., Skinner, R., Montague, D., Badger, T., & Lumpkin, C. (2002) Immunohistochemical study of osteopontin expression during distraction osteogenesis in the rat. *Journal histochemistry and cytochemistry*, 50(4), 567 – 574. Doi: 10.1177/002215540205000414

Persaud, A., Maus, A., Strait, L., & Zhu, D. (2022) 3D bioprinting with live cells. *Engineered regeneration,* 3(3), 292 – 309. Doi: 10.1016/j.engreg.2022.07.002

Persson, M., Lehenkari, P., Berglin, L., Turunen, S., Finnila, M., Risteli, J., Strifvars, M., & Tuukkanenm J. (2018) Osteogenic differentiation of human mesenchymal stem cells in a 3D woven scaffold. *Scientific reports*, 10457. Doi: 10.1038/s41598-018-28699-x

Petetta, F., & Ciccocioppo, R. (2020). Public perception of laboratory animal testing: Historical, philosophical, and ethical view. *Addiction Biology*, *26*(6), e12991. Doi: 10.1111/abd.12991

Pines, M., & Hurwitz, S. (1991) The role of the growth plate in longitudinal bone growth. *Poultry science*, 70(8), 1806 – 1814. Doi: 10.3382/ps.0701806

Piwocka, O., Musielak, M., Ampula, K., Piotrowski, I., Adamczyk, B., Fundowicz, M., Suchorska, W., & Malicki, J. (2024) Navigating challenges: optimising methods for primary cell culture isolation. *Cancer Cell International*, 24, 28. Doi: 10.1186/s12935-023-03190-4

Plessis, A., Broeckhoven, C., Guelpa, A., & Le Roux, S. (2017) Laboratory x-ray micro-computed tomography: a user guideline for biological samples. *Gigascience*, 6(6), 1 – 11. Doi: 10.1093/gigascience/gix027

Poon, C. (2022) Measuring the density and viscosity of culture media for optimised computational fluid dynamics analysis of in vitro devices. *Journal of the mechanical behaviour of biomedical materials*, 126, 105024. Doi: 10.1016/j.jmbbm.2021.105024

Pragnere, S., Essayan, L., El-Kholti, N., Petiot, E., & Mattei, C. (2024) In-vitro bioprinted 3D model enhancing osteoblast-to-osteocyte differentiation. *Bio fabrication*, 17(1). Doi: 10.1088/1758-5090/ad8ca6

Prankel, S. (2012). The Costs and Benefits of Animal Experiments: An Evaluation with Bias. *Animals: An Open Access Journal From MDPI*, *2*(1), 25. Doi: 10.3390/ani2010025

Prasanna, L. C., Bothra, Y. S., Ramakrishna Bhat, K. M., & Managuli, V. (2025). Exploring the bone tissue: Instrumental methods for characterisation and biomedical research application. *Translational Research in Anatomy*, *38*, 100374. Doi: 10.1016/j.tria.2024.100374

Prasher, A., Shrivastava, R., Dahl, D., Sharma-Huynh, P., Maturavongsadit, P., Pridgen, T., Schorzman, A., Zamboni, W., Ban, J., Blikslager, A., Dellon, E., & Benhabbour, S. (2021) Steroid eluting oesophageal-targeted drug delivery devices for treatment of eosinophilic esophagitis. *Polymers*, 13(4), 557. Doi: 10.3390/polym13040557

Pratt, I., & Cooper, D. (2017) A method for measuring the three-dimensional orientation of cortical canals with implications for comparative analysis of bone microstructure of bone microstructure in vertebrates. *Micron*, 92, 32-38. Doi: 10.1016/j.micron.2016.10.006

Preim, B., & Botha, C. (2014) Surface rendering, chapter 6. *Visual computing for medicine: Theory, algorithms, and applications*. 2nd Edition, 229 – 267.

PTC (2025) Artificial intelligence (Ai) in CAD. https://www.ptc.com/en/technologies/cad/artificial-intelligence (Accessed 17/06/2025)

Puchtler, H., Meloan, S., & Terry, M. (1969) On the history and mechanism of alizarin and alizarin red S stains for calcium. *Journal of histochemistry and cytochemistry*. 17(2), 110 – 124. Doi: 10.1177/17.2.110

Qin, L., Liu, W., Cao, H., & Xiao, G. (2020) Molecular mechanosensors in osteocytes. *Bone research*, 8, 23. Doi: 10.1038/s41413-020-0099-y

Qosim, N., Dai, Y., Williams, G. R., & Edirisinghe, M. (2024). Structure, properties, forming, and applications of alginate fibres: A review. *International Materials Reviews*. Doi: 10.1177/09506608241280419

Quarles, D., Yohay, D., Lever, L., Caton, R., & Wenstrup, R. (1992) Distinct proliferative and differentiated staged of murine MC3T3-E1 cells in culture: An in-vitro model of osteoblast development. *Journal of bone and mineral research,* 7(6), 683 – 692. Doi: 10.1002/jbmr.5650070613

Rahman, T., Wood, N., Pei, Z., Qin, H., & Mohan, P. (2025) Effects of extrusion pressure during 3D printing on viability of human bronchial epithelial cells in 3D printed samples. *Biomimetics*, 10(5), 297. Doi: 10.3390/biomimetics10050297

Rahmani, R., Santangelo, G., Jalal, M., Catanzaro, M., Samodal, J., Bender, M., & Stone, J. (2024) A simple 3D printed model for intracranial vascular anastomosis practice and the Rochester bypass training score. *Operative neurosurgery*, 26(3), 341 – 345. Doi: 10.1227/ons.0000000000000931

Ramiro-Gutierrez, L., Santos-Ruiz, L., Borrego-Gonzalez, S., Becerra, J., & Diaz-Cuenca, A. (2016) *In-vitro* stimulation of MC3T3-E1 cells and sustained drug delivery by a hierarchical nanostructured SiO_2-CaO-P_2O_5 scaffold. *Microporous and mesoporous materials*, 229, 31 – 43. Doi: 10.1016/j.micromeso.2016.04.018

Rania, M., Yong, H., Jia, Y., Jingwen, C., Han, W., Guixiang, Z., & Xiangyang, S. (2016) Synthesis of diatrizoic acid-modified Laptonite® nanodiscs for CT imaging applications. *RCS Advances*, 6(62), 57490 – 57490. Doi: 10.1039/c6ra11755d

Ravinetto, R., & Singh, J. (2023) Responsible dissemination of health and medical research: some guidance points. *BMJ Evidence-based methods*, 28(3), 144-147. Doi: 10.1136/bmjebm-20222-111967

Remmers, S., Wildt, B., Vis, M., Spaander, E., Vries, R., Ito, K., & Hofmann, S. (2021) Osteoblast-osteoclast co-cultures: a systematic review and map of available literature. *PLoS one*, 16(11), e0257724. Doi: 10.1371/journal.pone.0257724

Rengier, F., Mehndiratta, A., Tengg-Kobligk, H., Zechmann, C., Unterhinninghofen, R., Kauczor, H., & Giesel, F. (2010) 3D printing based on imaging data: review of medical applications. *International Journal of computed assisted radiology surgery*, 5(4), 335-341. Doi: 10.1007/s11548-010-0476-x

Ressler, A. (2022). Chitosan-Based Biomaterials for Bone Tissue Engineering Applications: A Short Review. *Polymers*, *14*(16), 3430. Doi: 10.3390/polym14163430

Revete, A., Aparicio, A., Cisterna, B., Revete, J., Luis, L., Ibarra, E., Gonzalez, E., Molino, J., & Reginensi, D. (2022) Advancements in the use of hydrogels for regenerative medicine: properties and biomedical applications. *International journal of biomaterials*, 3606765. Doi: 10.1155/2022/3606765

Rho, J., Ashman, R., & Turner, C. (1993) Youngs modulus of trabecular and cortical bone material: ultrasonic and micro tensile measurements. *Journal of biomechanics*, 26(2), 111 – 119. Doi: 10.1016/0021-9290(93)90042-D

Riberio de Barros, H., Cardoso, M., Camargo de Oliveria, C., Franco, C., Belan, D., Vidotti, M., & Riegel-Vidotti, I. (2016) Stability of gum arabic-gold nanoparticles in physiological simulated pHs and their selective effect on cell lines. *RSC advances*, 12. Doi: 10.1039/c5ra24858b

Riberio, A., Blokzijl, M., Levato, R., Visser, C., Castilho, M., Hennink, W., Vermonden, T., & Malda, J. (2017) Assessing bioink shape fidelity to aid material development in 3D bioprinting. *Biofabrication*, 10(1), 014102. Doi: 10.1088/1758-5090/aa90e2

Rickard, D., Sullivan, T., Shenker, B., Leboy, P., & Kazhdan, I. (1994) Induction of rapid osteoblast differentiation in rat bone marrow stromal cell cultures by dexamethasone and BMP-2. *Developmental biology*, 161(1), 218 – 228. Doi: 10.1006/dbio.1994.1022

Rimann, M., Laternser, S., Gvozdenovic, A., Muff, R., Fuchs, B., Kelm, J. M., & Graf-Hausner, U. (2014). An in vitro osteosarcoma 3D microtissue model for drug development. *Journal of Biotechnology*, *189*, 129-135. Doi: 10.1016/j.jbiotec.2014.09.005

Rodriguez, V., Picotto, G., Rivoira, M., Rigalli, A., & Talamoni, N. (2024) The combined treatment of insulin and nargingin improves bone properties in rats with type 1 diabetes mellitus. *Applied physiology, nutrition, and metabolism*, 49, 213 – 222. Doi: 10.1139/apnm-2023-0267

Rosello-Diez, A., & Joyner, A. (2015) Regulation of long bone growth in vertebrates; it is time to catch up. *Endocrine reviews*, 36(6), 646 – 680. Doi: 10.1210/er.2015 – 1048. Doi: 10.1210/er.2015-1048

Rotbaum, Y., Puiu, C., Rittel, D., & Domingos, M. (2019). Quasi-static and dynamic in vitro mechanical response of 3D printed scaffolds with tailored pore size and architectures. *Materials Science and Engineering: C*, *96*, 176-182. https://doi.org/10.1016/j.msec.2018.11.019

Ruberte, J., Schofield, P., Sundberg, J., Rodriguez-Baeza, A., Carretero, A., & Mckerlie, C. (2023) Bridging mouse and human anatomies: A knowledge-based approach to comparative anatomy for disease model phenotyping. *Mammal genome,* 34(3), 389 – 407. Doi: 10.1007/s00335-023-10005-4

Rubin, G. (2014) Computed tomography: revolutionising the practice of medicine for 40 years. *Radiology*, 273(25). Doi: 10.1148/radiol.14141356

Rucci, N. (2008) Molecular biology of bone remodelling. *Clinical cases in mineral and bone metabolism*, 5(1), 49 – 56.

Ruedinger, F., Lavrentieva, A., Blume, C., Peplanova, I., & Scheper, T. (2015) Hydrogels for 3D mammalian cell culture: a starting guide for laboratory practice. *Applied microbiology and biotechnology*, 99(2), 623 – 636. Doi: 10.1007/s00253-014-6253-y

Rungrojwittayakul, O., Kan, J., Shiozaki, K., Swamidass, R., Goodacre, B., Gooodacre, C., & Lozada, J. (2019) Accuracy of 3D printed models created by two technologies of printers with different designs of model base. *Journal of prosthodontics*, 29(2), 124-128. Doi: 10.1111/jopr.13107

Rutkovskiy, A., Stenslokken, K., & Vaage, I. (2016) Osteoblast differentiation at a glance. *Medical science monitor basic research*, 22, 95 – 106. Doi: 10.12659/MSMBR.901142

Rutten, L., Macias-Sanchez, E., & Sommerdijk, N. (2024) On the role of glycosylation of type I collagen in bone. *Journal of structural biology*, 216(4). Doi: 10.1016/j.jsb.2024.108145

Safadi, A., Livne, E., & Reznick, A. (1997) Characterisation of alkaline and acid phosphatases from skeletal muscles of young and old rats. *Archives of gerontology and geriatrics*, 24(2), 183 – 196. Doi: 10.1016/S0167-4943(96)00751-0

Sagoe, P., Velazquez, E., Espiritiusanto, Y., Gilbert, A., Orado, T., Wang, Q., & Jain, E. (2023) Fabrication of PEG-PLGA microparticles with tunable sizes for controlled drug release application. *Molecules*, 28(18), 6679. Doi: 10.3390/molecules28186679

Sakr, M., Siddiqua, S., Shin, S., & Kim, K. (2025) Synthesis and characterisation of a nanoclay reinforced gelatine-based hybrid hydrogel. *Journal of biomaterial research A*, 113(1), e37870. Doi: 10.1002/jbm.a.37870

Saleh, L., Carles-Carner, M., & Bryant, S. (2018) The in-vitro effects of macrophages on the osteogenic capabilities of MC3T3-E1 cells encapsulated in a biomimetic poly(ethylene glycol) hydrogel. *Acta biomaterials*, 71, 37 – 48. Doi: 10.1016/j.actbio.2018.02.026

Salmon, P., Ohlsson, C., Shefelbine, S., & Doube, M. (2015) Structural model index does not measure rods and plates in trabecular bone. *Frontiers in endocrinology*, 6. Doi: 10.3389/fendo.2015.00162

Samchenko, Y., Terpilowski, K., Samchenko, K., Golovkova, L., Oranska, O., & Goncharuk, O. (2024) Calcium alginate/laponite nanocomposite hydrogels: synthesis, swelling, and sorption properties. *Coatings*, 14(12), 1519. Doi: 10.3390/coatings14121519

Sanzari, I., Buratti, E., Huang, R., Tusan, C. G., Dinelli, F., Evans, N. D., Prodromakis, T., & Bertoldo, M. (2020). Poly(N-isopropylacrylamide) based thin microgel films for use in cell culture applications. *Scientific Reports*, *10*(1), 1-14. Doi: 10.1038/s41598-020-63228-9

Sarabi, M., Yetisen, A., & Tasoglu, S. (2023) Bioprinting in microgravity. *ACS biomaterials science engineering,* 9(6), 3074-3083. Doi: 10.1021/acsbiomaterials.3c00195

Saraf, S. K., & Kumaraswamy, V. (2013). Basic research: Issues with animal experimentations. *Indian Journal of Orthopaedics*, *47*(1), 6. Doi: 10.4103/0019-5413.106882

Satoh, M., & Hasegawa, Y. (2022) Factors affecting prepubertal and pubertal bone age progression. *Frontiers in Endocrinology*, 13, 967711. Doi: 10.3389/fendo.2022.967711

Sayed, S., Faruq, O., Hossain, M., Im, S., Kim, Y., & Lee, B. (2019) Thermal cycling effect on osteogenic differentiation of MC3T3-E1 cells loaded on 3D-porous biphasic calcium phosphate (BCP) scaffolds for early osteogenesis. *Materials science engineering part C: materials and biology applied.* 105, 110027. Doi: 10.1016/j.msec.2019.110027

Scan2CAD (2024) The role of artificial intelligence (AI) in the CAD industry. https://www.scan2cad.com/blog/cad/ai-cad/ (Accessed 17/06/2025)

Schaart, J., Lindert, M., Roverts, R., Nijhuis, W., Sommerdijk, N., & Akiva, A. (2024) Cell-induced collagen alignment in a 3D in-vitro culture during extracellular matrix production. *Journal of structural biology,* 216(2), 108096. Doi: 10.1016/j.jsb.2024.108096

Schaeffer, N., & Dykema, J. (2011) Questions for surverys. *Public Opinion Quarterly*, 75(5), 909-961. Doi: 10.1093/poq/nfr048

Schneckenburger, H., & Richter, V. (2021) Challenges in 3D live cell imaging. *Photonics*, 8(7), 275. Doi: 10.3390/photonics8070275

Schwab, A., Levato, R., D'Este, M., Piluso, S., Eglin, D., & Malda, J. (2020) Printability and shape fidelity of bioinks in 3D bioprinting. *Chemistry reviews*, 120(19), 10850 – 10877. Doi: 10.1021/acs.chemrev.0c00084

Scimeca, M., Bischetti, S., Lamsira, H., Bonfiglio, R., & Bonanno, E. (2018) Energy dispersive x-ray microanalysis: a powerful tool in biomedical research and diagnosis. *European journal of histochemistry,* 62(1), 2841. Doi: 10.4081/ejh.2018.2841

Scott, M., Nguyen, V., Levi, B., & James, A. (2011) Current methods of adipogenic differentiation of mesenchymal stem cells. *Stem cell development*, 20(10), 1793 – 1804. Doi: 10.1089/scd.2011.0040

Sefa, A., Espiritu, J., Cwieka, H., Greving, I., Flenner, S., Will, O., Beuer, S., Wieland, D., Willumeit-Romer, R., & Zeller-plumoff, B. (2023) Multiscale morphological analysis of bone microarchitecture around Mg-10Gd implants. *Bioactive Materials*, 30, 154 – 168. Doi: 10.1016/j.bioactmat.2023.07.017

Segeritz, C., & Vallier, L. (2017) Cell Culture: Growing cells as model systems *in-vitro*. *Basic science methods for clinical researchers,* 151 – 172. Doi: 10.1016/B978-0-12-8030777-6.00009-6

Segovia-Gutiérrez, J. P., Agudo, J. A. R., Binder, N., Weidler, P. G., Kirschhöfer, F., Fink-Straube, C., Utz, J., & Germann, N. (2025). Dynamic mechanical analysis of alginate/gellan hydrogels under controlled conditions relevant to environmentally sensitive applications. *Carbohydrate Polymers*, *352*, 123180. Doi: 10.1016/j.carbpol.2024.123180

Self, T., Ginn-hedman, A., Kaulfus, C., Newell-Fugate, A., Weeks, B., & Heaps, C. (2020) Iodine-enhanced micro-computed tomography of atherosclerotic plaque morphology complements conventional histology. *Atherosclerosis*, 313, 43-49. Doi: 10.1016/j.atherosclerosis.2020.09.012

Semicheva, A., Ersoy, U., Vasilaki, A., Myrtziou, I., & Kanakis, I. (2024) Defining the most potent osteoinductive culture conditions for MC3T3-E1 cells reveals no implication of oxidative stress or energy metabolism. *International journal of molecular sciences,* 25(8), 4180. Doi: 10.3390/ijms25084180

Sequeira, L., Nguyen, J., Wang, L., & Nohe, A. (2020) A novel peptide, CK2.3, improved bone formation in ovariectomized Sprague Dawley rats. *International journal of molecular sciences*, 21, 4874. Doi: 10.3390/ijms21144874

Serdar, C., Cihan, M., Yucel, D., & Serdar, M. (2021) Sample size, power and effect size revisited: simplified and practical approaches in pre-clinical, clinical and laboratory studies. *Biochemia Medica*, 31(1), 010502. Doi: 10.11613/BM.2021.010502

Serguienjo, A., Wang, M., & Myklebost, O. (2018) Real-time vital mineralisation detection and quantification during in-vitro osteoblast differentiation. *Biological procedures online*, 20, 14. Doi: 10.1186/s12575-018-0079-4

Shah, K., Stern, M., Stern, A., Pathak, J., Bravenboer, N., & Bakker, A. (2016) Osteocyte isolation and culture methods. *Bonekey reports*, 5, 838. Doi: 10.1038/bonekey.2016.65

Shao, C., Chen, L., Tang, R., Zhang, B., Tang, J., & Ma, W. (2021) Degradation and biological performance of porous osteomimetic biphasic calcium phosphate *in-vitro* and *in-vivo*. *Rare metals*, 41, 457 – 468. Doi: 10.1007/s12598-021-01814-0

Shi, S., Cheng, X., Wang, J., Zhang, W., Peng, L., & Zhang, Y. (2009). RhBMP-2 Microspheres-Loaded Chitosan/Collagen Scaffold Enhanced Osseointegration: An Experiment in Dog. *Journal of Biomaterials Applications*. Doi: 10.1177/0885328208090013

Shim, J., Iwaya, C., Ambrose, C., Suzuki, A., & Iwata, J. (2022) Micro-computed tomography assessment of bone structure of aging mice. *Scientific reports*, 12, 8117. Doi: 10.1038/s41598-022-11965-4

Shive, M., Broadbeck, W., & Anderson, J. (2002) Activation of caspase-3 during shear stress-induced neutrophil apoptosis on biomaterials. *Journal of biomedical materials research*, 62(2), 163 – 168. Doi: 10.1002/jbm.10225

Shiwarski, D., Hudson, A., Tashman, J., & Feinberg, A. (2021) Emergence of FRESH 3D printing as a platform for advanced tissue bio fabrication. *APL bioengineering*, 5(1), 010904. Doi: 10.1063/5.0032777

Si, J., Wang, C., Zhang, D., Wang, B., Hou, W., & Zhou, Y. (2020) Osteopontin in bone metabolism and bone diseases. *Medical Science Monitor*, 26, 919159-1 919159-9. Doi: 10.12659/MSM.919159

Sieberath, A., Della Bella, E., Ferreira, A. M., Gentile, P., Eglin, D., & Dalgarno, K. (2020). A Comparison of Osteoblast and Osteoclast In Vitro Co-Culture Models and Their Translation for Preclinical Drug Testing Applications. *International Journal of Molecular Sciences*, *21*(3), 912. Doi: 10.3390/ijms21030912

Singal, A., Grande, J., & Zhou, Y. (2013) Micro/nano-CT for visualisation of internal structures. *Microscopy today*, 21(2), 16 – 22. Doi: 10.1017/S1551929513000035

Sitarski, A. M., Fairfield, H., Falank, C., & Reagan, M. R. (2017). 3d Tissue Engineered In Vitro Models Of Cancer In Bone. *ACS Biomaterials Science & Engineering*, *4*(2), 324. Doi: 10.1021/acsbiomaterials.7b00097

Sitarski, A., Fairfield, H., Falank, C., & Reagan, M. (2018) 3D Tissue Engineered In vitro models of cancer in bone. *ACS biomaterials science engineering*, 4(2), 324 - 336. Doi: 10.1021/acsbiomaterials.7b00097

Skottke, J., Gelinsky, M., & Bernhardt, A. (2019) In-vitro co-culture model of primary human osteoblasts and osteocytes in collagen gels. *International journal for molecular science*, 20(8), 1998. Doi: 10.3390/ijms20081998

Smeets, S., Renaud, N., & Willenswaard, L. (2020) Nanomesh: A python workflow tool for generating meshes from image data. *The journal of open-source software,* 7(78), 4654. Doi: 10.21105/joss.04654

Smith, C., Voisin, S., Al Saedi, A., Phu, S., Brennan-Speranza, T., Parker, L., Eynon, N., Hiam, D., Yan, X., Scott, D., Blekkenhorst, L., & Lewis, J. (2020) Osteocalcin and its forms across the lifespan in adult men. *Bone*, 130, 115085. Doi: 10.1016/j.bone.2019.115085

Snuggs, J., Emanuel, K., Rustenburg, C., Janani, R., Partridge, S., Sammon, C., Smit, T., & Le Maitre, C. (2023) Injectable biomaterial induces regeneration of the intervertebral disc in a caprine loaded disc culture model. *Biomaterials science*, 11, 4630 – 4643. Doi: 10.1039/D3BM00150D

Soares, C., Midlej, V., De Oliveria, M., Benchimol, M., Costa, M., & Mermelstein, C. (2012) 3D and 3D-organised cardiac cells show differences in cellular morphology, adhesion junctions, presence of myofibrils and protein expression. *PLOS:one*. Doi: 10.1371/journal.pone.0038147

Soe, K., Delaisse, J., & Borggaard, X. (2021) Osteoclast formation at the bone marrow/bone surface interface: Importance of structural elements, matrix, and

intercellular communication. *Seminars in cell and developmental biology*, 112, 8 – 15. Doi: 10.1016/j.semcdb.2020.05.016

Soleymani, S., & Naghib, S. M. (2023). 3D and 4D printing hydroxyapatite-based scaffolds for bone tissue engineering and regeneration. *Heliyon*, *9*(9), e19363. Doi: 10.1016/j.heliyon.2023.e19363

Solidworks (2025) Evolve your design workflows with AI. https://www.solidworks.com/lp/evolve-your-design-workflows-ai (Accessed 17/06/2025)

Song, H. K., & Hwang, D. Y. (2017). Use of C57BL/6N mice on the variety of immunological researches. *Laboratory Animal Research*, *33*(2), 119. Doi: 10.5625/lar.2017.33.2.119

Sorgente, T., Biasotti, S., Manzini, G., & Spagnuolo, M. (2023) A survey of indicators for mesh quality assessment. *Computer graphics forum*, 42(2), 461 – 483. Doi: 10.1111/cgf.14779

Souter, P., Horner, A., & Cunningham, J. (2011) Quantification of in-vitro mineralisation using ion chromatography. *Analytical biochemistry*, 410(2), 244 – 247. Doi: 10.1016/j.ab.2010.11.41

Sovani, V. (2021) Normal bone marrow, its structure and function. *Diagnostic histopathology*, 27(9), 349-356. Doi: 10.1016/j.mpdhp.2021.06.001

Sroga, G., & Vashishth, D. (2012) Effects of bone matrix proteins on fracture and fragility in osteoporosis. *Current osteoporosis reports*, 10, 141 – 150. Doi: 10.1007/s11914-012-0103-6

Staehlke, S., Rebl, H., & Nebe, B. (2019). Phenotypic stability of the human MG-63 osteoblastic cell line at different passages. *Cell Biology International*, *43*(1), 22-32. Doi: 10.1002/cbin.11073

Stauber, M., & Muller, R. (2008) Micro-computed tomography: a method for the non-destructive evaluation of the three-dimensional structure of biological specimens. *Methods Molecular biology*, 455, 273-292. Doi: 10.1007/978-1-59745-104-8_19

Stealey, S., Gaharwar, A., & Zustiak, S. (2023) Laponite-based nanocomposite hydrogels for drug delivery applications. *Pharmaceuticals*, 16(6), 821. Doi: 10.3390/ph16060821

Stein, M., Elefteriou, F., Busse, B., Fiedler, I. A., Kwon, R. Y., Farell, E., Ahmad, M., Ignatius, A., Grover, L., Geris, L., & Tuckermann, J. (2023). Why animal experiments are still indispensable in bone research: A statement by the European Calcified Tissue Society. *Journal of Bone and Mineral Research: The Official Journal of the American Society for Bone and Mineral Research*, *38*(8), 1045. Doi: 10.1002/jbmr.4868

Steiner, L., Synek, A., & Pahr, D. (2020) Comparison of different micro-CT-based morphology assessment tools using human trabecular bone. *Bone reports*, 12. Doi: 10.1016/j.bonr.2020.100261

Stenvinkel, P., Painer, J., Johnson, R., & Natterson-Horowitz, B. (2019). Biomimetics - Nature's roadmap to insights and solutions for burden of lifestyle diseases. *Journal of Internal Medicine*, *287*(3), 238. Doi: 10.1111/joim.12982

Strauß, S., Schroth, B., & Hubbuch, J. (2022) Evaluation of the reproducibility and robustness of extrusion-based bioprinting processes applying a flow sensor. *Frontiers bioengineering and biotechnology,* 10, 831350. Doi: 10.3389/fbior.2022.831350

Subramaniam, M., Jalal, S., Rickard, D., Harris, S., Bolander, M., & Spelsberg, T. (2002) Further characterisation of human fetal osteoblastic hFOB 1.19 and hFOB/ER alpha cells: bone formation in vivo and karyotype analysis using multicolour fluorescent in situ hybridization. *Journal of cell biochemistry,* 87(1), 6 – 15. Doi: 10.1002/jcb.10259

Sudo, H., Kodama, H., Amagai, Y., Yamamoto, S., & Kasai, S. (1983) In-vitro differentiation and calcification in a new clonal osteogenic cell line derived from newborn mouse calvaria. *Journal of Cell Biology,* 96(1), 191-198. Doi: 10.1083/jcb.96.1.191

Sun, D., Gao, W., Hu, H., & Zhou, S. (2022) Why 90% of clinical drug development fails and how to improve it? *Acta Pharmaceutica Sinica. B*, *12*(7), 3049. Doi: 10.1016/j.apsb.2022.02.002

Sun, M., Liu, A., Yang, X., Gong, J., Yu, M., Yao, X., Wang, H., & He, Y. (2021) 3D cell culture – can it be as popular as 2D cell culture? *Advanced nano-biomed research*, 1(5), 2000066. Doi: 10.1002/anbr.20200066

Sun, Y., Li, J., Xie, X., Gu, F., Sui, Z., Zhang, K., & Yu, T. (2021). Macrophage-osteoclast associations: origin, polarization, and subgroups. *Frontiers immunology*, 12. Doi: 10.3389/fimmu.2021.778078

Suroweic, R., Allen, M., & Wallace, J. (2021) Bone hydration: how we can evaluate it, what can it tell us, and is it an effective therapeutic target? *Bone reports*, 16. Doi: 10.1016/j.bonr.2021.101161

Szwed-Georgiou, A., Plocinski, P., Kupikowska-Stobba, B., Urbaniak, M., Rusek-Wala, P., Szustakiewicz, K., Piszko, P., Krupa, A., Biernat, M., Gazinska, M., Kasprzak, M., Nawrotek, K., Mira, N., & Rudnicka, K. (2023) Bioactive materials for bone regeneration: biomolecules and delivery systems. *ACS biomaterials science & engineering*, 9(9), 5222 – 5254. Doi: 10.1021/acsbiomaterials.3c00609

Tack, P., Victor, J., Gemmel., P., & Annemans, L. (2016) 3D-printing techniques in a medical setting: a systematic literature review. *Biomedical engineering online*, 15, 115. Doi: 10.1186/s12938-016-0236-4

Tadros, S., Epsley, S., Mehta, S., Jones, B., Rajapakse, H., Madi, R., Alecxih, A., Kargilis, D., & Rajapakse, C. (2023) The application of advanced bone imaging technologies in sports medicine. *Radiology research and practice*, 7412540. Doi: 10.1155/2023/7412540

Taichman, R. (2005) Blood and bone: Two tissues whose fates are intertwined to create the hematopoietic stem-cell niche. *Blood*, 105, 7, 2631 – 2639. Doi: 10.1182/blood-2004-06-2480

Takahashi, N., Kobayashi, Y., & Udagawa, N. (2020) *Principals of bone biology: volume 1. Osteoclasts*, pp. 111 – 131. Doi: 10.1016/B978-0-12-814841-9.00005-1

Tan, S., Zhang, B., Zhu, X., Ao, P., Guo, G., Yi, W., & Zhou, G. (2014) Deregulation of bone forming cells in bone diseases and anabolic effects of strontium-containing agents and biomaterials. *Biochemistry research international*, 814057. Doi: 10.1155/2014/814057

Tang, L., Wang, L., Yang, X., Feng, Y., Li, Y., & Feng, W. (2021). Poly(N-isopropylacrylamide)-based smart hydrogels: Design, properties and applications. *Progress in Materials Science*, *115*, 100702. Doi: 10.1016/j.pmatsci.2020.100702

Tang, M., Berry, D., Miller, K., Ma, X., & Chen, S. (2022) Bioprinting of biomimetic tissue models for disease modelling and drug screening. *3D bioprinting and nanotechnology in tissue engineering and regenerative medicine*, 33-70. Doi: 10.1016/B978-0-12-824552-1.00002-5

Tenuta, M., Hasenmajer, V., Gianfrilli, D., & Isidori, A. (2025) Testosterone and male bone health: a puzzle of interactions. The *Journal of Clinical Endocrinology & metabolism*, dgaf191. Doi: 10.1210/clinem/dgaf191

Tevlek, A., Odabas, S., Celik, E., & Aydin, H. (2018) Preparation of MC3T3-E1 cell sheets through short-term osteogenic medium application. *Artificial cells, nanomedicine and biotechnology*, 46(2), 1145 – 1153. Doi: 10.1080/21691401.2018.1481081

Tharakan, S., Khondkar, S., Lee, S., Ahn, S., Mathew, C., Gresita, A., Hadjiargyrou, M., & Ilyas, A. (2022). 3D Printed Osteoblast–Alginate/Collagen Hydrogels Promote Survival, Proliferation and Mineralisation at Low Doses of Strontium Calcium Polyphosphate. *Pharmaceutics*, *15*(1), 11. Doi: 10.3390/pharmaceutics15010011

Thiagarajan, G., Begonia, M., Dallas, M., Lara-castillo, N., Scott, J., & Johnson, M. (2018) Determination of elastic modulus in mouse bones using a nondestructive micro-indentation technique using reference point indentation. *Journal of biomechanical engineering*, 140(7), 0710111 – 07101111. Doi: 10.1115/1.4039982

Thorpe, A., Boyes, V., Sammon, C., & Le Maitre, C. (2016a) Thermally triggered injectable hydrogel, which induces mesenchymal stem cell differentiation to nucleus pulposus cells: potential for regeneration of the intervertebral disc. *Acta Biomaterialia*, 36, 99 – 11. Doi: 10.1016/j.actbio.2016.03.029

Thorpe, A., Creasey, S., Sammon, C., & Le Maitre, C. (2016b) Hydroxyapatite nanoparticle injectable hydrogel scaffold to support osteogenic differentiation of human mesenchymal stem cells. *European cells and materials,* 32, 1 – 23. Doi: 10.22203/eCM.v032a01

Thorpe, A., Freeman, C., Farthing, P., Callaghan, J., Hatton, P., Brook, I., Sammon, C., & Le Maitre, C. (2018) In-vivo safety and efficacy testing of a thermally triggered injectable hydrogel scaffolds for bone regeneration and augmentation in a rat model. *Oncotarget,* 9, 18277 – 18295. Doi: 10.18632/oncotarget.24813

Tian, C., Yang, M., Xu, H., Zhu, M., Yue, N., Zhang, Y., Shi, R., Yao, J., Wang, L., Liang, Y., & Li, D. (2023). Stem cell-derived intestinal organoids: A novel modality for IBD. *Cell Death Discovery*, *9*(1), 1-16. Doi: 10.1038/s41420-023-01556-1

Tian, X., Li, M., Cao, N., Li, J., & Chen, X. (2009) Characterisation of the flow behaviour of alginate/hydroxyapatite mixtures for tissue scaffold fabrication. *Biofabrication*, 1, 045005. Doi: 10.1088/1758-5082/1/4/045005

Tilton, M., Camilleri, E. T., Astudillo Potes, M. D., Gaihre, B., Liu, X., Lucien, F., Elder, B. D., & Lu, L. (2023). Visible light-induced 3D bioprinted injectable scaffold for minimally

invasive tissue regeneration. *Biomaterials Advances*, *153*, 213539. Doi: 10.1016/j.bioadv.2023.213539

Timilsena, Y., Akanbi, T., Khalid, N., Adhikari, B., & Barrow, C. (2019) Complex coacervation: principles, mechanisms and applications in microencapsulation. *International journal of biological macromolecules,* 121, 1276 – 1286. Doi: 10.1016/j.ijbiomac.2018.10.144

Todo M, Arahira T. (2013) In vitro bone formation by mesenchymal stem cells with 3D collagen/β-TCP composite scaffold. *Annu Int Conf IEEE Eng Med Biol Soc*, 409 – 412. Doi: 10.1109/EMBC.2013.6609523.

Tolmacheva, N., Bhattacharyya, A., & Noh, I. (2024) Calcium phosphate biomaterials for 3D bioprinting in bone tissue engineering. *Biomimetics*, 9(2), 95. Doi: 10.3390/biomimetics9020095

Tomás, H., Alves, C. S., & Rodrigues, J. (2018). Laponite®: A key nanoplatform for biomedical applications? *Nanomedicine: Nanotechnology, Biology and Medicine*, *14*(7), 2407-2420. Doi: 10.1016/j.nano.2017.04.016

Tomco, M., Petrovova, E., Giretova, M., Almasiova, V., Holovska, K., Cigankova, V., Jenca, A., Jencova, J., Jenca, A., Boldizar, M., Balazsm, K., & Medvecky, L. (2017) *In-vitro* and *in-vivo* study of microporous ceramics using MC3T3-E1 cells, Cam assay and a pig animal model. *Anatomical science international,* 92, 569 – 580. Doi: 10.1007/s12565-016-0362-x

Tomiyama, T., Gu, P., Jin, Y., Lutters, D., Kind, C., & Kirmura, F. (2009) Design methodologies: industrial and educational applications. *CIRP Annals*, 58(2), 543-565. Doi: 10.1016/j.cirp.2009.09.003

Tornqvist, E., Annas, A., Granath, B., Jalkesten, E., Cotgreave, I., & Oberg, M. (2014) Strategic focus on 3D principles reveals major reductions in the use of animals in pharmaceutical toxicity testing. *PLoS* one, 9(7), e101638. Doi: 10.1371/journal.pone.0101638

Torres, B., Pérez, A., García, P., Jiménez, P., Abrigo, K., Valencia, P., Ramírez, C., Pinto, M., Almonacid, S., & Ruz, M. (2024). Fish Bones as Calcium Source: Bioavailability of Micro and Nano Particles. *Foods*, *13*(12), 1840. Doi: 10.3390/foods13121840

Tortelli, F., Pujic, N., Liu, Y., Laroche, N., Vico, L., & Camcedda. R. (2009) Osteoblast and osteoclast differentiation in an in-vitro three-dimensional model of bone. *Tissue engineering: Part A.* 15(9), 2773 – 2783. Doi: 10.1089/ten.tea.2008.0501

Tounsi, L., Shahabi, N., Patel, A. K., Abdelkafi, S., & Michaud, P. (2022). Structures, Properties and Applications of Alginates. *Marine Drugs*, *20*(6), 364. Doi: 10.3390/md20060364

Townsend, J., Beck, E., Gehrke, S., Berkland, C., & Detamore, M. (2019) Flow behaviour prior to crosslinking: the need for precursor rheology for placement of hydrogels in medical applications and for 3D bioprinting. *Progress in polymer science*, 91, 126-140. Doi: 10.1016/j.progpolymsci.2019.01.003

Tran, D., Ta, Q., Tran, M., Nguyen, T., Le, N., Hong, A., Park, H., Park, K. & Nguyen, D. (2024) Optimised synthesis of biphasic calcium phosphate: enhancing bone regeneration with a tailored β-tricalcium phosphate/hydroxyapatite ratio. *Biomaterials science*, 13, 969 – 979. Doi: 10.1039/D4BM01179A

Tresguerres, F., Torres, J., Lopez-Quiles, J., Hernandez, G., Vega, J., & Tresguerres, I. (2020) The osteocyte: a multifunctional cell within the bone. *Annals of anatomy,* 227, 151422. Doi: 10.1016/j.aanat.2019.151422

Trifonov, A., Shehzad, A., Mukasheva, F., Moaxxam, M., & Akillbekova, D. (2024) Reasoning on pore terminology in 3D bioprinting. *Gels*, 10(2), 153. Doi: 10.3390/gels10020153

Tripodi, N., Kelly, K., Husaric, M., Wospil, R., Fleischmann, M., Johnston, S., & Harkin, K. (2020) The impact of three-dimensional printed anatomical models on first-year student engagement in a block mode delivery. *Anatomical science education*, 13(6), 769 – 777. Doi: 10.1002/ase.1958

Tsutsumi, Y. (2021) Pitfalls and caveats in applying chromogenic immunostaining to histopathological diagnosis. *Cells*, 10(6), 1501. Doi: 10.3390/cells10061501

Udagawa, N., Takahashi, N., Akatsu, T., Sasaki, T., Yamaguchi, A., Kodama, H., Martin, J., & Suda, T. (1989) The bone marrow-derived stromal cell lines MC3T3-G2/PA6 and ST2 support osteoclast-like cell differentiation in cocultures with mouse spleen cells. *Endocrinology*, 125(4), 1805 – 1813. Doi: 10.1210/endo-125-4-1805

Ullah, F., Othman, M., Javed, F., Ahmad, Z., & Akil, H. (2015). Classification, processing and application of hydrogels: A review. *Materials science and engineering*: C, 57, 414 – 433. Doi: 10.1016/j.msec.2015.07.053

Unagolla, J. M., Gaihre, B., & Jayasuriya, A. C. (2023). In vitro and in vivo evaluation of 3D printed poly(ethylene glycol) dimethacrylate-based photocurable hydrogel platform for bone tissue engineering. *Macromolecular Bioscience*, *24*(4), e2300414. Doi: 10.1002/mabi.202300414

Urzì, O., Gasparro, R., Costanzo, E., Luca, A. D., Giavaresi, G., Fontana, S., & Alessandro, R. (2023). Three-Dimensional Cell Cultures: The Bridge between In Vitro and In Vivo Models. *International Journal of Molecular Sciences*, *24*(15), 12046. Doi: 10.3390/ijms241512046

Uysal, B., K Madduma-Bandarage, U. S., Jayasinghe, H. G., & Madihally, S. (2025). 3D-Printed Hydrogels from Natural Polymers for Biomedical Applications: Conventional Fabrication Methods, Current Developments, Advantages, and Challenges. *Gels*, *11*(3), 192. Doi: 10.3390/gels11030192

Valls-Esteve, A., Tejo-Otero, A., Adell-gomez, N., Lustig-Gainza, P., Fenollosa-artes, F., Buj-corral, I., Rubio-Palau, J., Manuera, J., & Krauel, L. (2023) Advanced strategies for the fabrication of multi-material anatomical models of complex paediatric oncologic cases. *Bioengineering*, 11(1), 31. Doi: 10.3390/bioengineering11010031

Valon, L., & Levayer, R. (2019). Dying under pressure: cellular characterisation and in-vivo functions of cell death induced by compaction. *Biology of the cell*, 111(3), 51 – 66. Doi: 10.1111/boc.2018000075

Van Norman, G. A. (2019). Limitations of Animal Studies for Predicting Toxicity in Clinical Trials: Is it Time to Rethink Our Current Approach? *JACC: Basic to Translational Science*, *4*(7), 845. Doi: 10.1016/j.jacbts.2019.10.008

Van Norman, G. A. (2019). Limitations of Animal Studies for Predicting Toxicity in Clinical Trials: Is it Time to Rethink Our Current Approach? *JACC: Basic to Translational Science*, *4*(7), 845-854. Doi: 10.1016/j.jacbts.2019.10.008

Vandamme, T. (2014) Use of rodents as models of human diseases. *Journal of pharmacy and bio-allied sciences*, 6(1), 2 – 9. Doi: 10.4103/0975-7406.124301

Vasarhelyi, L., Konya, Z., Kukovecz, A., & Vajtai, R. (2020) Microcomputed tomography-based characterisation of advanced materials: a review. *Materials today advanced*, 8. Doi: 10.1016/j.mtadv.2020.100084

Vazquez, M., Evans, B., Riccardi, D., Evans, S., Ralphs, J., Dillingham, C., & Mason, D. (2014) A new method to investigate how mechanical loading of osteocytes controls osteoblasts. *Frontiers in endocrinology*, 5, 208. Doi: 10.3389/fendo.2014.00208

Veneziano, A., Cazenave, M., Alfieri, F., Panetta, D., & Marchi, D. (2021) Novel strategies for the characterisation of cancellous bone morphology: virtual isolation and analysis. *American Journal of Biological Anthropology*, 175(4), 920-930. Doi: 10.1002/ajpa.24272

Venkatesan, J., Anil, S., & Murugan, S. (2021) 3D bioprinted alginate-based biomaterials for bone tissue engineering. *Journal of 3D printing in medicine*, 4(4), 175 – 179. Doi: 10.2217/3dp-2020-0029

Verdelis, K., Lukashova, L., Atti, E., Mayer-kuckuk, P., Peterson, M., Tetradis, S., Boskey, A., & Meulen, M. (2011) Micro-CT morphometry analysis of mouse cancellous bone: intra- and inter- system reproducibility. *Bone*, 49, 580 – 587. Doi: 10.1016/j.bone.2011.05.013

Viero, A., Biehler-Gomez, L., Messina, C., Cappella, A., Giannoukos, K., Viel, G., Tagliaro, F., & Cattaneo, C. (2022) Utility of micro-CT for dating post-cranial fractures of known post-traumatic ages through 3D measurements of the trabecular inner morphology. *Scientific reports*, 12, 10543. Doi: 10.1038/s41598-022-14530-1

Vijayakumar, P. (2020). Synthesis and characterization of hydroxyapatite nanoparticles and their cytotoxic effect on a fish vertebra derived cell line. *Biocatalysis and Agricultural Biotechnology*, *25*, 101612. Doi: 10.1016/j.bcab.2020.101612

Virzi, A., Muller, C., Marret, J., Mille, E., Berteloot, L., Grevent, D., Boddaert, N., Gori, P,. Sarnacki, S., & Bloch, I. (2019) Comprehensive review of 3D segmentation software tools for MRI usable for pelvic surgery planning. *Journal of digital imaging*, 33(1), 99 – 110. Doi: 10.1007/s10278-019-00239-7

Vis, M. A., Ito, K., & Hofmann, S. (2020). Impact of Culture Medium on Cellular Interactions in in vitro Co-culture Systems. *Frontiers in Bioengineering and Biotechnology*, *8*, 561429. Doi: 10.3389/fbioe.2020.00911

Volk, S., Shah, S., Cohen, A., Wang, Y., Brisson, B., Vogel, L., Hankenson, K., & Adams, S. (2014) Type III collagen regulates osteoclastogenesis and the quantity of trabecular bone. *Calcified tissue international*, 94(6), 621 – 631. Doi: 10.1007/s00223-014-9843-x

Vygotsky, L. S. (1978) Interaction between learning and development, zone of proximal development (In Mind and Society, 79-91), *Harvard University Press, Harvard UK.*

Waidi, Y., Kariim, I., & Datta, S. (2024) Bioprinting of gelatine-based materials for orthopedic application. *Frontiers bioengineering biotechnology,* 12. Doi: 10.3389/fbior.2024.1357460

Walker, E., McGregor, N., Chan, A., & Sims, N. (2021) Measuring bone volume at multiple densities by micro-computed tomography. *Bio-protocol*, 11(1), e3873. Doi: 10.21769/Bioprotoc.3873

Wan, H., Xiang, J., Mao, G., Pan, S., Li, B., & Lu, Y. (2024) Recent advances in the application of 3D-printing bioinks based on decellularized extracellular matrix in tissue engineering. *ACS Omega*, 9(23), 24219 – 24235. Doi: 10.1021/acsomega.4c02847

Wang, D., Christensen, K., Chawla, K., Xiao, G., Krebsbach, P., & Franceschi, R. (1999) Isolation and characterisation of MC3T3-E1 pre-osteoblast sub-clones with distinct in-vitro and in-vivo differentiation/mineralization potential. *Journal of bone mineral research*, 14(6), 893 – 903. Doi: 10.1359/jbmr.1999.14.6.893

Wang, L., You, X., Zhang, L., Zhang, C., & Zou, W. (2022). Mechanical regulation of bone remodelling. *Bone Research*, *10*(1), 1-15. Doi: 10.1038/s41413-022-00190-4

Wang, M., Gao, J., & Wang, X. (2017) High-quality mesh generation for human hip based on ideal element size: methods and evaluation. *Computer assisted surgery*, 22(1), 212 – 220. Doi: 10.1080/24699322.2017.1389399

Wang, N., Zhang, Y., Li, Z., Fu, Y., Yu, H., Liu, W., Xue, X., & Jiang, Y. (2021) Pixel2mesh: 3D mesh model generation via image-guided deformation. *IEEE transctions on pattern analysis and machine intelligence*, 43(1), 3600- 3613. Doi: 10.1109/TPAMI.2020.2984232

Wang, Q., Zhang, W., Peng, X., Tao, Y., Gu, Y., Li, W., Liang, X., Wang, L., Wu, Z., Wang, T., Zhang, H., Liu, X., Xu, Y., Liu, Y., Zhou, J., & Geng, D. (2022) GSK-3β suppression upregulates Gli1 to alleviate osteogenesis inhibition in titanium nanoparticle-induced osteolysis. *Journal of nanobiotechnology*, 20, 148. Doi: 10.1186/s12951-022-01351-7

Wang, W., & Yeung, K. W. (2017). Bone grafts and biomaterials substitutes for bone defect repair: A review. *Bioactive Materials*, *2*(4), 224. Doi: 10.1016/j.bioactmat.2017.05.007

Wang, X., Song, Y., Liu, Y., Sun, Y., Wang, Y., Wang, Y., & Lyu, P. (2016) Osteogenic differentiation of three-dimensional bioprinted constructs consisting of human adipose-derived stem cells in-vitro and in-vivo. *PLoS one*, 11(6), e0157214. Doi: 10.1371/journal.pone.0157214

Wankier, Z., Taylor, C., Drew, A., Kubiak, E., Agarwal, J., & Sinclair, S. (2021) Use of computer tomography imaging for analysing bone remodelling around a percutaneous

osseointegrated implant. *Journal of Orthopaedic Research*, 40(9), 2065-2075. Doi: 10.1002/jor.25247

Wathen, C., Foje, N., Avermaete, T., Miramontes, B., Chapaman, S., Sasser, T., Kannan, R., Gerstler, S., & Leevy, M. (2013) In vivo x-ray computed tomographic imaging of soft tissue with native, intravenous, or oral contrast. *Sensors (Basel)*, 13(6), 6957-6980. Doi: 10.3390/s130606957

Watkins, J., & Mathieson, I. (2009) The pocket podiatry guide: functional anatomy. *Connective tissues*, 4, 107 – 156. Doi: 10.1016/B978-0-7020-3032-1.00004-4

Wei, J., Yan, Y., Gao, J., Li, Y., Wang, R., Wang, J., Zou, Q., Zuo, Y., Zhu, M., & Li, J. (2022) 3D-printed hydroxyapatite microspheres reinforced PLGA scaffolds for bone regeneration. *Biomaterials advanced*, 133, 112618. Doi: 10.1016/j.msec.2021.112618

Wein, M. (2017) Bone lining cells: Normal physiology and role in response to anabolic osteoporosis treatments. *Current molecular biology reports*, 3, 79 – 84. Doi: 10.1007/s40610-017-0062-x

Weiskirchen, S., Schroder, S., Buhl, E., & Weiskirchen, R. (2023). A beginner's guide to cell culture: practical advice for preventing needless problems. Cells, 12(5), 682. Doi: 10.3390/cells12050682

White, K., Chalaby, R., Lowe, G., Berlin, J., Glackin, C., & Olabisi, R. (2021). Calcein binding to assess mineralization in hydrogel microspheres. *Polymers*, 13(14), 2274. Doi: 10.3390/polym13142274

Wickramasinghe, S., Do, T., & Tran, P. (2020) FDM-based 3D printing of polymer and associated composite: a review on mechanical properties, defects and treatments. *Polymers*, 12(7), 1529. Doi: 10.3390/polym12071529

Wildt, B., Ansari, S., Sommerdijk, N., Ito, K., Akiva, A., & Hofmann, S. (2019) From bone regeneration to three-dimensional in-vitro models: tissue engineering of organised bone extracellular matrix. *Current opinion in biomedical engineering,* 10, 105 – 115. Doi: 10.1016/j.cobme.2019.05.005

Williamson, A., Silva, A., Carmo, J., Le Maitre, C., Hall, J., & Aberdein, N. (2023) Impact of leptin deficiency on male tibia and vertebral body 3D bone architecture independent of changes in body weight. *Physiological reports*, 11(19). Doi: 10.14814/phy2.15832

Willner, I. (2017) Stimuli-controlled hydrogels and their applications. *Accounts of chemical research*, 50(4), 657 – 658. Doi: 10.1021.acs.accounts.7b00142

Wilson, D. I. (2017). What is rheology? *Eye*, *32*(2), 179. Doi: 10.1038/eye.2017.267

Wojtas, M., Lausch, A., & Sone, E. (2020) Glycosaminoglycans accelerate biomimetic collagen mineralization in tissue-based in-vitro model. *PNAS: biochemistry*, 117(23). 12636 – 12642. Doi: 10.1073/pnas.1914899117

Woo, S., Paek, K., Yoon, Y. M., Kim, H., Park, S. I., & Kim, J. A. (2025). Development of a BMU-on-a-chip model based on spatiotemporal regulation of cellular interactions in the bone remodelling cycle. *Materials Today Bio*, *32*, 101658. Doi: 10.1016/j.mtbio.2025.101658

Woo, S., Rosser, J., Dusevich, V., Kalajzic, I., & Bonewald, L. (2011) Cell line IDG-SW3 replicates osteoblast-to-late-osteocyte differentiation *in-vitro* and accelerates bone formation *in-vivo*. *Journal of bone and mineral research*, 26(11), 2634 – 2646. Doi: 10.1002/jbmr.465

Wray, A., Okita, N., & Ross, C. (2011) Cortical and trabecular bone, bone mineral density, and resistance to ex-vivo fracture are not altered in response to life-long vitamin A supplementation in aging rats. *The journal of nutrition*, 141(4), 660 – 666. Doi: 10.3945/jn.110.132126

Wu, C., Zhu, Y., & Woo, J. (2023) Advances in 3D bioprinting: techniques, applications, and future directions for cardiac tissue engineering. *Bioengineering*, 10(7), 842. Doi: 10.3390/bioengineering10070842

Wu, W., DeConick, A., & Lewis, J. (2011) Omnidirectional printing of 3D microvascular networks. *Advanced materials*, 23(24), H178 – H183. Doi: 10.1002/adma.201004625

Wu, Y., Wen, Y., Salamanca, E., Moe Aung, L., Chao, Y., Chen, C., Sun, Y., & Chang, W. (2024). 3D-bioprinted alginate-based bioink scaffolds with β-tricalcium phosphate for bone regeneration applications. *Journal of Dental Sciences*, *19*(2), 1116-1125. Doi: 10.1016/j.jds.2023.12.023

Wu, Z., Wang, B., Tang, J., Bai, B., Weng, S., Xie, Z., Shen, Z., Yan, D., Chen, L., Zhang, J., & Yang, L. (2020) Degradation of subchondral bone collagen in weight-bearing area of femoral head is associated with osteoarthritis and osteonecrosis. *Journal of orthopaedic surgery and research*, 15, 526. Doi: 10.1186/s13018-020-02065-y

Xi, R., Ali, M., Zhou, Y., & Tizzano, M. (2024) A reliable deep-learning-based method for alveolar bone quantification using a murine model of periodontitis and micro-computed tomography. *Journal of Dentistry*, 146, 105057. Doi: 10.1016/j.jdent.2024.105057

Xiao, G., Gopalakrishnan, R., Jiang, D., Reith, E., Benson, D., & Franceschi, R. (2009) Bone morphogenetic proteins, extracellular matrix, and mitogen-activated protein kinase signalling pathways are required for osteoblast-specific gene expression and differentiation in MC3T3-E1 cells. *Journal of bone and mineral research*, 17(1), 101 – 110. Doi: 10.1359/jmbr.2002.17.1.101

Xiao, L., Chenyang, Z., Xingzhu, L., Ping, L., & Yadong, Y. (2024) 3D bioprinting technology to construct bone reconstruction research model and its feasibility evaluation. *Frontiers: Tissue engineering and regenerative medicine*, 12. Doi: 10.3389/fbior.2024.1328078

Xie, R., Pal, V., Yu, Y., Lu, X., Gao, M., Liang, S., Huang, M., Peng, W., & Ozbolat, I. T. (2024). A comprehensive review on 3D tissue models: Biofabrication technologies and preclinical applications. *Biomaterials*, *304*, 122408. Doi: 10.1016/j.biomaterials.2023.122408

Xu, C., Lee, W., Dai, G., & Hong, Y. (2018) Highly elastic biodegradable single-network hydrogel for cell printing. *ACS applied materials & Interfaces,* 10(12), 9969 – 9979. Doi: 10.1021/acsami.8b01294

Xu, H., Liu, J., Zhang, Z., & Xu, C. (2022) A review on cell damage, viability, and functionality during 3D bioprinting. *Military medical research*, 9, 70. Doi: 10.1186/s40779-022-00429-5

Yahara, Y., Nguyen, T., Ishikawa, K., Kamei, K., & Alman, B. (2022) The origins and roles of osteoclasts in bone development, homeostasis and repair. *Development,* 149(8). Doi: 10.1242/dev.199908

Yamaguchi, N., & Knaut, H. (2022) Focal adhesion-mediated cell anchoring and migration: from *in vitro* to *in vivo*. *Development*, 149(10). Doi: 10.1242/dev.200647

Yang, B., Sun, H., Chen. P., Fan, N., Zhong, H., Liu, X., Wu, Y., & Wang, J. (2019) YAP1 influences differentiation of osteoblastic MC3T3-E1 cells through the regulation of ID1. *Journal of cellular physiology*, 234(8), 14007 – 14018. Doi: 10.1002/jcp.28088

Yang, R., Wang, R., Abbaspoor, S., Rajan, M., Turki Jalil, A., Mahmood Saleh, M., & Wang, W. (2023). In vitro and in vivo evaluation of hydrogel-based scaffold for bone tissue engineering application. *Arabian Journal of Chemistry*, *16*(7), 104799. Doi: 10.1016/j.arabjc.2023.104799

Yang, S., Li, Y., Ye, J., Wang, L., & Xu, M. (2025) Three-dimensional bioprinting utilising sacrifical material support and longitudinal printability evaluation through volumetric imaging. *Biomaterial advances*, 169, 214188. Doi: 10.1016/j.bioadv.2025.214188

Yang, Y., Ogando, C., See, C., Chang, T., & Barabino, G. (2018) Changes in phenotype and differentiation potential of human mesenchymal stem cells aging in-vitro. *Stem cell research & therapy*, 9(131). Doi: 10.1186/s13287-018-0876-3

Yao, Y., Zhou, D., Shen, Y., Wu, H., & Wang, H. (2021) Morphology-controllable amphiphilic cellulose microgels made from self-assembly of hydrophobic long-chain bromide-alkylated-cellulose/gelatine copolymer. *Carbohydrate polymers*, 269, 118265. Doi: 10.1016/j.carbpol.2021.118265

Yi, S., Liu, Q., Luo, Z., He, J. J., Ma, L., Li, W., Wang, D., Zhou, C., Garciamendez, C. E., Hou, L., Zhang, J., & Zhang, Y. S. (2022). Micropore-Forming Gelatin Methacryloyl (GelMA) Bioink Toolbox 2.0: Designable Tunability and Adaptability for 3D Bioprinting Applications. *Small*, *18*(25), 2106357. Doi: 10.1002/smll.202106357

Ying, G., Maharjan, S., Yin,Y., Chai, R., Cao, X., Yang, J., Miri, A., Hassan, S., Zhang, Y., & Jiang, N. (2018) Aqueous two-phase emulsion bioink-enabled 3D bioprinting of porous hydrogels. *Advanced materials*, 30(50), e1805460. Doi: 10.1002/adma.201805460

Yong-sang, L., Sung, K., Kyung, O., & Hong-soek, M. (2022) A comparative study of the accuracy of dental CAD programs in designing a fixed partial denture. *Journal of prosthodontics*, 31(3), 215-220. Doi: 10.1111/jopr.13406

Yoon, H., Park, S., Shin, H., Kim, K., Cho, Y., Moon, J., Kim, W., & Ryoo, H. (2025) Unravelling the dynamics of osteoblast differentiation in MC3T3-E1 cells: transcriptomic insights into matrix mineralisation and cell proliferation. *Bone*, 194, 117442. Doi: 10.1016/j.bone.2025.117442

You, S., Xiang, Y., Hwang, H., Berry, D., Kiratitanaporn, W., Guan, J., Yao, E., Tang, M., Zhong, Z., Ma, X., Wangpraseurt, D., Sun, Y., Lu, T., & Chen, S. (2023) High cell density

and high-resolution 3D bioprinting for fabricating vascularised tissues. *Science advances*, 9(8). Doi: 10.1126/sciadv.ade7923

You, Y., Niu, Y., Sun, F., Huang, S., Ding, P., Wang, X., Zhang, X., & Zhang, J. (2022) Three-dimensional printing and 3D slicer powerful tools in understanding and treating neurosurgical diseases. *Frontiers in surgery*, 9, 1030081. Doi: 10.3389/fsurg.2022.1030081

Yu, K., Chen, J., Fu, K., He, J., Zheng, J., & Zheng, Y. (2022) On the efficiency of the advancing-front surface mesh generation algorithm. *Computer-aided design*, 153, 103403. Doi: 10.1016/j.cad.2022.103403

Yuan, H., Fernandes, H., Habibovic, P., C Barradas, A. M., & Walsh, W. R. (2010). Osteoinductive ceramics as a synthetic alternative to autologous bone grafting. *Proceedings of the National Academy of Sciences of the United States of America*, *107*(31), 13614. Doi: 10.1073/pnas.1003600107

Yue, K., Trujillo-de Santiago, G., Alvarez, M. M., Tamayol, A., Annabi, N., & Khademhosseini, A. (2015). Synthesis, properties, and biomedical applications of gelatine meth acryloyl (GelMA) hydrogels. *Biomaterials*, *73*, 254-271. Doi: 10.1016/j.biomaterials.2015.08.045

Yuste, I., Luciano, F., Gonzalez-Burgos, E., Lalatsa, A., & Serrano, D. (2021) Mimicking bone microenvironment: 2D and 3D in vitro models of human osteoblasts. *Pharmacology research*, 169, 105626. Doi: 10.1016/j.phrs.2021.105626

Zamani, Y., Mohammadi, J., Amoabediny, G., Visscher, D., Helder, M., Zandieh-Doulabi, B., & Klein-Nulend, J. (2018) Enhanced osteogenic activity by MC3T3-E1 pre-osteoblasts on chemically surface-modified poly(ε-caprolactone) 3D-printed scaffolds compared to RGD immobilized scaffolds. *Biomedical biomaterials,* 14(1), 015008. Doi: 10.1088/1748-605X-aaeb82

Zandrini, T., Florczak, S., Levato, R., Ovsianikov, A. (2022) Breaking the resolution limits of 3D bioprinting: future opportunities and present challenges. *Cell Press: Trends in Biotechnology*, 41(5), 604-614. Doi: 10.1016/j.tibtech.2022.10.009

Zauchner, D., Müller, M. Z., Horrer, M., Bissig, L., Zhao, F., Fisch, P., Lee, S. S., Müller, R., & Qin, X. (2024). Synthetic biodegradable microporous hydrogels for in vitro 3D culture of functional human bone cell networks. *Nature Communications*, *15*(1), 1-12. Doi: 10.1038/s41467-024-49280-3

Zeng, G., Zhu, Y., & Chen, W. (2023) A brief review of micro-particle slurry rheological behaviour in grinding and flotation for enhancing fine mineral processing efficiency. *Minerals*, 13(6), 792. Doi: 10.3390/min12060792

Zhang, G. (2012). Biomimicry in biomedical research. *Organogenesis*, *8*(4), 101. Doi: 10.4161/org.23395

Zhang, H., Han, J., Sun, Y., Huang, Y., & Zhou, M. (2015) MC3T3-E1 cell response to stainless steel 316L with different surface treatments. *Materials science engineering part C: materials and biology applied.* 56, 22 – 29. Doi: 10.1016/j.msec.2015.06.017

Zhang, H., Luo, Y., Hu, Z., Chen, M., Chen, S., Yao, Y., Yao, J., Shao, X., Wu, K., Zhu, Y., & Fu, J. (2024). Cation-crosslinked k-carrageenan sub-microgel medium for high-quality embedded bioprinting. *Biofabrication*, 16(2). Doi: 10.1088/1758-5090/ab1cf3

Zhang, J., Wehrle, E., Adamek, P., Paul, G., Qin, X., Rubert, M., & Muller, R. (2020) Optimisation of mechanical stiffness and cell density of 3D bioprinted cell-laden scaffolds improves extracellular matrix mineralization and cellular organisation for bone tissue engineering. *Acta Biomaterialia*, 114, 307 – 322. Doi: 10.1016/j.actbio.2020.07.016

Zhang, J., Wehrle, E., Rubert, M., & Muller, R. (2021) 3D bioprinting of human tissues: biofabrication, bioinks, and bioreactors. *International journal of molecular science*, 22(8), 3971. Doi: 10.3390/ijms22083971

Zhang, L., & Yu, Y. (2023). Improving the stability of water-in-oil emulsions with medium internal phase by the introduction of gelatine. *Foods*, 12(15), 2863. Doi: 10.3390/foods12152863

Zhang, T., Lin, S., Shao, X., Zhang, Q., Xue, C., Zhang, S., Lin, Y., Zhu, B., & Cai, X. (2017) Effect of matrix stiffness on osteoblast functionalization. *Cell proliferation*, 50(3), e12338. Doi: 10.1111/cpr.12338

Zhang, T., Xu, J., Zhang, Y., Wang, X., Lorenzo, J., & Zhong, J. (2020) Gelatines as emulsifiers for oil-in-water emulsions: extractions, chemical composition, molecular structure, and molecular modification. *Trends in food science & technology*, 106, 113 – 131. Doi: 10.1016/j.tifs.2020.10.005

Zhang, X., Sun, M., Zhang, L., Dai, Y., & Wang, F. (2020) The potential function of miR0135b-medicated JAK2/STAT3 signalling pathway during osteoblast differentiation. *The Kaohsiung journal of medical sciences*, 36(9). Doi: 10.1002/kjm2.12217

Zhang, Y., Fan, W., Wang, K., Wei, H., Zhang, R., & Wu, Y. (2019) Novel preparation of Au nanoparticles loaded Laponite nanoparticles/ECM injectable hydrogel on cardiac differentiation of resident cardiac stem cells to cardiomyocytes. *Journal of photochemistry and photobiology B: Biology*, 192, 49 – 54. Doi: 10.1016/j.jphotobiol.2018.12.022

Zhang, Y., Wu, D., Zhao, X., Pakvasa, M., Tucker, A. B., Luo, H., Qin, K. H., Hu, D. A., Wang, E. J., Li, A. J., Zhang, M., Mao, Y., Sabharwal, M., He, F., Niu, C., Wang, H., Huang, L., Shi, D., Liu, Q. Ni, N., Fu, K., Chen, C., Wagstaff, W., Reid, R., Athiviraham, A., Ho, S., Lee, M., Hynes, K., Strelzow, J., He, T., & Dafrawy, M. (2020) Stem Cell-Friendly Scaffold Biomaterials: Applications for Bone Tissue Engineering and Regenerative Medicine. *Frontiers in Bioengineering and Biotechnology*, *8*, 598607. Doi: 10.3389/fbioe.2020.598607

Zhang, Y., Yu, T., Ding, J., & Li, Z. (2023). Bone-on-a-chip platforms and integrated biosensors: Towards advanced in vitro bone models with real-time biosensing. *Biosensors and Bioelectronics*, *219*, 114798. Doi: 10.1016/j.bios.2022.114798

Zhang, Z., & Wang, X. (2017) Current progress of 3D bioprinting based tissue engineering. *Quantitative Biology,* 5(2), 136 - 142. Doi: 10.1007/s40484-017-0103-8

Zhao, X., Zhou, X., Sun, H., Shi, H., Song, Y., Wang, Q., Zhang, G., & Xu, D. (2022) 3D printed Ti-5Cu alloy accelerates osteogenic differentiation of MC3T3-E1 cells by stimulating the M2 phenotype polarization of macrophages. *Frontiers in immunology*, 13, 1001526. Doi: 10.3389/fimmu.2022.1001526

Zhao, Y., Li, Y., Mao, S., Sun, W., & Yao, R. (2015) The influence of printing parameters on cell survival rate and printability in micro extrusion-based 3D cell printing technology. *Biofabrication*, 7(4), 045002. Doi: 10.1088/1758-5090/7/4/045002

Zhao, Z., Moay, Z. K., Setyawati, M. I., Rakshit, M., Kathawala, M. H., & Ng, K. W. (2020). Composite Hydrogels in Three-Dimensional in vitro Models. *Frontiers in Bioengineering and Biotechnology*, *8*, 543064. Doi: 10.3389/fbioe.2020.00611

Zheng, C., & Zhang, M. (2023) 3D-printed PCL/β-TCP/CS composite artificial bone and histocompatibility study. *Journal of orthopaedic surgery and research*, 18, 981. Doi: 10.1186/s13018-023-04489-8

Zhou, B., Jiang, X., Zhou, X., Tan, W., Luo, H., Lei, S., & Yang, Y. (2023). GelMA-based bioactive hydrogel scaffolds with multiple bone defect repair functions: Therapeutic strategies and recent advances. *Biomaterials Research*, *27*, 86. Doi: 10.1186/s40824-023-00422-6

Zhou, K., Dey, M., Ayan, B., Zhang, Z., Ozbolat, V,, Kim, M., Khristov, V., & Ozbolat, I. (2021) Fabrication of PDMS microfluidic devices using nano clay-reinforced Pluronic F-127 as a sacrificial ink. *Biomedical materials*, 16(4), 045005. Doi: 10.1088/1748-605X/abe55e

Zhou, K., Sun, Y., Yang, J., Mao, H., & Gu, Z. (2022) Hydrogels for 3D embedded bioprinting: a focused review on bioinks and support baths. *Journal of materials chemistry B,* 10, 1897 - 1907. Doi: 10.1039/D1TB02554F

Zhou, L., Li, Y., Tu, Q., & Wang, J. (2023) A 3D printing mold method for rapid fabrication of artifical blood vessels. *Colloids and surfaces A: physicochemical and engineering aspects*, 662, 130952. Doi: 10.1016/j.colsurfa.2023.120952

Zhu, H., Monavari, M., Zheng, K., Distler, T., Ouyang, L., Heid, S., Jin, Z., He, J., Li, D., & Boccaccini, A. (2022) 3D bioprinting of multifunctional dynamic nanocomposite bioinks incorporating Cu-Doped mesoporous bioactive glass nanoparticles for bone tissue engineering. *Small,* 18(12), 2104996. Doi: 10.1002/smll.202104996

Zhu, J., Sun, H., Wo, J., Xu, F., Lu, Deng, B., Zhu, Y., & Yuan, F. (2020) Duration of electrochemical deposition affects the morphology of hydroxyapatite coatings on 3D-printed titanium scaffold as well as the functions of adhered MC3T3-E1 cells. *Journal of orthopaedic science*, 25(4), 708 – 714. Doi: 10.1016/j.jos.2019.09.008

Zhu, M., Wang, Y., Ferracci, G., Zheng, J., Cho, N., & Lee, B. (2019) Gelatin methacryloyl and its hydrogels with an exceptional degree of controllability and batch-to-batch consistency. *Scientific reports*, 9, 6863. Doi: 10.1038/s41598-019-42186-x

Zhu, S., Chen, W., Masson, A., & Li, Y. (2024) Cell signalling and transcriptional regulation of osteoblast lineage commitment, differentiation, bone formation, and homeostasis. *Cell discovery*, 10, 71. Doi: 10.1038/s41421-024-00689-6

Zhu, Y., Yu, X., Liu, H., Li, J., Gholipourmalekabadi, M., Lin, K., Yuan, C., & Wang, P. (2024). Strategies of functionalized GelMA-based bioinks for bone regeneration: Recent advances and future perspectives. *Bioactive Materials*, *38*, 346. Doi: 10.1016/j.bioactmat.2024.04.032

Zinck, N., & Franz-Odendaal, T. (2020) Accurate whole-mount bone and cartilage staining requires acid-free conditions. *American association for anatomy*, 304(5), 958 – 960. Doi: 10.1002/ar.24526

Zonderland, J., & Moroni, L. (2021) Steering cell behaviour through mechanobiology in 3D: A regenerative medicine perspective. *Biomaterials*, 268. Doi: 10.1016/j.biomaterials.2020.120572

Zschenker, O., Streichert, T., Hehlgans, S., & Cordes, N. (2012) Genome-wide gene expression analysis in cancer cells reveals 3D growth to affect ECM and processes associated with cell adhesion but not DNA repair. *PLoS one*, 7(4), e34279. Doi: 10.1371/journal.pone.0034279

Zwierzyna, M., & Overington, J. (2017) Classification and analysis of a large collection of in-vivo bioassay descriptions. *PLOS computational biology*, 13(7), e10005641. Doi: 10.1371/journal.pcbi.1005641

Appendix

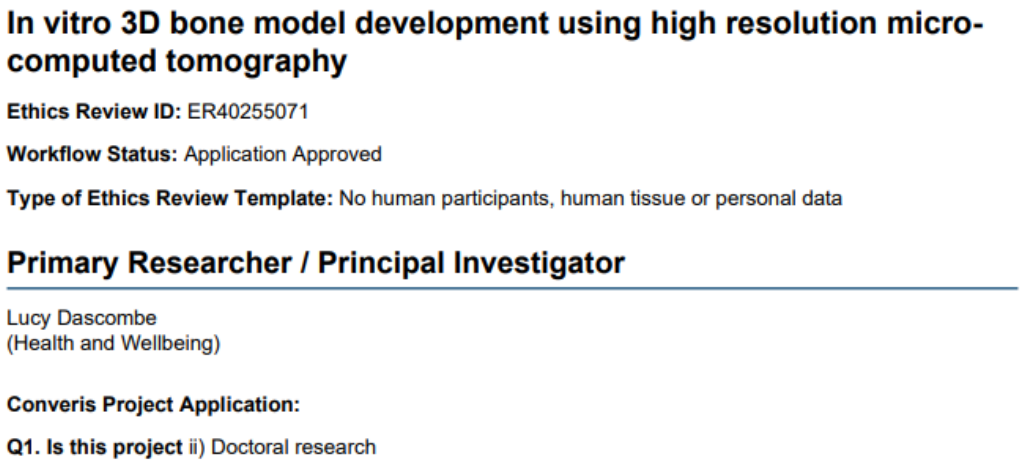

In vitro 3D bone model development using high resolution micro-computed tomography

Ethics Review ID: ER40255071

Workflow Status: Application Approved

Type of Ethics Review Template: No human participants, human tissue or personal data

Primary Researcher / Principal Investigator

Lucy Dascombe
(Health and Wellbeing)

Converis Project Application:

Q1. Is this project ii) Doctoral research

Figure S1. Ethical approval for PhD research.

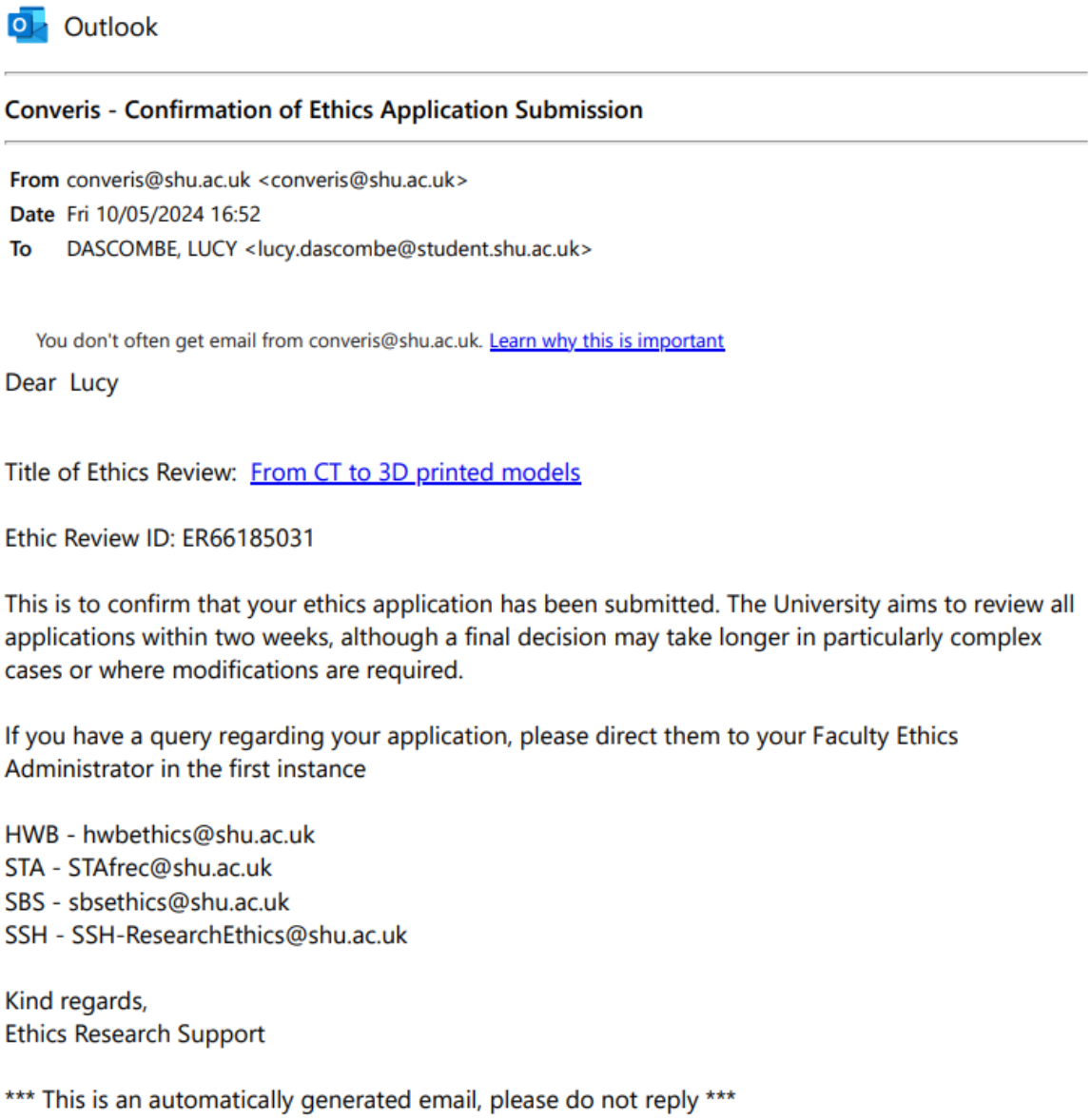

Outlook

Converis - Confirmation of Ethics Application Submission

From converis@shu.ac.uk <converis@shu.ac.uk>
Date Fri 10/05/2024 16:52
To DASCOMBE, LUCY <lucy.dascombe@student.shu.ac.uk>

You don't often get email from converis@shu.ac.uk. Learn why this is important

Dear Lucy

Title of Ethics Review: From CT to 3D printed models

Ethic Review ID: ER66185031

This is to confirm that your ethics application has been submitted. The University aims to review all applications within two weeks, although a final decision may take longer in particularly complex cases or where modifications are required.

If you have a query regarding your application, please direct them to your Faculty Ethics Administrator in the first instance

HWB - hwbethics@shu.ac.uk
STA - STAfrec@shu.ac.uk
SBS - sbsethics@shu.ac.uk
SSH - SSH-ResearchEthics@shu.ac.uk

Kind regards,
Ethics Research Support

*** This is an automatically generated email, please do not reply ***

Figure S2. Ethical approval for questionnaire-based research.

The following attached documents are the participant information guide (S3), pre-questionnaire (S4), post-questionnaire (S5) and participant learning handout (S6) as delivered to participants in accordance with chapter 4 – Dissemination of micro-CT to 3D CAD model workflow.

Sheffield Hallam University | Biomolecular Sciences Research Centre

University of Sheffield

Participant information guide

Sheffield Hallam University, Biomolecular Sciences Research Centre

Study title:

From CT to 3D printed models

Principal Investigator:

Lucy Dascombe, Sheffield Hallam University (L.Dascombe@shu.ac.uk)

Research team:

Tim Nichol, Sheffield Hallam University (T.Nichol@shu.ac.uk), Christine Le Maitre, University of Sheffield (C.Lemaitre@sheffield.ac.uk), Nicola Aberdein, Sheffield Hallam University (N.Aberdein@shu.ac.uk)

To help you make an informed decision regarding your participation, this guide will explain what the study is about, the possible risks and benefits, and your rights as a participant. If you do not understand something in this guide, please clarify with the principal investigator before agreeing to participate in this study. You may wish to save this guide for your records.

What is the study about?

You are invited to participate in a research study to determine the dissemination of knowledge from the process of Micro-computed tomography reconstruction to translation into a 3D printable model utilising appropriate software packages. Micro-CT is a high-resolution imaging technique that facilitates the planar capture of dense in-organic components, which can then be reconstructed into a 3D model to allow quantitative analysis. From this, the 3D model can be exported as a standard tessellation language (STL) model and rendered using computed assisted design software. CAD Autodesk® meshmixer and Fusion 360 offer user friendly interfaces that can tailor micro-CT scans into 3D printable models, for a variety of end-point outcomes, including 3D bioprinted *in vitro* model for biomedical testing. Participants will be informed on this process during a workshop completed at bone research society meeting (10/07/24) presented by the principal investigator.

You are welcomed to complete a pre-workshop questionnaire that investigates base knowledge of the aforementioned techniques, and upon participation in the workshop are offered to complete a post-workshop questionnaire to determine knowledge learnt from the session. Completion of the questionnaires will assist with the principal researcher assessing the effectiveness of dissemination of knowledge that has been

developed during the process of doctoral research, and how this method supports in the wider scientific community.

What does participation involve?

Participation in this study is optional, but if consent is provided participants are invited to complete a pre-workshop questionnaire, attend the from CT to 3D models workshop at bone research society meeting (10/07/24), and complete a post-workshop questionnaire. Participation with the questionnaires does not alter the opportunity to attend the outlined workshop. Responses will be used in a doctoral research thesis. No risks are associated with completion of the questionnaires.

What personal data gets collected?

No personal data will be collected from the researching team associated with this study. Participants who complete the pre-workshop questionnaire will be provided with a unique identification code and asked to provide the unique identification code on the post-workshop questionnaire. Only the research team will have access to the responses to the questionnaires, and this information will be stored in a secure internal drive. Principal investigator is responsible for this information.

Who should I contact if I have questions regarding my participation in the study?

If you have any questions or feedback regarding this study, or to withdraw from the study please contact Lucy Dascombe by email (L.Dascombe@shu.ac.uk).

Funding body acknowledgement

This research is funded and supported by Sheffield Hallam University (PhD studentship).

Ethical approval

This study has received ethical approval from Sheffield Hallam University, ER66185031. By completing this survey, you consent to the anonymous information collected for the purposes of this research study to be used for research purposes. Further information at https://www.shu.ac.uk/research/ethics-integrity-and-practice.

You should contact the Data Protection Officer if: you have query about how your data is used by the University; you would like to report a data security breach; you would like to complain about how the University has used your personal data DPO@shu.ac.uk. You should contact the Head of Research Ethics (Dr Ranchordas) if you have concerns about how the research was undertaken or how you were treated, at ethicssupport@shu.ac.uk

Postal address: Sheffield Hallam University, Howard Street, Sheffield S1 1WB. Telephone 0114 225 5555

From CT to 3D printed models – Pre-workshop questionnaire

Background: This study aims to assess the dissemination of knowledge delivered at bone research society meeting workshop titled 'From CT to 3D printed models'. Responses will be anonymously recorded by unique identifier codes and used to in partial fulfilment of a doctoral research thesis. Please refer to the participant information guide for further information.

Do you consent to participation in this study? Yes / No

Pre-questions

1. Are you familiar with the imaging technique of micro-computational tomography (Micro-CT)? Yes / No

   B) If yes, do you have practical experience in analysing data? Yes / No

   C) What software do you use?

   _____

   _____

2. Are you familiar with computer assisted design (CAD) software? Yes / No

   B) If yes, what software do you use?

   _____

   _____

3. Do you feel that transferring micro-CT data to 3D printable models would be useful for your research? Yes / Unsure / No

   B) why?

   _____

   _____

4. What type of 3D printer do you have access to?

_____

_____

5. What materials do you use to 3D print?

_____

_____

_____

6. What are you planning to 3D print?

_____

_____

7. What are your expectations for this workshop?

_____

_____

_____

_____

From CT to 3D printed models – Post-workshop questionnaire

Background: This study aims to assess the dissemination of knowledge delivered at bone research society meeting workshop titled 'From CT to 3D printed models'. Responses will be anonymously recorded by participant codes and used to in partial fulfilment of a doctoral research thesis. Please refer to the participant information guide for further information.

Do you consent to participation in this study? Yes / No

Participant code

_____

Post-questions

1. Did the workshop meet your initial expectations? Yes / No

   B) If no, what information could be provided?

   _____

   _____

2. Was the content of the workshop relevant to your research? Yes / No

   B) why?

   _____

   _____

3. Were the workshop materials easy to follow and helpful? Yes / No

   _____

   _____

   _____

4. Did the materials aid your understanding of the topics presented? Yes /

   No

_____

_____

_____

5. What was the most valuable part of the workshop for your research?

   _____

   _____

   _____

   _____

6. What techniques did you learn?

   _____

   _____

   _____

7. Do you feel confident in transferring micro-CT data to 3D printable models?

   Yes / Unsure / No

   _____

   _____

8. Are there any improvements you would suggest for future workshops?

   _____

   _____

   _____

From CT to 3D printed models

Lucy Dascombe, Professor Christine Le Maitre, and Dr Nicola Aberdein

Scope: 3D bioprinting is the construction of a 3D biological object, mixed with living cells, based on a computer-aided design model within XYZ spatial location. The aim of 3D bioprinting is to create a natural tissue-like 3D structure, typically for *in-vitro* experimentation.

Aims: Gain an understanding of the importance of various 3D model outputs, and how the different applications impact the downstream workflow.

Practice rendering 3D STL models through CAD software for 3D printing/bio-printing.

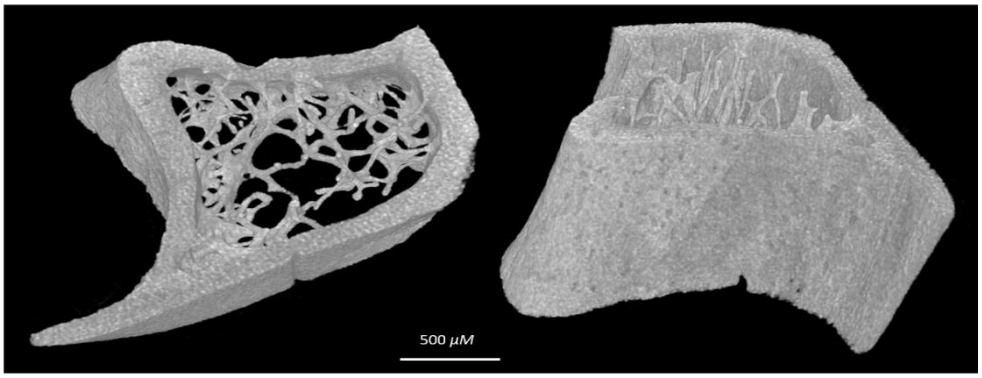

Key terms

Computational Tomography: computational tomography allows x-ray 3D imaging of in-organic materials, allowing geometry analysis in spatial location. Volumes of interest from reconstructed scans can be exported into standard tessellation language to allow computer aided design.

Computer Aided Design: Utilising software to aid in the innovation of creation, modification, analysis and optimisation of a 3D design or model.

Standard Tessellation Language: Translates complex designs by tiling the entire model surface with triangular data points into GCODE. This XYZ file format is most used for 3D printing / bioprinting.

Extrusion based bioprinting: 3D extrusion bioprinting is an additive manufacturing technique in which a 3D construct is generated by pneumatic pressure layer-by-layer based on a CAD model.

In-vitro 3D model: Complex 3D models represent tissue structures of the human body, allowing an accurate first line experimental model for biomedical experimentation.

CT Analysis – CTAn (Bruker)

Volume of interest selection: Volumes of interest selection is based on the area required for either analysis, or replication into a 3D model.

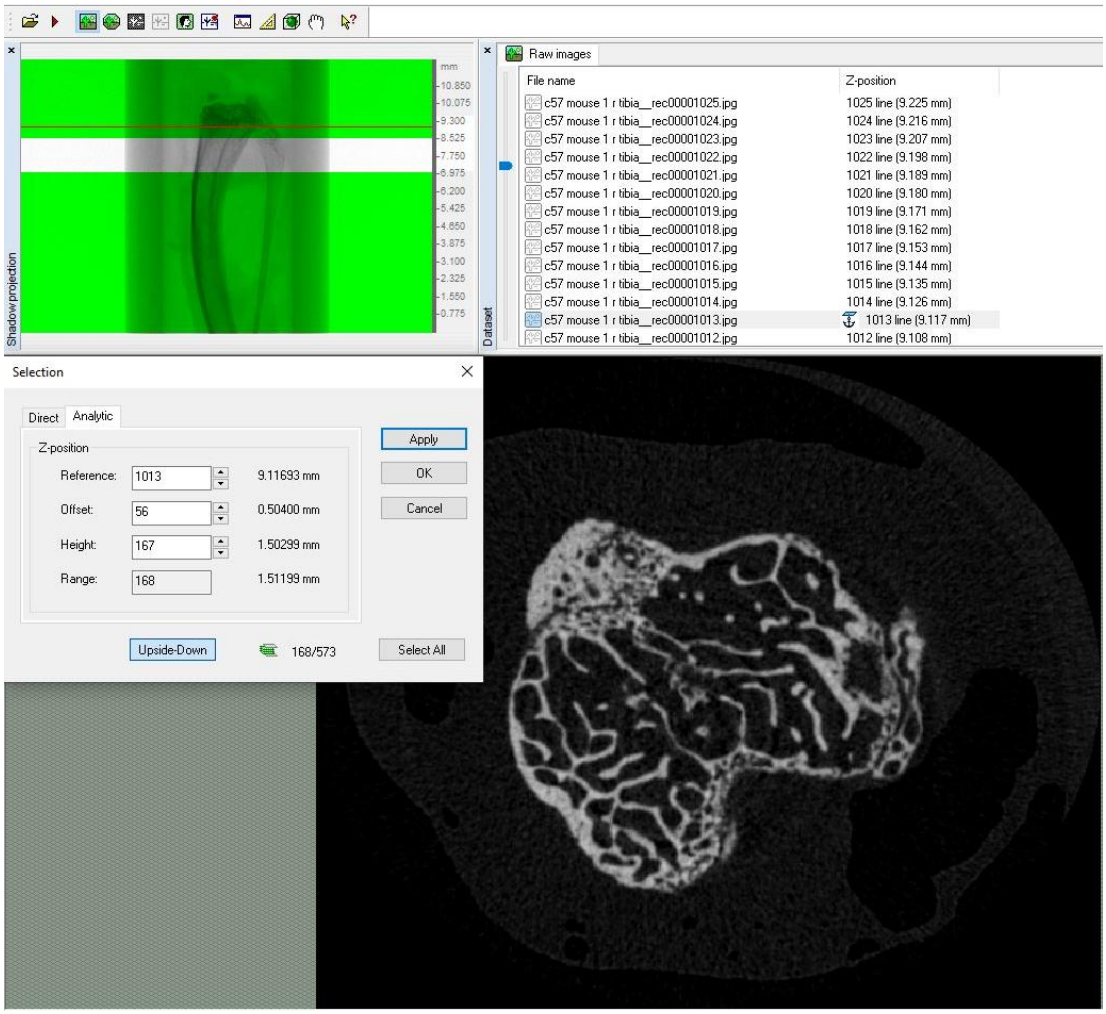

Current 2D slice is shown (bottom left of image). 2D slice library is shown (top left of image). For bones, landmark regions are selected (shown above). In the image projection (upper right of image), VOIs are shown in grey, current 2D slice is the red line, regions outside of the VOIs are shown in green.

Uploading objects into CTAn → open reconstructed file → if required, select 2D slice for landmark → right click on selected slice for analytical selection → input offset and volume of interest height → apply.

Region of interest segmentation: ROI can segment specific areas of interest, within the VOI. ROI allows reduced information, resulting in reduced processing and file sizes.

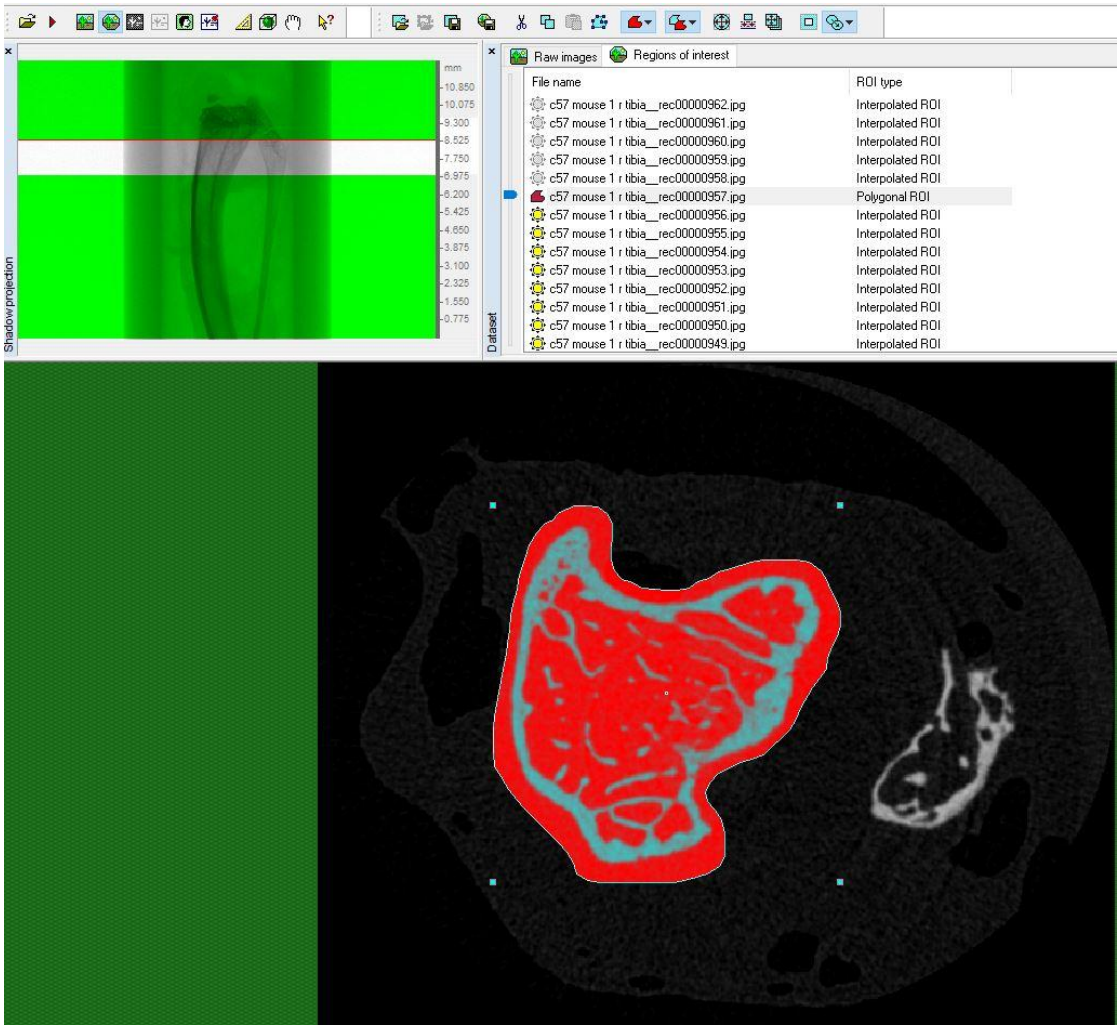

VOI selection → Region of interest tab (second cactus icon on the task bar) → draw manually a few slices throughout the VOI using a drawing pad or mouse → ROI will interpolate together; space bar allows toggle. Ensure each slice is checked to include the entire ROI → save images from ROI to generate a VOI → open VOI into CTAn

Consideration: *think about the final 3D print. What is the final height? How complex can the shape be? Increased complexity causes increased file size, and not all 3D printers/bio-printers will be able to produce complex shapes.*

Task list: Custom processing (green face on task bar) allows the information to be differentiated, highlighted, analysed and for outputs to be generated. Internal plug-ins are available in the interface. A particularly important task is the binary threshold selection (black and white cactus on task bar). By assigning an appropriate binary threshold, information is segmented.

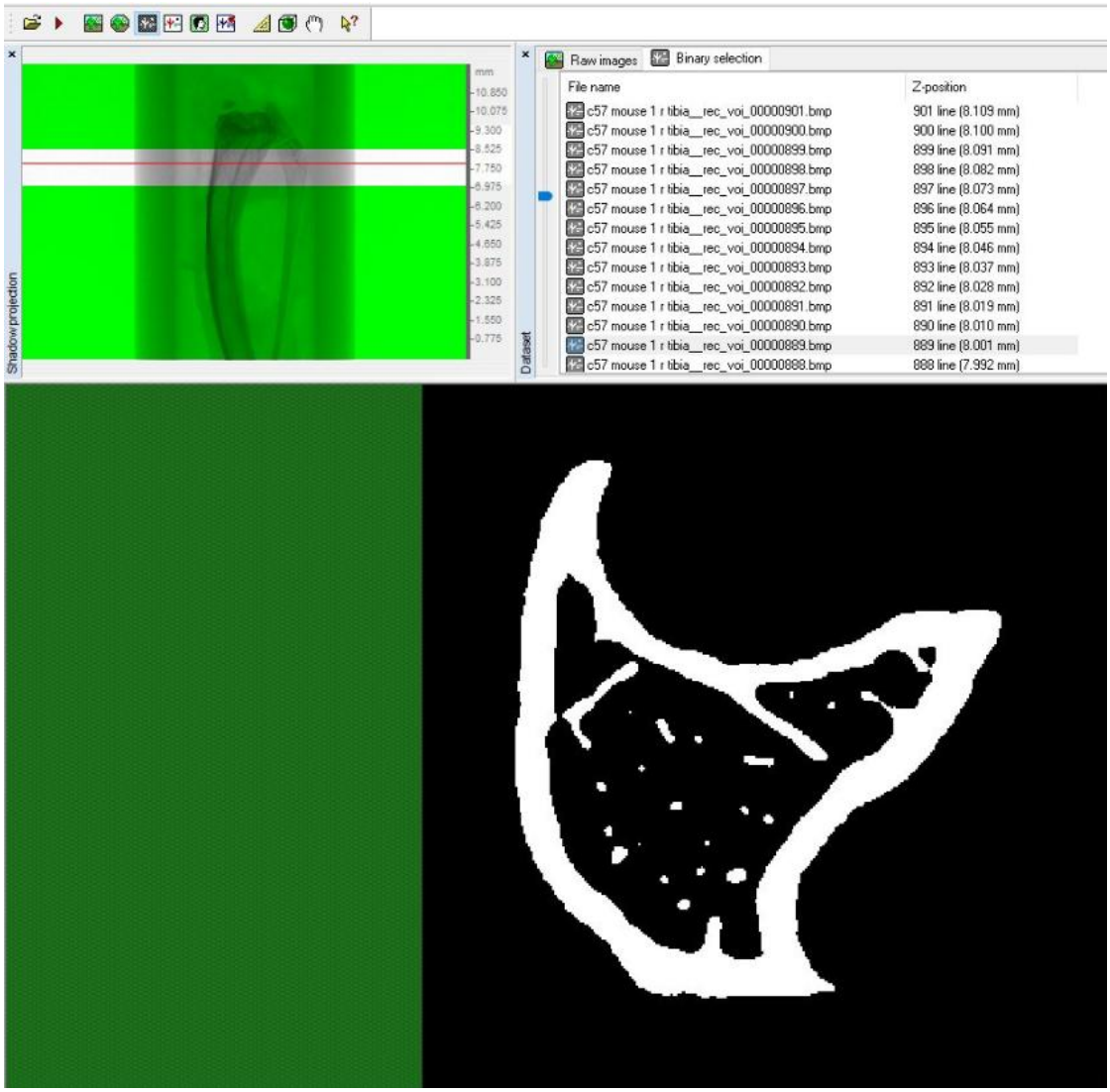

Binary selection → optimise the lower and upper threshold boundary to include information. Once selected → custom processing → internal plug-ins → thresholding → either '+' to action immediately or add to task list. If further segmentation / cleaning of the object is required, optimise with other internal plug-ins.

Recommended: Threshold 70 – 225, despeckle 'remove white speckles in 3D space with a volume less than 30 voxels in the region of interest'.

3D model selection: Within CTAn, internal plug-ins on the custom processing tab - different meshing algorithms are available: Marching cubes 33, double time cubed, adaptive rendering to produce various 3D model file types; STL, Ply, Ctm and p3g. Files can be exported as either ASCII or binary, with various units that provide exportation scale based on the scanning parameters. Choice of algorithms may impact meshing errors that require increased rendering.

Meshing algorithm	***Functionality***
Marching cubes 33	Entire VOI is split into cells. If the cell contains information, it is compiled into a 2D mesh with neighbouring information. The information is filtered into a 3D polygonal mesh to represent the triangular surface in-line with meshing rules.
Double times cubed	Comparative to marching cubes 33, with fewer cell regions and information.
Adaptive rendering	Comparative to marching cubes 33, however more control of locality and tolerance which defines accuracy between pixel boarders.

STL files follow the rules of tessellation:

1. The tessellation must tile a surface with no overlapping or gaps.
2. The tiles must be regular consistent polygons.
3. Each vertex must look identical.

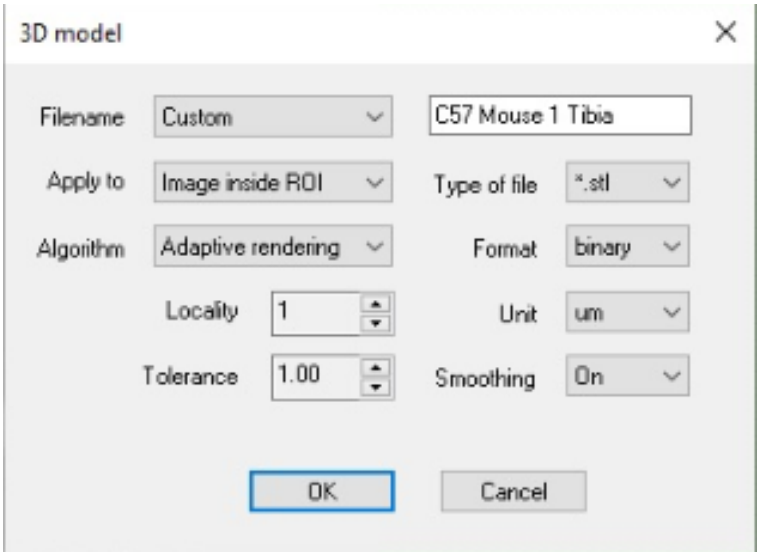

Recommended: Adaptive rendering, STL, binary, µm. Optimise to your own experimental requirements.

Considerations: Increased complexity of surface, or high-resolution scans may produce large output files which standard PCs, software, and benchtop 3D bioprinter can not process and read. Standard 3D bioprinters have limited printable resolution in comparison to imaging resolution of a CT scanner.

Computer assisted design (CAD).

Software selection: Different approaches can be applied to model rendering based on the software available, and the rendering of the model required. Autodesk® Meshmixer, TinkerCAD, Free CAD and Rhino are open-source CAD software with user friendly interfaces that allow basic model rendering whereas Autodesk® Fusion 360®, Autodesk® Inventor and SolidWorks requires a paid/education licence to assess but enables detailed analysis of models and rendering possibilities. List is not exhaustive.

Meshmixer: Simplistic CAD software that allows transformation of entire model size XYZ co-ordinates, fixing meshing errors and making the 3D model manifold (solid). The mouse allows different orientations, with the scroll wheel allowing +/- magnification.

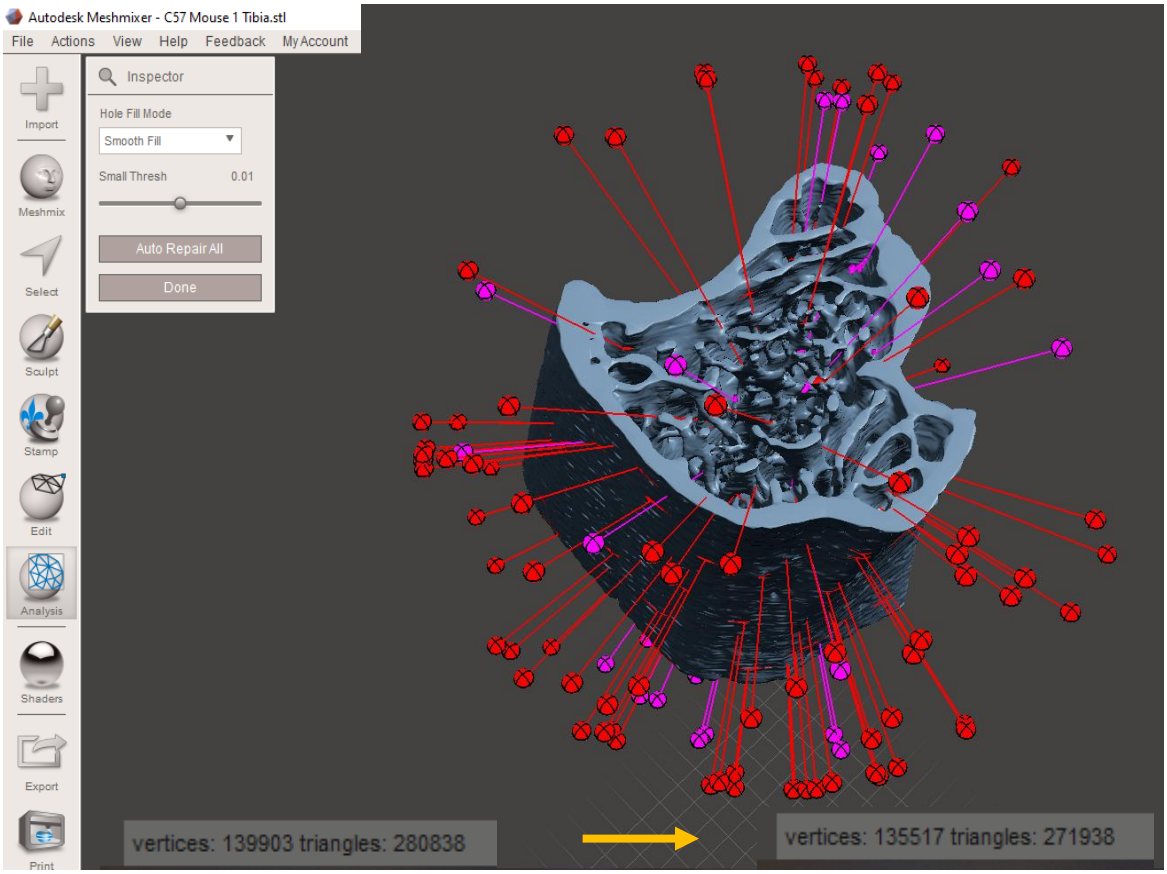

Importing the STL 3D model into Meshmixer shows object surface mesh information, and errors in the mesh (red & pink, represents thresh errors). Repairing mesh allows the structure to become manifold, with minimal errors likely to present in the printing process. Increased complexity can cause increased errors.

Repair mesh: Analysis → inspector → hole fill mode → smooth fill → auto repair all.

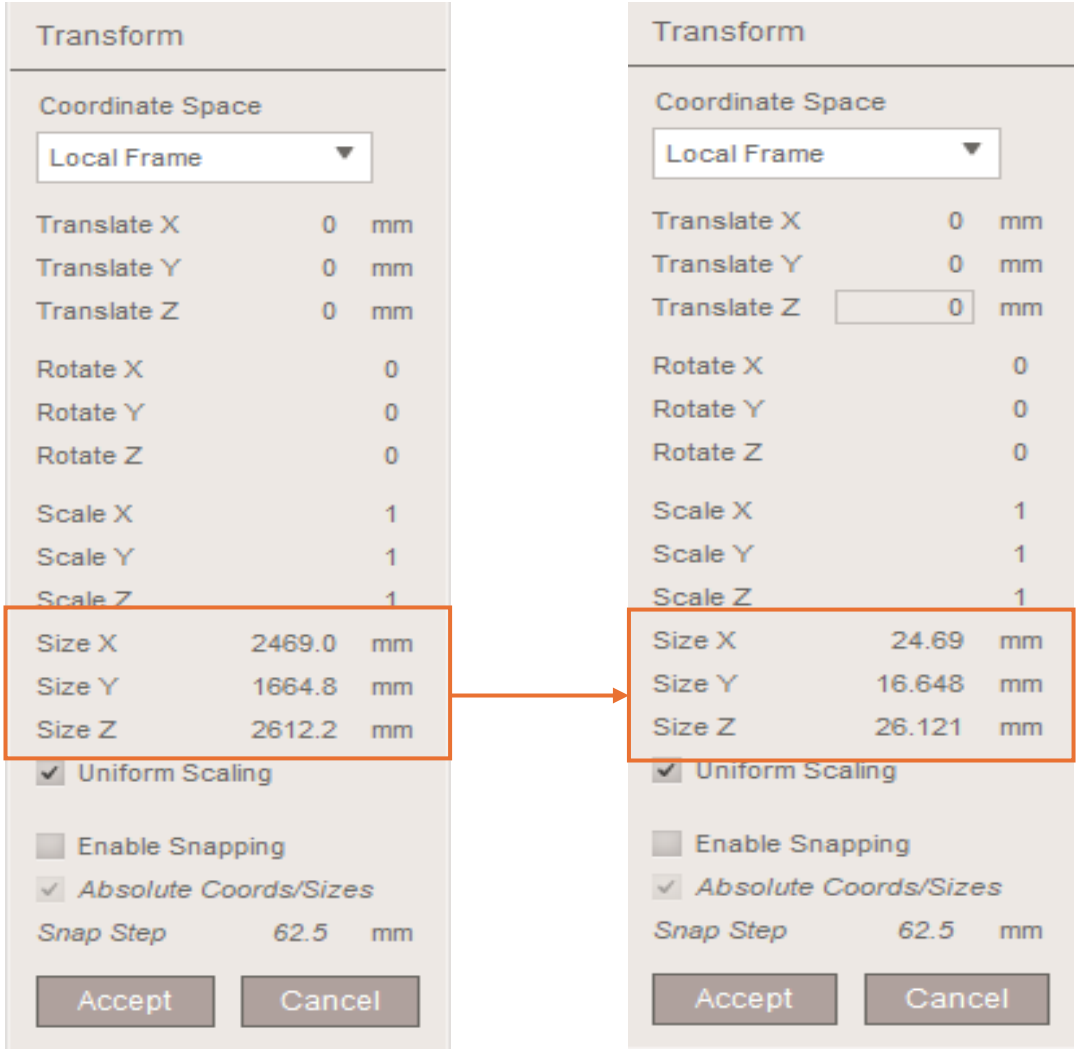

Transform size: Edit → Transform → coordinate space to local frame → original size XYZ stated, tick uniform scaling to ensure proportionate sizing.

Considerations: Transforming size by XYZ coordinates allows transformation with intact resolution of the original imaged model, to a scale appropriate for the method of 3D printing/bioprinting. For bioprinting - resolution is dependent on the biomaterial used, cells, and nozzle inner diameter. Larger builds can be achieved with 3D printing, dependant on material with less considerations.

Nozzle inner diameter = optimal filament width. E.g. 22G nozzle allows an absolute optimal filament width of 0.403 mm.

Majority of models for 3D bio-printing require making manifold (solid), with empty space causing increased, errors, tessellation, and file size. For 3D printing this is dependant on the model of creation.

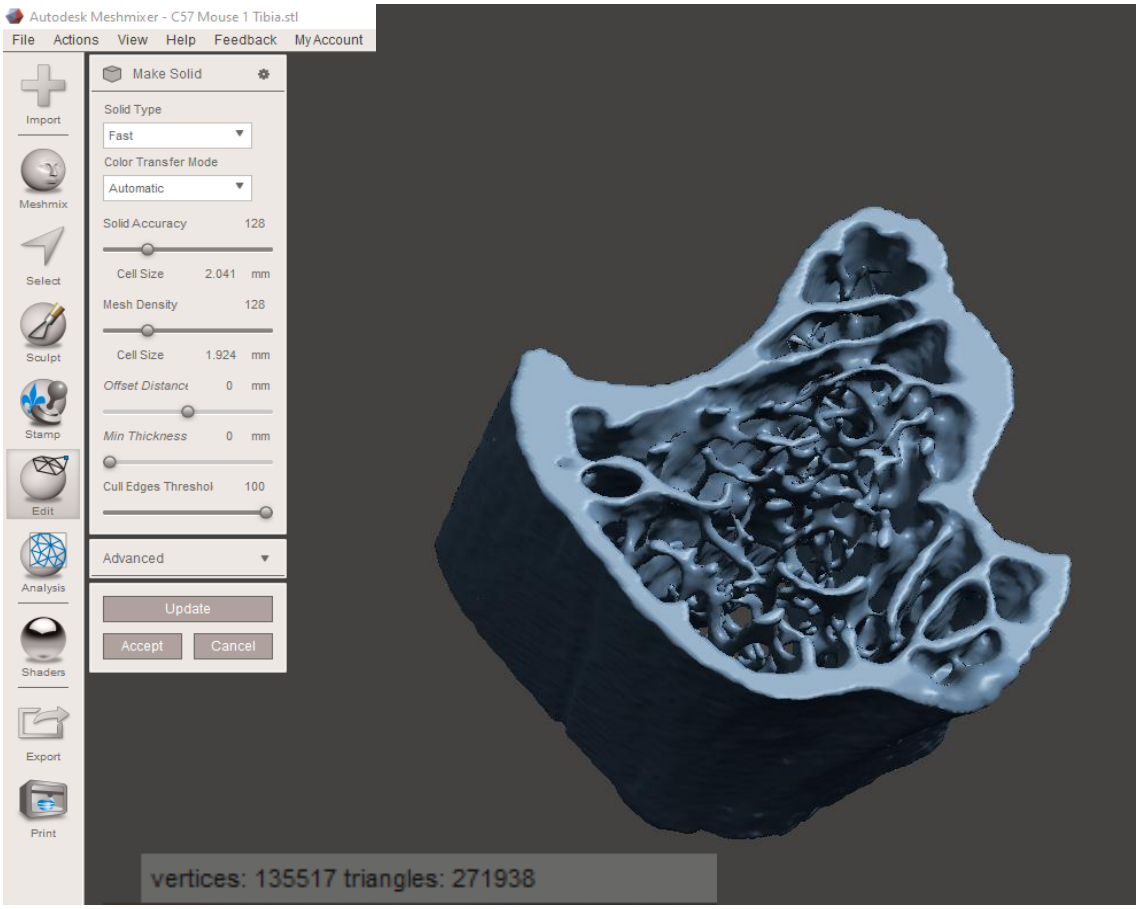

Making the model manifold (solid): *Solid type → Fast type reduces tesselation where as accurate type minimises changes to detail.*

Considerations: All options are optimisable to the desired render of the model. Retention or increase of detail may not always be required, as downstream processes (extrusion based bioprinting) may not allow translation of detail.

Unique features are available on meshmixer, such as free-hand sculpting, colouring, separating shells and making different slices of the model e.g., separation of trabecular and cortical bone. Strength, thickness, and stability assessment can also be completed. If the object is not connected, to the build plate, nodes/support beams can be generated – this is more applicable to 3D printing via overhangs in the analysis tab.

Once the model rendering is complete, to export the file as an STL: *File → export → file name, STL (choose between ASCII or binary, changes to file size).* Other file types include OBJ, dae, ply, smesh, amf, and wrl. Alternatively, if the PC with the CAD software is connected to the 3D printer, the option to send to printer is available.

Autodesk Fusion 360: Comprehensive CAD software that allows rendering of tessellation, objects, and construct surface. User friendly interface, with helpful user-guides throughout. To change the orientation of the model, use the mouse, scroll wheel for +/- magnification, and the features in the bottom middle of the interface.

To create a free account with an education-linked email

1. https://www.autodesk.com/education/edu-software/overview
2. Enter education linked (.ac.uk) email, and relevant information for the educational individual subscription.
3. Create account, note down the credentials ready for the workshop.

Alternatively, a 30-day free trial can be subscribed.

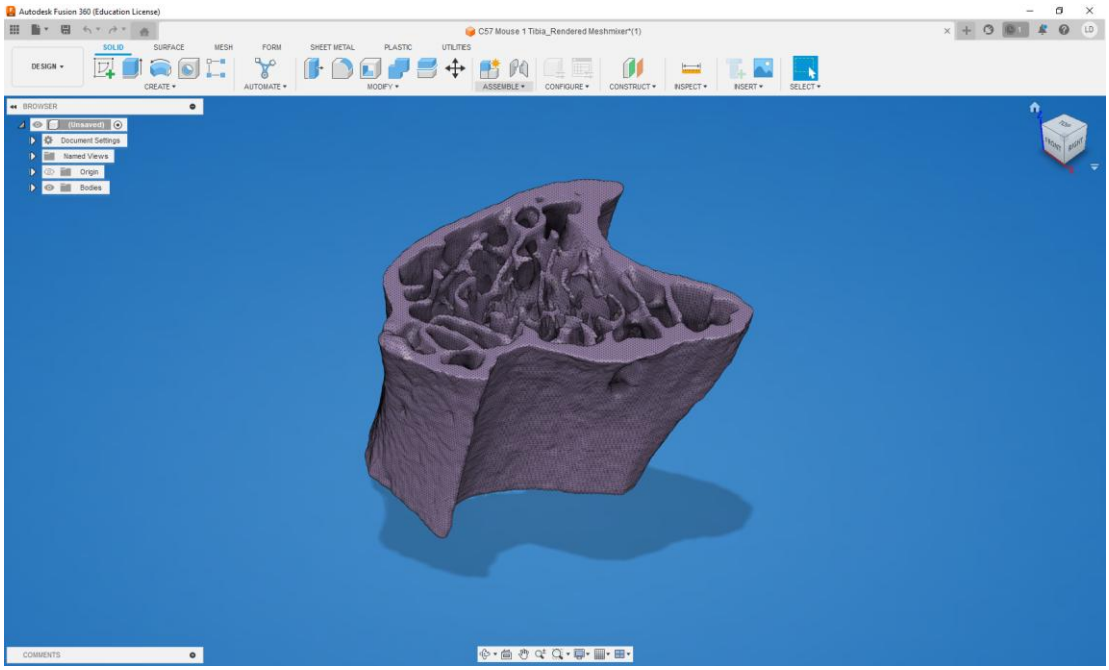

Import STL model: *file → open → open from my computer → select STL file.*

Mesh repair: *Design workspace → Mesh tab → repair → stitch and remove type recommended.*

Transformation of size: *Design workspace → solid tab → modify → scale (0.1 for a X10 reduction)*

Sometimes it is necessary to alter tessellation/mesh wireframe. Reducing mesh allows for a reduction in tessellation thereby file size and resolution, however drastic reduction can cause distortion of the original shape. Remeshing increases tessellation, which causes an increase in file size and resolution. The mesh capabilities are dependent on the 3D printer/bioprinter, and the material of the intended model.

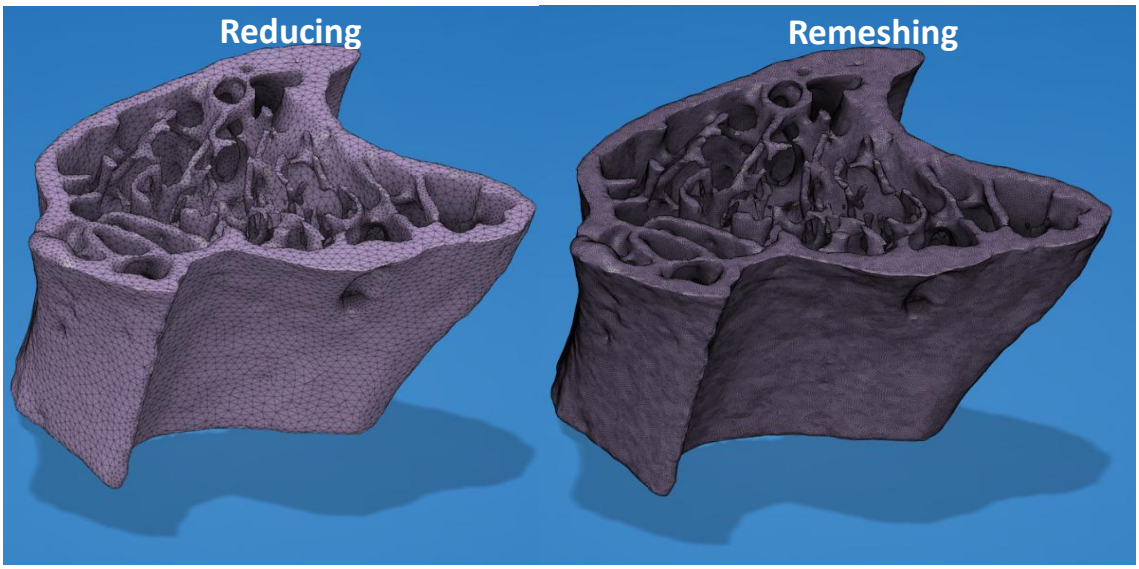

Reducing: *Design workspace → Mesh → Modify tab → Reduce → Proportion → Adaptive → shape proportion 5*

or

Remeshing: *Design workspace → Modify tab → Remesh → adaptive → Density of 1 → shape preservation 0.5.*

Considerations: The mesh capabilities are dependent on the 3D printer/bioprinter, and the material of the intended model. For bench top printers, the processor will not translate large file sizes. Increased tessellation will also increase print speed, as increased detail and complexity requires to be translated. For 3D bio-printing, biomaterial choice will heavily influence capabilities of complexity. Increasing mesh can introduce more error in tessellation. Ensure that the computer you intend to work on has high processing power (e.g., modern I7 processors), if not increased complexity in design may cause lower specification computers to fault.

3D designs with high complexity, it may be reasonable to remove 'objects' within the 3D model e.g. Tb structures that are not connected to a solid base, therefore would not translate into a solid structure. Generation of 'face groups' allows surfaces to be connected and removed. Only complete fast type, unless work is being completed on a high specification computer.

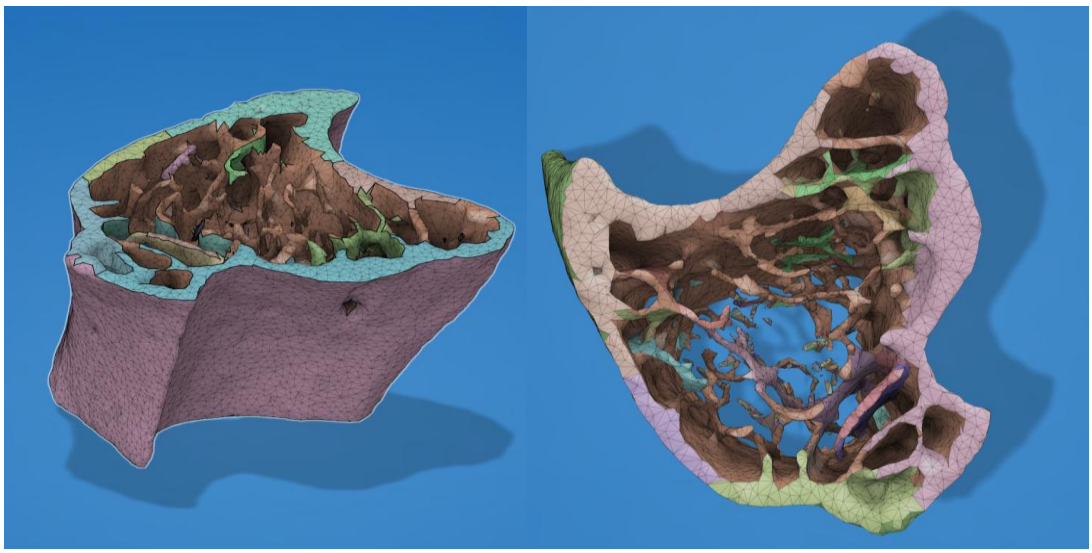

Face-groups: *Design workspace → Prepare tab → Mesh → Generate face groups → fast type → minimum face group needs to be optimised.*

Once face groups have been generated, inspect the model for any over-hangs, structures not connected to the main body of the model etc. To remove, select the tessellated structure, press CTRL, and delete. Use orbit and grab to change perspectives on the model, as well as zooming -/+.

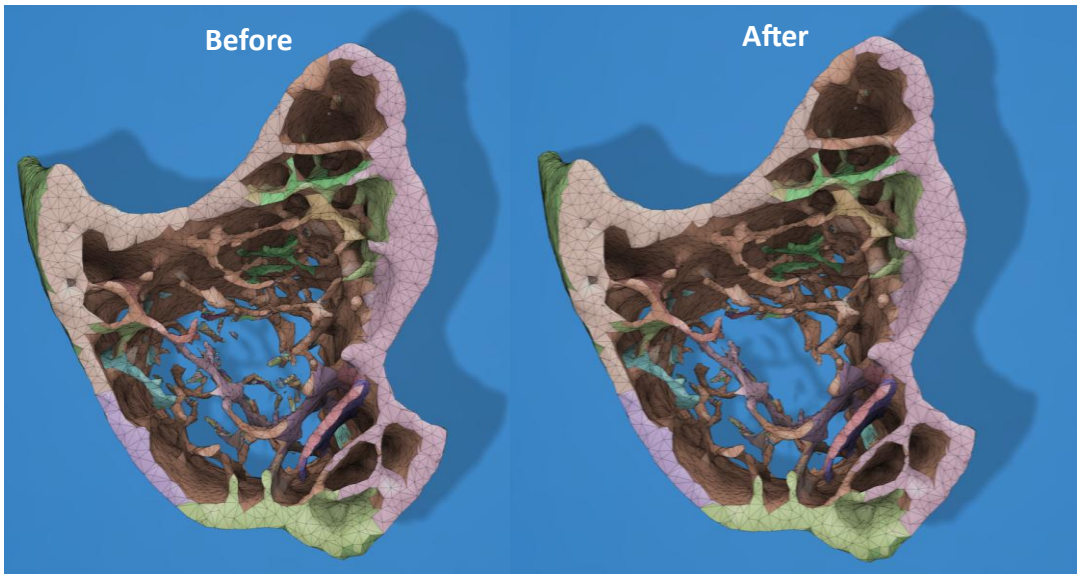

Removal of face groups*: Select un-supported group → CTRL + del.*

Considerations: As well as generation of separate face-groups, joining of face-groups allows a combined model. Although removing un-supported structures is beneficial for 3D bio-printing where biomaterials are not typically self-supporting, this alters the original structure.

Validating different measurements is important to validating the success of a print. Minimum width achievable for bio-printing is the nozzle inner diameter, with 3D printing dependant on the material usage.

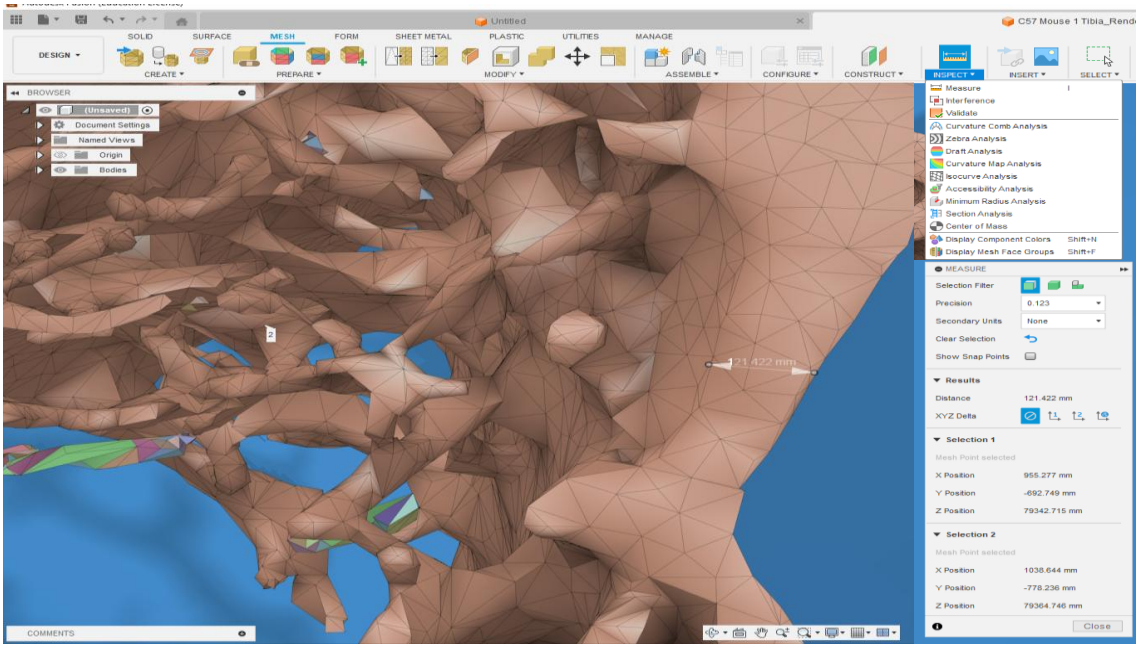

Measuring model: *Design → Mesh → Inspect → Measure → place two positions.*

Optional step: Supports can be generated to facilitate the 3D printing of a complex structure, this requires optimisation.

Generation of supports*: Manufacture workspace → set up → new set up → additive type (prepares model for 3D printing) → select printer and material (fusion contains a large library of existing 3D printers) → position the 3D model on the build plate → supports panel (Select support density, spacing and pattern) → preview → ok to generate tool path → post process to export GCODE model*

The features on fusion 360 are extensive. In this workshop, some design features have been explored. Unique features include generative design, render, animation, simulation, manufacture and drawing. All features include information, tutorials, and summaries. Alongside this, within the simulation workspace different computational tests can be completed on the 3D model generated – this is more applicable to 3D printing where the material is known and characterised by the software. This can assess

stress on the model (static, dynamic, nonlinear, and structural), variations of temperatures, and inclusion of fluid flow channels.

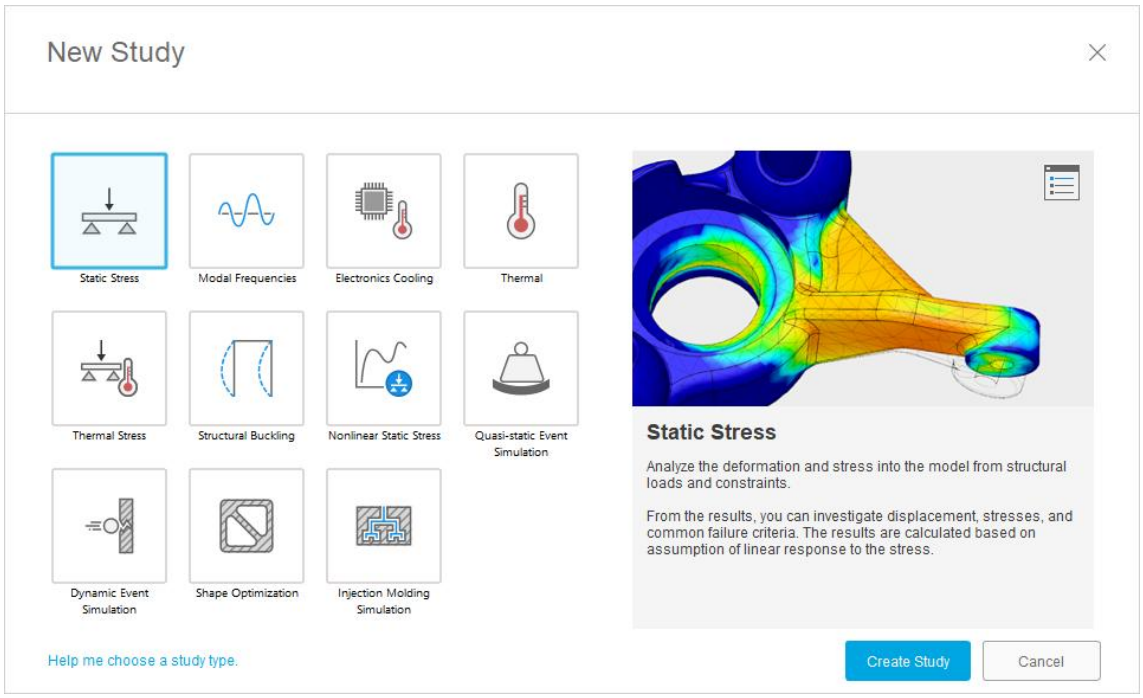

Once the final model has been rendered as appropriate, fusion 360 offers 14 different file types to export. Although STL is mostly accepted by 3D printers/bio-printers, some printers may have a specific file type compatibility.

Export the 3D model: *File → Export → select file type (STL) and destination.*

IgG controls for immunopositivity staining on MC3T3-E1 chamber slides represented no non-specific binding, supporting the immunopositivity detected in Figures 6.3.2 – 6.3.5.

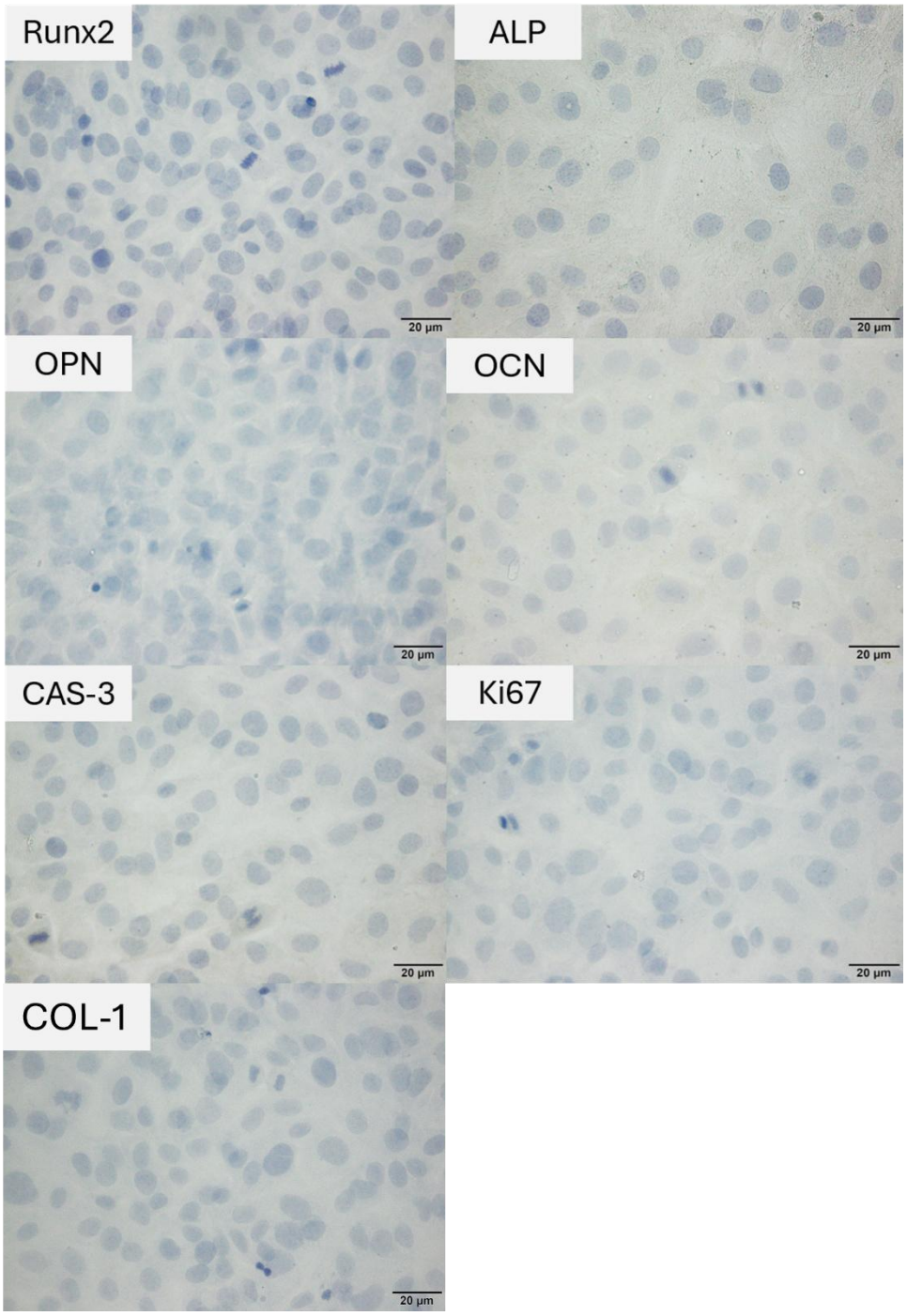

Figure S7. MC3T3-E1 monolayer immunocytochemistry IgG controls for characterisation over 21 days + ascorbic acid. *Each independent IgG control was tested at the same concentration of the antigen-specific antibody. Day 7 Chamber slides with 1x10^4 MC3T3-E1; Immunopositivity is represented by brown staining. Runt-related transcription factor-2, alkaline phosphatase, osteopontin, osteocalcin, caspase-3, ki-67 and type-1 collagen are shown. n = 3, representative image shown, scale bar represents 20 µm.*

IgG controls for immunopositivity staining on MC3T3-E1 bioprinted *in-vitro* 3D constructs represented no non-specific detectable binding for Runx2, ALP, OPN, CAS-3, Ki67 and COL-1. OCN featured non-specific binding of both antigen-specific and IgG control due to the high concentration of antibodies required as previously optimised for bones. Due to this, OCN for *in-vitro* 3D constructs were not included in the study. Supportive information for Figures 6.3.19 – 6.3.24.

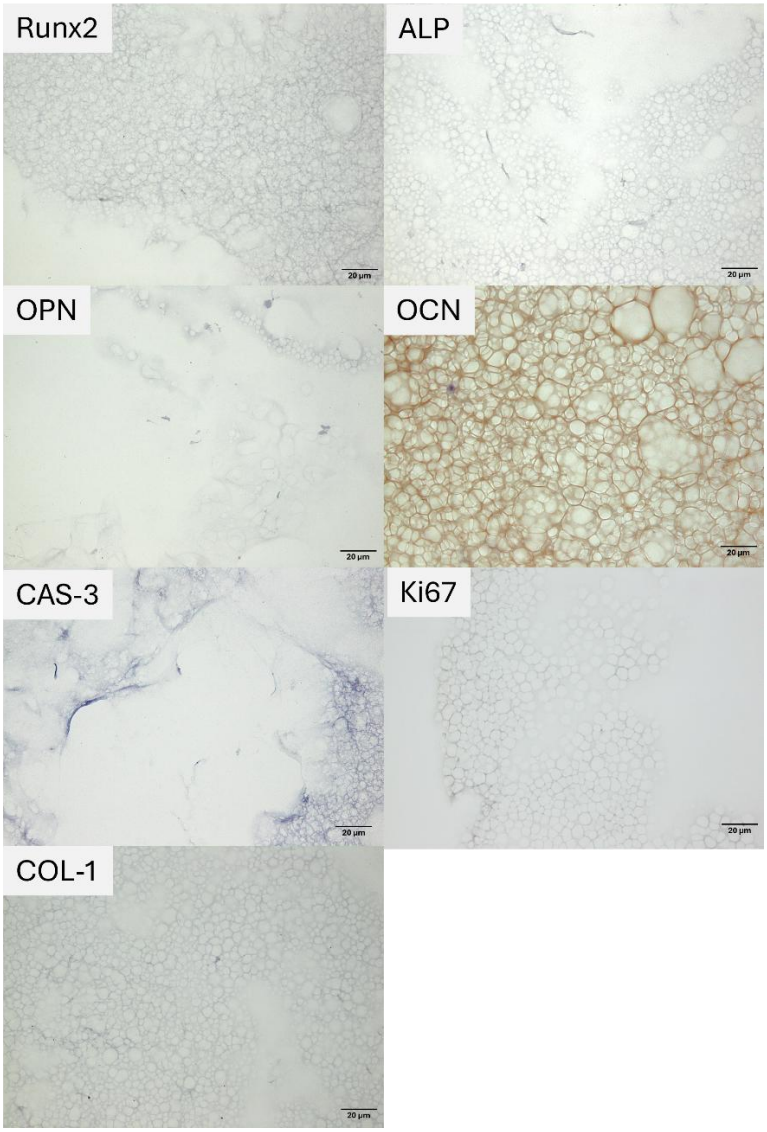

Figure S8. Randomly selected cellular conditions immunohistochemistry IgG controls for characterisation of in-vitro 3D bioprinted constructs. *Each independent IgG control was tested at the same concentration of the antigen-specific antibody. Non-specific binding and immunopositivity are represented by brown staining. Runt-related transcription factor-2, alkaline phosphatase, osteopontin, osteocalcin, caspase-3, ki-67 and type-1 collagen are shown. n = 3, representative image shown, scale bar represents 20 µm.*